STOCHASTIC MODELING OF MACRODISPERSION IN UNSATURATED HETEROGENEOUS POROUS MEDIA

A Final Project Report

Submitted to

U.S. Department of Energy

For

Grant No. DE-FG02-91ER61199

by

T.-C. Jim Yeh
Principal Investigator

Department of Hydrology and Water Resources
The University of Arizona
Tucson, Arizona 85721

DISCLAIMER

This report was prepared as an account of work sponsored by an agency of the United States Government. Neither the United States Government nor any agency thereof, nor any of their employees, makes any warranty, express or implied, or assumes any legal liability or responsibility for the accuracy, completeness, or usefulness of any information, apparatus, product, or process disclosed, or represents that its use would not infringe privately owned rights. Reference herein to any specific commercial product, process, or service by trade name, trademark, manufacturer, or otherwise does not necessarily constitute or imply its endorsement, recommendation, or favoring by the United States Government or any agency thereof. The views and opinions of authors expressed herein do not necessarily state or reflect those of the United States Government or any agency thereof.

MASTER

UNLIMITED

DISCLAIMER

Portions of this document may be illegible in electronic image products. Images are produced from the best available original document.

TABLE OF CONTENTS

TABLE OF CONTENTS - *CONTINUED*

TABLE OF CONTENTS - *CONTINUED*

TABLE OF CONTENTS - *CONTINUED*

LIST OF FIGURES

LIST OF FIGURES - *CONTINUED*

LIST OF FIGURES - *CONTINUED*

LIST OF FIGURES - *CONTINUED*

LIST OF FIGURES - *CONTINUED*

LIST OF TABLES

ABSTRACT

Spatial heterogeneity of geologic media leads to uncertainty in predicting both flow and transport in the vadose zone. In this work an efficient and flexible, combined analytical-numerical Monte Carlo approach is developed for the analysis of steady-state flow and transient transport processes in highly heterogeneous, variably saturated porous media. The approach is also used for the investigation of the validity of linear, first order analytical stochastic models. With the Monte Carlo analysis accurate estimates of the ensemble conductivity, head, velocity, and concentration mean and covariance are obtained; the statistical moments describing displacement of solute plumes, solute breakthrough at a compliance surface, and time of first exceedance of a given solute flux level are analyzed; and the cumulative probability density functions for solute flux across a compliance surface are investigated. The results of the Monte Carlo analysis show that for very heterogeneous flow fields, and particularly in anisotropic soils, the linearized, analytical predictions of soil water tension and soil moisture flux become erroneous. Analytical, linearized Lagrangian transport models also overestimate both the longitudinal and the transverse spreading of the mean solute plume in very heterogeneous soils and in dry soils.

A combined analytical-numerical conditional simulation algorithm is developed to estimate the impact of in-situ soil hydraulic measurements on reducing the uncertainty of concentration and solute flux predictions. In soils with large spatial variability and in dry soils, soil water tension measurements significantly reduce the uncertainty in the predicted solute concentration. Saturated hydraulic conductivity data are valuable in relatively wet soils. A combination of tension and saturated hydraulic conductivity data gives the best results, especially if some data are available on the unsaturated hydraulic conductivity function. It is also found that if soil heterogeneity is large, the conditional spatial moments of inertia of the mean concentration plume and the conditional mean breakthrough curves are poor means of depicting

the actual solute plume distribution and the actual solute flux. Nevertheless, conditional simulation is one of the most rational approaches for modeling unsaturated flow and transport, if in-situ data are available.

1. INTRODUCTION

In recent years consideration of the unsaturated zone has received increasing attention among scientists, regulators, and engineers involved with subsurface contaminant transport. Regarding groundwater pollution, the unsaturated zone acts as buffer but also as conveyor belt between the land surface, where most contaminants originate, and groundwater, which is a resource protected under a number of environmental regulations. Pesticides and fertilizers leach to the water table from agricultural areas; underground storage tanks leak petroleum products; landfills, septic tanks, waste water lagoons, and other man-made features are potential hazards to drinking water if the underlying aquifer is used as a potable water resource. For the cleanup of soil contamination and for the evaluation and control of waste storage and disposal sites, flow and transport processes in the area between the actual or potential contaminant source and the groundwater table must be well understood. Unsaturated flow processes above the water table play an important role in determining the pathways of a contamination plume before it reaches the aquifer, particularly in semiarid and arid regions where the unsaturated zone may be several tens of meters thick.

Modeling unsaturated flow and transport with mathematical or numerical methods is an important tool for predicting the infiltration and redistribution of soil water and the transport of solutes in the unsaturated zone. Flow and transport models are commonly used to support the decision making process in agricultural management, environmental impact assessment, toxic waste control, remediation design, and subsurface cleanup monitoring.

The modeling process, however, requires knowledge of the fundamental properties of porous media. Field research has shown that these porous media properties change continuously from location to location ("spatial heterogeneity"). Spatial heterogeneity may significantly influence flow and transport processes in the vadose zone. Modeling efforts must inherently cope with "uncertain" information i.e., information that has been extrapolated from

measurement locations to the surrounding areas because it is impossible to measure all soil properties at all locations. Since the model input is uncertain, the model results are uncertain and the validity of the modeling may be questioned.

In the past two decades, research efforts have been directed towards developing general quantitative concepts to describe the spatial heterogeneity of subsurface porous media. With mathematical tools the impact of model input uncertainty (due to heterogeneity) on the uncertainty of flow and transport predictions is quantified. Many of these research efforts have applied the so-called "geostatistical" description of porous media properties and used it for the "stochastic analysis" of model uncertainty. Geostatistics is a tool to quantify spatial variability of natural phenomena in terms of statistical parameters. Given the spatial variability of some environmental properties (model input) stochastic analysis, a particular form of mathematical analysis, finds the statistical parameters describing the spatial variability of and the prediction uncertainty about other environmental phenomena (model output). Most applications of the stochastic analysis of subsurface flow and transport processes have been with respect to groundwater.

Moisture movement in unsaturated or variably saturated soils is a physically more complex process than water flow in saturated porous media. The stochastic analysis of such processes in heterogeneous soils has therefore been limited to a relatively few, simplified analytical models. These models are known to be valid only if the spatial heterogeneity of the soil is moderate. None of the analytical stochastic models describing variably saturated flow and transport in heterogeneous porous media have been rigorously verified.

This work is an attempt to partially remedy the lack of stochastic tools that predict not only the most likely path and rate of water and solute movement in soils but also the spatial variability (i.e. uncertainty) of water movement and solute transport in the unsaturated zone. Combined analytical-numerical stochastic methods are developed, with which the characteristics and the prediction uncertainty of steady-state flow and transient transport in highly

heterogeneous soils can be assessed. The stochastic methods developed in this work are also able to predict the uncertainty about water movement and contaminant transport as a function of the number, location, and type of measurements taken at a particular field site of interest.

The scope of this work is two-fold: In part II, the stochastic framework is defined, within which the rest of this study operates. Analytical, quasi-analytical, and numerical tools are developed for the highly flexible analysis of many unsaturated flow and transport problems in moderately and strongly heterogeneous soils. In part III, these mostly numerical (computer modeling) tools are applied to verify existing analytical models of unsaturated flow and transport, to implement a numerical stochastic analysis of the spatial heterogeneity of soil hydraulic conductivity, soil water tension, soil water flux, and solute (or contaminant) transport as a function of the soil heterogeneity, and to demonstrate how the design of measurement and monitoring networks in the unsaturated zone may or may not reduce the uncertainty about these flow and transport variables.

The dissertation is organized into ten chapters. This introduction is both chapter one and part I. Part II consists of six chapters: In chapter 2, the concepts of probability and random variables are introduced. An attempt is made to link the physical phenomena "spatial heterogeneity" and "uncertainty" with the conceptual rigor of probability theory and stochastic analysis. The chapter is intended to give a detailed answer to the question of why we use stochastic analysis to understand model uncertainty. Chapter 3 then introduces, compares, and validates several numerical methods to artificially generate random, spatially heterogeneous soils that can be used to study the effects of soil heterogeneity on flow and transport variability. These methods are of very general nature and have found applications in a wide range of physics, engineering and earth-sciences applications and are commonly known as "random field generators". In chapter 4 a purely analytical stochastic theory of flow in unsaturated soils is developed based on similar work by other authors. The analytical unsaturated stochastic flow theory serves three important purposes: it is an inexpensive, approximate method to assess the

spatial variability of soil water tension and soil water flux; it is necessary for the application of existing transport theories to heterogeneous, unsaturated soils; and - as will be shown in chapter 7 - it is an invaluable catalyst needed to reduce the computation time associated with the numerical (computer) solution of the unsaturated, steady-state flow problem to just a fraction of the time hitherto necessary. In chapter 5 a computer simulation program is introduced that solves the physical equations governing variably saturated, flow and transport for any given random realization of a heterogeneous soil. Chapter 6 investigates several aspects of the numerical grid design for the finite element flow model introduced in chapter 5. Finally in chapter 7 an efficient combined analytical-numerical computer solution algorithm is described for the unsaturated stochastic flow problem based on the methods introduced in chapters 3 through 6.

Part III consists of three chapters, all of which are based on the conceptually simple but computationally expensive Monte Carlo method: a large number of "random" soils that are statistically identical to the field site of interest are generated. The flow and transport problems are solved for each soil, the individual results are compiled, and eventually analyzed statistically to give an overall assessment of the spatial variability of flow and transport in heterogeneous soils. The key to a successful Monte Carlo simulation is a high number of realizations (repetitions) such that the Monte Carlo results are truly representative of the stochastic nature of spatial heterogeneity and uncertainty. Monte Carlo analysis is therefore only possible with the efficient computational algorithms introduced in part II.

Chapter 8 is dedicated to the analysis of spatial variability and uncertainty of the unsaturated hydraulic conductivity, the soil water tension, and the soil moisture flux in a steady-state unsaturated flow regime. It compares the highly accurate numerical solutions with the analytical solutions of chapter 4 to discern the strengths and weaknesses of the analytical stochastic approach. In chapter 9 the nature of solute transport in heterogeneous soils is described and both the spatial variability of solute concentration as a function of time and the

temporal variability of solute flux as a function of space in heterogeneous soils is investigated. The analysis is specifically applied to a point or small pollution source (as opposed to a spatially extensive non-point pollution source). This chapter also compares the highly accurate numerical results with approximate analytical stochastic transport theories to highlight their advantages and disadvantages. Finally, in chapter 10, I investigate how prediction uncertainty can be reduced by measuring various soil properties in situ and by using a conditional stochastic method that honors the degree of deterministic knowledge available about a soil site. The results are contrasted with the unconditional stochastic analyses of chapters 8 and 9.

2. HETEROGENEITY, PROBABILITY, AND RANDOM FIELDS

2.1 Introduction: Heterogeneity and Stochastic Analysis

Spatial heterogeneity refers to the variation of a physical property in two- or three-dimensional space. This physical variation is encountered in many earth science applications; it is of particular interest when studying flow and transport processes in the unsaturated zone. When examining soil media, spatial heterogeneity is observed on many different scales such as the microscale of a single pore, the intermediate scale of laboratory experiments, the scale of field experiments, and the megascale, which encompasses entire regions. This work is not concerned with the spatial heterogeneity on the microscale or pore scale because the governing physical laws for porous media flow (chapter 4) are only valid on a scale larger than the microscale. Bear (1972) defined "Representative Elementary Volume" as the smallest volume over which there is a constant "effective" proportionality factor between the flux and the total pressure gradient or total head gradient. This proportionality factor is called the hydraulic conductivity of the REV. By definition of the REV, the hydraulic conductivity does not rapidly change as the volume to which it applies is increased to sizes larger than the REV. This is based on the conceptual notion that either no heterogeneity is encountered at a scale larger than the REV or that heterogeneity occurs on distinctly scales, the smallest of which is the REV (Marsily, 1986). The latter model assumes that within each scale relatively homogeneous regions exist. Within these homogeneous units heterogeneities can only be defined on a significantly smaller scale. Geologists refer to these different scales as facies (Anderson, 1991) while hydrologists commonly speak in terms of hydrologic units (Neuman, 1991). Analysis of a large number of hydrologic and geologic data from different sites associated with different scales has shown that the existence of discrete hierarchical scales for any particular geologic or hydrologic system vanishes in the global view as the multitude of different geologic or

hydrologic units allows for a continuous spectrum of scales (Neuman, 1990). This study is limited to the scale of a typical research field site; this is representative for many field contamination studies i.e., roughly the meter and decameter scale (10^0-10^2 m).

For the scale of the REV, mathematical models based on the physics of flow and transport in homogeneous porous media have been well-established in the literature and their accuracy has been verified in many laboratory experiments (c.f. Hillel, 1980). The physical meaning of the underlying model parameters is already well-understood (c.f. Jury, 1991). It is the fundamental mathematical treatment of flow and transport in **heterogeneous** porous media, which is of concern in this study.

Spatially heterogeneous properties can belong in either one of the following two classes depending on the problem formulation:

(a) porous medium properties that are **measurable** and that are seen as the **cause** of flow and transport behavior in soils such as pore geometry, the saturated permeability of the soil, the soil textural properties, and the soil water distribution;

(b) porous medium properties that are **predictable** based on physical laws or **functions** of class (a) properties e.g., the distribution of soil moisture flow and the solute concentration at some future time.

In very general terms, this dissertation is about the spatial heterogeneity of class (b) properties given some knowledge about the heterogeneity of class (a) properties. More specifically, the spatial heterogeneity of (and hence the uncertainty about) soil water tension, soil moisture flux, and solute transport in soils is computed based on some information about the spatial heterogeneity of the hydraulic properties of unsaturated porous media. Mathematically, spatial heterogeneity can be dealt with in one of three ways:

1. The local (REV-scale) porous media properties (soil property class (a)) are described at every point throughout the field area of interest. Then the classic flow and transport equation are used in a numerical model to obtain the output variables (soil property

class (b)). This approach requires an enormous amount of measurement data and is for all practical purposes impossible to implement.

2. Spatial heterogeneity is neglected and instead some form of "effective" parameter is determined to define the flow and transport problem on the scale of interest. Classical flow and transport solutions (analytical or numerical) are applied to solve the problem for a quasi-homogeneous domain with "effective" parameters. This is probably the most widely used approach in both soil and groundwater hydrology due to its relative simplicity and low computational cost. The disadvantage of the method lies in the uncertainty of the prediction, since the "real" field parameters may differ significantly from those assumed in the model.

3. An entirely new mathematical approach is developed that considers the limitations of our knowledge about the field site and that quantifies the uncertainty in the prediction of soil property class (b) given that only a small and economically reasonable amount of measurements are available from the field site (class (a) data or class (b) data). To that end, **spatial stochastic analysis** has been developed over the past three decades for a wide variety of similar problems not only in the treatment of unsaturated zone flow and solute transport but in the treatment of many earth science problems.

The stochastic approach is adopted in this study since the primary interest lies not only in making a best prediction but also in quantifying the uncertainty of the prediction. In this chapter probability theory is introduced together with some of its most important lemmas to show, how - in principle - spatial heterogeneity is conceptualized in form of a mathematical model. Based on probability theory, stochastic analysis (which is a particular form of mathematical analysis) allows the derivation of the probabilistic parameters describing the spatial heterogeneity of class (b) properties given the probabilistic parameters describing the heterogeneity of class (a) properties. A particular challenge arises, when deterministic measurement data of either class (a) or class (b) properties are given in addition to the

parameters describing the degree of heterogeneity. The additional deterministic information must be reflected in the derivation of the probabilistic parameters describing the spatial heterogeneity of class (b) properties. Conditional probability theory and conditional stochastic analysis will be introduced for this type of application.

Stochastic analysis is closely associated with the theory of random processes, which is a branch of mathematics called probability theory. Probability theory itself is a branch of mathematics called measure theory. "*Probability theory and measure theory both concentrate on functions that assign real numbers to certain sets in an abstract space according to certain rules.*" (Gray and Davisson, 1986 p.27). The treatment of spatial heterogeneity in terms of random processes is a highly abstract procedure, the appropriateness of which has been questioned. However, this treatment is justified by Athanasios Papoulis (1984, p. xi):

> *"Scientific theories deal with concepts, not with reality. All theoretical results are derived from certain axioms by deductive logic. In physical sciences the theories are so formulated as to correspond in some useful sense to the real world, whatever that may mean. However, this correspondence is approximate, and the physical justification of all theoretical conclusions must be based on some form of inductive reasoning."*

For a complete derivation of the concepts of random variables, random processes, and stochastic differential equations there is a vast amount of literature that has been published in this area for many different applications (see e.g. Gray and Davisson, 1986; Papoulis, 1984; Priestley, 1981). The intent of this chapter is to give the reader a full appreciation of the theoretical basis of random processes. This should allow a better understanding of the scope of stochastic modeling.

2.2 Principles of Probability Theory

Probability theory is a construct that allows rigorous quantification of rather imprecise

statements such as "tomorrow there may be rain", or "the contaminant plume may already have reached the groundwater table". Such statements are mostly based on past experiences in similar circumstances. The statements are about the chances of one particular result or outcome out of a total of two possible outcomes (a "sample space" of two outcomes), for example, groundwater is either contaminated or not.

There could be more than two possible results e.g., *a*: "groundwater is contaminated to the extent that it affects a well-field", or *b*: "it is contaminated without affecting any wells", or *c*: "it is not contaminated at all". In this example there are three possible outcomes, which form a set called the "sample space" $\Omega=\{a,b,c\}$ of all possible outcomes. The two outcomes with contaminated groundwater can be grouped together in a set or "event" $F=\{a,b\}$, which is equal to the event "groundwater is contaminated" in the very first example. The complementary set to the event $F=\{a,b\}$ is the event $F^c=\{c\}$: "groundwater is not contaminated". The latter event is a singleton set or a set with only one element (outcome). Another possible event is "no well is contaminated" i.e., the set $F=\{b,c\}$. This event also possesses a complementary set within the sample space Ω: $F^c=\{a\}$ or "groundwater is contaminated to the extent that it affects some wells". Yet another possible event is $F=\{a,c\}$ "some wells are contaminated or the groundwater is not contaminated at all", which has the complementary event $F^c=\{b\}$ "groundwater is contaminated without affecting any wells". Finally there is the trivial event $F=\{a,b,c\}$ "the contamination has either not reached the groundwater, has reached the groundwater but no wells, or has already reached the wells", which is equal to the sample space Ω. This event possesses the complementary event $F^c=\{\phi\}$, the so-called empty set with no elements at all. All possible events for the sample space $\Omega=\{a,b,c\}$ are now defined. Each of these events is a set. A set of all eight possible events (or sets) in the sample space Ω, can also be defined. In set theory "sets of sets" are called "classes" of sets, and the class of *all* eight possible sets mentioned above is called the "power set" of Ω. Since each set is also an event, the power set is called a "class **F** of events" or simply an "event space". To be precise, each set is called

an event only, if a probability measure P is assigned to the set. Only then the above probabilistic "experiment" is completely defined. As in this example, the theory of probability rests upon the principles of set theory.

In this simple example all basic elements necessary to define a probability problem, or - in mathematical terms - a "probability space" are encountered. Formally, a probability space consists of three basic, well-defined objects: The sample space Ω, which is a set of all possible elementary outcomes; the event space **F**, which is the group of all possible events F such that each event F_i is some combination of the elementary outcomes and such that the event space **F** is closed under certain set-operations e.g., if $F_i \in \mathbf{F}$ then $F_i^c \in \mathbf{F}$. Finally, the space $(\Omega,\mathbf{F})$ must be "measurable" such that there exists a probability measure P, which assigns a probability to each event F_i in the event space. The three fundamental axioms of the probability measure P are:

$$\begin{aligned} P(F) &\geq 0 \qquad \text{for all } F \in \mathbf{F} \\ P(\Omega) &= 1 \\ P\left(\bigcup_{i=1}^{\infty} F_i\right) &= \sum_{i=1}^{\infty} P(F_i) \qquad \text{if all } F_i \text{ are mutually exclusive} \end{aligned} \tag{2-1}$$

where the last equation is for both a finite event space (finite countable number of events) and an infinite event space (infinite number of events).

The above contamination example was a finite event space. An infinite number of events can occur in a discrete sample space e.g., the sample space $\Omega(\mathbf{N})$ of all integer numbers, or in a continuous sample space e.g., the sample space Ω of all spatial points in a particular soil cross-section. An event space **F** with an infinite number of events is called a "Borel Field" **B**. One of the most common Borel fields is the class $\mathbf{B}(\mathbf{R})$ of all open intervals on the real line.

A very useful probability measure for discrete events can be derived from the "probability mass function" (pmf) $p(\omega)$, which assigns a real number $p(\omega)$ to each elementary

outcome ω in the sample space Ω, and which has the following properties:

$$\begin{aligned} &p(\omega) \geq 0 \qquad \text{for all } \omega \in \Omega \\ &\sum_{\omega \in \Omega} p(\omega) = 1 \end{aligned} \tag{2-2}$$

The probability measure P(F) is defined as:

$$P(F) = \sum_{\omega \in F} p(\omega) \ , \ \text{all} F \in \mathbf{F} \tag{2-3}$$

Note that the pmf is not a probability measure since it is defined for the elementary outcomes themselves and not for a collection of sets. An example of a commonly used pmf is the *uniform pmf*: $\Omega = \mathbf{N}_n = \{0, 1, 2, ..., n-1\}$ and $p(k) = 1/n$, $k \in \mathbf{N}$.

Similarly the "probability density function" (pdf) $f(\omega)$ for continuous sample spaces is defined by:

$$\begin{aligned} &f(\omega) \geq 0 \ , \text{ all } \omega \in \Omega \\ &\int_{\Omega} f(\omega) d\omega = 1 \\ &P(F) = \int_{F} f(\omega) d\omega \ , \ F \in \mathbf{B} \end{aligned} \tag{2-4}$$

where P(F) is the probability measure for the continuous sample space **B**. The probability density function of a random variable is often expressed in functional form. The following pdfs are of importance in this study:

$$\textit{uniform pdf:}\quad f(\omega) = \frac{1}{b-a} \qquad \omega\in[a,b],\ [a,b]\in\mathbf{R}$$

$$\textit{normal pdf:}\quad f(\omega) = \frac{1}{\sqrt{2\pi\sigma^2}}\exp\left(\frac{-(\omega-\mu)^2}{\sigma^2}\right) \qquad \omega\in\mathbf{R} \tag{2-5}$$

$$\textit{lognormal pdf:}\quad f(\omega) = \frac{1}{\sqrt{2\pi\sigma^2\omega^2}}\exp\left(\frac{-(\log\omega-\mu)^2}{2\sigma^2}\right) \qquad \omega\in\mathbf{R}^+$$

$$\textit{Laplace pdf:}\quad f(\omega) = \frac{1}{2\beta}\exp(-|\omega-\alpha|) \qquad \omega\in\mathbf{R}$$

where μ and σ^2 are parameters of the normal and lognormal pdf. The normal pdf is also called the "Gaussian" pdf. α and β are parameters of the Laplace or double exponential pdf.

In the previous paragraphs the properties of the probability space (Ω,F,P) are defined and the pmf and pdf are introduced as tools to compute the probability measure P. The entire framework of stochastic analysis, which is a part of probability theory, rests like probability theory itself upon these definitions of the probability space, the basic operations of set theory, and the principles of mapping or functions. Mapping one probability space into another via some functional relationship is the key to the work presented in this dissertation, since the essence of stochastic analysis is the "connection of a system to a probability space with a description of the output" (Gray and Davisson, 1986, p.29) and the main objective of probability theory is "to find the probability of some new event formed by set-theoretic operations on given events, given a probabilistic description of a collection of events" (ibid.).

The first quoted statement was illustrated in the contamination example above. The second statement concerns itself both with the additivity property of the probability measure and with the mapping of a probability space into another probability space. The additivity property of P can be exemplified again with the contamination problem: Assuming the following probabilities are known: $P(\{c\})$ "the groundwater is not contaminated" is 20%, and the probability $P(\{b\})$ that "the groundwater is contaminated, but the contamination does not affect any wells" is 10%. What is the probability $P(\{a\})$ that "the groundwater is contaminated, and

the contamination has also reached some wells"? From (2-3) it can easily be seen that P({a})=P(Ω)-P({b})-P({c})=70%. Similarly the probability P({a,b}) of the event {a,b} "groundwater is contaminated" is then P({a,b})=P({a})+P({b})=80%.

Mapping (also called filtering, sampling, estimating, averaging, or measuring) is the process of mapping each element ω_A in a sample space Ω_A into another sample space Ω_B. An example is Ω_A = {a,b,c} of the contamination example. A second sample space Ω_B = {d,e,f} is defined such that *d*: "remedial action taken by EPA", *e*: "remedial action taken by fire department", *f*: "no remedial action taken". Also the following mapping (or function) is defined: g:ω -> Ω_B, such that g(a)=d, g(b)=d, g(c)=f i.e., if the groundwater is contaminated at all, EPA will take remedial action; if it is not (yet) contaminated, no remedial action will be initialized. The sample space Ω_A = {a,b,c} is called the domain of the function g, the sample space Ω_B = {d,e,f} is called the range of g, and the set of all g(Ω_A) in Ω_B, Ω_C = {d,f} is called the range space of g. g is a completely deterministic process, because it defines an exact mapping of the sample space Ω_A into the sample space Ω_B. Since each element of Ω_A is associated with a probability, g provides a tool to determine the probabilities in the range Ω_C of the domain Ω_A: The chances of {d} "EPA taking remedial action" are equal to the chances of {a,b} "groundwater is contaminated", which is 80%. Then the chances of "no action taken" are 20%.

Notice that the above example is not a one-to-one mapping and that there is no inverse mapping g^{-1}(d). Defining g(a)=d, g(b)=e, and g(c)=f, Ω_A is mapped "onto" Ω_B and the range Ω_B is equal the range space Ω_C = {d,e,f}. g is said to have an inverse function g^{-1}, because the mapping is one-to-one.

A mapping can occur between a discrete domain and a discrete range, between a discrete domain and a continuous range (albeit the range space is still discrete), between a continuous domain and a continuous range, and also between a continuous domain and a discrete range. The contamination example was of the first category. Considering, for example,

the amount of contaminant mass in the aquifer as a function of the outcome Ω_A would be a mapping between a discrete domain and the (continuous) real line $\mathbb{R}$. The stochastic analysis of unsaturated flow and transport processes is in principal the mapping of the sample space of soil hydraulic properties into the sample space of flow and transport properties.

2.3 Independence and Conditional Probabilities

Reconsider the initial contamination example with the sample space $\Omega_A=\{a,b,c\}$. The elementary events of this sample space are "mutually exclusive", since given one of the events {a}, {b}, or {c}, none of the others can occur at the same contamination site (in the same experiment): Either the groundwater and the wells are contaminated, or only the groundwater is contaminated or the groundwater is not contaminated at all. It is impossible that the groundwater is contaminated AND that it is not contaminated. The probability of one event F_a occurring, if any other mutually exclusive event F_b has occurred is therefore zero:

$$P(F_a \cap F_b) = P(F_a)P(F_b) = 0 \qquad (2\text{-}6)$$

In contrast, one speaks of "independent" events, if the probability of one occurring is independent of whether the other event occurred. Independent events must be from at least two different experiments, each of which has a well-defined sample space. Say, for example, there exist two identical contamination sites at different locations, with a given probability space (Ω,F,P) for each of the two sites. The two events occurring at the two sites are called "independent", since the probability of the event occurring at one site is independent of the probability of the event occurring at the other site. Then the probability of the event F_a at site A AND the event F_b at site B to occur concurrently is:

$$P(F_a \cap F_b) = P(F_a)P(F_b) \geq 0 \qquad (2\text{-}7)$$

Similarly a collection of events $\{F_i, i=1,k\}$ is called "mutually independent", if

$$P\left(\bigcap_{i=1}^{k} F_i\right) = \prod_{i=1}^{k} P(F_i) \qquad \textbf{(2-8)}$$

An example of the latter is the probability of wells contaminated at all of several contamination sites throughout an area, each of which has a probability space (Ω,F,P). If, however, two contamination sites are located very close to each other, the resulting events may not be independent. Then their combined probability space has to be taken into account. The combined probability space is also called the 'multivariate' probability space.

The conditional probability is the probability that an event F_a occurs given that another event F_b has already been determined to have taken place. It must be emphasized that conditional probabilities can be defined for events at the same site or of the same experiment, but also for events from two different sites or experiments if their combined or multivariate probability space is considered. For example, the probability $P(\{a\}|\{a,b\})$ of {a} "a well is affected by groundwater contamination", given that somehow it is known that the event {a,b} "groundwater is contaminated" has occurred is defined as:

$$P(\{a\}|\{a,b\}) = \frac{P(\{a\}\cap\{a,b\})}{P(\{a,b\})} = \frac{P(\{a\})}{P(\{a,b\})} \qquad \textbf{(2-9)}$$

More generally, the conditional probability of an event F_a given the occurrence of event F_b is:

$$P(F_a|F_b) = \frac{P(F_a\cap F_b)}{P(F_b)} \qquad \textbf{(2-10)}$$

It can be shown that conditional probabilities satisfy all the basic axioms of a probability space (2-1). An important property of conditional probabilities, which is derived from the above definition is "Bayes' theorem":

$$P(F_{A_i} | F_b) = \frac{P(F_b | F_{A_i})}{P(F_b | F_{A_1})P(F_{A_2}) + \ldots + P(F_b | F_{A_n})P(F_{A_n})} \qquad \textbf{(2-11)}$$

where the events F_{Ai} are mutually exclusive and the union of all events U $F_{Ai} = \Omega$. The event F_b is an arbitrary event in Ω. The denominator on the right hand side is called the "total probability" of the event F_b. It is the sum of all conditional probabilities of the event F_b given the collection of events $\{F_{Ai}, i=1,n\}$.

In the contamination example, the class of events {{a},{b},{c}} is one of several possible classes that are mutually exclusive and exhaustive of the sample space Ω (a "partition" of Ω). Assume soil samples were taken nearby the well. It is further assumed that the following conditional probabilities are known: If the well is affected by groundwater contamination, chances are 40% that the soil sample is also contaminated. If the groundwater is contaminated, but no wells are affected, chances are 30% that the soil sample is contaminated. If the groundwater is not contaminated at all, chances are 5% that the soil sample is contaminated. Bayes' theorem is used to determine the conditional probability of the event {a} "groundwater contaminated to the extent where it affects wells" given that the event {d} "soil sample contaminated" has occurred: The total probability of {d} (denominator of (2-11)) is:

$$P(\{d\}) = 0.4\ 0.7 + 0.3\ 0.1 + 0.05\ 0.2 = 0.32$$

Then the conditional probability

$$P(\{a\}|\{d\}) = 0.4\ 0.7\ /\ 0.32 = 0.875$$

In subsequent chapters, the concept of conditional probabilities is applied extensively to random variables and functions of random variables. Bayes' theorem plays a fundamental role in the development of this study.

2.4 Random Variables and Random Vectors

2.4.1 Random Variables

With the basic definitions of the probability space, of independence, of the conditional probability space, and of functions, we are well-equipped to proceed with the definition of a random variable X. The term random variable (RV) is actually improper, since by its formal definition a random variable is neither random nor a variable. Mathematically speaking a random variable $X(\omega)$ is a function that maps one to one any elementary outcome of an experiment (or probability space) $(\Omega,\mathbf{F},P)$ into a subset of the real line:

$$\begin{aligned} &X:\ \omega\in\Omega \rightarrow \mathbb{R} \\ &\text{such that: } X^{-1}(B) = \{\omega:\ X(\omega)\in B\} \in \mathbf{F},\ \text{if } B\in\mathbf{B}(\mathbb{R}) \end{aligned} \tag{2-12}$$

where $\mathbf{B}(\mathbb{R})$ is a Borel field on a subset of the real line (where the "subset" is an interval and may be the entire real line itself). In other words, every outcome ω in the abstract sample space Ω is assigned a real number B through the random variable $X(\omega)$. Ω is the domain to the random variable, and the subset $\mathbf{B}(\mathbb{R})$ of the real line $\mathbb{R}$ is the range of the random variable X.

As an example, let us consider a small core sample of soil . Ω_{K_s} is the sample space of all saturated permeabilities. Then $X:\omega \rightarrow \mathbf{B}(\mathbb{R})$, $\omega \in \Omega_{K_s}$, is the saturated permeability of this soil sample measured in units of [length/time]. X is a real number corresponding to the physical property in the soil core called saturated permeability. Other random variables measured on the soil core are e.g. the water content, the matric potential, and the unsaturated hydraulic conductivity. Generally random variables can be considered as "measurements of an experiment" of which the outcome is unknown *a priori.*

The probability distribution of the random variable X (which may be a pmf, a pdf, or a mixture of both) can be derived from the probability distribution of the underlying experiment Ω since the probability $P_X(b)$ that X takes on a value in b is the probability that the inverse of

X, X^{-1} takes on ω:

$$P_X(b) = P(X^{-1}(b)) = P(\{\omega : X(\omega) \in B\}) \qquad b \in \mathcal{B}(\mathbb{R}) \tag{2-13}$$

For most applications it is convenient to use the probability measure P_X rather than the original probability measure P_Ω i.e., one generally operates with the probability space $(\Omega_X, \mathcal{B}, P_X)$ where Ω_X is the range space of the random variable $X(\varpi)$. It is important, however, to keep in mind that the probability space of X is only inherited from the original sample space. There may be other random variables that are derived from the same original sample space Ω. When analyzing the relationship between different random variables, their origins must be considered since common origins generally suggest certain dependencies between RVs of the same sample space. As an example consider the above mentioned soil core itself as being from the sample space Ω_{core}, at which different random variables are measured: the saturated hydraulic conductivity, the unsaturated hydraulic conductivity, the soil water potential, the water content, etc. Each of these random variables is a different type measurement of the exact same physical soil core. Mathematically speaking all random variables are in the same domain Ω_{core}. Although the derived probability measures or probability distributions of these random variables may vary, they are not necessarily independent of each other.

The relationship between the pmf $p_X(x)$ of a discrete RV X and its probability distribution P_X is defined equivalently to (2-2):

$$\begin{aligned} p_X(x) &= P_X(x) \qquad , x \in \mathbb{R} \\ P_X(B) &= \sum_B p_X(x) \qquad , B \in \mathcal{B} \end{aligned} \tag{2-14}$$

and in the case of a continuous X with a pdf $f_X(x)$:

$$P_X(x) = \int_B f_X(x)dx \qquad , B \in \mathbf{B}$$

$$f_X(x_i) = \frac{dF_x(x)}{dx}\Big|_{x=x_i} \tag{2-15}$$

where

$$F_X(x) = P_X((-\infty,x])$$

$F_X(x_i)$ is called the cumulative distribution function (cdf) of X. It represents the cumulative probability of $X \leq x_i$. Note the following properties of the cdf:

$$\begin{aligned} F_X(\infty) &= 1 \\ F_X(-\infty) &= 0 \\ F_X(x_1) &\leq F_X(x_2) \text{ for } x_1 \leq x2 \\ P_X(x>x_i) &= 1 - F_X(x_i) \end{aligned} \tag{2-16}$$

The definition of the cdf allows for the construction of a relationship between the pdf and the probability measure of X such that one can be defined in terms of the other. The definitions of some of the most important pdfs including all those that will be used through the course of this study are already given in (2-5). Their respective cdfs are found by integration of the pdf over the half open interval $(-\infty,x]$.

The conditional cdf of a random variable X, given the event F_b is defined equivalently to (2-10):

$$F_X(x_i \mid F_b) = \frac{P(x \leq x_i \cap F_b)}{P(F_b)} \tag{2-17}$$

The conditional pdf of X is $f_X(x|F_b) = dF_X(x|F_b)/dx$. With these definitions Bayes' theorem for continuous random variables becomes:

$$f_X(x_i \mid F_b) = \frac{P(F_b \mid x=x_i)\, f_X(x_i)}{\int_{-\infty}^{\infty} P(F_b \mid x=a)\, f_X(a)\, da} \tag{2-18}$$

With Bayes' theorem the conditional pdf of a random variable X given an event F_b is determined from the unconditional pdf of the random variable X and from the conditional pdf of the event F_b given the outcome of the random variable X. Bayes' theorem establishes the foundation for conditional simulation (also see chapter 3, chapter 10).

Given the (unconditional or conditional) pdf $f_X(x)$ of a random variable X the (unconditional or conditional) mean or expectation of X are defined as:

$$\mu_X = E(X) = \langle X \rangle = \int_{-\infty}^{\infty} x\, f_X(x)\, dx \tag{2-19}$$

where the notation E() and < > are interchangeable and stand for 'expectation of'. The (unconditional or conditional) variance of X is defined as:

$$\sigma_X^2 = \langle (X-\mu_X)^2 \rangle = \int_{-\infty}^{\infty} (x-\mu_X)^2\, f_X(x)\, dx \tag{2-20}$$

From the definition of the variance of X it follows that

$$\sigma^2_X = \langle X^2 \rangle - (\langle X \rangle)^2 \tag{2-21}$$

The variance is the second-order central moment. Higher order central moments of X are defined as:

$$\langle (X-\mu_X)^n \rangle = \int_{-\infty}^{\infty} (x-\mu_X)^n f_x(x)\, dx \tag{2-22}$$

The skewness of X is obtained for n=3, and the kurtosis of X for n=4. In most of the

applications in this study, it is assumed that a random variable has a Gaussian (or normal) distribution function (2.5). Using the above definitions of the various moments, it is seen that the mean of X corresponds to the parameter μ in the Gaussian pdf, the variance of X corresponds to the parameter σ^2 in the Gaussian pdf, the skewness is 0, and the kurtosis is $3\sigma^4$. If one can reasonably assume that a random variable is Gaussian distributed, the actual form of the pdf is completely determined by the first two moments, the mean and the variance of X.

Before proceeding to describe random vectors and random processes, another important concept related to random variables must be introduced: functions of random variables. Functions of random variables - like the random variable itself - allow the derivation of probabilities of new random variables through functional relationships. Suppose that g(x) is a function of the real variable x. Then the random variable Y defined by

$$Y = g(X) \qquad \textbf{(2-23)a}$$

is also a random variable, since Y is also a function on the original sample space Ω through

$$Y(\omega) = g(X(\omega)) \qquad \textbf{(2-23)b}$$

if the domain of the RV Y is X. Depending on the nature of g(X) various methods exist to derive the probability of Y from the probability of X. In this study, partial differential equations describe the relationship between most random variables of interest. In subsequent chapters methods are introduced to derive the pdf of Y from a given pdf of X if Y and X are related through a partial differential equation.

2.4.2 Random Vectors

So far, only one random variable and its probability distribution has been considered. Now we turn to the probability measure (probability distribution) of two or more random variables $X_1, X_2, ..., X_n$. Note that throughout this study vectors are denoted by boldface letters.

A vector $\mathbf{X} = (X_1, X_2, ..., X_n)^T$ (^{T} indicates the transpose) is called a random vector if it is a finite collection of n random variables X defined on a common probability space $(\Omega,\mathbf{F},P)$ The range space of a random vector is $\mathbf{B}(\mathbb{R})^n$ or a discrete subset of $\mathbf{B}(\mathbb{R})^n$, since the vector has n dimensions. The probability measure P_X of a random vector is different from the probability measure P_X of a random variable, since a vector is the joint outcome of several different measurements. Hence, a "joint probability distribution" of the random vector **X** must be defined. The formal definition of the cumulative probability distribution function $F_X(x)$ of a random vector **X** with a continuous range space is:

$$F_X(x) = F_{X_1,X_2,...,X_n}(x_1,x_2,...,x_n)$$

$$= P_X(x: x\in(-\infty,x_i]; i=1,..n) = \int_{-\infty}^{x_1} ... \int_{-\infty}^{x_n} f_X(x)dx \qquad (2\text{-}24)$$

The corresponding joint pdf $f_X(x)$ is obtained by taking the total derivative of $F_X(x)$:

$$f_X(x) = \frac{\partial F_X(x)}{\partial x_1 \partial x_2 ... \partial x_n} \qquad (2\text{-}25)$$

The joint cumulative distribution describes the probability that the random vector **X** takes on a particular value $x = (x_1, x_2,..., x_n)^T$ or less. But the joint probability distribution can also be used to derive the probability distribution P_{Xi} of a random variable X_i within a random vector. This is called the "marginal probability distribution" $f_{Xi}(x_i)$ i.e., the probability distribution of the random variable X_i without regard for the outcome of any of the other random variables in the random vector **X**:

$$F_{X_i}(a_i) = P_{X_i}(x_i \le a_i) = F_X(\infty,\infty,...,\infty,a_i,\infty,...,\infty) \qquad (2\text{-}26)$$

The marginal probability density function $f_{Xi}(x_i)$ is found by integrating the joint pdf over all random variables other then X_i:

$$f_{X_i}(a_i) = \int_{-\infty}^{\infty} \cdots \int_{-\infty}^{\infty} f_X(x, x_i = a_i)\, dx_1 \ldots dx_{i-1} dx_{i+1} \ldots dx_n \qquad (2\text{-}27)$$

Equivalent definitions for the marginal and joint distributions can be derived for discrete range spaces of **X** (i.e. if the components X of **X** can take on a finite discrete set of real numbers only).

Like for random variables, mathematical models are used to describe the joint pdf of **X**. In section 2.2 several pdfs are introduced for single random variables. An important joint pdf is the "joint Gaussian" pdf or "multidimensional Gaussian" pdf, where "multidimensional" refers to the dimensions of the random vector. The formal definition of the multidimensional Gaussian pdf involves two parameters similar to the two parameters μ and σ^2 in the one-dimensional or univariate Gaussian pdf: If **m** is a n-dimensional column vector and C a n by n matrix that is symmetric and positive definite, then a joint pdf is said to be Gaussian if it has the following form for any **m** and C:

$$f_X(\mathbf{x}) = \frac{\exp[-\tfrac{1}{2}(\mathbf{x}-\mathbf{m})^T C^{-1}(\mathbf{x}-\mathbf{m})]}{\sqrt{(2\pi)^n \det C}} \qquad (2\text{-}28)$$

where detC is the determinant of C. The vector **m** corresponds to the mean of the random vector **X**. It can be shown that each entry $C_{ij} = C_{ji}$ (symmetry!) can be found by determining the "covariance" of X_i and X_j. The covariance is a second order moment defined as:

$$\mathrm{Cov}(X_i, X_j) = \langle (X_i - m_i)\,(X_j - m_j) \rangle \qquad (2\text{-}29)$$

Then $C_{ij} = \mathrm{Cov}(X_i, X_j)$. The covariance is a measure of the physical correlation between the random variable X_i and X_j e.g., between the saturated hydraulic conductivity and the matric potential in a soil core. Notice that $\mathrm{Cov}(X_i, X_j) = \mathrm{Var}(X)$ for i=j.

If the random variables of a random vector are independent of each other (2-8) then the joint pdf for continuous random variables becomes simply the product of the marginal

probability density functions:

$$f_X(x) = \prod_{i=1}^{n} f(x_i) \qquad (2\text{-}30)$$

Similarly, the joint pmf for a discrete random variable is the product of the marginal pmf. The probability distributions related to these independent pdfs and pmfs are called "product distributions". If the pdf or pmf for each of the independent random variables in the random vector are the same, the vector is called an "independent and identical distributed" (i.i.d.) random vector.

Like for random variables, one may define a function of a random vector:

$$Y = g(\mathbf{X}) = g(X_1, X_2, \ldots, X_n) \qquad (2\text{-}31)$$

where Y is a new random variable. This definition is then used to derive the probability distribution of Y in terms of the joint probability distribution of **X**.

Random vectors are used in this study in two different ways that are mathematically equivalent, but differ in their physical interpretation. Random vectors of random variables may represent different physical properties such as $\mathbf{X}=(K,h,\Theta)^T$, where K denotes the saturated hydraulic conductivity, h the matric potential, and Θ the moisture content of the soil core mentioned in previous examples. If, for example, this random vector has a joint Gaussian pdf, the joint probability measure is determined by specifying the mean $\mathbf{m} = (m_K, m_h, m_\Theta)^T$ of each of the random variables and the (cross-) covariance C between each of the physical properties in the same soil core.

Alternatively, a random vector may represent the same physical property at different spatial locations in the soil: $\mathbf{X}=(\Theta(x_1),\Theta(x_2),\ldots,\Theta(x_n))^T$. Since each spatial location - statistically speaking - represents the outcome of a joint experiment with its own (marginal) probability space Ω_x, each physical property at each spatial location x forms a random variable by itself. If, for example, the water content throughout a field site possesses a joint Gaussian pdf, then

the joint probability distribution is uniquely determined by the mean vector $\mathbf{m} = (<\Theta(\mathbf{x}_1)>, <\Theta(\mathbf{x}_2)>,...,<\Theta(\mathbf{x}_n)>)^T$ of Θ at each location separately (i.e. it doesn't have to be the same everywhere!), and the covariance matrix $\mathbf{C}_\Theta$ that defines the covariance between the Θs of each location pair.

While it is quite obvious that the saturated hydraulic conductivity and the soil matric potential at a location $\mathbf{x}$ in a soil domain are two different random variables with different marginal probability spaces, it must be emphasized here that without further assumptions the saturated hydraulic conductivity at one location is NOT the same random variable as the saturated hydraulic conductivity at another location and does not a priori possess the same marginal probability space! Similarly, the random variable "soil moisture" Θ at a time t_1 is not considered to be the same as the random variable Θ at a time t_2. Also note that there generally is an infinite number of either discrete or continuous physical locations $\mathbf{x}$ or times t, while the different physical properties are always a finite number of discrete variables. To distinguish between random vectors of different physical variables and random vectors of random variables in space and/or time, the terms 'random process' or 'random field' are used for the latter interpretation.

2.5 Random Processes and Random Fields

2.5.1 Definition

Random processes are an infinite collection of random variables where the random variables are indexed on a discrete or continuous "index set" $\mathbf{I}$. In our applications this index set always corresponds to time t or spatial location $\mathbf{x}$. The spatial location $\mathbf{x}$ is always denoted as a (lower case, bold print) vector of spatial coordinates and must not be confused with the probability $P_X(x)$ that the random variable X takes on a value x or the joint probability $P_{\mathbf{X}}(\mathbf{x})$ that the random vector $\mathbf{X}$ takes on a vector value $\mathbf{x}$!

The term "random process" or "stochastic process" is mostly used if the index set is the time variable, while the term "random field" is commonly applied for index sets of spatial locations. Formally, a random process is an indexed family of random variables $\{X(\varpi,t);\ \varpi\in\Omega,\ t\in I\} = X_t = X(t)$ defined on a common probability space (Ω,F,P). Equivalently a random field is denoted as an indexed family of random variables $\{X(\varpi,x);\ \varpi\in\Omega,\ x\in I\} = X_x = X(x)$ on a common probability space (Ω,F,P), where $I=\mathbb{R}^n$ or a discrete subset of $\mathbb{R}^n$, $n\leq 3$, indicates the spatial dimensionality. Since the only difference in the definitions of random fields (random processes) and random vectors is the number of components (infinite vs. finite family of random variables) equivalent probability measures are defined for random fields and random processes: process cumulative distribution functions, process density functions, marginal cumulative distribution functions and marginal probability density functions.

Realizations (samples) of random fields are a basic element of the numerical stochastic analysis as will be shown in subsequent chapters. Often, the realizations themselves are referred to as random fields. To avoid confusion and to distinguish the random fields from random realizations of random fields subsequent chapters will use the the term "random field variable" (RFV) to denote random fields that are families of random variables as defined above.

In numerical applications, random fields are always discretized in a finite domain. How do these finite discrete subsets relate to the infinite continuous random field? The "Kolmogorov extension theorem" shows that given a consistent family of finite-dimensional (joint) distributions

$$\{P(X(x_1),X(x_2),...,X(x_n));\ x_i \in I,i=1,...n\} \qquad (2\text{-}32)$$

there exists a random process or random field $\{X(x),\ x \in I\}$ described by these distributions. The term "consistent" distribution refers simply to fact that the joint distribution and the marginal distributions must be consistent in that one can be derived from the other through (2-26). This also includes the condition that "boxes" in n-space have positive probability.

Probability distributions are consistent, if they are described, for example, by the multidimensional Gaussian pdf. From the above theorem it then follows that a random field $\{\mathbf{X}(\mathbf{x}), \mathbf{x} \in \mathbf{I}\}$ is a "Gaussian random field" if ALL finite collections of samples of the random field $(\mathbf{X}(\mathbf{x}_1), \mathbf{X}(\mathbf{x}_2),...,\mathbf{X}(\mathbf{x}_n))^T$ are Gaussian random vectors i.e., satisfy (2-28) and the conditions stated for **m** and **C**.

To further distinguish between the covariances of the same physical property at different times or locations (covariance of a random field or random process) and the covariance between two different physical properties at the same or at different locations, the latter is from now on referred to as a "cross-covariance".

Random fields and processes - like random vectors - may consist of independent random variables. If each independent random variable possesses the same pdf or pmf, the random field (process) is called an i.i.d. random field (process). Note that for independent random variables $\langle X_i\ X_j \rangle = \langle X_i \rangle \langle X_j \rangle$. The the covariance of two uncorrelated random variables is 0.

2.5.2 Stationarity and Ergodicity of Random Processes

All basic probabilistic concepts encountered in the study of heterogeneous porous media via stochastic analysis are now defined. Before continuing with the introduction of two rather intriguing properties of random fields, two important questions are raised: What is the justification for treating porous medium properties as random variables? And how does the heterogeneous environment of a porous medium i.e., a soil cross-section, a field-lysimeter, the unsaturated zone underneath a particular field site, or the aquifer underneath a certain region, relate to the properties of random variables and random fields?

While the first question is often posed, it fails to address the central problem of environmental modeling, which is not the heterogeneity of natural systems, but the measurement

and/or estimation of the heterogeneous properties. Indeed the porous medium as it exists can be interpreted as being completely deterministic i.e., there is nothing random about the properties of the porous medium at any of its locations. The genesis of the pore morphology follows physical laws. All derived porous properties such as the permeability and the water content are also determined by physical principles. Hence, the heterogeneity of the soil does not in itself is completely deterministic.

The randomness lies in the lack of knowledge, and inability to acquire it fully, about what these porous medium properties exactly are. Soil physical or chemical properties are commonly determined by either an actual **measurement** of soil properties or by the intuitive, graphical, or mathematical **estimation** of soil properties from related data (inverse distance interpolation, kriging, etc.). Both measurement and estimation are associated with errors. The (physically deterministic) errors occurring during the measurement and/or estimation process have the properties of random variables and thus allow a rigorous analysis with statistical tools. This is the key to stochastic analysis and the bridge between reality and conceptual model. Stochastic analysis in subsurface hydrology is about modeling the limitations of our knowledge! How limited our knowledge is will in turn depend on the porous medium heterogeneity. The focus of this study are the **estimation** errors (and NOT the **measurement** errors) occurring in predictions of soil water tension, soil water flux, and solute transport. Without loss of generality measurement errors are neglected.

The beauty of the stochastic analysis is that it provides both a best estimate of the properties of interest (hydraulic conductivity, soil moisture, solute transport, etc.) and a quantitative measure describing the uncertainty of the best estimate. The probability distributions encountered in stochastic modeling are essentially a reflection of the fuzziness or uncertainty of our knowledge about the soil properties. Hence, the justification for treating porous media as random fields lies NOT in the physical nature of the porous medium (which is deterministic) but in the limitation of our knowledge ABOUT the porous medium. This is

not to say however that heterogeneity is unrelated to the statistical analysis. Indeed, the estimation error is a direct function of the soil heterogeneity: If the porous medium is relatively homogeneous, the properties of the soil at unmeasured locations are estimated with great certainty given a few sample data. On the other hand, if the porous medium is very heterogeneous and soil properties are correlated over only short distances, an estimation of the exact soil properties at unmeasured locations is associated with large errors. Hence, the heterogeneity of the soil is a measure of the estimation error or prediction uncertainty.

The second question addresses the practical problem of translating field measurements (a "sample") into statistical parameters defining random variables i.e., into a probability space that is representative of the spatial variability and hence the estimation error with regard to the physical property of interest. This leads to the general problem of deriving "ensemble" statistical parameters of random fields (which consist of an infinite number of random variables, each of which has an infinite number of possible outcomes) from a small sample that gives ONE measurement of each of an INFINITE number of random variables. At the most, using the definitions of the mean, the variance, the (cross-)covariance, and the higher order moments (2-22) "sample" statistical parameters and a "sample probability distribution" or histogram of the measured random field parameters can be computed. The sample statistics give a quantitative estimate of the degree of heterogeneity in the porous medium, which also is an estimate of the expected estimation error. Then two problems need to be addressed:

1. The sample taken from measuring MANY random variables ONCE must be related to the MANY possible outcomes of any particular ONE random variable $X(\mathbf{x})$ at location $\mathbf{x}$.
2. The sample statistics must be related to the ensemble statistics of the random field.

These two points are crucial to the stochastic analysis and in particular the first one must not be underestimated. Recall that a random field consists of an infinite number of random

variables, each of which has its own marginal pdf. The random variables in a random field need not have identical probability distributions. As will be seen in chapter 10, estimates of soil properties that are conditioned on field data are indeed always random fields with random variables whose pdf is a function of the location in space, since the uncertainty about field properties may vary from location to location (depending on whether the estimation is close to a measurement point or not)!

First, the question is addressed of how the measurement sample of different random variables (same physical property at different locations in the same single realization of a random field, namely the actual field site) can be taken to be equivalent to many measurements of the same random variable (same physical property at one location in many different hypothetical realizations of the site including the actual one). The definition of a random field as a collection of random variables in space says *a priori* nothing about the **spatial** relationship of the marginal probability distributions of the random variables that make up the random field, except for the condition that they must form a proper joint probability distribution. But an entire probability distribution for each and every random variable in the random field must be found. This poses a severe dilemma for the statistical treatment of many earth science problems: Only a single realization of the random field is available since all regional and subregional geologic, pedologic, and other environmental phenomena are unique and do not repeat themselves elsewhere. This is a very different problem from flipping a coin, an experiment that can easily be repeated (and measured) as many times as necessary to determine its sample probability distribution. To circumvent the dilemma it is assumed that the marginal probability distribution function of each random variable is identical at every location in the random field. In other words, one must assume that the likelihood that a physical property takes on a particular value B, is exactly the same everywhere in the field. This implies that the mean, the variance, and the other moments of the probability distribution are identical for every location in the random field. This property is called "stationarity" or "strict stationarity". A

formal definition is given:

$$P(X(\mathbf{x})\varepsilon B;\ \mathbf{x}\varepsilon I) = P(X(\mathbf{x}+\Delta\mathbf{x})\varepsilon B;\ \mathbf{x}\varepsilon I) \tag{2-33}$$

where B is an event of the Borel field $\mathbf{B}(\mathbb{R})$. In all the applications of this study, a weaker form of stationarity is assumed: "second order stationarity" or "weak stationarity" or "wide-sense stationarity", which requires that the mean and covariance (but not any higher order moment) are identical everywhere in the random field:

$$\langle X(\mathbf{x})\rangle = \langle X\rangle \qquad \text{, all } \mathbf{x}\varepsilon I \tag{2-34}$$

$$Cov_X(X(\mathbf{x}),X(\mathbf{x}+\Delta\xi)) = Cov_X(\Delta\xi) \qquad \text{, all } \mathbf{x},\Delta\xi\text{: } \mathbf{x},\ \mathbf{x}+\Delta\xi\ \varepsilon I \tag{2-35}$$

Two important examples of strictly stationary processes are the i.i.d. random field, which by definition has identical distributions for each of the random variables in the random field. A Gaussian random field is called weakly stationary if the mean $\mu_X(\mathbf{x})=\mu$ for all x, and the covariance $Cov(\mathbf{x}_1,\mathbf{x}_2)=Cov(\xi)$, $\xi = \mathbf{x}_2 - \mathbf{x}_1$ for all $\mathbf{x}_1$, $\mathbf{x}_2$ on the index set I. Since the Gaussian random field is completely defined by its first two moments, all higher order moments of the Gaussian random field must be stationary if the first two moments are stationary. Hence weakly stationary Gaussian fields are also strictly stationary.

The existence of stationarity in porous medium properties cannot be proven rigorously at any single field site. Data are often sparsely distributed. In the best of cases a linear or higher order trend can reasonably be removed from the data. For all practical purposes, it is therefore convenient to *hypothesize* that the field site is a realization of a weakly stationary random field (after removing an obvious trend). This is a reasonable assumption in many field applications. Once this working hypothesis is postulated, the sample of measurements at different locations is treated as if it were a sample of several realizations of the same random variable (i.e. at the same location).

Next, the sample moments must be related to the ensemble moments of the random

variable. This problem is treated by stochastic theorems related to convergence and to the law of large numbers (cf. Gray and Davisson, 1986). The definition of "convergence in the mean square" is: A sequence of random variables X_i, i=1,2,... (e.g. a random field) converges in the mean square to a random variable X if

$$\lim_{n\to\infty} \langle (X_i - X)^2 \rangle = 0 \tag{2-36}$$

Convergence in the mean square sense is mathematically also written as

$$\text{l.i.m.}_{n\to\infty} X_i = X \tag{2-37}$$

where l.i.m. stands for "limit in the mean". To solve the problem of relating sample statistics to ensemble parameters it is necessary that the sample statistics taken from a single realization indeed converge to the ensemble statistics of the random variables as the number of samples is increased:

$$\text{l.i.m.}_{n\to\infty}\left[\frac{1}{n} \sum_{i=1}^{n} X_i \right] = \mu_X \tag{2-38}$$

A random field or random process that satisfies this theorem is called "mean ergodic". A sufficient condition for weakly stationary random fields to be mean ergodic with a limiting sample average μ_X is that $C_X(0) < \infty$ and that $\lim_{n\to\infty} C_X(n\Delta x) = 0$. In other words a weakly stationary random field is mean ergodic, if the variance is finite and if random variables are uncorrelated at large separation distances (Papoulis, 1984).

Like stationarity, mean ergodicity cannot be measured in a single field site i.e., a single realization of the hypothetical random field. Rather mean ergodicity is taken as a working hypothesis i.e., it is assumed *a priori* that the measured sample statistics converge in the mean square to the true ensemble parameters as the number of samples increases.

Note that the above definition of a mean-ergodic random field is only a special case of

a more general ergodic theorem that states that the sample expectations converge to a constant (not necessarily the mean of any random variable in the random field) as the number of samples increases. Ergodic processes need not be stationary (e.g. a random field with underlying periodic trend) and similarly stationary random fields need not be ergodic (the sample expectations may not converge as the sample size increases such as in the flipping a coin experiment). For all applications in this study, however, both weak stationarity and mean-ergodicity are postulated as working hypotheses. Thus limited knowledge of a deterministic reality can be related to an abstract probability space. Once the step has been made from the sample to the probability space (via the working hypotheses stationarity and ergodicity) the tools available from the definitions of probability theory as stated in the previous sections are used to make probabilistic predictions about the current status of the porous medium at locations other than those from where measurements are available and to make probabilistic predictions about the future status at both unmeasured and measured locations. It should now be clear that a "probabilistic prediction" will not determine an actual value of a physical property. Rather it will give the moments (or probability distribution) of the random variable defined on the error of estimating a physical property.

Finally it is emphasized that the assumption of mean ergodicity (2-38) does not imply identity of the sample mean m_X based on n samples of a random variable X and the ensemble mean μ_X. For the same reason, the sample variance var_X or sample covariance cov_X are not identical to their respective ergodic limit σ_X^2 and C_X. The difference between the sample statistical parameters of X and its ensemble moments is generally referred to as parameter estimation error and will subsequently be neglected. Such parameter estimation errors, however, are recognized to be an important source of uncertainty in field applications of the stochastic approach.

2.5.3 Conditional Random Fields and Kriging

In section 2.3 the conditional probability space of random variables was introduced. The Bayesian theorems stated there are readily extended to random fields. Conditional probabilities in random fields are defined for separately for each random variable, given the exact outcome of other random variables. In this study, the conditional first and second moment (conditional mean and covariance) of a random variable are of particular interest. These two moments are sufficient to describe the conditional pdf if the underlying unconditional joint probability distribution is Gaussian.

Recall the (multivariate) **joint** cumulative probability distribution function $F_X(x_1,x_2,x_3,...,x_n)$ is defined as:

$$P_X(x_1,x_2,x_3,...,x_n) = \int\int\int...\int f_X(x_1,x_2,x_3,...,x_n)\, dx_1dx_2dx_3...dx_n \qquad (2\text{-}39)$$

with the unconditional expectation (first moment)

$$\langle X_i \rangle = \int_{-\infty}^{\infty} x_i f_X(x_i) dx_i \qquad (2\text{-}41)$$

and the unconditional covariance (second moment):

$$C_{ij} = \langle X_i' X_j' \rangle = \int_{-\infty}^{\infty}\int_{-\infty}^{\infty} x_i' x_j' \, f_X(x_i,x_j) dx_i dx_j \qquad (2\text{-}41)$$

where $x_i' = x_i - \langle X_i \rangle$ is the perturbation around the mean. The variance σ_X^2 is defined by (2-41) for i = j. The joint pdf is the derivative of the joint cumulative distribution function. Assume that m datapoints of the n datapoints of interest were already measured. Then the **marginal** probability density function $f_X(x_{m+1},x_{m+2},...,x_n)$ of the unknown data (RVs) $X_{m+1},...,X_n$ in the unknown ensemble of data $X_1,...,X_n$ is defined by (see 2-27):

$$f_X(x_{m+1},x_{m+2},\ldots,x_n) = \int_{-\infty}^{\infty}\int_{-\infty}^{\infty}\cdots\int_{-\infty}^{\infty} f_X(x_1,x_2,\ldots,x_n)dx_1dx_2\ldots dx_m \qquad (2\text{-}42)$$

With the help of these two distribution functions the **conditional** probability density function $f_X(x_{m+1},x_{m+2},x_{m+3},\ldots,x_n|x_1,x_2,x_3,\ldots,x_m)$ of the unknown data is defined given the actual values for the data at points $x_1,\ldots,x_m$:

$$f_X(x_{m+1},x_{m+2},\ldots,x_n|\ x_1,x_2,\ldots,x_m) = \frac{f_X(x_1,x_2,\ldots x_m,x_{m+1},\ldots,x_n)}{f_X(x_1,x_2,\ldots,x_m)} \qquad (2\text{-}43)$$

The conditional expectation $\langle X_i\rangle^c$ of X_i is defined as:

$$\langle X_i\rangle^c = \langle X_i|x_1,x_2,\ldots,x_m)\rangle = \int_{-\infty}^{\infty} x_i f_X(x_i|x_1,x_2,\ldots,x_m)\ dx_i \qquad (2\text{-}44)$$

and the conditional covariance (second moment) by

$$E_{ij} = \langle X_iX_j|x_1,x_2,..,x_m\rangle = \int_{-\infty}^{\infty}\int_{-\infty}^{\infty} x_ix_j f_X(x_i,x_j|x_1,x_2,..,x_m)\ dx_idx_j \quad i,j = 1,\ldots,n \qquad (2\text{-}45)$$

To make complicated matters simple, it is assumed that the unconditional joint pdf is multivariate normal and hence fully characterized by its first and second moments, the mean and the covariance. For practical reasons it is also assumed that the unconditional random process is stationary i.e., the first and second moment are not functions of the spatial location x. It is important to understand, however, that the conditional random process is NOT stationary, even if the unconditional probability field is stationary. In other words, even if the unconditional mean $\langle X\rangle$ and variance σ^2_X are independent of location x, the conditional mean $\langle X_i\rangle^c$, the conditional variance E_{ii}, and the conditional covariance E_{ij} are functions of location x_i.

Matheron (1971) contributed extensively to the theory of random variables in space, and developed a "best, linear, unbiased estimator" to estimate random variables in space from a few

known data, which has become widely known as "kriging" (c.f. Journel and Huijbregts, 1978). Essentially his analysis includes a derivation of the conditional moments of the random variables based on the concept of "regionalized variables" (Matheron's term for random variables in space). If the random field is Gaussian, then the algorithm for determining the conditional expectations in a random field is identical to kriging. Kriging is one of the main tools in geostatistics (Dagan, 1982). Kriging techniques have been developed for second order stationary fields with known constant mean (simple kriging), for intrinsic stationary fields i.e., random fields with constant but unknown mean and weakly stationary increments $(X_i - X_j)$ (ordinary kriging), for intrinsic stationary random fields with an underlying trend of known order (universal kriging), and for some non-Gaussian random fields (log-kriging, probability kriging, disjunctive kriging, and indicator kriging) (Matheron, 1971; Journel, 1983; Armstrong and Matheron, 1986; Journel, 1988; Kim, 1988). For the purpose of this study, it will be convenient to restrict ourselves to the case of a weakly stationary random process (random field) with a constant unconditional mean $\langle X \rangle$ and finite unconditional variance σ^2_X (simple kriging). The conditional expectation $\langle X_i \rangle^c$ (2-44) can then be computed by a linear estimate $\langle X_i \rangle^k$ (i.e. $\langle X_i \rangle^k$ is a linear function of the given data) such that the mean square of the estimation error $\langle e^2 \rangle$, $e = (X - X^k)$ is minimized (c.f. Papoulis, 1984, p.167ff.). The estimation of the conditional expectation is given by (Dagan, 1982):

$$\langle X_i \rangle^k = \langle X_i | x_1, x_2, ..., x_m \rangle = \langle X \rangle + \Sigma \lambda_{ij} (x_j - \langle X \rangle)$$

alternatively: (2-46)

$$\langle \mathbf{x}_2 \rangle^k = \langle \mathbf{X}_2 | \mathbf{x}_1 \rangle = \langle \mathbf{X}_1 \rangle + \Lambda_{21} (\mathbf{x}_1 - \langle \mathbf{X}_1 \rangle)$$

where $\mathbf{x}_1$ is the vector of known data of the RVs $\mathbf{X}_1 = (X_1,...,X_m)^T$ (at locations $\mathbf{x}_1,...,\mathbf{x}_m$) and $\mathbf{X}_2$ is the vector of unknown RVs $(X_{m+1},...,X_n)^T$ (at locations $\mathbf{x}_{m+1},...,\mathbf{x}_n$). In the geostatistics literature, $\langle \mathbf{X}_2 \rangle^k$ is referred to as the (simple) kriging estimator (Journel, 1988). The weights λ_{ij} in the weight matrix Λ_{21} are obtained by minimizing $\langle e^2 \rangle$, which leads to a linear system

of equations called the (simple) kriging system of equations:

$$\sum_{j=1}^{m} C_{ij}\,\lambda_{jk} = C_{ik} \qquad i = 1,2,...,m \qquad k = m+1,...,n$$

alternatively:

$$\mathbf{C_{11}}\,\Lambda_{12} = \mathbf{C_{12}} \tag{2-47}$$

where $\mathbf{C_{11}}$ is the covariance matrix between the known datapoints of $\mathbf{X_1}$ and $\mathbf{C_{12}}$ is the covariance matrix between known datapoints of $\mathbf{X_1}$ and points of unknown data $\mathbf{X_2}$. The kriging system has a solution only if $\mathbf{C_{11}}$ is a positive definite matrix (Journel and Huijbregts, 1978). To assure positive definiteness, the sample covariance data obtained from analysis of $\mathbf{x_1}$ are fitted to an optimal (i.e. best-fitting), valid (i.e. assuring positive definiteness) functional form of the covariance, such as the exponential, spherical, or gaussian models (Isaaks and Srivastava, 1989). The minimized "estimation error covariance" or "mean square error" corresponds exactly to the conditional covariance or simple kriging covariance and is given by:

$$E_{ij} = \langle X_i' X_j' | X_1, X_2, ..., X_m \rangle = C_{ij} - \sum_{k=1}^{m} C_{ik}\,\lambda_{kj} \qquad i,j = m+1,...,n$$

alternatively:

$$\mathbf{E_{22}} = \mathbf{C_{22}} - \Lambda_{21}\,\mathbf{C_{12}} \tag{2-48}$$

Note, that the individual entries in the conditional covariance or error covariance matrix $\mathbf{E_{22}}$ are equal to or smaller than the entries in the unconditional covariance matrix $\mathbf{C_{22}}$!

2.6 Spectral Representation of Random Variables

In the analysis of random processes (time series), "spectral analysis" has been an important tool for many different tasks and is a well-established field of probability theory (c.f. Priestley, 1981). Recently, spectral analysis has also become important for the study of

spatially variable processes (random fields). Introduced into the field of subsurface hydrology by Gelhar et al., (1974) to study groundwater systems, it has since been applied to a great variety of subsurface hydrologic problems (e.g. Bakr et al., 1978; Gutjahr et al., 1978; Gelhar and Axness, 1983; Yeh et al., 1985a,b; Li et al, 1992).

In principle, spectral analysis is founded on the concept that a single realization of a random process (RVs defined on a 1-dimensional time index) or of a random field (RVs defined on a n-dimensional location index, $n \leq 3$) is nothing but a superposition of many (even infinitely) different (n-dimensional) sine-cosine waves, each of which has different amplitude and frequency. Then any particular realization of a random field can be expressed either in terms of a spatial function or in terms of the frequencies and amplitudes of the sine-cosine waves and their amplitudes (called 'Fourier series' of a discrete process and 'Fourier transform' of a continuous process). The latter are collectively called the "spectral representation" of the random field. The spectral representation of a single random field realization can intuitively be understood as a field of amplitudes, where the coordinates are the frequencies of the sine-cosine waves. In other words, instead of an actual value for each location in space, the spectral representation gives an amplitude for each possible frequency (wave-length). Note that in n-dimensional space, $n \leq 3$, sine-cosine waves are defined by n-dimensional frequencies (with one component for each spatial direction) and therefore the spectral representation of a n-dimensional random field is also n-dimensional.

The spectral representation is defined deterministically i.e., it is not defined in a probability space and has by itself little to do with a stochastic solution: Each realization of a random field has its own spectral representation, since the amplitudes of the underlying sine-cosine waves are different for each realization. But obviously and following the rules already established in the previous sections the amplitudes of the sine-cosine waves can be defined as random variables with the frequency domain as the index field. In other words, a function of a spatial random field (which is defined on a probability space) is established rather than a

function of a realization of a random field (which is a deterministic function). One then deals with the probability space of the spectral representation, which in turn also is a random field, but defined in the frequency domain. Statistically speaking, the probability space of the spatial random field is mapped onto the probability space of the spectral random field.

The advantages of representing a random field in terms of its underlying spectral properties i.e., in terms of the probabilities of amplitudes and frequencies of the "waves" composing a random field, are many. But within the framework of this study two properties are particularly important:

1. The spectral representation of a spatially correlated random field i.e., of random variables with a joint probability distribution is - under certain conditions - a random field with random variables (amplitudes) that are uncorrelated i.e., they are completely defined by their univariate marginal distribution, the analysis of which is much easier than that of random variables with a multivariate joint distribution function.
2. Under certain conditions, the spectral transformation of a partial differential equation is a polynomial whose solution is found much easier than the solution to the partial differential equation in the spatial domain.

In this study, the tools of spectral analysis are used for three different but related tasks:

1. in a probabilistic sense to analytically derive the joint probability distributions of functions of random fields,
2. in a deterministic sense to numerically generate realizations of random fields of spatially variable parameters,
3. in a deterministic sense to obtain explicit solutions to partial differential equations defined by a particular (deterministic) realization of random fields.

In this section, the basic theorems of spectral analysis are introduced. In the following chapters they are applied to generate random fields (chapter 3), and to derive the joint probability distribution functions of parameters of interest in unsaturated flow and transport by applying

spectral analysis to the governing unsaturated flow equation (chapter 4). Finally, in chapter 7 a method is introduced that combines spectral and numerical analysis to efficiently obtain solutions of the unsaturated flow equation given a particular random field realization of the constitutive parameters.

For reasons discussed earlier, this study is solely concerned with stationary random fields. The spectral analysis of stationary random fields has been well-established in the literature and many fine texts can be found on the general subject (e.g. Priestley, 1981). Here only the basic theorems are introduced, which are necessary to understand the techniques applied to the stochastic analysis of flow and transport processes. For complete proofs and a broad introduction to the topic the reader is referred to the established literature (c.f. Priestley, 1981).

The spectral representation of a single realization X(x) of a random field with mean 0 is formally defined in terms of the Fourier-Stieltjes integral (Wiener, 1930):

$$X(x) = \int_{-\infty}^{\infty} e^{ikx}\, dZ(k) \qquad (2\text{-}49)$$

where the integral is n-dimensional, n≤3, and Z(**k**) is a (complex valued) function, called the Fourier-Stieltjes transform of X(**x**). The Fourier-Stieltjes integral must be chosen over the more common Fourier-Riemann integral

$$f(x) = \int_{-\infty}^{\infty} e^{ikx}\, g(k)\, dk \qquad (2\text{-}51)$$

where g(**k**) is the Fourier transform of f(**x**) since the Fourier-Stieltjes transform Z(**k**) of the random field X(**x**) is generally not differentiable such that dZ(**k**) = z(**k**) d**k**. Z(**k**) can be understood as an integrated measure of the amplitudes of the frequencies between (-∞, **k**] contributing to the realization X(**x**).

As already mentioned above, Z can also be interpreted as a random field consisting of

random variables $Z(\mathbf{k})$ defined in the frequency domain, where the random field Z is a stochastic function of the random field X i.e., each realization X_i is mapped into a realization of the spectral representation Z_i. In this probabilistic sense (2-49) essentially expresses the fact that "*(virtually) any stationary [random] process [random field] can be represented as (the limit) of the sum of sine and cosine functions with random coefficients dZ(k), or more precisely, with random amplitudes |dZ(k)| and random phases arg{dZ(k)}*" (Priestley, 1981, p.245). The new probability space $(\Omega_Z, \mathbf{F}_Z, P_z)$ of the random variables $Z(\mathbf{k})$ in (2-49) has several very important properties:

$$1.\quad \langle dZ(k)\rangle = \frac{1}{2\pi}\int_{-\infty}^{\infty} e^{-ikx}\langle X(x)\rangle dx$$

$$2.\quad \langle |dZ(k)|^2\rangle = S(k)dk \qquad \textbf{(2-51)}$$

$$3.\quad \langle dZ(k_1)dZ^*(k_2)\rangle = 0 \qquad \text{all } k_1 \neq k_2$$

The first property states that the mean $\langle dZ(\mathbf{k})\rangle$ of the random variables $dZ(\mathbf{k})$ is equal to the Fourier transform of the mean of the random variables $X(\mathbf{x})$. In subsequent applications, only zero-mean random processes are considered, hence the spectral representations are also of zero mean. The second property defines the variance ($S(\mathbf{k})\,d\mathbf{k}$) of the random variable $dZ(\mathbf{k})$. The term $S(\mathbf{k})\,d\mathbf{k}$ is a measure of the average "energy per unit area" or "power" contribution of the amplitude of a frequency $\mathbf{k}$ to the random field $X(\mathbf{x})$. $S(\mathbf{k})$ is called the "spectral density" or "spectrum" of the random field X. $S(\mathbf{k})$ depends purely on the probabilistic properties of the random field $X(\mathbf{x})$ and it can be shown that it is simply the Fourier transform of the covariance $C(\xi)$ of X. The third property states that the increments $dZ(\mathbf{k}_1)$ and $dZ(\mathbf{k}_2)$ at two different frequencies $\mathbf{k}_1$ and $\mathbf{k}_2$ are uncorrelated. Such a random field is also called an "orthogonal" random field.

Through (2-51) the first two moments of the random field $dZ(\mathbf{k})$ are defined solely in

terms of the first two moments of the stationary random field X(**x**). Hence, if the first two moments of the random field X(**x**) are known, then the first two moments of its spectral representation dZ(**k**) are known. Note that the spectral representation dZ(**k**) of a weakly stationary random field X(**x**) is only stationary to first order: The mean <dZ(**k**)> is constant (first property), but the variance S(**k**) of the random field dZ(**k**) is a function of the location **k** in the frequency domain (second property).

In summary of this last section, a new probability space, called the spectral representation of a random field, was defined on the known probability space of a random field. The mapping of a stationary, correlated random field X into its spectral representation dZ provides the important advantage of creating an equivalent dZ to the random field X that consists of orthogonal or uncorrelated random variables!

3. RANDOM FIELD GENERATORS

3.1 Introduction

The generation of spatially correlated samples of random fields plays a fundamental role in the numerical analysis of stochastic functions - whether these are 1-, 2-, or 3-dimensional. The purpose of random field simulation is to create numerical samples or "realizations" of stochastic processes with well-defined properties. The term "random field generator" is actually improper, because random fields are by definition probability spaces (see chapter 2) and can therefore not be discretely generated. For ease of reading and in reference to many other publications that deal with the generation of random realizations of a random field, the term "random field" is in this and all subsequent chapter used interchangeably with the term "realization". The random fields as defined in section 2.5.1 are henceforth referred to as random field variables (RFVs).

The simplest and most commonly available form of simulation is the random number generator on a calculator or computer. These readily accessible simulators generate independent, uniformly distributed random numbers i.e., samples of a single random variable X with a uniform, univariate distribution (e.g. Press et al., 1992). If X is not uniformly distributed it is a relatively easy task to transform these random numbers such that they follow any other desired univariate distribution.

The simplest case of a random field variable (random process) is an orthogonal RFV, which consists of random univariate samples at each location. This can be implemented easily with any good random number generator. A particular challenge arises, however, when the random variables $X_i=X(x_i)$, $X_j=X(x_j)$ $(i\neq j)$ are dependent i.e., when they are (spatially) correlated and defined through a joint or multivariate distribution. Not only do the generated random fields have to converge in the mean square to the desired ensemble mean and variance (and any

higher order moments if appropriate), they also have to converge in the mean square to the desired correlation structure as the number of samples increases. In this chapter, algorithms are introduced that generate such random fields.

In practice the joint probability distribution function is often inferred from field data obtained at the site of interest. The joint probability distribution is commonly described by invoking the ergodicity and stationarity hypotheses discussed in the previous chapter and by taking the sample mean and sample variance-covariance functions as the moments of the underlying multivariate pdf. To take full advantage of the field data the simulations must be conditioned on the information known about the particular points in space, where measurements were taken. This amounts to the generation of random variables with a conditional joint probability distribution function. The ensemble of conditional realizations is a subset of the ensemble of unconditional realizations. The conditional subset consists of all those samples in the unconditional set, that preserve the known data at the measured locations. As shown in the previous chapter the conditional joint distribution of the random variables is different from the unconditional multivariate pdf. The generation of conditional random fields therefore needs to go beyond the capabilities of an unconditional random field generator.

In this chapter several popular random field generators (RFGs) are described and compared. Random number generators (RNGs) are also tested. First an unconditional two-dimensional random field generator based on spectral representation and a fast Fourier transform is introduced. A conditioning method based on kriging estimation is presented next. The statistical performance of the spectral random field generator (SRFFT) is compared with the turning band method (TB), the matrix decomposition method (LU) and the sequential Gaussian simulation method (S). The numerical efficiency of these RFGs has been assessed elsewhere (Tompson et al., 1989).

3.2 (Unconditional) Two-Dimensional Random Field Generation by the Spectral Method

The purpose of a random field generator is to transform an orthogonal realization consisting of independently generated random numbers with a prescribed univariate distribution into a correlated random field with the desired joint probability distribution. If the distribution is Gaussian, the joint pdf is expressed by its first two moments, the mean and the covariance. In the previous chapter a transformation was introduced that is ideally suited for building a random field generator: the spectral representation dZ of a correlated RFV X is itself an RFV of independent random variables with a variance defined by the spectral density function of X, $S(\mathbf{k})\,d\mathbf{k}$. Recall that the spectral density $S(\mathbf{k})$ of X is the Fourier transform of the covariance function $C(\xi)$ of X where ξ is the separation distance. Hence, if random, zero-mean $dZ(\mathbf{k})$ are generated with a variance $S(\mathbf{k})\,d\mathbf{k}$ then their inverse Fourier transform yields a correlated random field with $X(\mathbf{x})$ that have zero-mean and the desired covariance function by virtue of (2-51). Random field generators based on Fourier transforms have first been introduced by Shinozuka (1972, 1991). Gutjahr (1989) describes a two-dimensional random field generator based on a fast Fourier transform algorithm, which has been adopted for our study.

In the previous chapter the spectral representation of a continuous, infinitely large random field was defined. In the numerical generation of random fields, however, one is limited both in the extent of the random field and in the number of points generated. Hence, (2-51) must be restated to accommodate *finite* random fields defined on a countable number of *discrete* grid-points. The following derivations are specifically for two-dimensional random fields. But the extension to higher dimensional random fields should be obvious and is straight forward.

For the purpose of this study realizations are generated on a rectangular domain defined over a regular grid centered around the origin with gridpoints being $\Delta\mathbf{x} = (\Delta x_1, \Delta x_2)^T$ apart. The

size of the domain is defined by M Δx such that the rectangle spans the area between $-M\Delta x$ and $(M-1)\Delta x$ and the number of gridpoints in the random field is 2M by 2M. Since the spectral representation of a stationary random field is only defined for an infinite domain, it is further assumed that the random field is periodic with period 2M in both dimensions. This has no direct impact on the generated random field. But it is a necessary assumption for the formal derivation of its spectral representation, because the analysis of an infinite process can be used for the generation of a finite random field. There is another reason for choosing the assumption of periodicity (after all, any other values for the random field outside $[-M\Delta x, (M-1)\Delta x]$) could have been assumed): Periodic functions are known to have a discrete rather than a continuous spectrum i.e., only a discrete set of frequencies contributes to the spectral representation of the periodic stationary random field. Hence, $dZ(\mathbf{k})$ exists only for discrete $\mathbf{k}$, for which it can be generated such that $\langle dZ(\mathbf{k})\rangle = 0$ and $\langle |dZ(\mathbf{k})|^2\rangle = S(\mathbf{k})\, d\mathbf{k}$.

The discretization of $X(x)$ limits the wavelengths "seen" by the discrete random field to all those that are at least of length $2\Delta x$ i.e., to all (angular) frequencies $\mathbf{k} \leq 2\pi/(2\Delta x)$. Higher frequencies cannot be distinguished from frequencies within this limit, an effect referred to as "aliasing". In other words, heterogeneities on a scale smaller than the discretization Δx are not resolved by the random field. Similarly, the longest possible wavelength "seen" by a finite random field is less than or equal to $2M\Delta x$ i.e., the lowest (angular) frequency is $\Delta \mathbf{k} = 2\pi/(2M\Delta x)$, and all other frequencies $\mathbf{k}$ must be multiples of $\Delta \mathbf{k}$. Hence, the spectral representation $dZ(\mathbf{k})$ of a finite, discrete random field $X(x)$ with $(2M)^2$ gridpoints in 2-D space is also a finite, discrete random field defined on a $(2M)^2$ grid in the 2-D frequency domain. Note that the discretization in $X(x)$ determines the size of the field of $dZ(\mathbf{k})$, while the finite size of $X(x)$ determines the discretization of $dZ(\mathbf{k})$. For discrete $dZ(\mathbf{k})$ the Fourier-Stieltjes integral (2-49) becomes a Fourier series such that

$$X(\mathbf{x}_n) = \sum_{m=-M}^{M-1} \sum e^{i\mathbf{k}_m \mathbf{x}_n} z(\mathbf{k}_m) \qquad (3\text{-}1)$$

where $z(\mathbf{k})$ are (complex valued) random Fourier coefficients with the same properties as $dZ(\mathbf{k})$ in (2-49), namely zero-mean, a variance $\sigma^2_{z(\mathbf{k})} = S(\mathbf{k})\,\Delta\mathbf{k}$, and all $z(\mathbf{k})$ independent for $\mathbf{k}_1 \neq \mathbf{k}_2$.

To ensure that $X(\mathbf{x})$ is a real valued random field, the $z(\mathbf{k})$ field must be constructed such that

$$z(-\mathbf{k}) = z^*(\mathbf{k}) \qquad (3\text{-}2)$$

i.e., random numbers $z(\mathbf{k})$ need only be generated for one half the size of the rectangle. The * stands for complex conjugate. Complex valued, Gaussian distributed $z(\mathbf{k})$ for discrete $\mathbf{k}_j$, $j=1,(2M)^2/2$ are obtained by generating two independent Gaussian random numbers α_j and β_j for each $\mathbf{k}_j$, each with zero-mean and variance ½, and construct

$$z(\mathbf{k}_j) = (S(\mathbf{k}_j)\,\Delta\mathbf{k})^{1/2}\,\frac{(\alpha_j + i\beta_j)}{2} \qquad (3\text{-}3)$$

for one half of the random field. The other half of the random field is obtained through the symmetry relation (3-2). It can be shown by inspection that the above construction of $z(\mathbf{k})$ satisfies the required properties (Gutjahr et al., 1989). After constructing a field $z(\mathbf{k})$ by the above method, which merely requires the generation of independent Gaussian distributed random numbers, the correlated random field $X(\mathbf{x})$ is obtained by performing the Fourier summation (3-1).

The double summation in (3-1) is most efficiently done by a numerical Fourier transform technique called the "Fast Fourier transform" or simply FFT (Brigham, 1988). FFT algorithms can be found in many computer libraries (e.g. IBM, 1993) and are described in books on numerical mathematics (e.g. Press et al., 1992). It suffices to say that FFT algorithms essentially perform a transformation as (3-1), but in a computationally very efficient manner.

Most available FFT algorithms are written using the frequency **u** as argument instead of the angular frequency **k**, where $\mathbf{k} = 2\pi\mathbf{u}$. Recall the following definitions of Fourier transform pairs from chapter 2:

$$C(\mathbf{x}_j) = \int_{-\infty}^{\infty}\int_{-\infty}^{\infty} e^{i\mathbf{k}\xi}\, S(\mathbf{k})\, d\mathbf{k} \tag{3-4}$$

$$S(\mathbf{k}) = \frac{1}{(2\pi)^2}\int_{-\infty}^{\infty}\int_{-\infty}^{\infty} e^{i\mathbf{k}\xi}\, C(\xi)\, d\xi \tag{3-5}$$

$$X(\mathbf{x}) = \int_{-\infty}^{\infty}\int_{-\infty}^{\infty} e^{i\mathbf{k}\xi} dZ(\mathbf{k}) \tag{3-6}$$

$$dZ(\mathbf{k}) = \frac{1}{(2\pi)^2}\int_{-\infty}^{\infty}\int_{-\infty}^{\infty} e^{i\mathbf{k}\xi}\, X(\mathbf{x})\, d\mathbf{x} \tag{3-7}$$

Changing the variables of integration from **k** to **u**, where $d\mathbf{k} = 2\pi d\mathbf{u}$, the above transform pairs become:

$$C(\xi) = (2\pi)^2 \int_{-\infty}^{\infty}\int_{-\infty}^{\infty} e^{i2\pi\mathbf{u}\xi}\, S(2\pi\mathbf{u})\, d\mathbf{u} \tag{3-8}$$

$$S(2\pi\mathbf{u}) = \frac{1}{(2\pi)^2}\int_{-\infty}^{\infty}\int_{-\infty}^{\infty} e^{-i2\pi\mathbf{u}\xi}\, C(\xi)\, d\xi \tag{3-9}$$

$$X(\mathbf{x}) = \int_{-\infty}^{\infty}\int_{-\infty}^{\infty} e^{i2\pi\mathbf{u}\mathbf{x}}\, dZ(2\pi\mathbf{u}) \tag{3-10}$$

$$dZ(2\pi \mathbf{u}) = \frac{1}{(2\pi)^2} \int_{-\infty}^{\infty}\int_{-\infty}^{\infty} e^{i 2\pi \mathbf{ux}} X(\mathbf{x})\, d\mathbf{x} \qquad (3\text{-}11)$$

Typical FFT algorithms also require that the summation in (3-1) is over the interval [0,2M-1] rather than over the interval [-M,M-1]. Using the periodicity assumption $z(m\,\Delta\mathbf{k})$, $m > M-1$, are obtained from:

$$z(m\Delta\mathbf{k}) = z((m-2M)\Delta\mathbf{k}), \qquad \text{all } m > M-1 \qquad (3\text{-}12)$$

Recalling that $\Delta\mathbf{k} = (2\pi)/(2M\Delta\mathbf{x})$ this leads to the following construction of the correlated random field $X(\mathbf{x})$ with entries $X(n_1\,\Delta x_1,\, n_2\,\Delta x_2)$, $0 \le n_1, n_2 \le 2M-1$:

$$X(n_1\Delta x_1, n_2\Delta x_2) = \sum_{m_1=0}^{2M-1}\sum_{m_2=0}^{2M-1} \exp\left(i\frac{2\pi\, m_1 n_1}{2M}\right) \exp\left(i\frac{2\pi\, m_2 n_2}{2M}\right) z(m_1,m_2) \qquad (3\text{-}13)a$$

where

$$z(m_1,m_2) = \left[\frac{2\pi}{2M\Delta x_1}\,\frac{2\pi}{2M\Delta x_2}\, S\left(\frac{2\pi\, m_1}{2M\Delta x_1}, \frac{2\pi\, m_2}{2M\Delta x_2}\right)\right]^{1/2} (\alpha_{m_1,m_2} + i\beta_{m_1,m_2}) \qquad (3\text{-}13)b$$

with α and β being zero-mean, independent, Gaussian distributed random numbers of variance ½. For this study, random fields are generated using (3-13) with the SCFT2 subroutine in the ESSL Fortran library to perform the FFT (IBM, 1993), and with the GAUSDEV and RAN2 subroutines from Press et al. (1992) to generate the random numbers α and β. The original implementation of this random field generator was generously provided by Allan Gutjahr (1989).

3.3 Conditional Two-Dimensional Random Fields

Assume an array of measurements $\mathbf{X}_1 = \{x_1,...,x_m\}$ is available and a two-dimensional conditional random field must be generated such that at locations $\{\mathbf{x}_1,...,\mathbf{x}_m\}$ the measured value

of the random variables $\mathbf{X}_1$ are reproduced with probability 1, and such that at all other locations $\{x_{m+1},...,x_n\}$ the generated random numbers $\mathbf{X}_2 = \{x_{m+1},...,x_n\}$ have a sample mean and sample covariance that converge in the mean to the conditional mean $\langle \mathbf{X}_2 \rangle^c$ and conditional covariance $\mathbf{E}_{22}$ (see section 2.5.3), respectively, in the limit as the number of random fields generated becomes infinite.

To implement the conditional random field generation, Delhomme (1979) used the following approach based on work by Matheron (1973) and Journel (1974, 1978): Initially, the measured data $\mathbf{X}_1$ are used to infer the moments (mean and covariance) of the unconditional joint pdf of the random field. Then an estimate of the conditional mean $\langle \mathbf{X}_2 \rangle^k$ is obtained by simple kriging (best linear unbiased estimate of the conditional mean, see section 2.5.3). The kriging weights Λ and the estimated conditional mean $\langle \mathbf{X}_2 \rangle^k$ are retained for the subsequent generation of conditional random fields $\mathbf{X}_s^c$, which are constructed through the following relationship:

$$\mathbf{X}_s^c = \langle \mathbf{X} \rangle^k + (\mathbf{X}_s - \langle \mathbf{X}_s \rangle^k) = \langle \mathbf{X} \rangle^k + \mathbf{e}_w \qquad (3\text{-}14)$$

where $\langle \mathbf{X} \rangle^k$ is the kriged random field given the simulated data $\mathbf{X}_{1s}$ from the unconditionally generated random field $\mathbf{X}_s$. $\mathbf{X}_s$ has a joint probability distribution defined by the measured moments. $\langle \mathbf{X}_s \rangle^k$ is the simulated equivalent to $\langle \mathbf{X} \rangle^k$: It preserves the data $\mathbf{X}_{1s}$ in the unconditionally generated random fields at and only at the locations $\{x_1,...,x_m\}$, where measurements are available in the real field site as well, and of the kriged estimates $\langle \mathbf{X}_{2s} \rangle^k$ at all other locations $\{x_{m+1},...,x_n\}$ given the unconditionally simulated data $\mathbf{X}_{1s}$. The difference $(\mathbf{X}_s - \langle \mathbf{X}_s \rangle^k)$ is a realization $\mathbf{e}_s$ of a possible estimation error incurred by estimating the data $\mathbf{X}_s$ through the kriged values $\langle \mathbf{X}_s \rangle^k$. The simulated error is added to the originally estimated conditional mean $\langle \mathbf{X} \rangle^k$ to obtain a possible conditional random field $\mathbf{X}_s^c$.

The simulated estimation error $\mathbf{e}_s$ has the same conditional moments as the real estimation error $\mathbf{e} = (\mathbf{X} - \langle \mathbf{X} \rangle^c)$ because the unconditional pdfs of the real and the simulated

fields are identical (neglecting the possibility of measurement and moment estimation errors), and because the conditioning occurs at the exact same locations both at the field site and in the simulations (Journel, 1974; Delhomme, 1979). Recall from (2-48) that the conditional covariance or error covariance $\mathbf{E}_{22}$ depends only on the location of the conditioning points $\mathbf{x}_1$ and on the unconditional covariance C, but not on the actual value of the conditioning data $\mathbf{X}_1$!

The unconditional random field generation and the kriging of the generated random field from the simulated measurement data are repeated for each realization. Each simulation will yield a random field of estimation errors $\mathbf{e}_s$, which can be added to the kriging estimate of the real data to obtain a conditional random field. For a large number of samples thus obtained, the sample variance of $\mathbf{X}_{2s}(\mathbf{x}_2)$ will converge in the mean square to the true conditional variance or kriging variance of $\mathbf{X}_2(\mathbf{x}_2)$ as shown by Delhomme (1979). It is obvious that this conditioning technique is independent of the method used to generate the unconditional random field and is as such unrelated to the spectral random field generator. The advantages of using this method together with the spectral random field generator will be discussed in chapters 7 and 10.

3.4 Alternative Methods of Random Field Generation

3.4.1 Turning Bands Method

The turning bands method was first proposed by Matheron (1973) to simulate unconditional random fields. Detailed descriptions of the turning bands method can be found elsewhere (e.g. Mantoglou and Wilson, 1982; Brooker, 1985; Mantoglou, 1987; Tompson et al., 1989). For completeness, a brief outline of the structure of the turning band method is given.

The principal advantage of the method is that it reduces the generation of a two- or three-dimensional, random, spatially correlated process to the generation of one-dimensional,

correlated line processes. The reduction in dimensionality is made possible by the fact that the transformation from a 3- or 2-dimensional covariance function into an equivalent one-dimensional covariance function can be uniquely defined (Matheron, 1973; Mantoglou and Wilson, 1982). After determining the equivalent 1-dimensional covariance, a one-dimensional, multivariate process Y(x) can be generated along a finite line by using an appropriate autoregressive or moving average algorithm (Bras and Rodriguez-Iturbe, 1985) or 1-dimensional spectral methods similar to the one described above (Mantoglou, 1987). To obtain the 2-dimensional random field, the one-dimensional simulation is repeated on a total of 16 (or more) equally spaced lines intersecting at their midpoints. Each of these lines is divided into small, discrete intervals of equal size. One random number is generated for each interval. The random value X(x) of a realization at any point x is computed by averaging the 16 corresponding line values:

$$X(x) = \frac{1}{\sqrt{16}} \sum_{j=1}^{16} Y(x_j, j) \qquad (3\text{-}15)$$

where j is the line number and x_j is located on line j such that x is orthogonal to x_j with respect to line j.

Conditional simulations with the turning bands method were among the first in hydrologic applications (Delhomme, 1979) and the method used is identical to the one described in section 3.3. for the spectral random field generator, since the actual conditioning is independent of the method used for unconditional random field generation.

3.4.2 Matrix Decomposition

3.4.2.1 Unconditional Simulation by Matrix Decomposition

An elegant approach to simulating unconditional as well as conditional random fields

is the matrix decomposition method (Clifton and Neuman, 1982; Davis, 1987; Alabert, 1987). Again, it is assumed that a valid unconditional covariance model is given (satisfying the conditions stated for (2-28)). The covariance between each two points in the random field domain is computed prior to the random field generation and stored in an unconditional symmetric covariance matrix C. For a random field consisting of n points, C has a dimension of n^2. Furthermore, it is assumed that the unconditional expected value $\langle X(x) \rangle$ is zero. Using, for example, the Cholesky algorithm for symmetric, positive definite matrices, the covariance matrix can be decomposed into a lower triangular matrix L and an upper triangular matrix U:

$$C = L\,U \qquad L = U^T \text{ (^{T} indicates the transpose operator)} \tag{3-16}$$

The product of the lower matrix L and a vector α of random, uncorrelated, univariate normally distributed random numbers α_i, i=1,...,n with zero mean and unit variance will then give a simulated random field X_s with the desired mean and covariance:

$$L\,\alpha = X_s \tag{3-17}$$

Proof :

$$\langle X_s \rangle = \langle L\,\alpha \rangle = L\,\langle \alpha \rangle = 0 \tag{3-18}$$

$$C_s = \langle X_s\,X_s^T \rangle = \langle L\,\alpha\,(L\,\alpha)^T \rangle =$$

$$\langle L\,\alpha\,\alpha^T\,L^T \rangle = L\,I\,U = L\,U = C \tag{3-19}$$

(I is the identity matrix)

After generating and decomposing the covariance matrix C once, any new realization of X is simply obtained by generating a new sample of the random vector α, which can easily be done with any good random number generator. Note that the method is independent of the dimensionality of the random field and that the covariance need not be stationary. Only 1st order (mean) stationarity is required for this method.

3.4.2.2 Conditional Simulation by Matrix Decomposition

The procedure can readily be extended to implement conditional simulations (Clifton and Neuman, 1982; Davis, 1987). Again $\mathbf{X}_1$ is a vector of known data-values and $\mathbf{X}_{2s}$ are the unknown random values that are conditionally simulated. The covariance matrix and its decomposition (3-16) is expanded in the following form:

$$\mathbf{C} = \begin{bmatrix} \mathbf{C}_{11} & \mathbf{C}_{12} \\ \mathbf{C}_{21} & \mathbf{C}_{22} \end{bmatrix} = \begin{bmatrix} \mathbf{L}_{11} & \mathbf{0} \\ \mathbf{L}_{21} & \mathbf{L}_{22} \end{bmatrix} \begin{bmatrix} \mathbf{U}_{11} & \mathbf{U}_{12} \\ \mathbf{0} & \mathbf{U}_{22} \end{bmatrix} \tag{3-20}$$

that is, the following four equations:

$$\mathbf{C}_{11} = \mathbf{L}_{11}\,\mathbf{U}_{11} = \mathbf{L}_{11}\,\mathbf{L}_{11}^{T} \tag{3-21a}$$
$$\mathbf{C}_{12} = \mathbf{L}_{11}\,\mathbf{U}_{12} = \mathbf{L}_{11}\,\mathbf{L}_{21}^{T} \tag{3-21b}$$
$$\mathbf{C}_{21} = \mathbf{L}_{21}\,\mathbf{U}_{11} = \mathbf{L}_{21}\,\mathbf{L}_{11}^{T} \tag{3-21c}$$
$$\mathbf{C}_{22} = \mathbf{L}_{21}\,\mathbf{U}_{12} + \mathbf{L}_{22}\,\mathbf{U}_{22} \tag{3-21d}$$

and as shown for the unconditional simulation (3-17):

$$\begin{bmatrix} \mathbf{L}_{11} & \mathbf{0} \\ \mathbf{L}_{21} & \mathbf{L}_{22} \end{bmatrix} \begin{bmatrix} \alpha_1 \\ \alpha_2 \end{bmatrix} = \begin{bmatrix} \mathbf{X}_1 \\ \mathbf{X}_{2s}^{c} \end{bmatrix} \tag{3-22}$$

However, $\mathbf{X}_1$ is known and α_1 need not be generated! Instead, the values α_1 are computed by solving the first of the two equations in the matrix (3-22):

$$\alpha_1 = \mathbf{L}_{11}^{-1}\,\mathbf{X}_1 \tag{3-23}$$

where $\mathbf{L}_{11}$ and $\mathbf{X}_1$ are given. α_2 is generated in the same way as α in the unconditional simulation. Then the conditional values $\mathbf{X}_{2s}^{c}$ are computed by solving the second of the the two equations in (3-22):

$$\mathbf{L}_{21}\,\alpha_1 + \mathbf{L}_{22}\,\alpha_2 = \mathbf{X}_{2s}^{c} \tag{3-24}$$

The procedure is further simplified by expressing all terms in (3-24) as functions of $\mathbf{L}_{11}$, the covariance submatrices of C, and the known data array $\mathbf{X}_1$:

$$\mathbf{L}_{21} = \mathbf{C}_{21}\,\mathbf{U}_{11}^{-1} = (\mathbf{U}_{11}^{-1})^{T}\,\mathbf{C}_{12}^{T} = \mathbf{L}_{11}^{-1}\,\mathbf{C}_{12} \tag{3-25}$$

$$L_{22}\,U_{22} = C_{22} - L_{21}\,U_{12} = C_{22} - L_{11}^{-1}\,C_{12}\,(L_{11}^{-1}\,C_{12})^T \qquad (3\text{-}26)$$

Collecting (3-23), (3-25), and (3-26) in (3-24), the conditional simulation becomes:

$$X_{2s} = L_{11}^{-1}\,C_{12}\,L_{11}^{-1}\,X_1 + L_{22}\,\alpha_2 \qquad (3\text{-}27)$$

Thus, the initial steps to conditional simulation are:

1. decompose C_{11},
2. invert the resulting matrix L_{11}, and
3. decompose (3-26) in order to obtain L_{22}.

Once all these matrices are determined, new realizations of conditional X_{2s}^c are obtained by simply generating new α_2 with a Gaussian random number generator and solving (3-27). It can be shown that the moments of X_{2s}^c are exactly the conditional moments defined in (2-46) and (2-48) (Alabert, 1987; Harter, 1992).

As an alternative to the above approach, Clifton and Neuman (1982) suggested to obtain the kriging estimate X_2^k of the points to be simulated. Then an error e_s with covariance $E_{22} = (L_{22}\,U_{22})$ is generated taking advantage of the matrix decomposition method introduced in (3-17):

$$L_{22}\,\alpha_2 = e_s \qquad (3\text{-}28)$$

Although based on the same theoretical foundation as the suggestion by Alabert (1987), just one matrix (E_{22}) needs to be decomposed instead of 2 as outlined in (3-27). However, C_{11} must be inverted to obtain the kriging weight matrix Λ_{12} and the kriging estimates X_2^k (2-46). (3-28) is very general in that its application is not limited to simple kriging. Ordinary or universal kriging estimates with the ordinary or universal kriging covariances can be applied as well as others e.g., Bayesian estimates for inverse modeling (the latter was implemented by Clifton and Neuman, 1982).

3.4.3 Gaussian Sequential Simulation

Sequential simulation was first implemented by Journel and Gomez-Hernandez (1989). Their version of the sequential simulator was specifically designed to generate stationary random fields with a non-parametric probability distribution ("indicator simulation"). Gomez-Hernandez (1991) presented a sequential simulator for the generation of multivariate normal random fields. The Gaussian simulation technique goes back to the definition of unconditional and conditional probabilities (2-42) and (2-43): Rearranging equation (2-43), the joint probability $f_X(x_1,x_2,...,x_n)$ is expressed as a function of the marginal distribution of the known data $x_1,....x_m$ and the conditional distribution of the unknown RVs $X_{m+1},..., X_n$:

$$f_X(x_1,x_2,..x_m,x_{m+1},...,x_n) = f_X(x_{m+1},xm+2,...,x_n|x_1,x_2,...,x_m)\ f_X(x_1,x_2,...,x_m) \qquad (3\text{-}29)$$

The equation is expanded into a sequence of lower order conditional probability terms:

$$\begin{aligned} &f_X(x_1,x_2,...x_m,x_{m+1},...,x_n) = \\ &f_X(x_n|x_1,x_2,....,x_{n-1})\ f_X(x_{n-1}|x_1,x_2,....,x_{n-2})\ f_X(x_{n-2}|x1,x2,....,x_{n-3}) \\ &.....f_X(x_{m+1}|x_1,x_2,....,x_m)\ f_X(x_1,x_2,...,x_m) \end{aligned} \qquad (3\text{-}30)$$

It is this form of the joint probability density function, which gives rise to the sequential simulator: The conditional probability function of each $f_X(x_{m+i}|x_1,...,x_m,x_{m+1},...,x_{i-1})$, $m < m+i \leq n$, can be expressed as a product of (i-1) **univariate** conditional density functions and the unconditional density function of the known data $x_1,...,x_m$. Hence the simulation algorithm for a realization is the following:

1. select a datapoint x_{m+1}^c to be generated,
2. find the conditional density for that datapoint given the measured data $x_1,...,x_m$ and draw

from it x_{m+1}^c,

3. select a second datapoint x_{m+2}^c to be generated,

4. find the conditional density for that datapoint given the measured data $x_1,...,x_m$ **and** given the already generated datapoint x_{m+1}^c and draw from it x_{m+2}^c,

5. repeat the procedure until a conditional sample has been drawn for all points.

For each realization, steps 1.-5. are implemented independently. The procedure as such is entirely general and can be applied to any random process.

The procedure is again illustrated for the multivariate normal, stationary, zero-mean random process. Specifically it is shown how 'to draw [a random number x_{m+i}] from [a univariate conditional] density function' (Gomez-Hernandez, 1991, p.42). First, the moments of the univariate conditional density function $f_X(x_{m+i}|x_1,...,x_m,x_{m+1},...,x_{m+i-1})$, $m < m+i \leq n$, must be specified. By definitions (2-46) and (2-48), the conditional mean and covariance are given by the kriging estimate x_{m+i}^k and the kriging covariance E_{ij}. The kriging estimate x_{m+i}^k is computed from **both** measured $x_1,...,x_m$ **and** already generated data $x_{m+1}^c,...,x_{m+i-1}^c$:

$$X_{m+i}^k = \Sigma\ \lambda_{ij} X_i + \Sigma\ \Lambda_{il} X_l \qquad j = 1,...,m;\ \ l = m+1,...,m+i- \tag{3-31}$$

As the conditional density is univariate, only the kriging variance E_{ii} (2-48) is relevant:

$$E_{ii} = \sigma^2_X - \Sigma\ C_{il}\ \lambda_{li} \qquad k = 1,...,m,...,m+i-1 \tag{3-32}$$

The important difference between this and all previously described methods is that a **univariate** conditional random variable is generated, which by definition renders the consideration of the error **co**variance i.e., the spatial correlation structure of the error, superfluous. $X_{(m+i)s}^c$ is simulated by first obtaining the kriging estimate X_{m+i}^k and then adding a random error $e_{(m+i)s}$, which is drawn from a zero-mean, univariate normal distribution with variance E_{ii} (3-32):

$$X_{(m+i)s} = X^{k}_{m+i} + e_{(m+i)s} \tag{3-33}$$

No covariance matrices are involved in the generation of the error $e_{(m+i)s}$ thus reducing the task of random field generation to generating independent, univariate random numbers.

Note that the procedure can be equally applied to unconditional simulation and conditional simulation. In unconditional simulations, the first point is generated as an independent random variable with the desired unconditional mean and variance. A second datapoint is generated conditioned on the first one in the manner described by (3-33), and so on. In a conditional simulation the generation of random fields begins with the already measured data. Subsequent datapoints are generated as in an unconditional simulation through the conditional relationship (3-33). For further details of the method, see Gomez-Hernandez (1991).

3.5 Performance Analysis of the SRFFT, LU, TB, and S Random Field Generators

3.5.1 Design of the Performance Analysis

Random field generators must generate truly independent realizations X(x) of an RFV such that the sample joint probability distribution of the random field realizations converges in mean square to the desired ensemble probability distribution (the pdf of the assumed probability space) in the limit as the number of realizations becomes infinite. Generally, two conditions must be fulfilled for a random field generator to give statistical results that converge in the mean to the desired ensemble moments of the RFV:

1. the random number generator (RNG) must be able to generate independent normally distributed random numbers with given mean μ and variance σ^2 in the limit as the

sample size becomes large.

2. the numerical implementation of the random field generator (RFG) must be free of deterministic artificial patterns caused by the generating algorithm.

The first condition can be tested separately and should be tested prior to a performance analysis of a random field generator. Random number generators are common in many scientific programming libraries. Two random number generators are tested both of which produce independent random samples distributed uniformly between 0 and 1: the random number generator SURAND in the Engineering and Scientific Subroutine Library (ESSL) available with the Fortran compilers for IBM workstations (IBM, 1993) and the random number generator program RAN2 described by Press et al. (1992). The normally distributed random numbers are obtained after a transformation achieved through the subroutines SNRAND (IBM, 1993) and GAUSDEV (Press et al., 1992) both of which use the Box-Muller method to obtain a normal deviate from a uniform deviate (Knuth, 1981).

Random number generators are not truly random. They rely on a deterministic formula to generate a new random number. Both random number generators tested are based on a congruential algorithm which algebraically alters a given number. Initially this number is directly or indirectly supplied by the user. In subsequent generations within the same program execution the number is taken from the preceding generation of a random number (Knuth, 1981). Sparing the details of the algorithms, note that one of the most important properties of good random number generators is the independence of subsequently generated random numbers and the time to recurrence i.e., the number of random numbers generated before any previously generated random number is generated a second time. Once the seed to a random number is regenerated the second time, the following sequence of random numbers will be exactly the

same as the sequence of random numbers generated after the first occurrence and hence will repeat itself *ad infinitum*. Since all computers have finite accuracy, they can only generate a finite number of different discrete numbers. Thus, every random number generator will eventually generate a random number that has already occurred before. The length of the random number sequence to the first recurrence is desired to be large, much larger than the number of samples actually generated in an application to assure the independence of the samples. Theoretically, infinite sequences can be achieved by appropriately shuffling small parts of the sequence (Press et al., 1992). For SURAND and RAN2 no recurrence of the initial seed was found within the following 10^{12} numbers, after which the test was interrupted.

A number of methods exist to test random number generators (Knuth, 1981). Sharp and Bays (1992) test the independence of consecutive random numbers by plotting the two-dimensional coordinates given by any two consecutive random numbers as dots into a map (see Orr, 1993). Biasedness can then often be discovered (although not always) if certain patterns develop. Unbiased uniform random number generators should fill such a map evenly. Figure 3.1 shows a sample of 20000 pairs generated with SURAND and RAN2. There is no obvious artificial pattern in the samples and - at least qualitatively - they are indeed from a uniform distribution. The CPU-times of both random number generators are comparable. In cooperation with Orr (see Orr, 1993) three other congruential random number generators were tested with similar results: DPRAND by Maclaren (1992), which is a portable random number generator like RAN2, and the random number generators in the IMSL library (1991) and NAG library (1990).

All five random number generators are tested by the author within the spectral random field generator (original FORTRAN code provided by Gutjahr, 1989) and within the LU-

decomposition based random field generator (FORTRAN code developed by the author) and as shown below, no specific bias was detectable due to the random number generator.

In this study the spectral random field generator is used for reasons that will become obvious in chapter 7. To assure its proper performance a large Monte Carlo simulation with 1000 samples was performed on a square grid with 64^2 gridpoints. The mean μ and variance σ^2 are 0 and 1, respectively. The covariance is isotropic and exponential (Isaacs and Srivastava, 1990):

$$C(\xi) = \sigma^2 \exp(-\frac{|\xi|}{\lambda}) \qquad (3\text{-}34)$$

where λ is a parameter called the "integral scale" of the covariance function and is here specified to be five gridpoint increments, a commonly chosen discretization of the random field. Commonly, the integral scale is referred to as the "correlation length" or "correlation scale" of C. For comparison, an equivalent Monte Carlo simulation is performed with a LU-decomposition based random field generator. Both the SRFFT and the LU Monte Carlo simulation are performed once with each of the five random number generators. Orr (1993) provided test-results from identically implemented TB and S Monte Carlo simulations using the DPRAND random number generator. The turning bands method is based on FORTRAN code by Zimmermann and Wilson, 1990. The sequential simulator in C code has been provided by Gomez-Hernandez (1991).

For the evaluation of the Monte Carlo simulations, a postprocessor was developed that is designed to collect the following sample moments:

* (spatial) mean and variance of each realization by summing over all values in a realization.

* (spatial) sample covariance of each realization by inverting the procedure of the spectral random field generator: take a Fourier transform of the realization X(x) to obtain the spectral representation dZ(k), take the expected value of the spectral representation with its conjugate to obtain the spectral density function, and compute the spatial sample covariance from the inverse Fourier transform of the sample spectral density function (Gutjahr, 1989).

* (local) mean and variance at location l as a function of the number of realizations (10, 20, 50, 100, 200, 500, and 1000 samples).

* (local) sample covariance at point l by performing the following summation over all N realizations for N=10, 20, 50, 100, 200, 500, and 1000 samples:

$$Cov_l(k) = \frac{1}{N}\sum_{n=1}^{N} X_l^n X_k^n - \frac{1}{N}\sum_{n=1}^{N} X_l^n * \frac{1}{N}\sum_{n=1}^{N} X_k^n \qquad (3\text{-}35)$$

where here n is an index to X and not a power of X. The points k surrounding the point l consist of all the points in a squared window of side-length 32 (33 points) centered on point l. This summation was implemented only for the 31 by 31 points in the center of the 64^2 grid. This sampling pattern avoids problems with boundaries and allows the evaluation of the local sample covariance on a complete squared window.

The sample moments are further evaluated statistically to give several summary moments:

* the average of the spatial means of each realization (which is exactly equal to the spatial average of the local means) gives the total mean of all numbers generated in the Monte Carlo simulation and must converge in the mean square to zero as the number of realizations (samples) increases.

* the average of the spatial variances is expected to be smaller or equal to the local

variances (due to spatial correlation), and the spatial average of the sample local variances must converge in the mean square to the desired local ensemble variance as the number of runs in the Monte Carlo simulation increases.

* the average of the local sample covariances (over all locations) must converge in the mean square to the desired exponential covariance function. Like the average spatial variance, the average of the spatial sample covariances is expected to be smaller or equal to the specified covariance. The average spatial covariance normalized by the average spatial variance, however, must be equal to the specified (normalized) exponential covariance function. The deviation of the average local covariance function from the specified exponential covariance function is computed. The local deviations are integrated over the entire domain of the two-dimensional covariance to obtain a mean deviation from theoretical covariance. Given the set of 31^2 local covariances, each of which is a 33^2 point two-dimensional field, the variance of the sample local covariance is calculated as a function of the separation point k and integrated over all k to obtain the average variance of the local covariance.

* the minimum and maximum of all local or spatial moments give a range of possible sample moments. The range is expected to decrease as the number of samples in the Monte Carlo simulation increases.

3.5.2 Summary Performance of the RNGs and RFGs

First, the summary moments are evaluated from the Monte Carlo simulations with the spectral (SRFFT) and the LU-decomposition (LU) random field generators (RFGs) using the

five different random number generators (RNGs) mentioned above.

Figure (3.2a) shows the total sample mean as a function of the number of SRFTT Monte Carlo realizations (NMC) for each of the five random number generators. The differences in sample means shown for the different RNGs reflects the sample moment variability, since each RNG generates a different sequence of random realizations. Initially, the differences are large due to the limited number of samples. Note that although there are 64^2 = 4096 samples of random numbers within each realization, these 4096 samples are not independent of each other and the spatial sample mean does not converge to the ensemble mean as fast as that of NMC * 4096 uncorrelated random samples. With all five random number generators the total sample mean (spatial mean of the local sample means) converges to zero as the number of realizations increases. A very similar behavior is seen in the total mean of the LU generator (Figure 3.3a). The convergence rate of the different RNG-based Monte Carlo simulations is the same for both random field generators: after 10 realizations the total sample mean varies within the range [-0.1, 0.1]; after 100 realizations the range decreases to [-0.025, 0.025]; and after 1000 realizations it reaches the limits [-0.01, 0.01]. No particular bias (i.e. numerical artifact) is found in any of the five RNGs with any of the two RFGs regarding the total sample mean. The decrease in the range of the sample mean is consistent with the theoretical decrease of the variance of the sample mean as a function of the sample size (Haan, 1977; see chapter 8).

Both the average of local sample variances and the average of the spatial sample variances converge (in the mean square sense) to the ensemble variance specified as the number of realizations becomes large (Figures 3.2c, 3.3c). Due to the spatial correlation the mean spatial variance is approximately 5% lower than the mean local variance with both the

SRFFT and LU generators. Unexpectedly, however, it is found that the mean local variance for all five RNGs in the SRFFT generator converges to values between 0.94 and 0.95, which is approximately 5% below the specified unit variance. The mean local variance of the LU generator converges to 1 for all five RNGs. Hence the erroneous sample variance in the SRFFT simulations are solely due to the procedure in the SRFFT random field generation and not due to the random number generators used. This is an important drawback of the SRFFT generator, which is addressed in more detail below.

The range of local variances for the SRFFT and the LU random field generators are comparable (Figures 3.2b, 3.3b and independent of the RNG used: After 10 realizations, local variances vary approximately between [0.1, 4], after 100 realizations the range is limited to [0.5, 1.8], and after 1000 realizations the range is approximately [0.7, 1.3]. The decrease in variability is due to the greater number of samples from which each local variance is computed. On the other hand the number of samples from which the spatial variance is computed is always 4096, and with each realization a sample of the statistics "spatial variance" is added. The range of these samples therefore slightly increases as more realizations are added (Figures 3.2d and 3.3d). At 1000 realizations the spatial variances vary approximately between [0.6, 1.7] for both the SRFFT and the LU generator. Again, the minimum and maximum spatial variance of the SRFFT random fields are approximately 5% lower than those of the LU simulations. For all variance computations none of the RNGs produces results significantly different from others.

The total average deviation of the sample local covariance from the specified exponential covariance (averaged over all points k in the covariance field l AND averaged over all covariance realizations l) varies around 0 and converges to near 0 as the number of realizations increases. Results for the SRFFT and the LU simulations are very similar,

independent of the RNG generator chosen (Figures 3.2e and 3.3e). This shows that the deviation of the variance in the SRFFT simulations from the specified variance does not occur for the entire sample covariance. Indeed, a comparison of the mean local sample covariance obtained from a SRFFT simulation with the exponential covariance specified shows that the erroneous deviation of the SRFFT sample covariance function is limited to the center (origin) of the covariance function i.e., to the variance itself (see below).

The average variance, and the maximum, and minimum variance of the sample covariance function, averaged over all points in the sample covariance, decrease such that their logarithms (the logarithm of the mean, the minimum, and the maximum) decrease linearly with the logarithm of the number of Monte Carlo realizations (Figures 3.2f and 3.3f), which is in good agreement with the statistical analysis: the standard deviation of the sample moments of independent random variables theoretically decreases proportional to $1/n^{\frac{1}{2}}$ (c.f. Haan, 1977). The results for the SRFFT and the LU simulations are again nearly identical and independent of the random number generators used.

Using the postprocessing program developed by this author, Orr (1993) also computed summary statistics for the turning bands (TB) and the sequential simulator (S), with which he had implemented Monte Carlo simulations under the same conditions as the above described SRFFT and LU simulations. Only the DPRAND subroutine was used as random number generator (Maclaren 1992). A comparison of the summary statistics of the four Monte Carlo simulations with the DPRAND random number generator and the SRFFT, the LU, the TB, and S random field generators are shown in Figures 3.4a through 3.4f. In general both the TB and S simulations give results that are - for all practical purposes - identical to the SRFFT and LU simulations. Neither the TB nor the S simulations show any bias regarding the mean local

variance, which is generally too low for the SRFFT simulations (Figure 3.4c). The only notable exception is a relatively high average deviation of the sample covariance from the specified covariance in the S simulations (Figure 3e): After 1000 realizations the mean deviation in the S simulation is approximately five times higher than in any of the other RFG simulations, and approximately 2.5 times larger than in any of the simulations with the other four RNGs in the SRFFT and LU RFGs (compare Figure 3.4e with Figures 3.2e and 3.3e). This may indicate that the Sequential Simulator produces a slightly higher sample covariance than specified, either overall, or in a small region within the covariance field.

In conclusion, the summary statistics indicate that any of the five random number generators tested will produce reliable results. With respect to the summary statistics, all four random field generators produce results that converge in the mean square sense to the desired ensemble distribution when the number of realizations is large. The two exceptions are: First, the covariance of the SRFFT simulations is significantly lower (about 5%) at and only at the origin of the covariance field. In other words, the variance is too low while all covariances between two different points are statistically accurate. Second, the S simulations may produce a seemingly significant overall deviation in the covariance field such that the sample covariances are on average larger than the specified covariance. The summary statistics have also shown that unless the number of Monte Carlo realizations exceed several hundred or even a thousand runs, local statistics (such as the local mean, variance, and the local covariance field) have a very wide spread and their local statistical significance is questionable.

3.5.3 Local Performance Analysis of the RFGs

The purpose of an analysis of the local moments is to investigate possible spatial bias in the realizations due to the particular random field generator. With the experiences from the above summary analysis it is sufficient to limit the analysis of the two-dimensional datasets to Monte Carlo simulations with N = 1000 realizations. First a single sample realization of each RFG simulation is presented together with its spatial covariance field. Then the local mean, the local variance, the local covariance, and finally the average of the local covariances, and the average of the spatial covariances are analyzed. The author gratefully acknowledges the work by Orr (1993), who implemented the TB and S simulations.

Figure 3.5 shows a representative single realization of each RFG simulation. No particularly disconcerting features are observed. Similar observations were made for other realizations, and generally found no particular notable bias within any one realization. Their spatial covariances (obtained by spectral analysis as described above) are generally more or less symmetrical and exponential near the very center (the origin of the covariance field) but also characterize some of the strong spatial features in the particular random realization e.g., the east-west trending valleys in the particular TB realization (Figure 3.6). It must be emphasized that any realization generated with any one of the RFGs may produce more or less dominant features that are then reflected in the sample covariance function (due to the limited field size). The summary statistical analysis has shown, however, that *overall* these features are well within the theoretically possible sample space. The following analysis will investigate, whether any *local* artifacts exists that are due to the numerical algorithms.

The local mean of 1000 realizations with each RFG are shown in Figure 3.7. The

standard deviation of the local sample means e.g., in the LU simulation, is 0.0329. This compares well with the theoretical standard deviation of the sample mean taken from a Gaussian distribution, which is 0.0316 for a sample-size of 1000 (c.f. Haan, 1977). In accordance with stochastic theory the sample means are a random field variable themselves. The correlation structure of the sample mean field is not quite unlike that of the underlying random fields, something that is observed throughout the remainder of this study. The sample mean field (actually a realization of the sample mean RFV) shows no particularly strong trend or non-stationarity or other artificial patterns.

Similarly, the local variances of 1000 realizations are themselves a random field realization with a familiar looking random pattern that reflects the fact that the correlation structure of the variance field is - like that of the mean field - similar to the correlation structure of the underlying random fields (Figure 3.8). Again no particular trend, non-stationarity, or pattern is observed that may be an artifact of the particular random field generator. The only exception is a very notable streak-line structure in the variance field of the TB simulation. From the left lower origin four lines extend radially throughout the variance field, dividing it into five equally sized pieces (with the exception of the leftmost and the lowest piece, which are only about half the size of the three others). The lines reflect four of the 16 turning bands used for the generation of the random field and are characterized by higher than normal variance on the counterclockwise side and a lower than normal variance on the clockwise side along the imaginary line. These patterns have been reported elsewhere and can be partly eliminated by increasing the number of turning bands. Orr (1993) implemented an alternative TB algorithm provided by Zimmerman (personal communication) and indeed found no artificial patterns in the sample variance (random) field (Figure 3.15) when using 32 lines.

A sample local covariance field (actually also a realization of the sample local covariance RFV) centered around the (48,48) coordinate of the random field is shown in Figure 3.9 for each of the four RFGs. Despite the relatively large number of realizations (many hydrogeologic and soil physical applications of the Monte Carlo method are limited to a few tens or a few hundred simulations), the local covariance functions exhibit a significant amount of randomness. More importantly perhaps they show anisotropy and other irregular structures with all of the four RFGs. This is expected since the statistical significance of 1000 independent samples of the covariance product sum (2-29) is relatively weak. Recall that a similar variability is observed for the local sample variance, which has a sample range of ± 0.2 (or ± 20% of the specified standard deviation).

To obtain a larger sample base, all 31^2 local covariance fields such as those in Figure 3.9 are averaged to obtain a mean local covariance field. The 31^2 local covariance fields are not statistically independent due to the correlation structure of the random field. Nevertheless the mean local covariance field has a very regular structure (Figure 3.10) since the sample error is now much smaller than the range [0,1] of the underlying covariance function. The shapes of three of the four mean local covariance fields is very similar to the specified isotropic exponential covariance function. The TB simulator generates anisotropic random fields with the correct variance, but longer correlation than specified in the horizontal direction and shorter correlation than specified in the vertical direction. Furthermore, a strong lineation is visible, when the difference is plotted between the mean sample local covariance of the TB simulation and the exponential covariance (Figure 3.11). As discussed above for the local variance, this artificial TB pattern is believed to be due to the small number of turning bands chosen for the simulation. Orr (1993) reports that these patterns vanish when a much larger number of turning

bands is used with an improved version of the TB generator program. Careful visualization reveals that the mean covariance field of the improved program is indeed very accurate, but the lineations in the deviation from the exponential covariance still exist, albeit at a much smaller amplitude than before (Figure 3.15). The SRFFT simulator has a significant deviation only at the origin of the covariance field i.e., the variance is biased, while all covariances of non-zero lag seem to converge to the specified structure (Figure 3.11). After correspondence with the author of the original SRFFT generator, Allan Gutjahr, it is not entirely clear what causes this particular bias. A larger size of the random field domain reduces the error. Similarly, the mean covariance field of the sequential simulator is somewhat more stretched out than expected, which possibly explains the positive bias in the total deviation from the specified covariance (see summary statistics discussion). Overall, the LU generator gives the most unbiased mean local sample covariance field.

Figure 3.12 depicts the local variance of the sample covariances corresponding to the local mean of the 31^2 superpositioned local covariance fields in Figure 3.10. All generators have the largest variance near the origin due to the large absolute value of the mean covariance field near and at the origin. Overall the LU generator exhibits the smallest variance. The S simulator exhibits relatively large variances throughout a large central part of the covariance field. Both the S and TB generators also exhibit areas of large variance near the edges of the covariance field, where the absolute value of the covariance is near 0. Again not too much significance should be given to these patterns without sampling from much larger populations i.e., without analyzing a Monte Carlo simulation based on a sample size several orders of magnitude larger.

Finally, the average of the first 50 spatial covariance field samples are analyzed, each

of which was obtained from a spectral analysis of a single random field realization (Figure 3.13). The SRFFT, S, and LU generators have average spatial covariance fields very similar to the average local covariance fields in Figure 3.10. The TB generator, however, exhibits both strong anisotropy and the familiar starlike pattern in its mean spatial covariance. The deviation of the mean spatial covariance from the specified exponential covariance (Figure 3.14) clearly shows the location of the 16 turning bands in the TB generator. Again, the same bias can qualitatively be observed in the improved version of the TB generator (Figure 3.15).

3.6 Conclusion

In summary of the moment analysis it is found that all random number generators tested perform equally well. Of the four random field generators tested, the LU-decomposition based simulation showed the least artificial bias. The local moment analysis confirmed that the SRFFT generator produces sample covariances that are very close to the specified covariance with the exception of the variance (covariance of zero-lag), which is on average about 5% too low. The error is probably due to the limited domain size. The sequential simulator produces sample covariances that are on average slightly larger than the specified covariance throughout most of the sample covariance field. Otherwise both the SRFFT and the S simulator produce random fields that are consistent with the probability space specified. The second order moments of the turning band simulator exhibited significant artificial patterns due to the starlike distribution of the 16 turning bands used. An improved code and the choice of a larger number of turning bands gave results comparable to those found for the other three RFGs (see Orr, 1993, for details).

The CPU-efficiency of the four RFGs varies greatly, while the choice of the RNG has no significant effect on the computation time. The CPU time for 1000 realizations of the SRFFT and the LU simulators were 1112 sec. and 1920 sec., respectively, on an IBM RS6000/320 system. The computation time of the SRFFT is proportional to the number of random fields that are generated. In contrast, the LU simulator initially requires large amounts of computation time just for the decomposition of the covariance matrix. The CPU time for 10 realizations of the LU simulator is 360 sec. compared to only 29 sec. for 10 realizations of the SRFFT simulator. Unfortunately, no CPU-times are available for the simulations with the TB and S simulators by Orr (1993). Tompson et al. (1989) evaluated the computing efficiency of the TB method as compared to the SRFFT method and concluded that the SRFFT will be at least as efficient as the TB method for random fields on the order of less than 10^5 points. For very large random fields, the TB simulator is more efficient, and Gomez-Hernandez (1989) claims similar efficiency for the sequential simulator. The comparative efficiency of the four different RFGs will mainly depend on the number of points generated in each field and on the number of realizations.

While the LU generator gives very good results, its disadvantage is that it requires the decomposition of a covariance matrix of size N^2, where N is the total number of points in the random field (4096 in the above examples). For smaller random fields (<5000 points) with many realizations this is indeed a very effective way of random field generation, since the covariance matrix must only be decomposed once for an entire simulation. Each realization then simply requires the generation of random numbers and the multiplication with the L matrix (3-17). For large random fields, the LU-decomposition becomes too cumbersome, if not impossible.

The largest drawback of the SRFFT generator is the overhead in the FFT, since the actual random field is only $(1/2)^2$ (in two dimensions) or $(1/2)^3$ (in three dimensions) of the size of the spectral field due to the symmetry (3-2) required to obtain real random fields. Gutjahr (1989) points out that the imaginary part of the inverse Fourier transform of the spectral representation is also an independent realization with the required properties i.e., one transform generates two independent realizations of the same random field. For our purposes the SRFFT is sufficiently accurate (in the statistical sense) and CPU-efficient to justify its use for the simulation of heterogeneous soils.

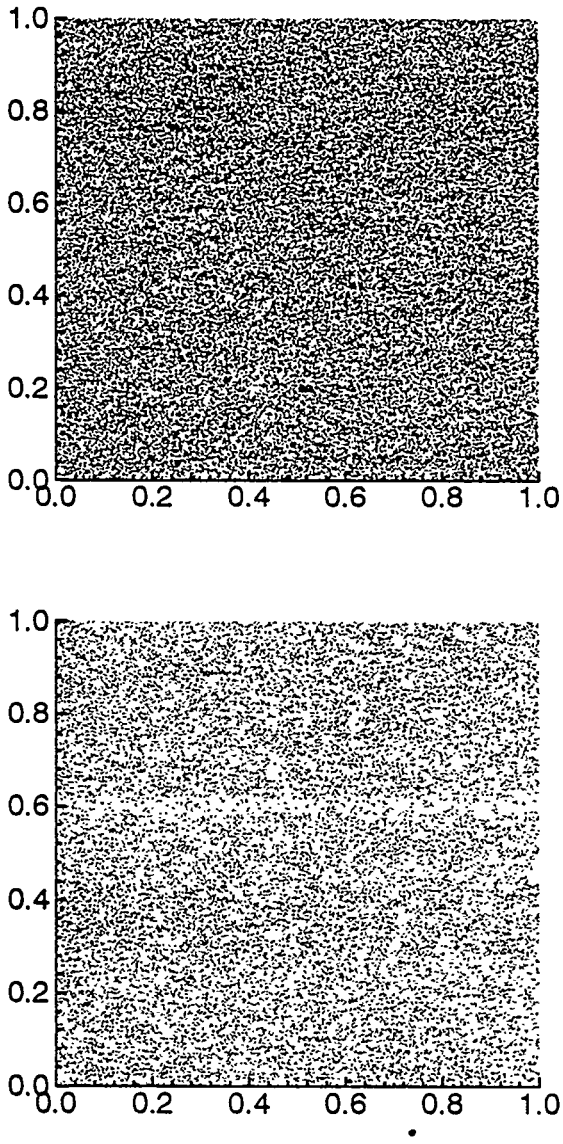

Figure 3.1: Dot diagrams of the RAN2 (top) and ESSL (bottom) random number generators. Each of the 100,000 points represents two consecutive, uniformly distributed random numbers.

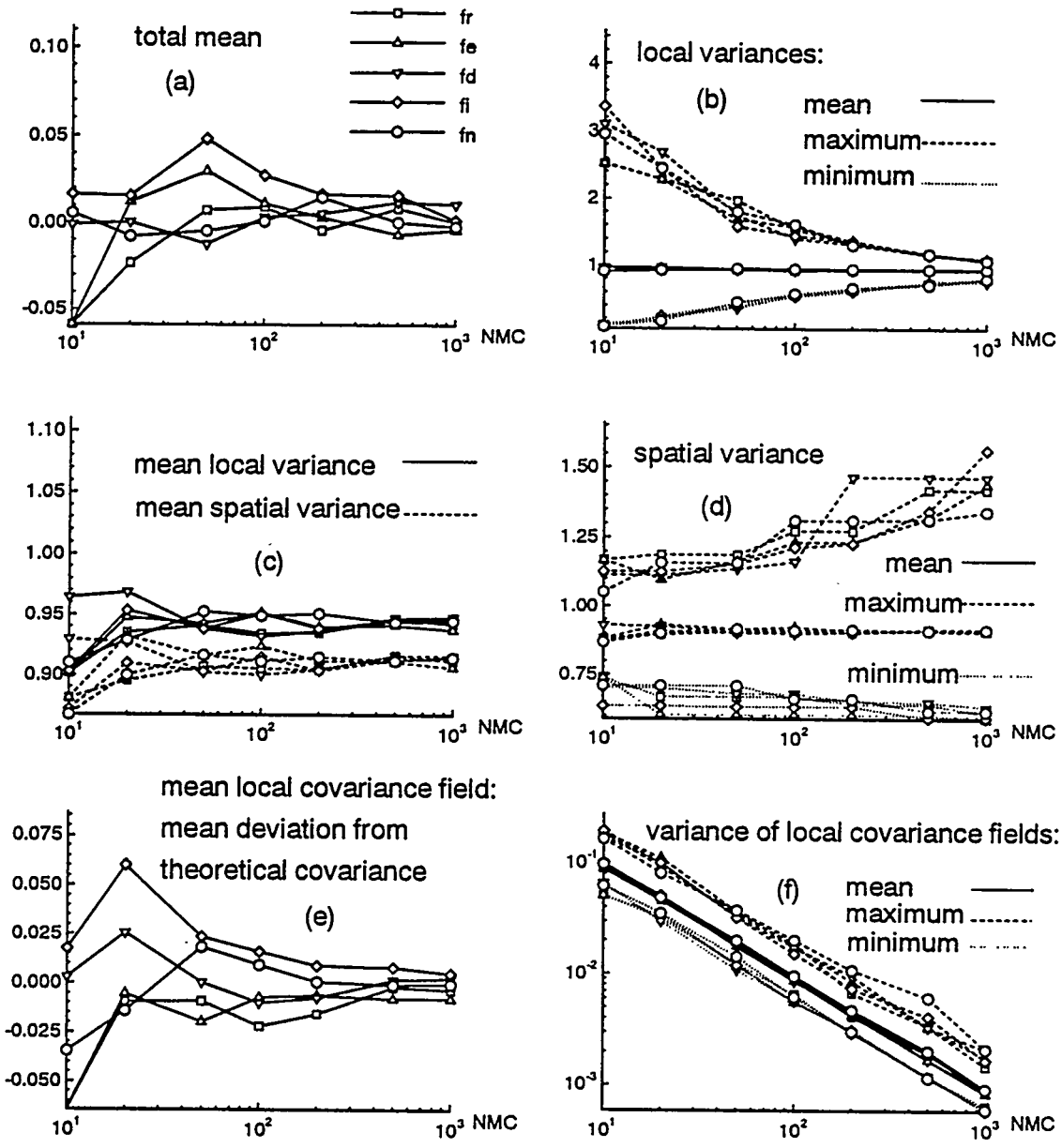

Figure 3.2: Summary moments of the sample mean, variance, and covariance as a function of the number of Monte Carlo realizations, NMC. Local sample moments are taken at the same point over all realizations. Spatial samples are taken from a single realization by sampling over all points. All simulations are implemented with the SRFFT simulator. Different symbols refer to different random number generators: fr - RAN2, fe - ESSL library, fd - DPRAND, fi - IMSL library, fn - NAG library. The f in the labeling refers to SRFFT.

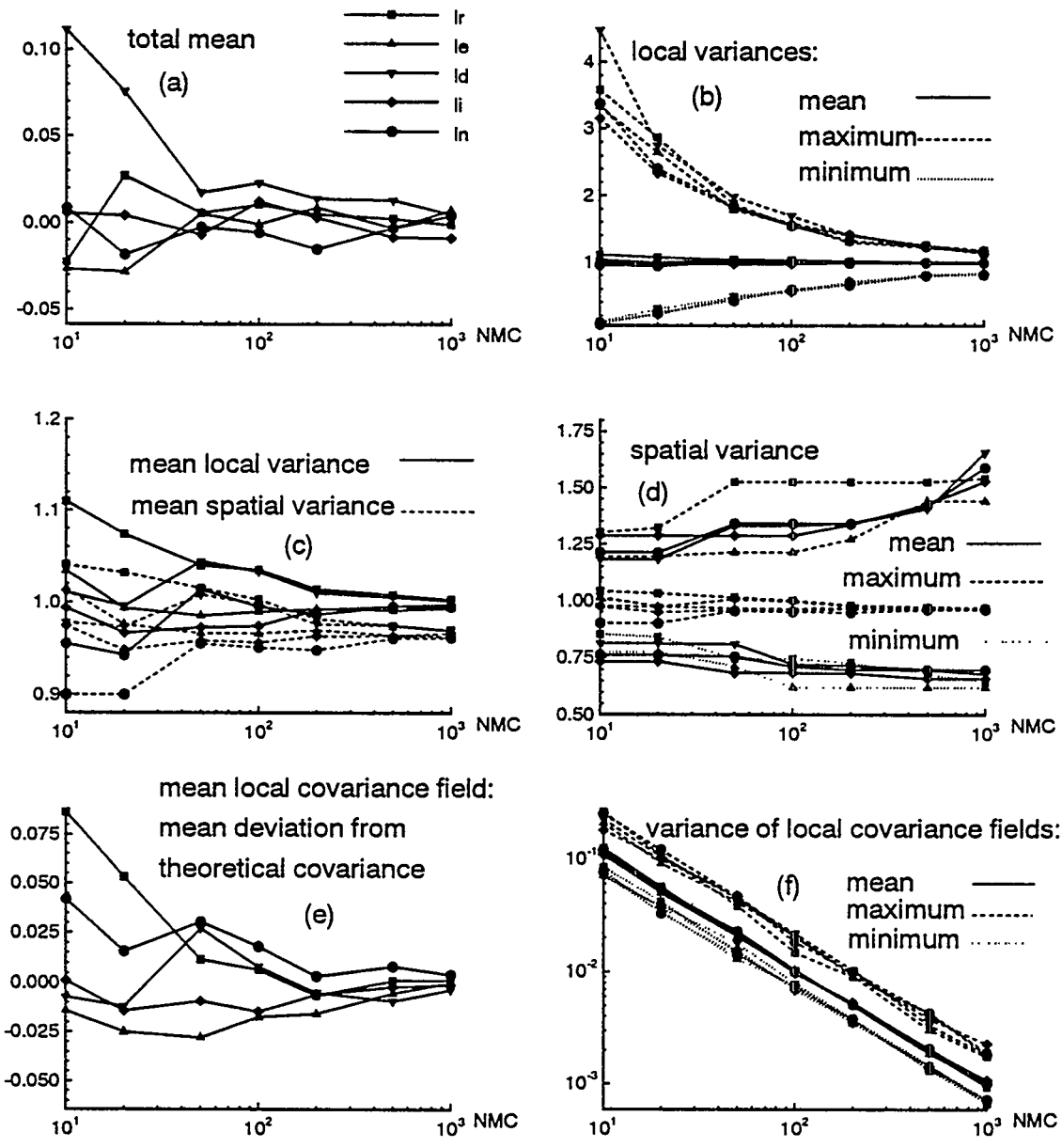

Figure 3.3: Summary moments of the sample mean, variance, and covariance as a function of the number of Monte Carlo realizations, NMC. The simulation results shown here are from simulations with the LU random field generator. The l in the labeling stands for "LU random field generator", otherwise the labeling is identical to Figure 3.2.

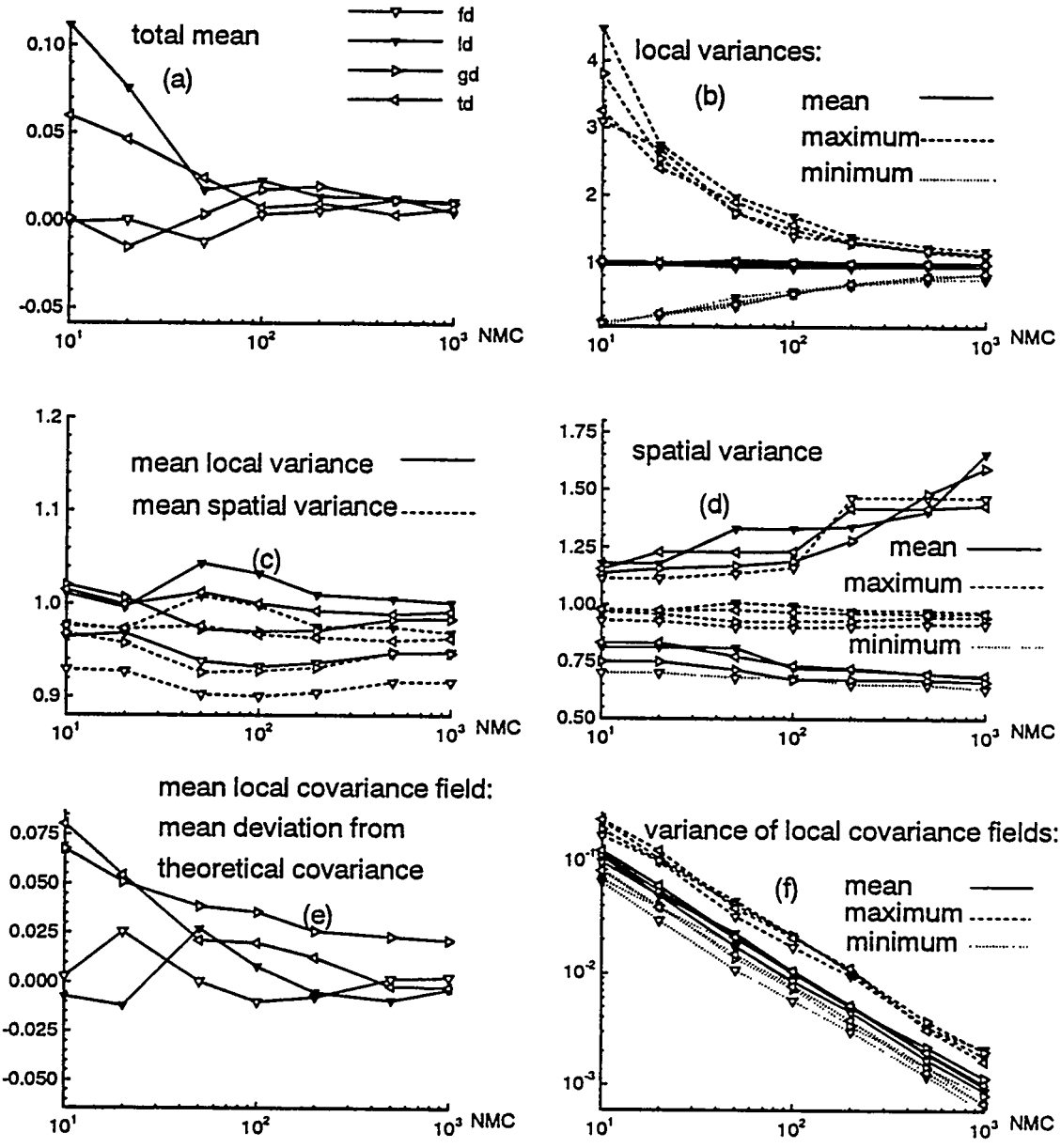

Figure 3.4: Same as Figures 3.2 and 3.3. Here the four different RFGs are compared using the same random number generator (DPRAND). "g" and "t" are the labels for the GCOSIM and the TB simulator, respectively.

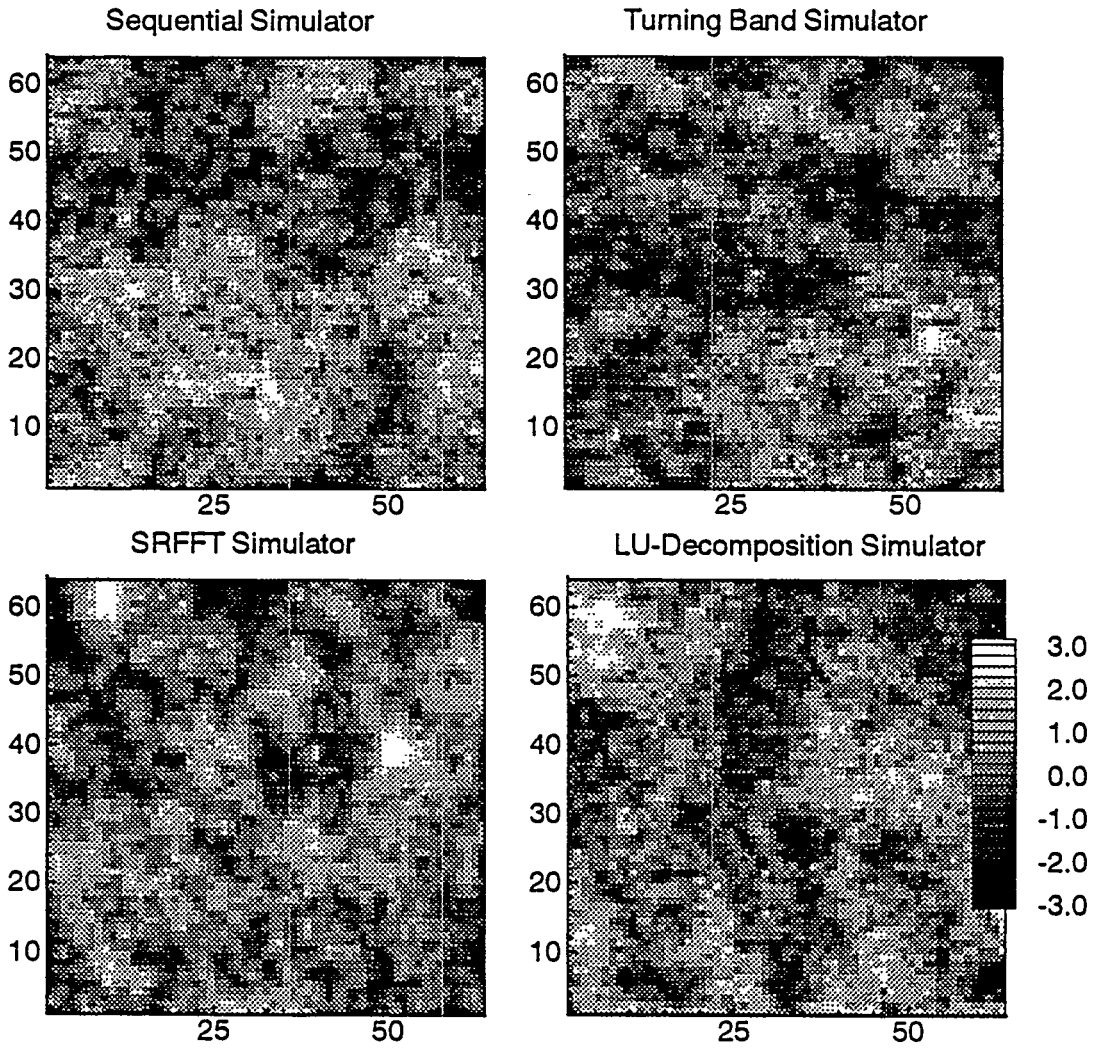

Figure 3.5: Sample Gaussian random field realizations with one realization of each tested RFG. The mean is specified to be 0; the variance is specified to be 1; the correlation function is exponential with $\lambda = 5$.

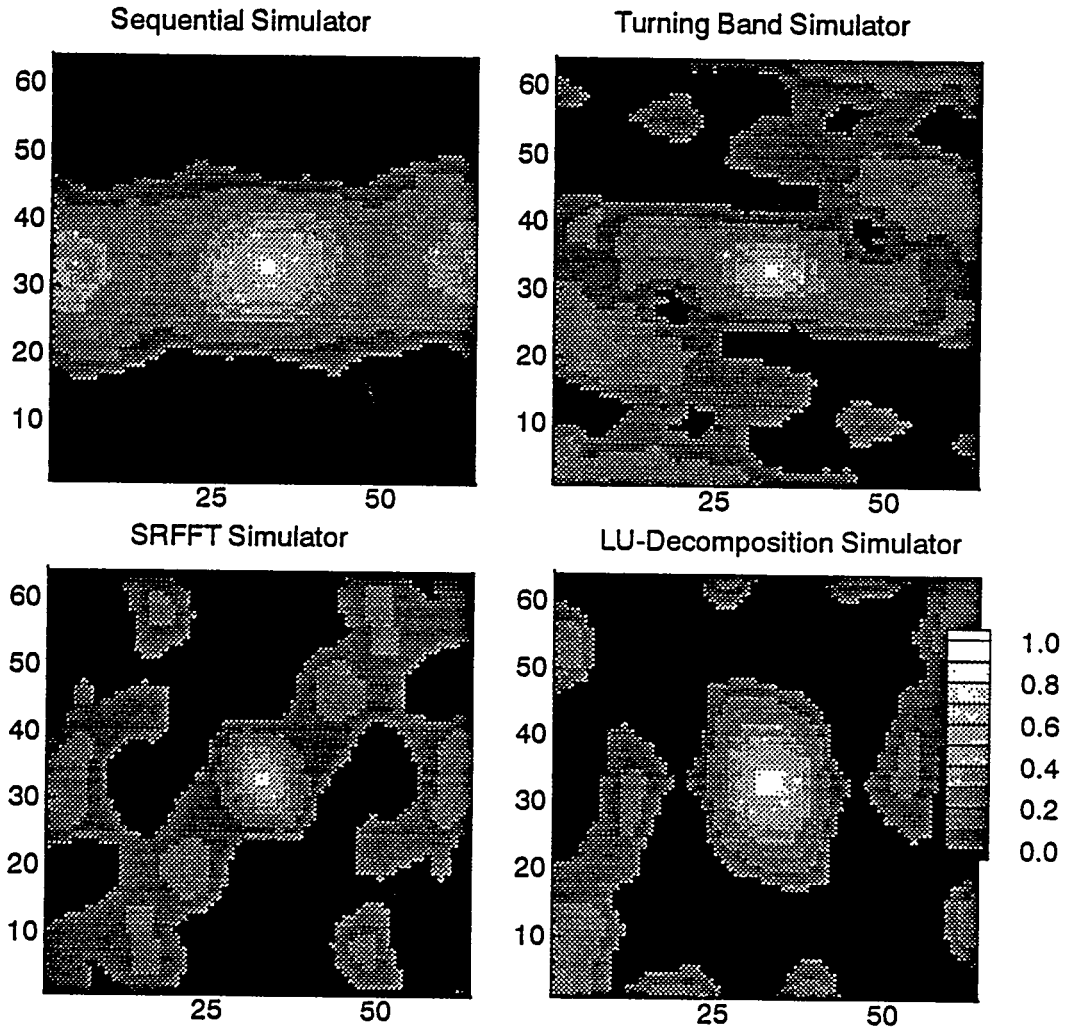

Figure 3.6: Spatial covariance of the sample random field realizations in Figure 3.5 (also see section 3.4.1).

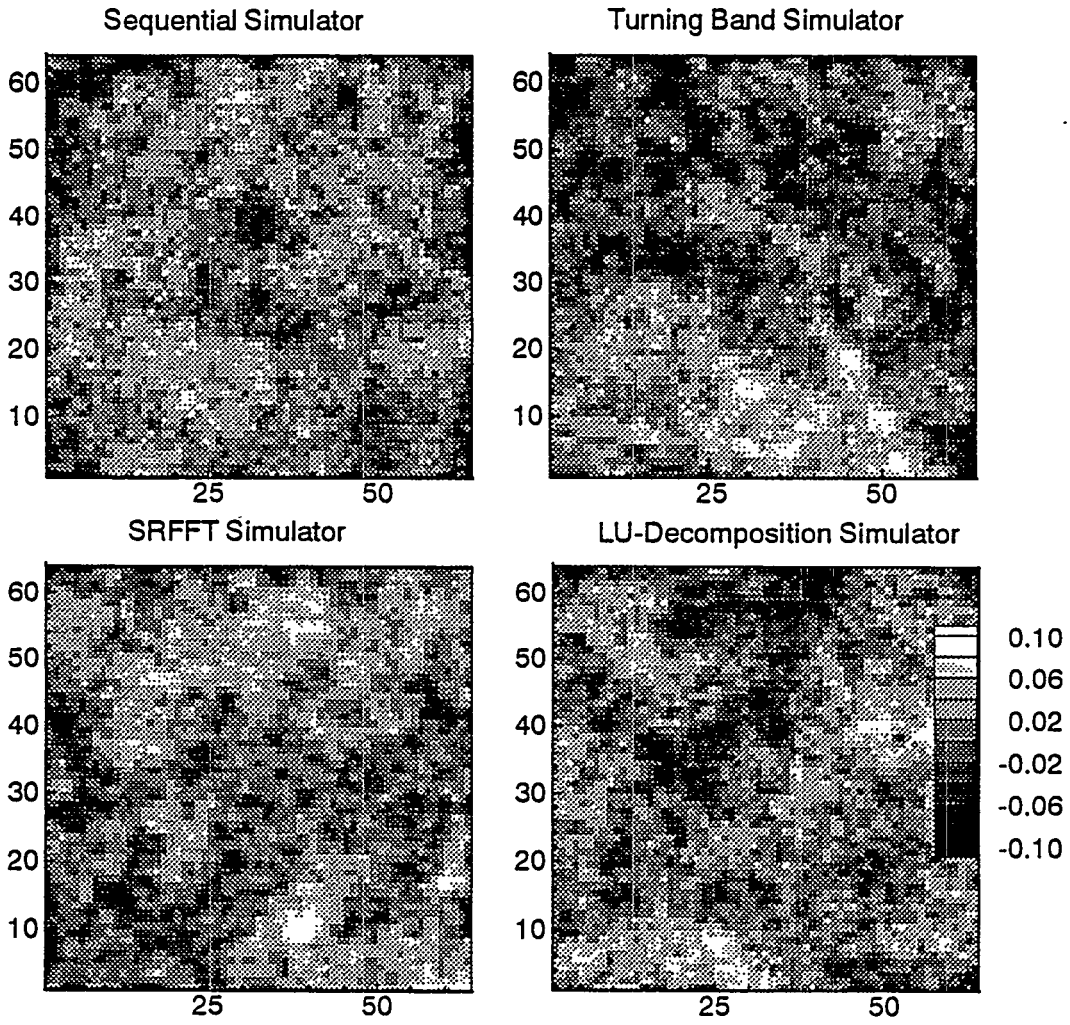

Figure 3.7: Local sample mean of each RFG after 1000 runs.

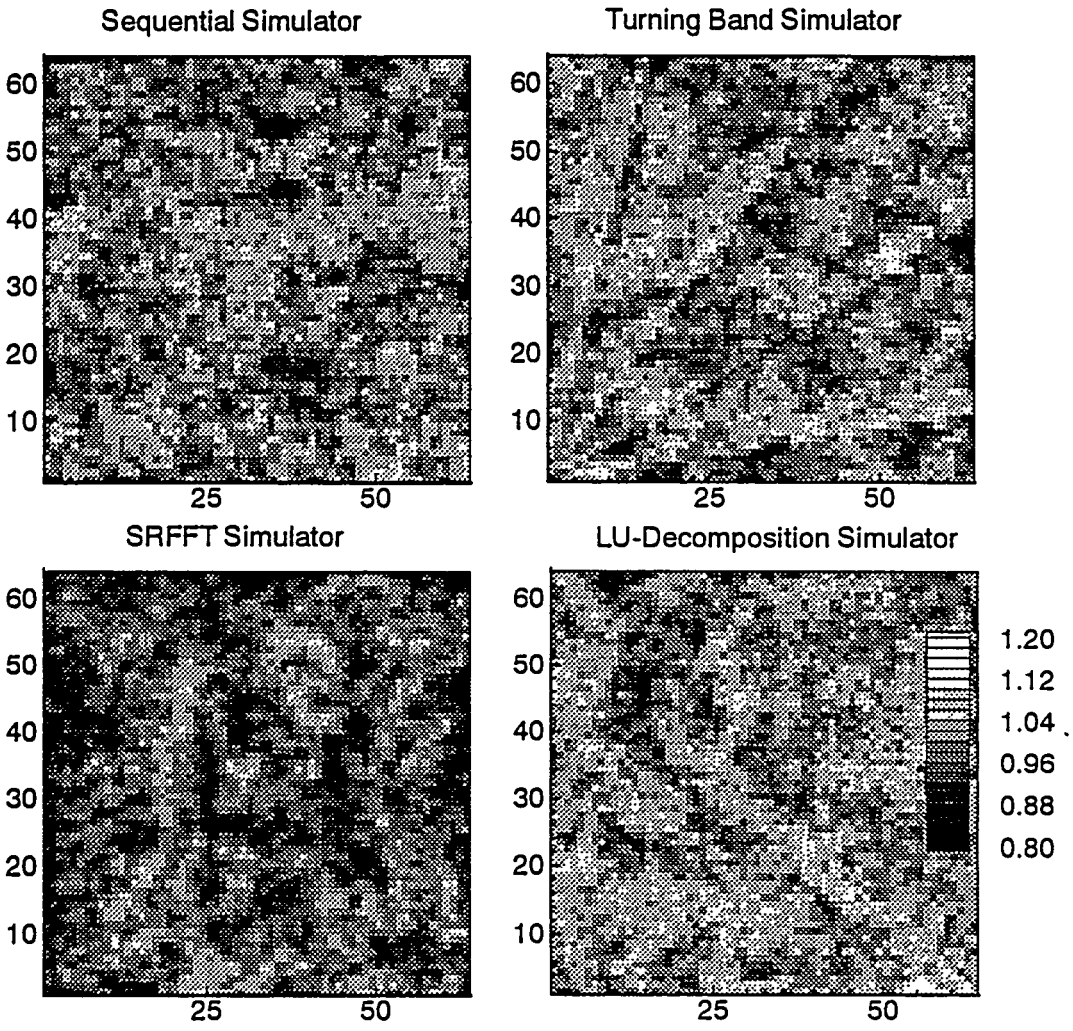

Figure 3.8: Local sample variance of each RFG after 1000 realizations.

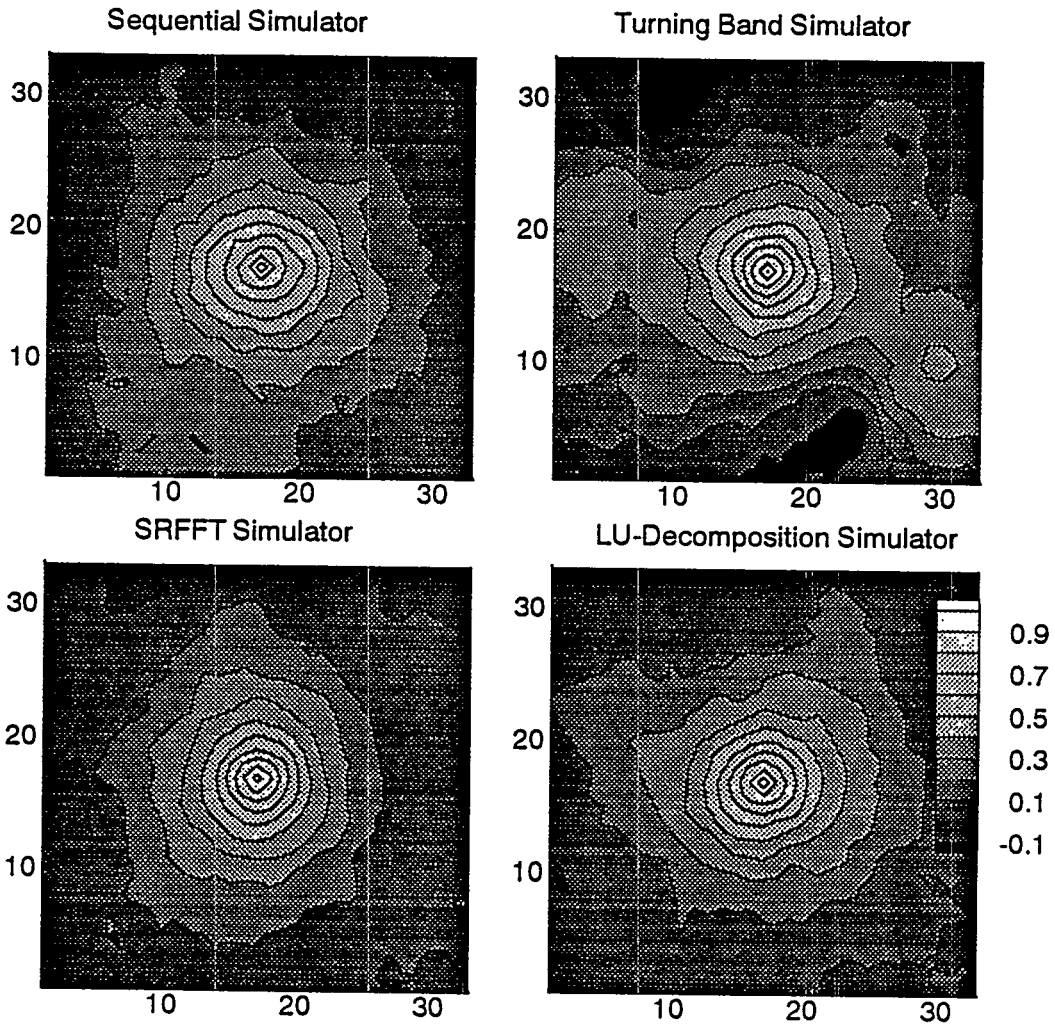

Figure 3.9: Sample local covariance field showing the covariance between point (48,48) and the surrounding 33^2-1 points. The results are based on 1000 realizations.

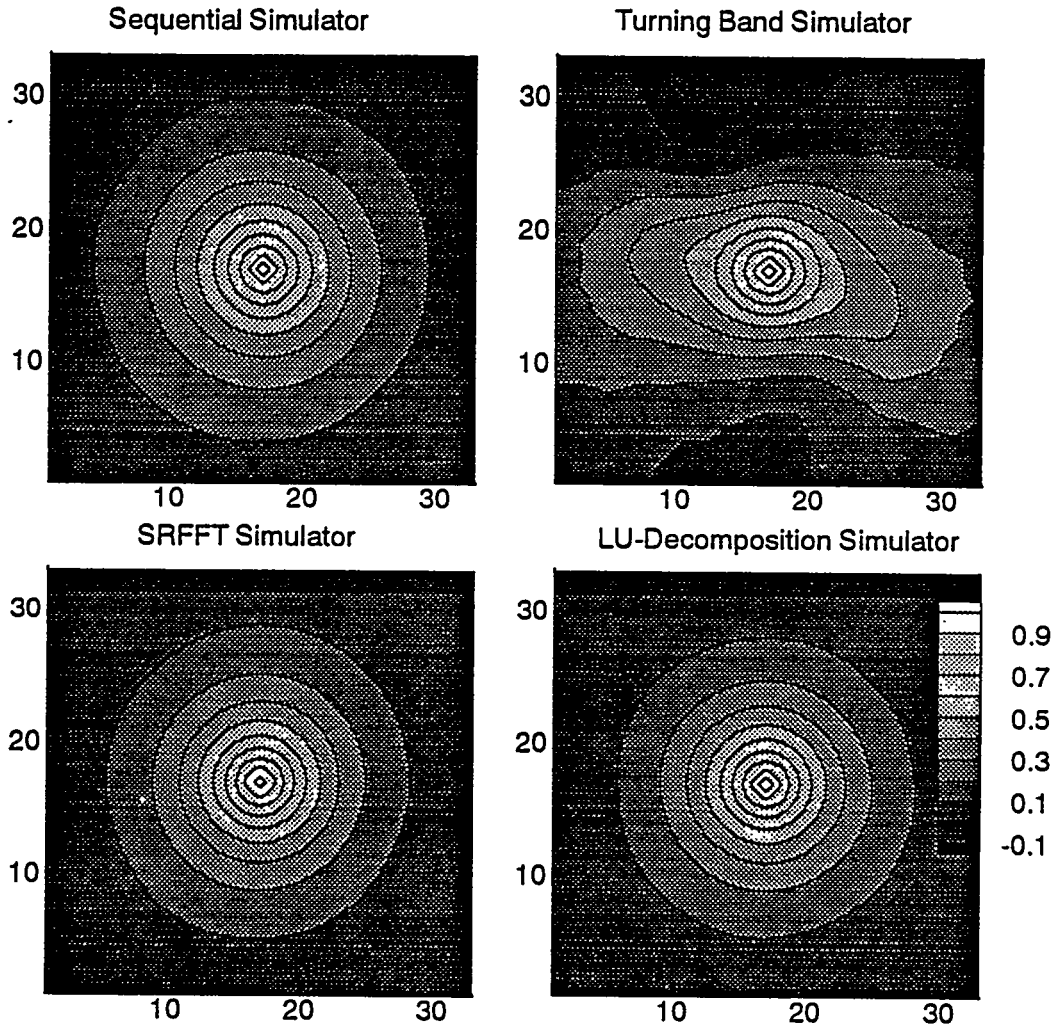

Figure 3.10: Mean of all 31^2 sample local covariance fields (such as those shown in Figure 3.9). Each sample local covariance field is based on 1000 realizations.

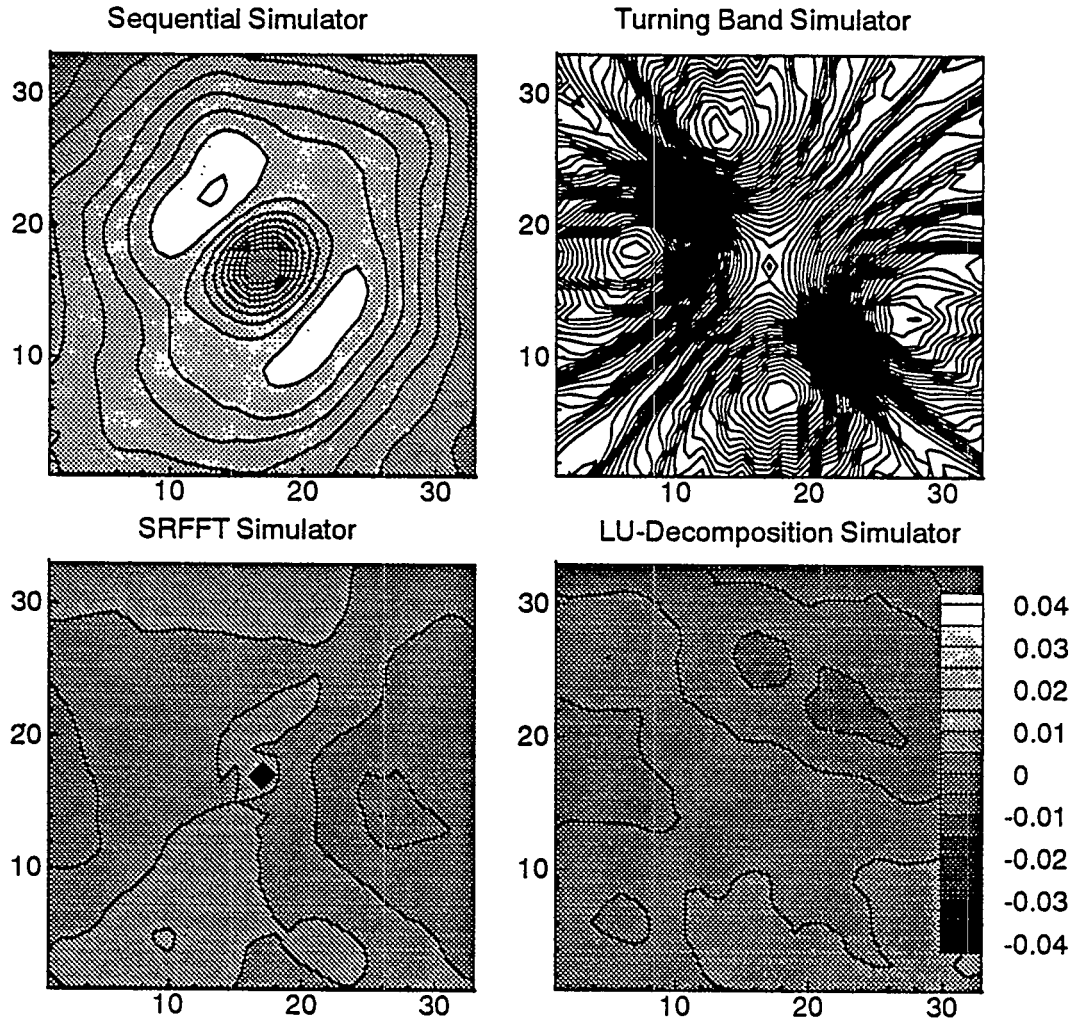

Figure 3.11: Deviation of the mean sample covariance fields (Figure 3.10) from the exponential covariance function. The color flooding is omitted from the plot for the TB simulator. For the TB plot the total number of contour levels has been increased to 61 (instead of 17) to visualize the lineation in the sample covariance. The range of the contours in the TB plot is [-0.13,0.18]. In the TB plot the deviation is negative near the top and bottom of the plot and positive towards the left and right side (see Figure 3.10).

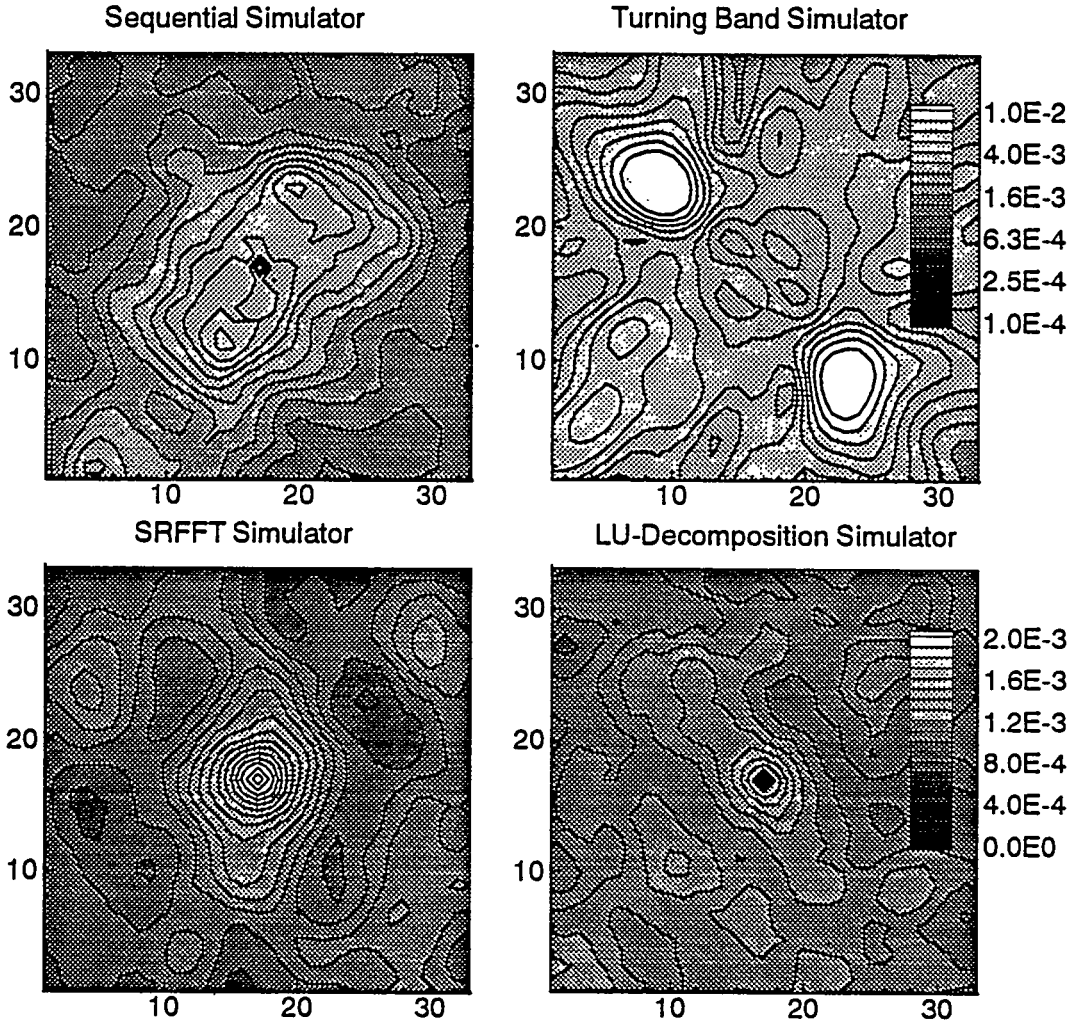

Figure 3.12: Variance of the sample covariance fields. The variance is obtained by superposing all sample covariance fields. Then the variance is computed for each point in the covariance field similar to the local variance of the random fields. The Turning Band Plot has a different gray-scale than the other three plots (label inserted). It has a larger range and is based on an exponential scale.

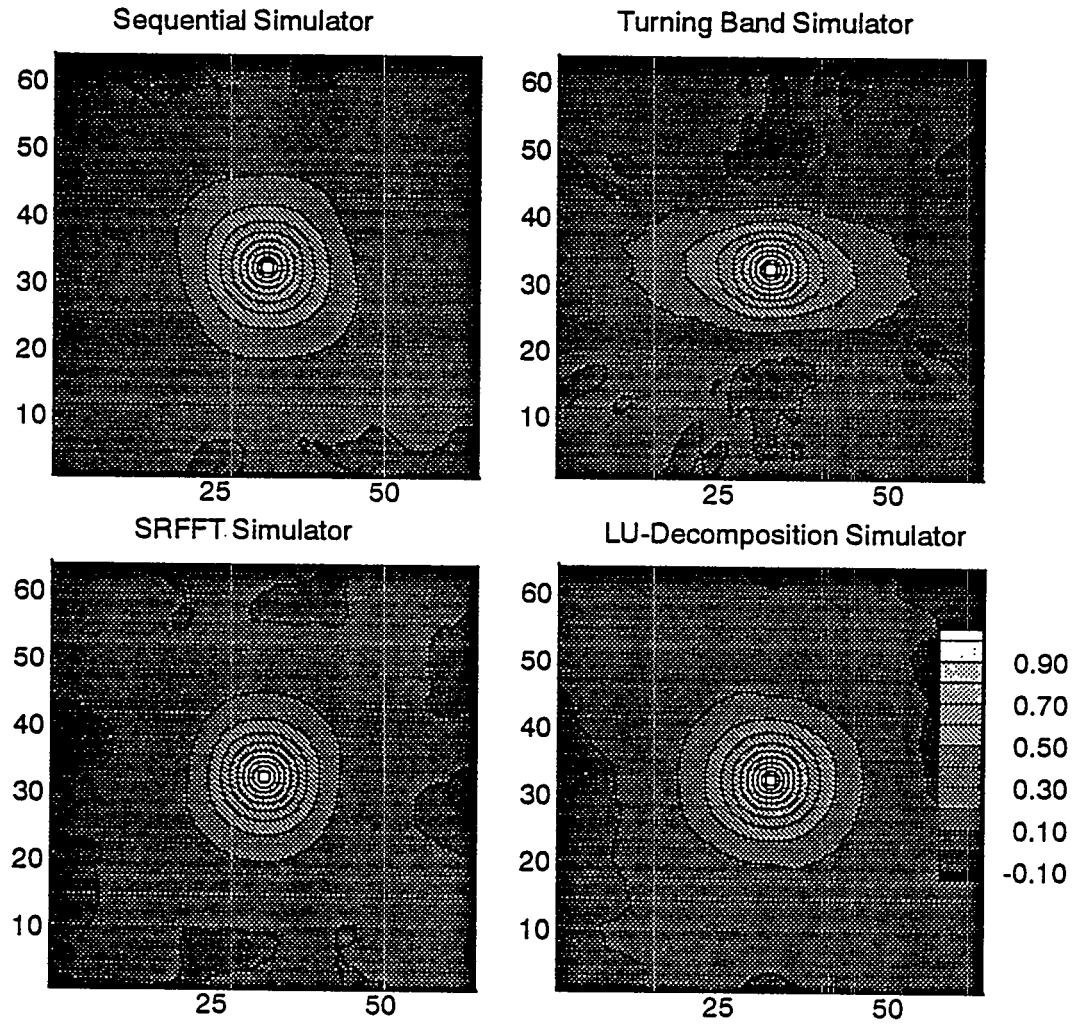

Figure 3.13: Mean of 50 spatial covariance fields such as the ones shown in Figure 3.6.

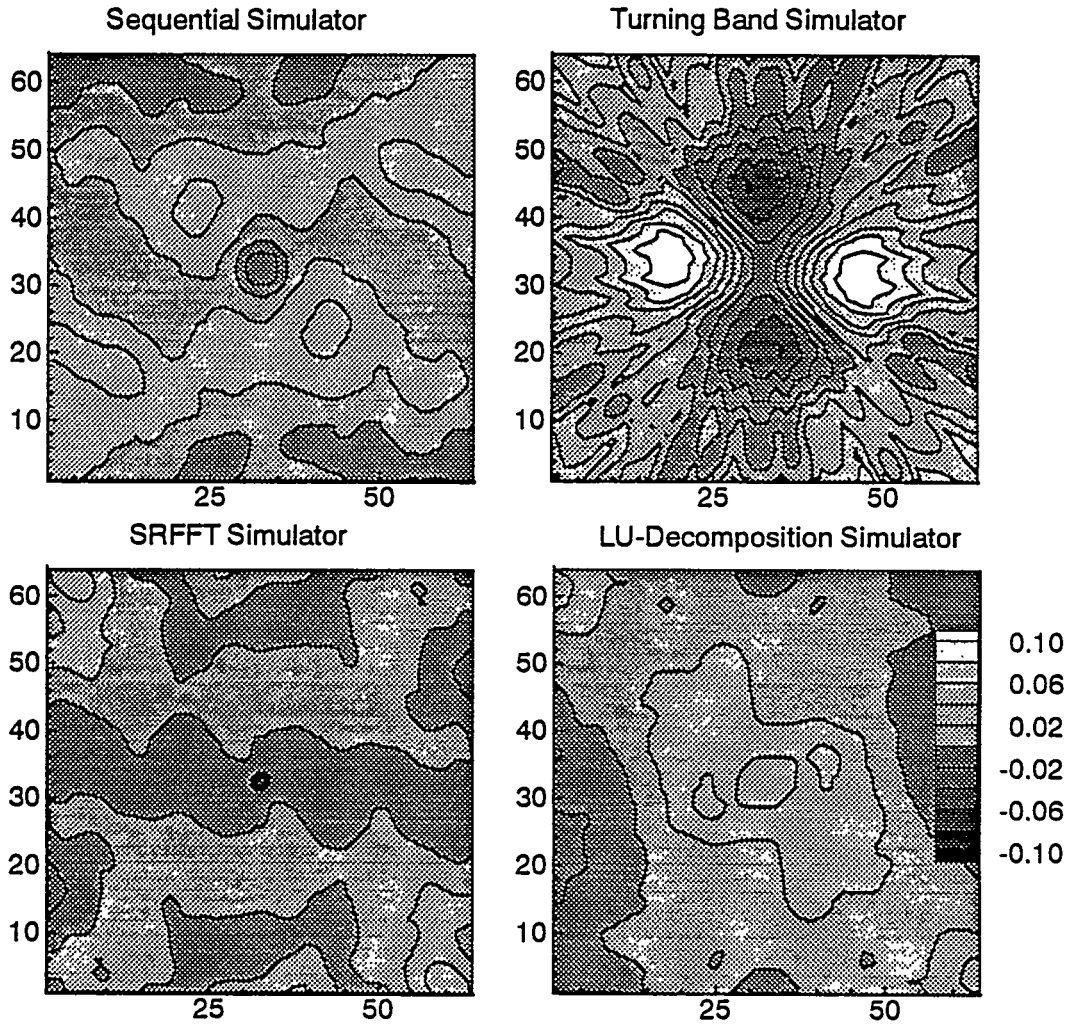

Figure 3.14: Deviation of the mean spatial covariance in Figure 3.13 from the exponential covariance function.

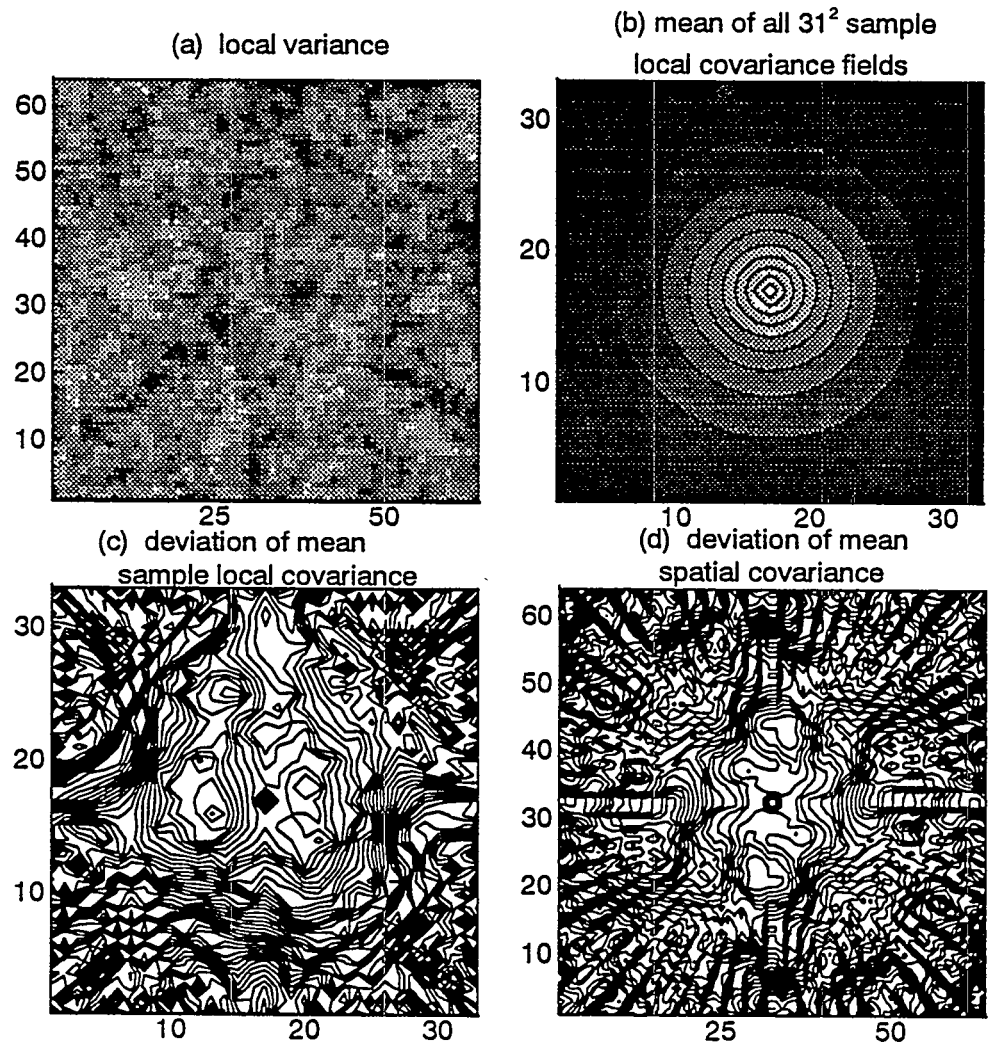

Figure 3.15: Selected results for the improved version of the TB simulator. The plotting variable and the flooding and contour ranges are identical to those of the LU simulator in Figure 3.8 (a), Figure 3.10 (b), Figure 3.11 (c), and Figure 3.14 (d). In the latter two plots, the overall range of the deviations is similar to that of the LU simulations. But small lineations remain as shown by the contour lines.

4. STOCHASTIC THEORY OF UNSATURATED FLOW IN TWO DIMENSIONS

4.1 Mathematical Problem Formulation

Flow in two-dimensional porous media under variably saturated conditions is generally modeled by Richards equation (Hillel, 1980):

$$\frac{\partial}{\partial x_i}\left[K_i(h)\frac{\partial(x_2+h)}{\partial x_i}\right] = C(h)\frac{\partial h}{\partial t} \qquad i=1,2 \qquad (4\text{-}1)a$$

where x_1 and x_2 are the horizontal and vertical coordinates, respectively. Note that the denoting of the vertical direction as x_2 (rather than x_1) is unusual (see Yeh, 1985a,b), but is chosen here for consistency with the notation for the numerical model (chapter 5). For the clarity in subsequent chapters, the subscripts x and z are used interchangeably with the subscripts 1 and 2, where appropriate. x_2 is positive upward, h is the matric potential (negative for unsaturated condition). $K_i(h)$, the principal unsaturated hydraulic conductivity, and the moisture capacity term, $C(h)=d\theta/dh$, are functions of h. For simplicity of notation and without loss of generality, it is assumed that the principal axes of anisotropy in the hydraulic conductivity coincide with the principal coordinate axes.

Under steady-state conditions the right-hand side of (2) vanishes and the solution becomes independent of the water retention function $\theta(h)$:

$$\frac{\partial}{\partial x_i}\left[K_i(h)\frac{\partial(x_2+h)}{\partial x_i}\right] = 0 \qquad i=1,2 \qquad (4\text{-}1)b$$

Like the groundwater flow equation, Richards equation is based on the principles of Darcy's law (conservation of momentum):

$$q_i = -K_i(h)\frac{\partial(h + x_2)}{\partial x_2} \qquad i=1,2 \qquad (4\text{-}2)$$

and mass continuity (conservation of mass) :

$$-\nabla \mathbf{q} = \frac{\partial m_w}{\partial t} = C(h)\frac{\partial h}{\partial t} \qquad (4\text{-}3)$$

q_i is the flux per cross-sectional area $A_i \perp x_i$, and $\partial m_w/\partial t$ is the change of the total mass of water per unit time. Unlike the parameters in the saturated flow equation, the parameters in Richards equation are functions of the matric potential h and hence equations (3-1a) and (3-1b) are nonlinear equations. Parametric relationships must be constructed to relate the unsaturated hydraulic conductivity K, the moisture content θ, and the moisture capacity function C to the matric potential (head) h. Since the moisture capacity function C(h) is defined in terms of θ and h, two functions $K_i(h)$ and $\theta(h)$ are sufficient to complete the transient equation (3-1a). A single function $K_i(h)$ suffices to complete the steady-state equation (3-1b).

Water retention $\theta(h)$ and saturated hydraulic conductivity K_s are commonly measured from soil samples. The measured $\theta(h)$ are used to find the parameters of a theoretical function such that the function will best fit the empirical data. The following class of functions has become particularly useful in describing actual field data (VanGenuchten, 1980):

$$\Theta = \left[\frac{1}{1+(|\alpha h|)^n}\right]^m \qquad m=1-1/n \qquad (4\text{-}4)$$

where

$$\Theta = \frac{\theta-\theta_r}{\theta_s-\theta_r} \qquad (4\text{-}5)$$

θ_s is the moisture content at saturation and θ_r is the residual moisture content. m is a fitting parameter related to the tortuosity of the flow path and the correlation between pores. α is a parameter mainly associated with the pore size distribution.

Unlike the water retention relationship or the saturated hydraulic conductivity, the unsaturated hydraulic conductivity K(h) is much more difficult to measure both in the field and in the laboratory. Since K(h) depends on similar porous medium properties as θ(h), several models have been developed to determine K(h) as a function of the known water retention relationship. Mualem (1976) suggested the relationship:

$$K(\Theta)=K_s \sqrt{\Theta} \left[\int_0^{\Theta} \frac{1}{h(x)} dx \Big/ \int_0^{1} \frac{1}{h(x)} dx \right]^2 \qquad (4\text{-}6)$$

From this and (4-4) VanGenuchten (1980) derived the following K(h) model:

$$K(h) = K_s \frac{[1-(|\alpha h|)^{n-1} [1+(|\alpha h|)^n]^{-m}]^2}{[1+(|\alpha h|)^n]^{\frac{m}{2}}} \qquad (m=1-1/n) \qquad (4\text{-}7)$$

Equations (4-4) an (4-7) are commonly known as the VanGenuchten model and have been used to describe a number of scientific field sites related to the study of soil heterogeneity (Anderson and Cassel, 1986; Field et al., 1984; Hopmans and Stricker, 1989; Wierenga et al., 1989, 1991). While the VanGenuchten model has provided the flexibility needed to describe many field soils, its functional form does not lend itself to the analytical study of soil moisture movement. Analytical solutions to Richards equation (4-1) can be derived only with simpler models. The exponential model first suggested by Gardner (1958) provides a powerful class of K(h) functions:

$$K(h) = K_s \exp(\alpha h) \qquad (4\text{-}8)$$

Again, α is related to the pore-size distribution and will in the remainder of the text be referred to as the pore-size distribution parameter. In the Gardner model K_s is related to, but need not be taken as, the saturated hydraulic conductivity. This should be kept in mind, as K_s is simply referred to as "saturated hydraulic conductivity" throughout this text.

Russo (1988) developed the following θ(h) model that is consistent with Gardner's

exponential model for K(h) (4-8) and with Mualem's pore-size distribution model (4-8):

$$\theta = \theta_r + (\theta_s - \theta_r)[e^{-0.5\alpha|h|}(1 + 0.5\alpha|h|)]^{2/(m+2)} \qquad (4\text{-}9)$$

Equations (4-8) and (4-9) are sometimes referred to as the Gardner-Russo model (Russo, 1988).

In the stochastic analysis of unsaturated flow and transport in heterogeneous soils, $K_s(x)$, $\alpha(x)$, $m(x)$, $\theta_s(x)$, and $\theta_r(x)$ become random field variables (RFVs, see chapter 2.5.1). The RFVs are defined by their probability distribution functions. Field studies have shown that the saturated hydraulic conductivity K_s, the pore-size distribution parameter α, and the tortuosity factor m are lognormally distributed (White and Sully, 1992). Little is known about the variability of θ_s and θ_r and the sensitivity of the head and flux solutions to the variability of the parameters defining the water retention functions (4-4) and (4-9). Analytical models commonly neglect the spatial variability in θ or state their results in terms of the flux rather than in terms of pore-velocity (Mantoglou et al., 1987a,b,c; Russo, 1993a; Yeh et al., 1985a,b). For the sake of clarity and since it is not the purpose of this study to investigate the impact of spatially variable θ on the transport behavior of solutes in unsaturated soils, the variability in θ_s, θ_r, m, α, and h in (4-4) and (4-9) will henceforth be ignored. A constant water content θ is assumed throughout the domain. Furthermore, K_s and therefore K(h) are assumed to be locally isotropic i.e., $K_1(x,h) = K_2(x,h)$. In the remainder of this work, K_s and α are the only independent parameters that are assumed spatially variable in the governing equations (4-1) and (4-2) with (4-8) and (4-9) being the constitutive equations.

The numerical steady-state analysis of flow and transport in this study is based on the use of Gardner's exponential K(h) function (4-8), since this K(h) model also allows the derivation of approximate (1st order) analytical solutions. The practicality of using Gardner's K(h) model may be questioned (White and Sully, 1992). But this study is geared towards investigating rather fundamental problems in the numerical stochastic treatment of unsaturated flow and transport. It is justified to confine the numerical modeling to some of the constraints

of analytical tools since the theoretical analysis of steady-state unsaturated flow and transport is an important part of this study:

- approximate analytical solutions allow a preliminary evaluation of the physical importance of various parameters to the stochastic head and flux solutions (this chapter);
- approximate analytical solutions are used as initial solutions to the numerical solver to improve the CPU-efficiency of the Monte Carlo analysis by up to two orders of magnitude (see chapter 7);
- analytical solutions serve to validate the numerical models within a range of variability for which analytical solutions are known to be rather accurate (see chapter 6, 8, and 9);
- the range of validity of the approximate analytical solutions is investigated empirically by comparison to numerical solutions for highly heterogeneous soils (see chapter 6, 8, and 9);

Yeh et al. (1985a,b,c) presented a thorough analysis of one- and three-dimensional steady-state unsaturated flow in heterogeneous soils based on Gardner's K(h) model with constant α and with normally distributed α. The following will, for the first time, give a thorough analysis of two-dimensional flow in heterogeneous soils under the more justifiable assumption that α is a lognormally distributed field parameter. In addition spectral analysis will be applied to determine the first and second moments of the unsaturated hydraulic conductivity and of the velocity components. The analytical extension of these results to three dimensions as in Yeh et al. (1985a,b) is straightforward.

4.2 First-Order Perturbation Analysis of the Governing Stochastic Equation

This analysis is based on a first-order perturbation approach similar to the work by Bakr et al. (1978), Gelhar and Axness (1983), and Yeh et al. (1985a,b). Equation (4-1b) can be rewritten as

$$\frac{\partial^2 h}{\partial x_i} + \frac{\partial \log K(h)}{\partial x_i}\frac{\partial h}{\partial x_i} + \frac{\partial \log K(h)}{\partial x_1} = 0 \qquad (4\text{-}10)$$

where i=1, 2. Throughout the dissertation, the notation 'log' refers to the natural logarithm (unless otherwise noted). The following perturbation notation is used for the random variables $\log K_s$, $\log\alpha$, and h:

$$\begin{aligned} \log K_s(\mathbf{x}) &= f = F(\mathbf{x}) + f'(\mathbf{x}) \\ \log\alpha(\mathbf{x}) &= a = A(\mathbf{x}) + a'(\mathbf{x}) \\ h(\mathbf{x}) &= H(\mathbf{x}) + h'(\mathbf{x}) \end{aligned} \qquad (4\text{-}11)$$

where F(x), A(x), and H(x) are the expected values of $\log K_s(x)$, $\log\alpha(x)$, and h(x), respectively, and f'(x), a'(x), and h'(x) are zero-mean, second order stationary perturbations at location x. For the sake of brevity, the explicit dependency of the RFVs, their mean, and their perturbation on the location x will be omitted from now on.

In general H is not uniform in space, but the gradient of H, $J_i=\partial H/\partial x_i$, is assumed to be independent of location. The unsaturated hydraulic conductivity is then given by

$$\begin{aligned} \log K(h) &= \log K_s + \alpha h \\ &= F + f' + (H + h')\exp(A + a') \end{aligned} \qquad (4\text{-}12)$$

Writing exp(A+a') = exp(A) exp(a') and expanding the exponential perturbation term in a Taylor series gives:

$$\exp(a') = 1 + (a') + \frac{(a')^2}{2!} + \ldots \tag{4-13}$$

Writing the geometric mean of α as $\Gamma=\exp(A)$ and truncating the Taylor series to first order, the unsaturated hydraulic conductivity can also be approximated by a lognormally distributed random variable:

$$\log K_s = Y + y' = F + f' + (1+a')\,\Gamma\,(H+h') \tag{4-14}$$

where Y is the mean of logK(h) and y' is a zero-mean, second order stationary random perturbation. Expanding the product terms and again neglecting second-order terms the first-order perturbation approximation of the unsaturated hydraulic conductivity is obtained:

$$Y + y' = F + f' + H\Gamma + \Gamma h' + H\Gamma a' \tag{4-15}$$

Using (4-15) in (4-10) the stochastic form of Richards equation becomes:

$$\frac{\partial^2(H+h')}{\partial x_i^2} + \frac{\partial}{\partial x_i}[(F+f'+H\Gamma+\Gamma h'+H\Gamma a')\frac{\partial(H+h')}{\partial x_i}] + \frac{\partial}{\partial x_2}(F+f'+H\Gamma+\Gamma h'+H\Gamma a') = 0 \tag{4-16}$$

Expanding the product terms, neglecting second and higher order terms, and noticing that the derivatives of the mean of stationary random field variables are zero, the first order stochastic Richards equation is:

$$\frac{\partial^2 h'}{\partial x_i} + J_i\frac{\partial f'}{\partial x_i} + \Gamma J_i^2 + 2\Gamma J_i\frac{\partial h'}{\partial x_i} + \Gamma J_i^2 a' + \Gamma H J_i\frac{\partial a'}{\partial x_i} + \frac{\partial f'}{\partial x_2} + \Gamma J_2 + \Gamma\frac{\partial h'}{\partial x_2} + \Gamma a' J_2 + \Gamma H\frac{\partial a'}{\partial x_2} = 0 \tag{4-17}$$

Taking the expected values, the mean Richards equation is:

$$\Gamma J_i^2 + \Gamma J_2 = 0 \tag{4-18}$$

Subtracting the mean equation from the stochastic equation, the governing perturbation equation

becomes:

$$\frac{\partial^2 h'}{\partial x_i} + J_i\frac{\partial f'}{\partial x_i} + 2\Gamma J_i\frac{\partial h'}{\partial x_i} + \Gamma J_i^2 a' + \Gamma H J_i\frac{\partial a'}{\partial x_i} + \frac{\partial f'}{\partial x_2} + \Gamma\frac{\partial h'}{\partial x_2} + \Gamma a' J_2 + \Gamma H\frac{\partial a'}{\partial x_2} = 0 \qquad (4\text{-}19)$$

This study is particularly concerned with cases involving gravity drainage conditions i.e., the average gradient of the total potential $\Phi=(h+x_2)$ is unity and the average gradient of h is zero in all directions: $J_i = 0$. Although the entire following analysis can be carried out for any constant mean gradients J_i, only the solutions for zero mean head gradient will be given. In that case H is uniform in space i.e., independent of location. The governing perturbation equation then simplifies to:

$$\frac{\partial^2 h'}{\partial x_i} + \frac{\partial f'}{\partial x_2} + \Gamma\frac{\partial h'}{\partial x_2} + \Gamma H\frac{\partial a'}{\partial x_2} = 0 \qquad (4\text{-}20)$$

Note that this is a linear equation. The linearization has been achieved by dropping the higher order perturbation products.

The head covariance function, the cross-covariance function between f' and h', and the covariance and cross-covariance functions of flux related RFVs are obtained from a spectral analysis of the respective second order stationary random processes. Continuous parameter stationary processes in infinite domains can be represented by Fourier-Stieltjes integrals (see chapter 2):

$$a'(\mathbf{x}) = \int_{-\infty}^{\infty}\int_{-\infty}^{\infty} e^{i\mathbf{k}\cdot\mathbf{x}}\, dZ_{a'}(\mathbf{k})$$

$$f'(\mathbf{x}) = \int_{-\infty}^{\infty}\int_{-\infty}^{\infty} e^{i\mathbf{k}\cdot\mathbf{x}}\, dZ_{f'}(\mathbf{k}) \qquad (4\text{-}21)$$

$$h'(\mathbf{x}) = \int_{-\infty}^{\infty}\int_{-\infty}^{\infty} e^{i\mathbf{k}\cdot\mathbf{x}}\, dZ_{h'}(\mathbf{k})$$

$dZ_p(\mathbf{k})$ are orthogonal complex stochastic processes, p = f', a', or h', where:

$$\langle dZ_p(k)\rangle = 0$$

$$\langle dZ_p^*(k_m)\, dZ_p(k_n)\rangle = 0 \qquad m \neq n \qquad (4\text{-}22)$$

$$\langle dZ_p^*(k_m)\, dZ_p(k_n)\rangle = S_{pp}(k)dk \qquad m = n$$

where * indicates complex conjugate. In other words, the process $dZ_p(\mathbf{k})$ is a zero-mean univariate Gaussian random variable. Any $dZ_p(\mathbf{k}_m)$ is statistically independent of $dZ_p(\mathbf{k}_n)$ for $m \neq n$ and has a variance $S_{pp}(\mathbf{k})\, d\mathbf{k}$. $S_{pp}(\mathbf{k})$ is the Fourier transform of the covariance functions for the spatial random processes $X_p(\mathbf{x}) = f'(\mathbf{x})$, $a'(\mathbf{x})$, or $h'(\mathbf{x})$. Similarly the cross-spectral density $S_{pq}(\mathbf{k}) = \langle dZ^*_p(\mathbf{k})\, dZ_q(\mathbf{k})\rangle$ is the Fourier transform of the cross-covariance function between the processes p and q (p, q = f', a', or h'). The general relationship between the (cross-) covariance and the (cross-) spectral density is defined by (3-4):

$$C_{pq}(\xi) = \int_{-\infty}^{\infty}\int_{-\infty}^{\infty} e^{i\mathbf{k}\cdot\xi}\, S_{pq}(\mathbf{k})\, d\mathbf{k} \qquad (4\text{-}23)$$

Note that $C_{pq}(\xi) = C_{pq}(x, x+\xi)$. This can be shown by using the definition for $S_{pq}(\mathbf{k}) = \langle dZ^*_p(\mathbf{k})\, dZ_q(\mathbf{k})\rangle$ and expanding the complex exponential in (4-23) to $\exp(i\mathbf{k}(x-x+\xi))$, which leads to

$$C_{pq}(\xi) = < \int_{-\infty}^{\infty}\int_{-\infty}^{\infty} e^{-ik\pi} dZ_p^*(\mathbf{k}) \int_{-\infty}^{\infty}\int_{-\infty}^{\infty} e^{ik(x+\xi)} dZ_q(\mathbf{k}) >$$
$$= < X_p^*(\mathbf{x})\ X_q(\mathbf{x}+\xi) >$$
$$= < X_p(\mathbf{x})\ X_q(\mathbf{x}+\xi) > \qquad (4\text{-}24)$$

Using (4-22) and (4-23), (cross-) covariance functions of dependent variables are obtained from their spectral representations $dZ_p(\mathbf{k})$, which in turn are functions of the independent random fields $dZ_{f'}(\mathbf{k})$ and $dZ_{a'}(\mathbf{k})$.

Using the spectral representation of the random variables f'(x), a'(x), and h'(x) (4-21) to expand the governing first order perturbation equation (4-20), and taking the derivatives with respect to the spatial coordinates, the partial differential equation becomes an integral equation:

$$\int_{-\infty}^{\infty}\int_{-\infty}^{\infty} e^{-ik\pi}[(-(k_1^2 + k_2^2)+ik_2\Gamma)dZ_{h'} + (ik_2)dZ_{f'} + ik_2H\Gamma dZ_{a'}\ ] = 0 \qquad (4\text{-}25)$$

[As with the spatial RFVs and for the sake of clarity, the dependency of dZ_p on $\mathbf{k}$ is implicitly assumed and not denoted explicitly.] Because of the uniqueness of the spectral representation theorem, the integral (4-25) is only zero, if the expression in square brackets becomes zero. The solution to (4-25) is an explicit closed form expression for the relationship between the Fourier amplitudes of the independent RFVs a', f', and the dependent RFV h':

$$dZ_{h'} = \frac{ik_2(dZ_{f'} + H\Gamma dZ_{a'})}{(k_1^2 + k_2^2 - i\Gamma k_2)} \qquad (4\text{-}26)$$

The reader is reminded that this is an exact solution to the first order perturbation equation governing steady-state unsaturated flow in an infinite, vertically two-dimensional domain under gravity drainage. It is also an exact, but trivial solution to the fully perturbed Richards equation with arbitrary boundary conditions at an infinite distance in the limit as $\sigma^2_{f'}$->0 and $\sigma^2_{a'}$->0. For $\sigma^2_{f'}$<<1 and $\sigma^2_{a'}$<<1 the above solution may be taken as a valid approximation of the

solution to the nonlinear Richards equation, since higher order perturbation products that were disregarded during the derivation of (4-26) are indeed negligibly small.

4.3 Moment Analysis of Unsaturated Flow

4.3.1 Head

The previous section derives an explicit spectral head solution for the first order perturbation flow equation. The mean head H is assumed to be a known constant parameter (gravity drainage). The variance and covariance of the head are obtained from an inverse Fourier transform of the spectral density, which can be computed numerically (see section 4.4). The spectral density is related to the spectral representation through (4-22c). Hence the remaining step in the derivation of the head variance-covariance function is to take the expected value of the products of $dZ_{h'}$ and its conjugate complex $dZ_{h'}^*$:

$$S_{hh} = \langle dZ_{h'}^*, dZ_{h'} \rangle = \frac{k_2^2 \, (S_{ff} + 2H\Gamma S_{fa} + H^2\Gamma^2 S_{aa})}{(k_1^2+k_2^2)^2 + \Gamma^2 k_2^2} \qquad (4\text{-}27)$$

Although not explicitly stated (for reasons of brevity) S_{hh} and all following spectral density functions S_{pq} are functions of $\mathbf{k}$. Also for simplicity of notation, the ' are dropped from the subscripts to the spectral density S and the covariance function C. S_{ff} and S_{aa} are the Fourier transforms of the covariance functions C_{ff} and C_{aa}, respectively, and can be obtained analytically for some covariance functions (Bakr, 1978; Mizell, 1981). The cross-spectral density S_{fa} depends on the desired cross-correlation between f'(x) and a'(x+ξ). A more general treatise on generating cross-correlated random fields can be found in Robin et al. (1993).

When $C_{aa}/\sigma_a^2 = C_{ff}/\sigma_f^2$ i.e., the correlation functions of a' and f' are identical, a' and f' are related through the following relationship:

$$a' = \zeta \left(\rho f' + \sqrt{1-\rho^2}\, w' \right) \tag{4-28}$$

where $\zeta = \sigma_a/\sigma_f$, ρ is the local correlation between f'(x) and a'(x), and w'(x) is a random process uncorrelated to f'(x) but with the same covariance function. Then it is easily seen by inspection that

$$dZ_{a'} = \zeta \left(\rho dZ_{f'} + \sqrt{1-\rho^2} dZ_{w'} \right) \tag{4-29}$$

From this it follows immediately that

$$\begin{aligned} S_{aa} &= \zeta^2 S_{ff} \\ S_{af} &= \zeta \rho S_{ff} \end{aligned} \tag{4-30}$$

and the head spectral density function simplifies to:

$$S_{hh} = \frac{k_2^2}{(k_1^2 + k_2^2)^2 + \Gamma^2 k_2^2} \left(1 + 2\rho\zeta H\Gamma + (\zeta H\Gamma)^2\right) S_{ff} \tag{4-31}$$

The cross-spectral densities between f' and h' and between a' and h' are:

$$S_{fh} = \langle dZ_f^*, dZ_{h'} \rangle = (-\Gamma k_2^2 + i\, k_2 (k_1^2 + k_2^2)) \frac{(S_{ff} + H\Gamma S_{fa})}{(k_1^2 + k_2^2)^2 + \Gamma^2 k_2^2)} \tag{4-32}$$

$$S_{ah} = \langle dZ_a^*, dZ_{h'} \rangle = (-\Gamma k_2^2 + i\, k_2 (k_1^2 + k_2^2)) \frac{(S_{af} + H\Gamma S_{aa})}{(k1^2 + k_2^2)^2 + \Gamma^2 k_2^2)} \tag{4-33}$$

If the correlation functions of a' and f' are identical, definition (4-29) is used to replace S_{aa} and $S_{af} = S_{fa}$ in (4-32) and (4-33), and to write S_{ah}:

$$S_{ah} = \frac{\zeta\rho + \zeta^2 H\Gamma}{1 + \zeta\rho H\Gamma} S_{fh} \tag{4-34}$$

Note that $S_{fh}^* = S_{hf}$, and $S_{ah}^* = S_{ha}$ which can be seen by inspection of (4-24). Since the cross-

spectral densities S_{fh} and S_{ah} are even in the real parts, but odd in the quadrature spectra with respect to k_2, the resulting cross-covariances are symmetric in the direction normal to the mean flow x_1, but asymmetric in the direction parallel to mean flow x_2 i.e., $C_{fh} \neq C_{hf}$ and $C_{ah} \neq C_{ha}$!

All the necessary moments to determine the parameters of the multivariate Gaussian probability density function of the matric potential h are now defined. These analytical relationships are strictly valid only for small perturbations with $\sigma^2_f << 1$ and $\sigma^2_a <<1$.

4.3.2 Unsaturated Hydraulic Conductivity

Recall the first order perturbation approximation of the logarithms of unsaturated hydraulic conductivity given in (4-15). Taking the expectation of (4-15) the equation for the 1st order mean unsaturated hydraulic conductivity Y is:

$$Y = F + H\Gamma \tag{4-35}$$

Subtracting (4-35) from (4-15), the perturbation y' of the unsaturated hydraulic conductivity becomes:

$$y' = f + \Gamma h' + H\Gamma a' \tag{4-36}$$

Again the spectral representations of f', a', and h' (4-21) are used to obtain a spectral representation of y':

$$dZ_{y'} = dZ_{f'} + \Gamma dZ_{h'} + H\Gamma dZ_{a'} \tag{4-37}$$

Then the spectral density of y', S_{yy}, is the expectation of the product of $dZ_{y'}$ with its complex conjugate:

$$S_{yy} = S_{ff} + \Gamma^2 S_{hh} + (H\Gamma)^2 S_{aa} + 2H\Gamma S_{fa} + \Gamma(S_{fh} + S_{fh}^*) + \Gamma H\Gamma(S_{ah} + S_{ah}^*) \tag{4-38}$$

where * indicates complex conjugate. When $C_{aa} = \zeta^2 C_{ff}$ relationships (4-29) and (4-30) are applied to obtain the spectral density S_{yy} in terms of S_{ff}:

$$S_{yy} = \left[1 + \frac{-k_2^2\Gamma^2}{(k_1^2 + k_2^2)^2 + \Gamma^2 k_2^2}\right](1 + 2\rho\zeta H\Gamma + (\zeta H\Gamma)^2)\, S_{ff} \tag{4-39}$$

Similarly, the cross-spectral density S_f is

$$S_{fy} = S_{ff} + \Gamma S_{fh} + H\Gamma S_{fa} \tag{4-40}$$

As with the cross-spectral densities S_{fh} and S_{ah} , S_f and hence C_f are nonsymmetric functions and care must be taken to apply the correct definition of the lag (4-24), when using these cross-covariance functions.

4.3.3 Pore Velocity

Pore velocity is defined by dividing the Darcy flux (4-2) with the soil water content θ:

$$v_n = \frac{-K(h)}{\theta}\frac{\partial(h + x_2)}{\partial x_n} \tag{4-41}$$

Using the first order approximation of K(h) given in (4-15), assuming that the mean head is the same everywhere (gravity drainage), and expanding esp(y') into a first order Taylor series similar to that of esp(a') in (4-13), the velocity components are approximated by:

$$v_1 = \frac{-K_m}{\theta}(1 + y')\, j_1'$$
$$v_2 = \frac{-K_m}{\theta}(1 + y')(1 + j_2') \tag{4-42}$$

where $K_m = \text{esp}(Y)$ and $j_n' = \partial h'/\partial x_n'$. The expected value of (4-42) gives the stationary first order mean velocity components:

$$V_1 = \langle v_1 \rangle = 0$$
$$V_2 = \langle v_2 \rangle = \frac{-K_m}{\theta} \tag{4-43}$$

Subtracting the expressions in (4-43) from the stochastic representation of the velocity v in (4-42), first order, zero mean velocity perturbations are obtained:

$$v_1' = \frac{-K_m}{\theta} j_1'$$
$$v_2' = \frac{-K_m}{\theta}(y' + j_2') \tag{4-44}$$

By simple inspection, and noting that $dZ_{j'n} = ik_n dZ_{h'}$, it is seen that the corresponding spectral representations of the velocity components are

$$dZ_{v_1'} = \frac{-K_m}{\theta}(ik_2 dZ_{h'})$$
$$dZ_{v_2'} = \frac{-K_m}{\theta}(dZ_{f'} + H\Gamma dZ_{a'} + (\Gamma + ik_1)dZ_{h'}) \tag{4-45}$$

Recall that $S_{v1.v1} = \langle dZ_{v1}^* \, dZ_{v1} \rangle$ and $S_{v2.v2} = \langle dZ_{v2}^* \, dZ_{v2} \rangle$. Then the Fourier transforms of the velocity covariance functions are:

$$S_{v_1v_1} = \frac{K_m^2}{\theta^2} k_1^2 S_{hh}$$

$$S_{v_2v_2} = \frac{K_m^2}{\theta^2} [S_{ff} + (H\Gamma)^2 S_{aa} + (\Gamma^2 + k_2^2) S_{hh} + 2H\Gamma S_{fa} \tag{4-46}$$

$$+ (\Gamma + ik_2) (S_{fh} + H\Gamma S_{ah}) + (\Gamma - ik_2) (S_{hf} + H\Gamma S_{ha})]$$

In the special case $C_{aa} = \zeta^2 C_{ff}$, (4-29) and (4-30) are used to obtain the spectral densities of the velocity components in terms of S_{ff}:

$$S_{v1.v1} = \frac{K_m^2}{\theta^2} \frac{k_1^2 k_2^2}{(k_1^2 + k_2^2) + \Gamma^2 k_2^2} (1 + 2\rho\zeta H\Gamma + +(\zeta H\Gamma)^2) S_{ff}$$

(4-47)

$$S_{v2.v2} = \frac{K_m^2}{\theta^2} \left[1 - \frac{k_2^2(\Gamma^2 + k_2^2) + k_1^2 k_2^2}{(k_1^2 + k_2^2) + \Gamma^2 k_2^2}\right] (1 + 2\rho\zeta H\Gamma + +(\zeta H\Gamma)^2) S_{ff}$$

Other cross-spectral density functions involving the velocity are computed equivalently.

4.4 Obtaining 2-D (Cross-)Covariance Functions from (Cross-) Spectral Density Functions by Inverse Fast Fourier Transforms

The (cross-) covariance function $C_{pq}(\xi) = \langle X_p(x)\, X_q(x+\xi)\rangle$ and the (cross-) spectral density function $S_{pq}(\mathbf{k})$ as used in this and previous chapters are defined by the Fourier transform pair (3-4) and (3-5) in chapter 3:

$$C_{pq}(\xi) = \int_{-\infty}^{\infty}\int_{-\infty}^{\infty} e^{i\mathbf{k}\cdot\xi} S_{pq}(\mathbf{k})\, d\mathbf{k} \tag{3-4}$$

$$S_{pq}(\mathbf{k}) = \frac{1}{2\pi^2}\int_{-\infty}^{\infty}\int_{-\infty}^{\infty} e^{i\mathbf{k}\cdot\xi} C_{pq}(\mathbf{k})\, d\xi \tag{3-5}$$

The inverse Fourier transforms (3-4) of the (cross-) spectral density functions derived in the

previous sections are implemented numerically since a rigorous analytical evaluation of the double Fourier integrals is very difficult if not impossible. In the past, spectral density functions derived for saturated flow and for unsaturated flow with constant α or normally distributed α have either been evaluated for ξ=0 only (Yeh et al., 1985a,b), by numerical integration (Yeh et al., 1985a,b; Russo, 1993a), or analytically for a specific class of S_{ff} (Bakr et al., 1978; Mizell, 1981). Russo (1993a) used the spectral densities of the head h' and its gradient j_n' and the cross-spectral densities involving f', a', h', and j_n' given by Yeh et al. (1985b). The respective (cross-)covariances are evaluated numerically, and the covariance functions of y', v_1', and v_2' are derived as functions (superpositions) of these numerically evaluated covariance and cross-covariances. The superposition of several numerically evaluated covariance and cross-covariance functions to obtain the unsaturated hydraulic conductivity and velocity covariances is very error prone, particularly for $C_{v2,v2}$, the covariance of the velocity component parallel to mean flow. If the numerical evaluation of the inverse Fourier transforms of the expressions in Yeh et al. (1985b) is not implemented with great accuracy, the additive errors resulting in the numerically obtained (cross-) covariances from which $C_{v2,v2}$ is computed may become considerable. In contrast, the spectral density $S_{v2,v2}$ derived here (4-46) is exact in the first order sense, and only one Fourier integral needs to be evaluated.

Unlike in the above mentioned studies, advantage is taken of a numerical technique called (inverse) "fast Fourier transform" (FFT), which has already been encountered in the previous chapter on random field generators. FFT algorithms were introduced five decades ago (Press et al., 1992). The development of their fundamental theoretical framework and various techniques for their implementation have since evolved into a field of science itself (Brigham, 1988). FFT algorithms are readily available for many computer platforms and programming languages (also see chapter 3.5). The FFT algorithm is SCFT2 provided by the Engineering and Scientific Solutions Library (ESSL) (IBM, 1993) that is part of the Fortran compiler for the IBM RS/6000 workstations.

As with all FFT algorithms, the SCFT2 algorithm is defined in terms of the spatial frequency u instead of the spectral wave-number k, where

$$k = 2\pi u \tag{4-48}$$

Introducing a new variable $\hat{S}_{pq}(\mathbf{u}) = (2\pi)^2 S_{pq}(2\pi\mathbf{u})$, substituting k with u, and noting that in two dimensions $d\mathbf{k} = (2\pi)^2 d\mathbf{u}$, the Fourier transform pair (3-4) and (3-5) becomes (compare to (3-8) and (3-9):

$$\hat{S}_{pq}(\mathbf{u}) = \int_{-\infty}^{\infty}\int_{-\infty}^{\infty} e^{-i2\pi\mathbf{u}\cdot\xi}\, C_{pq}(\xi)\, d\xi \tag{4-49}$$

$$C_{pq}(\xi) = \int_{-\infty}^{\infty}\int_{-\infty}^{\infty} e^{i2\pi\mathbf{u}\cdot\xi}\, \hat{S}_{pq}(\mathbf{u})\, d\mathbf{u} \tag{4-50}$$

In the numerical Fourier transform the continuous function under the integral is evaluated at a finite number of discrete arguments i.e., the integral is discretized into a sum, and truncated at sufficiently large positive and negative limits of the summation variable. The discretization and the truncation involve numerical errors, as will be seen later. The covariance function is discretized into a regular two-dimensional grid with an equal number of gridpoints in each direction:

$$\xi_n = n\Delta\xi \qquad n=-M,M-1 \tag{4-51}$$

Similarly, the spectral density function is discretized on a regular two-dimensional grid with an equal number of grid-points in each direction:

$$u_m = m\Delta u \qquad m = -M,M-1 \tag{4-52}$$

The spacing of the frequencies $\Delta\mathbf{u}$ is a function of the total length of the spatial grid $2M\Delta x$, since the lowest possible frequency (the frequency with the longest possible wavelength) in the discretized domain has a length equal to the side-length of the spatial domain (see chapter 3.2):

$$\Delta u = \frac{1}{2M\Delta\xi} \tag{4-53}$$

Similarly the highest possible frequency or Nyquist frequency is the reciprocal of twice the spatial discretization:

$$u_M = \frac{1}{2\Delta\xi} \tag{4-54}$$

To obtain the covariance function, a spatial discretization $\Delta\xi$ must be defined *a priori*. The gridpoints are then specified by

$$u_m = \frac{m}{2M\Delta\xi} \tag{4-55}$$

and since the spectral density functions in section (3.3) are defined in terms of **k**:

$$k_m = \frac{2\pi m}{2M\Delta\xi} \tag{4-56}$$

Most numerical FFTs pack the arrays for C_{pq} and S_{pq} not from -M to M-1, but from 0 to 2M-1 such that the values from -M to -1 are packed into the area M to 2M-1. In other words, for the purpose of the FFT $\hat{S}_{pq}$ is packed as follows:

$$\begin{aligned}
\hat{S}_{pq}(2M-m_1,2M-m_2) &= \hat{S}_{pq}(-m_1,-m_2) \qquad 1 < m_1,m_2 < M \\
\hat{S}_{pq}(m_1,2M-m_2) &= \hat{S}_{pq}(m_1,-m_2) \quad 1 < m_1,m_2 < M \\
\hat{S}_{pq}(2M-m_1,m_2) &= \hat{S}_{pq}(-m_1,m_2) \quad 1 < m_1,m_2 < M
\end{aligned} \tag{4-57}$$

and equivalently C_{pq}:

$$\begin{aligned}
C_{pq}(2M-n_1,2M-n_2) &= C_{pq}(-n_1,-n_2) \quad 1 < n_1,n_2 < M \\
C_{pq}(n_1,2M-n_2) &= C_{pq}(n_1,-n_2) \quad 1 < n_1,n_2 < M \\
C_{pq}(2M-n_1,n_2) &= C_{pq}(-n_1,n_2) \quad 1 < n_1,n_2 < M
\end{aligned} \tag{4-58}$$

The reasons for the packing order are explained, for example, in Brigham (1988).

Now the approximate inverse Fourier transform of $S(\mathbf{k})$ can be obtained by replacing

the integrals in (4-49) by a double summation, expanding $\hat{S}_{pq}(\mathbf{u})$ in terms of $S_{pq}(\mathbf{k})$ and replacing **du** by $\Delta\mathbf{u}$:

$$C_{pq}(n_1\Delta x_1, n_2\Delta x_2) =$$

$$\sum_{m_1=0}^{2M-1}\sum_{m_2=0}^{2M-1} e^{\frac{i2\pi}{2M}m_1n_1} e^{\frac{i2\pi}{2M}m_2n_2} S_{pq}\left(\frac{2\pi}{2M\Delta x_1}m_1 , \frac{2\pi}{2M\Delta x_2}m_2\right) \frac{2\pi}{2M\Delta x_1}\cdot\frac{2\pi}{2M\Delta x_2} \tag{4-59}$$

which is the definition of the Fourier transform SCFT2 in ESSL:

$$y(n_1,n_2) =$$

$$\text{scale}\sum_{m_1=0}^{l1-1}\sum_{m_2=0}^{l2-1} x(m_1,m_2)\, e^{\text{isign}\frac{-i2\pi}{l1}m_1n_1} e^{\text{isign}\frac{-i2\pi}{l2}m_2n_2} \tag{4-60}$$

where

$$y(n_1,n_2) = C_{pq}(n_1,n_2)$$

$$x(m_1,m_2) = S_{pq}(2\pi m_1/(2M\Delta x_1), 2\pi m_2/(2M\Delta x_2))$$

$$\text{scale} = (2\pi)^2/(4M^2\Delta x_1\Delta x_2) \qquad l1 = l2 = 2M \qquad \text{isign} = -1$$

From (4-51) and (4-52) it is seen that the discretization in the spatial domain determines the truncation in the frequency domain, while the truncation in the spatial domain determines the discretization in the frequency domain. Truncation and discretization error are therefore inseparable since both need to be avoided in both domains if the FFT is to be an accurate estimate of the Fourier integral (4-49) (see e.g. Robin et al., 1993). A discretization in the spatial domain such that $\lambda_f = 10\xi$ and $M=100\,\lambda_f$ gives a sufficiently accurate estimate of (4-49). Discretizing ξ such that $\lambda_f = 20\xi$ and $M=100\,\lambda_f$ or $\lambda_f = 10\xi$ and $M=200\,\lambda_f$ does not significantly change the results. Pseudo-analytical solutions of the covariance and cross-covariance functions obtained after a numerical FFT of the analytical spectral density functions given in this chapter are shown in subsequent chapters 6 and 8.

5. MMOC2 - A NUMERICAL MODEL FOR WATER FLOW AND TRANSPORT IN VARIABLY SATURATED POROUS MEDIA

For the numerical simulation of flow and transport through a vertical cross-section of a heterogeneous soil, the combined flow and transport model described by Yeh et al. (1993) (henceforth referred to as "MMOC2") is used and modified for the purposes of this study. This chapter summarizes the main features of MMOC2 and the conceptual changes from the description in Yeh et al. (1993). For the details of MMOC2 the reader is referred to the original publication.

The numerical flow model solves the governing equation for two-dimensional flow in porous media, and handles saturated as well as unsaturated or partially saturated flow (Neuman, 1973):

$$\frac{\partial}{\partial x_i}\left(K_{ij}(h,x)\frac{\partial}{\partial x_j}(h+x_2)\right) = \left(C(h,x)+\beta_s S_s(x)\right)\frac{\partial h}{\partial t} - q_s \qquad (5\text{-}1)$$

where i,j = 1,2. x_1 and x_2 are the horizontal and vertical spatial coordinates, respectively, with x_2 pointing upward (see notation in previous chapters). $K_{ij}(h)$ is the hydraulic conductivity tensor, which reduces to an isotropic, spatially variable, single parameter K(h,x) for all purposes of this study i.e., only locally isotropic phenomena are investigated. K(h,x) is a function of the soil matric potential only under unsaturated conditions (see chapter 4) and it equals the saturated hydraulic conductivity $K_s(x)$ under saturated conditions. β_s is an index for saturation and is 0 under unsaturated conditions ($h < 0$) and 1 for saturated conditions $h \geq 0$. C(h,x) is the soil water capacity function and $S_s(x)$ is the specific storage capacity of the saturated soil. The numerical solution of the flow equation - transient or steady-state ($\partial h/\partial t=0$) - is achieved through the Galerkin finite-element technique (FE) using triangular or rectangular elements.

For this study, only rectangular elements are used, over which bilinear shape-functions are defined. The nonlinear equations can be solved either by the Picard or by the Newton-Raphson technique. For the purpose of this study the Newton-Raphson method is chosen since it gives satisfactory results at high computational efficiency. The Picard scheme is not used in any applications of this study. The resulting linear matrix equation is solved through an incomplete LU-decomposition of the coefficient matrix as a preconditioner to the conjugate gradient method. Automatic time stepping is implemented for a more efficient handling of transient infiltration processes.

After the matric potential is found by solving (5-1), MMOC2 also solves Darcy's equation (4-2) by a Galerkin finite element method using the same bilinear shape functions as for the solution of the flow equation (5-1). The FE solution of Darcy's equation guarantees a continuous flux field q(x) throughout the domain, which is advantageous when solving the transport equation.

Transport of solutes through porous media is governed by the advection-dispersion equation:

$$\frac{\partial}{\partial x_i}\left(D_{ij}\frac{\partial c}{\partial x_j}\right) - q_i\frac{\partial c}{\partial x_i} - \lambda R c = \theta R\frac{\partial c}{\partial t} \qquad (5\text{-}2)$$

for i,j=1,2. D_{ij} is the local dispersion tensor computed as a function of the local flux $q(x) = (q_i(x)\, q_j(x))^{1/2}$:

$$D_{ij} = (\alpha_L - \alpha_T)\frac{q_i q_j}{q} + \alpha_T q \delta_{ij} + D_0 \qquad (5\text{-}3)$$

α_L is the longitudinal dispersivity and α_T is the transverse dispersivity. $\delta_{ij}=1$ for i=j, $\delta_{ij}=0$ otherwise, is the Kronecker delta. D_0 is the apparent molecular diffusion. λ is a non-selective, first-order decay rate constant. R is the retardation coefficient and is related to the equilibrium sorption coefficient K_d by:

$$R = (1 + \rho_b K_d) \qquad (5\text{-}4)$$

The modified version of MMOC2 used for this study solves equation (5-2) by applying a one-step reverse particle tracking method to solve the advective part of (5-2) and a Galerkin finite element method to solve the dispersive transport (Neuman, 1984). The transport model described by Yeh et al. (1993) includes terms for kinetic adsorption and desorption processes, which have been omitted from this model version, since such processes have not been investigated in this study. Notice that in (5-4) a non-selective decay term has been added to the transport equation, not originally contained in the model by Yeh et. al (1993). The decay and the sorption partitioning terms are part of the advective transport formulation solved numerically by the particle tracking method described in Yeh et al. (1993).

This version of MMOC2 also changes an option affecting the particle tracking near boundaries: Unlike described by Yeh et al. (1993) the backward particle tracking algorithm assumes that particles at no-flow boundaries are *not* reflected back into the domain, since the applications in this study never use a no-flow boundary specifically to simulate a symmetry boundary. Only under the symmetry-assumption is a reflection of particles at no-flow boundaries justified. Finally, for reasons of both accuracy and efficiency, the time-step in the transport simulation is selected such that the displacement $\Delta X = |v\Delta t|$ of each particle per time-step is at the most the distance between two nodes Δx, i.e. the Courant number $\Delta X/\Delta x$ is always smaller than 1.

The model has been tested for a wide range of boundary and initial conditions by Yeh et al. (1993). Local dispersion in all applications of this study is presumed to be on the order of 1/10 to 1/100 of the element-length. Such a small dispersion is sufficiently well reproduced by simply relying on numerical dispersion and setting the input dispersion coefficient to zero. Calculation of the dispersive terms in equation (5-2) is computationally very expensive. Solving the advective transport equation only, and using numerical dispersion *in lieu* of solving

the dispersion equation in (5-2), saves a considerable amount of computation time in Monte Carlo simulations. However, the exact amount of numerical dispersion varies both with velocity and from location to location and cannot be exactly quantified. While local dispersion plays an important role in spreading an initially small contamination plume, the macrodispersion or overall spreading of the contamination plume in most of this study's applications is several orders of magnitudes larger than the spreading due to numerical dispersion or otherwise specified local dispersion. The spreading of a plume in heterogeneous media is predominantly controlled by the heterogeneities in the soil. Hence, while the existence of local dispersion is important, its exact amount is relatively insignificant if it has an upper bound that is comparable to the actual local dispersion desired. Figure 5.1 shows an application of MMOC2 to a hypothetical contamination problem in a heterogeneous soil. The finite elements are squares with a side-length of 10 cm. The first simulation omitted the computation of the dispersive portion in equation (5-2). In the other simulations shown, the local dispersivities were assumed to be isotropic. Simulations with dispersivities of 0.001 cm, 0.01 cm, 0.1 cm, and 1 cm were implemented, and it is obvious that only local dispersivities of 0.1 cm or 1/100 of the element-length and larger disperse the plume stronger than numerical dispersion alone. From several such experiments it is found that the empirical, numerical dispersivity in simulations of transport through heterogeneous soils is on the order of 1/10 to 1/100 of the element size. In most applications in this study the element size varies between 10 cm and 30 cm. Hence, the numerical dispersion is equivalent to a local dispersivity on the order of 1 mm to 1 cm, which is realistic for many soils. This justifies the use of particle tracking alone to solve (5-2).

6. GRID DESIGN AND ACCURACY IN NUMERICAL SIMULATIONS OF VARIABLY SATURATED FLOW IN RANDOM MEDIA: REVIEW AND NUMERICAL ANALYSIS

6.1 Introduction

Most numerical stochastic models are based either on the Monte Carlo technique or on single large realizations. The numerical stochastic models technically consists of three major parts or modules:

1.) Random fields are generated to represent realizations of the stochastic input variables (random field variables, RFV, see section 2.5.1 and chapter 3) such as the saturated hydraulic conductivity.

2.) Using the random field(s) as input, a standard finite difference or finite element model (or any other numerical technique) is applied to solve the flow equation deterministically i.e., to compute the dependent variables (head and flux) at each location in space and time - the latter only for transient simulations (see chapter 5). Step 1 and 2 may be repeated several times to obtain a sample of realizations that will be large enough to represent the ensemble with only a small statistical error (Monte Carlo simulation). By invoking the ergodicity assumption (chapter 2) a single large simulation is sometimes used by itself to represent the ensemble (Ababou, 1988; Russo, 1991).

3.) The last step of a stochastic simulation will be to employ statistical analysis on the deterministic results i.e., to find, for example, the histogram, mean, variance, and covariance of the resulting random fields of output variables (see e.g. chapter 3.4).

A number of design criteria have to be considered to assure that the Monte Carlo analysis will be accurate when analyzing unsaturated flow in heterogeneous media (numerical stochastic

approach). Discretization of the numerical grid and the time stepping have long been recognized as an important input parameter to assure the accuracy of numerical models for unsaturated flow in homogeneous media (Fletcher, 1988). The grid design of Monte Carlo simulations must in addition assure results that are also accurate in the stochastic sense. The working hypothesis that will be tested in this chapter is that the grid design for Monte Carlo simulations (which are evaluated for their statistical information content) is different from that required for deterministic simulations (which are evaluated for their absolute information content). In this chapter, grid design criteria for the stochastic simulation of unsaturated flow are developed based on the empirical statistical analysis of single large simulations for which the ergodicity assumption can be invoked.

From the perspective of the numerical modeler the deterministic approach is merely a special case of the stochastic approach. As shown above, the deterministic method is embedded in the stochastic approach as one of three major modules. Hence, the list of important design parameters includes several critical elements that are unique to the stochastic approach:

module 1: The simulated random fields have to converge in mean square to the desired moment and statistical distribution specifications. This restricts the choice of the minimum relative correlation length $\lambda' = \lambda/\mathbf{b}$ (λ: vector of directional correlation lengths; vectors are indicated by lower boldface letters; **b**: vector of the length of a block in each dimension; a block is a discrete, homogeneous unit within the heterogeneous domain). When using SRFFT or TB type random field generators the convergence requirement will in general impose certain limits on the minimum relative size of the random field $\mathbf{d}' = \mathbf{d}/\lambda$ (**d**: length vector of the domain size e.g., depth and width of a vertical 2-D simulation domain). The generated random field should be free of any artificially introduced patterns such as the line-patterns resulting from some versions of the turning bands random field generator (see chapter 3.4)(Gutjahr, 1989; Tompson et al., 1989).

module 2: The general formulation of the finite difference or finite element solution

algorithm, the element size Δx, and the time-stepping Δt must be chosen to assure stability, consistency, and convergence of the solution. Since the unsaturated flow problem is nonlinear, special demands are placed on the element size Δx and the dimensionless size of the random blocks $b/\Delta x$ in the simulated domain. These criteria are distinctly different from criteria used to model saturated flow, as discussed below. In transient simulations of unsaturated flow, the time-step Δt must also be chosen with care.

module 3: For the stochastic analysis, effects from deterministic boundary conditions, the stationarity and ergodicity of the simulation, and the degree of resolution of the heterogenous field have to be taken into account. The limits imposed by these requirements are often mutually dependent because computing resources are limited. The relative correlation length $\lambda' = \lambda/b$, for example, is a measure of the resolution of the heterogeneous field: the larger λ', the finer the structure of the random field i.e., more of the true variance of the continuous random field variable will be captured by the simulation. However, the total size of the random field domain must also be large with respect to the correlation length to assure that the spectrally generated random fields accurately represent the desired moments (SRFFT method, chapter 3), to minimize boundary effects, and to meet the requirements of the ergodicity assumption in a single large realization (see chapters 2 and 3). Given a maximum domain size $d/\Delta x$ (dictated by the limits of the computer), an optimal compromise choice for the two parameters d/λ, λ/b, and $b/\Delta x$ has to be found.

While stochastic numerical models are increasingly applied to analyze the effects of heterogeneities in the unsaturated zone, there is little guidance in the literature regarding the design of the numerical grid used for such simulations. Commonly, vertical discretization is chosen on the order of a few centimeter, while horizontal discretization maybe on the order of several tens of centimeters. Also, few analytical or empirical results are available for determining a meaningful relative correlation length λ'. The smallest perturbation resolved by any numerical grid has a wavelength twice the element-size (see chapter 3). Thus, the statistical

resolution requirement that $\mathbf{b} << \lambda$. The resolution λ' is commonly chosen to be between two and five (e.g. Ababou, 1988; Hopmans, 1989; Russo, 1991).

While such design criteria have been applied to stochastic simulations of unsaturated flow, most have originally been developed for solving the saturated flow equation. The immediate application of these criteria to also solve Richards equation (4-1) seems not warranted without a closer examination of the difficulties that may arise from the nonlinear character of Richards equation. The purpose of this chapter is to closely examine some of the most important numerical design criteria mentioned. Two-dimensional, heterogeneous, unsaturated steady state flow in a single, large vertical flow domain is simulated i.e., the stationarity and ergodicity assumptions are invoked (see also Ababou, 1988; Russo, 1991). The difficulties encountered in deriving analytical solutions limit closed form stochastic analyses to first or second order approximations (Yeh et al., 1985a,b; Ababou, 1988; this work, chapter 4). This limitation renders most analytical solutions unsuitable for comparison with numerical simulations in highly disordered media. For the same reasons, it is also difficult to develop exact modeling criteria based on a rigorous truncation and error analysis of the nonlinear numerical model.

A common way to empirically establish certain grid design criteria, is to vary the grid parameters and to compare the results among themselves (Hopmans et al., 1988) and possibly with analytical solutions, if these are available. The obvious drawback of the method is that the criteria may only apply to a particular situation. My hope, however, is that the following examples will establish some general guidelines regarding the design of stochastic computer simulations. Numerical experiments are implemented to analyze the sensitivity of stochastic solutions with respect to:

* the absolute length of the grid-elements Δx
* the number $\mathbf{b'} = \mathbf{b}/\Delta x$ of elements within each homogeneous block
* the size $\lambda' = \lambda/\mathbf{b}$ of each block relative to the correlation length of the

stochastic input variables

* the size $\mathbf{d' = d/\lambda}$ of the simulation domain relative to the correlation length of the stochastic input variables

Known limitations on grid-design are summarized in section 6.2. The details of the simulations are given in section 6.3. Results are discussed in section 6.4. Analytical solutions developed in chapter 4 will be used to verify the numerical solutions. A comparison with simulations by other authors is made in section 6.5. A summary is given in section 6.6.

6.2 Review of Some Theoretical Considerations Regarding Numerical Accuracy

6.2.1 Grid Size

Well known criteria to assure accurate and stable solutions are only available for determining the maximum element-size and the time-step in some deterministic FD or FE methods (Fletcher, 1988). Ababou (1988) derived a grid discretization or Peclet number based on an error and truncation analysis of the particular finite difference model he developed for the simulation of unsaturated, transient flow. For vertical flow in a soil described by Gardner's model for K(h), the grid Peclet number was found to be:

$$\alpha \Delta x_2 < 2 \qquad (6\text{-}1)$$

If this or other similar criteria are strictly applied to the simulation of flow in heterogeneous soils, the largest possible value of α in the random field dictates the discretization in space. Similar arguments can be made for the discretization in time. Since α is commonly on the order of 10^{-3} to 10^{-1} cm^{-1}, vertical discretization in an unsaturated heterogeneous flow model is often chosen to be between 2 cm and 10 cm (Ababou, 1988; Hopmans et al., 1988; Ünlü et al., 1990; Russo, 1991). For horizontal grid lengths Δx_1, Hopmans et al. (1988) found little difference in the stochastic results of two sets of Monte Carlo simulations with Δx_1 = 12.5 cm and Δx_1 = 25 cm, respectively. Other authors chose similar horizontal grid-lengths without

further specifying the reasons for their choice. The vertical grid discretization in Hopmans et al. (1988) is determined by reducing Δx_2 systematically until no change is observed in the results.

However, the numerical errors resulting from any particular choice of finite difference or finite element method are only one of a number of possible error sources in the stochastic simulation. An important limitation arises from the discrete, finite representation of continuous RFVs. The finite number of nodes or elements from which the statistical output moments are computed in a numerical simulation (single realization or Monte Carlo) introduce significant error in the sample statistics (see chapter 8). Therefore, if only a small number of elements will violate the discretization constraints imposed for purely numerical reasons, the statistical results should not be altered significantly. This would allow to weaken the Peclet constraint (6-1) imposed on the grid-design, which is otherwise determined by the largest α value in the random field. Depending on the input parameters, the weakened constraint may allow a considerably larger grid-size than a strict application of (6-1), particularly if α or - for that matter - any pore-size distribution parameter is distributed log-normal, as found in field applications (e.g. Wierenga et al., 1991; White and Sully, 1992).

6.2.2 Block Subdiscretization

Block subdiscretization is a technique applied specifically to nonlinear problems. For the purpose of this study, blocks are defined as the largest homogeneous, discrete units in a random field to distinguish them from the elements in a finite element or finite difference grid. A block is either equivalent to an element or it is subdivided into several elements. The technique of subdividing a (homogeneous) block into several elements is often used for the one-dimensional simulation of infiltration into vertical soil columns consisting of several (random or deterministic) layers of material with different physical properties (e.g. Hern and Melancon,

1986; Yeh and Harvey, 1990). Each layer is modeled by a small stack of cells or elements to accurately capture the non-linear behavior of the matric potential within each layer (Figure 6.1). Examples of using block subdiscretization in a two-dimensional, layered problem are found in Hopmans et al. (1988). Subdiscretization has not been applied to multidimensional heterogeneous fields, where the physical parameters vary in both the horizontal and vertical directions. There, the common modeling rule is not to subdiscretize - in other words: each block is associated with one element (e.g.: Ababou, 1988; Ünlü et al., 1990; Russo, 1991).

Figure 6.1 shows a typical matric potential distribution in layered media. Layers of coarse material exhibit a small fringe at the bottom, within which the matric potential changes drastically, while the head in layers of fine material changes only gradually. The thickness of the fringe is mainly determined by the slope of the unsaturated hydraulic conductivity function. Assuming Gardner's hydraulic conductivity model (4-8), the slope of the hydraulic conductivity curve is characterized by α (Yeh and Harvey, 1990). The thickness of the fringe Δr is approximately of the order $1/\alpha$ (White and Sully, 1992). Hence, for large α, which is characteristic for coarse textured soils, the fringe is much thinner than for small α, which is characteristic for fine textured soils.

If n elements are chosen to be required within the hypothetical thickness of a fully developed fringe $\Delta r \approx 1/\alpha$, then:

$$\Delta r = n\,\Delta x \approx 1/\alpha \quad \text{thus:} \quad \alpha\Delta x \approx 1/n \tag{6-2}$$

This simple heuristic criterion is slightly more stringent than the one inferred from the stability analysis by Ababou (1988, p.423; also see (6-1)) and depends on the number n chosen. In applications with correlation lengths much larger than $1/\alpha$ it may be appropriate to discretize heterogeneity on a scale larger than that required for Δx. In those cases a discretization of blocks (which represent the scale of heterogeneity) into several elements may seem justified. However, in the same case random fields can also be generated with a discretization equal to the required element size and several tens of elements per correlation length. No

subdiscretization is needed if the typical block-length b (usually 15%-20% of the correlation length) satisfies the condition $\alpha b \approx 1/n$. Numerical examples are used to analyze the effect of subdiscretization.

6.2.3 Correlation Length

Each block in the simulation domain represents a finite, homogeneous portion of the total domain, within which smaller scale variability is neglected. In geostatistics, these blocks are referred to as "support". Although the term 'support' is closely related to the measurement of certain data (estimation problem), it is here also used as term for the homogeneous blocks in a simulated random field (simulation problem).

In geostatistics it is well-known that the choice of the (measurement) support is crucial to the evaluation of the statistical properties of a RFV e.g., the mean and covariance, because statistical properties are strongly related to the size and shape of the support. Similarly, the size and shape of the simulation support (blocks) has significant impact on the statistical results of the simulation e.g., the mean and covariance of the matric potential h. The simulation should be designed such that the numerical model captures both the spatial variability of K_s and α (input) and the spatial variability of h and **q** (output) with sufficient accuracy. A compromise must be found between representing the natural spatial variability with sufficient accuracy and keeping the computing cost at a minimum.

Geostatistical methods provide simple analytical tools to determine how close the spatial variability of the block values is to the total spatial variability of all the points in a real soil profile. Block values are assumed to be the arithmetic average of all point values within a block. D.G. Krige derived a fundamental relationship that relates the variability of such block values e.g., within a soil profile (the domain of interest), with the variability of all the points within the same soil profile (Journel and Huijbregts, 1978):

$$\sigma^2 (p/d) = \sigma^2 (p/b) + \sigma^2 (b/d) \qquad (6\text{-}3)$$

where σ^2 (p/d) is the total variance (of the point values) within the domain, σ^2 (p/b) is the variance of the point values within the block, and σ^2 (b/d) is the variance of the block values within the domain. In applications to subsurface flow problems the arithmetic average, used to derive (6-3), rarely gives an accurate estimate of "effective" values of conductivity on the block scale (Yeh et al., 1985a,b; Gomez-Hernandez, 1991; Desbarats, 1992). The linear geostatistical approach is used here only as an approximation to illustrate the importance of sufficiently resolving heterogeneities. Journel and Huijbregts (1979) applied the variogram to derive the relationship between 2nd order moments of the point random variable X and the block-averaged random variable X_Ω. In a second order stationary random field, the variogram γ is related to the covariance by:

$$\gamma(\xi) = (\sigma^2 - C(\xi)) \qquad (6\text{-}4)$$

A random function that is regularized on the support Ω centered around the point x is defined as:

$$X_\Omega(x) = 1/\Omega \int_\Omega X(y)\, dy \qquad (6\text{-}5)$$

The variogram $\gamma_\Omega(b)$ of X_Ω (x) is derived from the variogram $\gamma(p)$ of the point-values by (Journel and Huijbregts (1979, p. 89)):

$$\gamma_\Omega(b) = \gamma(p) - \gamma(p,\Omega) \qquad (6\text{-}6)$$

Note the similarity of this equation with equation (6-3). $\gamma(p,\Omega)$ is the mean variogram of all points within each block (support) Ω. It is equivalent to the difference between a point variogram (the spatial variability of the point values) and a variogram based on block values (spatial variability of the blocks). $\gamma(p,\Omega)$ is defined by auxiliary functions (see e.g. Journel and Huijbregts, 1979). For rectangular blocks with sides l and L, the auxiliary function is of the following form:

$$\gamma(p,\Omega)=F(L,l)=\frac{2}{L}\int_0^L(L-u)\alpha_\gamma(u;l)du \qquad (6\text{-}7)$$

F(L,l) can be evaluated using charts, numerical solutions, or analytical solutions (Zhang et al., 1990). α_γ is a shape function. Equation (6-7) is used to determine how many blocks per correlation lengths are needed to represent the point variability within a specified error. For example, if the error should not be more than 10%, and assuming an exponential variogram, then $\lambda/b = 15$. A maximum difference between point and block variance of 5% is obtained with a resolution of 30 blocks per correlation length, $\lambda/b = 30$. On the other hand, a resolution of $\lambda/b = 4$ captures only about 70% of the total variance. In such situations considerable error is expected in the estimation of the true variances of the output variables.

Applied to soil water flow, the problem is far more complex than illustrated here, since the above approach (6-7) is based on Bayesian estimation theory, without direct involvement of the physical problem. Also note that point variability is neither a measurable quantity nor a quantity of much interest. It is the upscaling from the field scales of interest to the scales of a simulation that is of importance. The problem of upscaling data based on measurement support to "effective" parameters for the simulation support (blocks) has been discussed elsewhere in the literature (e.g. Rubin and Gomez-Hernandez, 1990). But the simplified analysis given here is helpful to illustrate the principle concern.

6.3 Numerical Simulation

6.3.1 Model Parameters, Initial and Boundary Conditions

Objectives for the numerical simulations here are: (1) model verification: to investigate whether single large field numerical solutions that use a conservative grid-design are comparable to analytical stochastic solutions. (2) grid-design study: to implement a sensitivity

analysis by varying several design-related parameters and using field-site related values.

The simulations are based on Gardner's exponential conductivity function (4-8) and the assumption that α is lognormally distributed. In this chapter it is assumed that the RFVs $\log K_s$ and $\log\alpha$ in Gardner's model are perfectly correlated. Then, K_s and α can be derived from a single random field Z by:

$$X = \exp(\mu_X + \sigma_X Z) \tag{6-8}$$

Z is a N(0,1) normally distributed random process with zero mean, unit variance, and with an exponential covariance structure (2-28) defined by the integral scale λ. The correlation structure is preserved by the transformation such that logX (log: natural logarithm) satisfies the same correlation function as Z. X is the lognormal random process to be derived ($X = K_s, \alpha$). μ_X is the specified mean of the logarithm of the RFV X and σ_X the square root of the variance of the logarithm of X. The mean of $\log K_s$ (where K_s is in [cm/d]) and $\log\alpha$ (α in [1/cm]) are chosen to be 5.5 and -4, respectively. For the model verification the variances for $\log K_s$ and $\log\alpha$ are 0.09 and 0.0009, respectively. For the grid design analysis the variances of $\log K_s$ and $\log\alpha$ are 4 and 0.25, respectively, which is representative of field conditions.

The random fields are generated using the spectral random field generator described in chapter 3. For the purpose of the grid-design sensitivity analysis, which is based on single large random field realizations, differences in the sample input moments from simulation to simulation must be avoided. To achieve a better preservation of the specified moments, the sample mean m_g and the sample standard deviation s_g are computed from the generated random field Z_g. Then the following transformation is applied to obtain Z in (6-8) from Z_g:

$$Z = (Z_g - m_g)/ s_g \tag{6-9}$$

The numerical solution of Richards equation, given the random field input of $\log K_s$ and $\log\alpha$, is obtained using MMOC2 (chapter 5). All non-variable input parameters to the model are listed in Table 6.1. The parameters are similar to those found for the field conditions at the Las Cruces trench site (Wierenga et al., 1989, 1991). The finite element net in all simulations

consists of 200 by 200 quadrilateral elements (rectangles or squares). The boundary conditions are:

a. $q_2 = -10$ [cm/d] at $x_2 = max$, i.e. constant flux at the top boundary

b. $\Delta h / \Delta x_1 = 0$ at $x_1 = 0$ and $x_1 = max$, i.e. no flow across the vertical boundaries

c. $\Delta h / \Delta x_2 = 0$ at $x_2 = 0$, i.e. unit hydraulic gradient across the bottom boundary.

x_1 and x_2 are the horizontal and vertical coordinates, respectively, x_2 increasing in upward direction. The steady-state solutions to (4-1 b) are computed by solving the transient solution of an initial value problem (4-1 a) at sufficiently large time. A direct numerical solution of the steady-state Richards equation is not possible due to the heterogeneity of the parameters (see also chapter 7). In addition, near static conditions may develop far from the true steady state (Neuman, 1972).

6.3.2 Model Verification

The model verification consists of a single Monte Carlo realization with a small rectangular element size $\Delta x_1 = 5$ [cm] and $\Delta x_2 = 2$ [cm], a correlation length $\lambda_1 = 50$ [cm], $\lambda_2 = 20$ [cm], and block-size = 1 element. This problem configuration is in conservative agreement with simulations presented by other authors (e.g. Ababou, 1988; Hopmans et al., 1988; Ünlü et al., 1990). To ensure that the perturbations of all RFVs are small, the variances of $\log K_s$ and $\log\alpha$ are 0.09 and 0.0009, respectively.

6.3.3 Grid-Design Analysis

A number of parameters are varied in order to investigate the limits of numerical stochastic models: The element-length Δx, the element shape $\Delta x_1/\Delta x_2$, the block-size **b**, the

relative correlation length λ/b, and consequently the relative domain size d/λ. For the grid-design study the variance of $\log\alpha$ was chosen such that the maximum α does not exceed 0.2 [1/cm]. Strictly applying the grid-Peclet number (6-2) limits the grid-size to less than 10 cm. In the experiments here the criterion is tested by varying the grid-size from 0.5 cm to 256 cm. The block sizes chosen were 1 element, 2 by 2 elements, and 4 by 4 elements. The (relative) correlation length λ/b varied from the standard 4 and 5 block-lengths to 40 block-lengths. Because the total size of the finite element grid was kept constant (200 by 200 elements), the corresponding domain length varied from 50 λ to only 5 λ. A complete overview of the various simulations is given in Figure 2. Note that up to three simulations are implemented with different grid-size Δx at approximately equal correlation length λ.

Most simulations are implemented with square blocks of 1 and 2 by 2 elements. The simulations with 4 by 4 elements per block are limited to $\lambda = 5$ and 10 block-lengths. Rectangular elements are tested for $\Delta_{x2} = \{2\ [cm], 4[cm]\}$ with $\Delta_{x1} = \{2\Delta x_1, 4\Delta x_1, 8\Delta x_1\}$ and $\lambda x_1 = 10\ \Delta x_1$, $\lambda x_2 = 10\ \Delta x_2$.

All simulations use the same seed for the random field simulator. Simulations based on the same number of blocks but different block-lengths b (i.e. different element-size Δx) have an identical random structure. The length-scale of the random structure, however, is different. Simulations based on the same number of blocks but different (relative) correlation length λ/b have similar pattern structures but each with the prescribed correlation length λ. In addition, a Monte Carlo simulation with 30 realizations is implemented with $\Delta x_1 = \Delta x_2 = 4$ [cm], $\lambda = 40$ [cm], and block-size = 1 element.

6.4 Results and Discussion

6.4.1 Random Field Generator

The random field generator is known to generate random fields free of numerical artifacts if sufficient discretization of the spectral domain is chosen (see chapter 3). The normalization of the generated random fields (6-9) further decreases the sampling error. The realizations do not contain any obvious artificial structures. None of the random fields exhibit any significant trends and all satisfy the stationarity and normality assumption. The directional sample autocorrelation functions (Yevjevich, 1972) show in more detail the quality of the random fields given various domain sizes for the grid design study (Figure 6.3). The sample correlation functions compare very well with the exponential correlation function, if $D/\lambda \geq 20$ (Figure 6.3c,d). For $D/\lambda \leq 10$ the sample autocorrelation function deviates from the exponential function and shows significantly shorter correlation lengths (Figure 6.3a,b). In this particular realization the horizontal autocorrelation function is less affected by sampling bias than the vertical sample autocorrelation function thus inducing a slight anisotropy. For $D/\lambda = 5$ a significant gap exists between the two curves (Figure 3a). The limitation of the SRFFT based random field generator to large dimensionless domain-sizes ($\lambda' \geq 10$) was discussed in chapter 3.

6.4.2 Comparison with Analytical Solutions (Model Verification)

The simulation runs for the model verification are evaluated with respect to the mean, variance, and covariance, which are compared to analytically derived moments. In chapter 4, the spectral density functions of the head, of the unsaturated hydraulic conductivity, and of the flux components are derived. The mean of the unsaturated hydraulic conductivity and of the flux components are also computed for given constant mean head. In the numerical simulation

no head boundaries are specified, only the mean flux is known. An analytical first order approximation of the mean head is obtained from the relationship for the mean unsaturated hydraulic conductivity (4-35):

$$H = (Y - F) / \Gamma \tag{6-10}$$

F is the mean of $\log K_s$ and Γ the geometric mean of α. Y is the mean of the unsaturated log conductivity, which can be written in terms of the mean vertical flux (4-43):

$$\exp(Y) = K_m = \langle q_z \rangle \tag{6-11}$$

For mass continuity the mean vertical flux must be equal to the specified boundary flux (10 [cm/d]) across the top boundary since no flux occurs across the vertical boundaries. With F = 5.5 and Γ = 0.018 [1/cm], the analytical mean pressure head is -174.6 cm, which compares excellently to the mean pressure head of -174.3 cm in the numerical simulation (Table 6.2). The mean values of the other output RFVs are also essentially identical with the first order analytical solution.

The analytical variances are computed from their respective spectral densities by a fast Fourier transform. For the numerical evaluation of the Fourier transforms, spectral density functions are calculated on a 1024^2 grid such that its transform, the covariance function has a resolution of 11 points per correlation length λ_f and a size of 102.4 λ_f in each direction (see chapter 4). The exponential input covariance function is also computed as a FFT of its analytical spectral density function to assess the accuracy of the numerical Fourier transform. The variance obtained for $\log K_s$ through the FFT is 3% below the fully analytical equivalent, which was specified to be 0.09. The accuracy does not improve significantly by increasing the number of points per correlation length or by increasing the size of the FFT domain. Other FFT-analytical solutions from the 1st order perturbation analysis for this verification case are assumed to have a similar margin of accuracy.

Table 6.3 shows that the sample variance of $\log K_s$ (from the random field generator) is within 1% of the specified variance due to the normalization (6-9). The sample variances

of logK and the vertical flux are 6% and 14% larger than their analytical variances, respectively. In contrast the head and horizontal flux variances are by 4% and 9% lower, respectively, than the analytically determined variances. Given the small error of the numerical Fourier transform the remaining 5% to 10% variability in the sample variance must be attributed to sample error. Recall that the 200^2 samples are not mutually independent and the sample size must therefore be considered limited.

The horizontal and vertical sample autocorrelation functions are shown in Figure 6.4 together with the analytically derived autocorrelation functions. The autocorrelation function is obtained from the covariance function by dividing the covariance with its variance. For short separation distances ($\xi' < 2$, where $\xi' = \xi/\lambda_{logK_s}$) the sample correlation of $logK_s$ is in excellent agreement with the analytical exponential correlation function. At larger ξ' the sample correlation in this realization is weaker than expected from the ensemble (analytical) correlation function. This is due to the proportionally smaller sample size from which the correlation is computed as the separation distance increases (Yevjevich, 1972). The smaller sample sizes are associated with larger sampling errors.

A similarly good agreement at shorter separation distances is seen for the correlation functions of the unsaturated hydraulic conductivity logK and the horizontal flux q_h. In contrast, the correlation functions of the head and the vertical flux are significantly different from the ensemble correlation functions even at short lag distances. Since the size and discretization of the FFT domain in the evaluation of the spectral density function is sufficiently accurate, the difference between the ensemble and sample correlation functions must be attributed to sample errors in the simulation. The error of the numerical results is likely due to the limited size of the simulation domain. Both the horizontal and vertical head ensemble correlation functions and the vertical ensemble correlation of v_v have very long correlation lengths relative to the total domain length. The total domain length both vertically and horizontally is 20 λ_f. The vertical and horizontal correlation lengths of the head and the horizontal correlation length of

q_v are three to five times larger than for $\log K_s$. The domain length is therefore only about six times the correlation length of the head. Since the deterministic flux boundaries increase the variance of the head near the boundary (Rubin and Dagan, 1989) it is not surprising to see a generally shorter correlation length in the sample correlation functions of the head and the vertical velocity.

Apart from the effects of the limited domain size, the simulations are in excellent agreement with the analytical solutions. The results confirm that the numerical model gives sufficiently accurate solutions under a conservative grid-design. Inaccuracies stem from the limited size of the sample domain given the relatively strong and far-reaching correlation of the head and the vertical velocity.

6.4.3. Grid-Design Sensitivity Analysis

6.4.3.1 Effects on the 1st Moment (Mean)

The analysis focuses on the sensitivity of the head, flux, and unsaturated hydraulic conductivity moments with respect to the various design parameters. Figure 6.5 depicts the sample means of both the input and the output random fields as a function of $\alpha_g \lambda_f$. α_g is given as input parameter. λ_f is directly obtained from the random field sample. This is done in an attempt to minimize the impact of varying sample error (6.4.1) occurring due to different relative domain lengths. The correlation length λ of all stochastic variables is computed from the sample covariance functions (Yevjevich, 1972) by iteratively solving the equation:

$$\mathrm{Cov}(\lambda) = \sigma^2 e^{-1} \qquad (6\text{-}12)$$

This definition of the correlation length λ coincides with the definition of the integral scale if the sample correlation satisfies an exponential correlation function.

The mean values for the input parameters are fairly constant. They show some sample variation due to the different sizes of the random fields generated. Of the output parameters the

horizontal mean flux $<q_h>$, the vertical mean flux $<q_v>$, and the mean of the unsaturated hydraulic conductivity <logK> are constant and independent of the grid-size chosen if $\Delta x \leq 16$ cm. The mean head varies significantly depending on the grid-design but also between Monte Carlo runs of the same grid-design. For elements larger than 16^2 [cm^2], all sample mean values are decreasing. The only exception is $<\log K_s>$, the independent parameter, and $<q_h>$, which always is close to 0. In particular the mean vertical flux $<q_v>$ decreases significantly at large element lengths although it shows very little sample variation at all for smaller elements. Since the flux at the top boundary is specified as 10 [cm/d] and no flux occurs across the vertical boundaries, the decrease in the mean vertical flux rate is an indication of significant numerical mass balance problems. For elements with Δx = 256 [cm] the decrease in mean vertical flux is more than 20% of the specified flux rate at the top boundary. For the same element size, the mean head decreases by 15 cm or 30% of the observed standard deviation.

The first order approximations of the head disagree even for small element sizes. The first order mean head is 174.6 [cm] (see section 6.4.2), while the numerically obtained mean heads range between 150 and 165 [cm] (based on computations with element lengths of 16 [cm] and less). While the variance of the output RFVs (unsaturated hydraulic conductivity and head) is relatively small, the large variance of the input parameters $\log K_s$ and $\log\alpha$ introduce significant analytical error into the first order approximations of the mean head. This demonstrates the limitations of the first order solutions derived in chapter 4 (see also chapter 8).

6.4.3.2 Variance and Covariance

HEAD: The normalized head variance σ^{*2}_h as a function of α_g and λ_f is computed in a form similar to the one suggested by Yeh (1985b, eqn. 26a):

$$\sigma_h^{*2} = \frac{\sigma_h^2}{\sigma_f^2 \lambda_f^2} \qquad (6\text{-}13)$$

The normalized head variance for block-size **b'** = 1 (**b=Δx**) is shown in Figure 6.6 together with the analytical function obtained from an evaluation of the first order spectral density of the head. The first order analytical approximation of the 2nd moments of the head and other output parameters are computed assuming a mean head of 155 [cm], which is representative for the mean heads of the numerical computations.

It is assumed that the numerical results for small element size and large λ/b are as accurate in the high input variance case (grid-design analysis) as in the low input variance simulation (model verification, Figure 6.4)). Although there are quantitative differences, the empirical head sample variance follows a stochastic function similar to the analytical variance function. Figure 6.6 shows that for small values of λ_f the first order approximation overestimates the normalized sample variance of the head, while it largely underestimates σ^{*2}_h for large λ_f. For block-size **b'**=1, the choice of the relative correlation length $\lambda' = \lambda/b$ has a consistent influence on σ^{*2}_h: The larger λ' , the lower the normalized head variance. Doubling λ' decreases the normalized variance of the head by approximately 10% with the only exception being the case λ/b=40. In other words, the higher resolution of the spatial variability in $\log K_s$ and $\log\alpha$ leads to a slightly lower head variance relative to the variance of the independent RFV $\log K_s$. It is interesting to note that unlike the mean head values the normalized head variance does not seem to be significantly altered by large element sizes.

The simulations with block size 2*2el. (**b'=2Δx**) and 4*4el. (**b'=4Δx**) give results very similar to the single element block simulations (Figure 6.7) regarding the general shape of the empirical variance function. However, here the relative correlation length λ' has the opposite effect: The larger the resolution of perturbations (higher λ') the larger the normalized head variance. For 2*2el. blocks the normalized head variance increases by 5% to 10% when

doubling the relative correlation length. For 4*4el. blocks, the same increase in relative correlation length causes a 30% to 40% increase in the normalized head variance. Since a change in relative correlation length changes the number of random points generated (and hence the sample size), it is not clear from these results whether the differences are statistically significant and due to the change in λ' or due to the change in the relative block-size **b'**.

To assess the statistical significance of the results, a small Monte Carlo simulation is implemented with $\mathbf{b'}=\Delta\mathbf{x}$, $\lambda' = (10, 10)$ to investigate the variability of the sample statistics. Figure 6.7 indicates the range of values in the normalized head variance for 90% of the 30 Monte Carlo samples. The large range of values for the *normalized* head variance is the combined effect of the variability in sample head, in sample correlation length λ_f, and in sample $\log K_s$ variance (see (6-13)). The smallest and largest non-normalized sample head variances differ by a factor of 2. In the Monte Carlo simulation the input λ_f is 40 [cm]. The sample λ_f varies from 34 to 57 [cm]. The sample variance of $\log K_s$, σ^2_f, ranges from 3.6 to 4.5. The range of sample mean head values obtained from each of the Monte Carlo runs is equivalent to approximately 1/2 the head standard deviation. This shows that a single large field simulation can only give rough estimates of the head variance. The range of the sample moments is much larger even than the total range covered by the simulations with different element-, block-, and correlation length. Hence, the differences for the various choices of element size, relative correlation length λ_f', and block size **b'** observed for element-lengths not exceeding 32 cm are statistically of limited significance. For a high level of accuracy, the choice of the relative input correlation length will certainly have to be considered, but then a single large field realization even with 40,000 elements is inadequate. A greater statistical significance can only be achieved by evaluating a large number of Monte Carlo runs and by comparing the results of entire Monte Carlo simulations rather than those of single large realizations. This is beyond the scope of this chapter. However, the results for different element size Δx but identical resolution λ_f' and block-size **b'** are directly comparable, since they

are based on the same set of random numbers.

For the (output) correlation length λ_h of the matric suction head the results are similar: In general, $\log\lambda_h$ is linearly proportional to $\log\lambda_f$ (Figure 6.8). For large element sizes (large λ_f) only insignificant deviations from a log-linear relationship are observed. Like σ_h^2, λ_h shows a dependence on the choice of the relative (input) correlation length λ': As λ' increases from 5 to 40, λ_h decreases, independent of the block-size chosen. Comparing the correlation structure for various block-sizes, it seems that the results are not sensitive to the block-discretization e.g., for $\mathbf{b} = \Delta x$ and $\lambda = 10\mathbf{b} = 10\Delta x$ the head correlation is the same as for $\mathbf{b} = 2\Delta x$ and $\lambda = 5\mathbf{b} = 10\Delta x$. The exact match is mere coincidence, given that the first simulation was based on a random field of 40,000 numbers, while the latter simulation was based on a random sub-field of only 10,000 numbers.

FLUX: The simulated normalized empirical flux variances $\sigma_{q^*}^2$:

$$\sigma_q^{*2} = \frac{\sigma_q^2}{\sigma_f^2 \bar{K}_m^2} \qquad (6\text{-}14)$$

where:

$$K_m = \exp(F)$$

are approximately 30% to 50% above the theoretical 1st order analytical results if $\alpha_g\lambda_f < 1$. The differences between the numerical and the analytical results increase as $\alpha_g\lambda_f$ increases. The normalized vertical flux variance deviates even qualitatively from the stochastic analytical results at correlation lengths corresponding to element sizes $\Delta x > 16$ cm indicating large numerical errors with discretizations in excess of much more than 16 cm. The increase in vertical flux variance for the larger element sizes coincides with the decrease in the mean vertical flux, further indicating that the vertical flux moments of all output moments are the most sensitive to the element size. The actual (non-normalized) vertical flux variance (like the vertical flux mean) is approximately constant for $\Delta x \leq 16$ cm (Figure 6.9).

The horizontal flux variance follows a similar stochastic form as the analytical solution

over the range of all correlation lengths/element sizes. The sensitivity of the flux variances to element-length Δx, block-size b', and relative correlation length λ' is in general slightly smaller than the sensitivity of the head variance to these parameters. Although not explicitly shown in Figure 6.8, the normalized flux variance of both the vertical and the horizontal flux decreases as the relative correlation length λ' increases. However, the range of variances obtained from different random fields in the Monte Carlo simulation again indicates the weak statistical significance of those results due to the sample error associated with one single large realization when assessing uncertainty of unsaturated flow.

A plot of the vertical and horizontal correlation length λ_{qv} vs. λ_f reveals a very strong correlation to the input correlation length over most of the range tested. Strong deviations from a log-linear type correlation between λ_{qv} and λ_f occur for $\Delta x \geq 64$ cm (Figure 6.10). Figure 6.11 shows the same results for the horizontal flux q_h. Unlike λ_{qv} the numerically determined correlation length of the horizontal flux λ_{qh} slows rather than accelerates its growth relative to λ_f for $\lambda_f > 100$ cm. The analytically derived λ_{qv} and λ_{qh} show a similar nonlinear dependence.

These results for the correlation length of the two flux components as an integrated measure of the covariance function are rather independent of the block-size chosen. The block-size itself has a small influence on the results. Given the range of possible outcomes of the normalized flux variance from a small Monte Carlo simulation, both the influence of the block-size and of the relative correlation length are almost negligible.

UNSATURATED K: A plot of the variance of logK against $\alpha_g\lambda$ and a plot of the correlation length of the unsaturated hydraulic conductivity against the input correlation length of logKs reveals that the unsaturated hydraulic conductivity are little sensitive to the tested grid-design options for $\Delta x \leq 32$ cm (Figure 6.12a-c). As for other statistical output parameters, the variation of sample moments within a single Monte Carlo simulation exceeds the variations observed due to different grid-design. Since the dependence of the logK moments on block size and relative correlation length is much less than the uncertainty arising from the small sample

size and hence from the variability in the sample moments there is little further insight these simulations can shed.

As expected, a strong linear dependence exists between λ_y and λ_r. The shape of the unsaturated variance function is similar to the vertical flux variance function. Note that the vertical flux has a correlation length approximately equal to the input correlation length, while the correlation length of the unsaturated hydraulic conductivity is only about half of λ_r (Figure 6.12b,c). The analytically determined correlation lengths (1st order) are generally larger than the numerical ones. Only at large $\lambda_r > 32$ cm both the horizontal and the vertical correlation length of logK are above the analytical results and also deviate from the linear correlation with λ_r.

6.4.3.3 Rectangular vs. Square Elements

To investigate the numerical effect of the ratio between the horizontal and vertical length of an element, an anisotropic field is simulated once with rectangular blocks consisting of several square elements and once with rectangular blocks consisting of a single rectangular element. Each block consists of only one row of elements in the vertical direction. The block-side ratios b_1/b_2 in the five cases examined are 2, 4, and 8. The relative correlation length λ' is 10 in both the vertical and horizontal directions. Table 6.3 compares several selected results obtained with the square element solutions vs. the rectangular element solutions. For the block-size ratios in these examples there is a remarkable agreement between both types of element shape. The difference in output parameter variance is generally less than 5% of the respective total variance. While the variance of the unsaturated log hydraulic conductivity is slightly smaller for square elements than for rectangular elements, all other variances are slightly larger for square elements than for rectangular elements. The differences in the correlation length are on the order of 1%. The correlation length of the square elements is always slightly smaller

than for rectangular elements. Overall no particularly strong bias is found associated with different element shapes.

6.5 Comparison with Other Heterogeneous Flow Simulation Studies

The general framework of the numerical experiments is similar to simulations reported by Hopmans et al. (1989), Ünlü et al.(1990), and Russo (1991). The grid-design analysis not only allows the assessment of the effect of various design parameters but also sheds some valuable insight into the stochastic analysis of flow in heterogeneous porous media. In the following paragraphs the results from section 6.4 are compared with the Monte Carlo simulation results obtained by the above authors.

Russo (1991) and Russo and Dagan (1991) (referred to here as R&D) simulate and evaluate an infiltration event in heterogeneous, unsaturated media in two dimensions with a single large domain simulation. Their computer simulation solves Richards equation with θ, the water content, instead of the matric potential h as dependent variable. The input RFVs are generated based on the similar media theory (Warrick et al., 1977), which requires one random field from which all random input variables are derived (compare to (6-8)). Unlike the simulations here, their simulation was based on VanGenuchten's constitutive equations for $K(\theta)$ and $\psi(\theta)$. Their grid-discretization was within the framework tested here (Δx=20 cm, Δz=2 cm). The simulation was based on a grid with just over 30,000 nodes with a relative domain size $\mathbf{d}'$ =(15, 80) in the horizontal and vertical direction, respectively. Since the resulting correlation length of the water content is similar to the input correlation of the scaling factor, the simulation results of the water content moments have less sampling error than the head moments in the simulations implemented here. But no attempt is made to characterize the sample variance of either the input or the output stochastic sample parameters.

In their analysis R&D suggest that

$$(\sigma^2 \lambda)_y = (\sigma^2 \lambda)_f \qquad (6\text{-}15)$$

reasoning that under unsaturated conditions the correlation length of the conductivity decreases and the variance increases. Clearly, the simulations here demonstrate that the relationship does not necessarily hold. R&D concluded that the unsaturated hydraulic conductivity variance increases reciprocal to the decrease in correlation length as the soil dries out. However, the behavior of σ^2_y among others depends primarily on the set of unsaturated hydraulic conductivity functions generated and on the mean hydraulic head in the simulation. This is true for both Gardner's and VanGenuchten's expression of K(h) and will be determined by the mean and variance chosen for the parameters in the K(h) expression. Field evidence qualitatively supports these findings (White and Sully, 1992). In the simulations described above σ^2_y is smaller than the variance for the saturated hydraulic conductivity σ^2_f: The correlation of f and logα causes a continuous decrease of the unsaturated conductivity variance as the mean head decreases until it reaches a minimum near $h_{min} = -1/(\alpha_g \zeta)$ (see Figure 6.13). At heads drier than h_{min} the unsaturated conductivity variance increases with decreasing head. While the reduction of σ^2_y is an artifact of the selected model, it should be understood that parameters are generally chosen to fit measured data with the K(h) function. In particular, if Gardner's exponential expression is chosen, the parameter logK_s should not be mistaken for the actual saturated hydraulic conductivity. Gardner's function is known to work well only for a limited range of suction values. If a wide range of h is expected to occur during the simulations, VanGenuchten's or other K(h) relations may be more satisfying. In general, however, a statement like (6-15) is not warranted given the strong dependence of σ^2_y on the K(h) function.

As a consequence of the hypothesis (6-15), R&D also discuss the possibility that unsaturated transport variability may be governed by similar laws as saturated transport due to the fact that the "*Lagrangian analysis [...] is of general nature and applies to saturated and unsaturated flow as well.*" In particular they find for their simulation, that

$$\sigma_{qv}^2/\langle q_v \rangle^2 \lambda_{qv} = \sigma^2_f \lambda_t \qquad (6\text{-}16)$$

The results in section 6.4 partially supports their conclusion. Indeed remarkably close agreement with (6-16) is found if the variance and correlation length of f=logK$_s$ is replaced with the variance and correlation length of y=logK (Figure 6.14). However, (6-16) does not hold for logK$_s$ as suggested by R&D. This precludes an *a priori* determination of the longitudinal dispersivity from σ^2_f and λ_f alone. A linear regression curve through the experimental values also exhibits a slope slightly larger than 1, which does not seem to be caused by the larger Δx alone (see the case, where $\mathbf{b} = 1\Delta x$).

A further hypothesis tested by R&D suggests that according to theoretical results suggested originally for saturated flow, the unsaturated flux moments are characterized approximately by:

$$CV_{qz}^2 = \sigma_{qv}^2/\langle q_z\rangle^2 = 0.375\ \sigma^2_f \qquad (6\text{-}17)$$

In neither Russo's nor the simulations in 6.4 does this particular relationship hold. But if σ^2_{logKs} is again replaced with σ^2_{logK} the agreement between the numerical results and (6-21) is quite good: In the simulations of section 6.4 $CV_{qz}^2/\sigma^2_{logK}$ varies from 0.24 to 0.31 for the simulations with single element blocks, from 0.25 to 0.40 for 2*2 element-blocks, and from 0.28 to 0.34 for the 4*4 element blocks. This supports the hypothesis that the stochastic theory developed for the saturated velocity field may hold for the unsaturated field, with logK replacing logKs (Figure 6.15) (see also chapter 9).

The results presented here are also in agreement with some of the findings of Hopmans et al. (1988) (referred to here as Hopmans), who simulated 2-D infiltration into one- and two-layered soils. In their simulations of the one-layered case, the simulated soil consists of a set of random soil property block-columns, each of which is subdivided into homogeneous (finite difference) elements. They find that the head values converged quickly to the ensemble moments. Only 10 Monte Carlo simulations with 50 random soil columns (approximately corresponding to a single realization with 500 random soil columns) were needed to achieve convergence, a result that is in clear contrast with the findings of section 6.4. As shown

previously even a single realization of 40,000 random blocks may not be considered to give results of the accuracy reported by Hopmans. The reason for the apparent discrepancy between Hopmans results and those reported here are the following: (1.) The bottom boundary condition in Hopmans simulation is fixed with respect to the head, thereby greatly reducing the head variance in most of the simulation domain. (2.) Hopmans' random fields are random only in the horizontal direction. The variance in Hopmans simulation varies between 80 and 400 cm^2 compared to a range from less than 5 cm^2 to more than 1000 cm^2 in the simulations presented here. In contrast to the strong horizontal head correlation of the simulations in this study, the correlation length in Hopmans' simulation was only slightly larger than the input correlation length and did not exceed 3 Δx or 1/15 of the domain size in the horizontal direction (Hopmans et al, 1988, Figure 5).

Hopmans used correlation lengths (in the definition of (6-12)) of 2 blocks and 4 blocks. Like in the simulations of this study, a small but discernable difference was found in the head correlation length that might be attributed to the better resolution of the heterogeneous properties: Their table 5 also indicates a slight decrease in the correlation length of the head as the relative input correlation length increases.

The results in 6.4 regarding the stability of the mean head and flux confirm similar findings of Ünlü et al. (1990) (here referred to as Ünlü). Their one-dimensional, vertical, transient flow simulations showed a similar behavior of the head and flux variance as a function of the input variance as Hopmans simulations and the simulations ins section 6.4. Furthermore, the simulations in this study confirm the conclusion of Ünlü, that the flux variance in mean flow direction increases, if the correlation length in mean flow direction increases, while the vertical flux variance decreases, if the correlation length in the horizontal direction increases: In the simulations with varying element-width Δx_2, but element-"thickness" Δx_1 (and consequently a change of λ_{x2} but not of λ_{x1}) the simulations with larger λ_{x2} have a significantly smaller variance in q_{x1}, while the variance of q_{x2} increases. In all other simulations, the

simultaneous change in width and thickness of the element (to keep the square form) and hence in λ caused a decrease in σ^2_{qh}, but an increase in σ^2_{qv} for any constant λ/b and $b/\Delta x_1$. Although discernable, the increase in the vertical flux variance is by far not as drastic as observed in the 1-dimensional simulations of Ünlü. This is expected due to the higher degree of freedom in the flow-path for the 2-D simulations (see also Yeh, 1985a).

6.6 Conclusion and Summary

The previous analysis of several dozen flow simulations with varying element-size, block-size, and correlation-length allows valuable insight into the accuracy of numerical stochastic solutions and its dependence on grid-design. The simulation further sheds some light on previous analyses by various authors.

As part of the model verification the numerical solutions for the stochastic moments of the head and flux (mean, variance, and covariance) are found to compare well with the analytical results for 2-D flow that were derived in chapter 4. The only disagreement found between analytical and numerical results are the covariance functions of the head and the vertical flux. Both the head and the vertical flux have very long correlation lengths, several times longer than the input correlation length λ_f. The size of the domain (200 by 200 elements or 20 by 20 correlation lengths) is found to be inadequate to unbiasedly sample the head and vertical flux. As a result the numerical covariance functions are of significantly shorter correlation length than the analytical covariances for the head and the vertical velocity.

The grid design sensitivity analysis was implemented with parameters chosen to be representative of field conditions. The conservative grid-design simulation results served as comparative basis for the sensitivity analysis. Since the input parameters have a large variance, the analytical solutions derived in chapter 4 cannot serve as a direct verification tool for the grid design sensitivity analysis. Instead it may serve as a guideline only. Indeed, the moments of

the numerical simulation significantly differ from the analytically determined moments, even for the same conservatively chosen grid-design. But the general qualitative dependency between stochastic input and output parameters was found to be similar.

The element-size was found to have little influence on the head solution accuracy as long as 32 cm thickness and width was not exceeded. Numerical oscillations significantly distort the head and unsaturated hydraulic conductivity moments only if simulations are based on element-sizes of 64 cm and larger. The vertical flux moments are more sensitive to the grid-design than the head moments and require an element size of 16 cm or less in the vertical direction. A grid-Peclet number $\alpha\Delta x < 2$, derived for the quasi-linear form of Richards equation, gives a very safe margin if it is strictly applied such that the condition is met for all elements. Based on the findings of section 6.4 a weaker grid-Peclet number restriction can be formulated:

$$\alpha_g \Delta x < 0.5 \tag{6-18}$$

where α_g is the geometric mean of α. This criterion is simple to implement, gives larger freedom in the choice of the element-size and still provides accurate solutions. For most practical purposes, this allows grid-sizes of up to 20 cm and more in the vertical direction. The element size in the horizontal direction is by far not as critical, and horizontal element lengths of e.g. 4 cm and 32 cm give identical results.

The subdiscretization into multi-element blocks for better resolution of the nonlinear head variations gave little improvement in the accuracy of the solutions. The differences to the simulations with single-element blocks were subtle and statistically of little significance. If $b=\Delta x$ is sufficiently small to give a good resolution of the heterogeneities (i.e. $b/\lambda \leq 0.1$), and if Δx satisfies the grid-Peclet criterion to avoid oscillations, the error introduced by linear head interpolation between element nodes is reduced sufficiently to be neglected.

The simulations have shown that the choice of a larger relative correlation length has a discernable albeit small effect on the head and flux variance and covariance: With large λ/b

the stronger coherence of random input parameters reduces the discrete jumps in hydraulic properties between neighboring blocks. Hence, the nonlinearity in the matric potential field decreases, while its numerical approximation improves. As a result the output variance of the head tends to increase due to a higher resolution of the perturbations and the output head correlation length decreases. In contrast, the flux variance decreases as the perturbation resolution increases. The differences have a weak statistical significance but are in accordance with findings by Hopmans et al. (1988).

By comparing several single large realizations it was found that simulations, which are based on a singe large realization, give stochastic results that are associated with considerable sampling error. Although only results for a limited number of Monte Carlo realizations are available, the variations of the sample correlation lengths and sample variances of head and flux indicate that a single realization with 10^4 - 10^5 elements and a side-length of 20 λ_f does give results with a sampling error of up to a factor 2.

With respect to previously implemented research, the simulations confirm the hypothesis by Russo and Dagan (1991), that the unsaturated velocity field may be subject to the same stochastic processes formulated for the saturated case. By consistently replacing the moments of logKs with the moments of logK, it was shown that the Lagrangian unsaturated flux moments presented in Russo and Dagan (1991) are related to the unsaturated hydraulic conductivity moments in a manner very similar to that found under saturated condition. The simulations in this chapter are not considered a complete proof of their hypothesis because other factors, like the infiltration rate and the geometric mean of α, may strongly influence the results as well. Here these parameters were kept constant. It would be particularly interesting to investigate the proposed relationships for water movement in dry soils. Most importantly, however, it is also shown that their assumption (6-15) does not generally hold. In contrast to the suggestion by Russo and Dagan (1991), it is therefore not possible to derive the moments of the flux field directly from the moments of the input random field of logKs.

Further research is certainly necessary to obtain a better understanding of numerical grid-design in stochastic simulations of unsaturated flow. This research has not addressed the impact of the infiltration rate on grid-design or the effect of different constitutive functions and constitutive parameters. The soil flow simulations only addressed accuracy for steady-state conditions in a relatively moist soil. The results underline the necessity of a careful grid-design evaluation to avoid numerical errors but also indicate that much more rigorous Monte Carlo simulations are necessary to accurately assess the impact of grid-design. At computation times exceeding 6 to 10 hours even on a dedicated workstation such Monte Carlo simulations are very limited in the number of realizations. The next chapter will introduce a numerical technique that accelerates the numerical computation time by up to two orders of magnitude. With such improvements in the computational techniques, Monte Carlo simulations can easily be implemented with hundreds of realizations. Chapter 8 will present the analysis of unsaturated flow with multiple realization Monte Carlo simulations.

Table 6.1: Non-variable input parameters common to all simulations of the model verification and grid design analysis.

input parameter	model verification	grid design analysis
mean $\log K_s$	5.5	5.5
variance $\log K_s$	0.09	4.0
mean $\log\alpha$	-4.0	-4.0
variance $\log\alpha$	0.0009	0.25
saturated water content	0.3	0.3
residual water content	0.3	0.3

Table 6.2: Comparison of the sample mean; obtained from a single large scale simulation with the analytical moments obtained from the 1st order perturbation analysis (chapter 4).

MEAN	analytical-1st order	simulation
logKs	5.500	5.513
logK	2.303	2.313
head [cm]	-174.6	-174.3
hor. flux [cm]	0.000	-0.02264
ver. flux [cm]	-10.00	-9.999
VARIANCE		
logKs	0.08742 (0.09)	0.09148
logK	0.03488	0.03694
head [cm^2]	16.59	15.92
hor. flux [$(cm/d)^2$]	0.3828	0.3471
vert. flux [$(cm/d)^2$]	0.5907	0.6708

Table 6.3: Comparison of the sample variance and correlation length for rectangular elements (1st row) and square elements (2nd row). Each column represents a different block-size indicated in the top row. All units are based on [cm] and [days].

rectang./square	4 x 2 cm^2	8 x 2 cm^2	16 x 2 cm^2	8 x 4 cm^2	16 x 4 cm^2	32 x 4 cm^2
σ^2 logK	0.440	0.410	0.388	0.387	0.353	0.339
	0.439	0.406	0.385	0.385	0.350	0.338
σ^2 head	35.9	61.1	103	78.1	134	22.2
	36.4	54.6	104	78.5	128	223.1
σ^2 qh	5.20	4.85	4.07	4.61	3.95	3.08
	5.38	5.12	4.46	4.78	4.19	3.39
σ^2 qv	8.85	6.22	3.74	8.16	5.28	2.72
	8.85	6.73	4.12	8.17	5.74	3.07
λ logKs	31.8	63.6	127.2	63.6	127.2	254
	31.8	63.6	127.2	63.6	127.2	254
λ logK	14.7	28.6	57.1	27.2	532.6	110
	14.7	28.5	57.3	27.2	523.9	111
λ head	68.0	75.8	106	83.1	114.4	183
	68.7	66.3	105	83.3	111.3	181
λ qh	14.3	23.1	37.9	26.7	42.7	73.0
	14.1	23.+	37.2	26.4	42.5	71.5
λ qv	10.0	17.4	27.1	19.0	31.3	48.8
	10.2	17.8	26.1	19.3	31.9	45.4

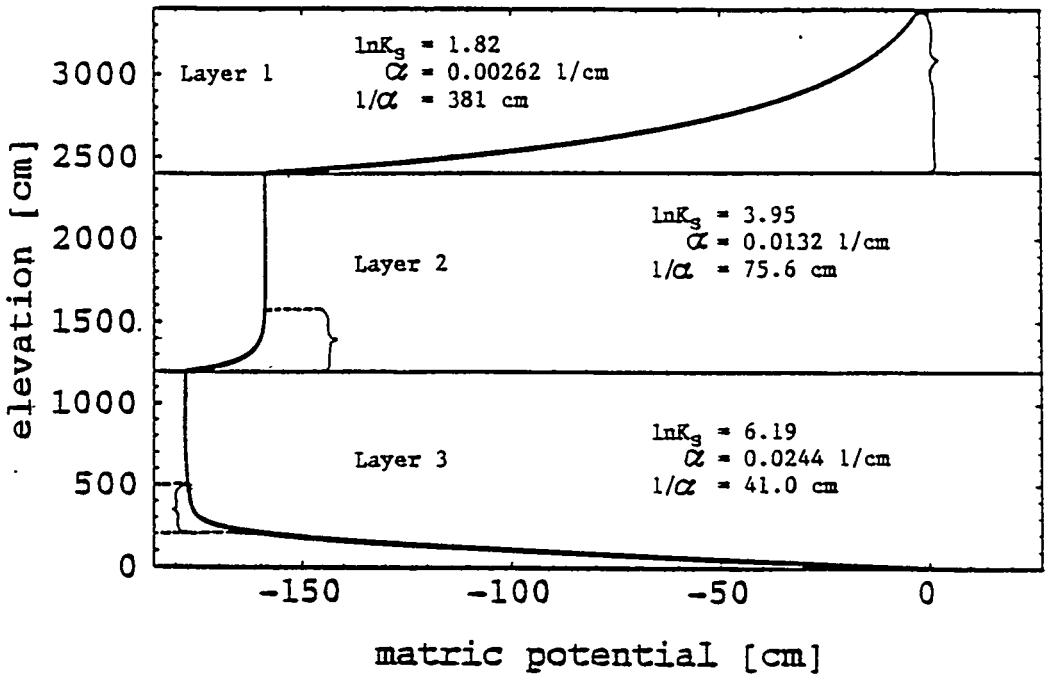

Figure 6.1: Matric potential distribution in a 3-layered soil column. Layer 1 is a very low permeable soil with small α. Permeability and α increase with each of the subsequent two-layers. Inversely, the nonlinear portion of the capillary fringe decreases. Layer 3 requires smaller discretization than layer 2 or layer 1 to accurately capture the nonlinear portion of the matric potential curve.

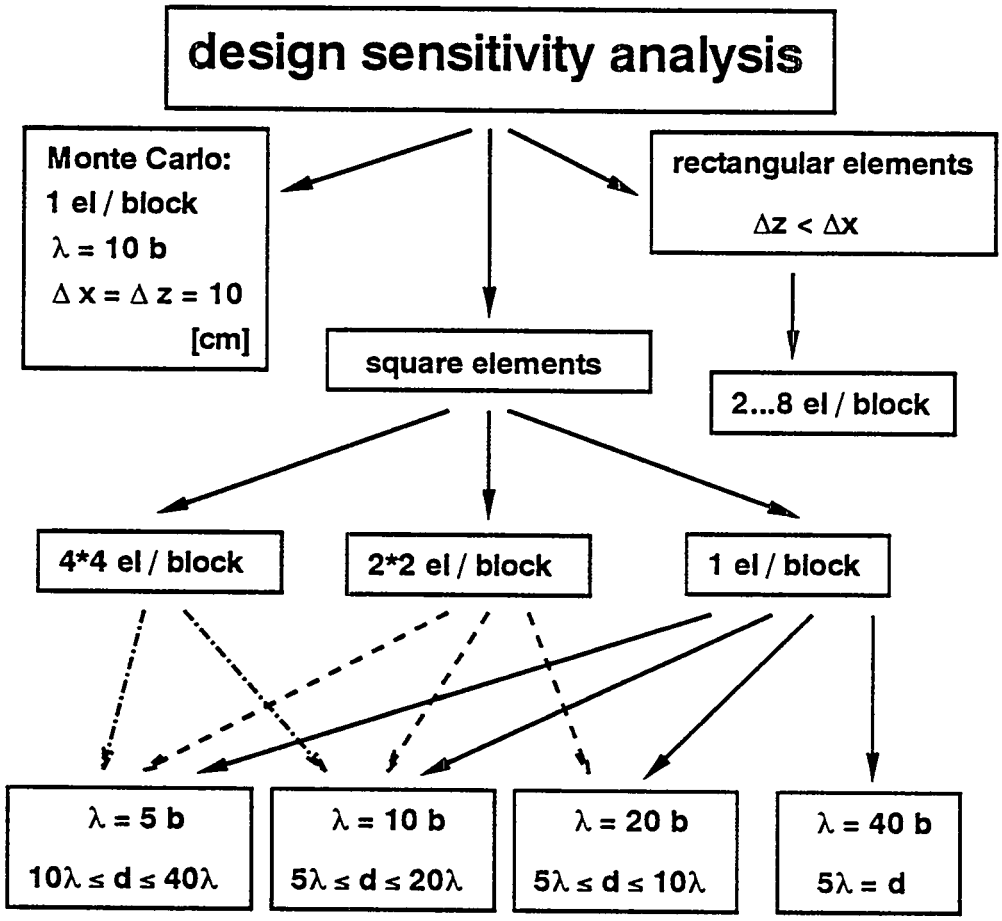

Δx -> {0.5, 1, ..., 256} [cm]

Δx, Δz: element width, height

b: block length

λ: correlation length

d: domain length

Figure 6.2: Overview of the simulation concept for the grid design sensitivity analysis

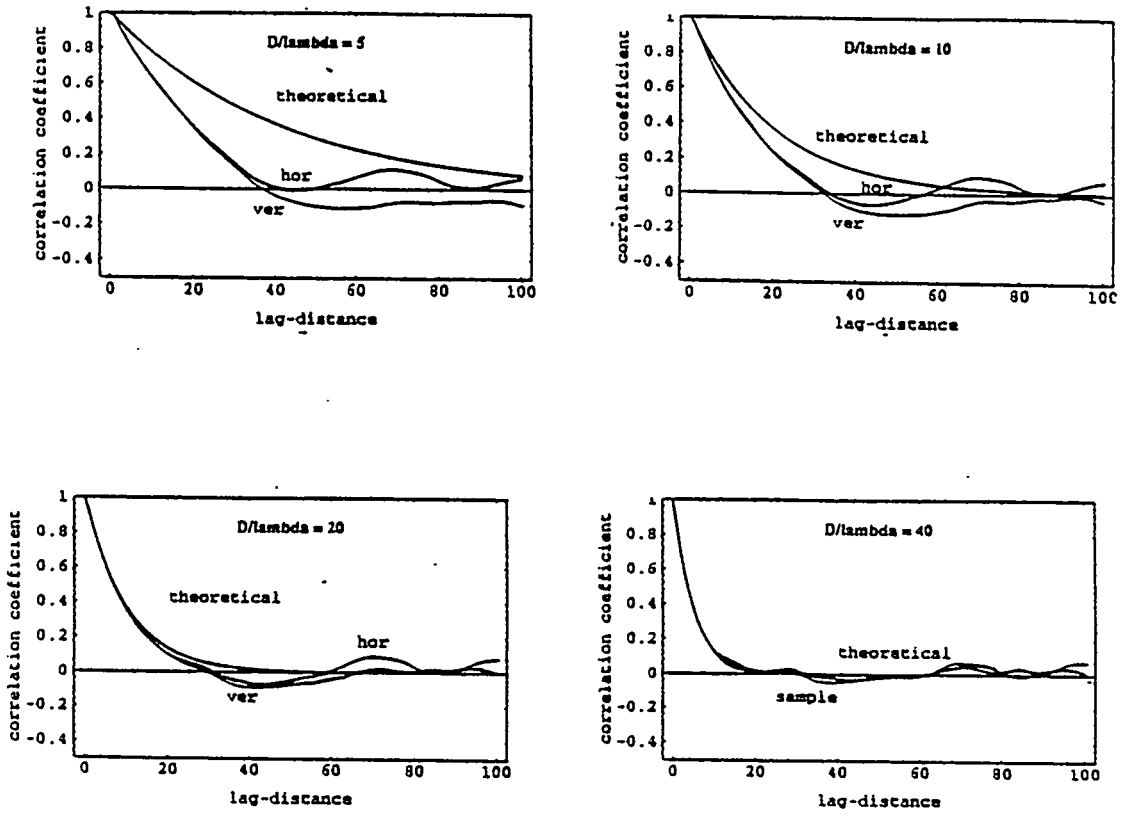

Figure 6.3: Two-point autocorrelation function of the random field for various relative domain sizes D/λ. The absolute domain size is 200 by 200 grid points. The autocorrelation function is computed by spatial averaging for lag-distances up to half the length of the random field.

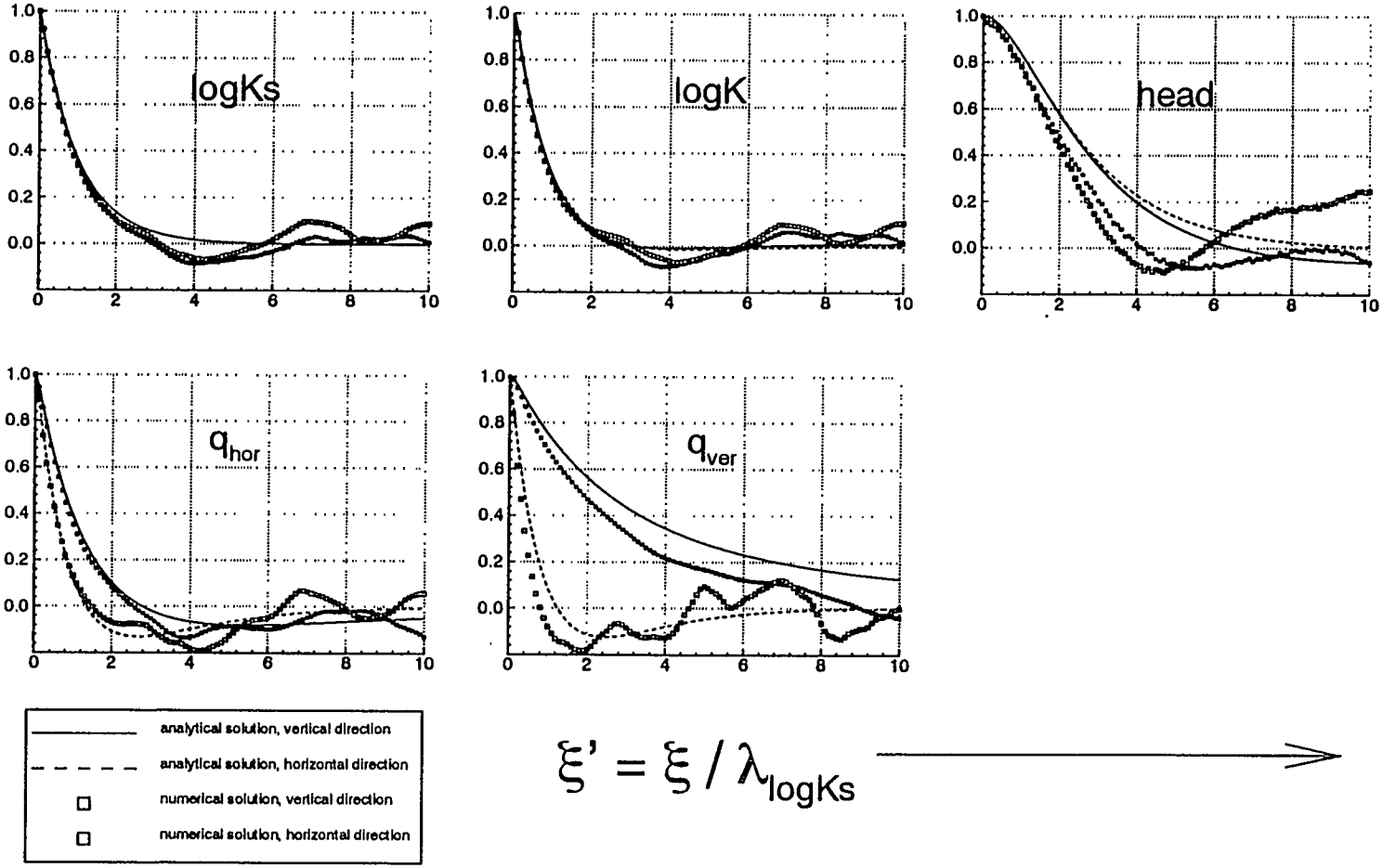

Figure 6.4: Theoretical autocorrelation function in comparison with the numerical sample autocorrelation of the input and output RFVs.

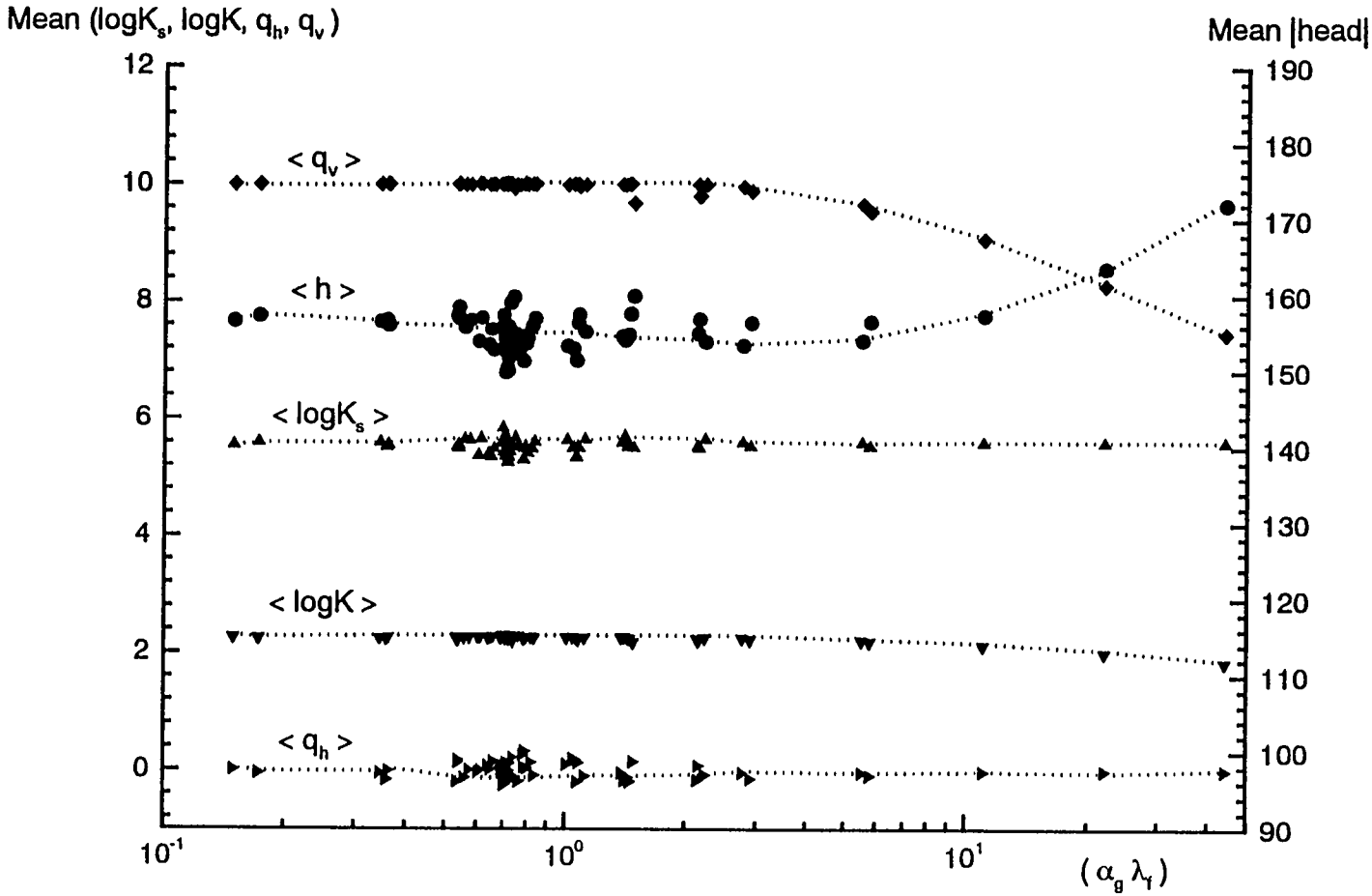

Figure 6.5: Sample mean of input and output RFGs for each realization as a function of the sample correlation length λ_f of f = logKs given $\alpha_g = 0.018$ [cm^{-1}].

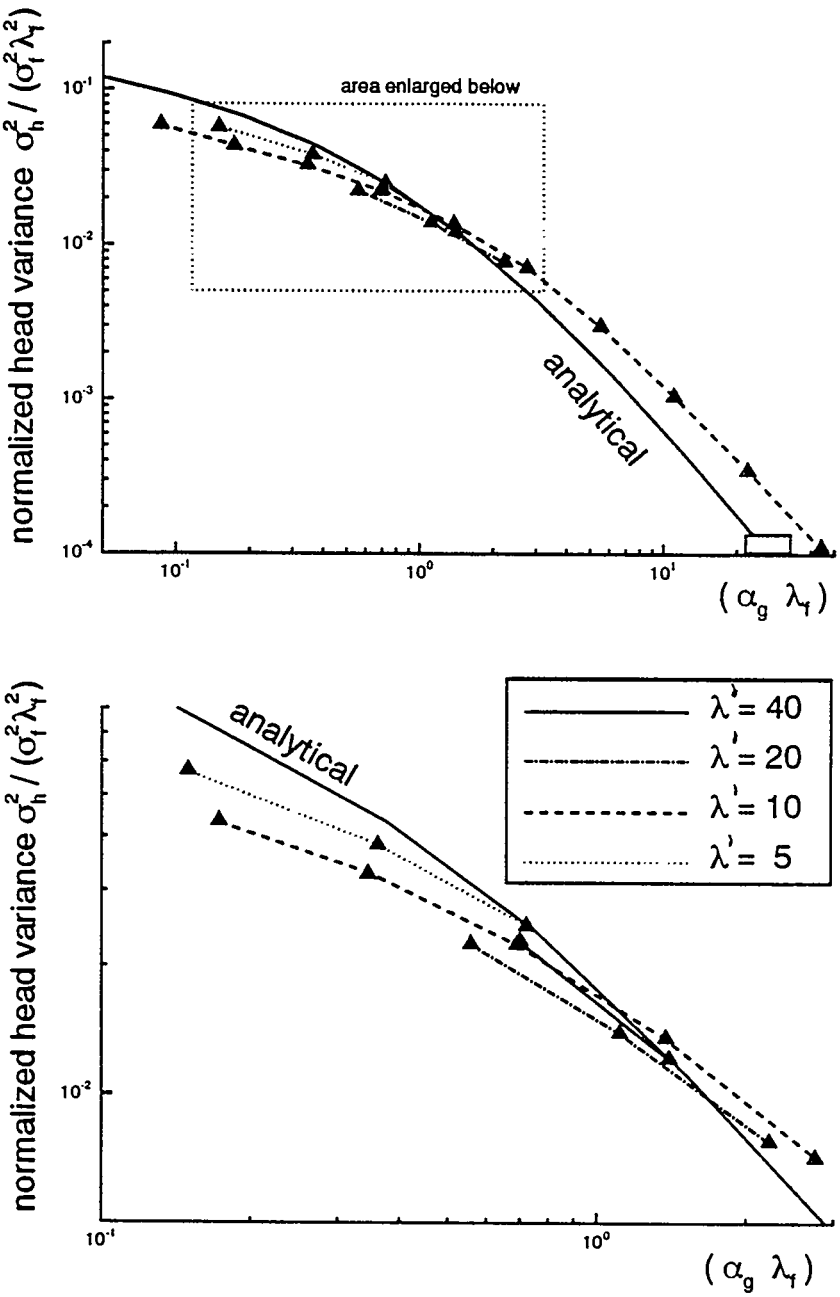

Figure 6.6: Normalized head variance as a function of $\alpha_g \lambda_f$, where λ_f is the sample correlation length of f=logK_s. Only simulations with block-size b=Δx are shown.

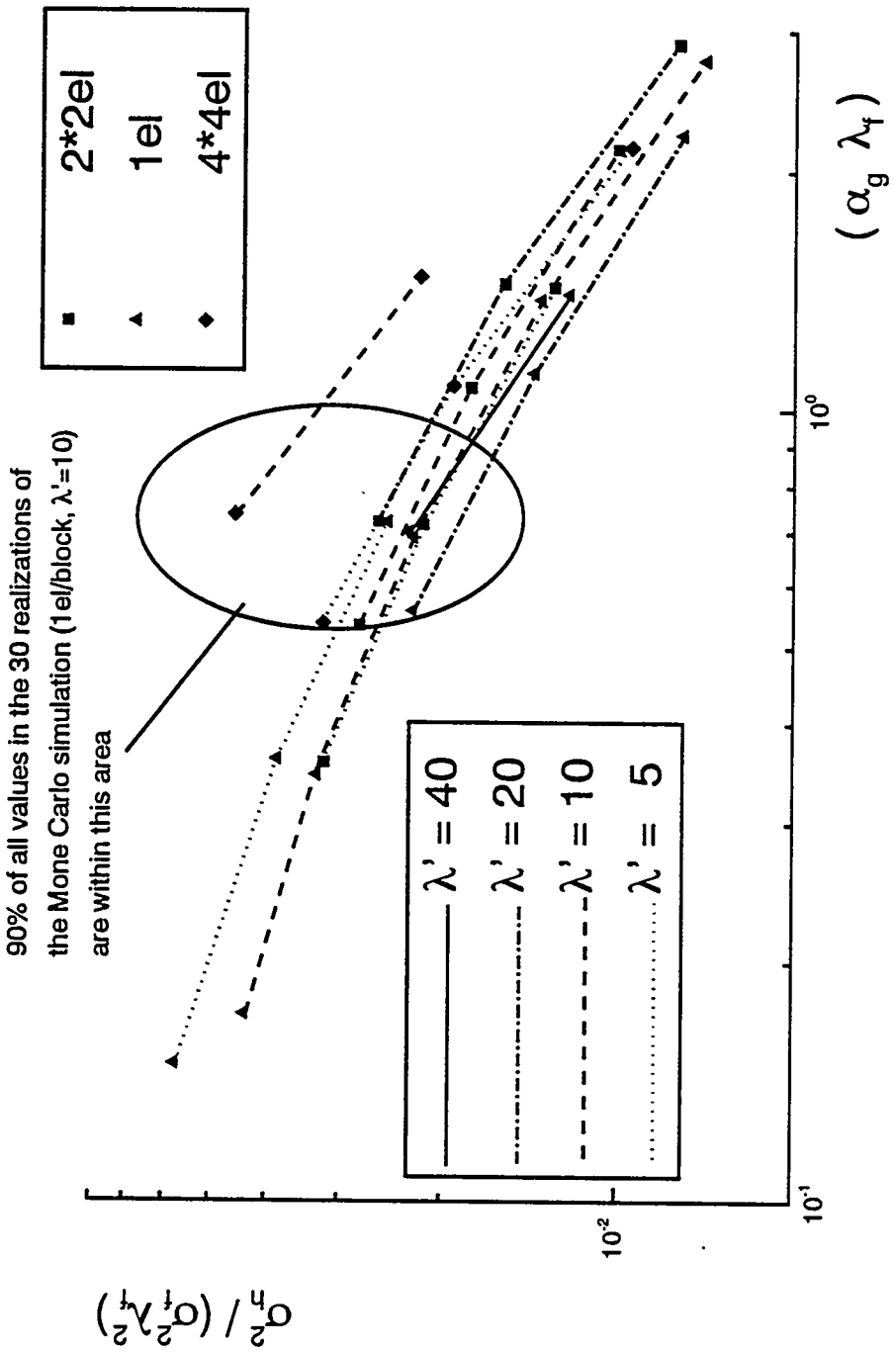

Figure 6.7: The normalized head variance as shown in Figure 6.6, but for various block-sizes b: b=Δx (1 element/block), b=2Δx (2*2 elements/block), b=4Δx (4*4 elements/block)

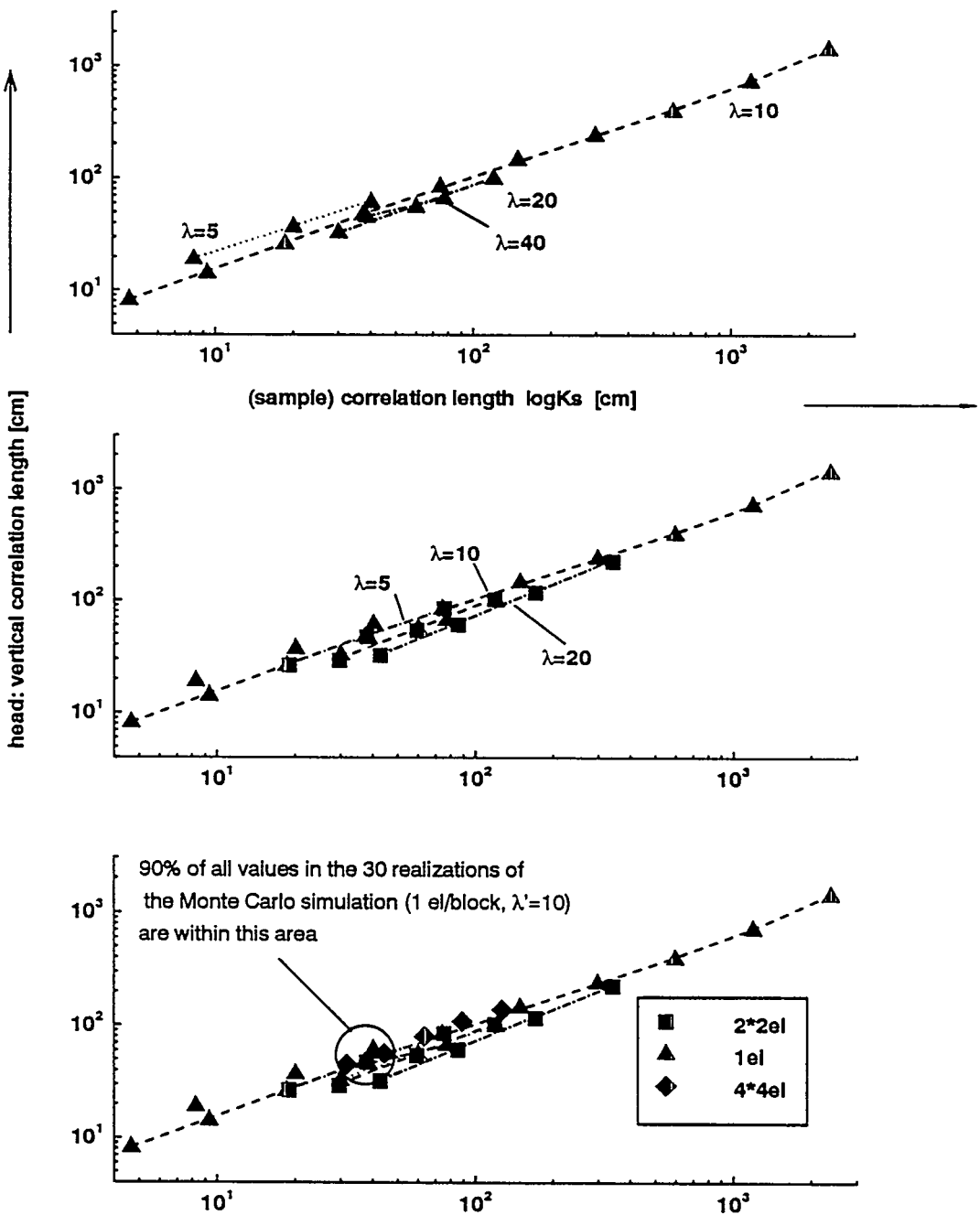

Figure 6.8: Vertical correlation length of the sample head values for each simulation.

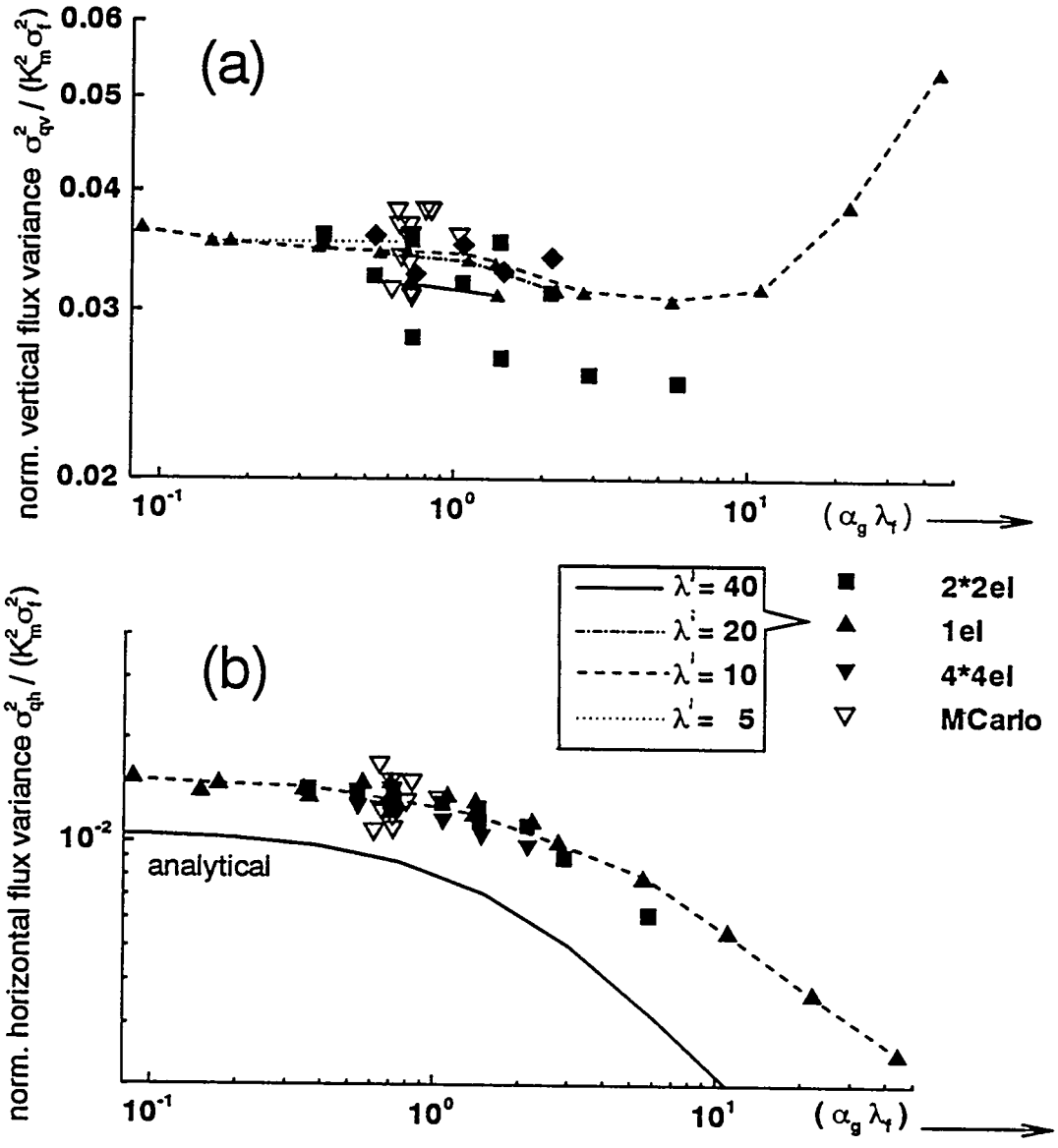

Figure 6.9: Normalized variances of the vertical (a) and horizontal (b) flux. Results from all simulations and from 7 of the 30 Monte Carlo realizations are plotted. The straight line below the numerical data is a first order perturbation solution.

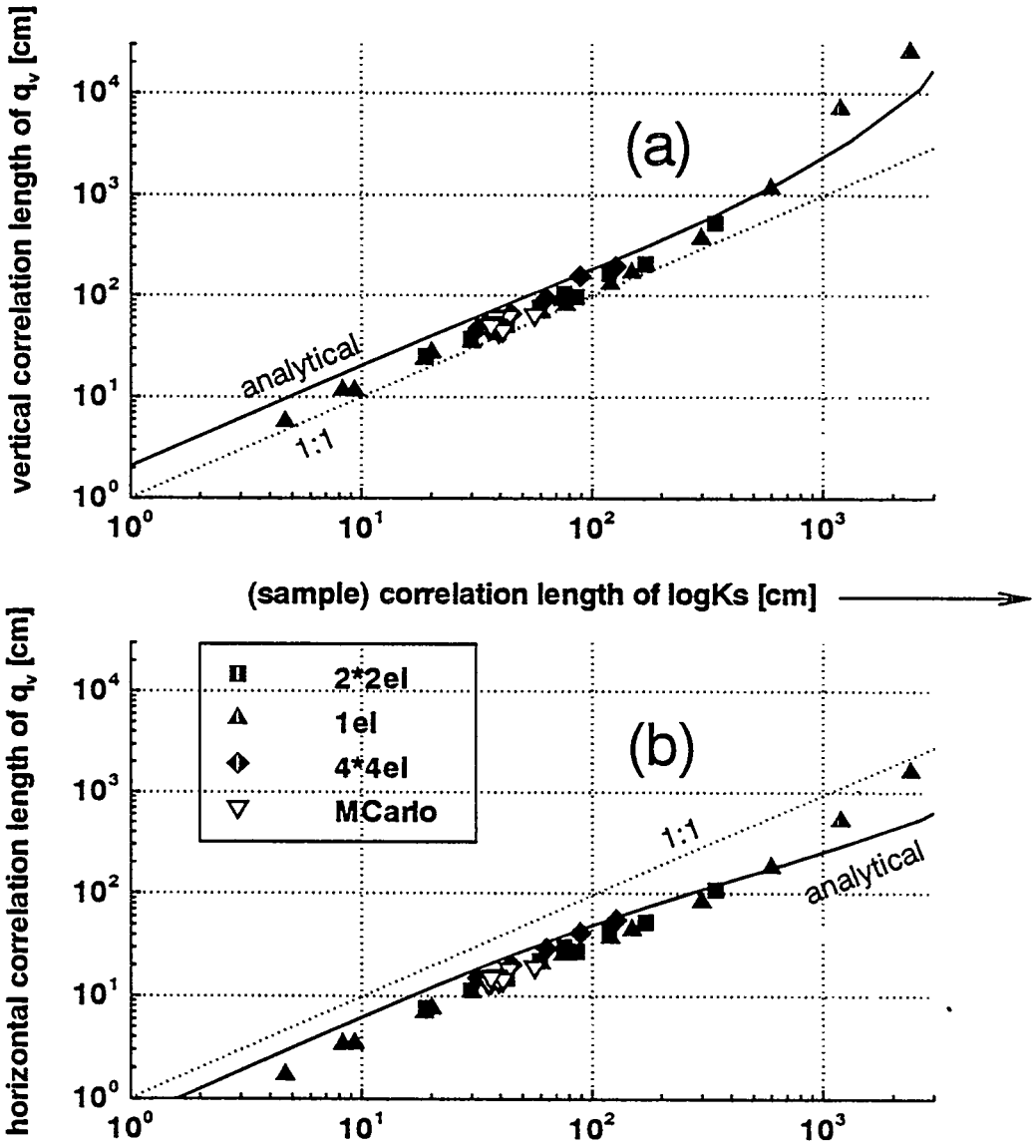

Figure 6.10: Vertical (top) and horizontal (bottom) sample correlation length of the vertical velocity. The solid line is obtained from the first-order perturbation analysis.

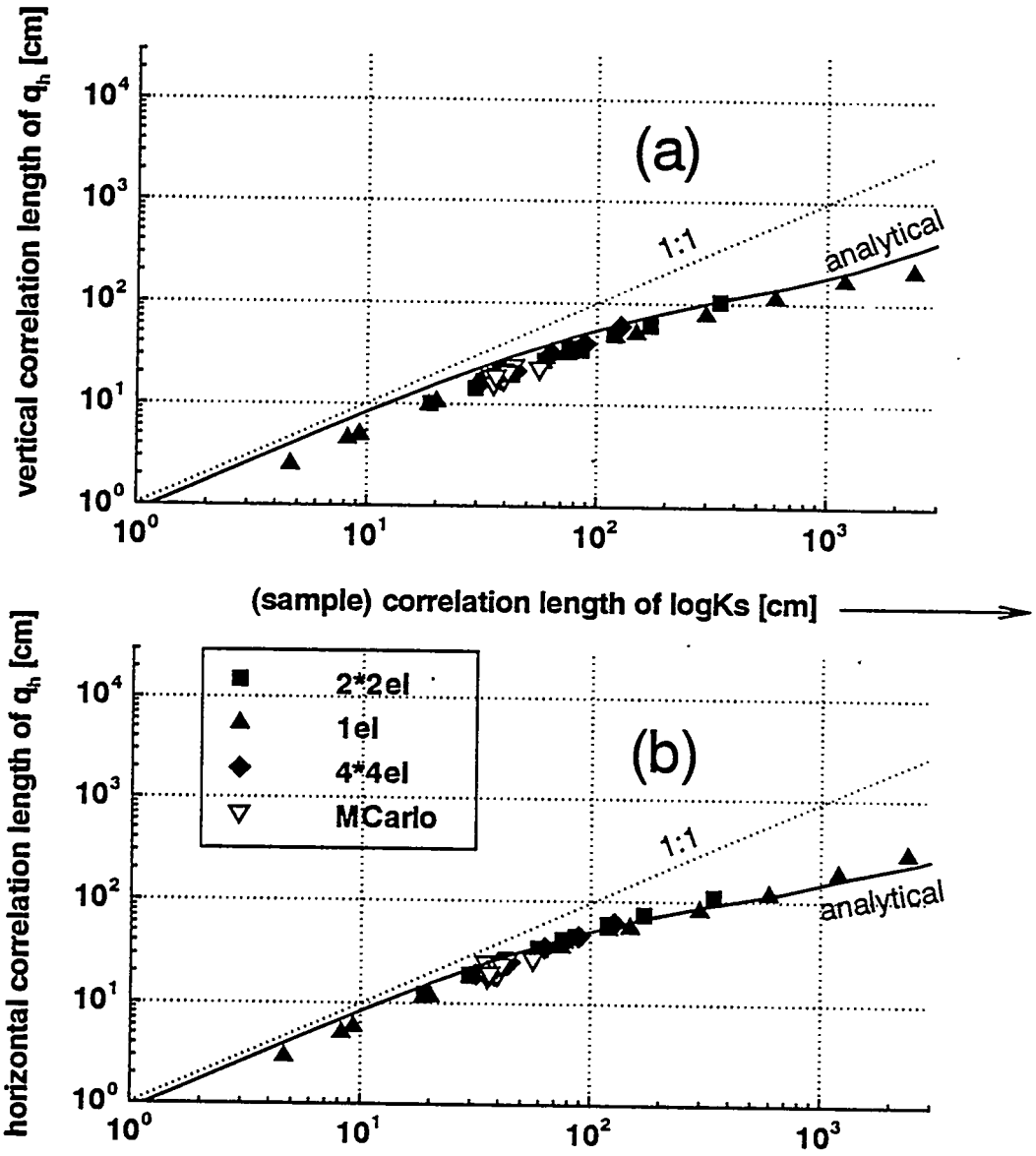

Figure 6.11: Vertical (a) and horizontal (b) sample correlation length of the horizontal velocity.
The solid line indicates the first order perturbation solution.

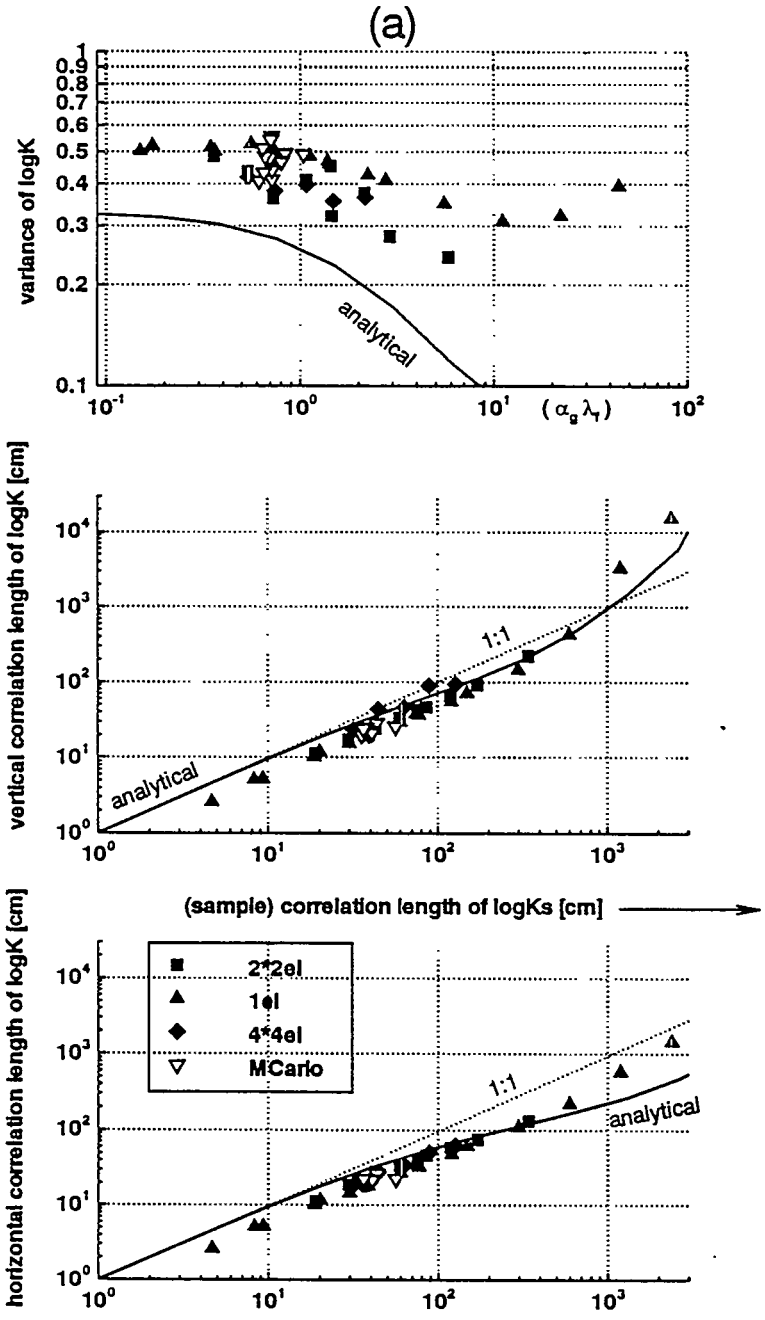

Figure 6.12: Variance (a), vertical (b) and horizontal (c) sample correlation length of the unsaturated hydraulic conductivity y = logK. The solid lines represent the first-order perturbation solutions derived in chapter 4.

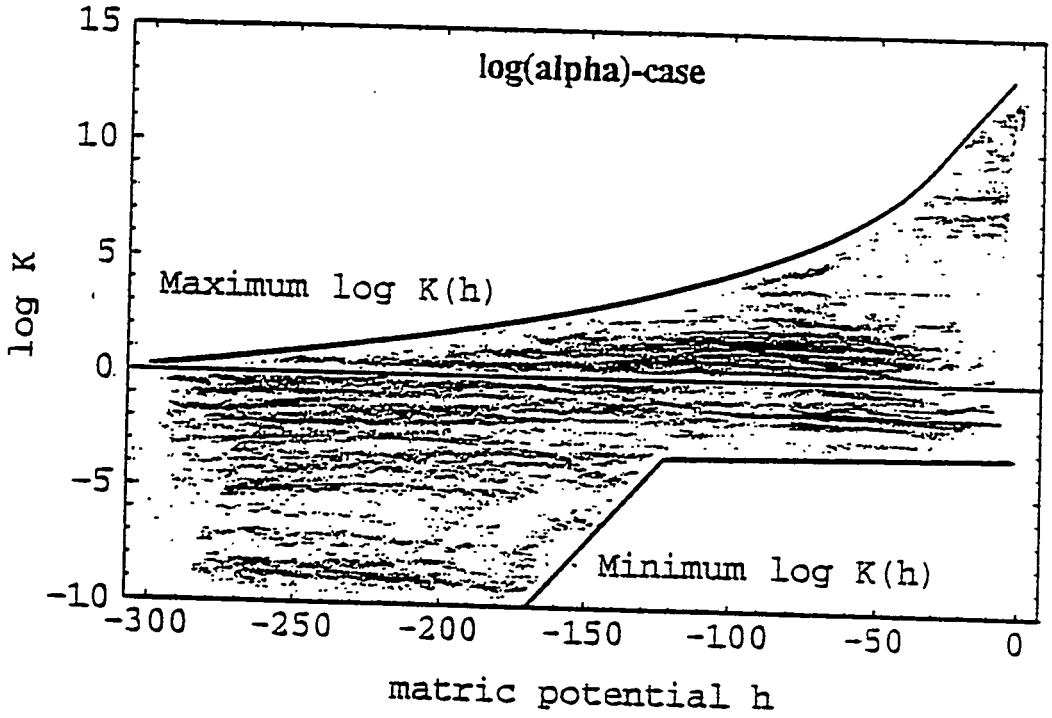

Figure 6.13: Envelope of all possible unsaturated hydraulic conductivity curves in run 1 of the logα-case Monte Carlo simulation.

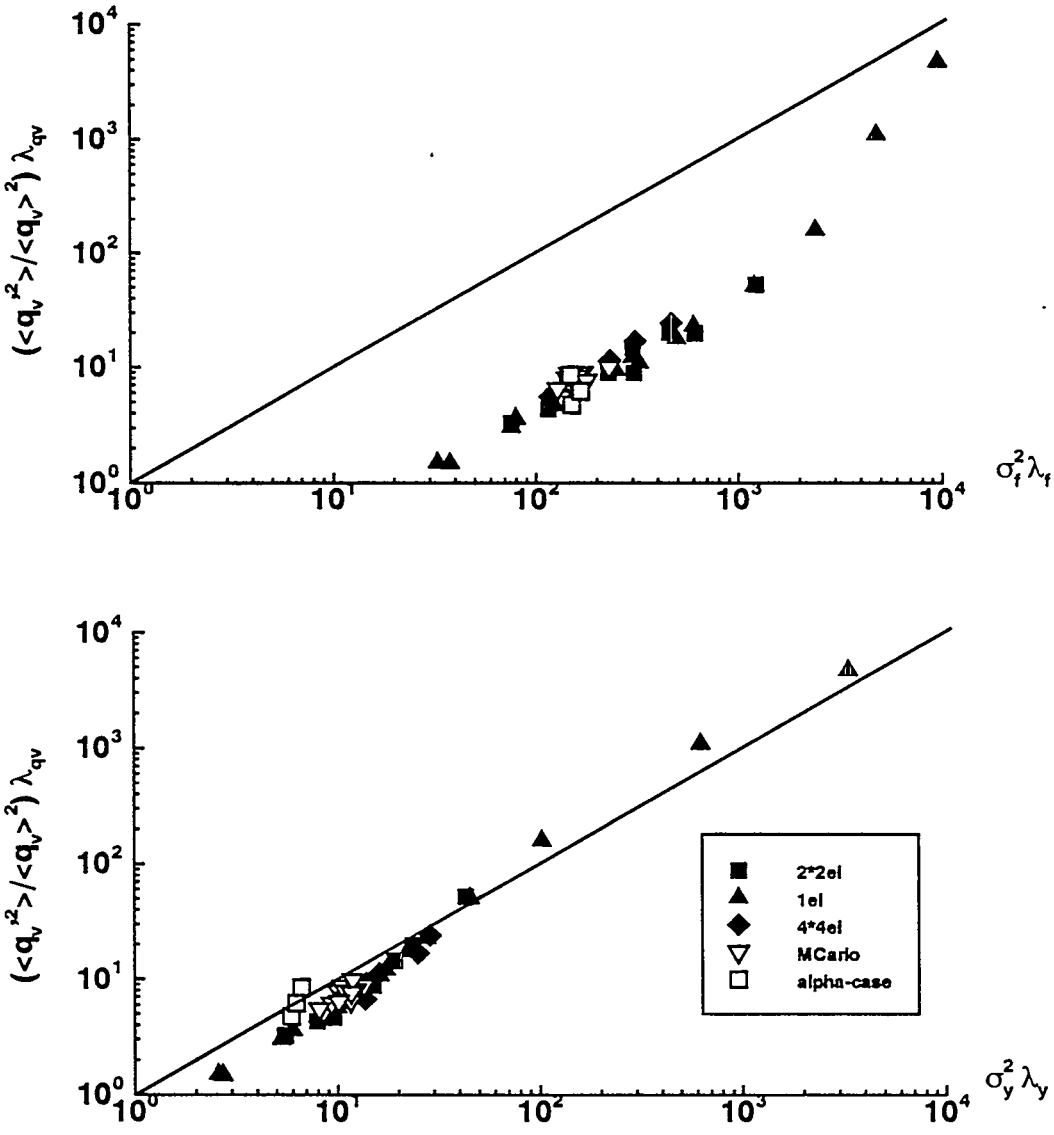

Figure 6.14: The Lagrangian flux field equation (6-16) using sample parameters of the saturated hydraulic conductivity (top) and of the unsaturated hydraulic conductivity (bottom).

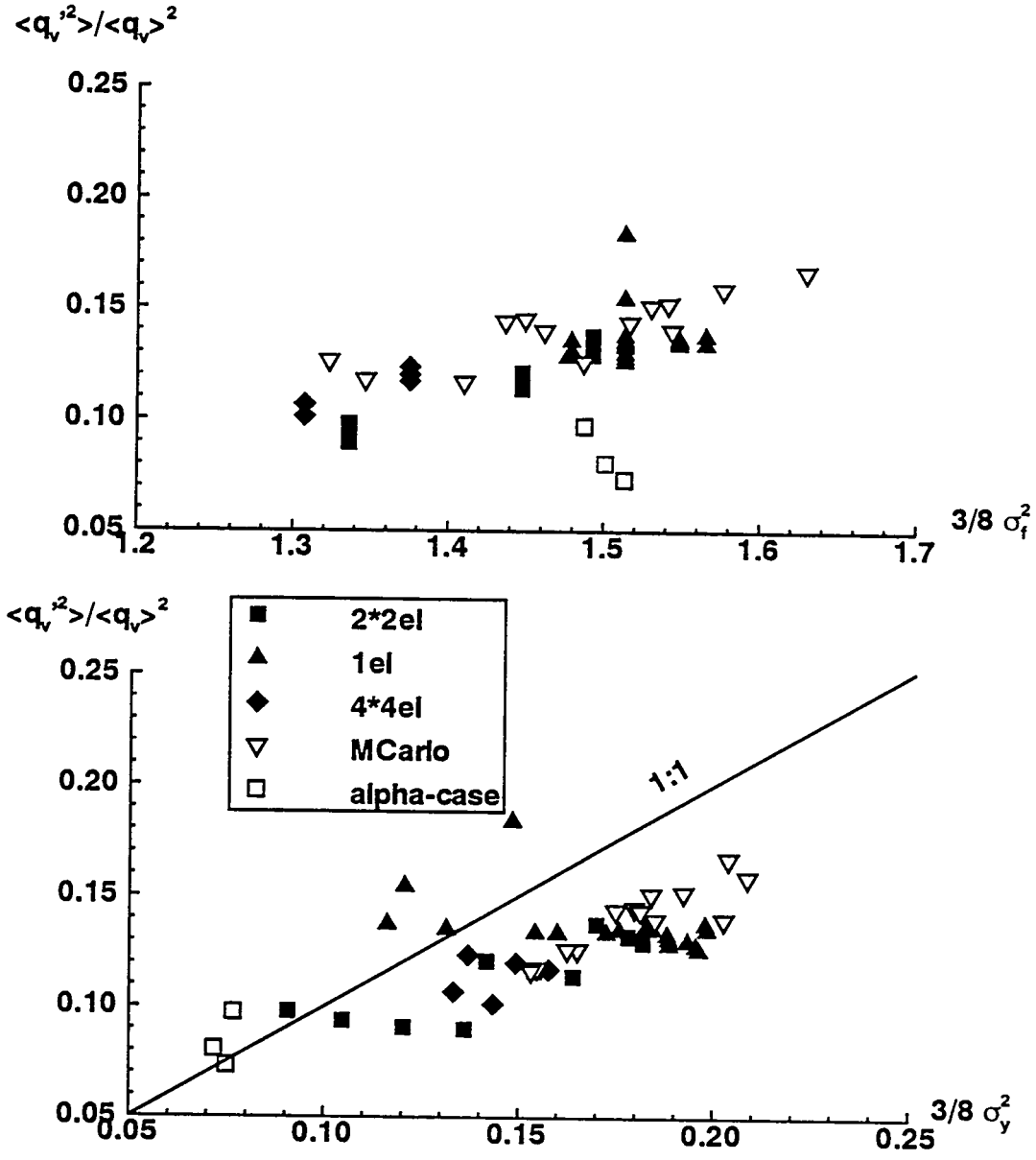

Figure 6.15: Squared coefficient of variation of the vertical flux compared to 3/8 σ_f^2 (top) and to 3/8 σ_y^2 (bottom); see equation 6-17.

7. AN EFFICIENT METHOD FOR SIMULATING STEADY UNSATURATED FLOW IN RANDOM POROUS MEDIA: USING AN ANALYTICAL PERTURBATION SOLUTION AS INITIAL GUESS TO A NUMERICAL MODEL

7.1 Introduction

Effects of soil heterogeneity have been the focus of both field and theoretical research for the past decade (e.g., Hills et al., 1991; Hopmans et al., 1988; Mantoglou and Gelhar, 1987; McCord et al., 1991, Russo, 1991; Ünlü et al., 1990; Wierenga et al., 1991; Yeh et al., 1985a,b; Yeh et al., 1986). Analytical models are essential tools for investigating the effect of heterogeneity on flow and transport in the unsaturated zone. However, the nonlinearity of the governing flow equation, the degree of nonlinearity, and the spatial variability in the unsaturated hydraulic properties make the development of analytical solutions difficult. Analytical solutions are only available for some special cases, such as one-dimensional steady-state and transient infiltration in layered soil with Gardner type unsaturated properties (Yeh, 1989; Warrick and Yeh, 1990; Srivastava and Yeh, 1991). For more general problems one often relies on numerical techniques such as finite difference and finite element methods (c.f. Fletcher, 1988; Anderson and Woessner, 1992).

The finite element or finite difference equations for unsaturated media are commonly written in form of a linearized matrix equation such as:

$$\mathbf{A}(\mathbf{x}^{m})\mathbf{x}^{m+1} = \mathbf{b}(\mathbf{x}^{m}) \tag{7-1}$$

where m indicates the outer, nonlinear iteration level, **A** is the linear coefficient matrix, **x** the vector of unknown values, and **b** the vector of known terms. Direct (non-iterative) or indirect

(iterative) methods are used to solve the inner, linear part of (1) numerically. In general, direct algorithms require a large amount of computer storage. Hence, most numerical techniques employ so-called indirect or iterative methods for solving the linear part of eqn. (7-1) to improve CPU-efficiency and to reduce the memory-requirements for the computer.

The non-linear solution is essentially found by repeating the linear solution to (7-1) at increasing iteration levels m until the convergence criteria $|x^{m+1} - x^m| < \delta$ (a prescribed tolerance) is met. Several techniques have been developed based on (7-1) such as the Picard method and the Newton-Raphson method (Ortega and Rheinbolt, 1970).

If (7-1) were to represent a transient problem, both the inner and outer iteration procedure would start from the initial conditions of the boundary value problem and march through time. For a steady-state problem, the iterative procedure initially requires an approximate solution $\mathbf{x}^1$ (initial guess or initial solution). The initial guess has little bearing on the final solution. But it can reduce the number of iterations if the guess solution is close to the actual solution. In the case of nonlinear equations no guarantee exists, even under the absence of round-off errors, that the outer or nonlinear iteration methods will converge under some predefined conditions. In general, the initial guess must be close to the solution to avoid divergence of the outer iteration scheme. The degree of similarity between initial and actual solution that is required for convergence depends on the degree of heterogeneity and nonlinearity in the boundary value problem.

The solution of the perturbation flow problem (4-1b) for heterogeneous media with either the Picard or the Newton-Raphson method is mostly impossible, since it is difficult to prescribe an initial guess that consistently leads to convergence in the solution of (7-1). One may circumvent this difficulty by using either a transient time-marching approach (i.e., solving the steady-state flow problem by the transient approach) or a pseudo-transient approach (Fletcher, 1988) together with simple uniform or linearly varying initial solutions. Both techniques diagonalize the matrix and expand the radius of convergence but they require

numerous time steps to obtain an approximate steady-state solution. In the solution of Richards equation (4-1a), a trade-off between the choice of C(h) and the size of the time-step Δt limits options for CPU-time improvements, when the pseudo-transient method is used. As a result, such approaches often require large amounts of CPU time (chapter 6 in this work; Ababou, 1988, p.649, p.684, pp.681ff.). In the past, convergence problems and CPU time requirements often limited the investigation of the effect of heterogeneity in unsaturated soils. While numerical methods have enjoyed relatively widespread use for saturated problems, numerical stochastic analysis of unsaturated flow and transport has been an exercise with very limited applications (chapter 6). It is desirable to obtain the steady-state solution to (4-1b) without resorting to time-marching methods to improve CPU efficiency.

To alleviate the convergence and CPU time problems, it is suggested that a very powerful initial guess can be provided by solving an approximate problem to which the analytical solution is known (to ASIGN: to use an Analytical [or Approximate] Solution as Initial Guess to the Numerical solver). In this chapter, it is demonstrated how the first order spectral solution can be used to provide such an initial guess to solve the 2-D steady-state Richards equation (4-1)b with Gardner's K(h) model (4-8) numerically in a very efficient manner. The advantage of the approach over the pseudo-transient approach utilized in chapter 6 is demonstrated through several examples.

7.2 Formulation of the Initial Guess Solution

In chapter 4, a first order perturbation solution to the steady-state Richards equation (4-1b) is developed based on spectral analysis. (4-26) gives the spectral solution of the steady-state head given the spectral representation of lognormally distributed input random fields of $\log K_s$ (log: natural logarithm) and α. The necessary random fields can be generated with any of the random field generators described in chapter 3. This requires a Fourier transform of the

random fields of f' and a' to obtain dZ_f and dZ_a in (4-26). By generating the random fields with the SRFFT method, dZ_f and dZ_a are obtained directly by virtue of (3-3) and dZ_h is easily obtained by the explicit relationship provided in (4-26). Inverse FFTs are applied to each of the three discrete z-fields representing f', a', and h' just like in the SRFFT random field generator (3-13). Not only has a set of input random fields f' and a' been generated; the approximate solution h' is also available. The f' and a' random fields are the input random fields for the numerical model, and h' is used as initial guess solution to the numerical solver. Only the use of the first order head solution as initial guess has allowed for obtaining steady-state solutions of (4-1b) without using pseudo-transient or transient methods. I call the process of solving the governing nonlinear partial differential equation by a combination of analytical and numerical techniques ASIGNing (using an Analytical Solution as Initial Guess to a Numerical solver). Figure 7.1 gives a schematic overview of the ASIGNing process.

The versatility of the approach is demonstrated for two different solutions of (4-1b) and (4-8): the case of *lognormally* distributed α ($\log\alpha$-case), and the case equivalent to Yeh et al. (1985a,b), where α is *normally* distributed (α-case). The former is given in (4-26). The latter is derived here: With $\alpha = A + a'$, the unsaturated hydraulic conductivity is given by:

$$\begin{aligned} \ln K(h) &= \ln K_s + \alpha h \\ &= F + f' + (A + a')(H + h') \end{aligned} \tag{7-2}$$

and the governing first order perturbation equation under mean unit gradient conditions is (compare to (4-20)):

$$\frac{\partial^2 h'}{\partial x_i^2} + A\frac{\partial h'}{\partial x_1} + H\frac{\partial \alpha'}{\partial x_1} + \frac{\partial f'}{\partial x_1} = 0 \qquad i=1,2 \tag{7-3}$$

The corresponding spectral solution for the head perturbation is derived equivalently to (4-26):

$$dZ_{h'} = \frac{ik_1 (dZ_{f'} + HdZ_{\alpha'})}{(k_1^2 + k_2^2 - iAk_1)} \qquad (7\text{-}4)$$

The perturbation of the normally distributed α is denoted by a' and the perturbation of the lognormal α by γ' to distinguish between the two cases.

7.3 Example Problems

To investigate the capability of ASIGNing at various degrees of soil variability and to compare the efficiency of the ASIGNed steady-state solution with the hitherto standard (pseudo-) transient numerical solution method a principal parameter set is chosen that allowed variations in the moments of $\log K_s$, α, and $\log\alpha$ over several orders of magnitude. The values of both the deterministic and the stochastic parameters are summarized in Table 7.1. The examples are for two-dimensional cross-sections of 64 elements width and 64 elements depth. The size of the elements is 10 cm by 10 cm resulting in a total domain size of 6.4 m by 6.4 m. In all simulations an exponential isotropic covariance function is specified to characterize the random field variables (RFVs) f', a', and γ':

$$\mathrm{Cov}(\mathbf{b}) = \sigma^2 \exp\left(\frac{-|\mathbf{b}|}{\lambda}\right) \qquad (7\text{-}5)$$

where σ^2 is the variance of the RFV, $\mathbf{b}$ is the two-dimensional vector of the separation distance, and λ = 50 cm is the isotropic correlation length.

The mean of α, (arithmetic mean A for normal α, geometric mean Γ for lognormally distributed α), determines the degree of nonlinearity in (4-1b). Initially, two values are chosen for A: 0.01 cm^{-1}, which is typical for fine sandy to loamy soils (α-case(1)); and 0.001 cm^{-1}, which is typical for fine-grained silty and clay rich loamy soils (α-case(2)). With α-case(1) the effect of different boundary conditions is investigated. The α-case(2) and the $\log\alpha$ case are

used to demonstrate the efficiency and flexibility of the method with respect to various possible applications.

Alternative boundary conditions are:

(a) of the Dirichlet type (prescribed head) on all boundaries;

(b) of the Dirichlet type at the top and bottom of the domain, but with zero-flux on the vertical boundaries;

(c) of the Dirichlet type at the bottom boundary, zero-flux at the vertical boundaries, and a prescribed flux of q = 7.4 cm/h at the top boundary (then H ≈ -150 cm);

(d) unit-gradient conditions at the bottom boundary, zero-flux at the vertical boundaries and prescribed flux q = 7.4 cm/h at the top boundary;

(e) water-table boundary at the bottom (uniform Dirichlet, h_{BC} = 0), all other boundaries are Dirichlet boundaries;

(f) water-table boundary at the bottom (uniform Dirichlet, h_{BC} = 0), zero-flux at the vertical boundaries, and Dirichlet boundary at the top;

(g) The logα-case is tested with boundary condition (a) and parameters similar to the α-case(1) (see Table 7.1).

For the combined ASIGNing method each Dirichlet boundary (except the water table condition) is equal to the perturbed random head boundary produced by the quasi-analytical solution for an infinite domain. In the transient solutions all head boundaries are uniformly set to H = -150 cm, which is the mean head used in all example problems. All of the above boundary value cases are run at variances σ^2_f = 0.1, 1.5, and 6. Some cases are also repeated at σ^2_f = 0.01, 0.5, 1.0, and 3.0. The geometric mean of K_s is 33.1 cm/h in α-case(1) and 4.5 cm/h in α-case(2). a' and γ' are assumed to be correlated to logK_s with proportionality constants ζ = 0.001 and 0.1, respectively. It is chosen such that none or only minor portions of the domain become saturated, even at large matric potential variances. Partial saturation poses no computational problem to the numerical code MMOC2, but unsaturated conditions are

the focus of this work. The α-case(1) is also implemented with σ^2_f = 1.5 for domain sizes ranging from 32^2 to 256^2 elements to demonstrate the applicability of ASIGNing to small as well as large numerical grids. All simulations are performed twice: One simulation with the transient approach using the transient option of MMOC2 and one simulation with the ASIGNing method, which combines the quasi-analytical solver with the steady-state version of MMOC2. Except for the boundary conditions, all deterministic/stochastic parameters and the constitutive equations for K(h) and θ(h) are identical for the initial analytical, the steady-state, and the transient solutions of each example problem. The random fields of f' and a' or γ' produced to obtain the initial guess via (7-4) or (4-26), respectively, are used as random field input to the steady-state and transient numerical solutions (Figure 7.1).

7.4 Results and Discussion

7.4.1 The Quasi-Analytical, the ASIGNed, and the Transient Numerical Solution in Comparison

It is generally known that the first-order perturbation equations (4-20) and (7-3) are a valid approximation to the nonlinear Richards equation (4-1b) for variances of f' << 1.0 (Yeh et al. 1985a). Hence, for problems involving only small perturbations, the quasi-analytical spectral solution technique itself is expected to be satisfactory. Figure 7.2 shows that the head field from the quasi-analytical spectral solution to (7-4) is indeed in very good agreement with the ASIGNed solution to (4-1b) at σ^2_f = 0.1. At higher variances, the approximate solution deviates significantly from the "true" (numerical) solution of Richards equation, in particular with respect to the head gradients. Harter et al. (1992) showed that the velocity fields derived from the quasi-analytical head solution to (7-4) have artificial sources and sinks for σ^2_f> 0.25. In contrast, the numerical solution implicitly guarantees a mass-balanced head distribution which will result in a divergence-free velocity field. It is the inaccuracy in the head gradient

field, which prevents the spectral solution to (7-3) to be a useful tool for transport simulations in highly variable media. Nevertheless the overall spatial head distribution pattern is well preserved by the quasi-analytical spectral solution (7-4), even at large variances (Figure 7.3). This may explain, why the quasi-analytical solution provides an initial guess that allows a direct numerical steady-state solution of (4-1b) much beyond the usual limits of the first order perturbation approach.

With regard to solution uniqueness, all ASIGNed solutions are in excellent agreement with the those obtained by the time-marching approach. As an example, Figure 7.4 compares the ASIGNed with the late transient solution for α-case(1) under boundary conditions (c) at σ^2_f = 6.0. The only differences in the two solutions are near the bottom of the domain due to different constant head boundary conditions: The ASIGNed solution has a random head boundary given by the initial guess. The transient approach is based on a uniform head boundary condition with H = -150 cm.

7.4.2 Efficiency of the ASIGNed Solutions

The experiments show that the quasi-analytical spectral solution method to obtain (4-26) and (7-4) is an extremely CPU-efficient algorithm to obtain approximate solutions to (4-1b) (Figure 7.5). Due to its spectral nature the number of computational steps is finite and independent of σ^2_f. The savings in CPU-time over the transient time-marching numerical solution of (4-1a) is on the order of three magnitudes and more: The quasi-analytical solution of (7-3) on a discretized grid of 64*64 points takes less than 1 second on an IBM RS6000/560 workstation, while the CPU-time of the transient finite element solution with 64*64 elements is on the order of tens of minutes for σ^2_f= 0.1 (for a comparison of the performance of the IBM RS6000/560, see Tripathi and Yeh, 1993)

At higher variances numerical solutions must be sought to correctly solve Richards

equation (4-1) and the main purpose of ASIGNing is to reduce the CPU-time requirements of the numerical solution. Indeed, the CPU-time savings of the combined approach (ASIGNing) over the transient simulation technique are of a factor 20 to 30 at any input variance (Figure 7.5). The computation time of the initial guess (1.5 sec of which almost 1 second is input/output) is almost negligible compared to the ASIGNed numerical solution time.

While the first example in Figure 7.5 contrasts two technically identical problems since both the ASIGNed steady-state and the transient solutions are subject to Dirichlet boundary conditions, the physical problems solved are different: The transient solution assumes a uniform head of -150 cm all around its domain. The assumption of such uniform head boundaries is questionable, since in most unsaturated flow and transport applications little is actually known about the head boundaries of the domain. The ASIGNed steady-state solution, however, takes advantage of the random head boundaries provided by the initial guess, thus solving for a quasi-infinite domain. In practice, the use of random head boundaries provided by (7-4) or (4-26) is much more realistic than uniform head boundaries. The random type head boundaries are consistent in first order with the random input parameter fields $\log K_s$ and α, With the random boundary head approach one can simulate a soil domain that has no definite boundaries. Many authors have circumvented uniform Dirichlet boundaries by specifying flux boundaries (Neumann conditions) around the domain, which are generally more CPU-expensive to solve. The CPU-savings of the combined approach with random Dirichlet conditions over the transient approach with at least three Neumann conditions are approximately two orders of magnitude (Figures 7.5 vs. 7.6).

In the examples tested, both the ASIGNed steady state and the time-marching (transient) solutions cost increasing CPU-time as more and more Neumann conditions are introduced. But throughout the range of variability ASIGNing remains a much more efficient technique (Figure 7.6). Surprisingly perhaps, the most significant time-savings (two orders of magnitude) under otherwise identical boundary conditions are obtained for the water-table scenario with no-flow

conditions on the vertical boundaries (Figure 7.7). The head-field in this case is not only heterogeneous, but also deviates from the uniform mean-head assumption implicit in the initial solution (7-4). This shows the broad applicability of ASIGNing.

The only boundary conditions, for which no ASIGNed steady-state solution is obtained are those which involve a unit-gradient boundary condition at the bottom of the cross-section. The unit-gradient boundary is a Cauchy or mixed type condition. Ünlü et al. (1990) have shown for the one-dimensional case that unit gradient boundary conditions are associated with head variances that are higher than those associated with other types of boundary conditions, which may explain the convergence problems of ASIGNing in this case.

Figure 7.8 shows that the efficiency of the proposed method decreases only slightly as the size of the domain increases from 1,000 to over 65,000 elements. For any domain-size, the proposed method is particularly powerful at high variances when compared to the traditional transient solution CPU-time. The method also applies successfully to the logα-case. Table 7.2 provides some example CPU-times for both the logα-case and for the α-case(2) with much smaller mean α. The efficiency of the method is comparable to the cases shown in Figure 7.5.

With regard to the overall efficiency of ASIGNing over the common transient method it should be noted that the convergence-criteria of the transient method is not coded into the model (such as a stopping rule of the type $\text{Max}|h_{t+1} - h_t| < \delta$), since transient solutions may change very little per time-step without having necessarily reached steady state. Rather, the transient heads are continuously evaluated at seven points uniformly distributed over the domain. From this head record, the actual CPU-time for the transient approach is determined retroactively. In practice, the pseudo-transient approach may require significantly more CPU-time than indicated in Figures 7.5 to 7.8 and in Table 7.2, since the number of time-steps required to approach steady-state are generally not a priori known.

7.4.3 Limitations of ASIGNing

The above examples have shown that ASIGNed solutions can be obtained over a wide range of variances. But it must be emphasized that the success of the method is not unlimited due to the first order character of the analytical solution. As indicated before, terms of second and higher order that were neglected in deriving the perturbation equation (7-3) and (4-20) become significant at higher variances of f' and/or a'. Hence the (initial guess) solutions (7-4) and (4-26) deviate more strongly from the steady-state solution to (4-1b) as the perturbations increase (compare Figures 7.2 and 7.3). Once the difference between the two solutions is larger than the convergence radius of the Newton-Raphson method, a direct steady-state solution is impossible to obtain even with the quasi-analytical initial guess. The experiences with the above examples have shown that ASIGNing is successful up to variances of 5 in the (natural) logarithm of the unsaturated hydraulic conductivity, $\sigma^2_{y'}$ with $A \leq 0.01$ [cm^{-1}] and $\sigma^2_{a'} \leq 0.006$. Since α determines the degree of nonlinearity, the mean and variance of α or $\log\alpha$, and its correlation to f' are expected to be critical to the success of ASIGNing.

To explore the limits of the method, additional ASIGNed simulations are implemented with independent random parameters f', a', and γ' and a wider range of means and variances in α as before. First, the $\log\alpha$-case described above is repeated with independent parameters f' and γ'. The variances of the independent γ' in these cases are 1/100 of the variance $\sigma^2_{f'}$ specified, just as in the first $\log\alpha$ case with dependent random fields. The CPU times required for the two cases with low $\sigma^2_{f'}$ are 50% larger than those for the dependent case. Convergence is achieved except for the case of $\sigma^2_{f'}$=6.0. In this independent $\log\alpha$ case, convergence is obtained with $\sigma^2_{f'} \leq 4.5$, which results in an unsaturated logK variance $\sigma^2_{y'} \leq 5$.

To separate the effects of f' and γ' at a given geometric mean $\alpha_g = 0.01$ [cm^{-1}], the largest $\sigma^2_{\gamma'}$ for which convergence is achieved is determined at each of three different $\sigma^2_{f'}$. At $\sigma^2_{f'} = 0.1$ and 1.5 solutions are obtained if $\sigma^2_{\gamma'} \leq 0.5$, although the range in head variance in

the two cases spans from 1470 cm^2 to 2300 cm^2, respectively, and the range of unsaturated hydraulic conductivity variances spans from 1.9 to 3.5, respectively. For $\sigma^2_{f'} = 4$, solutions are obtained with $\sigma^2_{\gamma'} \leq 0.2$. At $\sigma^2_{f'} = 4.7$, the maximum usable $\sigma^2_{\gamma'}$ reduces to $2*10^{-5}$. Increasing the geometric mean of α from 0.01 to 0.1 [cm^{-1}], which is typical of a coarse sand, shows that convergence in ASIGNing is limited to slightly smaller variances of γ'. At variances $\sigma^2_{f'} = 1$, 5.3, and 7.4, the maximum usable $\sigma^2_{\gamma'}$ are 0.024, 0.01, and 0.0001, respectively, resulting in unsaturated hydraulic conductivity variances $\sigma^2_{y'} = 3.0$, 4.0, and 4.2.

In the case of independent, normally distributed α the first order perturbation solution is not based on an approximation similar to (4-13). Here, ASIGNing is also successful for a large range of $A = \langle\alpha\rangle$ without loss of CPU-efficiency. At $\sigma^2_{f'} = 1.0$ and $A = 0.1$ [cm^{-1}], the largest possible $\sigma^2_{a'}$ is 0.01 ($\sigma^2_{logK'} = 2.0$, $\sigma^2_{h'} = 235$ cm^2), and at $A = 0.5$ [cm^{-1}] it is 0.007 ($\sigma^2_{logK'} = 0.77$, $\sigma^2_{h'} = 9$ cm^2). At smaller variances of a' and $A = 0.1$ [cm^{-1}] ASIGNed solutions are generally possible if $\sigma^2_{y'} \leq 4.3$. These limits are obtained for the particular seed used to generate the random numbers α_j and β_j in (3-3). For other seeds the limits vary slightly and should therefore be taken as guidelines only.

The experiments show that three parameters seem to be most important to define the range of solutions for which ASIGNing is possible: The variance of the unsaturated hydraulic conductivity, the mean of α and the variance of α, where the latter two parameters mainly identify the degree of nonlinearity in (4-1). For the mean of $\alpha \leq 0.01$ or the mean of $\log\alpha \leq -4.6$, cases resulting in $\sigma^2_{y'} \leq 4$ (or even 5) are solvable with ASIGNing as long as e.g., in the $\log\alpha$ case the variance of $\gamma' \leq 0.5$. At $\alpha_g = 0.1$ and for a given $\sigma^2_{f'}$ ASIGNing is successful for any $\sigma^2_{\gamma'}$ such that $\sigma^2_{y'}$ does not exceed 4. The α-case remains solvable for $\sigma^2_{a'} \leq 0.01$ at $A = 0.1$ [cm^{-1}]. These findings seem to be independent of the correlation between f' and a' or γ', independent of $\sigma^2_{f'}$ (if $\sigma^2_{y'}$ does not exceed 3 to 4), and independent of the resulting head variance. At higher A the restrictions on the maximum conductivity variance are tighter, but overall the method has been shown to be successful for a broad range of parameters

encountered under realistic field conditions.

7.4.4 Extensions of ASIGNing

It has already been emphasized that the boundary value problem for the initial guess, which is given by the analytical solutions (7-4) or (4-26), is different from the boundary value problems stated above for the numerical solver of (4-1b). For all the above boundary value problems the analytical solution provides an initial guess based on the assumption of an unbounded domain, while the numerical solutions are all subject to bounded domain conditions. It is important to understand that the quasi-analytical solutions for all of the cases tested serve only as first approximations and are not a defining part of the numerical solution. The set of boundary conditions is intended to show the variety of boundary conditions for which the analytical solutions may successfully be used as initial guess such that the steady-state finite element simulation of (4-1b) converges directly.

Theoretically, it is possible to generate quasi-analytical solutions not only with different boundary conditions than the numerical solutions, but also with a different input set { F^*, $\sigma^{2*}_{f'}$, A^* , $\sigma^{2*}_{a'}$, H^* } to better approximate the solution of (4-1b) subject to the input parameter set { F, $\sigma^2_{f'}$, A, $\sigma^2_{a'}$, H }. This approach may be taken because the spectrally generated random fields of {f',a'} and {f'*,a'*} are identical in structure not only when different mean values are specified but also for different variances, if the same seed is used for the spectral random field generator: Recall from (2-49) that $dZ_p(\mathbf{k})$, p = f', a' are independent random numbers with a variance equal to the spectral density $S_{pp}(\mathbf{k})d\mathbf{k}$. Since the spectral density function $S_{pp}(\mathbf{k})$ is the Fourier transform $\mathcal{F}$ of the covariance function (7-5), where σ^2_p is independent of location x or spectral wave number k, it can easily be shown that the spectral density is a linear function of the variance σ^2_p:

$$S_{pp}(\mathbf{k}) = \sigma^2_p \, \mathcal{F}(Cor_{pp}(\mathbf{b}) \tag{7-6}$$

where $Cor_{pp}(\mathbf{b}) = Cov_{pp}(\mathbf{b})/\sigma^2_p$ is the normalized correlation function. Then both $dZ_p(\mathbf{k})$ and their inverse fast Fourier transforms $f'(\mathbf{x})$ and $a'(\mathbf{x})$ are linearly dependent on σ^2_p. The quasi-analytical head solution h' will also produce identical structures for different σ^2_p. They merely differ in the amount of excitation in their perturbed structure as shown by the quasi-analytical solutions in Figures 7.2 and 7.3. The same is not true for the head solution to (4-1b) due to its nonlinear character. Yet the structures are similar as shown by the ASIGNed head solution in Figure 7.2 produced from random fields of correlated f' and a' with $\sigma^2_{f'} = 0.1$ and the ASIGNed head solution shown in Figure 7.3 which is based on random fields with $\sigma^2_{f'} = 6.0$.

It is therefore conceivable to generate the initial guess solution with a meaningful, but arbitrary set of parameters { F^*, $\sigma^{2*}_{f'}$, A^* , $\sigma^{2*}_{a'}$, H^* }, to produce a certain structure in the initial head h', which is closer to the solution of (4-1b) subject to { F, $\sigma^2_{f'}$, A, $\sigma^2_{a'}$, H } than an initial head that is also based on { F, $\sigma^2_{f'}$, A, $\sigma^2_{a'}$, H }. The practical procedure is then as follows: After obtaining the initial head h' with an arbitrary set { F^*, $\sigma^{2*}_{f'}$, A^* , $\sigma^{2*}_{a'}$, H^* }, one regenerates f' and a' with the same seed, but the input set { F, $\sigma^2_{f'}$, A, $\sigma^2_{a'}$, H }, and then proceeds to solve the steady-state numerical solution with the latter random fields of f' and a' but the former h' as initial guess. The water-table problem α-case(1) with the boundary condition (f) is a simple example of such an application: The initial head solution is based on a uniform mean head H^*, the numerical simulation solves a problem of vertically varying H(z). The number of variations in this method is potentially endless and depends directly on the problem type. Further research is warranted, but it is beyond the scope of this paper to further investigate those possibilities.

In principal, ASIGNing can also be applied for cases where a solution to (4-1b) is sought with an unsaturated conductivity function K(h) different from (4-8). In this case the moments of the parameters K_s and α in (4-8) have to be determined such that the head field from (7-4) is similar to that solving (4-1b) with the desired K(h) function. A prominent example is the use of Van Genuchten's constitutive relationships for K(h) and θ(h) (Van

Genuchten, 1980) in the numerical solution of (4-1b). While Gardner's equation for K(h) (4-8) is necessary for the derivation of (7-4), it is in many practical circumstances of rather limited use while Van Genuchten's K(h) model has generally been more applicable to field soils. ASIGNing a Van Genuchten based solution to (4-1b) may be possible by defining equivalent parameters f' and a' for (4-8) analytically (Russo et al., 1991). This is cumbersome, however, since an equivalent f' and a' need to be determined for each random replicate of VanGenuchten parameters. Alternatively, the equivalent moments { F^*, $\sigma^{2*}_{f'}$, A^* , $\sigma^{2*}_{a'}$ } of the K(h) parameters in (4-8) can be graphically matched by trial and error with those desired for the VanGenuchten K(h): The parameter set { F^*, $\sigma^{2*}_{f'}$, A^* , $\sigma^{2*}_{a'}$ } is manually adjusted such that a random sample of Gardner's K(h) curves best matches against a random sample plot of Van Genuchten's K(h) curves (e.g. Ababou, 1988, p.652). The latter approach may be time-consuming for a single simulation, and a transient solution is probably obtained faster. In most cases, however, ASIGNing will be used as part of a Monte Carlo simulation and a single trial and error definition of a suitable parameter set for obtaining the initial guess may solve hundreds of Monte Carlo runs.

7.5 Conclusions

In many instances and particularly in the case of heterogeneous, steady, non-linear problems, numerical solutions take prohibitive amounts of CPU-time or lead to divergence in the iterative solution process. Typically, a uniform initial guess is provided by the user, even if the steady solution is non-uniform. For problems involving heterogeneous parameter-fields e.g., flow through variably permeable porous media, such an initial guess is commonly so different from the solution that steady solution techniques fail and transient time-marching or pseudo-transient methods must be employed, which are associated with high computation time.

A quasi-analytical spectral solution technique was developed, which is a first-order

linearized perturbation approximation to the governing non-linear stochastic equation. This quasi-analytical solution is used as an initial guess solution in a finite element model which solves the nonlinear governing flow equation (4-1b) (ASIGNing: Analytical Solution as Initial Guess to Numerical solver). ASIGNing renders up to two orders of magnitude of CPU-time savings. To my knowledge this is the first time stochastic analytical solutions have been combined with their respective numerical solutions. It was shown that the method can successfully be applied to a wide range of field conditions with average α ranging from 0.001 [cm^{-1}] to 0.1 [cm^{-1}] and the variance of the log unsaturated hydraulic conductivity being as large as 5. An even wider range of applications is conceivable, if the parameters for the initial guess solutions are determined separately. In this chapter examples are shown, where the set of parameters for both the initial guess and the numerical solution are identical (with the exception of the mean head). ASIGNing works for correlated and uncorrelated f' and a' fields alike, and can be adopted to solve problems involving normal or lognormally distributed α. The success of this particular combination of a quasi-analytical with a numerical method is very encouraging since the nature of the technique is very general and many related problems in fluid dynamics may be solved similarly.

Another advantage of this particular approach is that random fields are generated intrinsically instead of separately. Furthermore, the first order perturbation solution used here as initial guess allows to model vertical soil domains with random head boundaries thus eliminating boundary effects to the degree to which the first order solution is accurate. Alternatively, partial boundary conditions can be introduced through conditional simulation techniques, a possibility that is investigated in chapter 10. CPU-time enhancements of one and a half to two orders of magnitude allow for the first time the implementation of Monte Carlo techniques to solve unconditional and conditional stochastic unsaturated flow and transport problems. Subsequent chapters will explore several different such applications of ASIGNing.

Table 7.1: Parameters for the numerical experiments

	α-case(1) and logα-case	α-case(2)
mean $\log K_s$ [cm/d]	3.5	1.5
variance σ^2_f	0.1 - 1.5 - 6.0	1.5
mean α: A [1/cm]	0.01	0.001
$\zeta_{\alpha' f}=\sigma_{\alpha'}/\sigma_f$	0.001	0.0002
mean logα: Γ [1/cm]	-4.6	-
$\zeta_{\gamma' f}=\sigma_{\gamma'}/\sigma_f$	0.1	-
mean head: H [cm]	-150	-150

Table 7.2: Results of the α-case(2) and the logα-case experiments

	σ^2_f (saturated hydraulic cond.)	$\sigma^2_{[\log K]'}$ (unsatur. hydraulic cond.)	CPU-time[sec] (pseudo-transient)	CPU-time [sec] (steady state with ASIGNing)
α-case(1)	0.1	0.062	559	16.6
α-case(1)	1.5	0.97	758	34.8
α-case(1)	6.0	4.05	N/A*	211
α-case(2)	1.5	1.36	695	24.6
logα-case	0.1	0.062	563	16.6
logα-case	1.5	0.96	743	39.4
logα-case	6.0	3.99	N/A*	63.9

* N/A: transient solution did not converge

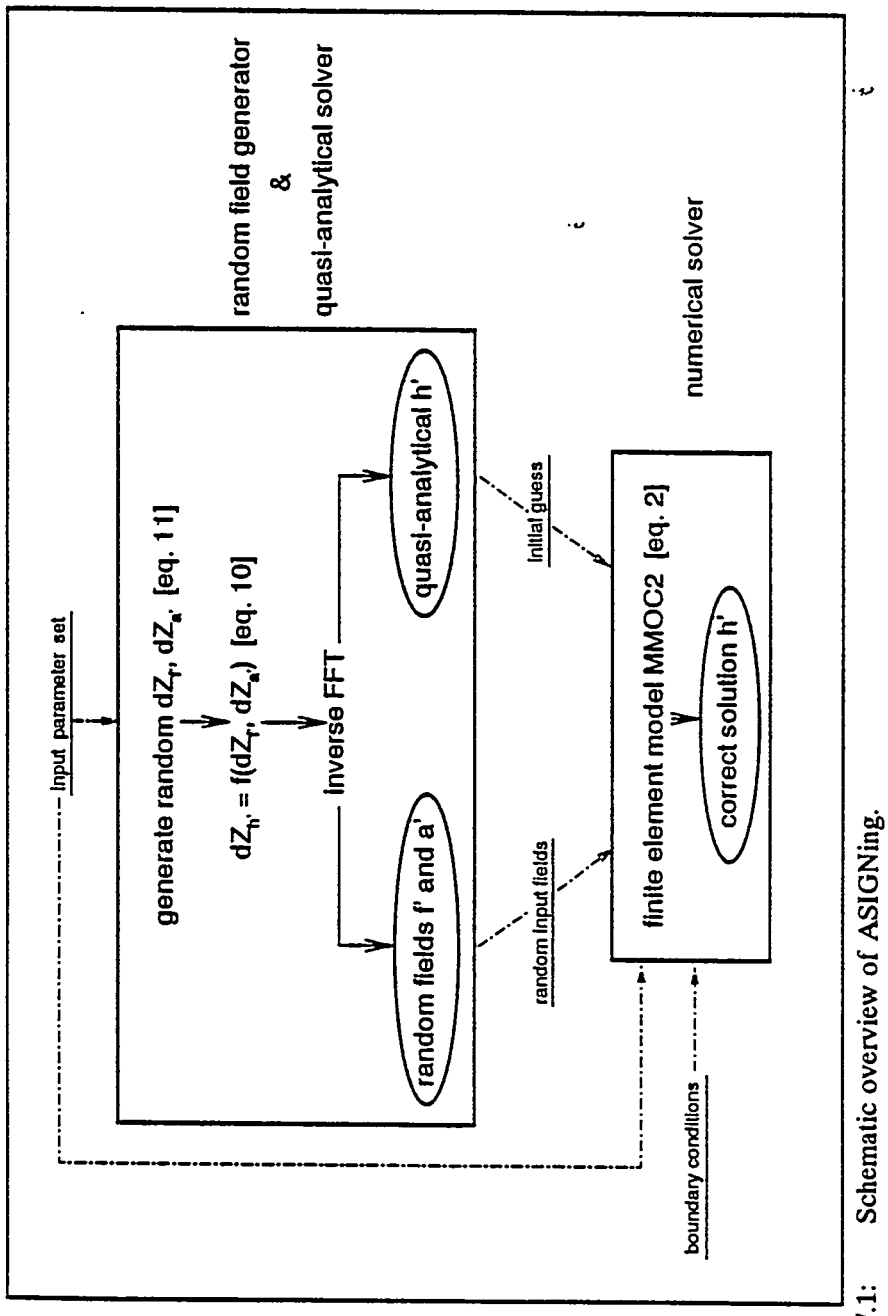

Figure 7.1: Schematic overview of ASIGNing.

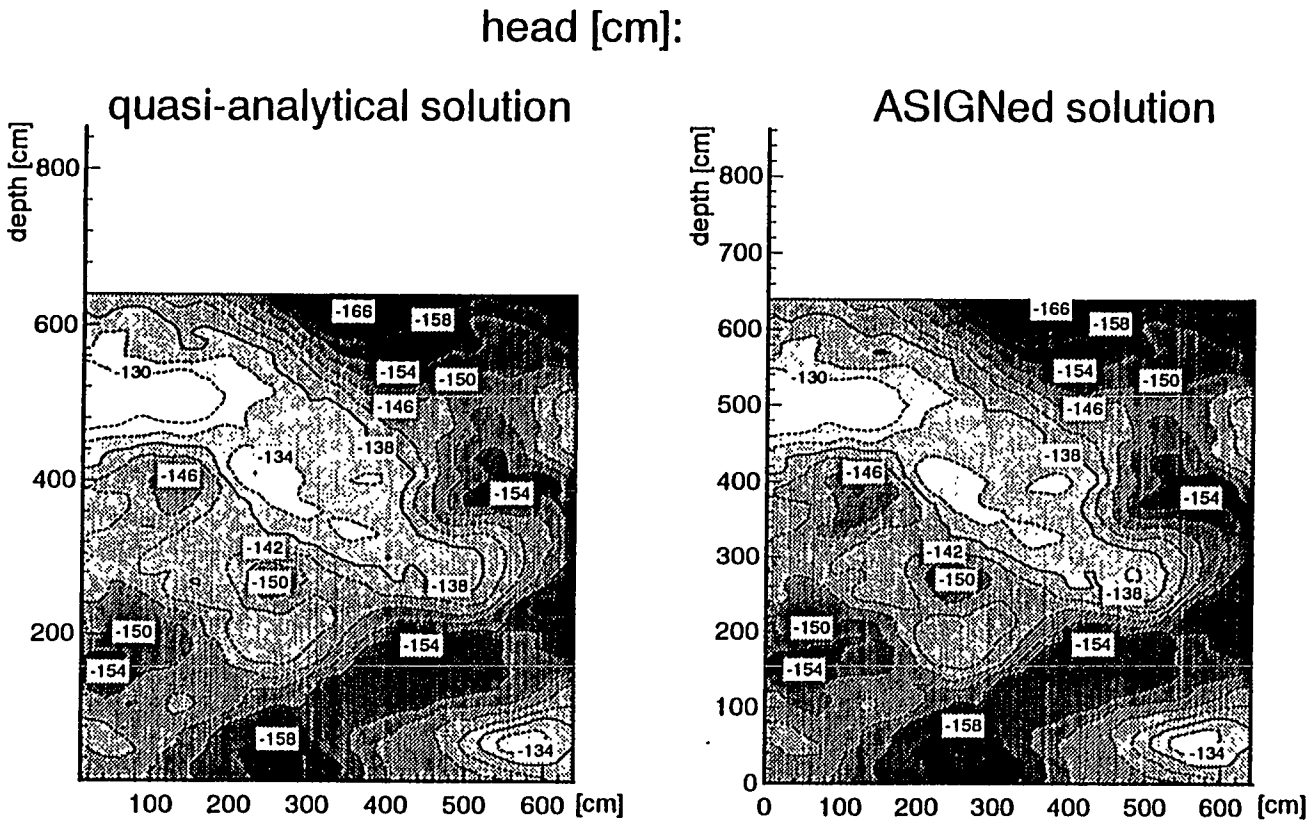

Figure 7.2: Low variability: Comparison of the 1st order perturbation solution obtained by the quasi-analytical spectral method with the ASIGNed finite element solution to Richards equation under boundary condition (a) at σ^2_f = 0.1. The labels indicate the head [cm] at the nearest contour line.

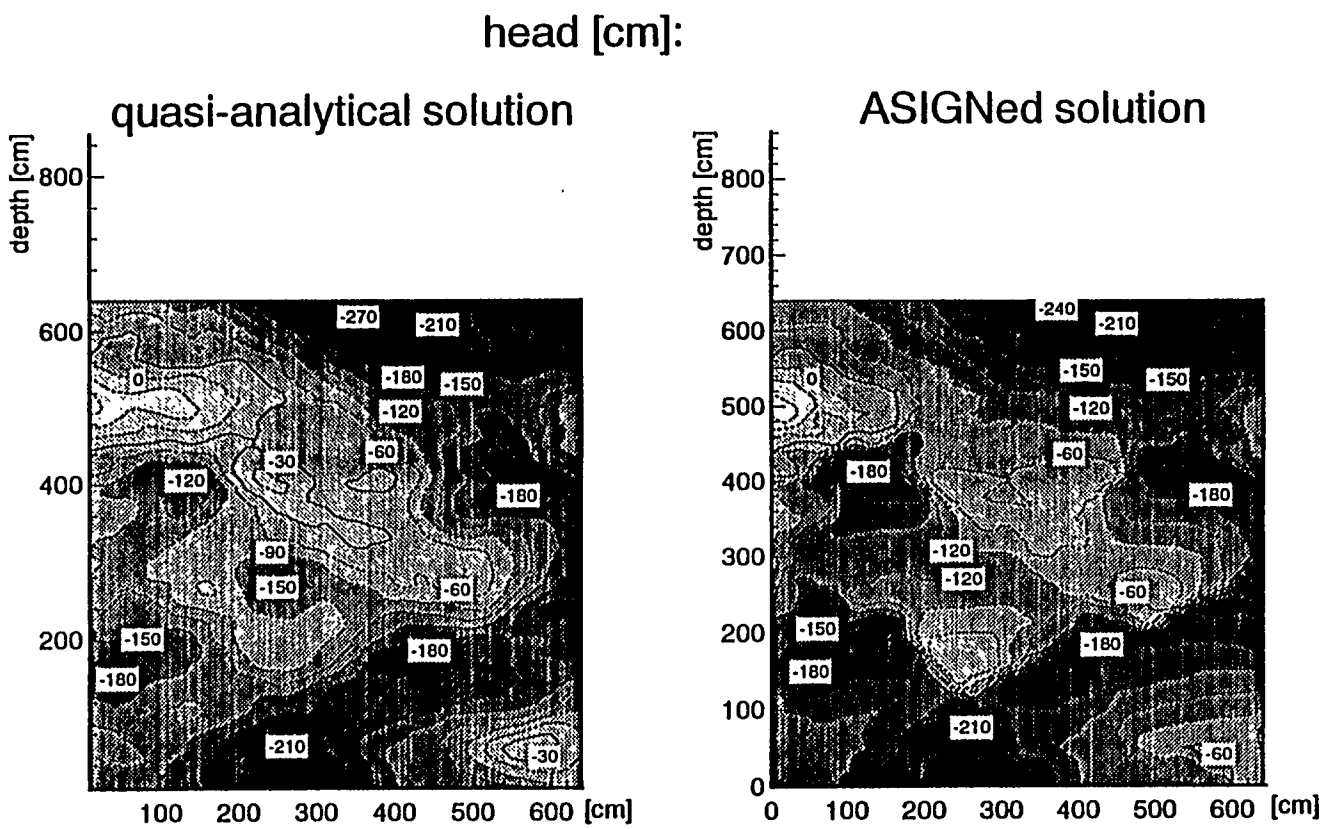

Figure 7.3: High variability: Comparison of the 1st order perturbation solution obtained by the quasi-analytical spectral method with the ASIGNed finite element solution to Richards equation under boundary condition (a) at σ^2_f = 6.0. The labels indicate the head [cm] at the nearest contour line.

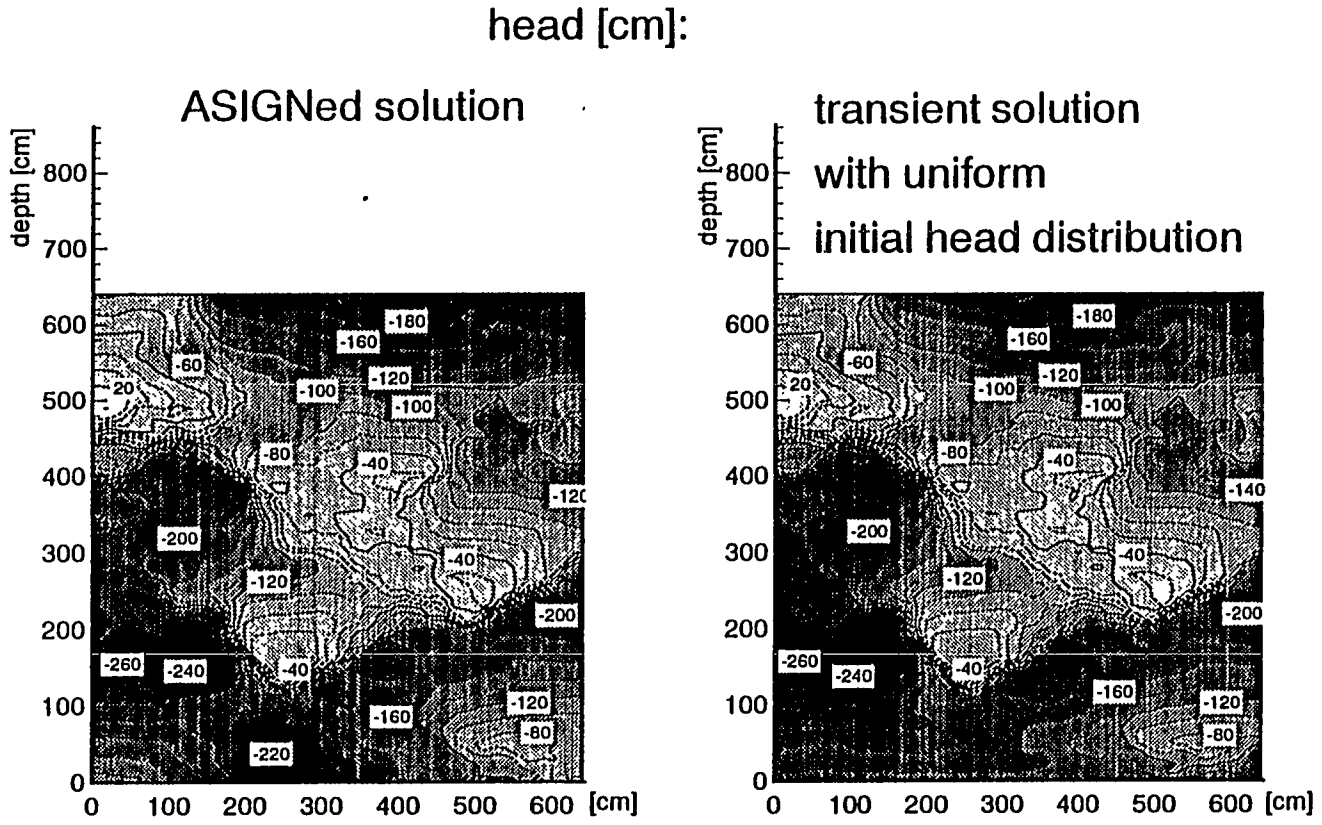

Figure 7.4: Boundary condition (c) with three flux-type boundaries: Comparison of the ASIGNed steady state finite element solution to the Richards equation with that obtained by transient time-marching at $\sigma^2_f = 6.0$. The labels indicate the head [cm] at the nearest contour line.

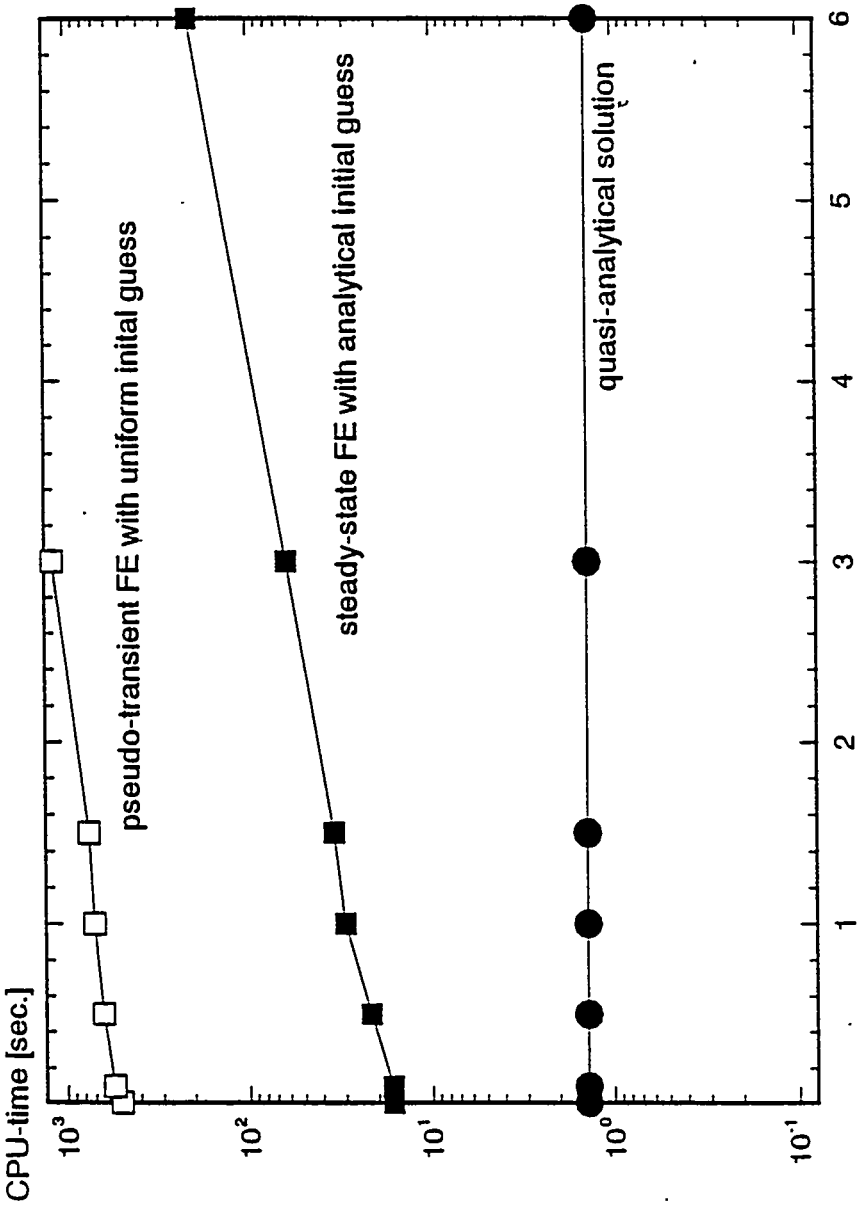

Figure 7.5: CPU-time in seconds as a function of σ^2_f for the quasi-analytical spectral method, the ASIGNed numerical solution (without computation of the initial guess), and the transient numerical solution with a uniform initial head distribution. The numerical cases are computed with boundary condition (a).

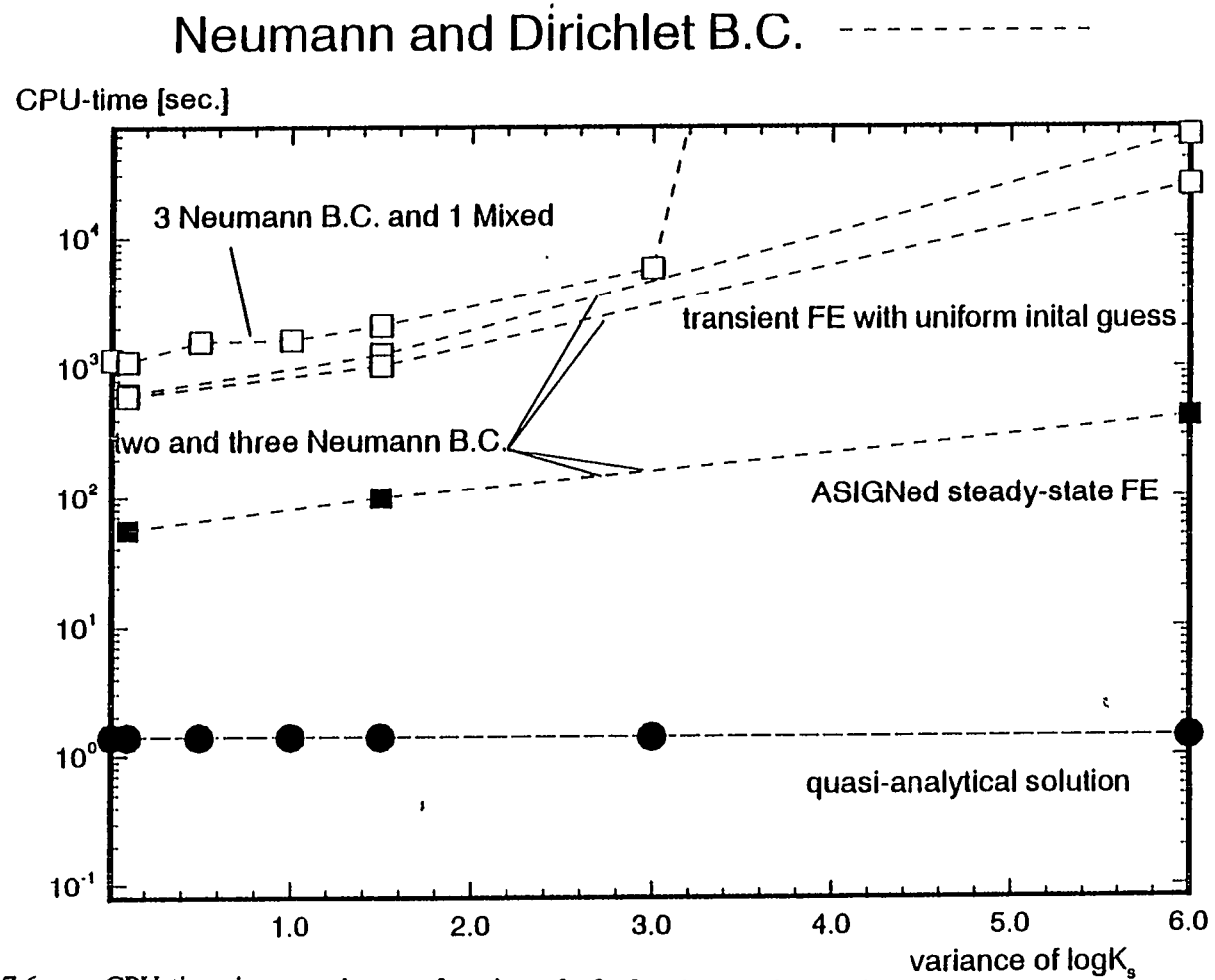

Figure 7.6: CPU-time in seconds as a function of σ^2_f for the quasi-analytical spectral method, the ASIGNed numerical solution (without computation of the initial guess), and the transient numerical solution with a uniform initial head distribution. The numerical cases are computed with boundary conditions (b) and (c). No convergence in the ASIGNed solution was achieved for boundary condition (d).

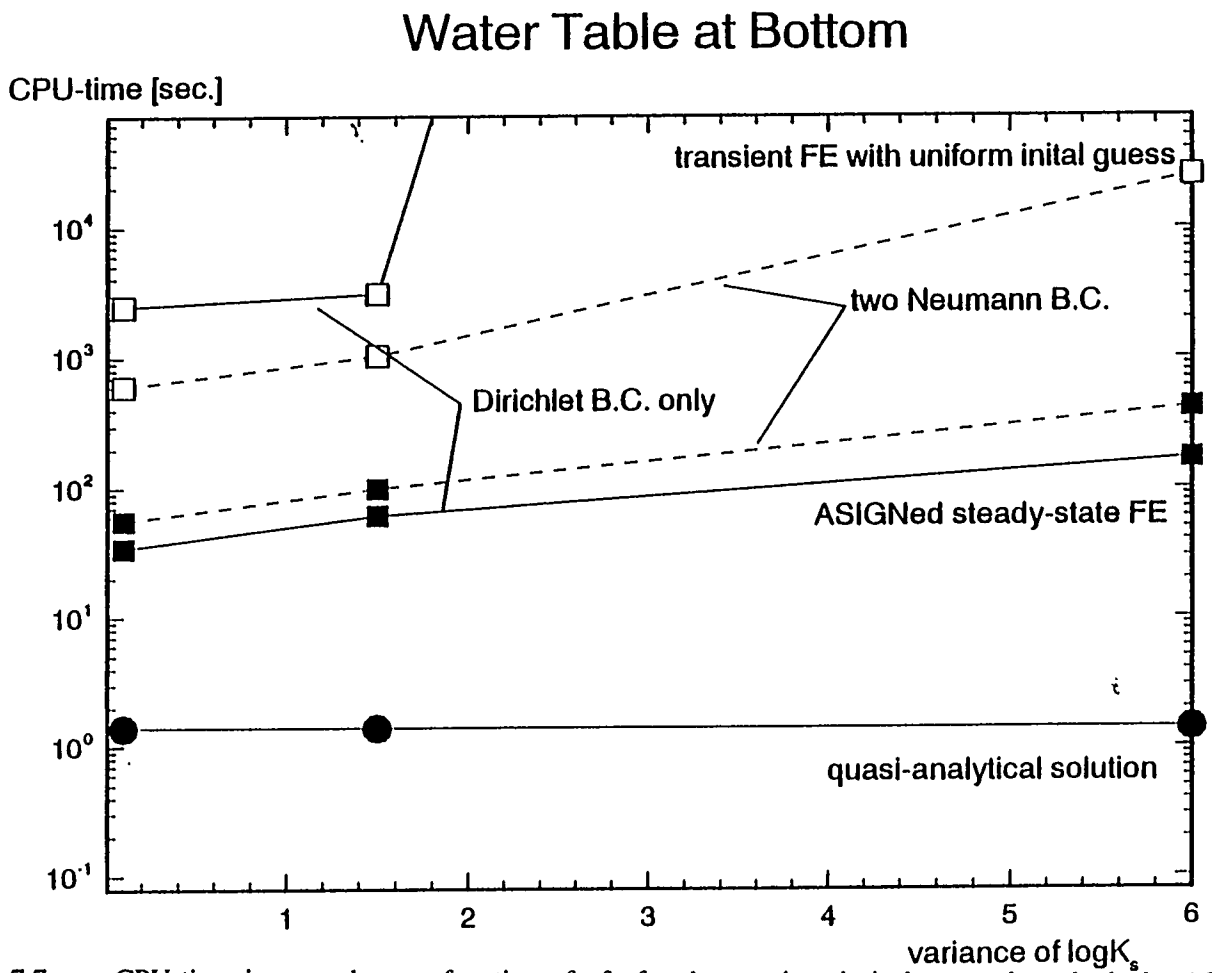

Figure 7.7: CPU-time in seconds as a function of σ^2_f for the quasi-analytical spectral method, the ASIGNed numerical solution (without computation of the initial guess), and the transient numerical solution with a uniform initial head distribution. The numerical cases are computed with boundary conditions (e) and (f).

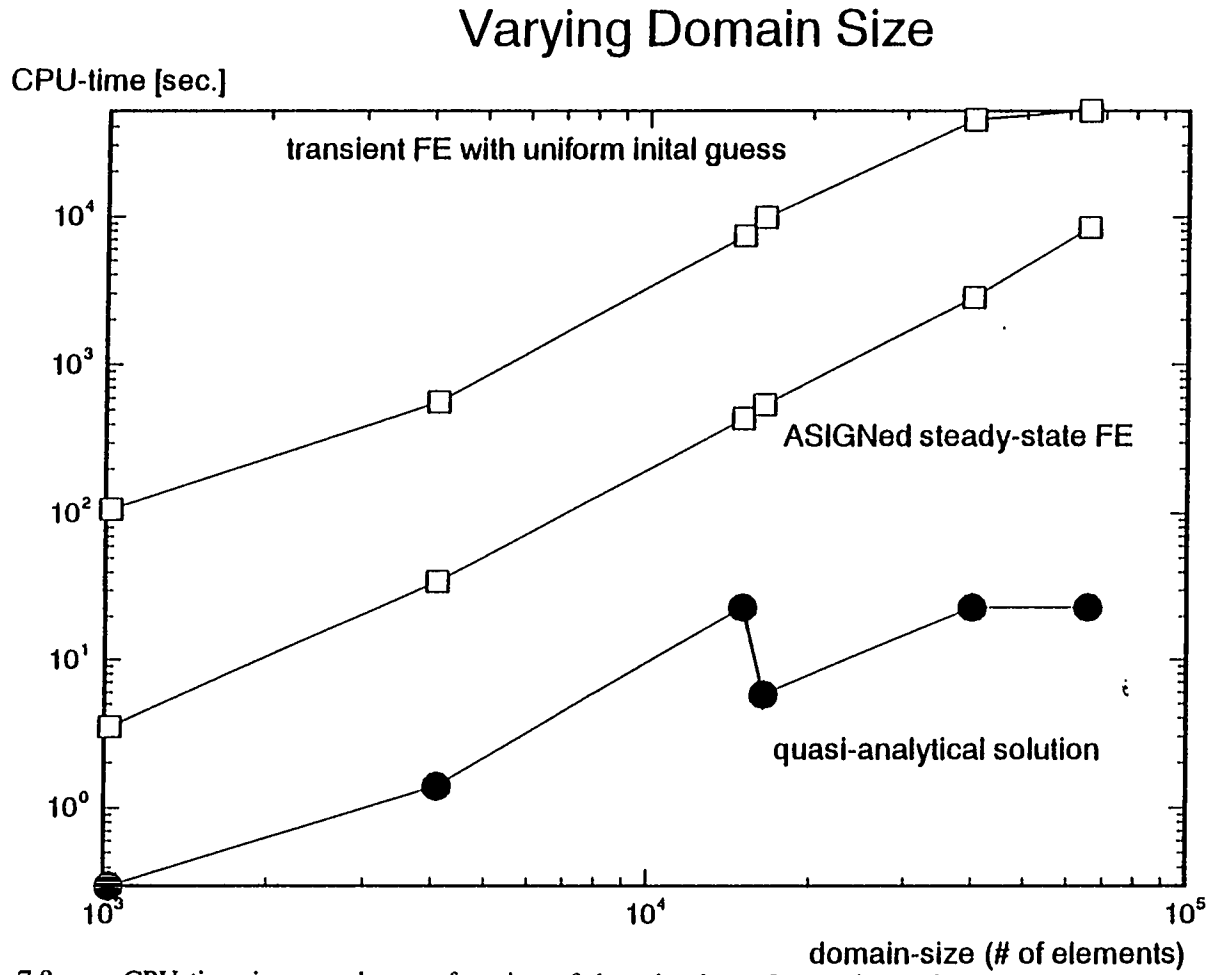

Figure 7.8: CPU-time in seconds as a function of domain size: Comparison of the quasi-analytical spectral method, the ASIGNed numerical solution (without computation of the initial guess), and the transient numerical solution with a uniform initial head distribution. The numerical cases are computed with boundary conditions (a).

8. STOCHASTIC ANALYSIS OF STEADY-STATE FLOW IN HETEROGENEOUS UNSATURATED SOILS VIA INTENSIVE MONTE CARLO SIMULATION

8.1 Introduction

Spatial heterogeneity of soil textural properties causes a potentially high degree of variability in the soil moisture flux. In general, the amount of field information that is available to understand or predict moisture flux in the heterogeneous unsaturated zone is limited. Consequently, the modeling of infiltration events and of soil moisture transport to the water table is associated with uncertainty. In many applications quantification of the uncertainty by stochastic analysis is necessary to assess certain hazards or risks. Statistical models enable us to quantify the average soil textural properties, their variability, and their spatial correlation (chapter 2). They are utilized as input for the stochastic analysis of the physical principles governing soil moisture movement. Stochastic analysis provides a statistical description of the variability of soil moisture movement.

Over the past two decades field studies at numerous sites have been used to determine statistical models for describing the variability of soil texture, saturated and unsaturated hydraulic conductivity, soil moisture content, and soil water tension (Ahuja et al., 1984; Anderson and Cassel, 1986; Burden and Selim, 1989; Byers and Stephens, 1983; Cameron, 1978; Ciollaro and Comegna, 1988; Field et al., 1984; Greenhotlz et al., 1988; Greminger et al., 1985; Hopmans et al., 1988; Lauren et al., 1988; Mulla, 1988; Naney et al., 1988; Nielsen et al., 1973; Russo et al., 1981; Russo, 1984; Saddiq et al., 1985; Smettem, 1987; Vieira et al., 1981; Wagenet and Addiscott, 1987; Wierenga et al., 1989). The basic tenet of these field studies has been that the soil hydraulic parameters, which relate unsaturated hydraulic conductivity to soil moisture content and soil water tension, may vary by orders of

magnitude over very short distances (decameters to meters). They are best characterized by a lognormal probability density function (White and Sully, 1992). The variability in soil moisture content and in soil water tension (here generally referred to as suction head or simply 'head') has been found to be very significant with coefficients of variation that often exceed 70%.

This chapter is concerned with the stochastic analysis of these spatially variable field properties. In the stochastic context, the spatially variable physical properties are referred to as random field variables (RFVs, see section 2.5.1) to emphasize that they are not deterministic but described by a probability density function (pdf) (see chapter 2). The stochastic analysis here focuses on characterizing the mean, variance, and covariance of the dependent RFVs K (unsaturated hydraulic conductivity), head h, and moisture flux v as a function of the two RFVs K_s (saturated hydraulic conductivity) and α (soil pore size distribution parameter). The physical equations relating K_s and α to K, h, and v are the exponential unsaturated hydraulic conductivity model by Gardner (1958) (eqn. 4-8), the governing unsaturated flow equation (Richards equation, eqn. 4-1), and Darcy's law (eqn. 4-2) (see chapter 4).

In the past, several approaches have been suggested for the stochastic analysis of unsaturated flow problems. These approaches are either based on purely analytical methods or on numerical computer models. Analytical methods (Yeh et al., 1985a,b; Mantoglou et al., 1987a,b,c; Yeh, 1989; also see chapter 4) offer the advantage of providing general mathematical solutions (in form of equations) and an explicit insight into the interdependencies of the statistical parameters for the RFVs K_s, α, K, h, and v. Analytical solutions are limited, however, to quasi-infinite soils of mild to moderate variability ($\sigma_y^2<1$, y=logK; log refers to the natural logarithm). In contrast, the numerical stochastic analysis of unsaturated flow provides almost unlimited flexibility in designing the model to match with the particular conditions at a field site or to address particular problems of fundamental interest that are difficult to address analytically (Ababou, 1988; Hopmans et al., 1988; Ünlü et al., 1990; Polmann et al., 1991; Russo, 1991). The Monte Carlo technique is particularly attractive, since

no stationarity assumptions are needed (Hopmans et al., 1988). Monte Carlo simulations are common in the stochastic analysis of groundwater flow and transport problems (e.g. Freeze, 1975; Delhomme, 1979; Smith and Freeze, 1979; Smith and Schwartz, 1980, 1981a,b; Clifton and Neuman, 1982; Rubin, 1990; Rubin, 1991a,b). The flexibility, however, comes at the expense of rigor and - more importantly - at the expense of potentially enormous computational costs. Single numerical solutions of the nonlinear, heterogeneous flow problem and in particular the steady-state solution are expensive to obtain, let alone multiple solutions in a Monte Carlo simulation (chapter 6). It is therefore not surprising that the numerical analysis of unsaturated flow in heterogeneous soils has been limited both in the number of studies published and in the number of random realizations implemented for each study.

Recently, Harter and Yeh (1993) have developed an efficient combined analytical-numerical method (called ASIGNing) that reduces the cost of computing the solution to Richards equation (K, h) and Darcy's law (v) by two orders of magnitude, even for highly heterogeneous input random fields K_s and α (chapter 7). In this chapter, ASIGNing is applied as the cornerstone to Monte Carlo simulations with a large number of realizations (N=1000). The objective is to obtain highly accurate stochastic solutions of the dependent RFVs K, h, and v in two-dimensional, vertical, steady-state unsaturated flow-fields of moderately to strongly heterogeneous soils in order to implement a stochastic analysis with respect to the statistical input parameters describing the lognormally distributed RFVs K_s and α. Accuracy here refers not only to the numerical accuracy, but also to the statistical accuracy of the sample moments obtained from the Monte Carlo simulation (compare to chapter 6). The study is intended to provide new insight to the problem of variably saturated flow in highly heterogeneous porous media and to critically assess the assumptions and the range of validity of the analytical stochastic steady-state flow model by Yeh (1985a,b), which has here been adopted for 2-D flow and the particular case of α having a lognormal pdf (chapter 4). All past studies of unsaturated flow in heterogeneous porous media have been limited to soils with a variance of y no larger

than one ($\sigma_y^2 \leq 1$). Field studies have shown that the variance of the logarithms of the saturated and unsaturated hydraulic conductivity often exceed 1 and may be as large as 3, sometimes even higher (Nielsen et al., 1973; Vieira et al., 1981; Anderson and Cassel, 1986; Ciollaro and Comegna, 1988; Lauren, 1988; Wierenga et al., 1989). In this study hypothetical isotropic and anisotropic soils are investigated with σ_y^2 ranging from 0.01 to 3.2. The variability in y may be due to the dryness of the soil (large mean soil water tension), or due to a high variability in K_s and α, or due to a combination of these.

It is expected that the results will be useful for the assessment of soil moisture movement in variably saturated soils, and also for the assessment of unsaturated transport since the second-order moments characterizing unsaturated flow are also used to estimate solute transport in heterogeneous porous medium (Russo, 1993a,b; Dagan, 1982, 1984; Rubin, 1990, 1991a, 1992) (see chapter 9). Among others, the proposed model allows accurate estimates of the head covariance function and of the cross-covariance function between head, K_s, and α for arbitrary boundary conditions. These (cross-) covariances are necessary to implement conditional simulations of unsaturated flow and transport (chapter 10).

Polmann et al. (1991) have pointed out the importance of model-generated data both to validate analytical models and to improve our understanding of unsaturated flow processes: Large amounts of data are difficult to obtain in the field and problems of sampling accuracy and soil heterogeneity become intertwined. In contrast, "*a simulation experiment based on model-generated data enables us to focus on individual sources of heterogeneity while holding others fixed. If carried out systematically, this approach can identify the critical factors which control moisture movement through heterogeneous soils*" (ibid., p.1448). The following analysis is presented in this spirit.

First a rigorous definition is given for the term Monte Carlo and some simple measures are introduced to determine the sample accuracy of numerical stochastic results as a function of the number of realizations. Then an outline is given of the actual implementation of the

Monte Carlo simulations. The results are presented separately for each of the dependent RFVs logK, h, and v. The general statistical properties of each of these RFVs are discussed, the sample error associated with the Monte Carlo simulation is determined, boundary effects are investigated, the dependency of the RFVs on the independent parameters is analyzed and compared with the analytical stochastic model introduced in chapter 4.

8.2 Monte Carlo Simulation

8.2.1 Definition and Theoretical Sampling Accuracy

The Monte Carlo method is defined as a random sampling procedure used to numerically evaluate the integral:

$$G = \int_{\Omega} g(X)p(X)dX \qquad \textbf{(8-1)}$$

where G is the expected value of the random variable g(**X**) defined in the sample space Ω. g(**X**) is an analytical function of a vector **X** of random variables or random field variables with a joint-pdf p(**X**). The numerical integration by Monte Carlo is performed as a *game of chance* (Kalos and Whitlock, 1986), where N sets of random (field) variables **X** are sampled from the joint-pdf f(**X**). In Monte Carlo sampling is equivalent to generating a random number or random field (chapter 3). The integral above is approximated by the sum:

$$G_N = \frac{1}{N}\sum_i g(X_i) \qquad \textbf{(8-2)}$$

G_N is the sample mean. Through the fundamental theorem of large numbers it is guaranteed that $<G_N>$ converges in the mean square to G (< > indicates expected value)

If $\mathbf{X}_i$ is independent of $\mathbf{X}_j$, $i \neq j$, and if it is known *a priori* that g(**X**) has a Gaussian pdf or if N is very large, the sampling error (variance) ε_G^2 of the normally distributed sample mean G_N is (Haan, 1977; Kalos and Whitlock, 1986):

$$\varepsilon_G^2 = \frac{\sigma_g^2}{N} \tag{8-3}$$

where σ_g^2 is the variance of g(X). Note that the sample moments are assumed to have a Gaussian distribution rather than the commonly applied t-distribution, which is justified since samples of at least 40 independent measurements are subsequently evaluated. Since σ_g^2 is not known, it must be estimated by:

$$var_g = \frac{1}{N}\sum g^2(X_N) - (\frac{1}{N}\sum g(X_N))^2 \tag{8-4}$$

The sample variance var_g itself has an associated sampling error. For the square-root s_g of var_g, the sampling error (variance) $\varepsilon_{s.g}^2$ of the sample standard deviation s_g is approximately (Yevjevich, 1972):

$$\varepsilon_{s.g}^2 \approx \frac{\sigma_g^2}{2N} \tag{8-5}$$

For the sample variance var_g itself, simple heuristic considerations lead to the following expression of the expected sampling error (standard deviation) $\varepsilon_{v.g}$ given $\varepsilon_{s.g}$:

$$\varepsilon_{v.g} = \frac{(\sigma_g + \varepsilon_{s.g})^2 - (\sigma_g - \varepsilon_{s.g})^2}{2} \tag{8-6}$$

which simplifies with the help of (8-5) to:

$$\varepsilon_{v.g} \approx \frac{2\sigma_g^2}{\sqrt{2N}} \tag{8-7}$$

(8-3) and (8-7) can be used to estimate the sampling errors of past Monte Carlo studies of unsaturated moisture movement. Ünlü et al. (1990) implemented Monte Carlo simulations with 50 realizations of the moisture redistribution process in a one-dimensional soil column. The column consisted of 100 random soil layers of varying soil properties. The study addressed

the sensitivity of the head and vertical flux moments to the statistical input parameters and to the boundary conditions. Using (8-3) with N=50 and the sample head variances reported by the authors, the 95% confidence interval ($\pm 2\varepsilon_G$) for sample mean head ranges from ±0.2 cm to ±10 cm (±28% of the sample standard deviation). This is a small range given that the mean suction head varies over several hundred centimeters along the vertical column, but relative to the standard deviation it is rather significant.

The same accuracy of sample mean heads is found for Hopmans et al. (1988) who used 10 realizations of a two-dimensional, hypothetical soil cross-section consisting of 50 vertically homogeneous columns i.e., with vertically constant K_s and soil pore size distribution, but variable mean head. The analysis was used to derive the nonstationary head and flux distribution moments as a function of the distance above water-table by averaging over all 10 samples in all 50 columns in the same horizontal layer. For a conservative estimate of the associated sampling error it can be assumed that after a horizontal distance of roughly 10 soil columns the local head and flux moments are completely independent of each other. Then, N = 10 * 50/10 = 50 (the number of realizations times the number of independent soil columns per realization), the same as in Ünlü et al. (1990).

The 95% confidence interval of the sample variance ($\pm 2\varepsilon_{v,g}$) in these two studies ranges from 60% to 140% of the ensemble standard deviation (as represented by the square-root of the sample variance). The same confidence interval applies to the sample covariance functions computed in Hopmans et al. (1988). While the results from both studies may be considered accurate for practical purposes, the sampling error of the mean and variance in head and flux is large enough to question the use of these results for comparison with analytical results.

From (8-7) it is straightforward to determine that the number of realizations necessary to reduce the 95% confidence interval of the sample variance (or covariance) to within ±10% and ±5% of the ensemble variance is $N \geq 800$ and $N \geq 3200$, respectively. In other words, roughly 1000 realizations are necessary to estimate the local sample variance (covariance) such

that in 19 of 20 Monte Carlo simulations the sample error is less than 10% of the ensemble variance. If the variance is obtained not only by averaging over the N samples at x, but also by averaging spatially, less realizations are needed and the confidence interval will depend on the spatial correlation of the RFVs. Spatial averaging, however, assumes that the field is weakly stationary i.e., that the ensemble mean G and ensemble variance σ_g^2 are identical for all x in the simulation domain. In this study, the primary interest is to obtain the sample mean, variance, and covariance separately for each x so that stationarity of the dependent RFVs does not have to be assumed *a priori*.

8.2.2 General Computational Procedures

Applied to the unsaturated flow problem, g(X) is any of the random field variables logK, h, and v. X is a vector of the two RFVs K_s and $\log\alpha$. Note that the mean and variance of the RFV g(X) and the sampling errors ε_G and $\varepsilon_{s,g}$ are functions of location x unless stationarity is assumed. To obtain the sums (8-2) and (8-4) individual realizations $\mathbf{X}_i$ of the Gaussian distributed RFVs $f=\log K_s$ and $a=\log\alpha$ must be generated. For each realization of f and *a*, the corresponding random field solutions of y, h, v_x (horizontal flux), and v_z (vertical flux) are computed by using the ASIGNing technique described in chapter 7. The results are evaluated not only to determine the first and second moment of the pdfs, (8-2) and (8-4), but also the histograms of both the independent RFVs f and *a* (for control) and the dependent RFVs y, h, v_x, and v_z. The local sample covariance field of a RFV g centered around point x, $cov_g(\mathbf{x},\xi)$, is computed by:

$$cov_g(x,\xi) = \frac{1}{N}\sum_i^N \left[g_i(x)g_i(x+\xi) - G_N(x)G_N(x+\xi)\right] \qquad \textbf{(8-8)}$$

And similarly the local cross-covariance field for two RFVs g and g' is defined as:

$$cov_{gg'}(x,\xi) = \frac{1}{N}\sum_{i}^{N} g_i(x)g_i'(x+\xi) - G_N(x)G_N'(x+\xi) \qquad (8\text{-}9)$$

Here, g and g' denote any of the RFVs f, a, y, h, v_x, and v_z. Note that unlike in any previous numerical studies of unsaturated flow, the sample covariance and cross-covariance is evaluated over the sample space N and does not involve any spatial averaging. During the Monte Carlo simulation, the sums in (8-2), (8-4), and (8-8), (8-9) are updated after each realization i.e., the outcomes $g_i(x)$, $g_i^2(x)$, $g_i(x)g_i(x+\xi)$, and $g_i(x)g_i'(x+\xi)$ are added to the sum of their outcomes from previous realizations j<i, respectively. For efficient data management, the actual results of each realization are discarded once all sums and histograms (see below) have been updated. After the Monte Carlo simulation is completed, the sample means, variances, and (cross-)covariances (8-2), (8-4), (8-8), and (8-9) are obtained explicitly from the respective sums.

The sample mean G_N and sample variance var_g are themselves two-dimensional realizations of RFVs and summary statistics can be obtained by spatially averaging over the sample mean field and the sample variance field. For N=1000, the spatial average of the local moments (average sample mean and average sample variance) has a very narrow confidence interval i.e., it is a very accurate estimate of the true mean and variance of the dependent RFV's provided that the mean and variance fields are found to be weakly stationary. Since the statistical input parameters F, A, H, σ_f^2, and σ_a^2 in this study are all independent of location, the statistical moments of y, h, and v must also be weakly stationary. In the weakly stationary Gaussian case, the spatial variance of the sample mean field, $var(G_N)$, and the standard deviation of the sample variance field, $std(var_g)$, also provide an estimate of the sampling error and should be similar to (8-3) and (8-7) if the sample moments indeed converge in the mean square sense (see chapter 2). For better comparison, the spatial variance of the local sample means is normalized by the expected sampling error ε_G^2, where the latter is obtained by using the average sample variance $\langle var_g \rangle$ rather than the (unknown) ensemble variance σ_g^2 in (8-3).

Then the dimensionless actual sample error of the sample mean is defined as:

$$\varepsilon_G'^2 = N \frac{var(G_N)}{<var_g>} \tag{8-10}$$

where N is the number of realizations in the Monte Carlo simulation. Similarly, the dimensionless actual sample error of the sample variance is defined by using (8-7):

$$\varepsilon'_{var,g} = \frac{\sqrt{2N var(var_g)}}{2<var_g>} \tag{8-11}$$

As in (8-10) and (8-11) an apostrophe ' with a statistical moment subsequently indicates that the moment has been normalized and that it is dimensionless.

The sample covariance and cross-covariance fields are computed in a window of half the side-length of the simulation domain centered around each of nine sample locations $\mathbf{x}$ (Figure 8.1). In other words, (cross-)covariance values around $\mathbf{x}$ are computed only for separation distances $|\xi|$ not exceeding one-fourth of the domain-length in each principal direction. The choice of the locations $\mathbf{x}_i$ and the size of the windows surrounding them is dictated by several objectives: to provide local sample (cross-)covariance fields that can be checked for spatial trend; to spread the locations $\mathbf{x}_i$ as far apart as possible to minimize correlation between the sample (cross-)covariance fields; and finally to provide equally sized sample fields. The latter is necessary to obtain average (cross-)covariance fields $C_{gg'}(\xi)$ for each lag distance ξ:

$$C_{gg'}(\xi) = 1/9 \sum_{i=1}^{9} cov_{gg'}(x_i, \xi) \tag{8-12}$$

The window for the covariance and cross-covariance fields around the center point $\mathbf{x}_{center}$ of the simulation domain is chosen to be as large as the simulation domain itself to provide additional information on $cov_{gg'}(\mathbf{x}_{center}, \xi)$ at lag distances up to one-half of the domain size in each dimension.

Finally, two classes of histograms are computed: The local histogram of the RFVs at x_{center} and the total histogram of all outcomes of each RFV regardless of location. The histograms are updated after each realization. Figure 8.2 shows a simple flow-chart of the Monte Carlo simulation procedure.

8.3 Simulation Parameters and Implementation

This study is geared towards the equivalent of a formal stochastic analysis and not towards a particular field application. Nevertheless, it is imperative to implement the numerical analysis such that the demands of actual model applications are addressed. An intensive study of field heterogeneity in an arid soil was implemented by Wierenga et al. (1989, 1991) near Las Cruces, New Mexico. Measurements of the in situ and laboratory saturated hydraulic conductivity, soil water content, and soil water retention function provide valuable information about the magnitude of field soil variability. The saturated hydraulic conductivity was found to be on the order of 10^0 - 10^5 cm/d and to have a lognormal distribution. Variances in $\log K_s$ (natural based logarithms) range from as small as 0.1 to as large as 3 depending on the measurement method and the soil layer. The overall variability of $\log K_s$ at the Las Cruces site is approximately 1.5. A geostatistical analysis of these $\log K_s$ data reveals that the correlation structure can be modeled by an exponential covariance function with an integral scale of a few meters in the horizontal direction and an integral scale of a few decimeters in the vertical direction. To describe the spatial variability of pore-size distribution related parameters, Wierenga et al. (1989) fitted the VanGenuchten model (4-4) to the empirical retention curves obtained from soil cores. A statistical analysis of their data shows that the VanGenuchten α is lognormally distributed with a geometric mean Γ = 0.04 and variance σ_s^2 = 0.3. The VanGenuchten n is also best fitted by a lognormal distribution with a geometric mean n of 1.6 and a variance in log(n) of 0.02. Covariance functions similar to that of $\log K_s$ were found for

the parameters characterizing the pore-size distribution (unpublished study report, Harter, 1991). This information of spatial variability of unsaturated hydraulic properties in the field provided the basis for the design of the Monte Carlo simulations.

The input parameters for all Monte Carlo simulations (MCSs) in this study are (Table 8.1): the variances of f and a, σ_f^2, σ_a^2, the correlation between a and f, ρ_{af}, the geometric mean Γ of the soil parameter α (eqn. 4-8), the horizontal and vertical grid discretization, Δx, Δz, and the horizontal and vertical correlation scales of f (and a), λ_{fx}, λ_{fz}. Only steady-state gravity flow is considered. Each Monte Carlo simulation is designed to simulate one particular, hypothetical soil site. The different sites (simulations) are arbitrarily labeled as #M, where $M \in \{2,3,...,31\}$. To keep matters simple and transparent, a base soil site is defined (#3). From site to site, one or a few of the input parameters are systematically varied. Only the differences to the base site are listed in Table 8.1.

Recall from chapter 7, that the ASIGNing technique allows the use of random Dirichlet type boundaries by setting the head on the boundaries equal to the spectrally derived solution. The solution for a particular sample of random fields f and a is obtained quasi-analytically in the spectral domain (Harter and Yeh, 1993; see also chapter 7) The underlying assumption is that the RFV h is weakly stationary, normally distributed, and that boundaries are at infinity. The spectral solution for the head is defined through the spectral representations of f and a, and through the ensemble means Γ and H. The mean vertical flux is controlled through Γ, H, and the covariance function of f and a.. This type of boundary condition allows the simulation of a finite portion of a quasi-infinite domain, which is consistent with many field applications. Boundary conditions are rarely known with certainty.

Within the steady-state unsaturated flow profile the spatial variability of the soil water content θ is neglected. For simplicity a constant $\theta=1$ is used in the numerical simulations. Then the pore velocity is equal to the Darcian flux **q** and is automatically normalized with respect to the (constant) soil water content. This greatly simplifies the flux analysis and - in

subsequent chapters - will prove advantageous in the analysis of solute transport through unsaturated media, since the results are very general and independent of the relationship between θ and h. Note that this assumption does not neglect the change in water content from a very wet to a very dry soil. It only postulates that the water content spatial variability at a given H is negligible. The velocity distribution can also be normalized with respect to the mean saturated hydraulic conductivity, the only other RFV depending on units of time, since the choice of the time-units is arbitrary. Setting the mean saturated hydraulic conductivity to 1[cm/day], the actual steady-state results for the velocity distribution given a mean saturated hydraulic conductivity of x [cm/day] are obtained by multiplying the velocity with x.

The mean pressure head in the base soil is -150 cm and varies in other simulations from -100 cm to -3000 cm. The mean pressure head is chosen to avoid partial saturation of significant parts of the soil domain if the soil is very heterogeneous. Partial saturation poses no problem to the Monte Carlo simulation, but cannot be taken into account by the first order stochastic analysis to which the numerical results are compared. The base site has a unit variance of f, σ_f^2=1. In other soils, σ_f^2 is as small as 0.01 and as large as 4. The geometric mean Γ of α is 0.01 cm^{-1} with a variance σ_a^2 = 0.01 such that $\zeta = \sigma_a/\sigma_f = 0.1$. All simulations are implemented using the exponential covariance function (7-5) for f and *a*. The RFV *a* is either perfectly correlated with f (ρ_{af}=1) or - as in the base soil site - independent of f (ρ_{af}=0). It has a correlation scale that is always identical to that of f. In the sensitivity analysis the geometric mean of α is increased to values as large as 0.1 cm^{-1} and the variance of *a* varies between 10^{-4} and 0.6. The correlation scale is systematically varied from as little as 12.5 cm in both the horizontal and vertical direction to as much as 300 cm in the horizontal and 50 cm in the vertical. The base soil is isotropic with a correlation scale λ_f = 50 cm. The discretization of the base soil site yields squared finite elements of $(10)^2$ cm^2 or $1/5^{th}$ of the correlation scale in each dimension. The vertical discretization (Δz=10 cm) is chosen according to the results of the grid design analysis in chapter 6. Different finite element discretizations are also selected

to test the grid-design with the Monte Carlo approach (as opposed to the single simulation technique used in chapter 6). An isotropic case is simulated with $\Delta x = \Delta z = 2.5$ cm and a correlation scale $|\lambda_f| = 12.5$ cm in each direction (#19). The effect of horizontal discretization on the stochastic results is tested by comparing an anisotropic case (λ_{f_x}=300 cm, λ_{f_z} = 50 cm) with Δx =30 cm and Δz=10 cm (#12) with the same case, but different horizontal discretization Δx =10 cm (#11).

8.4 Random Field Generator: Evaluation

The performance of the random field generator used to generate the two-dimensional input random fields of K_s and α has been discussed in chapters 3 and 6. The spectral generator produces numerically undistorted random fields with sample moments that are in excellent agreement with the specified ensemble moments. The only significant weakness of the technique described in chapter 3 is a small reduction in the variance of the random fields: The sample variance is generally 5% lower than specified, while the sample covariance reproduces the desired covariance structure at non-zero lags with very good accuracy. No consistent error is observed for the sample mean. These results from chapter 3 are confirmed by the sample moments obtained for f and a in the unsaturated flow simulations. The histograms of f and a show a smooth Gaussian-like distribution, and no consistent artificial spatial pattern is observed in the two-dimensional map of the input sample moments (Figure 8.3d,h). In the base soil #3, the local sample mean $F_{1000}(\mathbf{x})$ of f varies from -0.1 to 0.1 with a (spatial) standard deviation of the sample mean of 0.033. The expected standard deviation (8-3) of the sample mean is ε_F = 0.032 (N=1000) (Figure 8.3a). The local sample variance of f varies from 0.8 to 1.1 with a spatial average of 0.94, which is 6% below the specified ensemble variance (Figure 8.3b). The spatial standard deviation of the local sample variance is 0.043 which is very close to the expected $\varepsilon_{v,f}$ = 0.042 (8-7). Similar results are found for the sample moments of a. The

average sample covariance function (8-8) for f and *a* are isotropic (Figure 8.3c,g) and a cross-section shows that they are in excellent agreement with the specified exponential covariance function (Figure 8.6).

8.5 Stochastic Analysis of the Unsaturated Hydraulic Conductivity

The stochastic analysis of the dependent variables y, h, v_x, and v_z is organized in the following manner: Using primarily the results from the base soil site #3, general observations are summarized regarding the structure of the random fields, the structure, stationarity, and sampling error of the sample mean and sample variance fields, and the structure of the covariance fields. The covariance fields are qualitatively compared with analytically obtained covariance functions (chapter 4). The histograms are described to draw conclusions about the empirical pdf of the dependent parameters. Then a quantitative analysis is implemented regarding the stochastic dependence of the mean, the variance, and the covariance of the dependent RFVs on the variances σ_f^2, σ_a^2, the correlation ρ_{af} between *a* and f, the mean head H, the geometric mean Γ of α, the horizontal and vertical correlation scales λ_{fx} and λ_{fz} of f, the anisotropy aspect ratio $\nu = \lambda_{fx}/\lambda_{fz}$, and the grid discretization Δx and Δz. The numerical results are directly compared with the first order analytical solutions.

8.5.1 General Observations

Sample mean and sample variance field. At site #3, the sample mean and variance fields of y have the random character of individual realizations (Figure 8.3i,k). The dimensionless errors (8-10) and (8-11) of the sample mean and sample variance are 1.21 and 0.99, respectively. Almost identical sampling errors are observed for other soils with the same or less variability in y. At the anisotropic soil sites, the dimensionless error of the sample mean

reduces to 0.82 due to the smaller size of the simulation domain relative to the correlation scale of f (see Table 8.1). No significant trend or other artificial spatial features indicates a deviation from second order stationarity. Second order stationarity for y and other dependent RFVs is expected since the random head boundary conditions are weakly stationary and the mean vertical flow therefore uniform. Notice that the sample mean and variance of y on the boundary are not notably different from the interior of the simulation domain. However, for soils with larger aspect ratio ν than the base soil site #3 or larger variability σ_y^2 or both, the variance within $0.5\lambda_{fz}$ from the bottom boundary and within $2\lambda_{fz}$ from the top boundary tends to be lower than in the rest of the domain by up to approximately 30%. A similar variance reduction is observed within $0.2\lambda_{fx}$ of the horizontal boundaries. These boundary effects on the sample variance of y increase $\varepsilon'_{v.g}$ to 1.26 in the highest variance soil (#21) while reducing $\varepsilon'_G{}^2$ to 0.67. No significant boundary effects are observed for the sample mean Y of y at any soil site.

The average reduction of σ_y^2 at and near the boundary is due to setting the head values on the boundary equal to the first order approximation of the head, given the random fields of f and a. The statistical moments of the head on the boundary are therefore not entirely consistent with those in the interior of the domain. As will be discussed below, the head and velocity variances near the boundary increase significantly for soils with high variability in moisture flux due to the approximate nature of the first order quasi-analytical head boundary conditions. It is not clear, however, why there is a reduction and not an increase in σ_y^2 near the boundary (relative to the interior).

Sample covariance. For all soils the sample covariance field C_{yy} of y is very similar to the input covariance field C_{ff} reflecting the physical observation that the random fields of y have a very similar random structure as the random fields of f and a (compare e.g., Figure 8.3i,k vs. Figure 8.3a,b). At the isotropic soil sites (isotropic with respect to f), C_{yy} has a very small, but notable anisotropy with larger vertical than horizontal correlation scale (Figure 8.6).

The correlation lengths in both directions are approximately 10% smaller than λ_f. The horizontal covariance is of the "hole-covariance" type i.e., it becomes negative at some lag distance and then tends asymptotically to zero. The vertical covariance of y remains positive for all lag-distances. In the anisotropic soils with $\nu > 1$, the situation reverses to a hole-type covariance function in the vertical direction and an exponential type covariance function in the horizontal direction. Again, the correlation lengths are approximately 10% smaller than those for f (Figure 8.7). These findings are in excellent agreement with the theoretical covariance function derived in chapter 4. In Figure 8.5d a single sample covariance C_{yy} is plotted for an anisotropic wet soil with ν=3 and σ_f^2=0.95 (#31) to illustrate the qualitative agreement between the analytical solution and the numerical results. Similar qualitative agreement of the sample C_{yy} with the analytical C_{yy} is found at all sites. The correlation function ρ_{yy} is also in good quantitative agreement for all soil sites, even those with strong variability (compare Figure 8.6, a mildly heterogeneous, isotropic soil, with Figure 8.7, a strongly heterogeneous, anisotropic soil).

Histogram. The histograms of y at all soil sites indicate that y is Gaussian-like distributed i.e., the unsaturated hydraulic conductivity seems lognormally distributed (Figure 8.3m). Only at the driest soil site (#21), which is also the soil with the highest variability in y, the histogram has a slight tail towards lower y. No distribution tests were implemented.

8.5.2 Moment Analysis of the Unsaturated Hydraulic Conductivity

For the stochastic analysis, only the spatially averaged sample moments are considered. To eliminate the non-stationary effects near the boundary, the average sample mean and variance of each dependent RFV are obtained by averaging over the center 33 by 33 nodes (h,v_x, v_z) or the center 32 by 32 elements (y). y is computed for each element from Gardner's equation (4-8) by arithmetically averaging the head values on the four nodes surrounding the

element.

Since the correlation functions of f and *a* are identical within each soil site, inspection of 4-31, 4-39, and 4-47 in chapter 4 suggests that the variances of all dependent parameters of interest - h, y, v_x, and v_z - can be normalized by the variance factor σ^2:

$$\sigma^2 = \sigma_f^2 (1 + \rho \zeta \Gamma H + (\zeta \Gamma H)^2) \qquad \textbf{(8-13)}$$

Note that σ^2 is not identical with either the saturated conductivity variance σ_f^2 nor with the unsaturated conductivity variance σ_y^2. The dimensionless unsaturated hydraulic conductivity variance $\sigma'_y{}^2$:

$$\sigma_y'^2 = \frac{\sigma_y^2}{\sigma^2} \qquad \textbf{(8-14)}$$

as well as the dimensionless variances of the other dependent RFVs are in first order independent of the mean soil water tension H, the correlation ρ_{af}, and the variances of f and *a*. The analytical, dimensionless variances and covariance functions of all RFVs including y are therefore only functions of the correlation scales of f and the geometric mean Γ of α. The numerical analysis shows, however, that the actual stochastic relationship between the dependent RFV second moments and the independent RFV pdfs is more complex than suggested by the analysis in chapter 4. The following results will illustrate this for the unsaturated hydraulic conductivity variance. The stochastic analysis of other RFVs is given in subsequent sections.

Dependence on input variance. The average sample mean Y of the log unsaturated hydraulic conductivity changes proportional to H such that for all sites the first order approximation of Y (4-35), $Y=F+H\Gamma$, holds very accurately (deviations of less than 1%). Figure 8.8b shows the normalized soil variances σ_y^2 as a function of the input variance σ_f^2, aspect ratio v, and vertical correlation scale λ_{fz}. All soils have the same mean tension head H = -150 cm. The random fields of f and *a* are independent. The variance ratio $\zeta=\sigma_a/\sigma_f$ is 0.1. It is obvious from Figure 8.8b that the results are not quite independent of the actual magnitude of the

variances in f and *a*. For the three least variable soil sites (σ_f^2=0.01, 0.11, 0.95), the actual σ_y^2 is approximately 4% smaller than the first order results indicating (as expected) a very good agreement between the numerical and the analytical results (Table 8.2) considering that the variance of the input random fields is also approximately 4%-5% smaller than specified.

With increasing σ_f^2, the dimensionless σ'^2_y increases more or less linearly. In the anisotropic soils the increase relative to the analytical solution is larger. At σ_f^2=3.6, the numerical σ'^2_y is 4% larger than the analytical σ'^2_y in the isotropic soil and 10% and 16% larger in the anisotropic soils with λ_{fz}=50 cm and 30 cm, respectively. A careful analysis of these results reveals that the differences partly stem from an increasing difference in the sample mean head (used for the normalization (8-14)) at higher variances. The difference between the actual (dimensional) and analytical σ_y^2 does not exceed 11%, even for the most variable soils (σ_y^2=3.2) including the dry sites that are not shown here.

The dependence on σ_a^2 alone is demonstrated by comparing the isotropic base site (σ_a^2=0.01, #3) with a soil having σ_a^2=0.64 (#26). In the latter soil the difference between the actual and analytical σ_y^2 (dimensional) is 16%.

Overall, the MCSs indicate that the first order analytical estimate of the mean Y of the unsaturated hydraulic conductivity is very accurate even for strongly heterogeneous soils. The analytical solutions underestimate σ_y^2 at large variances of f and *a*. For practical purposes, the 10%-16% error of the analytical solution in very heterogeneous flow fields (large σ_y^2) is negligible.

Dependence on soil water tension and the correlation between f and a. Again, the first order approximation of Y gives very accurate predictions (to within 1%) of the observed Y. Apart from the differences between analytical and numerical solutions for σ_y^2 discussed in the previous paragraph, neither the mean head, nor the correlation coefficient ρ_{af} have a remarkable effect on σ'^2_y. Due to the particular form of the variance factor σ^2, the variance of all RFVs goes to 0 for ρ_{af}=1 as $H \rightarrow -1/\zeta\Gamma$. At soil water tensions that are more negative than this limit,

the variances of all RFVs increase again (see also chapter 9). It is found that these results indeed hold for the numerical simulation. In correlated soils, the first order solution for the moments of y is accurate over a larger range of soil tensions than in uncorrelated soils. Only at a very dry head (H=-3000) with a large σ_y^2, the dimensionless σ'^2_y increases relative to the analytical solution (Figure 8.9b).

Dependence on Γ and the correlation scale of the soil. The second moments of the dependent RFVs depend nonlinearly on Γ and λ as shown in Figure 8.10b and are also found to be in good agreement with the first order analytical solution, even for large $\Gamma = 0.1$ cm^{-1}.

Dependence on aspect ratio and grid discretization. The difference between the numerical and analytical σ_y^2 increases for larger aspect ratio ν and longer vertical correlation scale λ_{fz}. Figure 8.11b and shows that overall the variance of y decreases as the aspect ratio increases, as expected from the first order analysis. Different horizontal element discretization (#11 vs. #12) does not influence the results for y.

8.6 Stochastic Analysis of the Soil Water Tension

8.6.1 General Observations

Sample mean and sample variance field. The sample mean and variance fields of the soil water tension have a very different random character compared to y, f, or *a* (compare Figure 8.3i,k with Figure 8.4a,b): The visual patterns are much less erratic and significantly broader with only a few relatively large areas of randomly high and low sample values. This pattern is a reflection of the much less erratic nature of the underlying realizations of h, which exhibit a similarly smooth pattern (see Figures 7-2 through 7-4 in chapter 7).

The dimensionless error of sample mean and sample variance, ε'^2_G and $\varepsilon'_{v.g}$, are 0.66 and 1.09, respectively at the isotropic base soil site (#3). Recall that the dimensionless error reflects the spatial variability of the sample mean and sample variance within the simulation

domain relative to the expected variability in an infinite domain. The low error of the sample mean is caused by the strong correlation of the head sample mean values within the simulated domain; the sample domain is small relative to λ_h (approximately 3 λ_{hx} and 5 λ_{hz}). In the anisotropic soils (anisotropy in f), ε'^2_G becomes even smaller ranging from 0.22 in the less variable soils (e.g. #12) to 0.46 in the most variable soils (e.g. #22). This significant reduction in the sample error comes despite the fact that e.g., for the anisotropic soils with ν=6, the correlation scales are λ'_{hx}=2 and λ'_{hz}=3, which means that the relative domain size (measured in λ_h) remains approximately the same as in the isotropic soils. The low ε'^2_G indicates that the sample error associated with the *average* sample mean approaches that of the *local* sample mean. The variance sample error $\varepsilon'_{v.g}$ is approximately 1. In the anisotropic soils of moderate variability it generally is within 5% of 1, and increases to 1.1 in the isotropic soils. In the strongly variable soils $\varepsilon'_{v.g}$ increases up to 1.4.

Boundary effects are insignificant at the base soil site (Figure 8.4a,b). But in more heterogeneous soils and particularly in soils of stronger horizontal anisotropy, the variance increases by up to 30% in a boundary region that is λ_{fz}=2 thick near the horizontal boundaries, but only λ_{fx}=0.2 wide near the vertical boundaries. In other words, the boundary effect is particularly dominant into the direction of mean flow. The variance increase is due to the larger variance in the first order head perturbation solution on the boundary (see discussion below). The artificial impact of the first order random head boundary in the anisotropic and strongly heterogeneous soils is - spatially - much less dominant than constant head or flux boundary conditions, which have traditionally been used in Monte Carlo simulations. For the saturated case, Rubin and Dagan (1988, 1989) estimate that the boundary effects of such non-random boundaries vanishes only at a distance of at least $1\lambda_f$ to $2\lambda_f$ from the boundary.

Covariance sample field. The "smoothness" of the realizations of h and of the pattern in the sample mean and variance fields is quantitatively captured by the covariance function, which has a much larger correlation scale than f in both the horizontal and vertical direction

(Figure 8.4c). Even for the isotropic base soil #3, the head covariance C_{hh} is anisotropic with $\lambda'_{hx} = \lambda_{hx}/\lambda_{fx}$=4.5 and $\lambda'_{hz} = \lambda_{hz}/\lambda_{fz}$=2.5. The anisotropy is reflected in the horizontally elongated pattern structure of the sample mean and variance fields in Figure 8.4a,b. The numerically obtained covariance function is well predicted by the analytical covariance function for the head C_{hh} (Figure 8.5a,b). The covariance function is similar to an anisotropic Gaussian function, particularly near the origin, which explains the smoothness of the random head fields (Figure 8.6). For larger lag distances both the analytical and numerical covariance fields deviate from the oval shape of the Gaussian covariance. In the vertical direction, the head covariance is a "hole"-type function (see discussion of C_{yy}) regardless of the type of soil investigated here. The limitation of the domain size does not allow an assessment of the type of covariance function in the horizontal direction. The differences between numerical and analytical covariance functions are primarily due to sampling variability and due to the different variances. The normalized head correlation functions ρ_{hh} from the first order analysis and the Monte Carlo analysis are in good agreement not only for mildly heterogeneous soils (σ_y^2=0.1, #8, see Figure 8.6), but also for highly heterogeneous soils (σ_y^2=3.2, #22, Figure 8.7). For strongly heterogeneous soils of any anisotropy ratio, the analytical correlation function tends to underestimate the vertical correlation of the Monte Carlo results. In anisotropic soils this is also true for the head horizontal correlation.

Histograms. The histogram for the total of sample head values is not significantly different from the histogram for the head values sampled at the center of the simulation domain. Figure 8.4d shows the total sample histogram for the base soil site. At this and most other soil sites, the histogram follows the symmetric Gaussian pdf, which confirms a basic assumption of previous analytical studies of flow in heterogeneous soils (Yeh et al., 1985a,b,c; Mantoglou et al., 1987a,b,c). Only in the most heterogeneous soils (those with the highest σ_h^2) and in soils with a large Γ (=0.1 in #30) an almost negligible but consistently notable tail towards more negative head values develops.

8.6.2 Moment Analysis of the Soil Water Tension

Dependence on input variance of f and a. In the least variable soil (isotropic soil site #2 with σ_f^2=0.01) the average mean head deviates less than 0.1% from the mean head (-150 cm) prescribed for the first order perturbation solution on the boundary. As the variance of f and *a* increase, the mean head drops slightly to -150.9 cm in the isotropic base soil site with σ_f^2=1 (#3) and to -156.3 cm in one of the most variable, wet anisotropic soil sites with σ_f^2=4 (#22). In drier soils the difference between prescribed and average measured mean head does not exceed 1%, even if the head variance is very large (e.g. #21). The actual sample mean head is not sensitive to any of the other input parameters. The rest of this section will therefore only discuss the dependence of the sample head variance on the various input statistics.

For the least variable three isotropic soil sites, the results of the head variance are shown in Table 8.2 together with the analytical head variance solution. For those three soils the largest difference between numerical and analytical head variance is observed for the least variable soil. There, the variance in the Monte Carlo is 4% higher than the analytical variance σ_h^2. At σ_f^2=1 (#3) the difference is reduced to 2%. For practical purposes, the first order analytical solution is considered accurate for isotropic soils of $\sigma_f^2 \leq 1$.

The normalized head variance σ'^2_h is:

$$\sigma'^2_h = \frac{\sigma_h^2}{\sigma^2 \lambda_{fz}^2} \qquad (8\text{-}15)$$

where the variance factor σ^2 is defined in (8-13). Figure 8.8a shows that the numerical head variance in the isotropic soils is well modeled by the analytical head variance even at σ_f^2=3.6. In the anisotropic soils, the head variance is also very accurately predicted from theory for σ_f^2=1, but decreases linearly (relative to the first order solution) at higher variances. The decrease is the strongest for those soils with the highest aspect ratio, such that for a wet soil

with ν=6 and 6.7, and with σ_f^2=3.6 the head variance in the Monte Carlo simulation is only 75% of the analytically obtained variance. This is consistent with the boundary effects observed particularly in the anisotropic soils.

The robustness of the first order head perturbation solution at variances up to σ_f^2=1 has previously been discussed in the literature, but with respect to saturated groundwater flow. Dagan (1985) computed second order corrections for the head moments in an infinite aquifer and found that for σ_f^2=1 first order head moments are within 10% of the second order head moments. Gutjahr and Gelhar (1981) concluded from their analysis that the spectral first order approximation of the head moments in saturated porous media is valid even for variances σ_f^2 much larger than unity. As Gelhar (1986) noticed, no such evaluation has been made for the spectral analysis of unsaturated flow. While this study does not address the issue analytically, the simulations clearly indicate the general trend: First order analysis will significantly overestimate σ_h^2 at large σ_f^2 and σ_a^2. It may be argued that the difference is due to the small simulation domain. However, the average sample variance as well as the sample variance in the center of the simulation domain change insignificantly, when the vertical and horizontal domain size is increased to 150 nodes and 100 nodes, respectively.

Dependency on mean soil water tension. In anisotropic soils the numerically obtained σ'^2_h decreases as the soil becomes drier and as σ_y^2 increases (Figure 8.9a). For the driest soil (#21: H=-3000 cm, ν=6, σ_y^2=3.2) the decrease is approximately 25% i.e., almost the same as for the highly heterogeneous wet soils (#22: H=-250 cm, ν=6, σ_y^2=3.2). The overall effect of mean soil water tension on the actual variance of the head depends on ρ_{af} as discussed in the analysis of y. For mean head much more negative than the critical head H=-1/$\zeta\Gamma$, the head variance will increase in any soil but not as strong as suggested by the form of the variance factor σ^2 (8-13).

Dependency on Γ and vertical correlation scale. A similar deviation from the first order results is not observed for varying vertical correlation scale or increased coarseness of the

soil texture (larger average pore size distribution parameter Γ), if σ_f^2 does not significantly exceed unity. As Figure 8.10a shows, there is excellent agreement between first order analysis and Monte Carlo analysis.

Dependency on aspect ratio and grid discretization. The effects of aspect ratio are also well modelled by the first order approximation (Figure 8.11a) if $\sigma_f^2=1$. As the aspect ratio ν increases, σ_h^{2} decreases slightly relative to the analytical solution. A threefold increase in the horizontal element size (#12 vs. #11) increases the head variance slightly (about 2%).

8.7 Stochastic Analysis of the Velocity

8.7.1 General Observations

Sample mean and variance fields. The random structure of the horizontal and vertical velocity fields are very peculiar and distinctly different from those of other RFVs. In Figure 8.12, a single realization of corresponding v_x and v_z fields in the base soil site (#3) are shown. The horizontal velocity map has a distinctly symmetric pattern of diagonally trending narrow stripes with strong negative velocities (dark NE-SW trending "canyons") and counter-diagonally trending narrow stripes with strong positive velocities (white NW-SE trending "cloud streamers") in an otherwise relatively homogeneous velocity field with very small horizontal velocities. The vertical velocity map, in contrast, is not quite unlike the map of a braided channel network in a river valley or of the preferential flow paths that have been reported to occur in soils: While most portions of the soil domain have relatively small vertical velocities (lightly colored areas), high velocities (dark areas) form a braided network of narrow channels with a predominantly vertical direction. The diagonal streaks of v_x and the vertical braided channels of v_z reappear in the sample mean and sample variance maps (Figure 8.4e,f,i,k), but in a much more vivid, livelier, more interwoven, and more erratic manner. Graphically speaking, the laziness of the landscape in the individual realizations is replaced by a vivid

pattern in the sample mean and variance fields. This is in contrast to the observations for the sample mean and variance fields of f, a, y, and h, which are all very similar in character to individual realizations.

Individual realizations are relatively homogeneous over large areas (the laziness) with extreme values (the canyons and clouds and river channels) interrupting them at a spatial interval that is on average significantly longer than the transverse size of the channels and streaks. In the sample mean and variance fields the diagonal and cross-diagonal streakline pattern and the vertical braided channel pattern are preserved, but the transverse extent of the channels and streaks is narrower, the frequency of streaks and channels has increased, and they are much less continuous.

What is the explanation for the particular pattern of the individual realizations and the character of the sample mean and variance fields? And what is its significance? Before analyzing the statistical description of the velocity RFV, it is important to pursue these questions to better understand the physical nature of moisture movement in heterogeneous soils.

The horizontal and vertical velocity realizations depicted in Figure 8.12 must be seen as a unity since they are two components of a single vector v. The areas of very large positive and negative horizontal velocity occur in those parts where the vertical velocity is also large (indicated by the channels) but where the channels are inclined relative to the vertical axis. In the isotropic soil of Figure 8.12, the horizontal component of the velocity is rarely much larger than the vertical component, therefore the diagonal orientation of the streaks (instead of a horizontal or near horizontal orientation). Since most of the flow is vertical, the vertical velocity map can be seen as almost representative of v. The velocity map in Figure 8.12b indicates that soil moisture movement in spatially variable but statistically homogeneous (chapter 2) soils tends to be along preferential flow paths i.e., the majority of soil moisture moves through only a small portion of the entire soil domain. In a large part of the soil domain, moisture flux is relatively small. The simulations show that the concentration of

moisture flux into small channels increases as the heterogeneity of the soil increases or as the soil becomes drier. Similar patterns of flow channeling are shown by Moreno et al. (1989) who modeled Darcian flow in a two-dimensional, single fracture with varying aperture and high variability of fracture resistance (which is inversely related to the conductivity). Channeling has also been observed in field soils, where channeling due to soil heterogeneity and channeling due to wetting front instability (fingering) together may greatly enhance the variability of the flux field (Glass et al., 1988).

From these physical observations it is expected that both the vertical and horizontal velocity distribution have a non-Gaussian, highly skewed distribution. As discussed in more detail below, the velocity components are indeed non-Gaussian, lognormal-like distributed (Figure 8.13). Hence the usefulness of the first and second moments as measures of the pdf of v is limited. Since the sample mean and variance are obtained through arithmetic averaging, the large velocity areas of individual realizations carry much weight in the sample mean and variance. The maps of the two sample moments become like a collection of the many streaks and channels of the individual realizations.

Boundary effects. The sample mean and sample variance fields of the velocity have boundary effects that quantitatively are very strong, even at the base soil site, where no significant boundary effects are observed for other RFVs (Figure 8.4e,f,i,k). Directly on the boundary, extremely low and high values occur in the sample mean of both velocity components. The sample variance of the velocity is much higher at the boundary than in the interior of the domain: at the base site (#3) by up to an order of magnitude for σ_{vx}^2 and a factor 5 for σ_{vz}^2. The spatial extension of the boundary effects are particularly strong for σ_{vx}^2 into the mean flow direction: along the horizontal boundaries they are significant within $1\lambda_{fz}$ (Figure 8.14a,b). Along the vertical boundaries and for all boundaries around the σ_{vz}^2 map the effect is limited to $0.5\lambda_{fz}$ and less. The boundary effect has a spatially larger extent in the anisotropic soils of equivalent heterogeneity, which increases with the variability of y. If σ_y^2

= 3, the boundary effect significantly increases σ_{vx}^2 and σ_{vz}^2 within almost $3\lambda_{fz}$ from the bottom boundary and within almost $2\lambda_{fz}$ from the top boundary (Figure 8.14e,f). For this soil the velocity variance on the boundaries is three orders of magnitude larger than in the interior of the domain. The spatial extent of the boundary effect on the velocity moments is slightly smaller than the spatial extent of constant flux boundary conditions in saturated flow (compare Figure 8.14 to Bellin et al., 1992, Figure 3).

The very strong though spatially limited boundary effects on σ_v^2 are again caused by the approximate nature of the first order head perturbation solution used as Dirichlet boundary conditions in the numerical model. But while the statistical moments of the first order head approximation are in excellent agreement with those of the Monte Carlo simulation for $\sigma_f^2 = 1$, the velocities derived from the first order perturbation head distribution along the boundary are extremely erratic. A simple method to circumvent the erroneous boundary effects in transport simulations is described in chapter 9.

Covariance fields. The covariance fields for v_x and v_z are a reflection of the diagonal and counter-diagonal patterns, and of the braided vertical patterns, respectively, of the high velocity areas (Figure 8.4g,l). For increasing aspect ratios, the two diagonal main axes of the horizontal covariance function become flatter (Figure 8.5e,f) indicating that the diagonal flow patterns observed in the isotropic soil (Figure 8.4g) tend to become more horizontal as the aspect ratio increases. For mildly to moderately heterogeneous soils such as the base soil (#3), the analytical covariance functions obtained from the first order spectral density functions for the two velocity components are in very good qualitative, if not quantitative agreement with the numerically derived velocity covariance functions (Figures 8.5 and 8.6).

In soils (wet or dry) with $\sigma_y^2 > 1$, the vertical and horizontal cross-sections of the analytical velocity correlation functions deviate significantly from the numerically determined solutions. The numerically obtained horizontal velocity correlation function is almost identical in the transverse (horizontal) and the longitudinal (vertical) direction, while first order analysis

predicts a much shorter transverse correlation scale and a much larger longitudinal correlation scale. The numerical vertical velocity correlation function has also a much shorter longitudinal correlation scale than the analytical correlation function. Only the transverse hole-type correlation of v_z is very accurately predicted for all soils (compare Figures 8.6 and 8.7).

Histograms. The histogram for v_z is - as expected - skewed (see, for example, Figure 8.4m). The velocity statistics are obtained on the untransformed RFVs. Logarithms were not taken during the simulation due to the fact that neither the vertical nor the horizontal velocity component is restricted to either positive or negative values only. A graphical method to investigate whether the vertical velocity is indeed lognormal-like distributed consists of a plot of the histogram on a lognormal axis (Figure 8.13). For very small input variances of f (σ_f^2 =0.01) the histogram of v_z can either be interpreted as normal or as lognormal (Figure 8.15), but at higher variances, the histogram is always skewed on the arithmetic scale, even for mildly heterogeneous soils (e.g. σ_f^2 = 0.11, #8, see Figure 8.15). This result is in accordance with the histograms obtained from Monte Carlo simulations of saturated flow in two- and three-dimensional heterogeneous media by Bellin et al. (1992) and Levin (1994). Figure 8.16 shows the total histogram as well as the histogram of the center point of the simulation domain for v_x and v_z. The two types of histograms are generally identical. The histogram for the center point is of course based on only N=1000 values, while the total histogram is based on 4 million data (64^2 N). Even the histogram plotted on the logarithmic axis has a significant skewness if the soils are dry or very heterogeneous (Figure 8.16h,i). In the soils with very high variability, a significant amount of vertical velocities is positive (upward) (Figure 8.16h,i,k).

The horizontal velocity histogram plotted on an arithmetic scale (Figure 8.4h) seems to be Laplacian (symmetric exponential decay, chapter 2), but plotting the histograms of $|v_x|$ on the logarithmic scale reveals that the pdf for v_x must be differentiable for $|v_x| \rightarrow 0$ (Figure 8.16a-e). The histogram of v_x resembles a Gaussian function only if the unsaturated hydraulic conductivity variance is very small (σ_y^2<0.2). This is in contrast to the findings of Bellin et

al. (1992) and Levin (1994) who argue that the horizontal velocity component in their simulations has a normal pdf even in very heterogeneous saturated porous media. However, visual inspection of the numerical velocity cdf and the Gaussian cdf in Figure 7d of Bellin et al. (1992) indicates that their transverse velocity pdf qualitatively tends away from the Gaussian pdf towards a similar shape shown for the unsaturated velocity pdf e.g. in Figure 8.4h!

8.7.2 Moment Analysis of the Velocity

Dependence on input variance of f and a. Due to the mean vertical, uniform flux, the mean horizontal velocity must be 0. In all simulated soils, the average sample mean horizontal velocity V_x is at least three orders of magnitude smaller than the mean vertical V_z and can therefore indeed be considered as being negligible. The first order analytical mean V_z is equal to:

$$V_z = \frac{K_m}{\theta} \tag{8-16}$$

where K_m =exp(Y) is the geometric mean of the unsaturated hydraulic conductivity. The first order analysis, of course, assumes that both the vertical and horizontal velocities have a normal distribution. Nevertheless, the difference between analytical and average sample V_z in the isotropic soils with $\sigma_f^2 \leq 1$ is 2% at the most (Table 8.2). For the most heterogeneous soils (#9) the Monte Carlo V_z is 10% larger than (8-16). In contrast, the average sample V_z in the anisotropic, wet soils with ν=6.0 and ν=6.7, σ_f^2=1, is more than 20% smaller than the analytical V_z and decreases to less than 50% of (8-16). The decrease in the average arithmetic sample mean velocity relative to the analytical mean velocity must be explained with the neglect of higher order moments in (8-16) and with the lognormal distribution of v_z, which yields a preferential flow pattern as the variance increases, particularly in anisotropic soils. The numerical results show that the average steady state flux in highly heterogeneous soils depends

strongly on the aspect ratio.

For a better physical explanation, v_z must be analytically evaluated to higher order than in chapter 4. Yeh et al. (1985b) used a mixed first and second order approach to determine the effective hydraulic conductivity K_e in a vertically uniform flow field. The effective conductivity is defined as $K_e=<q_z>/J_z$, where $<q_z>$ is the mean vertical flux and J_z is the mean vertical total potential gradient. All of the simulations here preserve the mean unit gradient condition. Since the soil water content in all simulations is constant and identical to 1, the average sample mean V_z from the MCS becomes the effective hydraulic conductivity. As Figure 2 in Yeh et al. (1985) indicates, K_e/K_m is expected to be slightly larger than 1 in isotropic soils, but only about 0.5 for $\nu=10$ ($\Gamma\lambda_{fz}$ = 0.5). Qualitatively and quantitatively, their findings are therefore confirmed by the numerical simulations.

The average sample velocity variances σ_{vx}^2 and σ_{vz}^2 differ by 0% and -3% from the analytical solutions for the least variable soil (#2, $\sigma_f^2=0.01$). In isotropic, wet soils with $\sigma_f^2=0.1$ and 1 (#8, #3), the differences of the numerical to the analytical solutions are of similar magnitude (Table 8.2). Again a more rigorous analysis can be performed by using the dimensionless variances of v_x and v_z, which are defined by:

$$\sigma'^2_{vx} = \frac{\sigma^2_{vx}}{\sigma^2 K_m^2}$$
$$\sigma'^2_{vz} = \frac{\sigma^2_{vz}}{\sigma^2 K_m^2} \qquad (8\text{-}17)$$

where the variance factor is defined in (8-13). The numerical σ'^2_{vz} and σ'^2_{vx} are plotted in Figure 8.8c,d for wet soils with three different anisotropy ratios. The Monte Carlo σ'^2_{vx} increases significantly in all soils as σ_f^2 increases. In the most heterogeneous soils, the average sample σ'^2_{vx} exceeds the analytically predicted by a factor of 5 in the two anisotropic soils and by a factor of 2.5 in the isotropic soil. The Monte Carlo σ'^2_{vz} in the isotropic strongly variable soil is also larger than predicted (factor of 1.5), while it decreases with the variance

of f in the anisotropic soil. The results are difficult to interpret, since the RFVs are not normally distributed. But they clearly show the limitations of the perturbation approach with respect to the velocities.

Dependence on mean soil water tension. The stochastic dependence on the mean head found in the MCS deviates from the analytical results in a similar way, if both the previous and these results are stated not in terms of σ_f^2 and H, but in terms of σ_y^2: The deviations become stronger as σ_y^2 increases, which may be due to either a larger soil textural variability or a drier soil. The magnitude and direction of the deviations are independent of whether the higher σ_y^2 is due to large negative H or due to high σ_f^2 (Figure 8.9c,d). Recall that for ρ=1, the variance of the RFVs theoretically decreases to 0 at H=-1000 cm.

Dependence on Γ *and the vertical correlation scale.* The average sample velocity variance follows a similar stochastic function as the theoretical curve but decreases not as quickly with increasing $\Gamma\lambda_{fz}$ as predicted by 1st order analysis (Figure 8.10c,d).

Dependence on aspect ratio and grid discretization. The velocity variance decreases with increasing aspect ratio, just as the mean vertical velocity decreases. At σ_f^2=1, the influence of the horizontal correlation scale on the accuracy of the analytical solution is negligible. Grid discretization has no significant impact on the solution (Figure 8.11c,d).

8.8 Stochastic Analysis of the Cross-Covariance Functions

Cross-covariances are of interest for various reasons. First, many analytical stochastic models of unsaturated or general porous media flow and transport rely on first-order analytical formulations of the cross-covariances (e.g. Dagan, 1984, 1987; Yeh et al., 1985a,b; Mantoglou et al., 1987a,b; Rubin, 1990; Cvetkovic et al., 1992; Russo, 1993a,b). Second, the cross-covariance is necessary for the implementation of conditional simulation, which will be described in chapter 10. The cross-covariances of common interest are C_{fh}, $C_{f,vx}$, and $C_{f,vz}$.

Figure 8.17 shows an anisotropic example (#31) of single sample fields (not the average covariance field!) of each of those cross-covariances. The cross-covariances have features, which are only partially reflected in their respective horizontal and vertical cross-sections. By inspection of Figure 8.17 it can be seen that the horizontal and vertical cross-sections of $C_{f,vx}$ and $C_{h,vx}$, for example, would have little information content if taken horizontally or vertically through the origin. Unlike the covariance fields, the cross-covariances are neither symmetric with respect to the origin, nor symmetric with respect to the major coordinate axes. The complex structure of the cross-covariance functions will make it difficult to define such cross-covariances from field measurements, unless a large number of samples are taken throughout the area of interest.

Of practical interest is the fact that all cross-covariances except $C_{f,vx}$ and $C_{h,vx}$ are much stronger in the vertical direction than in the horizontal direction. Hence the information content of one variable with respect to another variable is predominant within the same vertical region but bears less predictive capacity with respect to other variables in the same horizontal region. Another important feature to be noticed is the non-zero lag-distance at which the highest absolute cross-correlation is reached. Also, the correlation can be either negative or positive. For example, head values have a positive correlation to f values that are approximately $3\lambda_f$ further upward and a strong negative correlation to f values that are approximately $1\lambda_f$ downward from the location of the head measurement. There is comparatively small cross-correlation into the horizontal direction. The cross-correlation between f and h at the same location is only about half of the strongest cross-correlation between f and h at the optimal distance. The knowledge of the particular structure of the cross-covariance function is helpful in the design of monitoring networks, in particular if conclusions on the state of one RFV are drawn from the state of another RFV (see chapter 10).

The relatively large differences between numerical and analytical solutions for the cross-covariances of the two least variable isotropic soils (approximately 10% to 20%, see Figure 8.6)

are due to a simplification in the computation of the numerical sample cross-covariance. The RFVs f and *a* are element properties while the RFVs h,v_x, and v_z are node properties. Since y depends on both nodal and elemental properties (h,f, and *a*), nodal properties must be extrapolated to the element or vice versa. For the sampling procedure here, the head values h_i^k of the four nodes i, i=1...4, around an element k are averaged, and y is obtained as elemental property of f, *a*, and the average head $\bar{h}^k$ in a particular element. Averaging the head values introduces a small reduction in the variance of the unsaturated hydraulic conductivity. However, since the head values have a strong spatial correlation, the variance reduction can be neglected. In the sampling process for the sample cross-covariance (8-9) it is assumed - for simplicity - that the location of an element is identical to the location of the lower left node of that element. The error in the cross-covariance fields relating nodal with elemental properties stems from the discrepancy between the assumed identity of element and node location.

Note that the correlation ρ_{af} has a significant impact on the cross-covariances of f, h, and v_z: In the correlated soils the vertical cross-covariance structure of C_{fh} and $C_{f,vz}$ inverts itself at $H_{min}=-1/\zeta\Gamma$, such that in dry soils C_{fh} has a minimum at negative lag distances and a maximum at positive (upward) lag distances. The cross-correlation between f and the (negative, downward) vertical velocity becomes positive at lower head pressure, because under dry conditions soils with high saturated hydraulic conductivity and coarse texture (large α) are assumed much less permeable than soils with low saturated hydraulic conductivity and fine texture (low α). In the uncorrelated soils the correlation between f and h and f and v_z weakens as the soil dries out, which can be seen by comparing, for example, the cross-covariance C_{fh} for the correlated soil at -2000 cm (#24) and the uncorrelated, anisotropic soil at -1000 cm (#15). Both have approximately the same absolute maximum of 30 cm, although the head variance in the uncorrelated soil is almost twice as large as in the correlated soil (Figure 8.18).

8.9 Summary and Conclusions

For the first time, intensive Monte Carlo simulations of unsaturated, steady-state gravity flow have been implemented for a large range of different soils. The Monte Carlo simulations take advantage of the ASIGNing technique introduced in chapter 7, which combines the efficiency of spectral perturbation analysis with the flexibility and accuracy of finite element modeling. It allows for the fast simulation of steady-state head and flux in two-dimensional vertical soils. It is applicable to a great variety of different soils and is therefore well-suited for the stochastic simulation of unsaturated flow at actual field sites. The approach is here used for a stochastic analysis of the unsaturated hydraulic conductivity, the soil water tension, and the soil water flux. The simulations are all implemented with 1000 realizations on a finite element domain of 64*64 rectangular elements. To avoid aliasing effects in the fast Fourier transform of the random field and initial guess generator, the size of the initial random field is at least 10 by 10 correlation scales λ_f and in most cases exceeds 20 by 20 λ_f as recommended by Gutjahr et al. (1989). The large amount of realizations for each Monte Carlo simulation results in a very small variability of the sample moments, which allows for both a numerical model validation and an evaluation of first order analytical solutions that were introduced almost a decade ago (Yeh et al., 1985a,b, chapter 4), but have never been rigorously tested for their validity in mildly and strongly heterogeneous soils. By comparing the spatial variability of the local sample mean and variance with the expected variability of the sample moments it was shown that the Monte Carlo simulations indeed converge and that the theoretical variability (8-3) and (8-7) of the sample mean and sample variance provide good estimates of the actual sample error. While the analysis here is limited to the case of exponential input covariance functions, the numerical and analytical methods introduced in this work are both applicable to arbitrary input covariance functions and arbitrary correlation structures between $\log K_s$ and $\log\alpha$. In many field situations, these covariance and cross-covariance functions are obtained from

geostatistical analysis (Isaaks and Srivastava, 1990). Both the analytical and numerical approach can in principle also be used to analyze flow in unsaturated soils of multidirectional flow with arbitrary, spatially constant mean head gradients (see also Yeh et al., 1985b).

Beyond the analytical solutions of chapter 4, the Monte Carlo model introduced in this chapter provides not only more accuracy, but mainly the flexibility offered by the finite element model with respect to boundary conditions and the particular probability distributions of the input parameters. Moreover, the combination of spectral analysis and numerical model (ASIGNing) makes it possible to simulate quasi-infinite domains or semi-infinite domains (e.g. with random head vertical boundaries, flux boundary at the top and water table at the bottom). The analysis has shown that even for very heterogeneous flow fields (large σ_y^2=3.2) the use of the initial first order perturbation solution as random head boundary adversely affects the results within no more than one or two correlation scales from the boundaries, which is similar to the effect of using constant head or constant flux boundaries. In mildly to moderately heterogeneous flux fields ($\sigma_y^2 \leq 1$), the use of random head boundaries obtained by first order analysis is less biased than the use of constant head or flux boundary conditions, if deterministic boundary conditions are not truly justified. Mixed deterministic/random boundaries can also be introduced by conditioning as demonstrated in chapter 10. Arbitrary boundaries could also be specified including non-stationary boundary conditions (e.g. above a water table).

The analytical solutions derived in chapter 4 for the mean and variances of the dependent RFVs y, h, and v are found to be - for all practical purposes - very similar to the numerical solutions if the resulting variance of y is less than 1.0. (mildly variable flow). The two-dimensional covariance and cross-covariance functions are also in good agreement with numerically sampled models. For $\sigma_y^2 \geq 1$ (moderately to strongly variable flow) the analysis of chapter 4 provides some general insights, but the actual, fully nonlinear (numerical Monte Carlo) solutions differ in parts very significantly. The most important findings of the stochastic analysis of the dependent RFVs and the comparison with the analytical solutions of chapter 4

are summarized here:

The first and second moments of y are very robust with respect to first order perturbation analysis. Even for very heterogeneous flow, the differences between Monte Carlo and perturbation analysis were less than 16%. The moments of the unsaturated head are generally also well estimated by the first order analysis. If $\sigma_y^2>1$ i.e., if a soil is either strongly variable in the saturated hydraulic conductivity and in the soil pore parameter α or if it is a dry soil, the variance of the head is significantly overestimated by the perturbation analysis (up to 30 %). The head correlation function is in very good agreement with the numerically obtained correlation field throughout the simulations. At large lag-distances, the sample ρ_{hh} in the Monte Carlo simulation is slightly higher than predicted, possibly because of boundary effects in the numerical simulation. The sample pdfs of h and y are always found to be Gaussian, except for very high σ_α^2, where y showed a small but notable skewness.

The probability distributions of the two velocity components are skewed. The vertical velocity is best described by a lognormal pdf. At very high σ_y^2, however, the sample pdf (histogram) of v_z extends beyond zero velocity and shows that a significant number of nodes with upward velocities exists. Such a pdf cannot be modeled with the lognormal function. The pdf of v_x is symmetric and has an exponential decay as $|v_x|$ increases. However, it is differentiable for $v_x \rightarrow 0$ as shown by plotting the pdf of $\log|v_x|$. Since the first order perturbation analysis assumes normal RFVs, it is generally much less accurate in predicting the flux (velocity) than in predicting the head and the unsaturated hydraulic conductivity at equal variability of y. Only the decrease in mean vertical velocity is well predicted by using the mixed order effective hydraulic conductivity analysis of Yeh et al. (1985b).

The Monte Carlo sample correlation fields and the analytically determined correlation functions for the velocity are in good qualitative agreement for all the tested soils. The covariance function of the horizontal velocity is symmetric with respect to the origin, but has its major axes diagonal to the major axes of anisotropy. The vertical velocity covariance is

strongly anisotropic with a larger vertical than horizontal correlation scale, even if the underlying hydraulic soil properties are isotropic. The covariance functions of the two velocity components reflect the peculiar flow structure in heterogeneous soils, which was shown to take place in a preferential or channel type flow pattern. Even though the underlying random structure of the soil is statistically homogeneous, most of the moisture mass is transported through only a small fraction of the soil. This is in good agreement with field findings (Glass et al., 1988) and the numerical analyses of flow in single fractures with high variability in their conductivity (Moreno et al., 1989).

Similar second order moments for h, y, v_x, and v_z are found for wet, texturally heterogeneous soils and dry, texturally rather homogeneous soils with an equal degree of unsaturated logK heterogeneity. The similarity does not extend to the cross-covariances, which depend not only on the mean head, but also on the correlation between f and a. For $\rho_{af}=0$ the cross-correlation between f and h, and between f and v_z weakens with increasing soil-water tension. If $\rho=1$, the unsaturated hydraulic conductivity parameters are completely determined by h and f. Consequently a strong correlation not only between f and h, but also between f and v_z exists even in dry soils. The use of tension measurements for the conditional simulation of f and a random fields is discussed in chapter 10.

The grid-discretization criteria developed in chapter 6 have been proven to provide accurate solutions not only in the context of single large simulations, but also for Monte Carlo simulations with a large number of realizations. A fairly coarse vertical discretization of 10 cm has been shown to provide results of accuracy equal to that of a fine discretization (2.5 cm).

In conclusion this study has shown both the applicability and limitations of the first order perturbation solutions developed in chapter 4 for two-dimensional heterogeneous soils with lognormally distributed α. ASIGNing provides a flexible tool to implement Monte Carlo simulations efficiently on today's available workstations.

Table 8.1

Input parameters for the various hypothetical soil sites: σ_f^2: variance of f=logK_s, σ_a^2: variance of a = logα, ρ_{af}: correlation coefficient between f and a, Γ: geometric mean of α, Δx: horizontal discretization of finite elements, Δz: vertical discretization of finite elements, λ_{fx}: horizontal correlation length of f, λ_{fz}: vertical correlation length of f.

name	σ_f^2	σ_a^2	ρ_{af}	Γ	H	Δx	Δz	λ_{fx}	λ_{fz}
#3	**1.0**	**0.01**	**0**	**0.01**	**-150**	**10**	**10**	**50**	**50**
#2	0.01	10^{-4}							
#4			1						
#6					-1000				
#8	0.12								
#9	4.0	0.04							
#10			1		-3000				
#11			1					300	
#12			1			30		300	
#13						20		200	30
#15					-1000	30		300	
#19						2.5	2.5	12.5	12.5
#20							2.5		12.5
#21			1		-3000	30		300	
#22	4.0	0.04				30		300	
#23			1		-3000	20		200	30
#24			1		-2000	30		300	
#25	4.0	0.04				20		200	30
#26		0.64							
#27	20	0.09	1	10^{-4}	-1.8E5	30		300	
#28	2.25	0.04				30		300	
#29						30		300	
#30				0.1	-100				
#31						15		150	

Table 8.2

Comparison of the numerical and first order analytical stochastic solutions for the mean and variance of the dependent RFVs head h, unsaturated hydraulic conductivity y, horizontal velocity v_x, and vertical velocity v_z. #2, #8, and #3 are three different Monte Carlo simulations with σ_f^2 = 0.01, 0.1, and 1.0, respectively. All other parameters are identical to base case #3 (Table 8.1).

	#2 numerical - analytical		#8 numerical - analytical		#3 numerical - analytical	
h: mean	-150.1	-150.0	-150.4	-150.0	-150.9	-150.0
variance	11.2	10.6	157	150	1079	1060
y: mean	-1.499	-1.500	-1.503	-1.500	-1.498	-1.500
variance	8.53E-2	8.90E-2	.121	.126	.858	.887
v_x: mean	-3.18E-5	0.00000	-1.03E-4	0.00000	-4.35E-4	0.00000
variance	5.49E-5	5.49E-5	8.03E-4	7.78E-4	7.23E-3	5.49E-3
v_z: mean	-.2232	-.2231	-.2230	-.2231	-.2293	-.2231
variance	1.71E-4	1.76E-4	2.44E-3	2.50E-3	1.93E-2	1.76E-2

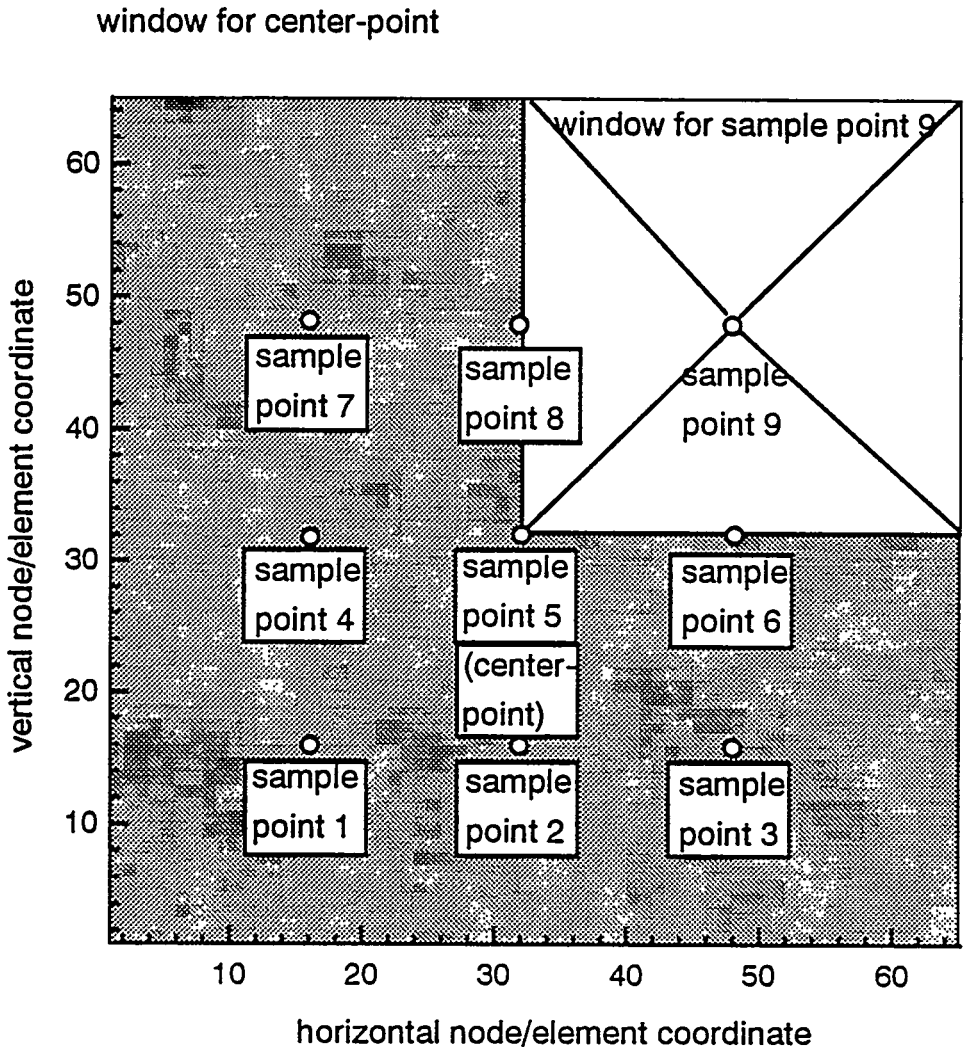

Figure 8.1: Location of the sampling points for which local covariance and cross-covariance fields are obtained. The local (cross-)covariance fields are computed in a 31 by 31 window around each sample point. The center point has the entire field as window.

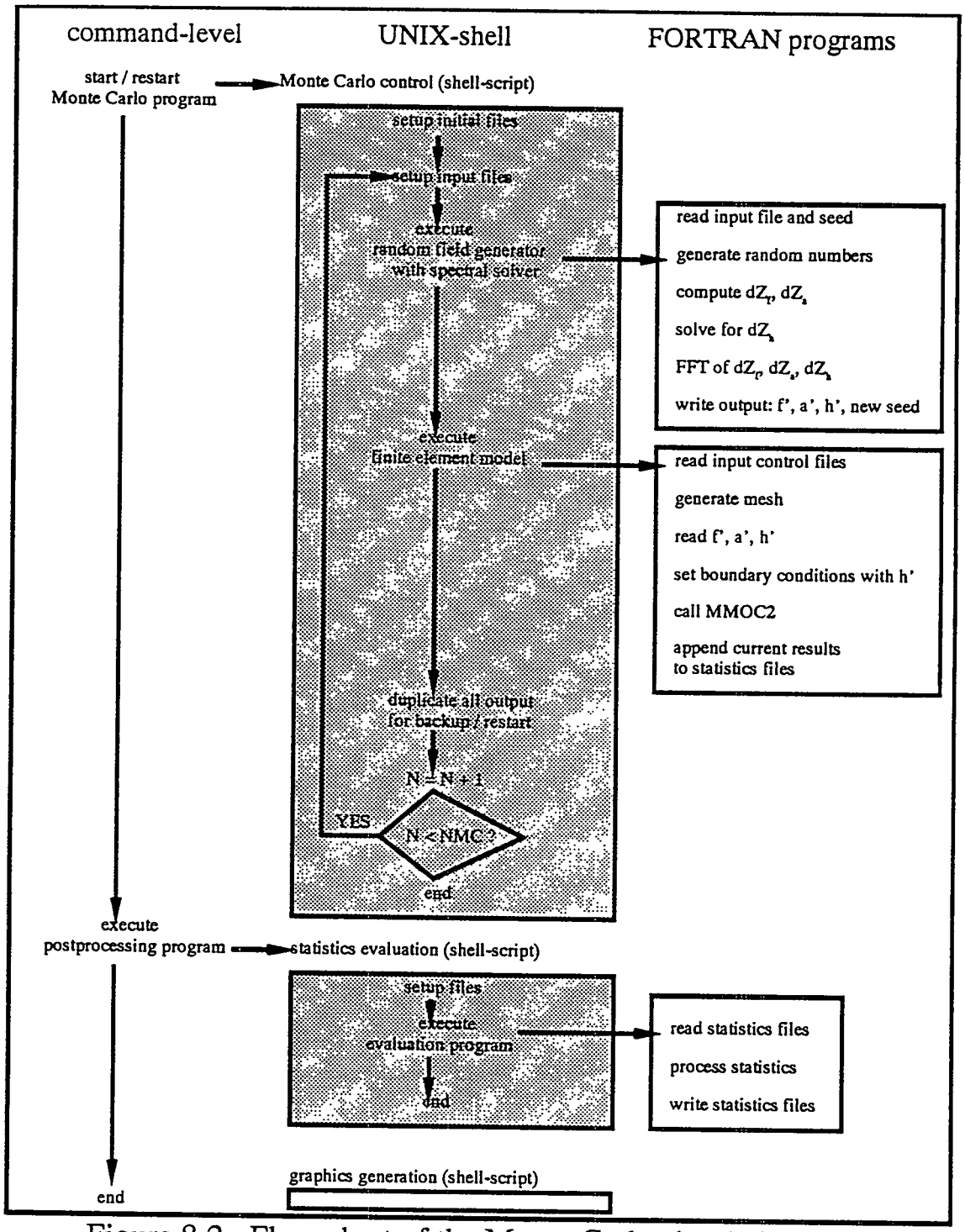

Figure 8.2: Flow chart of the Monte Carlo simulation

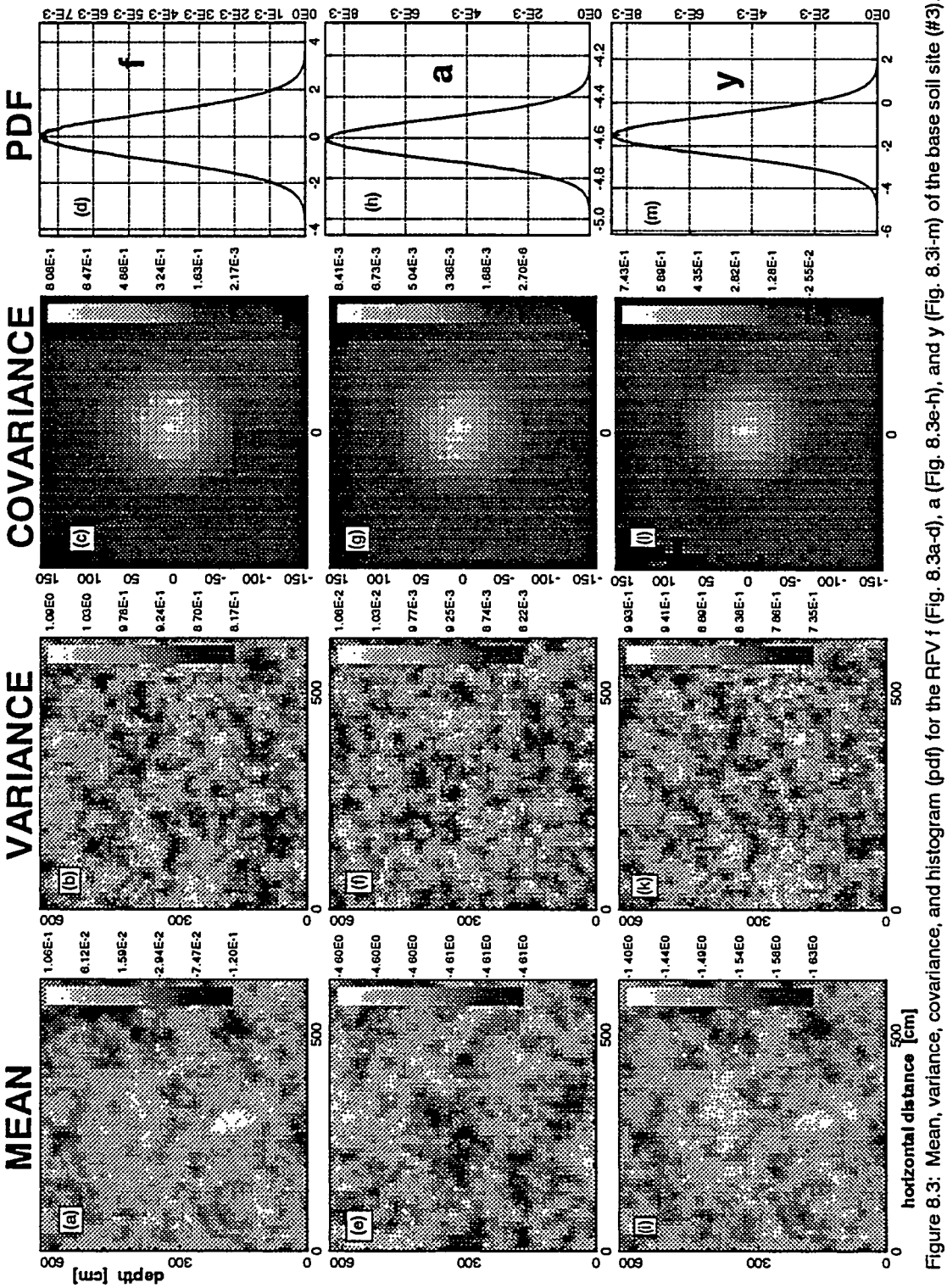

Figure 8.3: Mean, variance, covariance, and histogram (pdf) for the RFV f (Fig. 8.3a-d), a (Fig. 8.3e-h), and y (Fig. 8.3i-m) of the base soil site (#3).

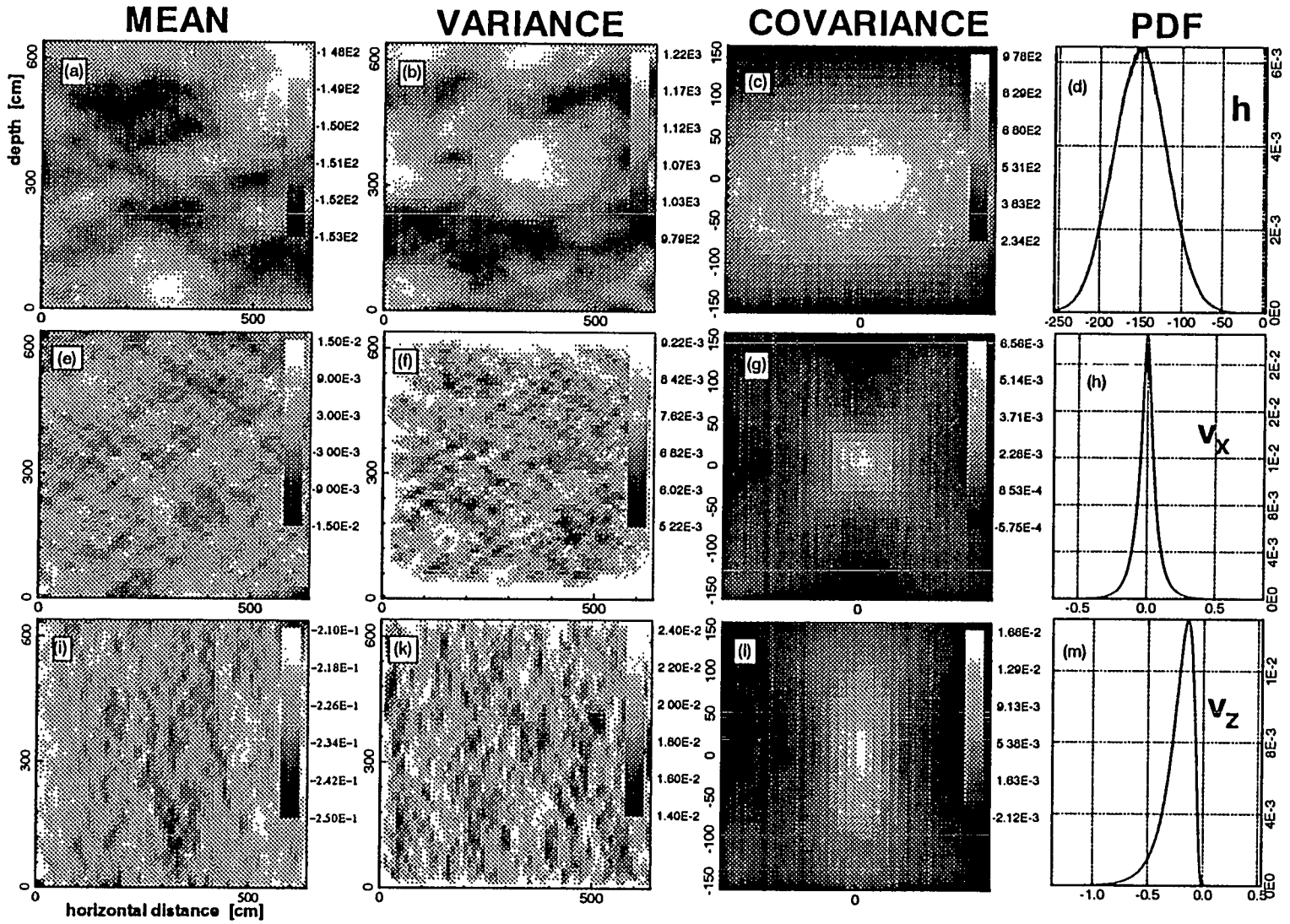

Figure 8.4: Mean, variance, covariance, and histogram (pdf) for the RFV h (Fig. 8.4a-d), v_x (Fig. 8.4e-h), and v_z (Fig. 8.4i-m) of the base soil site (#3).

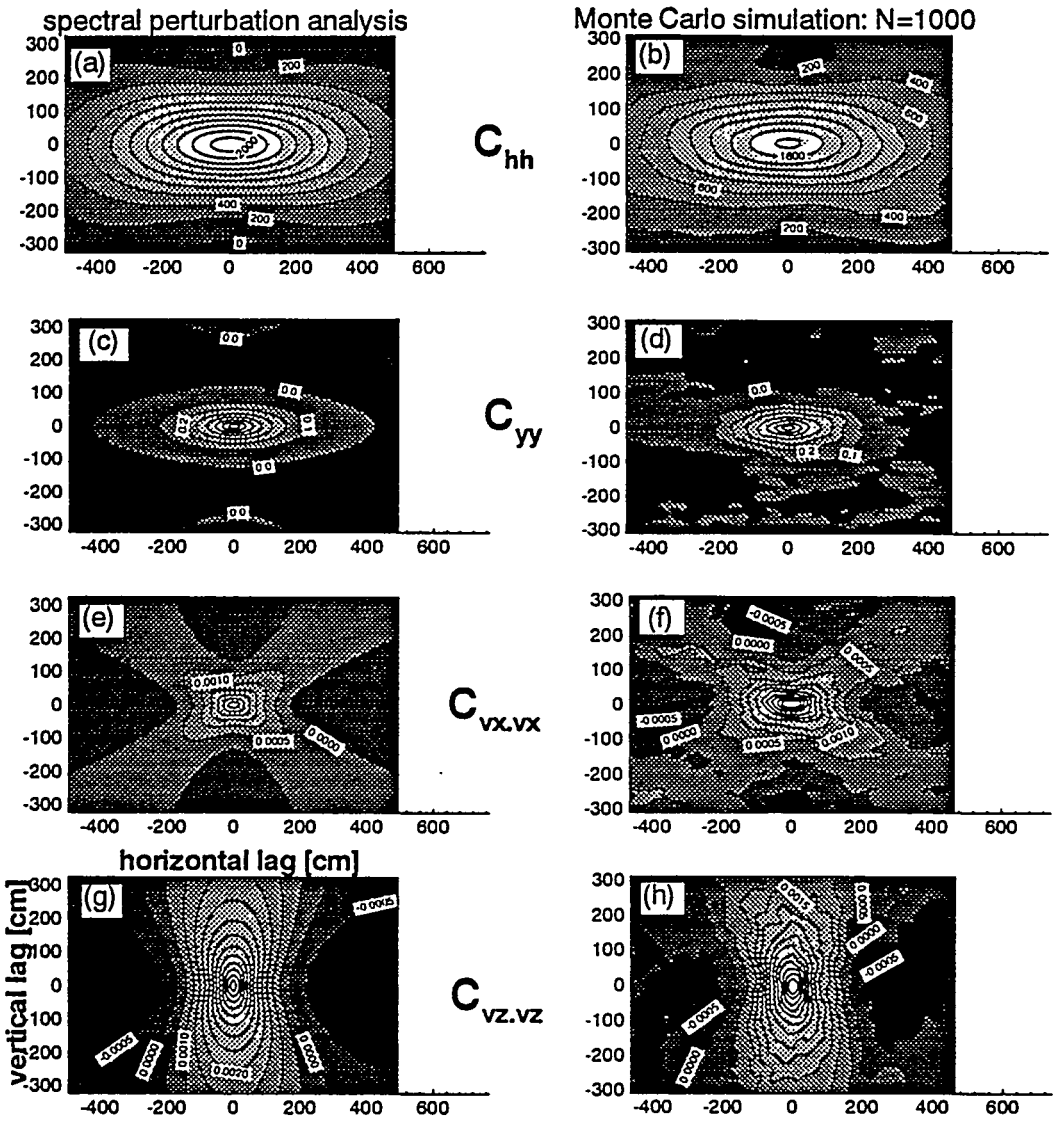

Figure 8.5: Analytical ensemble covariance fields (left) and Monte Carlo sample covariance fields (right) around the center-point of the simulation domain in an anisotropic soil site (#31: λ_x=150 cm, σ_f^2=1, H=-150 cm).

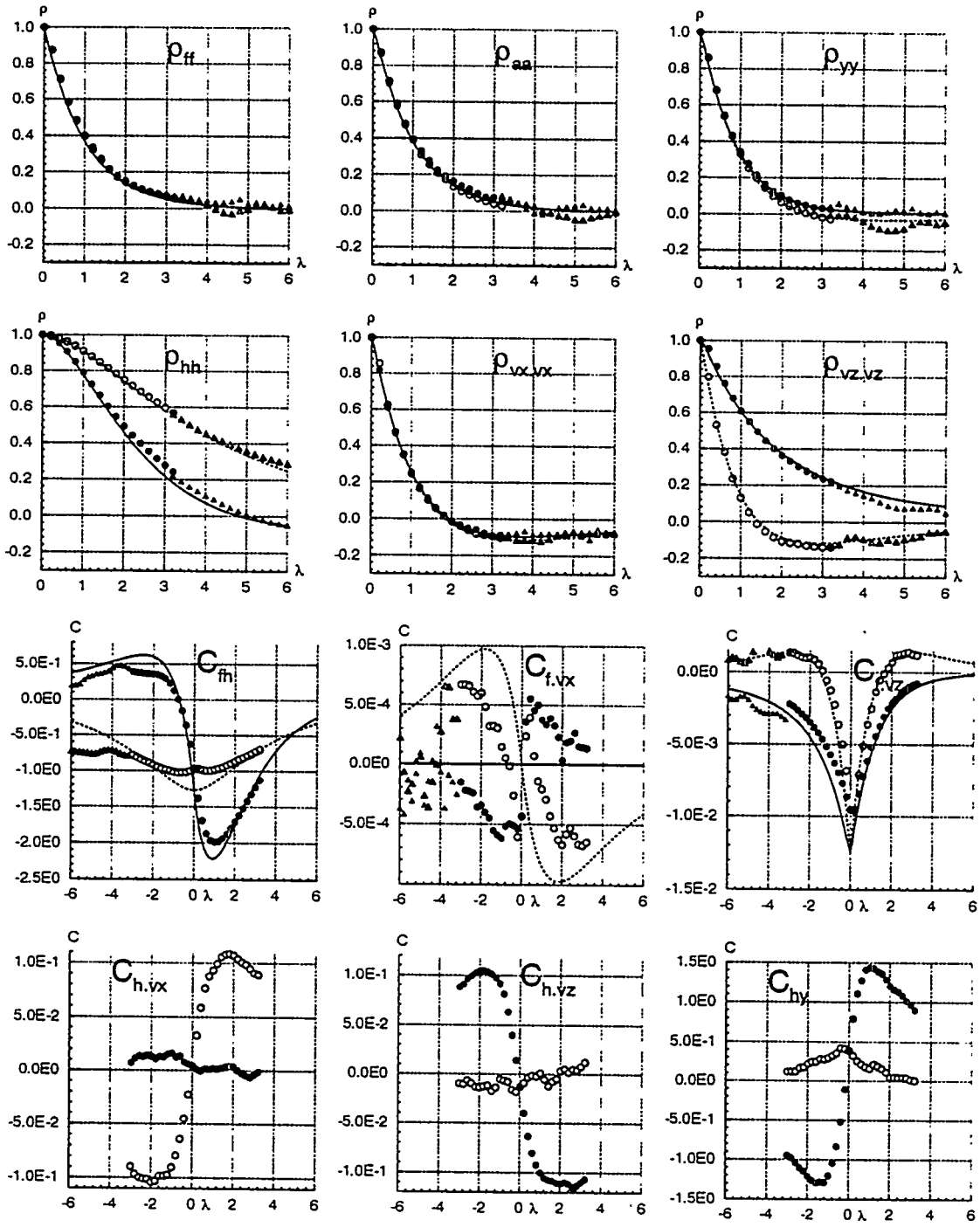

Figure 8.6: Cross-sections of the correlation functions ρ and cross-covariance functions C for the #8 soil site. Horizontal and vertical first order analytical functions are indicated by dashed and solid lines, respectively. Horizontal and vertical MC sample functions are noted with hollow and solid symbols, respectively. Circles are average sample functions, triangles are from the center-point correlation and cross-covariance samples (see text).

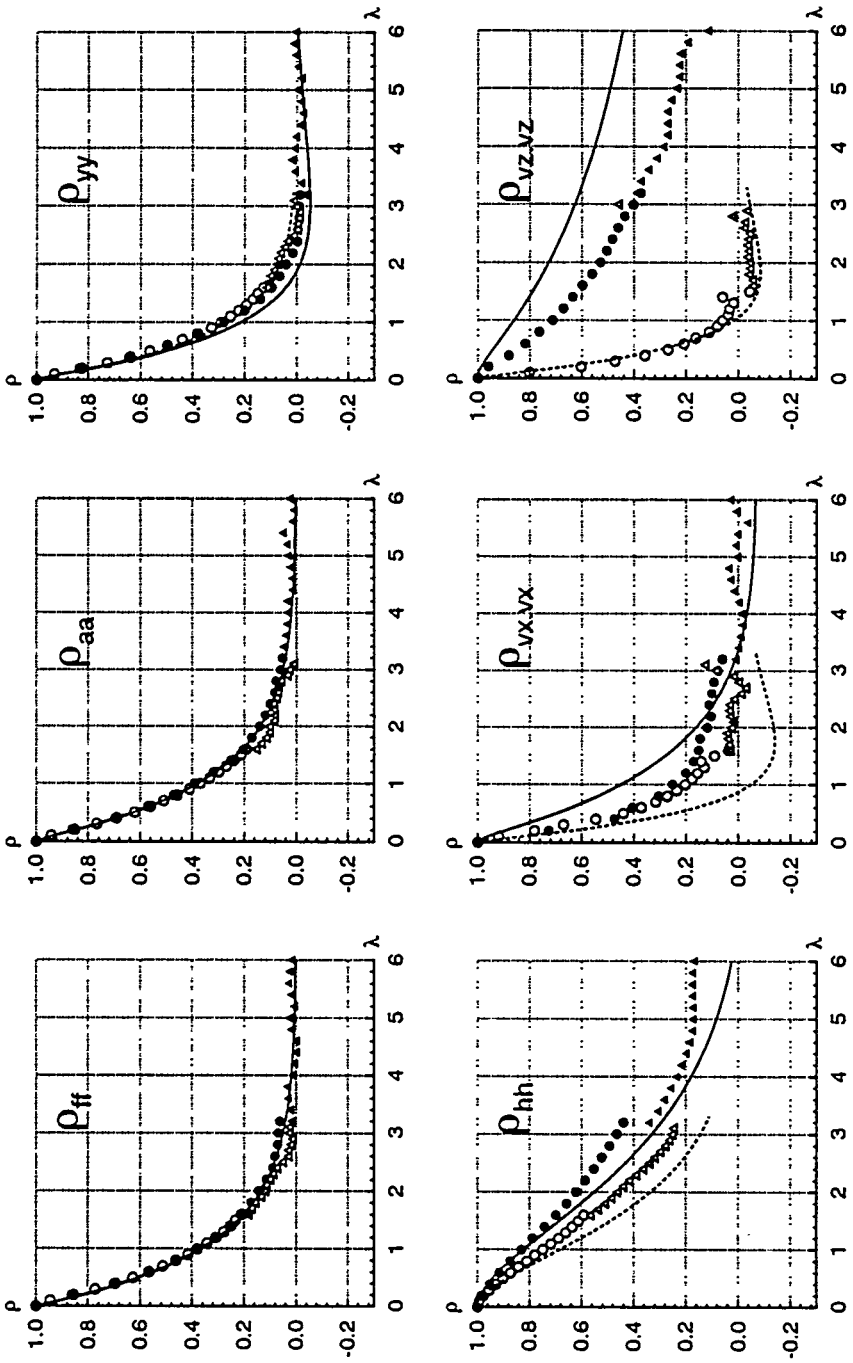

Figure 8.7: Analytical correlation functions (see chapter 4) (lines) and Monte Carlo sample correlation functions (symbols) for an anisotropic, highly variable, wet soil (#22). Legend as in Figure 8.6.

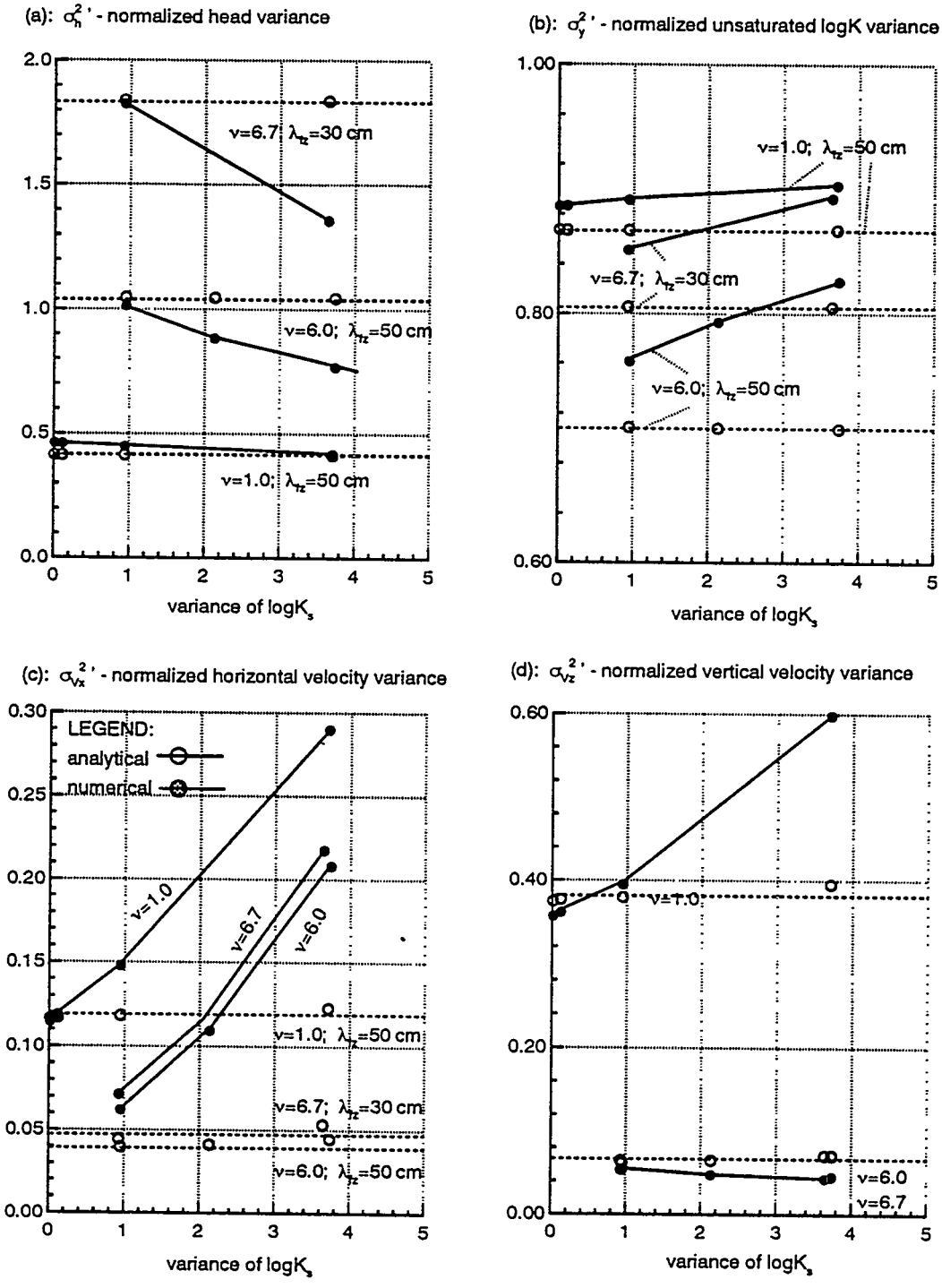

Figure 8.8: Dimensionless variances of the dependent RFVs as a function of the variance of the RFV f (=logK$_s$).

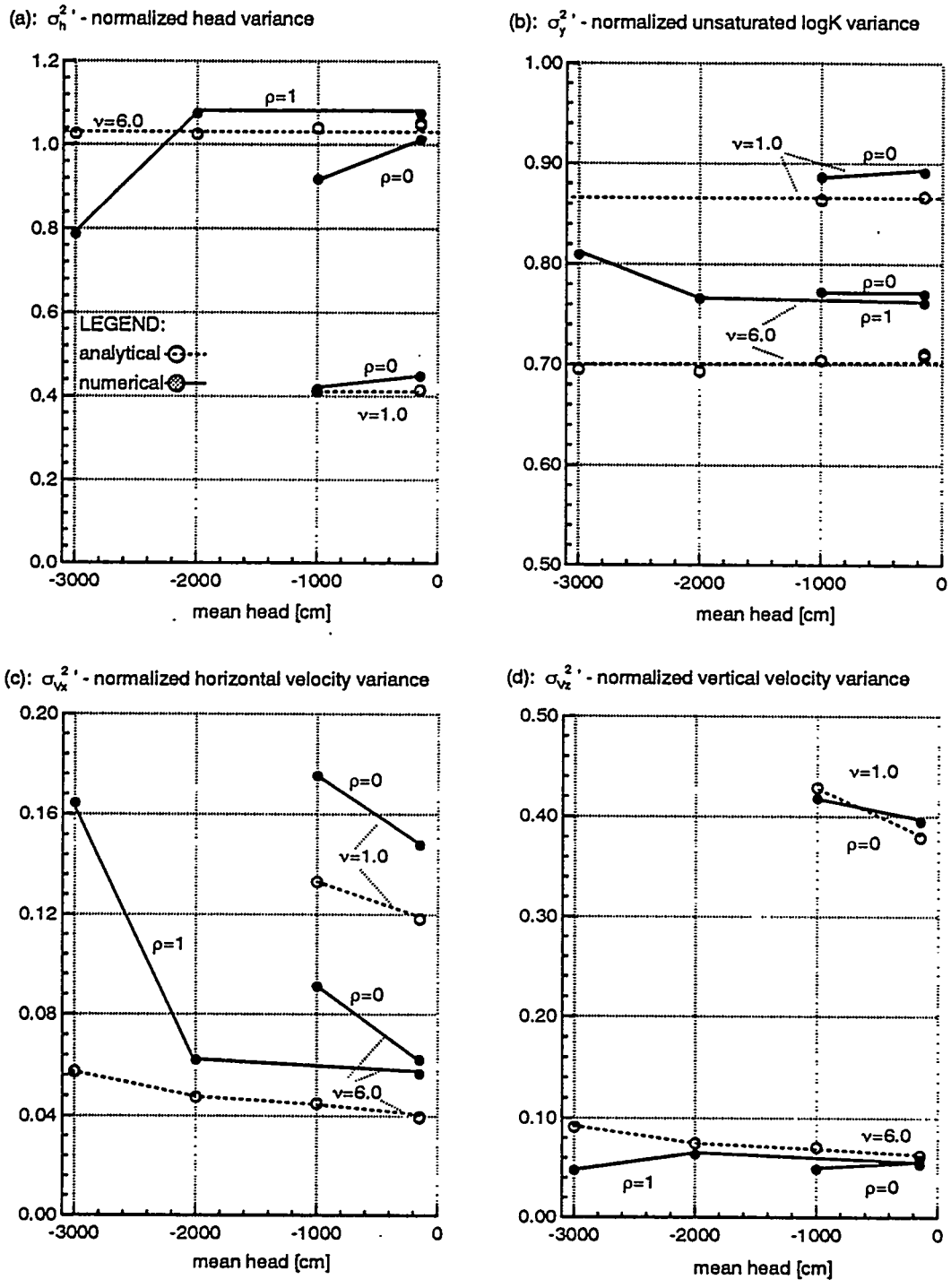

Figure 8.9: Dimensionless variances of the dependent RFVs as a function of the mean head.

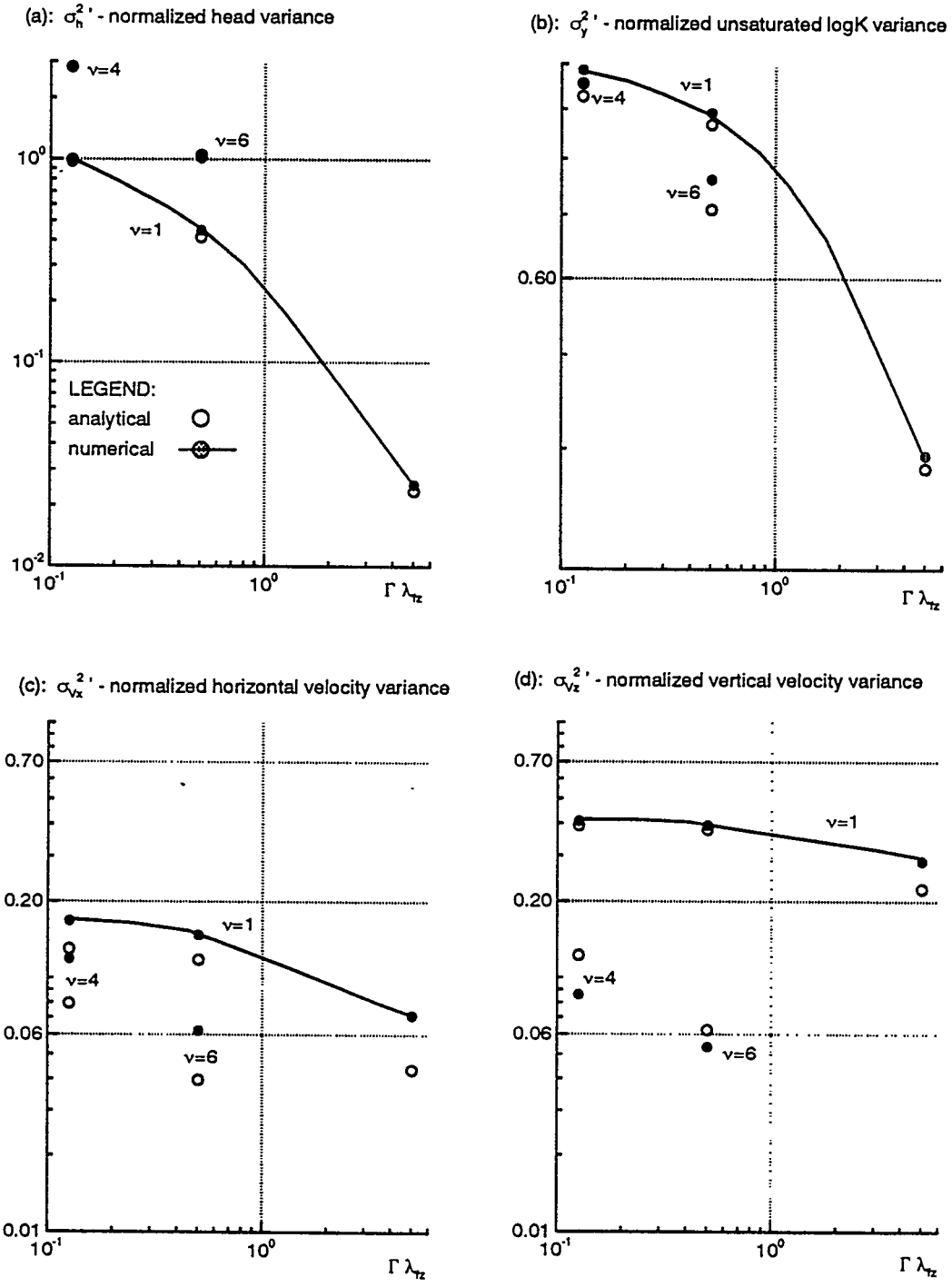

Figure 8.10: Dimensionless variances of the dependent RFVs as a function of $\Gamma\lambda_{fz}$, where Γ is the geometric mean of α and λ_{fz} is the vertical correlation scale of f.

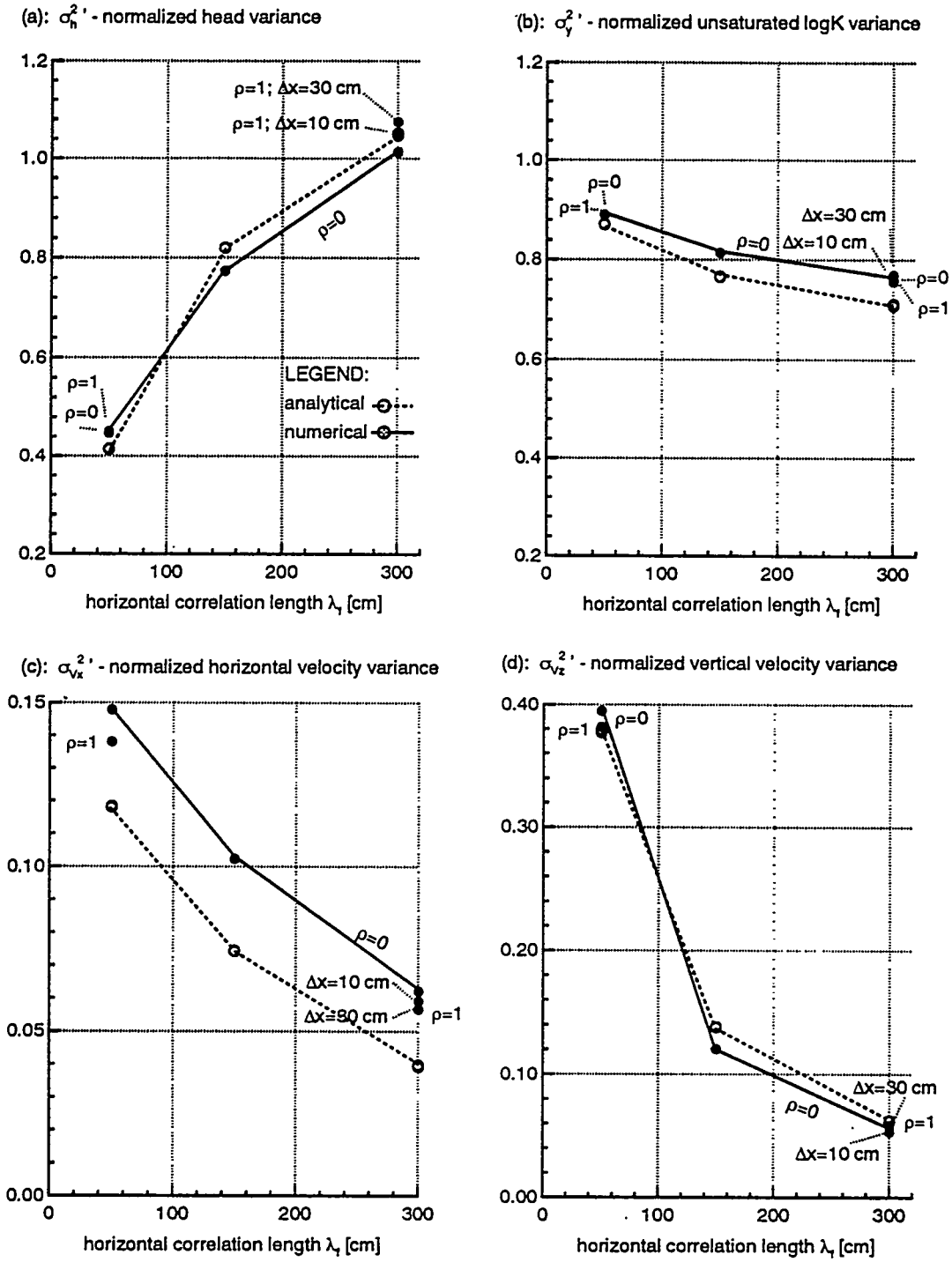

Figure 8.11: Dimensionless variances of the dependent RFVs as a function of the horizontal correlation scale of f. The vertical correlation scale of f is 50 cm.

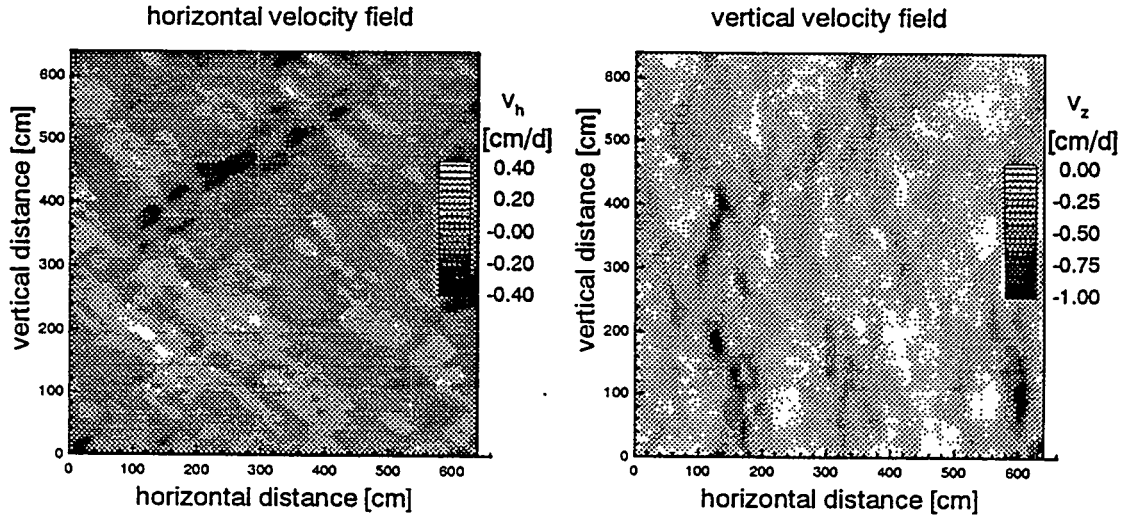

Figure 8.12: Single solution for v_x (left) and v_z (right) from a random field realization of f and α for the isotropic base soil site (#3).

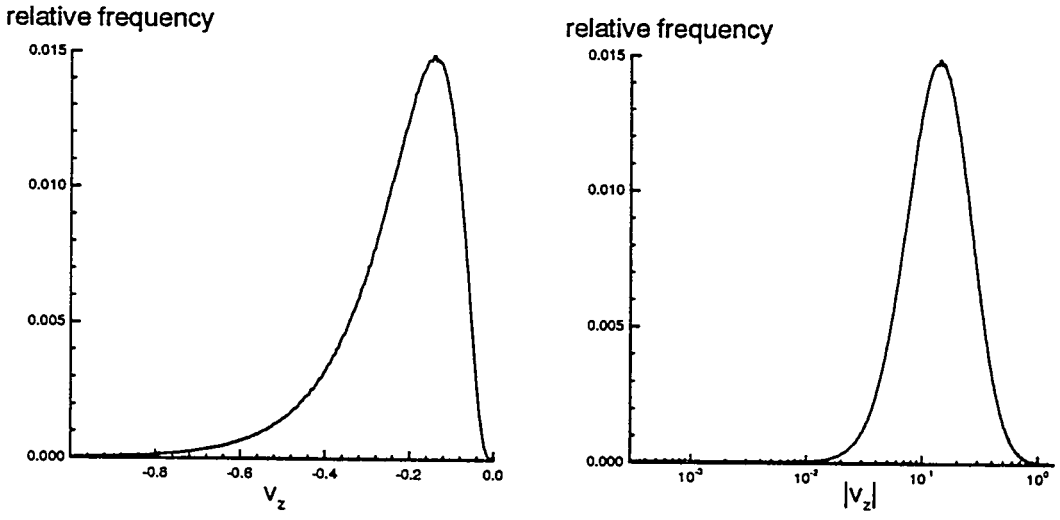

Figure 8.13: Histogram of v_z at the isotropic base soil site (#3) on an arithmetic scale (left) and on an absolute logarithmic scale (right).

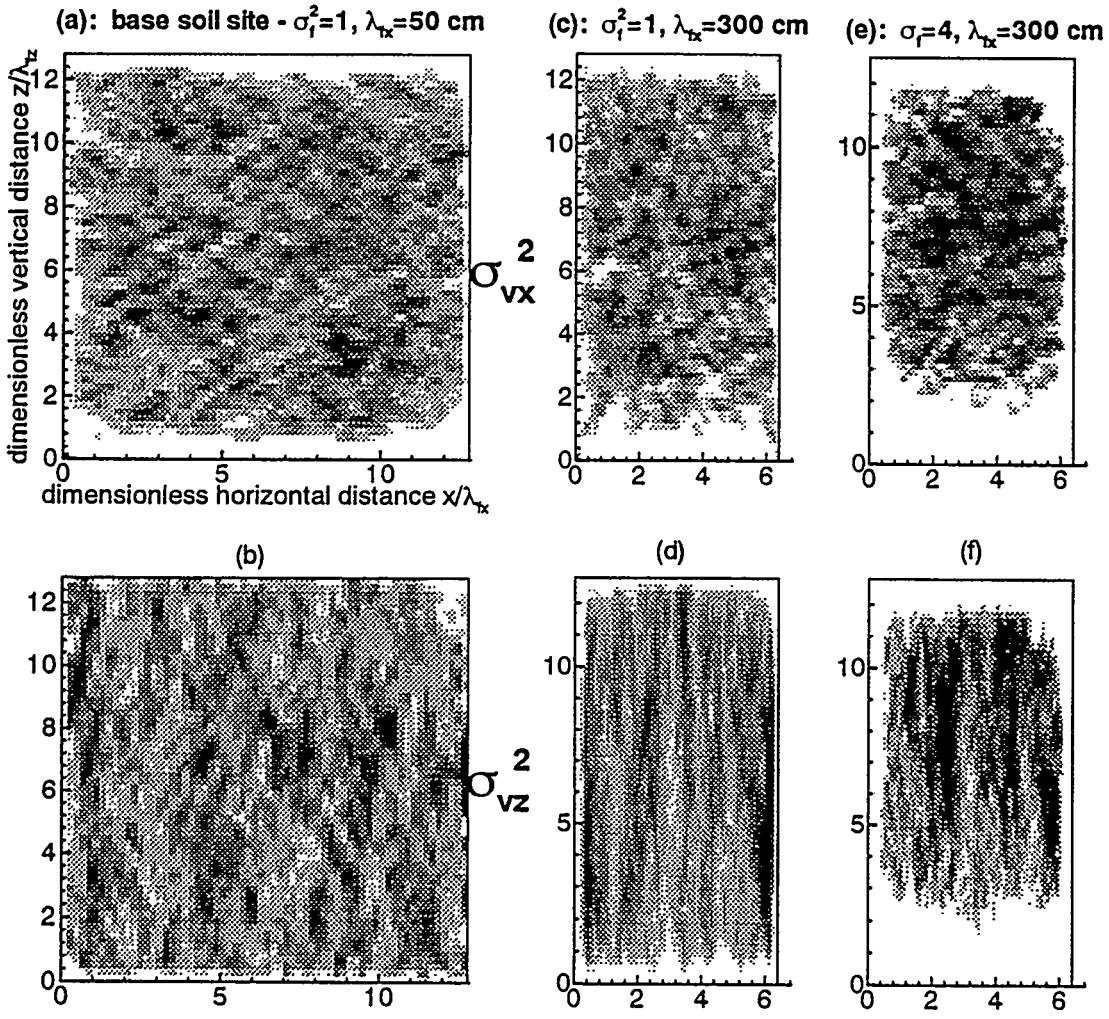

Figure 8.14: Influence of the first order perturbation head boundaries on the horizontal (top) and vertical (bottom) velocity variance for the isotropic base soil (#3, Fig. 8.14a,b), an anisotropic soil (#29, Fig. 8.14c,d), and an anisotropic high f-variance soil (#22, Fig. 8.14e,f). The boundary effect is indicated by the (white) high velocity variance areas near the boundary. Darker shades indicate lower variance.

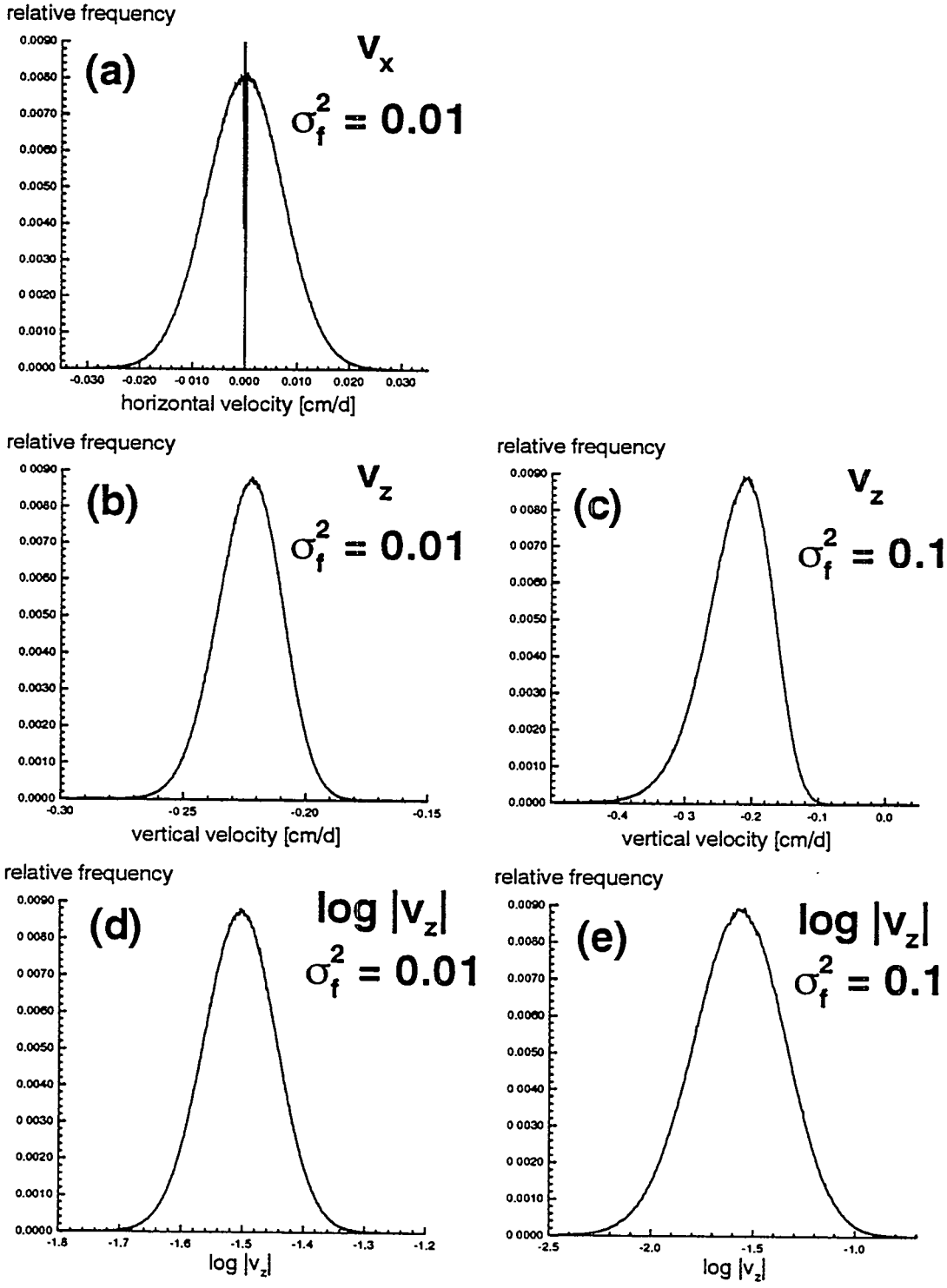

Figure 8.15: Histograms of the horizontal velocity at $\sigma_f^2 = 0.01$ (a). Histograms for the vertical velocity are given for $\sigma_f^2 = 0.01$ (b) and 0.1 (c). The latter histograms are also plotted both on a logarithmic scale (Fig 8.15d,e).

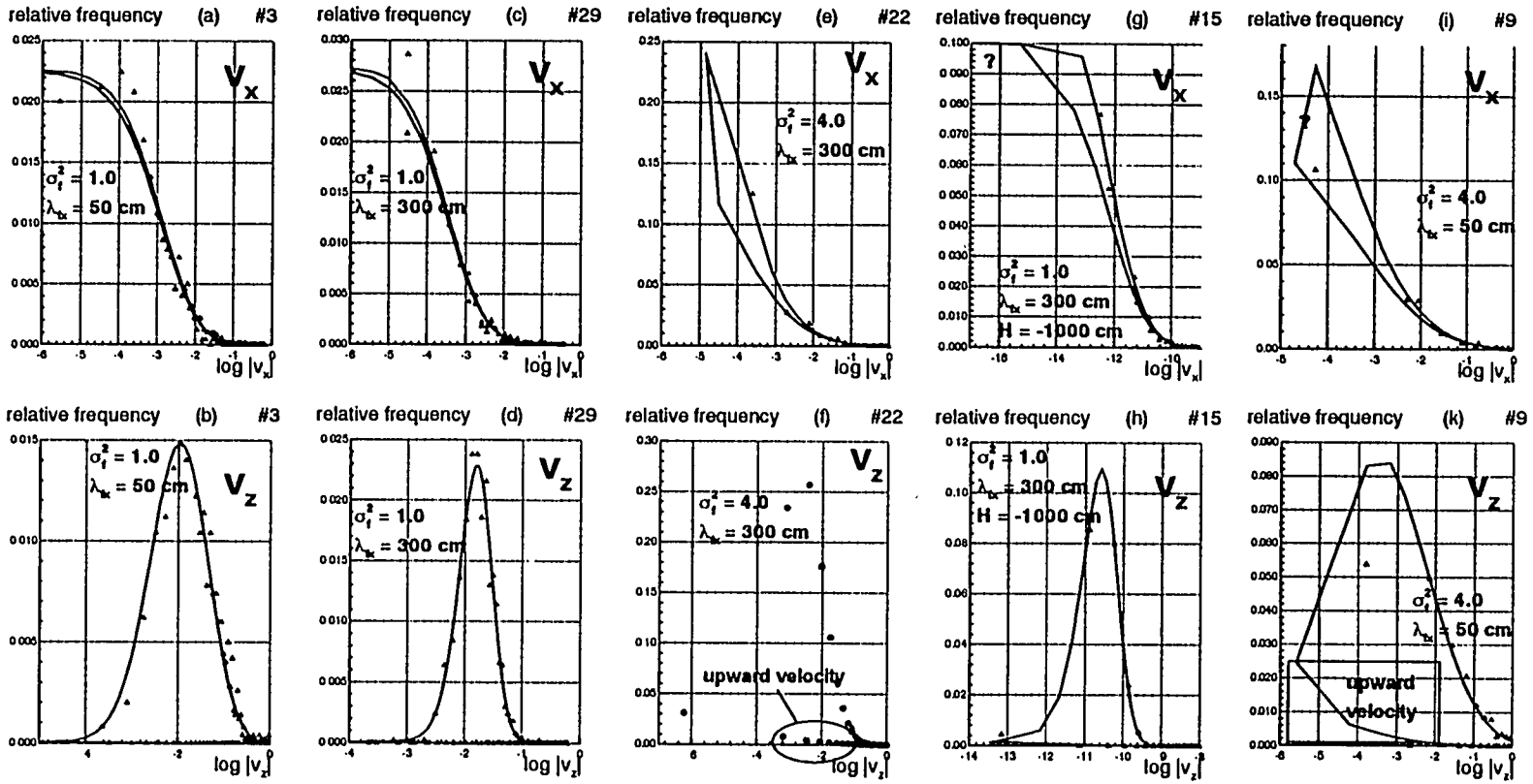

Figure 8.16: Horizontal velocity (top) and vertical velocity (bottom) histograms for soil site #3 (isotropic base soil), soil site #29 (anisotropic), soil site #22 (anisotropic, f-high variability), soil site #15 (anisotropic, dry), and soil site #9 (isotropic, high f-variability). In all three simulations ρ=0, λ_{fz}=50 cm.

Where not explicitly noted, H = -150 cm. Solid lines and circles are histograms for all data. Triangles are histograms obtained from the center-point in the domain.

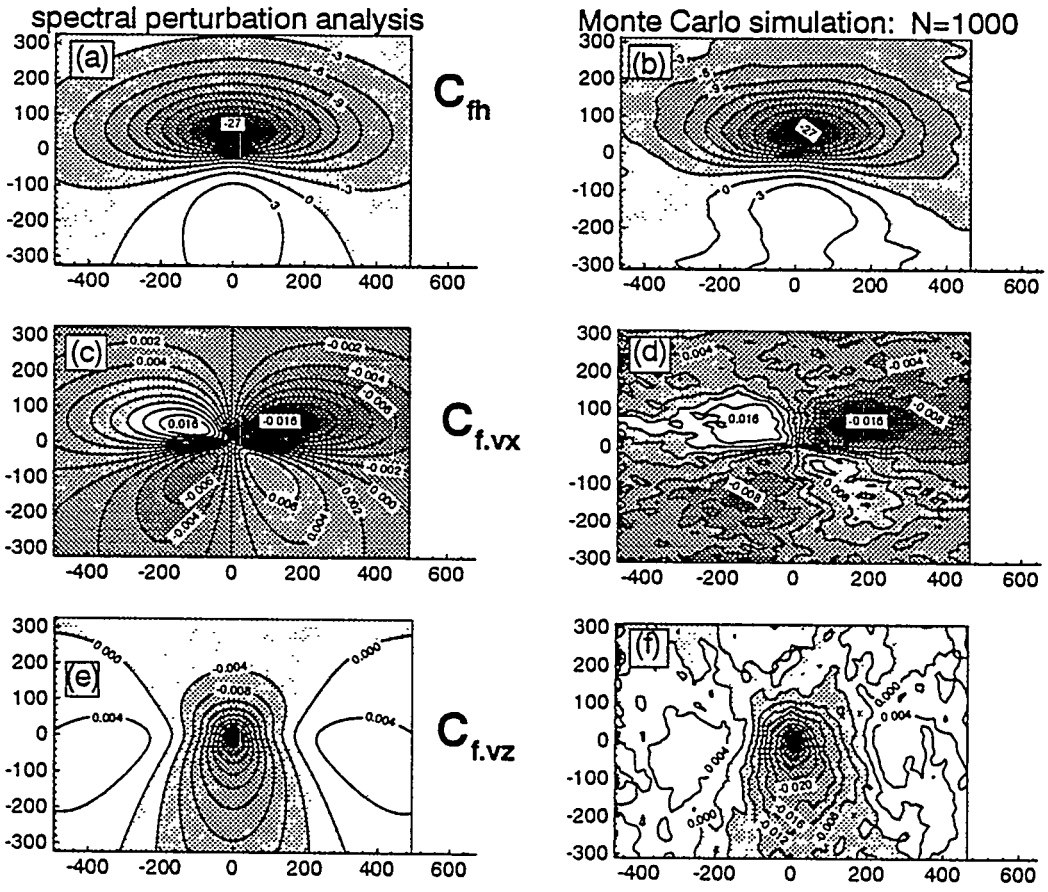

Figure 8.17: Anisotropic variation (#31: λ_x=150 cm) of base soil site. First order analytical ensemble cross-covariance fields (left) and numerical sample cross-covariance fields (right) for cross-covariances between f at the center-point and h, v_x, and v_z in the entire domain. Axes labels are lag-distances in [cm].

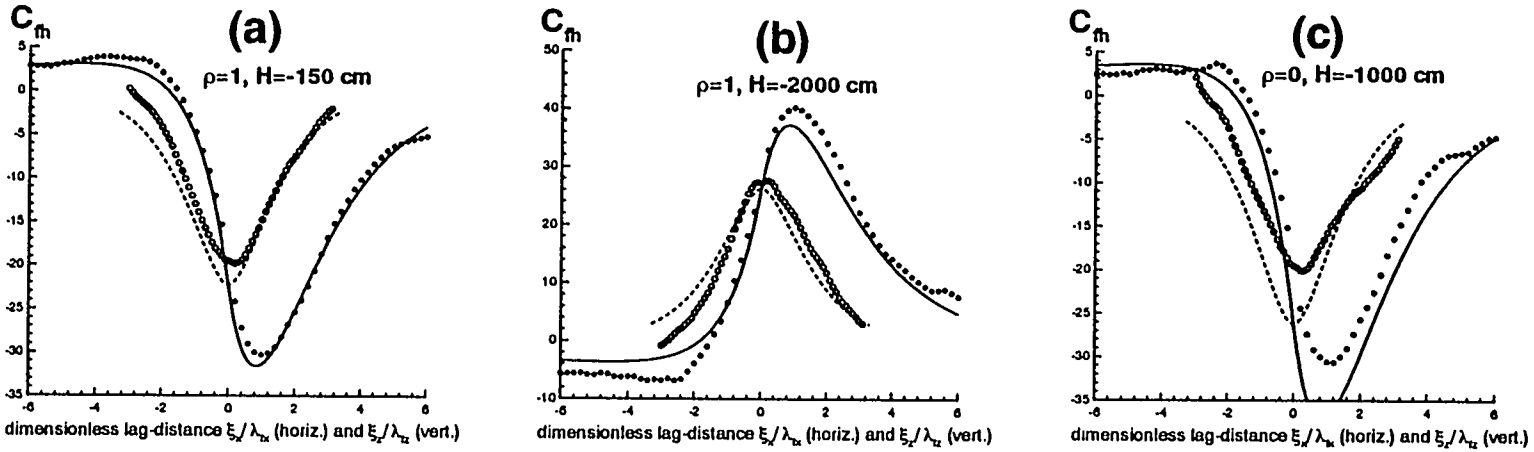

Figure 8.18: Comparison of the cross-covariance C_{fh} in three different anisotropic soils of equal textural heterogeneity but different correlation between f and logα (ρ_{af}) and at different mean head H (from left to right: #12, #24, #15). Legend as in Figure 8.6.

9. MONTE CARLO SIMULATION OF SOLUTE TRANSPORT FROM SMALL SOURCES IN DEEP, VARIABLY SATURATED SOILS

9.1 Introduction

Contamination of groundwater resources has been one the largest environmental concerns of the last decade. Most pollution sources, whether they are agricultural, domestic, or industrial, non-point or point pollution sources, are at or near the surface. Much of the pollutants must therefore travel through the unsaturated zone between the surface and the groundwater before reaching the water table. A thorough understanding of the transport processes in the unsaturated zone is essential to assess the contamination risk of groundwater resources and to predict the travel time from a pollution source to a drinking water well.

The advection-diffusion equation (ADE, eqn. 5-1) is generally used to describe the movement of solutes in the unsaturated zone. Like the study of groundwater pollution the assessment of solute and contaminant transport through the unsaturated zone is hampered by the uncertainty caused by the heterogeneous structure of the geologic material. However, the list of soil properties that determines solute displacement and plume spreading includes more than just the saturated hydraulic conductivity, since the unsaturated hydraulic conductivity depends directly on the soil water tension or the soil water content. In the previous chapter some of the effects of soil spatial variability on the soil water tension and velocity distribution in the soil were studied. Field studies have shown that the heterogeneity of the soil moisture flux leads to variable, time- and scale-dependent parameters in the ADE.

Stochastic transport models have been developed to describe average solute displacement and plume spreading in variable flux fields (e.g. Gelhar and Axness, 1983; Dagan, 1982, 1984; Neuman et al., 1987). The objective of these stochastic models is to cast

solute transport in heterogeneous geologic media into an equivalent quasi-homogeneous ADE i.e., to define the mean transport velocity and the average plume-spreading in terms of the statistical parameters that describe the spatially random velocity field. Stochastic analysis of transport in porous media such as Dagan (1984, 1988), Neuman and Zhang (1990), Rubin (19990), Zhang and Neuman (1994c) suggests that the effective dispersion or "macrodispersion" varies with time. These models have primarily been developed and applied to transport in groundwater, although they are in principle valid also for unsaturated flow.

Past efforts of modeling unsaturated solute transport have concentrated on the analysis of one-dimensional transport in steady state flow fields. A basic tenet of such models is the assumption that the soil consists of an ensemble of independent, homogeneous vertical stream tubes. For each stream-tube, the vertical flow and transport parameters are defined randomly. (Dagan and Bresler, 1979; Bresler and Dagan, 1981; Amoozegar-Fard et al., 1982; Jury, 1982; Simmons, 1982; Jury et al., 1986; Butters and Jury, 1989; Destouni and Cvetkovic, 1989, 1991). Horizontal solute displacement and lateral dispersion is neglected, an assumption that has been found valid mainly in applications to field-scale solute transport from non-point pollution sources through shallow soils. Destouni (1992) incorporated the effect of vertically variable saturated conductivity into the stream-tube model.

Field studies of multi-dimensional unsaturated transport have been documented by Ellsworth and Jury (1991) and by Wierenga et al. (1991). These studies have demonstrated the limitations of one-dimensional unsaturated transport models if the lateral extension of the plume is small relative to the depth of groundwater. Lateral solute spreading and plume contraction and expansion were found to be important mechanisms affecting the movement of the solute plume. The dispersion of solutes in a more general two-dimensional heterogeneous soil has been studied numerically by Russo (1991) and by Russo and Dagan (1991) who suggested that macrodispersion of unsaturated transport is amenable to the same stochastic transport analysis as those known for aquifer contamination. More recently, Russo (1993a) combined the three-

dimensional stochastic formulation of unsaturated flow in heterogeneous media by Yeh et al. (1985a,b) with the Lagrangian transport analysis by Dagan (1982, 1984) to derive analytical expressions for the displacement of the center of a plume and the average plume spreading. In a complementary study, Russo (1993b) derived the temporal moments of solute arrival time in a three-dimensionally heterogeneous soil based on the work by Cvetkovic et al. (1992).

Both spectral analysis of unsaturated flow and Lagrangian analysis of solute transport are limited to mildly heterogeneous media with a normally distributed velocity. The findings in the previous chapter suggest that the velocity pdf is neither normally distributed nor well described by the first order spectral perturbation analysis. It was found that spectral analysis may be much more limited with respect to predicting velocity moments than with respect to predicting the soil water tension distribution. While Russo's (1993a,b) analysis is a useful tool for the validation of numerical models and to obtain approximate estimates, it may be inappropriate for many field applications with highly heterogeneous soils.

In this study, transport through unsaturated soils is re-examined without assuming that the spatial variability is small, without limiting the study to one-dimensional transport of non-point pollution, and without depending on the assumption that transport is ergodic, which is invoked in the numerical study by Russo (1991) and which is necessary for analytical results such as those of Dagan (1984) to hold. Going beyond these restrictions allows one to analyze the behavior of plumes from sources of relatively small lateral extent occurring for example under leaky storage tanks and damaged liner systems. These sources can generally be viewed as point-sources. In contrast to solute plumes from non-point sources, the lateral solute movement plays an important role for point source plumes and is a significant source of uncertainty for transport models of heterogenous soils. Solute transport from small sources in heterogeneous porous media is not ergodic i.e., the mean concentration derived stochastically is not identical to the actual concentration. Plumes from small sources (lateral extent on the order of or smaller than the correlation scale of the soil hydraulic conductivity) require several

tens if not hundreds of correlation scales in mean travel distance before the ergodic condition is met and the concentration variance vanishes.

Therefore the Monte Carlo technique is applied to study the spatial and temporal variability of non-ergodic solute plumes in variably saturated porous media. A variety of different hypothetical soil sites is investigated to establish a stochastic analysis of the solute concentration, the solute flux, and the solute plume spreading as a function of the various independent parameters characterizing a spatially variable soil. For efficiency, the two-dimensional steady-state head and velocity distribution in a vertical soil profile is computed using the ASIGN approach (Harter and Yeh, 1993; see chapter 7). For each realization of a velocity field the movement of a small plume through the soil is predicted as a function of time. From a set of 300 realizations within each Monte Carlo simulation the local concentration moments (mean and variance) are computed over time, the first and second moments of each individual plume are monitored over time, and solute flux is recorded and statistically analyzed as a function of location and time. The technical implementation and design of the Monte Carlo simulations is described in section 9.2. In section 9.3, the results for the concentration moments and the solute plume spreading are reported and compared to the linear macrodispersion model by Dagan (1988). In section 9.4 solute flux and travel time in various soils are investigated and compared to the Lagrangian particle travel time model by Cvetkovic et al. (1992). Both the linear macrodispersion model and the Lagrangian travel time analysis are coupled with the linearized first order perturbation analysis of unsaturated flow described in chapter4. The chapter ends with summary and conclusions in section 9.5.

9.2 Implementation of the Monte Carlo Simulation and Statistical Methods

9.2.1 Transport Model

The same Monte Carlo procedure as described in chapter 8.2 is used for the stochastic analysis of transient transport. The procedure described in 8.2 computes steady-state, unsaturated velocity fields v(x) given spatially correlated random realizations of f and a with means F, A, variance σ_f^2, σ_a^2, and an exponential spatial correlation characterized by the horizontal and vertical correlation scales λ_{fx} and λ_{fz}, respectively. For each realization of v(x), transient transport is simulated with an algorithm based on the modified method of characteristics (MMOC) and described in Yeh et al. (1993). Chapter 5 gives an overview of the numerical procedure and describes the particular implementation used for this study. In this chapter, only transport of non-reactive solutes is analyzed. Recall from chapter 5 that only advective transport is computed (for efficiency), while local or "pore-scale" dispersion is introduced through numerical dispersion. The effective equation solved by MMOC given a random realization v(x) of the velocity field is:

$$\frac{\partial c(x,t)}{\partial t} + v(x)\nabla c(x,t) = \nabla\cdot(D_{num}(x)\nabla c(x,t)) \qquad (9\text{-}1)$$

Although the numerical dispersion $\mathbf{D}_{num}(\mathbf{x})$ cannot be rigorously quantified, preliminary numerical experiments showed that the resulting effective local dispersivity $\mathbf{d}_{num} = (\mathbf{D}_{num} / V_z)$ is on the order of 1/10 to 1/100 of the element size and therefore much smaller than the correlation scale of the velocity variations (see chapter 8). V_z is the mean vertical velocity. It will be shown later that the effective local dispersivity is only of minor importance for the overall plume movement. The main contribution of the effective local dispersivity is limited to the first few time steps i.e., very early time ($t \ll \lambda_{fz}/V_z$). At early time an initially small plume with uniform concentration c_0 is numerically dispersed over a larger area due to the sharp concentration gradient at the boundary of the plume. Numerical dispersion is caused by the

bilinear interpolation scheme employed in the modified method of characteristics to compute the concentration at locations not identical to those of finite element nodes. At later times, the concentration gradients are much smaller, and the plume movement is dictated predominantly by advective processes. While numerical dispersion is artificial, its net effect is consistent with many field findings and with the stochastic transport theories of Gelhar and Axness (1983), and Neuman et al. (1987), which explicitly account for pore-scale dispersion. Implicit (numerical) or explicit (parametric) local dispersion is expected to affect primarily the local concentration variance (Dagan, 1982) and the asymptotic (i.e. late time) magnitude of the lateral macrodispersion (Gelhar and Axness, 1983; Neuman et al., 1987).

9.2.2 Moment Analysis

In this analysis, the statistical description of three phenomena associated with solute transport is addressed: the statistical analysis of the spatial moments of the actual concentration plumes, the statistical moments of the local concentration, and the statistical moments of the solute flux at a given distance from the plume source. The first two phenomena are closely associated with the concept of macrodispersion (Dagan, 1982, 1984, 1988; Gelhar and Axness, 1983; Neuman et al., 1987) and are grouped together in the spatial analysis of solute transport. The latter analysis is often treated separately and deals primarily with the statistical analysis of particle travel times to a given distance from the source of the contamination (Cvetkovic et al., 1992; Russo, 1993b). Only recently, the spatial and temporal analysis of solute transport has been treated in a unified manner both numerically and analytically (Bellin et al., 1992; Zhang and Neuman, 1994a-d)

9.2.2.1 Spatial Concentration Distribution

Concentration is a non-stationary random field variable (RFV, see section 2.5.1) in space and time. Spatial plume moments and local statistical moments of the concentration distribution are therefore RFV functions of time. In this analysis the computation of the local concentration sample mean <c(x,t)> and of the local sample variance $\sigma_c^2(x,t)$ is limited to four discrete points in time (see below). The computation of local concentration moments is equivalent to the computation of local head sample moments (see chapter 8). No covariances and cross-covariances are computed. The spatial moments of the mass distribution in each solute plume are computed at each time-step of each realization. The zero order, first order, and second order spatial moments of an actual concentration plume are given as:

$$
\begin{aligned}
M_0(t) &= \sum_{i=1}^{NN} c(x^i,t)\theta(x^i)\Delta x^i\ \Delta z^i \\
M_x(t) &= 1/M_0 \sum_{i=1}^{NN} c(x^i,t)\theta(x^i)\Delta x^i\ \Delta z^i\ x^i \\
M_z(t) &= 1/M_0 \sum_{i=1}^{NN} c(x^i,t)\theta(x^i)\Delta x^i\ \Delta z^i\ z^i \\
M_{xx}(t) &= 1/M_0 \sum_{i=1}^{NN} c(x^i,t)\theta(x^i)\Delta x^i\ \Delta z^i\ (x^i)^2 \\
M_{zz}(t) &= 1/M_0 \sum_{i=1}^{NN} c(x^i,t)\theta(x^i)\Delta x^i\ \Delta z^i\ (z^i)^2
\end{aligned}
\qquad (9\text{-}2)
$$

$M_0(t)$ is the total mass in the finite element domain, where the finite element domain consists of NN nodes connecting rectangular elements of sidelength Δx and Δz. $\theta(x^i)$ is the arithmetic average of the water content in the four elements surrounding node i. In this study θ is assumed constant throughout the domain (chapter 8). $M_x(t)$ and $M_z(t)$ are the horizontal and vertical position, respectively, of the center of mass of the plume c(x,t). $M_{xx}(t)$ and $M_{zz}(t)$ are the horizontal and vertical moment of inertia, respectively. The moment of inertia is a measure

of the average plume spreading around the center of mass. The five spatial moments in (9-2) are computed for each time-step of each realization in the Monte Carlo simulation. Similar to the concentration moments, the spatial plume moments are a random process indexed on the real line representing time (see section 2.5). From the realizations of the random, time-dependent moment functions, sample means and sample variances are computed at 500 equal-distanced time intervals distributed over the total amount of simulation time (see below).

Due to the principle of mass conservation the sample mean $<M_0(t)>$ must be constant with time during the early part of the simulation when the solute plume is entirely confined within the boundaries of the finite element domain. Any variance in $M_0(t) > 0$ would indicate mass balance errors due to the numerical transport solving method. Computing the variance of $M_0(t)$ is therefore an important opportunity to assess potential mass balance errors in MMOC. The expected values of the first spatial moments, $<M_x(t)>$ and $<M_x(t)>$, are a measure of the average plume displacement and must coincide with the center of mass of the mean plume concentration $<c(x)>$. The mean of the second spatial moment $<M_{ii}(t)>$ (i=x,z) is a representative measure of the average spreading of the plume around its centroid. $<M_{ii}(t)>$ is not identical to the second moment $X_{ii}(t)$ of the mean concentration plume (c.f. Dagan, 1990). The first and second spatial moment X_i and X_{ii} of the mean concentration plume $<c(x,t)>$ are computed as in (9-2) with c(x,t) replaced by $<c(x,t)>$ and M replaced by X. From statistical principles for turbulent mixing (Fischer et al., 1979), illustrated by Kitanidis (1988) and Dagan (1990) for porous media transport, it follows that X_{ij} and $<M_{ij}>$ are related through:

$$<M_{ii}(t)> + var(M_i(t)) = X_{ii}(t) \qquad i=x,z \qquad (9\text{-}3)$$

where $var(M_i)$ is the sample variance of the first spatial moment M_i. $var(M_i)$ is a measure of the uncertainty regarding the actual center of a solute plume. Hence, the spatial spreading of the mean concentration plume X_{ii} is the sum of the expected moment of inertia of the actual plume plus the uncertainty about the center of mass of the plume (Figure 9.1). A general result

of stochastic transport analysis is the fact that only for plumes of large initial lateral spreading or at very late times the uncertainty regarding the center of the plume vanishes relative to the size of $<M_{ii}>$. Then $<M_{ii}>$ and X_{ii} become interchangeable. Such a plume is called ergodic (chapter 2).

9.2.2.2 Solute Flux Characteristics

While much research has been devoted to define the spatial concentration distribution in terms of $<c(x,t)>$ and $\sigma_c^2(x,t)$, the stochastic analysis of the solute mass flux s(x,t) has only recently been investigated (Dagan et al., 1992; Cvetkovic et al., 1992, Russo, 1993; Neuman, 1993; Zhang and Neuman, 1994c). Solute mass flux is an important variable in many regulatory applications, where interest is not so much focused on the spatial distribution of a contamination plume, but on the temporal distribution of solute mass flux across a compliance boundary. It is of particular interest in the study of unsaturated transport, since a common remediation and site assessment question is: When, where, and how much solute mass will arrive at the water table? What is the uncertainty of the prediction due to variable travel times that are caused by the spatial heterogeneity of the soil?

Solute flux s(x,t) is defined as the mass of solute per unit area and unit time passing through a surface element of unit normal η. Neglecting pore-scale dispersion, it can be related to the resident concentration c(x,t):

$$s(x,t) = s(x,t)\eta = c(x,t)\ \theta_e\ v(x)\eta \qquad (9\text{-}4)$$

(9-4) is adopted specifically for use in the numerical model, such that s(x,t) can easily be computed from the resident concentration c(x,t). The definition of (9-4) yields a flux-averaged concentration $c_q = \int (s\ \eta\ dA)/ \int (\theta_e\ v\ \eta\ dA)$ equal to the resident concentration. Setting the flux averaged concentration equal to the resident concentration is justified since the advective

mass flux is much larger than the dispersive mass flux (Parker and VanGenuchten, 1983). No diffusion is included in these simulations and since the effective dispersion is related to the seepage velocity, the effective dispersive mass flux is always smaller than the advective mass flux.

In this study, a number of statistical tools are employed to analyze solute flux at a given compliance surface CS (CS reduces to a line CL in two dimensional transport). The total solute mass flux S(t) is the integrated mass flux across the compliance surface:

$$S(t) = \sum_{n=1}^{NC} s(x_i,t)\Delta x_i \qquad (9\text{-}5)$$

where NC is the number of finite element nodes along the horizontal CS and Δx_i is the average element width to the left and right of node i, in other words, the concentration is linearly weighted between nodes. The mean $<S(t)>$ and variance $\sigma_S^2(t)$ of S(t) are computed from the individual realizations of the integrated mass breakthrough curves S(t). For this study, four CLs are defined at dimensionless vertical distances $Z' = Z/\lambda_{tz}$ = 5.4, 11.6, 17.8, and 23.8 from the solute source area.

In addition to the stochastic analysis of total mass breakthrough S(t), a stochastic analysis of solute mass flux arrival time $t_a(x,s_0)$, and solute peak flux time $t_p(x)$ is undertaken. The solute mass flux arrival $t_a(x,s_0)$ is the time at which the solute mass flux s(x,t) first exceeds some compliance mass flux s_0 at the location x on the CL. Nineteen different s_0 are defined (see below) for each of which, the mean $<t_a(x,s_0)>$, $<t_d(x,s_0)>$ and the variance $var_{ta}(x,s_0)$, $var_{td}(x,s_0)$ are computed. The peak flux time $t_p(x)$ is equal to the time of highest concentration or peak solute flux, since the velocity field is at steady-state. The moments of the arrival and peak time are investigated only at one horizontal compliance surface in the center of the simulation domain. The results are normalized with respect to the constant water content θ and the mean vertical velocity V_z. A more detailed discussion of the physical importance of these temporal moments is given in the analysis of the results.

9.2.3 Parameters and Model Design

The numerical simulations are implemented for a soil cross-section that is 12.8 m deep and between 7.6 m and 30 m wide depending on the expected horizontal solute spreading. The model simulates the instantaneous injection of a small source solute slug into the soil by specifying an initial concentration $c_0 = 1$ for a horizontal rectangle of 3 by 2 nodes (concentration is specified as a nodal property in the MMOC algorithm). The total applied mass therefore depends on the chosen grid-discretization. Since all results are normalized with respect to the total mass or the initial concentration, the results are only dependent on the ratio between the initial plume size and the correlation scale of the soil texture.

For the transport simulations a subset of the different soil-types investigated in the previous chapter is selected. All soils investigated here have a hypothetical vertical correlation length λ_{fz}=50 cm. The horizontal correlation length λ_{fh} varies from 50 cm to 300 cm. The discretization of the domain is 10 cm in the vertical. The horizontal discretization is 10 cm for λ_{fh}=50 cm, 15 cm for λ_{fh}=150 cm, and 30 cm for λ_{fh}=300 cm. Thus the size of the initial solute slug relative to the correlation scale of the saturated hydraulic conductivity is 40% in the vertical; 60% in the horizontal for the isotropic soils, and 30% in the horizontal for the anisotropic soils. The total size of the finite element domain is 128 elements vertically and between 76 and 100 elements horizontally. The horizontal domain size was chosen such that the solute plume would not spread beyond the vertical boundaries of the finite element domain. An overview of the different hypothetical soils is given in Table 9.1 together with the actual size and discretization of the respective flow and transport models. The same soil mc3 is used as base soil site as in the flow analysis (isotropic, unit variance in f). The variance of f varies from 0.01 to 4, the variance of a from 0.0001 to 0.04. The correlation ρ_{af} between f and a is either 1 or 0. The geometric mean of α (=Γ) is always 0.01 cm^{-1}. The average water tension varies from -150 cm to -3000 cm.

As for the flow analysis in chapter 8, the boundary conditions imposed on the solution of the steady state head field are of the random Dirichlet type. The random head boundaries are obtained from the first order spectral solution for the head given the particular realization of f and *a*. From the previous chapter it is known that the first order head boundaries significantly alter the velocity distribution in the vicinity of the boundary. These boundary effects would adversely affect transport across or near the boundary. To avoid the erroneous impact of the first order boundary, the solution of the flux is separated from the transport simulation. Steady-state flux is obtained for a finite element domain that is five to ten elements larger around each side than the finite element domain for the transport simulation. In other words, the boundaries of the transport model are located in the interior of the flow model. The size of the peripheral "cut-out" within the flow-model is determined from the results of the previous flow analysis (chapter 8, Figure 8.14). The number of rows or columns cut off of each side of the flow field is indicated in the right column of Table 9.1. For the transport model itself, no boundary conditions are necessary, since only advective transport is solved. The Monte Carlo simulations are based on 300 realizations of each soil site.

The previous chapter elucidated the dependence of the velocity field and its spatial variability upon the various parameters governing unsaturated flow. The spatial variability of the velocity field controls the uncertainty (or spatial variability) of solute flux and the solute concentration distribution through the physical dependence of concentration upon velocity expressed in the transport equation (eqn. 5-1). The velocity field is controlled by Darcy's law, and hence by the spatial variability of the unsaturated hydraulic conductivity y. The latter is the single most important parameter used to describe or predict the uncertainty in solute transport. Its spatial variability, as described in chapter 8, depends on the variance of the independent input parameters f and *a*, on their correlation scale and anisotropy ratio, and on the mean soil water tension H. For the evaluation of the transport simulation, the soils are therefore grouped into four categories, each of which addresses the sensitivity of stochastic transport to

one specific parameter:

1. category: isotropic, wet soil: #2, #8, #3, and #9. Only the variance of f and a change. The actual average sample variance of f is 0.01, 0.11, 0.95, and 3.62, respectively (see chapter 8). The variance of a is 10^{-4}, 10^{-2}, 10^{-2}, and $4*10^{-2}$, respectively.
2. category: anisotropic, wet soil: #12, #29, #28, #22. Again, only the variance of f and a change. For #29, #28, and #22, the variances of f and a are 0.95, 2.15, 3.67, and 10^{-2}, $4*10^{-2}$, $4*10^{-2}$, respectively. #12 and #29 have identical parameter variances, but unlike all other example soils #12 has perfectly correlated f and a random fields, which slightly reduces the unsaturated hydraulic conductivity variance relative to #29 (see chapter 8).
3. category: $\sigma_f^2=1$, wet soil: #3, #31, #29. Only the horizontal correlation scale of f (and a) change: For the three soils they are 50 cm, 150 cm, and 300 cm which results in aspect ratios $\nu = \lambda_{fh}/\lambda_{fz} = 1$, 3, and 6, respectively.
4. category: anisotropic dry soil: #15 and #21. These are both dry soils with mean soil water tensions H of -1000 cm and -3000 cm, respectively. The first soil is otherwise the same soil as #29, while the second soil is otherwise identical to #12, which has perfectly correlated f and a random fields. The two dry soils are contrasted with two wet soils of similar unsaturated hydraulic conductivity variance to investigate whether unsaturated transport can be characterized by σ_y^2 and C_{yy} alone: #15 is contrasted with #28 ($\sigma_y^2=1.5$ and 1.8, respectively), #21 is contrasted with #22 ($\sigma_y^2=3.2$ for both).

9.3 Spatial Analysis of Solute Transport under Uncertainty

9.3.1 General Characteristics of Solute Movement and of its Statistical Representation

The dynamics of the spatial distribution of solute concentration in unsaturated porous media and its direct dependence on the variability in velocity is illustrated in Figure 9.2 for

three anisotropic soils with distinctly different σ_y^2. In mildly heterogeneous soil the streamlines are more or less vertical (Figure 9.2a). Deviation from a parallel vertical flow pattern becomes stronger as the variability of y increases (Figure 9.2b,c). In more heterogeneous soils streamlines tend to cluster in preferential flow areas, and show a large variability over short distances. If the soil is very heterogeneous, the streamlines may exhibit a horizontal displacement of several meters (a few correlation scales, Figure 9.2c). Relative to its entry position, the maximum observed total horizontal displacement of a streamline at the bottom of the 12 m deep vertical section is 1 to 2 m for σ_y^2=0.74 (soil #29), on the order of 5 m for σ_y^2=1.48, and on the order of 10 m for σ_y^2=3.20. While the single realizations of streamlines depicted in Figure 9.2 bear limited statistical significance, they clearly illustrate the degree of uncertainty associated with making predictions about the travel path of a small solute plume and help to understand the results of the stochastic transport analysis. These examples also illustrate that parallel streamtube models are limited in their applications when modeling solute transport from point sources, because they neglect the horizontal displacement of solutes.

The individual solute plumes (Figure 9.2d-f) show the combined effects of travel path variability, local dispersion and travel velocity variability. Since the plume center of mass is an integrated measure of the entire plume displacement, its travel path varies less than the corresponding streamlines. With increasing variance, the solute plumes assume increasingly erratic shapes, and for the same travel time, the travel distance of the plume center of mass becomes more variable. The peak concentration of the plume strongly depends on the total travel distance of the individual plume. If the solute is initially placed into an area of low unsaturated permeability, the plume will travel only slowly for an extended period of time and disperse very little i.e., the peak plume concentration will remain high. In contrast, a solute plume that is initially placed into a relatively high permeability area will travel quickly, disperse, and the peak concentrations will drop rapidly.

The mean concentration from the Monte Carlo simulation (Figure 9.2g-i) indicates the

stochastically predicted location and spreading of the solute plumes at t'=10 ($t'=\lambda_{fz}/V_z$), the same time at which the snapshot of the actual plumes (Figure 9.2d-f) are taken. As expected, the mean plumes exhibit more spreading and lower peak concentrations than the actual plumes due to the variability var(M_i) (i=x,z) in the travel path of the plume center (9-3). For strongly variable soil flux ($\sigma_y^2>1$), Figure 9.2i qualitatively illustrates how var(M_i) contributes significantly to the total spreading X_{ii} of the mean concentration plume. In that case X_{ii} is a poor measure of the "typical" solute distribution M_{ii} (Kitanidis, 1994).

Small irregularities can be seen in the contours due to the random nature of the sample mean (Figure 9.2g-i). The irregularities in the mean plume shape and the skewness of the mean concentration along the vertical axis are more notable at higher σ_y^2, since the potential error of the sample mean concentration increases with increasing velocity and concentration variance. For $\sigma_y^2 > 1$, the Monte Carlo simulations (which are based on 300 realizations) become potentially very sensitive to outliers. Those realizations with very small unsaturated hydraulic conductivities at and/or immediately around the source produce solute plumes which move extremely slow and therefore have peak concentrations close to the initial concentration throughout the entire simulation time (Figure 9.3). Even one realization with a very slow moving plume may significantly bias the arithmetically averaged concentration at later times, since otherwise the concentration at the source quickly drops by several orders of magnitude. In the example problems all simulations with $\sigma_y^2 > 1.5$ show significant 'residual' mean concentrations at the source or within 1 correlation scale distance of the source. In this context, 'significant' is defined as any concentration larger than approximately 1/100th of the observed peak concentration. In these cases the concentration contours in the immediate vicinity of the source are also erratic and must therefore be attributed to outliers (see e.g. Figure 9.2h).

To investigate the accuracy of the sample mean concentrations calculated from 300 realizations, the rate of convergence in the Monte Carlo simulation is demonstrated for the most variable soil in this study (#21, $\sigma_y^2=3.2$) i.e., the soil for which the sample error is the largest.

Figure 9.3 shows the mean concentration at four different times computed from 300 realizations (Figure 9.3a-d) and from 100 realizations (Figure 9.3e-h). The contour map for 300 realizations is significantly smoother than the contour map for 100 realizations. Near the source and at the outermost contour level (<1% of peak mean concentration) the sample accuracy appears to be the least. Otherwise the dominant features of the mean plume are well-defined when based on 300 realizations. With only 100 realizations, the general pattern of the mean concentration distribution can already be seen, but there is also a large degree of erratic spatial variability. It is obvious that hundreds (if not thousands) of additional realizations would be necessary to completely remove the secondary peak near the source caused by an outlier within the first 100 realizations. However, 300 realizations are considered adequate to give relatively accurate results for the spatial moments of the mean plume and the mean breakthrough curve and its variance, because they are integrated measures. They are also adequate to give an approximate description of the spatial mean concentration distribution (Figure 9.3a-d,i).

Therefore it appears that the skewness in the vertical distribution of the mean concentration, which increases with σ_y^2, cannot be explained as an outlier problem. Another explanation for the skewed mean concentration distribution must be sought. Recall that the longitudinal velocities have approximately a lognormal pdf (chapter 8). The theory by Neuman (1993) and the results of Zhang and Neuman (1994d) show that a lognormal velocity pdf indeed causes a skewed shape of the concentration plume at early travel time. Zhang and Neuman (1994d, Figures 1 and 2) indicate that the skewness of the mean concentration plume vanishes after only one correlation scale in travel distance. However, their examples are for mildly heterogeneous media, in which case the Monte Carlo simulations here also produce a Gaussian mean concentration distribution (Figure 9.2g,h). For highly heterogeneous soils (σ_y^2=3.2), the skewness of the concentration plume along the longitudinal direction is very strong even at t'=10. Only at t'=20 the skewness appears to converge towards a more Gaussian distribution (Figure 9.3c). For soil site #15 (σ_y^2=1.5), the skewness is very strong at t'=5 (not shown), but

has almost disappeared at t'=10 (Figure 9.2h).

These observations have a significant practical aspect. The relatively high 'residual' mean concentrations at t'=10 for the large variance soils #9, #21, and #22 (σ_y^2>3) (see e.g. Figure 9.3) suggest that several hundred correlation scales of travel distance may be required before a solute plume achieves ergodicity. The use of stochastic transport models that are based on the ergodicity assumption is therefore not justified for small plume sources and highly variable soils, since the unsaturated zone is either not that thick or it is unlikely to be characterized by a stochastically homogeneous random medium throughout its vertical extent.

The variability of the concentration from realization to realization is illustrated by the variance maps (Figure 9.2k-m). The concentration variance, however, is not a good measure of uncertainty since the mean concentration is nonstationary. The concentration variance is largest near the center of the mean concentration plume simply because the concentrations are largest at the center of the plume. Also note that the largest variances are found in the second of the three example soils, which exhibits a σ_y^2 of less than half the largest σ_y^2 in the three examples of Figure 9.2. Intuitively it would expected that the uncertainty increases with σ_y^2. The discrepancy in the behavior of the peak variance is due to the fact that at higher σ_y^2 the peak mean concentration decreases thus countering the overall increase in concentration variability. Another problematic aspect of the concentration variance is that it is even more sensitive to outliers than the concentration mean due to its second order nature (e.g. Figure 9.2l). A considerably better measure of uncertainty is the concentration coefficient of variation $CV_c(x,t)$:

$$CV_c = \frac{\sigma_c}{<c>} \qquad (9\text{-}6)$$

where < > refers to sample averages and the evaluation is at x and t. The CV_c measures the variability of the concentration at location x and time t not in absolute terms but relative to the mean concentration at the same location and time. Unlike the concentration variance, the CV_c

has a *minimum* at or near the location of the peak mean concentration and increases with distance from the plume center. This is consistent with the analysis of concentration variability in saturated transport (Dagan, 1984; Rubin, 1991b). In terms of CV_c the uncertainty about the high concentrations in the center of the plume is the lowest while uncertainty about the very low mean concentrations at the edges of the plume is highest. The added advantage of using CV_c instead of σ_c^2 as a measure of uncertainty is its inherent ability to neutralize outliers of the type discussed above. Outliers not only increase the concentration mean but also the concentration variance near the plume source. The resulting CV_c remains very high (as expected) relative to the CV_c at the plume center. Overall the lower CV_c is much less sensitive to sampling error than either the variance or the mean.

The general shape of the CV_c plume shows a similar sensitivity to soil heterogeneity and soil moisture as the mean concentration plume. At the plume center the CV_c increases with σ_y^2 while it decreases at the periphery of the mean plume location (see chapter 10). With increasing aspect ratio vertical spreading decreases and horizontal spreading increases. The large CV_c (>1) in all areas except the plume center is yet another indication that the concentration RFV c(x,t) is not Gaussian distributed. Cushey et al. (1993) have also shown that the concentration in porous media has a non-Gaussian pdf. These findings must be taken into consideration when it comes to the practical meaning of both mean concentration and concentration coefficient of variation (or the concentration variance).

9.3.2 The Minimum CV_c - an Empirical Stochastic Analysis

As expected, the minimum CV_c (used as an indicator of the overall uncertainty) increases with the textural variability of the soil expressed by σ_f^2 (Figure 9.4a,b). Surprisingly, the minimum CV_c in the σ_f^2=0.01 soil is still significant throughout the simulated time-span (≈0.2). On the other end of the scale, the largest observed minimum CV_c are for anisotropic

soils of high variability in y and do not exceed 1.6 (#21, Figure 9.4c). The location of the minimum CV_c coincides with the location of the maximum mean concentration only for the two plumes with $\sigma_f^2<0.15$. For all other soils, the minimum CV_c location is lower than the point of maximum mean concentration (Table 9.2). Generally the distance between the two is less than $1\lambda_{fz}$. But for t'=20 the distance may be from $2\lambda_{fz}$ to $10\lambda_{fz}$, depending on the soil variability. Non-Gaussian vertical velocity pdfs and higher variability of the soil flux causes stronger skewness of the vertical mean concentration plume and larger distances between the two locations of maximum concentration and minimum CV_c.

The results are consistent with the theoretical findings of Rubin (1991b), who estimated the concentration mean and concentration coefficient of variation in a mildly heterogeneous saturated porous medium ($\sigma_y^2 = 0.21$). Under the assumption that the velocity pdf is Gaussian, it was concluded that the highest concentration variance and lowest CV_c coincide with the center of the mean concentration plume. The results here illustrate that Rubin's conclusion does not extend to porous media of higher variability and lognormally distributed velocities, where the minimum CV_c location has travelled further than the peak mean concentration location. The results are in contrast with those of Zhang and Neuman (1994d, Figure 1). In their analysis of solute transport with lognormally distributed longitudinal velocity, they came to the same conclusion as Rubin (1991b) i.e., the lowest CV_c occurs at the location of the largest <c>. Again it should be noted that their result is obtained for a mildly heterogeneous porous medium.

Unfortunately, no information on the CV_c is available for t'<5 or at any other times besides those at which the concentration distribution is recorded (t'=5,10,20,40; in case #28: t'=4, 8, 16, 31; $t' = \lambda_{fz}/V_z$). For illustration purposes the three data points of each soil site shown in Figure 9.4 are interpolated with a 3rd order polynomial on the interval t'=[4,20]. The CV_c decreases with time or remains almost constant in the isotropic soils (category 1, Figure 9.4a), but initially increases and later remains constant or decreases again in the anisotropic soils (category 2, Figure 9.4b). The minimum CV_c at t'=5 is higher in the isotropic soils than

in the anisotropic soils (category 3, Figure 9.4c). At later times (t'=10, 20) the observed difference in CV_c for different aspect ratios decreases, and in some instances the anisotropic soil will have a higher CV_c than the isotropic soil of comparable textural variability (compare σ_f^2=3.6, isotropic/anisotropic soils, Figure 9.4a,b). At the last output time (t'=40) all or most of the plume has passed through the domain, and the actual minimum CV_c of the plume cannot be observed. For soils of comparable σ_y^2, but different mean head (4th category), the temporal dynamic and magnitude of the minimum CV_c is very similar but not identical (Figure 9.4d).

In contrast to these findings, other analytical studies (Rubin, 1991b) and field analyses (Barry and Sposito, 1990), both for transport in the saturated zone, report a steady increase in the CV_c with time (maximum analyzed travel distance approximately 40λ). The argument was made that the deterministic effect of the source shape and location of the plume wears out over time. Thus one would observe increasing prediction uncertainty. Observations here suggest that the minimum CV_c in the tested soils may reach a maximum around or before t'=20, then decrease at a slow rate. However, the record is too short to be conclusive. In addition, the time span of the initial increase in minimum CV_c seems to be strongly influenced by the aspect ratio of the anisotropy and by the variance of the unsaturated conductivity.

9.3.3 Spatial Spreading of the Mean Plume, Mean Spatial Spreading of Plumes, and Variability of the Plume Center of Mass

In this section the stochastic dependence of the three moments X_{jj}, var(M_j), and $<M_{jj}>$ (j=x,z) on the heterogeneity and moisture content of the unsaturated zone is examined under fully nonlinear conditions (numerical Monte Carlo simulations). The results are used to assess the validity of what is called the linear macrodispersion theory.

Until recently, the thrust of stochastic analyses regarding transport in heterogeneous porous media has not so much dealt with the mean concentration and concentration variance

itself, as it has focused on the second spatial moment or moment of inertia X_{jk} of the ensemble mean concentration plume (9-2). Under the assumption of normally distributed velocities, the spatial distribution of the mean concentration is Gaussian, and X_{jk} is then intrinsically related to the apparent Fickian macrodispersion D_{jk} through:

$$D_{jk}(t) = \frac{1}{2}\frac{dX_{jk}(t)}{dt} \qquad (9\text{-}7)$$

With the aid of the time-dependent macrodispersion coefficient, the ensemble mean concentration can be estimated through a quasi-Fickian analysis i.e., by solving (5-1) or (9-1) with $D(t) = D_{jk}(t) + D_d$ in lieu of $D = D_d$, where D_d is the local (small-scale) dispersion coefficient. In all linear theories of macrodispersion (Gelhar and Axness, 1983; Dagan, 1984, 1988; Neuman et al., 1987), the second moment (moment of inertia) of the mean concentration plume is estimated analytically based on the following fundamental result of turbulent diffusion (Dagan, 1984, eqn. 3.20, 1988, eqn.3, A2; here formulated for two-dimensional, vertical, uniform flux):

$$X_{ij}(t) = \int_0^t \int_0^t C_{v_i v_j}(V_z t', V_z t'')\, dt'\, dt'' \qquad (9\text{-}8)$$

where j = x,z and V_z is the mean velocity in the vertical direction. $C_{vj,vj}$ is the covariance of the velocities at two locations x' and x'' corresponding to mean displacement at t' and t'', respectively. x' and x'' are assumed to be located along the travel path of the mean solute plume. This latter assumption is the most important restriction to the analysis, since it neglects any deviation of the actual plume from the mean travel path. Neuman and Zhang (1990) and Neuman (1993) have overcome the assumption by using a quasi-linear analysis and a Eulerian-Lagrangian approach, respectively. Equation (9-8) also assumes both Eulerian and Lagrangian stationarity of the velocity field (Dagan, 1988).

The stationarity conditions are met in the numerical transport simulations under

investigation. Also, in chapter 4 the second moment $C_{vj,vj}$ of the velocity is derived to first order for soils of arbitrary covariance functions in f and *a*. The velocity covariance function is obtained from a spectral analysis and a numerical fast Fourier transform of the resulting spectral density function. The mean travel velocity is given to first order in (4-43, 8-16). The second spatial moments of the mean plume (9-8) can therefore be readily computed. The validity of the linear macrodispersion theory over a wide range of soil heterogeneity is analyzed by comparing the analytical with the numerical results.

Since all example soils of the Monte Carlo analysis assume the same correlation functions for the input RFVs f and *a* (identical correlation scales), the covariance functions C_{yy}, $C_{v1,v1}$, and $C_{v2,v2}$ and by virtue of (9-8) also the spatial moments $X_{zz}(t)$ and $X_{xx}(t)$ are directly proportional to the variance factor σ^2 (see chapters 4 and 8):

$$\sigma^2 = \sigma_f^2 (1 + 2\rho H' + H'^2) \qquad (9\text{-}9)$$

$H' = \zeta\Gamma H$ is a dimensionless form of the mean soil water tension. The spatial moments can therefore be normalized with respect to four of the input parameters: the correlation between *a* and f, ρ_{af}, the ratio between the standard deviations of *a* and f, ζ, the mean head, H, and the input variance of f, σ_f^2, and of *a*, σ_a^2. The remaining input parameters are the geometric mean of α, Γ, and the vertical and horizontal correlation scales of f, λ_{fz} and λ_{fx}. Γ is constant throughout all simulations. The dimensionless spatial moments $X_{zz}' = X_{zz}/(\lambda_{fz}^2 \sigma^2)$ and $X_{xx}' = X_{xx}/(\lambda_{fz}^2 \sigma^2)$ for the three different anisotropy ratios in Table 9.1 give the analytical solution (9-8) to all hypothetical soils investigated here (Figure 9.5a,b). The initial dimensions of the plume are negligible for all but the least variable soil (σ_f^2=0.01) and are not taken into account in Figure 9.5.

As the aspect ratio ν increases, the longitudinal, vertical spatial spreading X_{zz}' computed from (9-8) decreases considerably. This is consistent with the theoretical results for three-dimensional saturated porous media (Dagan, 1988). At early time, the transverse,

horizontal spreading X_{xx}' is smaller in soils with larger ν. But the less anisotropic the soil, the earlier it reaches its maximum transverse macrodispersivity, which is also higher. Hence, at late time X_{xx}' is larger for soils with higher transverse anisotropy. The theoretical impact of anisotropy on X_{zz}' and X_{xx}' is considerably stronger than in three dimensions (compare to Russo, 1993a, Fig. 7). From the corresponding curves for the apparent longitudinal and transverse macrodispersivity $D_{ij}' = 0.5\, X_{ij}' / t'$ (Figure 9.5c,d) it is obvious that the asymptotic apparent macrodispersivity will only be reached after 100 to several hundred correlation scales travel distance. In a three-dimensional medium, the asymptotic value is reached significantly earlier (Russo, 1993a, Figure 8). The right vertical axis in Figure 9.5c,d is scaled to give the actual macrodispersivity α_{ij} for soils with $\sigma_f^2=1$, $\lambda_{fz}=50$ cm, H=-150cm, $\Gamma=0.01$ 1/cm, $\zeta=0.1$, and $\rho_{af}=0$ (soils #3, #31, #29). The asymptotic longitudinal macrodispersivity for these soils is 51 cm, and the maximum transverse dispersivity varies from 3 cm in the isotropic soil to 1.7 cm in the most anisotropic of the three soils. None of these theoretical results considers local dispersion i.e., $D_d = 0$.

From the linear theory, the spatial moments of the mean plume are expected to increase as the soil dries out, if $\rho_{af}=0$ (9-9). For correlated soils ($\rho_{af}=1$) the variance of y and hence the solute spreading decreases as the soil begins to dry out, reaches a zero variance at H' = 1 (9-9), and then increases for very dry soils (Figure 9.5e). Note that the variance of the correlated case reaches 0 only if the correlation functions for *a* and f are identical. The effect of decreasing soil moisture and increasing soil water tension becomes significant for H' > 0.01. At high soil water tensions H' > 100 the correlation between f and *a* plays an insignificant role and the scaling factor σ^2 grows with ($H'^2\, \sigma_f^2$).

Figure 9.6 shows the results for the spatial spreading X_{zz}' and X_{xx}' of the mean concentration plume in the numerical simulations. The results are shown separately for the four different simulation categories. For the isotropic soils, the fully non-linear solution deviates strongly from the linearized analytical solution for all $\sigma_f^2 \ll 1$ due to the influence of local

dispersion (whose dimensionless magnitude increases with $1/\sigma_f^2$ as σ_f^2 -> 0). The smaller the variability of the soil, the larger are both the longitudinal and transverse spreading relative to the theoretical result. For σ_f^2=0.95, the actual longitudinal spatial spreading of the mean concentration is very close to, but slightly smaller than the analytical solution. At higher soil variability the numerical results again increase relative to theory. However, for σ_f^2=3.6 the mean concentration plume reaches the outflow boundary very early resulting in an artificial deviation from the expected behavior in both the transverse and longitudinal spreading. For the anisotropic soils (second category), the lowest variance is σ_f^2=0.95 and as for the isotropic soils, an increase is observed in both the horizontal and vertical spreading with increasing soil variability. In contrast to the isotropic soils, the dimensionless vertical (longitudinal) spreading is much larger relative to the linear macrodispersion theory, even for σ_f^2=0.95, since the decrease in longitudinal spatial spreading with increasing ν is not as strong for the numerical results as for the analytical solutions (category 3). Similarly drier soils with larger $(1 + 2\rho\zeta\Gamma H + (\zeta\Gamma H)^2)$ exhibit a stronger deviation from the linear macrodispersion theory (category 4).

In general, the numerically obtained transverse X_{xx}' curves follow the same ups and downs with varying σ^2 as the longitudinal X_{zz}'. But the actual deviation from the linear theory is much larger in the transverse direction than in the longitudinal direction. The transverse spreading for σ_f^2=0.95 in an isotropic soil is approximately twice as large as the analytical prediction. This confirms similar results by Rubin (1991b) in a stochastic analysis of a groundwater transport site with σ_y^2=0.29. Based on a nonlinear stochastic transport model, Rubin found that the transverse spreading is approximately twice the value predicted by linear macrodispersion theory (Dagan, 1984, 1988). For the anisotropic soils, the transverse, horizontal spreading of the mean concentration plume from the Monte Carlo analysis is several times larger than predicted from (9-8). The underestimation of the horizontal mean plume spreading by (9-8) is significantly greater for the anisotropic soils than for the isotropic soils (category 3).

The variance var'(M_z) of the plume center of mass in the vertical direction is also larger than the analytical results for X'_{zz} with the exception of isotropic soils. It exhibits a very similar sensitivity though not as pronounced, to changes in soil variability, soil moisture, and anisotropy as the vertical spreading of the mean concentration plume (Figure 9.7a-d); a very small decrease from the isotropic soil σ_f^2=0.01 to the soils σ_f^2=0.95, and an increase in var'(M_z) for both anisotropic and isotropic soils with $\sigma_f^2 > 1$. In the wet, anisotropic soils with ν=6, var(M_z) is almost identical with the theoretical curve for X'_{zz}. As ν decreases, the increase in var'(M_z) is not as strong as in the theoretical X'_{zz}. On the other hand, a significant increase is observed in var'(M_z) for the two dry soils relative to wet soils of similar unsaturated conductivity variance. In the horizontal direction, the variance var'(M_x) of the plume center of mass is almost identical with the theoretical X'_{xx} for the isotropic soils, but several times larger than the theoretical X'_{xx} for all anisotropic soils. The disagreement between the two results increases significantly for higher σ_f^2 and for dry soils (Figure 9.7e-h).

The numerical results for the spatial moments of the mean concentration plume cannot be strictly compared with the theoretical results for the ensemble mean concentration, because the theoretical results do not account for the local dispersion D_d. Unfortunately, no definite number can be associated with $D_{num,jk} = D_{d,jk}$, but initial empirical results have shown that $\alpha_{num,jj} = D_{num,jj}/V_z$ is on the order of 1/10th or less of the element size in the j-th direction (see section 9.2.1). Since $D_{num,jk}$ is constant with time, a term $X_{num,jk} = 2tD_{num,jk}$ must be subtracted from the spatial moments of the mean concentration to obtain the actual X_{jk}. Note that the dimensionless $X'_{num,jk} = (2\alpha_{num,jk}\ t'\ )/(\lambda_{fz}\sigma_f^2\ )$. For small σ_f^2 the numerical dispersion therefore has a considerable impact on the spatial moments of the mean concentration. The initial findings on numerical dispersion are re-evaluated by assessing the observed mean spreading $<M_{jj}>$ around the center of mass of each plume. Taking into account the initial size of the plume $M_{jj}(0)$ the mean apparent dispersivity of plumes, α_{Mjj}, is:

$$\alpha_{Mij} = \frac{(<M_{ij}'> - M_{ij}'(0))\lambda_f \sigma^2}{2t'} \qquad (9\text{-}10)$$

($<M_{ij}'>$ - $M_{ij}'(0)$)/(2t') is plotted in Figure 9.8. For σ_f^2=0.01 the effect of numerical dispersion is largest relative to the effect of spatial variability. There, the mean apparent dispersivity is approximately constant with time and is 1.08 cm in the vertical and 0.12 cm in the horizontal. Since the element size is square with side-length 10 cm, the initial assumption that local dispersivity is on the order of 1 cm or less is confirmed. In other soils, α_{Mij} is significantly larger and is attributed mainly to the effect of spatially variable velocity fields.

9.4 Temporal Analysis of Solute Transport under Uncertainty

9.4.1 Integrated Breakthrough at a Compliance Surface

For many regulatory purposes, the distribution of a contaminant in the unsaturated zone is not as much of interest as the breakthrough of the contaminant or solute at the groundwater table, which is at some distance Z from the source area. Cvetkovic et al. (1992) introduced a theoretical multidimensional model based on the Lagrangian analysis of solute transport (Dagan et al., 1992) to predict the aerially integrated averaged breakthrough and its variance at an arbitrary compliance surface located normal to the mean flow direction at distance Z from a solute source of initial volume V_0 [a similar approach based on the theory by Neuman (1993) was used by Zhang and Neuman (1994c)]. Since the model requires stationarity in the velocity moments and a mean uniform flow field, it applies directly to the unsaturated transport experiments performed in this study. The simulations presented here are for two dimensions. Thus, the initial source is an area A_0 and the compliance surface CP reduces to a linear compliance level CL. The theoretical mean total solute flux $<S(t,Z)>$ and the variance of the total solute flux $\sigma_s^2(t,Z)$ across the CL at distance Z, at time t are obtained from the following

fundamental relationships (Dagan et al., 1992):

$$\langle S(t,Z)\rangle = c_0 \int_{A_0} g_1(t,Z-a,a)\, da$$

$$\sigma_s^2(t,Z) = c_0 \int\int_{A_0} g_2(t,Z-a',a'-a'') - g_1(t,Z-a',a')\, g_1(t,Z-a'',a'')\, da'\, da'' \qquad (9\text{-}11)$$

where c_0 is the initial, uniform solute concentration in the source area A_0, and a is the vertical coordinate of the location vector **a**. $g_1(t,Z\text{-}a,\mathbf{a})$ is the travel time probability density function (pdf) of a particle originating at **a** in A_0 and passing through the CL at time t. Correspondingly, the joint two-particle travel time pdf $g_2(t, Z\text{-}a',\mathbf{a}'\text{-}\mathbf{a}'')$ is the probability that two particles originating at **a'** and **a"** in A_0 traverse the CL at time t. The travel time pdfs depend on the statistics of the velocity. Cvetkovic et al. (1992) derive a first order approximation of the first two moments of the joint two-particle travel time pdf under the assumption that the travel path of a particle does not deviate significantly from the mean flow direction:

$$\langle\tau\rangle(Z) = \frac{Z}{V_z}$$

$$\sigma_{\tau,\tau'}(Z,a',a'') = \frac{1}{V_z^4} \int_{a'}^{Z}\int_{a''}^{Z} C_{v_z,v_z}(z'-z'',x'-x'')\, dz'\, dz'' \qquad (9\text{-}12)$$

where (a',x') and (a",x") are the vertical and horizontal coordinates of **a'** and **a"**. Using these travel time moments, Cvetkovic et al. (1992) then hypothesize that g_1 and g_2 are lognormal pdfs, an approximation that is strictly valid only for lognormal velocity pdfs as $Z \to 0$. They point out, however, that lognormal pdfs for g_1 and g_2 are consistent with the first order approximation (9-12) at all distances from the source, if the velocity field is lognormally distributed, an assumption that holds for the numerical simulations (chapter 8). The form of the lognormal pdfs g_1 and g_2 can be found e.g., in Bras and Rodriguez-Iturbe (1985). Using (9-12) with the linearized velocity covariance function $C_{vz,vz}$ derived in chapter 4, the double integrals in (9-11) can be obtained by numerical evaluation. Since $C_{vz,vz}$ varies smoothly and

is numerically evaluated with a discretization $\Delta x=0.1\lambda_f$ (chapters 4, 8), a very accurate estimate of the integrals (9-12) and (9-11) is obtained by applying an extended form of Simpson's rule first to (9-12) and subsequently to (9-11) using the same discretization as in $C_{vz,vz}$. In the evaluation, the vertical extent of the source area is taken into full consideration. A conceptually similar approach is taken by Russo (1993b) but based on a different derivation of $C_{vz,vz}$ and different integration procedures. From (9-12a) and (9-11a) he evaluated the mean (but not the variance) of the unsaturated breakthrough curve from a source of negligible longitudinal extension for a three-dimensional soil with normally distributed pore-size parameter α.

As in section 9.3, the travel time variance and covariance (9-12) can be obtained normalized with respect to λ_{fz} and the scaled input variance σ^2. But due to the nonlinear form of the lognormal pdfs g_1 and g_2, the mean and variance of the solute flux (9-11) would not be associated with the same normalization. Since solute flux has dimensions of mass per time, the dimensionless solute flux S' is defined as:

$$S' = \frac{S\lambda_{fz}}{M_0 V_z \theta} \tag{9-13}$$

For non-reactive, mass-conservative solutes, the area under the breakthrough curve S'(t') must be unity. The numerical mean breakthrough curves (mean BTCs) can be integrated up to t'=40. Only at Z'=5.4 breakthrough is completed in all but the most heterogeneous soil before t'=40. Mass balance errors in the Monte Carlo mean BTCs range from +1% to +5%. The mass-balance in the numerically evaluated analytical BTC (9-11) is accurate to within less than 0.1%. For Z'=11.6, the analytical ensemble solute flux moments (9-11) and the numerical sample solute flux moments are plotted in Figure 9.9 (as solid and dashed lines, respectively).

Numerical simulation results. For both isotropic and anisotropic soils, the mean BTC increases with soil heterogeneity (Figure 9.9a,b). The increased spreading is associated with lower and much earlier peak solute flux. In the isotropic soils, peak solute flux decreases from 0.25 to 0.06 as the variance of f increases from 0.11 to 3.62. In the anisotropic soils of

equivalent heterogeneity solute breakthrough is less disperse with higher peak concentrations. At σ_f^2=0.95, peak solute flux is 0.10 in the isotropic wet soil and 0.15 in the anisotropic (ν=6) wet soil. At σ_f^2=3.6, peak solute flux has reduced to 0.06 and 0.08, respectively. Very similar breakthrough is observed for the two pairs of wet and dry soils with similar σ_y^2 (Figure 9.9d). The dry soil #15 has a slightly more peaked breakthrough than #28, owing perhaps to its 17% smaller σ_y^2. In contrast, dry soil #21 shows a more smearing than wet soil #22, even though their σ_y^2 are identical. Some of the difference may be attributed to the 7% mass balance difference between #21 and #22 (#22 is the only soil with a relatively high mass balance error: +12%).

The skewness and spread of the mean BTC is reflected in the skewness and spread of the standard deviation of the solute flux (Figure 9.9e-h). The peak standard deviation does not decrease as rapidly with increasing σ_f^2 as the mean BTC, suggesting an increase in the solute flux coefficient of variation as the soils become more heterogeneous. The shape of the standard deviation curve (STDC) is almost bimodal with a small secondary peak after the maximum standard deviation occurred. The bimodality is more pronounced in the isotropic soils than in the anisotropic soils. Also in the isotropic soils, both peaks in the STDC occur before the mean BTC reaches its maximum (except in the soil with σ_f^2=0.11). In the anisotropic soils, the peak of the mean BTC falls between the two maxima of the STDC (Figure 9.9f). As for the mean BTC, little differences are observed in the STDC between the soils of the two wet/dry soil pairs (Figure 9.9h).

Comparison to analytical results. Surprisingly, perhaps, there is a good visual agreement between the sensitivity of the theoretically determined and the numerically obtained BTCs and STDCs to the variations of the soil hydraulic conductivity variance, change in soil water tension, and change in anisotropy (Figure 9.9). All theoretical BTCs are less disperse than the numerical results with a peak solute flux that is generally between 15% and 30% larger. Larger differences occur in soils with more heterogeneous flow patterns. Only in the

driest soil (#21) the difference exceeds 30% (approx. 70% more peak solute flux). The theoretical standard deviation is approximately twice as large as the numerical standard deviation with a tendency to a greater difference at low σ_f^2 and low ν. Both numerical and analytical STDC are much broader than the respective mean BTCs suggesting a very high uncertainty about the prediction of the frontal breakthrough and tailing of the mean plume. The bimodality of the STDC is not observed in the analytical results. The general observations made for the BTCs and STDCs at Z'=11.6 (Figure 9.9) are also made at other depths of the CL (an example is shown in Figure 9.10)

The smaller spreading of the mean theoretical BTC curve (when compared to the simulation results) is consistent with the observed difference between the longitudinal spatial moments from the analytical stochastic macrodispersion analysis and the numerically determined spreading of the mean concentration plume, the latter of which is generally found larger. As mentioned above the differences can be attributed to the first order approximations assumed in the derivation of (9-11). Note that the illustration of the numerical and analytical results of the least variable soil (wet, isotropic, σ_f^2=0.01) are omitted. For that soil site the analytical results show a very sharp peak, which is approximately twice as large as the numerical result. However, in the latter local dispersion plays a considerable role in the overall plume spreading since the spatial variability of the velocity field is almost negligible.

9.4.2 Local Compliance with Maximum Contamination Flux Levels

This section is concerned with the statistics of local solute breakthrough in contrast to the integrated breakthrough investigated in the previous section. The arrival time t_a of the compliance solute flux s_0 and the solute flux peak passing time t_p are used as parameters to describe the frontal part of the breakthrough curves at each location x of the CL (recall that x is defined for a line only). In fact, t_p is only a particular aspect of the t_a function. The choice

of these two parameters, instead of the entire local BTCs, has several advantages. The computational effort of storing and evaluating these data in a Monte Carlo simulation is orders of magnitudes smaller than the statistical evaluation of the local BTCs(x). In the numerical simulation, t_p is defined simply as a function of location and is therefore a very small array containing the same number of elements as a single row in the simulation domain. The arrival time t_a is also defined as a function of horizontal location on the CL, but it is parametrized with respect to the compliance solute flux. t_a is compiled for 19 levels of dimensionless solute flux s/s_0, varying logarithmically from 10^{-9} to 1. Hence, t_p is essentially a function defined for the two-dimensional plane $(x,s/s_0)$. Computationally, these are 19 times the amount of data stored for t_p. In contrast, the information of a solute BTC at (x,t), recorded for every time-step, takes as many data as there are time-steps for each grid-node on the simulated CL. These time-steps vary from realization to realization depending on the maximum Courant number (automatic time-stepping, chapter 5). For the assembly of the sum and sum of square arrays of these data variables (see above), the individual BTCs have to be interpolated onto a regular grid of the time-axis.

To illustrate the conceptual link between the arrival time function $t_a(x,s/s_0)$, the peak time function $t_p(x)$, and the BTC function $s/s_0(x,t)$, recall that all are functions in the same three-dimensional space defined by the real variables s/s_0, x, and t. The BTC function $s/s_0(x,t)$ has a unique solution for each (x,t) and can be visualized as a longitudinal (parallel to the t coordinate) trending "mountain" bulging above the (x,t) plane. The BTC function can be uniquely mapped by projecting the mountain onto a contour map in the (x,t) plane. In contrast, neither the function $t(x,s/s_0)$ nor the function $x(t,s/s_0)$ have unique solutions. For each x, s/s_0 is obtained twice (in the front and in the tail of the BTC(x) i.e. one can look at the mountain from the front or the back). And at each time, s/s_0 is obtained twice along the CL (to the left and to the right of the center of the breakthrough i.e. one can look at the mountain from the left or the right side). But if the three-dimensional cube spanned by $\mathbf{R}^3(s/s_0,x,t)$ is sliced such that

$t(x,s/s_0)$ has only a single solution (in other words by deciding that one is only interested in the shape of the mountain as it is seen either from the front or the back), either the frontal part of the solute flux "mountain" or the tail part of the solute flux "mountain" can be projected onto a contour map in the $(x,s/s_0)$ plane of the cube. The $t_a(x,s/s_0)$ function is the frontal projection of the solute flux "mountain". And $t_p(x)$ is the contour in the (x,t) plane along which the cut was made.

In the statistical analysis, there is a fundamental difference, however, between the mean BTC(x,t) function and the mean $t_a(x,s/s_0)$ function and their associated variances. The former will average the solute flux at a particular time and location, while the latter will average the time associated with a particular location and solute flux. From the analysis of the spatial mean concentration it has become obvious that the concentration not only has a truncated, but also highly skewed pdf as evidenced by the outlier problems. The meaning of averages and variances of non-Gaussian pdfs is questionable. In contrast, the pdf of the arrival time is not truncated (a zero arrival time is impossible) but it has the difficult property that arrival time is not necessarily defined for every location x and every solute flux s/s_0. At distance x certain solute fluxes s/s_0 (and any higher flux) never occur. From realization to realization, arrival time may or may not be defined for the location x and level s/s_0. In statistical terms, the empty set $\{\varnothing\}$ must be assigned a certain probability. While this poses difficulties in approaching the problem theoretically, an approximate solution for the numerical sampling in a finite sampling space (number of realizations) can be constructed by simply ignoring those samples at $(x,s/s_0)$ that are not defined. In the Monte Carlo simulation, a zero is added to the sum and sum of square arrays, if no solute flux ever occurred at a certain level and location during a particular transient transport realization. In addition a counting file is kept to count the number of occurrences of $t_a(x,s/s_0)$, which is equal to or smaller than the total number of realizations. The resulting sums and sums of squares are eventually divided not by the number of realizations but by the number of occurrences of $t_a(x,s/s_0)$.

Thus not only an average time and time variance is obtained, but also a histogram of the probability that s/s_0 is exceeded at location x, which is in essence an inverse cumulative distribution function ("iCDF" = 1-CDF) for s/s_0. Obtaining a iCDF for solute flux is extremely important for many regulatory purposes, which deal with the likelihood that a certain contamination level is ever exceeded after the installation of a potential contamination source or after completion of site remediation. In addition, the physical meaning of "expected time of solute flux exceedance" and the variability of the arrival time is in many instances more significant than the "expected solute flux at time t" and its potential variability. The probability of arrival time of a certain solute flux level is similar to assessing the probability that a solute particle originating from a contamination source will arrive within a certain time-frame. Many regulatory statutes require that a certain contamination level may not be exceeded at any given time after installment of a potential pollution source, or that certain contamination levels are unlikely to occur for X number of years after installment of the potential pollution source (Neuman, 1991). Such measures can be formulated as conditional probability measures of time of exceedance given a solute flux ($pdf(t_a)|s/s_0$) or as conditional probability measures of solute flux levels given a time ($pdf(s/s_0)|t_a$).

The evaluation of the local solute breakthrough is essentially complimentary to the spatial analysis of the concentration mean and variance. The results are expected to be analogous to the findings of the previous sections. The numerical evaluation of the arrival time of peak solute flux is shown in Figure 9.11 for the first, third, and last soil categories. All times are normalized with respect to the mean residence time Z/V_z. The average peak arrival time occurs earliest for the least heterogeneous soils (isotropic, wet, σ_f^2=0.01, 0.11), since the BTC in these soils are least skewed (Figure 9.11a, see also Figure 9.9a). Not much difference in $<t_p>$ is seen between these two soils. Notice that the peak arrival time for the highly heterogeneous soil (isotropic, wet, σ_f^2=3.62) is significantly later than for the other three soils. The peak solute flux occurs later at location on the CL further away from its center (where the

center x=0 is defined as being located vertically underneath the center of the plume source). The shape of the t_p contour is not very sensitive to soil heterogeneity indicating that the delay in peak arrival time at a location x (with respect to the $<t_p>$(x=0)) is the same no matter how heterogeneous the soil. With respect to the shape of the $<t_p>$ line, the anisotropy ratio of the soil is much more significant (Figure 9.11b). At higher anisotropy, the peak time on the sides of the CL will occur earlier than in isotropic soils due to the stronger horizontal spreading of the solute plume. Again the differences between dry and wet soils are insignificant if the flux field has a similar variability (Figure 9.11c). For all soils the variance of the peak arrival time does not vary with horizontal location, even though the mean arrival times are larger at larger x. The variance increases mainly with σ_f^2 and decreases only slightly with higher anisotropy (Figures 9.11d-f).

The mean arrival $<t_a>$ map, a front view or projection into the $(x,s/s_0)$ plane of the solute flux "mountain" generally has the expected behavior that a given solute flux level is exceeded earlier towards the center of the CL and later as |x| increases. The higher the solute flux level, the later it will on average be exceeded (Figure 9.12). Note that the solute flux is plotted on a logarithmic scale. Except for the very highest solute flux levels (the only ones distinguishable in the BTCs of Figure 9.9, where solute flux is plotted on an arithmetic scale), the mean time of first exceedance of a solute flux level is significantly earlier than 1. The mean arrival time (relative to the average residence time Z/V_z) for the lowest solute flux level ($s/s_0=10^{-9}$) is between 0.45 and 0.55 for all investigated soils. Only in isotropic soils with $\sigma_f^2<1.0$ the mean arrival time for any solute flux level never drops below 0.5. The mean arrival times increase in an almost linear fashion radially away from the ($x=0,s/s_0=10^{-9}$) point. For higher variances and larger anisotropies the shape of the "mountain" becomes broader (but not flatter owing to the log scale on the vertical axis). With increasing anisotropy and increasing σ_f^2, the earliest arrival time for the low solute flux levels decreases everywhere on the CL, although $<t_a>$ shows very little sensitivity in the anisotropic soils at x=0, once $\sigma_f^2 \geq 0.95$.

The highest solute flux levels are reached in the least variable soils, while the maps for the most highly variable soils (Figure 9.12e,f) prove that outliers are observed not only on the slow travel time end (see section 9.3), but also on the fast travel time end of time scales. In a reversion of the general trend that higher solute fluxes occur later, the highest solute fluxes in the three soils with $\sigma_f^2 > 0.9$ occur on average earlier than some lower flux levels. Since these high flux levels are associated with low likelihoods (see below), they can only be attained if the solute source is in a preferential flow area, which displaces the plume relatively fast past the CL. Due to the varying number of samples underlying the sample mean and sample variance, the estimation errors of the sample mean and sample variance of t_a may vary significantly and are expected to be high near the margin of the map, where the likelihood of exceedance is least. The more variable the soil, the more erratic are the contour lines of both the $<t_a>$ and the CV_{ta} maps (Figure 9.12 and 9.13).

The coefficient of variation CV_{ta} of solute flux exceedance time shows that the highest uncertainties are about the arrival times of the lowest solute flux levels at the center of the CL (Figure 9.13). The only exception are the two, mildly heterogeneous, isotropic soils (Figure 9.13a-b), where the CV_{ta} increases first and then decreases again, with larger distance form the center of the CL. Clearly, the CV_{ta} rises with soil variability. For the isotropic, wet soil with σ_f^2=0.11, the CV_{ta} varies from 0.3 to 0.5 (Figure 9.13a). In the anisotropic soils with σ_y^2=3.2, the CV_{ta} varies from 0.5 near the edges to 1.1 in the center of the CL (Figures 9.13e-f). Anisotropy decreases the uncertainty about the mean arrival time considerably for soils of comparable variability in σ_f^2. The observed decrease of uncertainty towards the edges of the "mountain" must be seen in connection with the decreasing likelihood of such solute fluxes ever to be exceeded. Figure 9.14 gives the sample probability that a solute flux level is ever exceeded. Each curve presents the iCDF of solute flux at a particular location x of the left half of the CL. Like the mean $<t_a>$, the iCDF is symmetric to the center of the CL. The rightmost curves represent the highest likelihood for the highest solute flux levels and are associated with

x=0. Each curve further to the left in the graphs of Figure 9.14 is for an increasing distance x from the center. The interval between locations x of neighboring iCDF plots is indicated as Δx. The iCDF is steepest for the soils of lowest variability indicating the least variance in solute flux. At each soil, the steepest iCDF is observed for the center location, which has the highest mean (rightmost curve) and the least variance. The further away from the center of the CL, the lower the mean solute flux and the smaller the slope of the iCDF, hence the larger the variance. Note that these plots are on a logarithmic scale for s/s_0. For a relatively homogeneous soil (Figure 9.14a), the iCDF is relatively symmetric with respect to the geometric mean s/s_0, and solute flux is lognormally distributed. At higher variances the top part of the slope of the iCDF decreases with a longer tail towards lower solute flux levels, indicating that on a logarithmic scale for s/s_0, the probability distribution of s/s_0 (derivative of the iCDF) is significantly skewed. Skewness also increases with distance from the center.

9.5 Summary and Conclusions

In this chapter solute transport from local sources of small lateral extent in unsaturated soils with steady-state mean uniform flow conditions is analyzed. A number of numerical Monte Carlo transport simulations were implemented for a variety of soil conditions. The sensitivity of solute transport and the uncertainty of its prediction is investigated for soils of varying variability in σ_f^2 and σ_a^2, for soils with anisotropy ratios ranging from $\nu=1$ to $\nu=6$, for soils of different mean soil water tension H, and for soils with correlated and uncorrelated f and a parameters. Several different aspects of solute transport have been addressed: The dynamics of the mean concentration plume and of the concentration variance, the spatial inertia moments of the mean concentration plume, the mean inertia moments of individual plumes around their center of mass, and the variability of the center of mass of individual plumes. The spatial description of solute transport was contrasted with the temporal description of solute

transport i.e., the solute breakthrough at a compliance surface or compliance level (CL) some distance away from the solute source. The mean and variance of the total mass flux across the CL is determined and an alternative interpretation of uncertainty with regard to the arrival time of a solute at a compliance surface is offered. Instead of predicting the uncertainty about the solute flux level at a given time, the uncertainty about the time of first exceedance of a given solute flux level is stochastically determined.

In agreement with theoretical predictions by Dagan (1986), the prediction of a solute plume of small initial extension (relative to the correlation scale of soil heterogeneity) is associated with large uncertainties. For highly heterogeneous soils ($\sigma_f^2>2$) the mean concentration plume is of dimensions that have little to do with the actual size of the plume. For soils with an unsaturated hydraulic conductivity variance $\sigma_y^2 = 3.2$, the variability in the vertical and horizontal displacement of the plume center at t'=10 accounts for 71% and 55%, respectively, of the spreading observed in the mean concentration. As a consequence, the predicted average peak concentration is almost an order of magnitude lower. At $\sigma_f^2=1$ and t'=10, the vertical and horizontal variability of the plume center displacement still accounts for 61% to 68% of the longitudinal and for 47% to 42% of the lateral mean concentration spreading, with the former limit being for isotropic soils and the latter for anisotropic soils of aspect ratio 6. Large residual mean concentration at less than 20 correlation scales from the source for t'=40 is an important indication that the variability of the displacement of the plume center accounts for significant amounts of the prediction uncertainty even at travel distances larger than 40 correlation scales. This conclusion is confirmed by the significant variability of the solute mass flux across the bottom boundary (23 correlation scales from the source) at t'=40.

The numerical results are contrasted with linear theoretical models of stochastic transport in porous media. To describe the spatial moments of the solute plume, a linear macrodispersion model is developed for the two-dimensional unsaturated transport under

investigation based on the analytical flow model developed in chapter 4 (see also Yeh et al., 1985a,b) and on the linear macrodispersion theory by Dagan (1984, 1988). For the solute breakthrough at a compliance surface the first order perturbation analysis of unsaturated flow is applied to the travel time analysis developed by Dagan et al. (1992) and Cvetkovic et al. (1992). Analytical predictions of the mean solute breakthrough curve and the variance of total solute flux at the unsaturated CL are obtained as a function of time.

The linear macrodispersion theory predicts that for soils with identical $\lambda_f=\lambda_a$ and Γ, the second spatial moments are directly proportional to the theoretical unsaturated hydraulic conductivity variance σ_y^2, since the second spatial moment and σ_y^2 both grow with $\sigma = \sigma_f^2 (1+2\rho H' + H'^2)$, where $H' = \zeta\Gamma H$ is a dimensionless measure of the mean soil water tension. From these theoretical considerations it is expected that a direct proportionality between the spatial moments of the concentration and the unsaturated hydraulic conductivity does not exist, when either the aspect ratio of the correlation scales or the geometric mean of α (=Γ) changes. It does also not hold, if the correlation functions for f and *a* are not identical. Together with the findings in chapter 8 (λ_y does not decrease significantly with respect to λ_f as the soil water tension increases) both the numerical and analytical results presented here contradict the hypothesis by Russo and Dagan (1991) that $\lambda_{yz}\sigma_y^2 \approx \lambda_{fz}\sigma_f^2$ independent of the mean soil water tension (see also chapter 6).

The numerical simulations have shown that the longitudinal spatial moments of the mean concentration in anisotropic soils with moderate to high variability are indeed more or less proportional to the unsaturated hydraulic conductivity. In isotropic soils, however, no direct proportionality is found between X_{zz} and σ_y^2. Only the variance of the vertical (longitudinal) location of the center of plume position is in all soils found to be directly proportional to σ and hence to σ_y^2. Otherwise the accuracy of the linear macrodispersion theory is limited. The actual mean concentration spreading is found to be not only larger than predicted by the theory, particularly in anisotropic soils, but also in contrast with the very concept of

"macrodispersion". The latter is based on the pseudo-Fickian advection-dispersion model i.e., a Gaussian spatial concentration distribution. The numerical simulations, however, show that the spatial distribution of the average concentration is non-symmetric and highly skewed along the longitudinal axis due to the lognormally distributed vertical velocity component. For the anisotropic soils of moderate to high variability and aspect ratio 6, the actual longitudinal spreading is 60% to 80% larger than predicted.

Numerically computed transverse mean plume spreading and displacement variance of the plume centers also varies nonlinearly with σ_y^2. Transverse spreading of the mean plume far exceeds the predictions of the linear macrodispersion theory. Like for longitudinal spreading, this study finds that the difference between theory and simulation of transverse spreading increases as the anisotropy ratio becomes larger. In a dry soil with aspect ratio 6 and σ_y^2=3.2, the horizontal spreading of the actual (numerical) mean plume is almost one order of magnitude larger than predicted by the theory, and most of the spreading is due to variability in the horizontal plume center displacement. Except for the case of the least variable soil examples, the larger actual mean plume spreading cannot be explained by the effect of local dispersion, which has been neglected in the macrodispersion model. Rather it is the well-known limitation of the macrodispersion model itself, which explains the difference. The main assumption of the linear macrodispersion model is that a particle deviates only insignificantly from the mean travel path, which is obviously erroneous for highly heterogeneous soils (see Figure 9.2c).

Although not specifically addressed in this study, the results do not confirm the findings of Bellin et al. (1992) who concluded from their numerical studies of saturated flow that the erroneous effects of linearized flow and linearized transport may cancel each other. However, their study was limited to the isotropic case with $\sigma_y^2=\sigma_f^2 \leq 1.6$. For those conditions the results in this study also indicate a good match between the theoretical model and the numerical results. Only under anisotropic conditions large differences between theoretical and numerical

solutions are found, even in mildly heterogeneous soils.

The findings with respect to the underestimation of horizontal spreading are consistent with Rubin (1990), Neuman and Zhang (1990), Tompson et al. (1990), and Zhang and Neuman (1994c). However, the same authors come to the conclusion that the linear macrodispersion model will overpredict longitudinal spreading of the mean concentration. Again, this is in contrast to the results here, where the macrodispersion model generally underestimates the longitudinal macrodispersion. The differences are attributed to the different anisotropy structure modeled here. The above mentioned papers model groundwater transport in isotropic and anisotropic porous media, where the mean flow is generally assumed to be parallel to the direction of strongest correlation. In contrast, mean flow in this study is normal to the direction of strongest correlation. Together with the results of Bellin et al. (1992) this may be an indication that the linear macrodispersion model best predicts transport in isotropic porous media, underpredicts longitudinal spreading for $\lambda_l/\lambda_t<1$ and overpredicts longitudinal spreading for $\lambda_l/\lambda_t > 1$, where λ_l/λ_t is the ratio of the correlation scales in longitudinal and transverse direction of mean flow.

Similar differences occur in the estimation of the spreading of the mean breakthrough curve across the CL. The theoretical model by Cvetkovic et al. (1992) based on lognormal two-particle joint travel time pdfs with first order parameters, underestimates the spreading of the mean breakthrough curve observed in the numerical simulation. It is generally very accurate in predicting the front end of the mean BTC, but overestimates the peak concentration by 15% to 30% and in highly heterogeneous soils up to 70%. All numerically obtained mean breakthrough curves exhibit considerably more tailing than predicted by the theory. The theory overpredicts the variance of the solute flux by a factor 2 resulting in conservative estimates of the uncertainty (measured in terms of the coefficient of variation) about the solute flux at time t. Overall I conclude that the linear macrodispersion model as well as the travel time model adopted here for unsaturated flow conditions will give reasonable estimates of the mean

concentration in space and mean solute flux across CL, if the purpose is to obtain rough estimates of the mean concentration plume and the mean BTC. For predicting uncertainties associated with extreme events (e.g., early arrival) or associated with very small concentrations, the theoretical models are insufficient.

The statistical analysis of the first time or arrival t_a of exceedance of a given solute flux s/s_0 at a location x of the CL has yielded additional insights into the stochastic behavior of solute transport. Not only is it a very attractive and efficient alternative to the numerical Monte Carlo evaluation of the local BTC(x). It also offers an important practical tool to predict the mean and uncertainty about the time when a given compliance level will be exceeded, an approach that has in the past neither been addressed theoretically nor numerically. The analysis of travel time variability that is suggested here also yields probability distribution functions for the likelihood that a given solute flux level will ever be exceeded at location x of the CL. However, it does not indicate for how long the compliance level is exceeded or what the total mass flux will be at x. The empirical sample probability of exceedance of solute flux levels has a form best described as a slightly skewed quasi-lognormal Gaussian CDF. The average $<t_a(s/s_0)>$, the time of first exceedance of s/s_0, shows that the same solute flux levels are reached later as the distance from the center of the CL increases. The least uncertainty is associated with predicting the arrival time of the highest solute flux levels at a location x, since high solute flux levels can only be attained, if the travel path is fairly direct and undistorted and hence, the travel time is relatively short (physical constriction). This must not be confused with the likelihood that such high solute flux levels occur. Indeed the high flux levels are the least likely. A weakness of the numerical approach to arrival time analysis is that the number of samples decreases with larger x and larger s/s_0. The statistical sample moments of t_a and t_p have therefore increasing sample error. Note that this type of analysis is different from the numerical or Lagrangian travel time analysis of particles such as e.g. in Smith and Schwartz (1981a) and Cvetkovic et al. (1992).

In light of the high variability of the plume center displacement, the strong skewness of the mean concentration plume, the non-Gaussian distribution of the concentration RFV c(x,t), and the very long travel times required for ergodicity to occur, the fundamental problem highlighted in this chapter is the high uncertainty of predicting solute transport with *any* unconditional stochastic model for unsaturated transport, if the soil flux variability becomes large ($\sigma_y^2 \geq 1$). The differences between the stochastically more accurate numerical simulations and the predictions of the macrodispersion and travel time theories may seem minor compared to the differences between the mean predictions and actual values of concentrations and solute fluxes. The conditional simulation approach introduced in the next chapter offers an alternative to the unconditional stochastic models applied in this chapter. But the detailed information obtained in this chapter about the variability of solute transport from small sources - under very idealized conditions - is in agreement with the empirical results reported in numerous field studies: It is generally difficult to model or predict the actual transport behavior of a solute in a heterogeneous soil to a high degree of accuracy.

Table 9.1

Input parameters for the various hypothetical soil sites used in the unconditional transport analysis: σ_f^2: variance of f=logK_s (log: natural logarithm), σ_a^2: variance of a = logα, ρ_{af}: correlation coefficient between f and a, Γ: geometric mean of α, Δx: horizontal discretization of finite elements, Δz: vertical discretization of finite elements, λ_{fx}: horizontal correlation length of f, λ_{fz}: vertical correlation length of f.

name	σ_f^2	σ_a^2	ρ	Γ	H	Δx	λ_x	cut
#3	**1.0**	**0.01**	**0**	**0.01**	**-150**	**10**	**50**	**5**
#2	0.01	10^{-4}						2
#4			1					5
#8	0.12							5
#9	4.0	0.04						10
#12			1			30	300	5
#15					-1000	30	300	5
#21			1		-3000	30	300	10
#22	4.0	0.04				30	300	10
#28	2.25	0.04				30	300	5
#29						30	300	5
#31						15	150	5

Table 9.2

Dimensionless distance z/λ_{fz} between the location of the minimum CV_c and the location of the maximum <c> as a function of dimensionless time $t'=tV_z/\lambda_{fz}$. The minimum CV_c is always located below the maximum <c> i.e., is travelling at a faster rate. Dimensionless times in parentheses refer to soil site #28.

soil type	σ_y^2	ν	t' = 5 (4)	t' = 10 (8)	t' = 20 (16)
#2	.01	1	0.0	0.0	0.0
#8	.10	1	0.1	0.0	0.0
#3	.85	1	0.8	0.6	0.4
#9	3.4	1	2.6	5.2	14.8
#31	.75	3	0.8	1.0	3.2
#12	.53	6	0.4	0.4	1.2
#29	.79	6	0.4	0.6	1.8
#15	1.5	6	0.8	1.6	1.4
#28	1.8	6	0.8	1.8	4.8
#22	3.2	6	2.6	9.6	5.2
#21	3.2	6	4.2	8.6	4.8

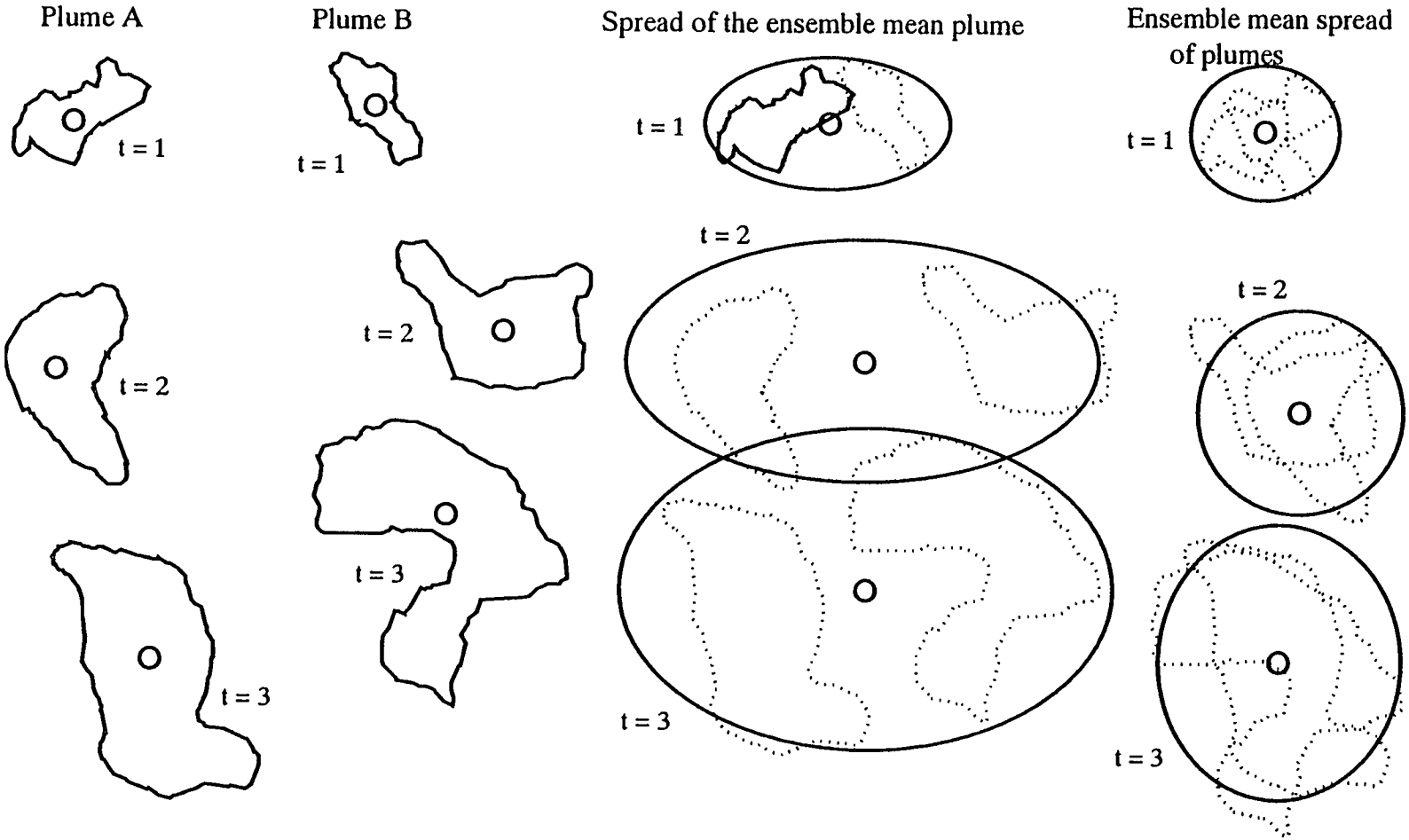

Figure 9.1: Spreading M of individual realizations of solute plumes, spreading X of the ensemble mean plume, and ensemble mean spreading <M> of plumes in steady state, statistically homogeneous porous medium.

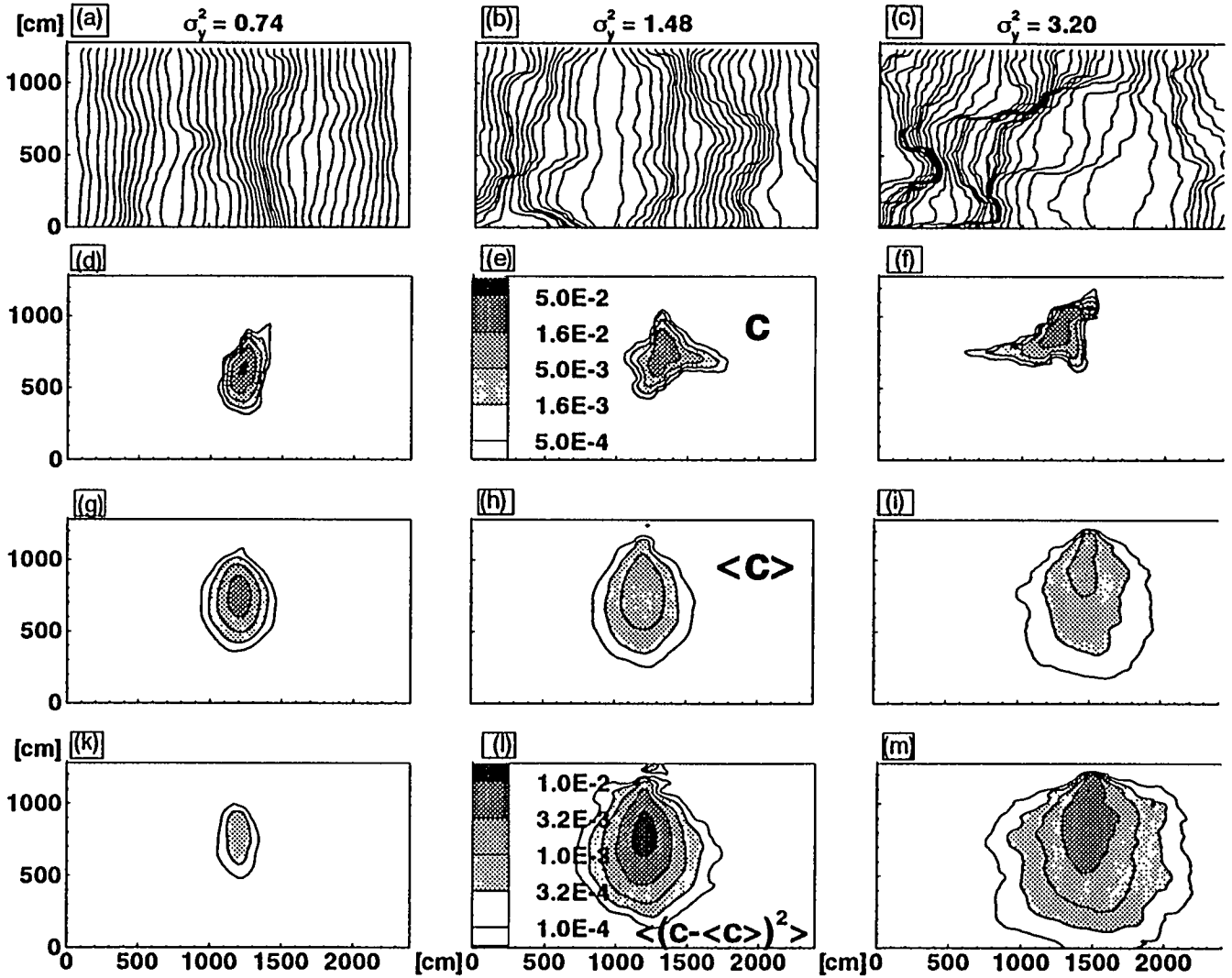

Figure 9.2: Single realizations of streamlines (a,b,c), corresponding realization of concentration levels at t'=10 (d,e,f), sample mean concentration (g,h,i) and sample concentration variance (k,l,m) for the three soils: #29 (left column), #15 (center column), and #22 (right colum).

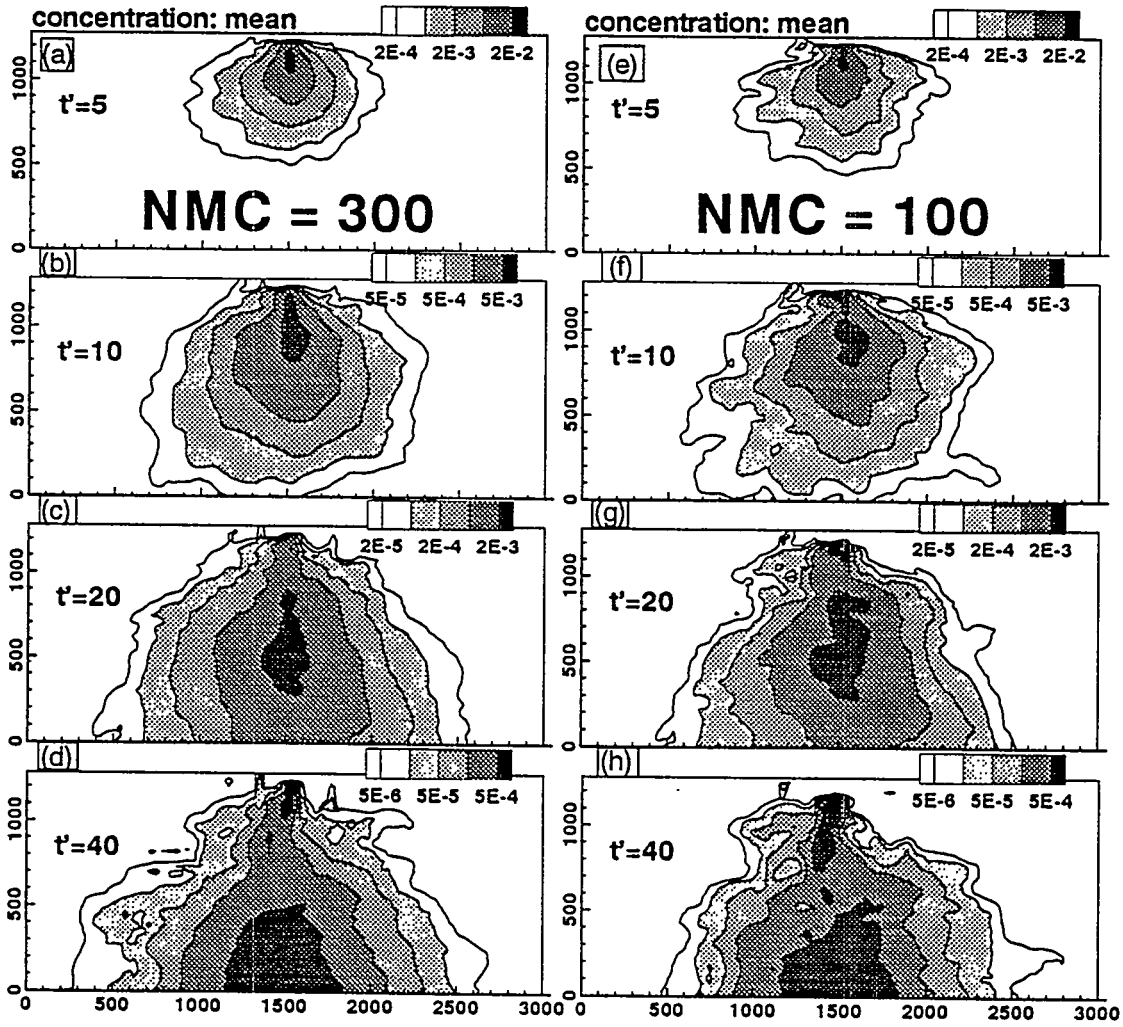

Figure 9.3: Sample mean concentration after 300 realizations (a-d, left column) and after only 100 realizations (e-h, right column) of transport in a strongly heterogeneous flow field (soil site #21, $\sigma_y^2 = 3.2$).

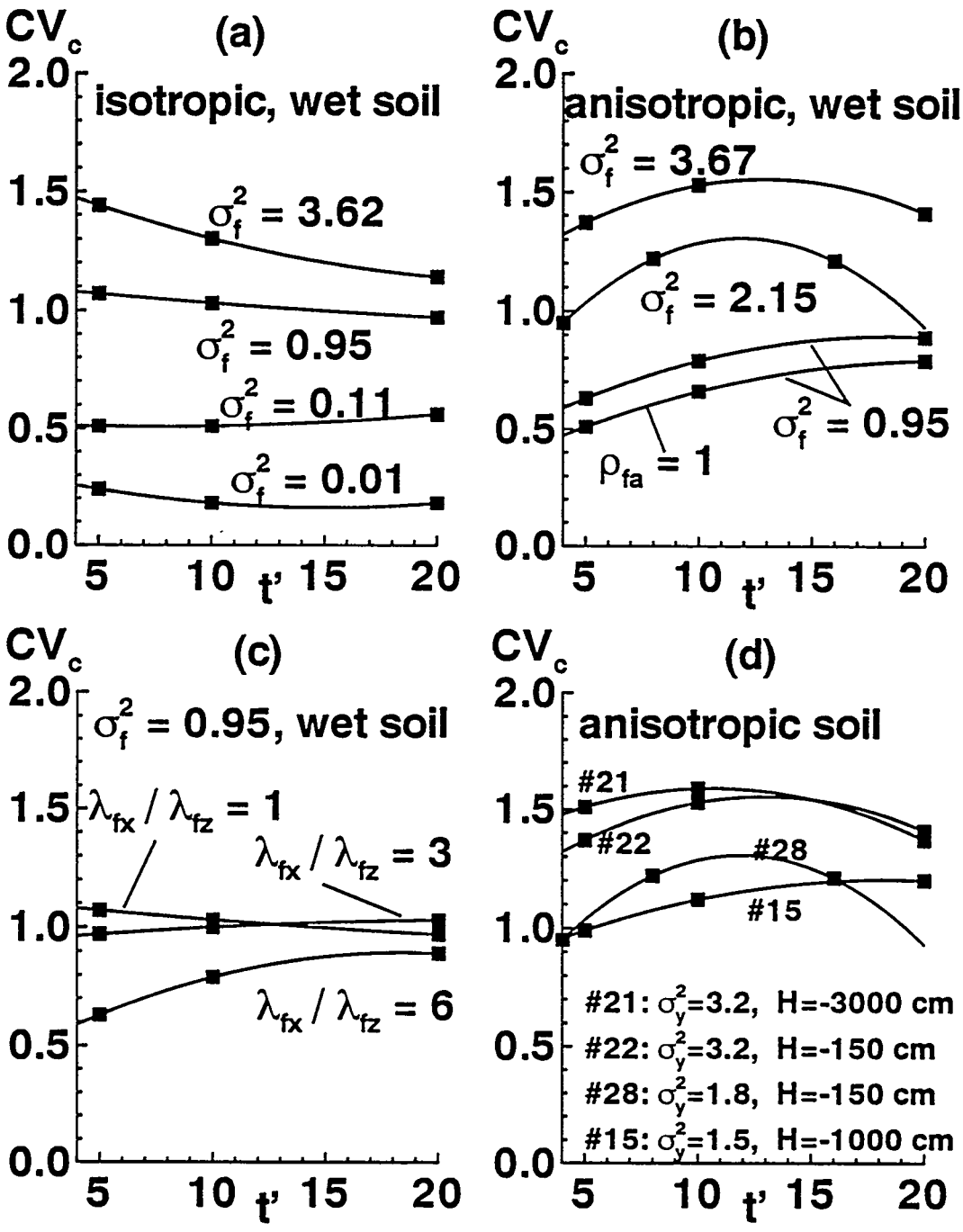

Figure 9.4: Minimum concentration coefficient of variation at or near the center of the mean plume. Except where indicated, f and a are not correlated ($\rho_{fa} = 0$).

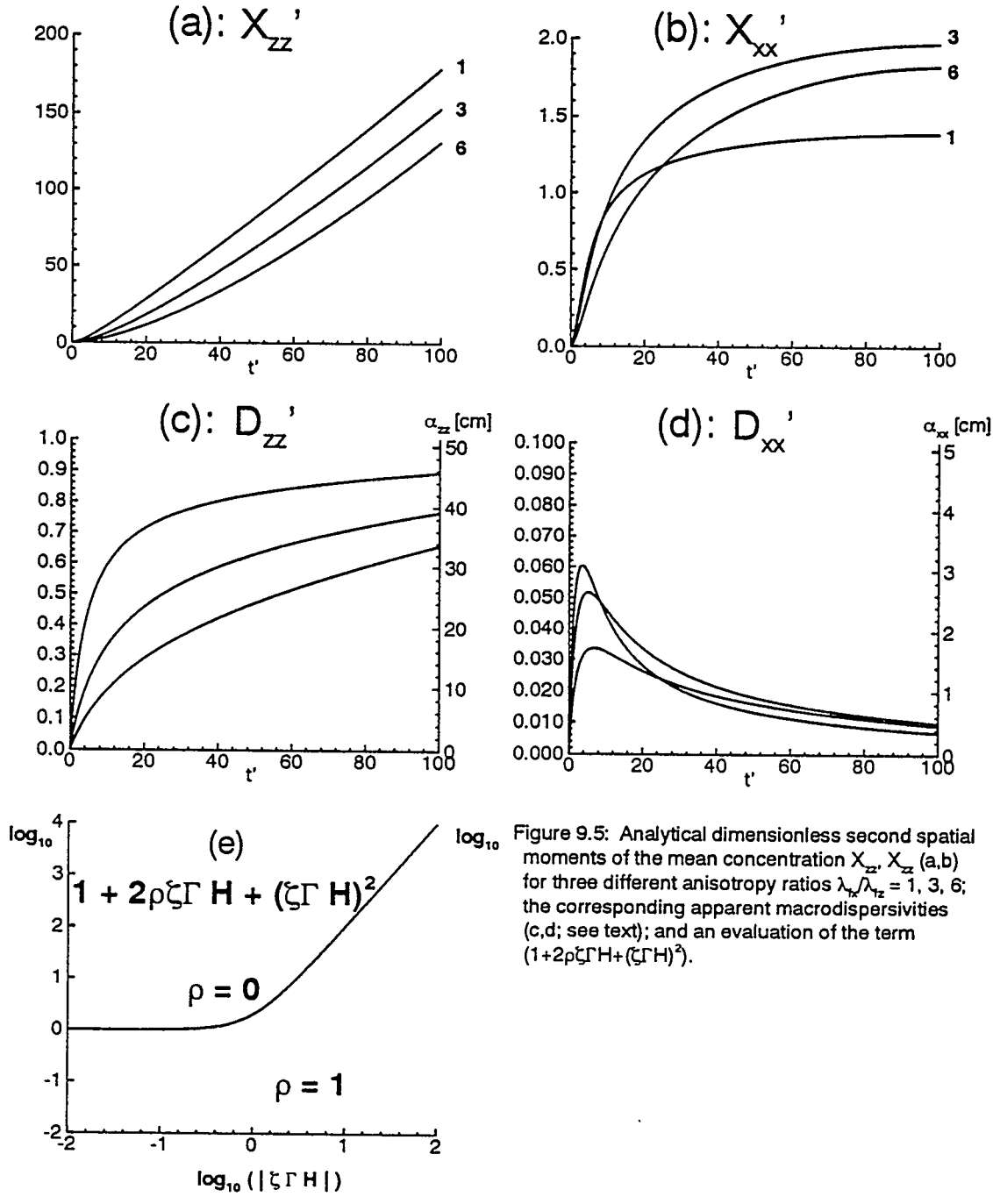

Figure 9.5: Analytical dimensionless second spatial moments of the mean concentration X_{zz}', X_{xx}' (a,b) for three different anisotropy ratios $\lambda_{hx}/\lambda_{hz}$ = 1, 3, 6; the corresponding apparent macrodispersivities (c,d; see text); and an evaluation of the term $(1+2\rho\zeta\Gamma H+(\zeta\Gamma H)^2)$.

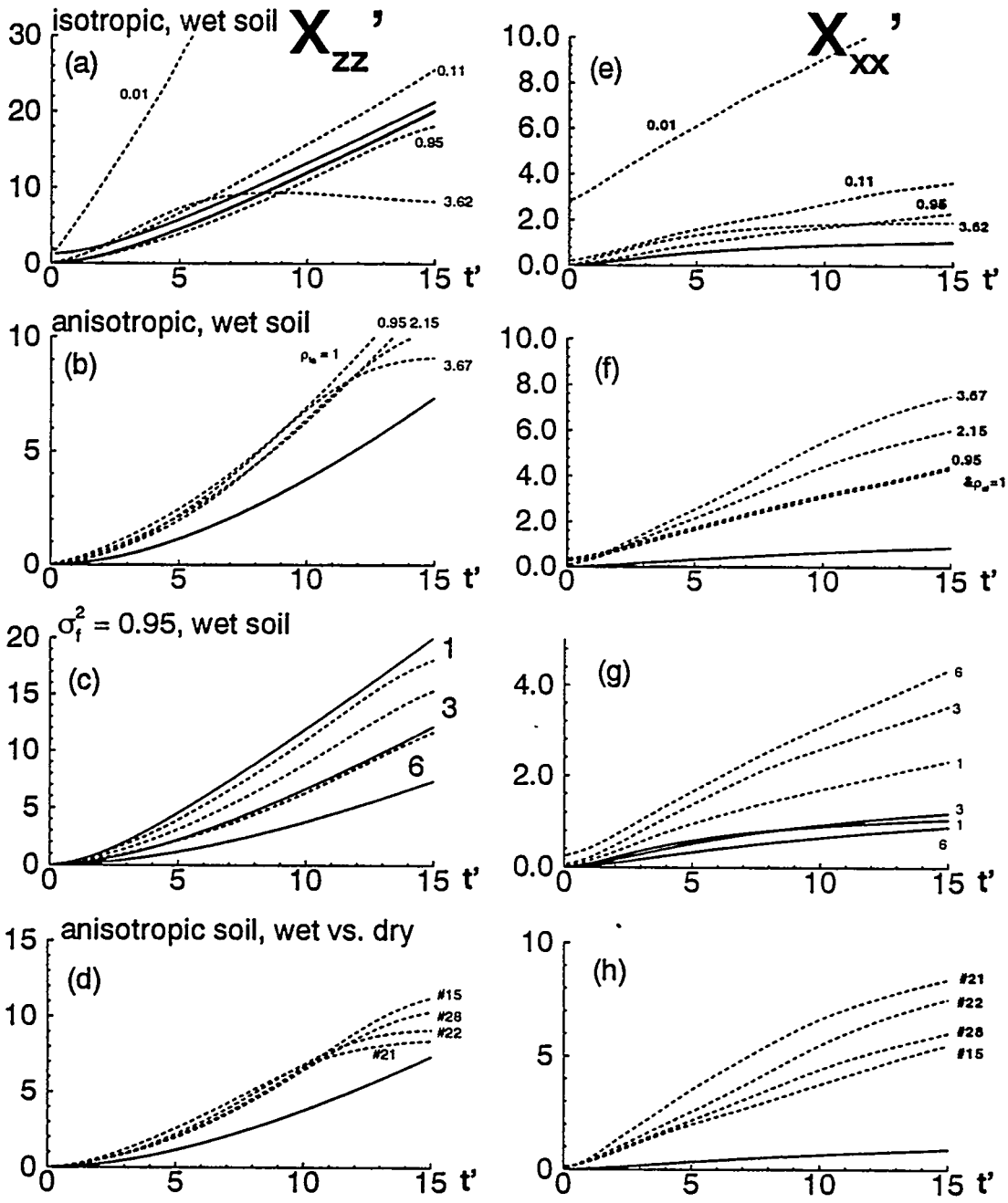

Figure 9.6: Vertical (a-d, left column) and horizontal (e-h, right column) mean concentration second spatial moment. Solid lines are analytical results, while dashed lines are from the Monte Carlo analysis. Labels are explained in Figure 9.4 and Table 9.1 (also see section 9.2.3).

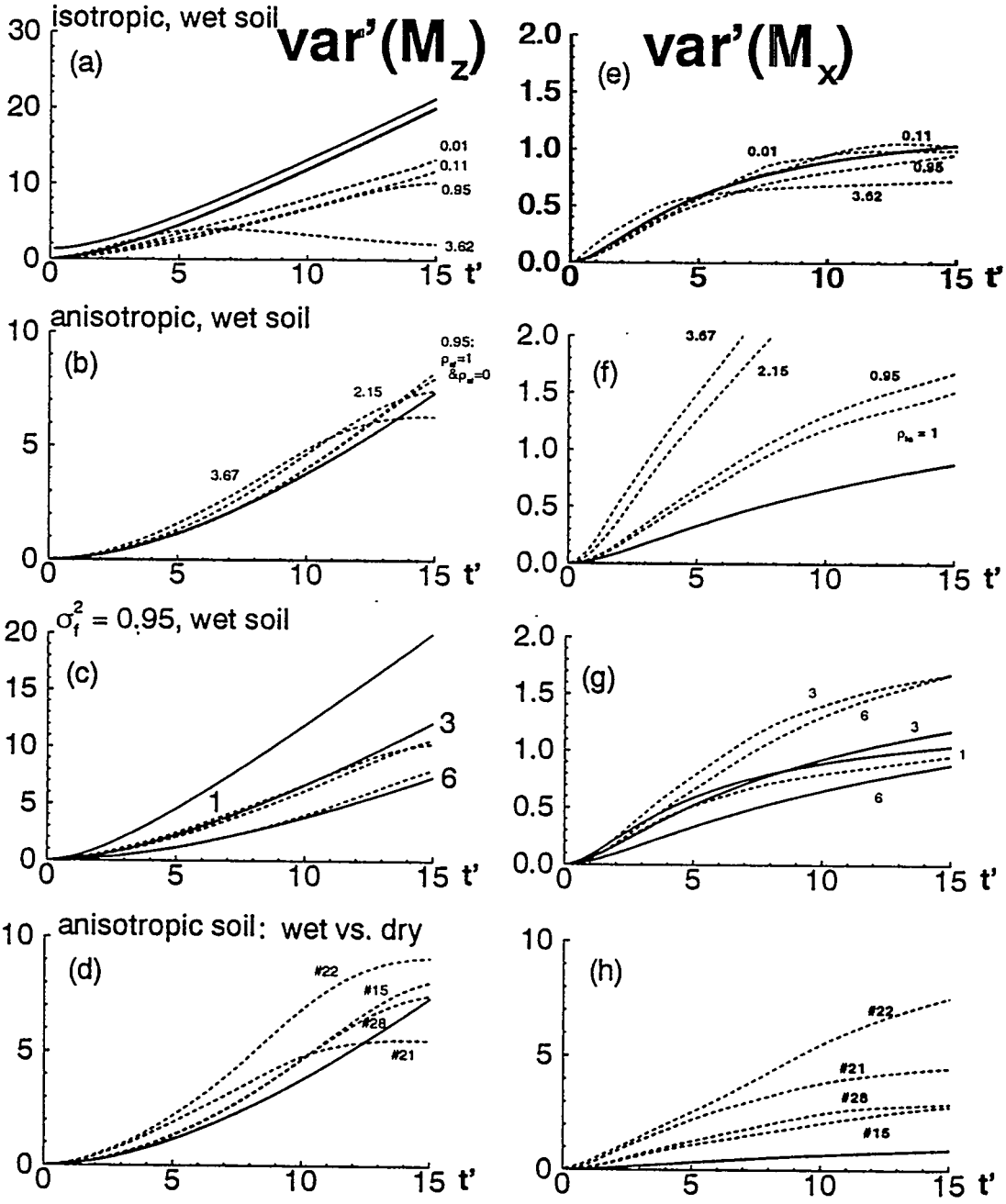

Figure 9.7: Vertical (a-d, left column) and horizontal (e-h, right column) variance of concentration center of mass. Solid lines are analytical results, while dashed lines are from the Monte Carlo analysis. Labels are explained in Figure 9.4 and Table 9.1 (also see section 9.2.3).

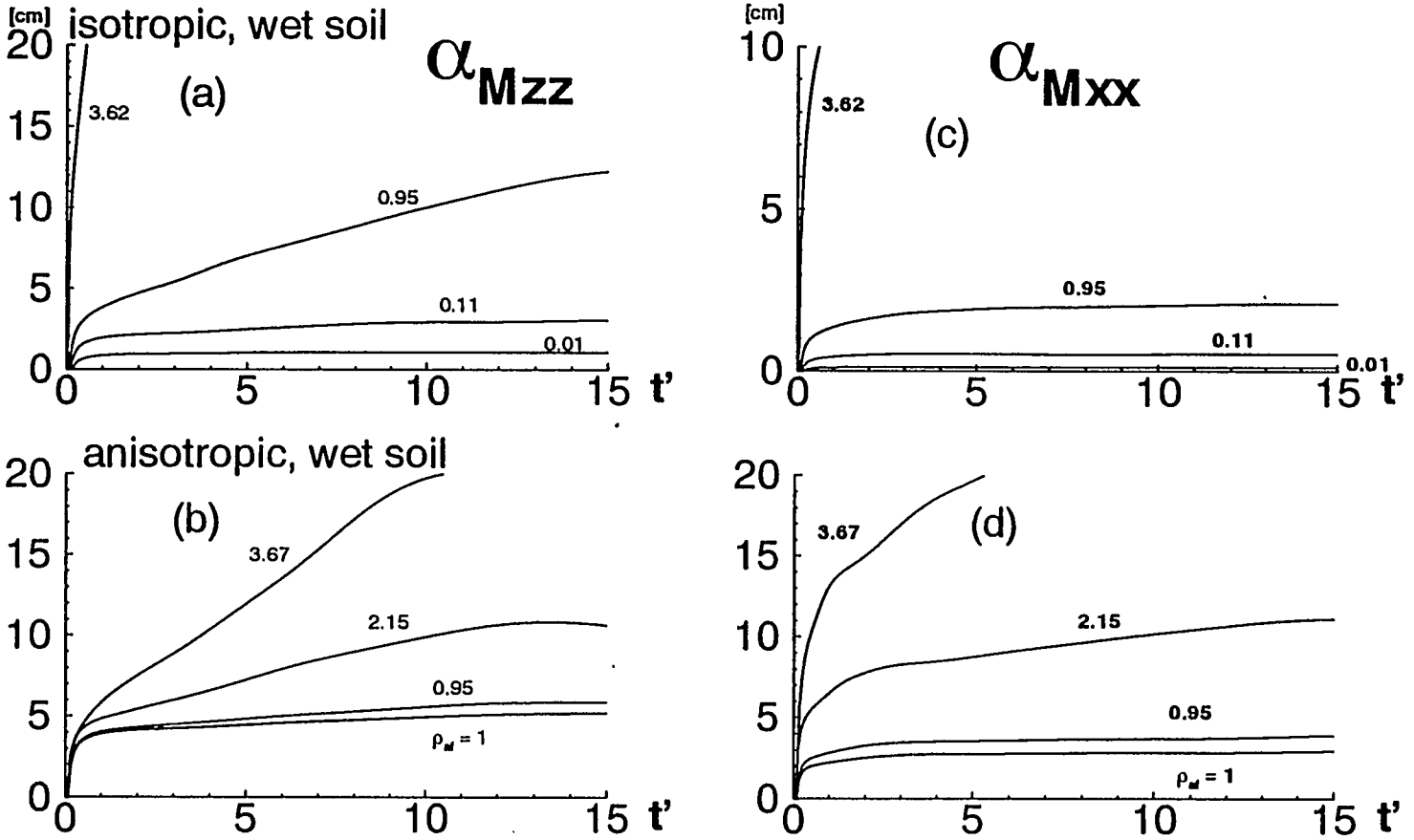

Figure 9.8: Vertical (a,b; left column) and horizontal (c,d; right column) mean apparent dimensional dispersivity in [cm] derived from the sample M_{zz} and M_{xx} of the Monte Carlo analysis. For labeling refer to Figure 9.4 and Table 9.1. For computation of α_{Mzz} and α_{Mxx} see text.

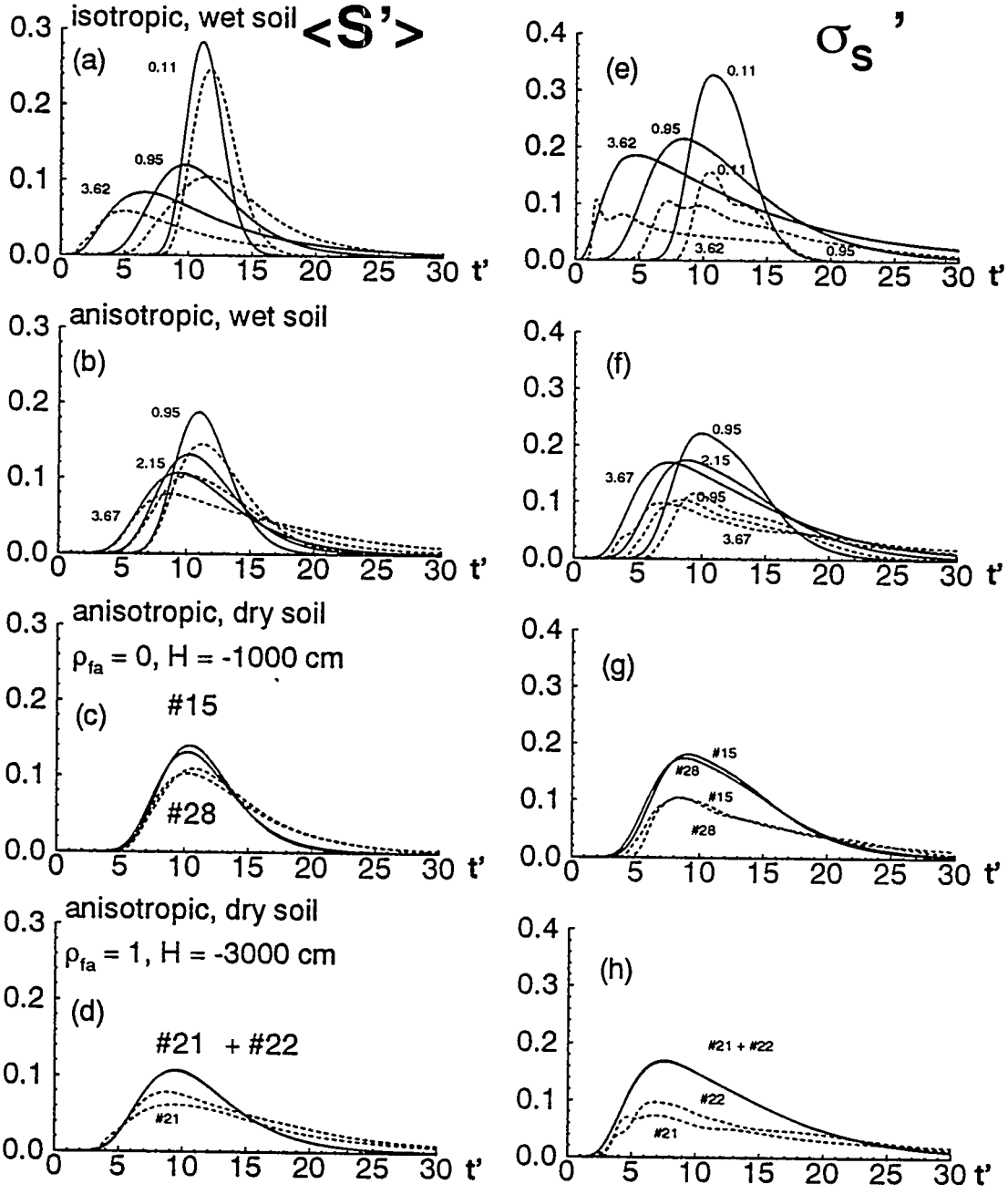

Figure 9.9: Mean solute flux (a-d; left column) and standard deviation of the solute flux (e-h; right column) at a distance z'=11.6 from the center of the source. Solid lines are the analytical model (eqn. 9-11), dashed lines are from the Monte Carlo analysis. For labeling refer to Figure 9.4.

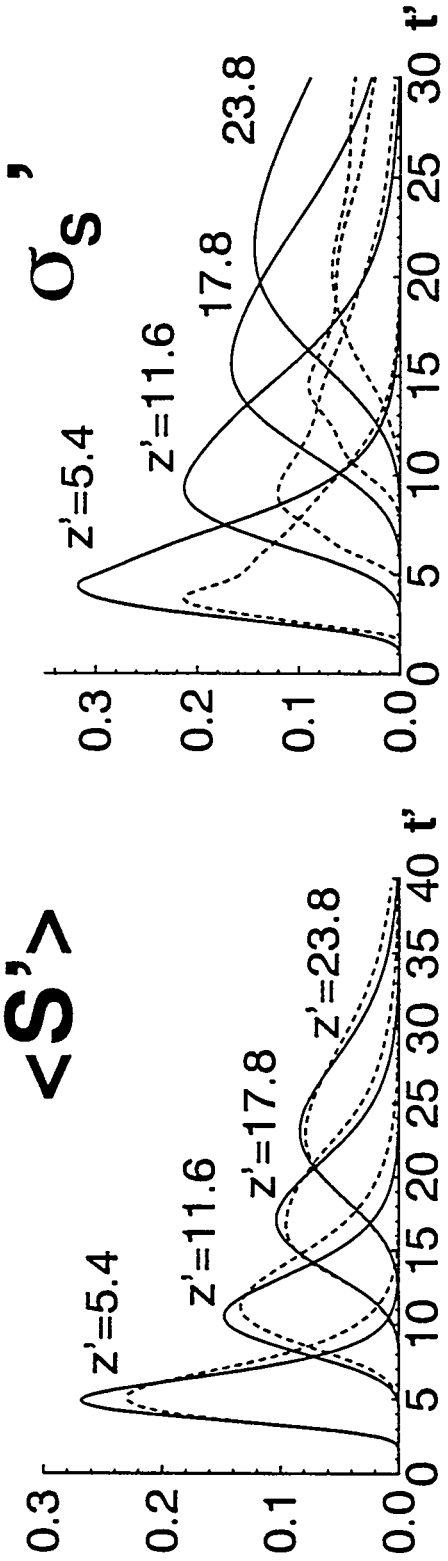

Figure 9.10: Mean solute flux and standard deviation of the solute flux at different distances z' from the center of the solute source. Soil #31: anisotropic, wet, $\sigma_f^2 = 0.95$, $\nu = 3$.

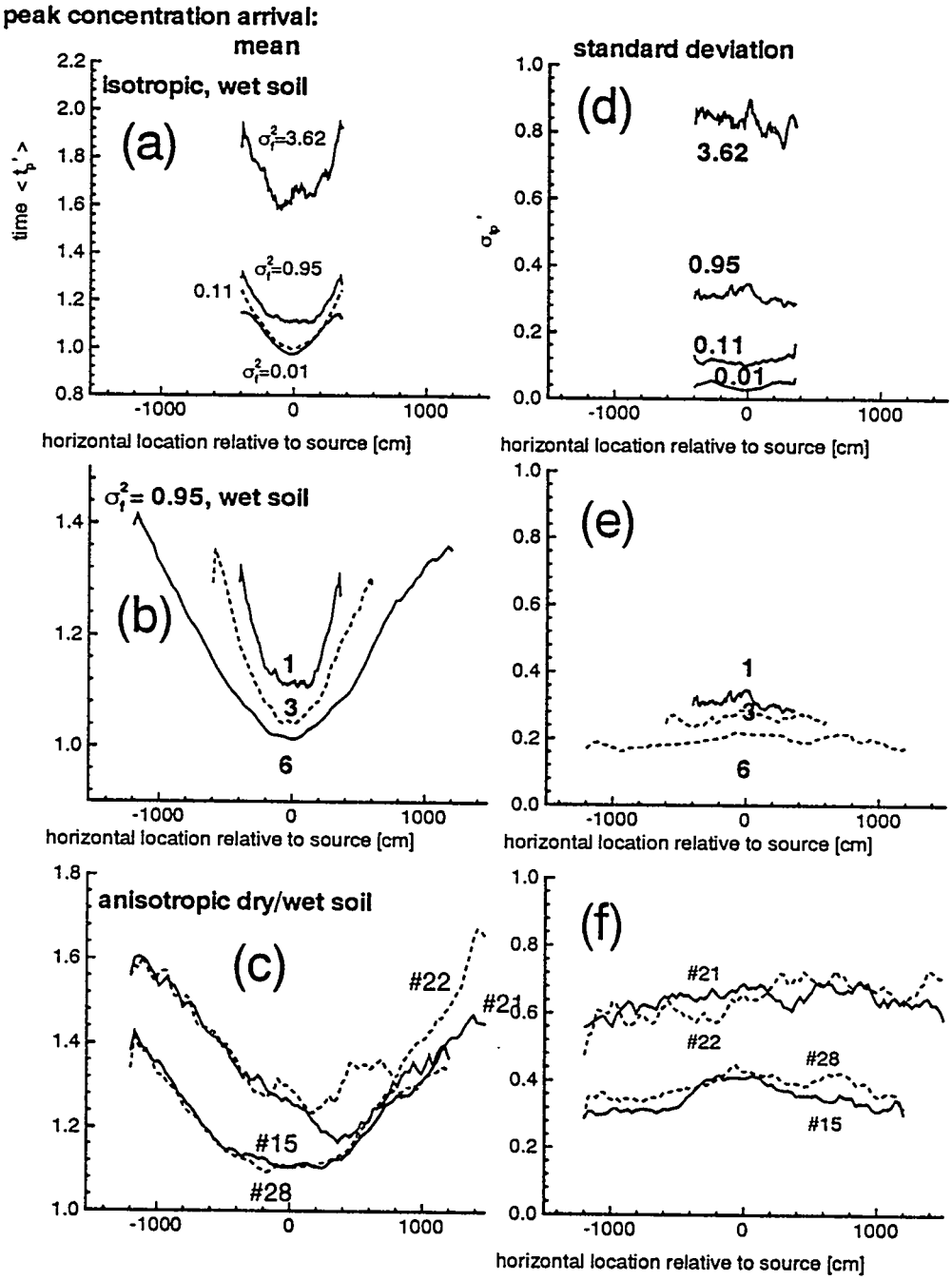

Figure 9.11: Mean (a-c; left column) and standard deviation (d-f; right column) of the arrival time t_p' of peak concentration at the compliance surface. All results are from numerical analysis. Labeling identical to previous Figures.

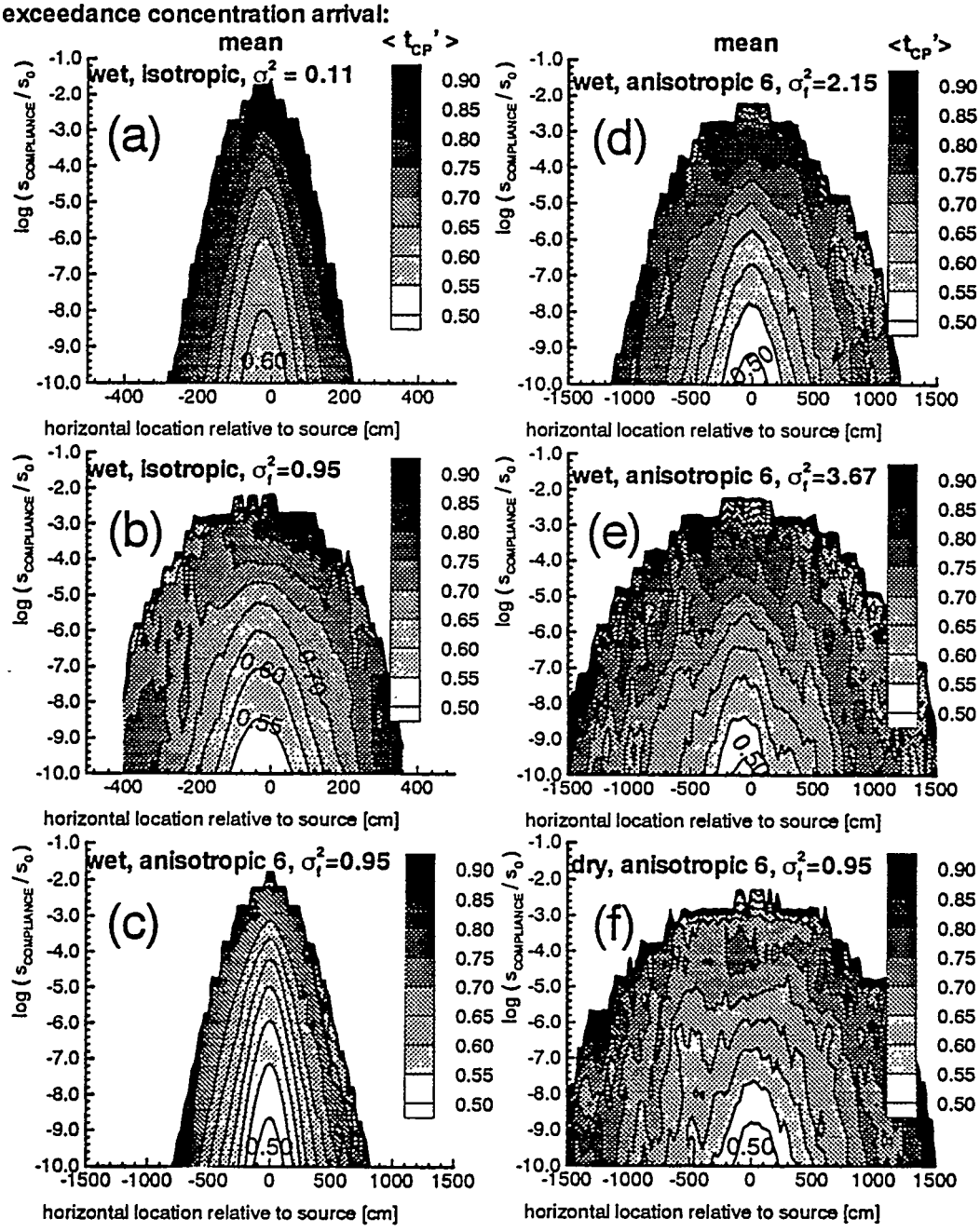

Figure 9.12: Mean arrival time $<t_{CP}'>$ of first exceedance of the compliance concentration. The arrival time is contoured as a function of compliance concentration (y-axis) and as a function of horizontal location (x-axis). The time is normalized with respect to the mean travel time to the CP surface.

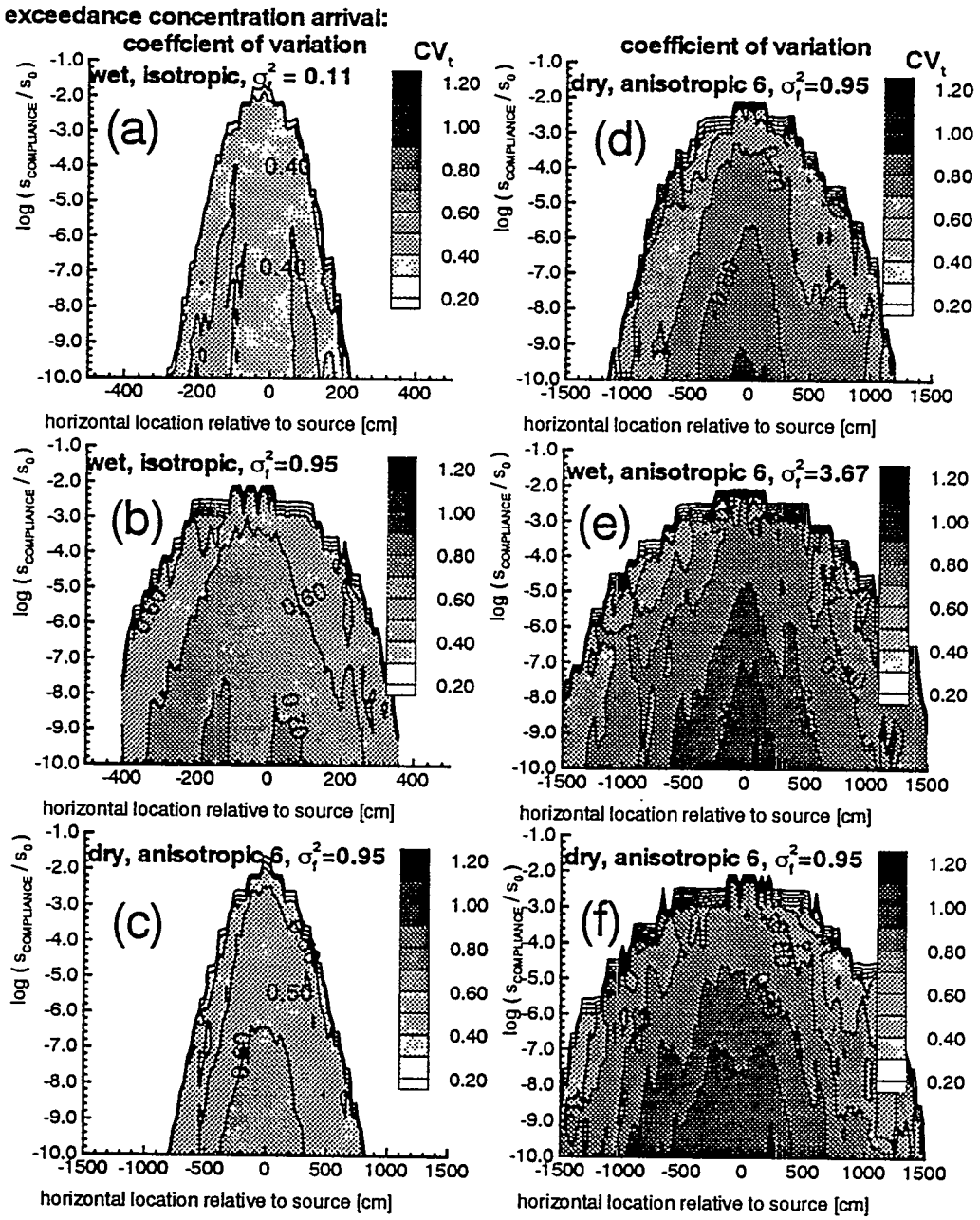

Figure 9.13: Coefficient of variation of arrival time CV_{tcp} of first exceedance of the compliance concentration. The CV of arrival time is contoured as a function of compliance concentration (y-axis) and as a function of horizontal location (x-axis).

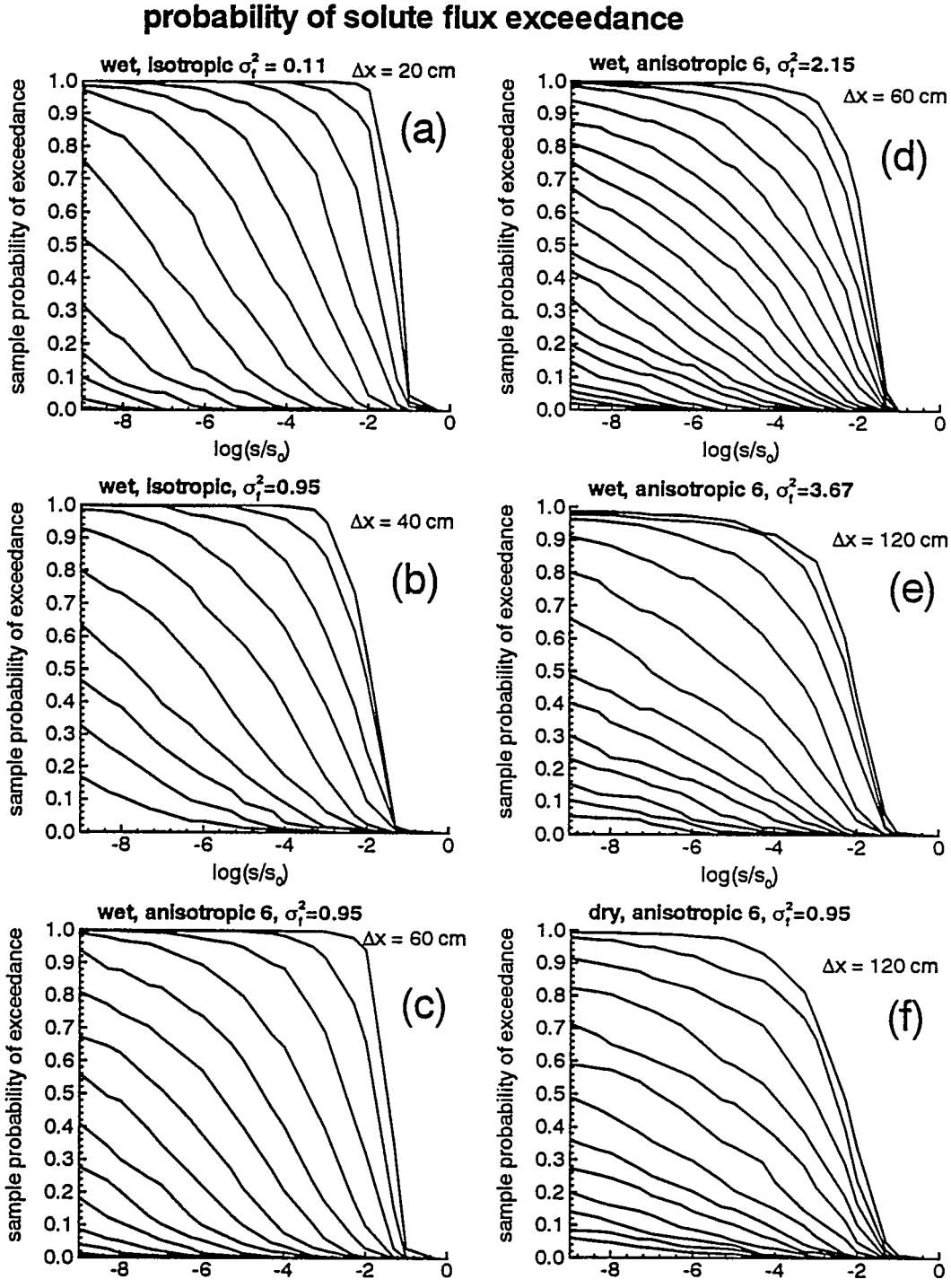

Figure 9.14: Probability of exceedance of solute flux s/s_0 at different horizontal distances x relative to the location of the source. The curve with the highest probability is at x=0. Subsequent curves are at distance x that are Δx apart from the neighboring curve.

10. CONDITIONAL SIMULATION OF UNSATURATED SOLUTE TRANSPORT

10.1 Introduction

The stochastic evaluation of solute transport is of interest where not only the expected behavior of contaminant movement but also the uncertainty associated with the mean concentration prediction must be evaluated. To obtain the statistical parameters of the input random field variables (RFVs, see section 2.5.1) K_s and α in (4-8), measurements must be taken to determine K_s and α at the site that needs to be evaluated (unless these data are available from similar or nearby sites). In many cases, measurements are also available that are related to those two parameters, although they represent a different physical quantity, for example soil tensiometer data or concentration measurements. Data of physical variables that are different from, but related to the constitutive parameters of unsaturated flow are often referred to as "indirect" information. The unconditional stochastic method presented in the previous two chapters ignores any available indirect data and considers only the statistical properties of the "direct" data. The approach is satisfactory in applications where either the lateral extent of the contamination source or the travel distance of interest is very large with respect to the correlation scale of the soil and if the soil is of only mild heterogeneity. In such cases, the actual solute plume is "ergodic" (see chapter 2) i.e., the stochastic mean concentration plume accurately predicts the actual plume and the concentration variance is zero. But for a point source or very localized contamination, the travel distance required for the plume to reach ergodicity may be exceedingly large. Dagan (1986) suggested that the ergodicity assumption is valid only after the plume has been displaced several hundred correlation scales. In the unsaturated zone, this may correspond to several tens of meters (see field studies referenced in the introduction to chapter 8). If soil heterogeneity is found on a number of distinct scales of

increasing order, ergodicity may not be achieved at all, even in the deep unsaturated zones encountered in semi-arid and arid environments (see chapter 9).

The non-ergodic mean plume concentration has a meaning much different from the ergodic mean plume concentration. It merely is a mass conservative, best estimate of the local, time dependent concentration probability. Unlike the pdf of other RFVs, the concentration pdf is difficult to determine due to the non-stationarity in space and time. Hence, the significance of the first two unconditional concentration moments is questionable if the variability is very large. To condition the stochastic evaluation of solute transport on all of the available information - including the deterministic value of single measurement data - is therefore a desirable approach not only to reduce the uncertainty of the concentration prediction but also to fully reflect the information content of the available field measurements.

Conditional stochastic analysis has been applied to a number of groundwater problems. Dagan (1982, 1984) derived analytical perturbation expressions for the conditional moments of the saturated hydraulic conductivity (input variable), the conditional head, and the spatial plume moments (output variables) in a Bayesian framework. The work accounted for local measurements of the hydraulic conductivity, of the head, and of the groundwater pore velocity. Delhomme (1979) used the geostatistical method to generate conditional random input fields of the saturated hydraulic conductivity (chapter 3; Journel, 1974). By generating random fields of K_s and solving the saturated flow equation numerically, he evaluated the conditional head moments through a Monte Carlo simulation. A similar approach was taken by Smith and Schwartz (1981) who not only analyzed the conditional head, but also the conditional solute arrival time to demonstrate the principal effect of conditioning. Binsariti (1980) and Clifton and Neuman (1982) used transmissivity and water table measurements to condition the transmissivity fields. They applied the statistical inverse method introduced by Neuman and Yakowitz (1978) to condition the hydraulic conductivity data on measurements of head. Clifton and Neuman (1982) reported a large decrease in prediction uncertainty with respect to the head

moments, when head measurements are included in the conditional approach. The first effort to condition hydraulic conductivity and the velocity field on concentration data was made by Graham and McLaughlin (1989). They presented a first order analytical stochastic solution based on spectral perturbation analysis and Kalman filtering. This work has to date been the only rigorous approach that allows for conditioning with concentration data. Indirect and direct information is used in the Lagrangian conditional transport analysis by Rubin (1991a), who uses a cokriging approach to obtain the conditional moments of the velocity from measurements of the saturated hydraulic conductivity and/or the head. The covariances and cross-covariances necessary for the cokriging are derived from a linear first order analysis based on Dagan's work (1984). Using the conditional velocity fields, the conditional spatial moments (center of mass and moment of inertia) of the contamination plume are evaluated in a Lagrangian framework by particle tracking. Zhang and Neuman (1994a,b,c,d) develop a new approach to obtain conditional concentration moments, conditional spatial moments of the mean concentration, and conditional solute flux moments based on the Eulerian-Lagrangian transport theory by Neuman (1993). Transmissivity and hydraulic head data are used in their work to condition the concentration moments.

To date, no attempt has been made to also analyze *un*saturated transport with conditional stochastic methods. Recently, an exact formalism to predict the conditional moments of transient unsaturated flow (but not transport) in heterogeneous media has been suggested (Neuman and Loeven, 1994). In principle, all of the above approaches lend themselves for an analysis of the conditional plume and concentration moments under unsaturated conditions. The main difficulty encountered in the numerical (Monte Carlo) approach on one hand is the prohibitive amount of computation time needed to obtain just one steady-state velocity field from the conditional random input fields of K_s and α. The difficulty of the analytical approaches on the other hand is the derivation of covariance and cross-covariance functions necessary to obtain the conditional velocity moments.

The work presented in the previous chapters has overcome both limitations: An efficient numerical approach to compute steady-state unsaturated velocity fields, given a heterogeneous realization of K_s and α, has been introduced (chapter 7; Harter and Yeh, 1993). This allows the efficient implementation of Monte Carlo simulations similar to the work by Smith and Schwartz (1981a,b). The stochastic moments of the unsaturated flow variables $f=\log K_s$, $a=\log\alpha$ (log: natural logarithm), and soil water tension (head) h have also been derived (chapter 4; Yeh et al., 1985a,b). With these theoretical moments, Rubin's (1991a) analysis of conditional plume moments can easily be extended to unsaturated flow. His semi-analytical approach, however, is limited to small perturbations. In this chapter the (nonlinear) numerical Monte Carlo technique is applied to derive various conditional stochastic transport parameters without having to linearize either the flow or the transport equation. Linearization is only used to generate conditional input random fields f and a given data of either f, a, or h. For the conditioning, a geostatistical inverse method called cokriging is applied (Myers, 1982; Kitanidis and Vomvoris, 1983).

Conditional simulation of unsaturated transport distinguishes itself from the conditional simulation of saturated transport not so much in the principle of the approach as in the inter-dependencies between input and output RFVs. The same measurement data play a different role depending on whether they are applied to saturated or unsaturated flow. In unsaturated flow two independent parameters (or more - depending on the choice of the constitutive relationship) define the actual local hydraulic conductivity. The unsaturated flow problem is inherently nonlinear i.e., head and conductivity are interdependent unlike in the saturated case, where the conductivity is independent of the head. It is therefore expected that the data measured in the field and used to condition the stochastic analysis have a relevant information content that is distinctly different from the saturated case. Much of the usefulness of one type of measurement will depend on the availability of other types of measurements. Measuring, for example, either the saturated hydraulic conductivity, or the soil pore size distribution parameter, or the soil

water tension each by itself should result in much less conditioning than the combined effect of all three measurements.

The main objective of this chapter is to investigate the role of both indirect information (soil water tension data) and direct information (K_s and α data), and the role of their spatial distribution (monitoring network or sampling strategy) on the uncertainty of the conditional stochastic prediction of non-reactive solute transport under variably saturated conditions in isotropic and anisotropic soils. A second objective is to discriminate the effect that conditioning has on the various measures of solute transport. Besides analyzing the local concentration moments (Rubin (1991a, Zhang and Neuman, 1994b), the conditioning effects on the spatial plume moments (Dagan, 1982; 1984), on the arrival time (Smith and Schwartz, 1981; Zhang and Neuman, 1994c), and on the integrated breakthrough (Zhang and Neuman, 1994c) at an arbitrary compliance surface are examined. The structure of this chapter is as follows: The theoretical background and the implementation of the conditional unsaturated flow and transport model is described in sections 10.2 and 10.3. The hypothetical field soil sites for the conditioning study are a subset of the example soils described in the previous chapter and are selected in section 10.4. The impact of different sampling strategies or monitoring network designs on the reduction in the spatial moments of solute transport is investigated in sections 10.5 through 10.8. Parameter uncertainty in the context of conditional simulation is addressed in section 10.9. Section 10.10 discusses the role of the spatial plume moments as a measure to judge the effect of conditioning. In many applications involving environmental compliance at a particular location or surface, the variable of interest is the solute arrival time or breakthrough curve and not the spatial plume distribution. In the two sections 10.11 and 10.12, the effect of conditioning on several local and integrated measures of solute travel time is studied. The conditional mean concentration prediction at a highly conditioned site is compared to the deterministic inverse modeling prediction in section 10.13. The chapter closes with a summary and conclusion.

10.2 Theory of Conditional Simulation by Cokriging

In chapter 3.3 a method was introduced to generate conditional random fields of the same random field variable (RFV) of which measurement data are available. In the context of this chapter the term conditioning is also applied to the process of generating random fields (and their dependent functions) that are not only conditioned on data from the same RFV (direct data e.g., random K_s fields conditioned on K_s data) but also or even exclusively on data from other physically related RFVs (indirect data e.g., random K_s fields conditioned on head data). The conditional simulation technique used in this study is based on the same principles and numerical techniques as the conditional simulation algorithm described in chapter 3.3, equation 3-14 (Journel, 1974; Delhomme, 1979). The important difference is that cokriging rather than kriging is employed because of the multivariate nature of the problem. The kriging equations are given in (2-46) through (2-48). The cokriging equations are identical to the kriging equations (2-46), (2-47) in chapter 2 (Carr and Myers, 1985). However, the array of measured data $\mathbf{X}_1$ in (2-46) contains data from more than one RFV e.g., from saturated hydraulic conductivity data *and* head data, while the array of unknown data $\mathbf{X}_2$ is - as in kriging - comprised of data exclusively from one RFV e.g., the saturated hydraulic conductivity K_s. Λ_{12} in (2-46) is the weight matrix of the measured data $\mathbf{X}_1$ with respect to the estimate $\mathbf{X}_2$, which is either of the same RFV as $\mathbf{X}_1$ (kriging) or of a different RFV (cokriging). In either case the kriging weight matrix Λ_{12} is computed by solving the covariance matrix equation (2-47). For the cokriging case, the cross-covariances between two RFVs must be known to determine the matrices $\mathbf{C}_{11}$ and $\mathbf{C}_{12}$ in (2-47). Note, that the covariance and cross-covariance functions must be positive definite, otherwise (2-47) has no general solution (Myers, 1982).

10.3 Conditional Monte Carlo Simulation: Methods

10.3.1 Principal Elements of the Monte Carlo Algorithm

The principal procedures in the conditional Monte Carlo simulation are identical to those of the unconditional Monte Carlo simulation introduced in chapters 8 and 9 (see Figure 8.2). Conditional realizations of f and a are generated and a conditional approximate solution h is computed explicitly. The realization of each of these three RFVs is passed to MMOC2, which computes the steady-state soil water tension through a finite element solution of Richards equation, the flux field through a finite element solution of Darcy's law, and the transient solute transport by using a modified method of characteristics (chapter 5). The procedure is repeated for 150 to 300 realizations (see below). Finally, the appropriate statistical sample parameters are computed from the output of the Monte Carlo simulation. The only difference between the conditional simulations in this chapter and the unconditional simulations in chapter 9 is the algorithm used to generate the random field realizations f and a and the approximate solution h, all of which must be conditioned on measurement data, which are provided as input. As in the previous chapter, the statistical parameters describing the RFVs f and a are assumed to be known. The next sections discuss the actual implementation of the conditional random field generator and the conditional extension of the ASIGN method described in chapter 7. A flow chart of conditional ASIGNing and Monte Carlo simulation is shown in Figure 10.1.

10.3.2 Generating Conditional Random Fields

The conditional random field generator developed for this study is an extension of the spectral random field generator described in chapter 3. Unconditional spectral representations dZ_f and dZ_a are generated. The unconditional realizations f and a are computed from their respective spectral representations via fast Fourier transform (FFT). The unconditional random

field realizations are needed to obtain the conditional random field realizations from (3-14). However, following the approach by Gutjahr et al. (1992), (3-14) is rearranged and the kriging equation (2-47) is used to explicitly write the kriged terms in (3-14). Then the algorithm for generating the conditional realization can simply be written as:

$$X_{2_s}^c = X_{2_s} + \Lambda_{21} (X_1 - X_{1_s}) \qquad \textbf{(10-1)}$$

where Λ_{21} is the kriging weight matrix, $\mathbf{X}_{2_s}$ is the unconditionally generated mean removed realization f or a. $\mathbf{X}_1$ is the array of field measured data (unconditional mean removed), which may include f, a, and h data. $\mathbf{X}_{1_s}$ is the array of unconditionally simulated data at the particular locations, where measurements of the same variable are available in the field site (also unconditional mean removed). $\mathbf{X}_{2_s}^c$ is the conditional mean removed realization f^c or a^c. (10-1) is computed once for each realization of each RFV.

If $\mathbf{X}_1$ contains any head measurements (soft conditioning) or if (10-1) is used to compute a linearized conditional solution $h_L^c = \mathbf{X}_{2_s}^c$ (conditional ASIGNing, see below), the unconditional realization h must be computed from the unconditional realizations f and a to fill $\mathbf{X}_{1_s}$ or $\mathbf{X}_{2_s}$ or both. Conditional flow simulation therefore requires that the unsaturated flow equation be solved twice: once to obtain the unconditional random field h from the unconditionally generated realizations f and a, and a second time to obtain the conditional nonlinear solution h^c from the conditional realizations f^c and a^c.

In the classical conditional approach, the unconditional head solution h is computed using standard finite difference or finite element models. A more efficient method would be to use ASIGNing (chapter 7), which combines the spectrally derived first order, linear approximation h_L of the head with the finite element model MMOC2. This is still a computationally very expensive conditioning algorithm. For this study a much more efficient alternative is chosen: The computation of the "true" nonlinear unconditional head h(f,a) with MMOC2 is omitted altogether. Instead the linear approximation $h_L(f,a)$ is used to fill either $\mathbf{X}_{1_s}$

or X_{2_a} or both on the right-hand side of (10-1). Recall that the linear head solution h_L is simply cogenerated with f and a by explicitly solving for $dZ_h(\mathbf{k}) = f(dZ_f(\mathbf{k}), dZ_a(\mathbf{k}), H, \Gamma)$ (4-26) and by applying the FFT on dZ_h. Using a linearized unconditional solution h_L in the conditioning process is consistent with the linear estimation procedure (10-1) from which the conditional random fields f^c and a^c are obtained.

10.3.3 Conditional ASIGNing

The conditional random field realization $h_L{}^c$ from (10-1) is used as initial approximation of the nonlinear finite element solution $h_{FE}{}^c$ to the unsaturated flow equation given the conditional realizations f^c and a^c. This is equivalent to the ASIGNing procedure for the unconditional flow simulation (chapter 7), and is therefore called conditional ASIGNing. The conditional random fields $h_L{}^c$ obtained from (10-1) are accurate enough to allow the numerical algorithm to converge very efficiently to the conditional finite element solution $h_{FE}{}^c(f^c, a^c)$. No rigorous study similar to that in chapter 7 has been implemented here to determine for which range of soil heterogeneity conditional ASIGNing leads to efficient numerical steady-state flow solutions. However, in this work conditional ASIGNing has successfully been applied to soils with $\sigma_y^2 \leq 3.2$.

It must be emphasized that the use of the spectrally derived linear head solution (4-26) leads to a double advantage in the conditioning algorithm (10-1): It allows for a very efficient evaluation of the unconditional head field (which reduces the CPU time by approximately three orders of magnitude compared to using MMOC alone, see Figures 7.6-7.8). The unconditional random head solution in turn is needed not only to condition f and a, but also to provide an initial approximation of the conditional head field such that the finite element solution converges approximately two orders of magnitude faster than without such an initial approximation (chapter 7). The computational savings achieved by using the linear, spectral

head solution h_L in this context are so enormous that an entire conditional Monte Carlo simulation of unsaturated steady-state flow with several hundred realizations can be carried out as CPU-efficiently as a single conditional realization based on finite element solutions alone (i.e. without using the linear, spectral head solution).

10.3.4 Covariances and Cross-covariances for the Cokriging Matrix Λ_{21}

To obtain the conditional random field X_{2s}^c, the difference term $(X_1 - X_{1s})$ in (10-1) is cokriged using the kriging matrix Λ_{21}, which remains identical for all realizations. Due to storage space limitations, however, the entries to the kriging matrix Λ_{21} are actually recomputed for every realization. With a field size of over 10,000 nodes (size of X_{2s} and X_{2s}^c) and up to almost 1000 data measurement points (a maximum 320 measurements of each of the three variables f, a, and h) (size of X_1 and X_{1s}), the size of the Λ_{21} matrix would exceed 10 million entries for each of the three RFV fields, which adds to the equivalent of 3*80Mb of memory when stored in double precision (8 byte per entry).

The cokriging matrix Λ_{21} is obtained by solving the covariance matrix equation (2-47). The solution is computed by inverting C_{11} using Cholesky decomposition. The inverted matrix is then multiplied with C_{12}. The subroutine SPPICD in ESSL (IBM, 1993) is used for the matrix inversion.

The cross-covariance functions C_{fh} and C_{ah} and the covariance function C_{hh} in the covariance matrices C_{11} and C_{12} can be computed from the analytical linear (cross-)spectral density functions S_{hh}, S_{fh}, and S_{ah} (chapter 4). In chapter 8 it was shown that these quasi-analytical, linearized (cross-)covariance functions are in qualitative agreement with the numerically determined, nonlinear sample functions, but differ in their absolute values if the perturbations are large. For the conditional simulation a modified quasi-analytical solution of the (cross-)covariances is developed based on a calibration of the quasi-analytical, linear (cross-

)covariances against the numerically determined sample (cross-)covariance functions. The analytical functions are multiplied by a correction factor (defined separately for each (cross-)covariance function and for each example soil) such that the modified analytical solutions match the numerical, nonlinear sample (cross-)covariance functions with minimal error. The calibration of the analytical cross-covariance functions is implemented by visual matching. The head covariance is calibrated such that the modified analytical solution for the variance exactly matches the numerically determined variance. Preliminary experiments were implemented and it was found that the results from the Monte Carlo simulation are very robust with respect to the potential error in the calibration procedure.

Calibrating the analytical (cross-)covariances rather than directly employing the empirical (cross-)covariance functions derived in chapter 8 has two advantages: The analytical cross-covariance functions are found to yield invertible covariance matrices C_{11}. However, no attempt has been made to rigorously prove that either the analytical (cross-)covariance functions or the calibrated (cross-)covariance functions yield positive definite matrix functions. This point needs to be further investigated. The second advantage is that the discretization and domain size of the empirical covariance function becomes irrelevant if the empirical functions are only used for calibration of the analytical functions. The transport simulations in the last and in this chapter, for example, are carried out in a domain roughly four times as large as the empirical unsaturated flow studies in chapter 8. Only the calibrated analytical (cross-)covariance functions provide values of C_{fh}, C_{ah}, and C_{hh} at the large lag-distances needed in this conditional flow and transport study. Since the small lag-distances are the most important ones in terms of cokriging, it is sufficient to use the empirical cross-covariance solution at short lag-distances to obtain a reliable, calibrated analytical cross-covariance functions even at large lag-distances.

10.3.5 Nodal and Elemental Properties in the Finite Element Model vs. Grid Properties in the Spectral Random Field Generator

In the finite element realization that serves as hypothetical field site (see next section), head h and concentration c are nodal values while the saturated hydraulic conductivity f and the pore size distribution parameter a are element properties. In contrast, the spectral random field generator and conditioning algorithm assume an identical grid and support for all variables. For the purpose of the conditional simulation it is simply assumed that the support scale of the nodal and elemental properties that are "measured" are identical, and that the bottom left node of each element has the same support and location as the element itself. This introduces a small error in the computation of the cross-covariances (which are functions of distances between measurement points; see chapter 9). The error is negligible since the element discretization is rather small compared to the correlation scale. To be consistent, the assignment of nodal and elemental properties in the finite element model from the conditional random field realizations f^c and a^c and the initial head h^c follows the reverse order: The f, a, and h value at the i^{th} column in the j^{th}row of the conditional random fields are assigned to the i^{th} element in the j^{th} element row (f, a) and to the i^{th} node in the j^{th} nodal row (h), which is the bottom left node to the i^{th} element in the j^{th} element row.

10.4 "Field Test Sites" and Sampling Strategies: Methodology

10.4.1 "Field Test Sites"

The so-called "field sites" that are investigated here are computer-generated hypothetical soil cross-sections (see also comment in the introduction to chapter 8). Computer-generated field-sites allow a rigorous analysis of the information content of measurement data that can be retrieved through conditional stochastic simulation. In the artificial field sites "field" hydraulic

properties and the movement of the contamination plume can be perfectly sampled. The physical processes governing the flow and transport of the so-called "real" plume and the random properties of the soil are perfectly known. Measurement errors, parameter estimation errors, and upscaling problems can for the moment be neglected.

A number of field sites are studied in this chapter to evaluate the amount of uncertainty reduction achieved by measuring relevant data *in situ*. Each "field-site" is a single, randomly chosen realization from the unconditional Monte Carlo simulations of the previous chapter. Only a subset of the soil types and moisture conditions simulated in chapter 9 is chosen for the purpose of conditional simulation. The subset includes isotropic, anisotropic, wet, and dry soils, soils with high textural variability and soils with moderate textural variability, soils with correlated f and *a*, and soils with uncorrelated f and *a* (soil sites from simulations #3, #12, #15, #21, #22, #28 in chapter 9, see also Table 9.1). Independent of the mean moisture content or the textural variability of the soil, soils with similar unsaturated hydraulic conductivity statistics are expected to behave alike not only with respect to the unconditional concentration moments (see chapter 9) but also with respect to the conditional concentration moments.

Soil #3 is isotropic with σ_y^2=0.86 and a weakly anisotropic covariance in y. All other soils are strongly anisotropic with a vertical correlation scale of f, λ_{fz}, equal to 50 cm and a horizontal correlation scale of y, λ_{fx}, equal to 300 cm. Soil #12 (wet, correlated f and a) has the lowest σ_y^2 = 0.53. Soils #28 (wet, uncorrelated f and a) and #15 (dry, uncorrelated f and a) have similar σ_y^2 = 1.76 and σ_y^2 = 1.47, respectively, although their textural variability (σ_f^2, σ_a^2) differs. Soils #21 (very dry, correlated f and a) and #22 (wet, uncorrelated f and a) both have a very high σ_y^2 = 3.12 and σ_y^2 = 3.16, respectively. These sites are grouped into four categories of soils: Isotropic soil with mild to moderate variability (#3), anisotropic soil with mild variability (#12), anisotropic soil with high variability (#28, #15), and anisotropic soils with very high variability (#21, #22).

10.4.2 Sampling Strategies

Two basic sampling networks were designed for each of the three parameters f, *a*, and h: a "sparse" and a "dense" sampling network. The sparse sampling network consists of measurement locations along three vertical columns near the plume source (e.g. tensiometer nests or boreholes) spaced 1 horizontal λ_{fx} apart with measurements at every $2\lambda_{fz}$ depth interval (e.g. Figure 10.5e). No data are sampled from an area within $2\lambda_{fz}$ of the bottom boundary of the simulation domain. The center column intersects the source area of the solute plume (see chapter 9). The total number of data points in the sparse network is 40.

A dense sampling network consists of double the data-density of the sparse sampling network i.e., 0.5 λ_{fx} in the horizontal and 1 λ_{fz} in the vertical. In the dense sampling network, the data are sampled throughout the entire simulation domain except the area within $2\lambda_{fx}$ of the vertical simulation domain boundaries (e.g. Figure 10.6a) resulting in a total of 320 data points per RFV. Measurements of K_s and α are obtained at identical locations. The sampling grid for the head measurements is shifted both in the vertical and horizontal direction such that a head measurement point is at the center between four adjacent K_s measurements (Figure 10.5i). The dense sampling network also includes measurements at all locations (nodes or elements) within and adjacent to the contamination source, which is defined on the nodal grid. Monte Carlo simulations are implemented with various combinations of f, a, and h sampling networks as listed in Table 10.1.

10.5 Conditional Simulation of Unsaturated Flow

The results of the conditional flow simulations are important to subsequently understand the behavior of the conditional solute plume, since conditioning directly affects the uncertainty about the prediction of the soil water tension h and the logarithm of the unsaturated hydraulic

conductivity y. The reduction of the velocity and concentration variance is only an indirect consequence of the conditioning. The effect of conditioning on the statistical moments of y, h, and the pore velocity v is demonstrated for the two conditional simulations A and G (Table 10.1) of field site #28, a highly variable, wet, anisotropic soil with uncorrelated f and a. Monte Carlo simulations of other field sites give qualitatively similar results. Field-site #28 (like all other sites except #3) is a vertical cross-section that is 12.8m deep and 24m wide, which is approximately as wide but twice as deep as the experimental Las Cruces trench site (Wierenga et al., 1991). The variability of f and a is 2.25 and 0.04, respectively. The two parameters are considered to be independent of each other. The geometric mean of alpha, Γ, is 0.01 cm^{-1}. Recall, that the soil is anisotropic with correlation scales for f and a of 3m and 50 cm in the horizontal and vertical direction, respectively. The cross-section is therefore about 26 λ_{fz} deep.

Figure 10.2a-d shows the actual field values of the maps of y, h, and the pore velocity components v_x and v_z at site #28. The cross-section of y has the typical random character described in chapter 8. In the center of the cross-section a high conductivity lens is layered immediately above a relatively low conductivity area (Figure 10.2a), which correlates with a partially saturated, very wet lens overlying a dry area with a relatively high tension (Figure 10.2b). The horizontal velocities reach some of their highest absolute values in this large, wet region, because flow is around the low conductivity area. Another distinct feature of the horizontal velocity field at the site is a strong positively diagonal downward/sideward flow immediately beneath the contamination source (Figure 10.2c). The vertical velocity field has the typical pattern of broad low velocity areas interrupted by relatively narrow vertical bands of higher velocities (Figure 10.2d, see chapter 8).

The main features are preserved in the mean predictions of the two conditional simulations A (Figure 10.2e-h) and G (Figure 10.2i-m). A is based on a dense data network of all three variables f, a, and h, while G is based on only 40 soil water tension data (sparse network) from three tensiometer nests. As the number of conditioning data decreases, the mean

prediction becomes more and more uniform, asymptotically approaching the stationary moments of the unconditional simulation. Since only head information is available to conditional simulation G, it is not surprising to find that the head data are those best preserved.

Figure 10.3a-d again shows the field site values of y, h, and v together with the variance distribution of the two simulation A (Figure 10.3e-h) and G (Figure 10.3i-m). In conditional simulation A, the variance of y (Figure 10.3e) decreases to less than 0.1 at the f and *a* measurement points (but not at the head measurement points) compared to an unconditional variance of 1.8. The extremely low variance is very local. Due to the anisotropic structure of the soil, the conductivity variance is reduced significantly stronger in the horizontal vicinity of the measurement points than in the vertical vicinity. Between rows of measurements, the conductivity variance increases to values of nearly 0.7 in conditional simulation A. In the sparse data conditional simulation G, the minimum local variance of y is several times larger than in conditional simulation A with values between 0.4 and 0.7 (Figure 10.3i).

The head variance in much of the area with tensiometer data is reduced to less than 150 cm^2 in conditional simulation A (Figure 10.3f) from 4900 cm^2 in the unconditional simulation (chapter 8). The head variance, however, is nowhere less than 120 cm^2. In conditional simulation G where no other data are used besides head, the variance reduction is not as strong with a minimum variance of less than 300 cm^2 (Figure 10.3k). Despite the use of conditioning head data, the head variance does not become zero at the measurement points. Neither does the mean head at those locations always coincide with the measured value (Figure 10.4a). This is an artifact of the linear conditioning procedure (Kitanidis and Vomvoris, 1983; Peck et al., 1988; Yeh et al., 1993; Gutjahr et al., 1994): The conditional realizations f^c and a^c are obtained through *linear* estimation (10-1) from head measurements (among others). But the conditional realization h^c is computed by solving the *nonlinear* flow equation (5-1). Note that the head measurement data cannot be applied as internal boundary conditions in the finite element solution.

Although not entirely consistent, the conditioning technique generally gives satisfactory results. It is weakest in areas where steep head gradients exist e.g., in the center of the simulation domain between the very wet and very dry areas mentioned above (Figure 10.4a). In those areas the head changes rapidly with distance, and if the location of the steep head gradient is not predicted with a very high accuracy, large head variances and a significant deviation of the mean head form the measured head are the result. At field sites with smaller σ_y^2, the discrepancy between measured and mean conditional head decreases (Figure 10.4b,c). Future work will have to assess how much more consistency is achieved by using a numerical nonlinear solution instead of a first order perturbation solver within the conditioning algorithm.

In the vicinity of datapoints the horizontal velocity variance is reduced stronger than the vertical velocity variance: from an unconditional variance of 0.02 $(cm/d)^2$ to less than 0.004 $(cm/d)^2$, a reduction of over 80% (Figure 10.3g,l). In contrast, the vertical velocity variance is reduced only to approximately 60%-80% of the unconditional variance (Figure 10.3h,m). The conditioning effect in the horizontal direction is very strong for the horizontal velocity, which can be particularly well seen in the results for simulation G. The vertical velocity components are well-conditioned by data in the immediate vertical vicinity, while conditional f, a, and h data have little effect on the vertical velocity in the nearby horizontal vicinity. This is not surprising since the vertical velocity covariance has a strong vertical correlation scale and a very short horizontal correlation scale (see chapter 8).

10.6 Sampling Network Design Impacts on Concentration Prediction

10.6.1 Organization of Graphical Output for Concentration Moments

The maps of the actual plumes, of the mean concentration m_c and of the concentration coefficient of variation CV_c are plotted in Figures 10.5 - 10.22. The organization of each of these figures is identical: Each figure is divided into twelve panels plotted in four rows and

three columns. Each panel shows a vertical cross-section of the soil site with the horizontal axis being the horizontal distance [cm] and the vertical axis being the vertical distance [cm]. Each vertical row represents the results of one Monte Carlo simulation (MCS) or of the actual plume movement. The variable that is mapped in the panels is indicated above the top panel of each column. Each panel in a column represents a different output time. It increases from top to bottom and is measured in dimensionless units $t' = V_z / \lambda_{fz}$. V_z is the (arithmetic) sample mean vertical velocity computed from the unconditional MCS for the particular soil site (chapter 8). λ_{fz} is the vertical correlation scale of f. t'=0 is the time of solute release. The initial area of uniform concentration is indicated by the small black box in each panel. The output times are identical to those of the unconditional MCSs in chapter 9 (see Table 9.2) and are indicated in the panels of the leftmost column of each figure. Each row corresponds to only one output time. The concentration maps are plotted with five gray-shaded contour levels, to which the labels are found at the right side of the rightmost column. The soil site number (#) to which the results belong is indicated in the bottom right corner. Note that the actual and mean concentration contour levels at a particular output time t' are identical for the maps of all MCSs of one site and correspond to the contour levels chosen for the actual plume. All concentration data are normalized with respect to the initial concentration c_0. The contour levels have logarithmic intervals (log base 10) and range over two orders of magnitude such that the maximum contour level is at the most 15% below the peak concentration of the actual field solute plume at time t' (e.g. if the peak concentration is 9.45E-2, the contour levels are from 9.00E-4 to 9.00E-2). In all panels showing CV_c maps, the CV_c contour levels are in increments of 0.3 in the interval from 0.5 to 2 as indicated by the labels on the right side of each figure. In addition, the minimum CV_c of each CV_c map is printed out explicitly and the location is indicated where necessary. The first panel in each column indicates the locations where conditional data are available for the MCS shown in that column. Open circles are datapoints, at which f and *a* data are measured. Black dots indicate soil water tension measurement points.

Unless it is the map of the actual plume, the second panel in each column indicates the type of MCS with the amount of data used for conditioning.

10.6.2 Solute Plume Movement at the Field Site

Again, field site #28 and the results from its Monte Carlo simulations are discussed at length in this section. The Monte Carlo simulations of other example soils are discussed more briefly in subsequent sections, where the emphasis is a comparative analysis. The plume dynamics at field site #28 are depicted in Figure 10.5a-d. Initially the plume moves diagonally downwards along a strong diagonal velocity field (Figure 10.2c,d), the tip of the plume splits into two at an early travel time and spreads horizontally as it reaches a large wet area located above a relatively dry lens in the center of the simulation domain (see previous section). At late time t'=31 residual concentration is found primarily within and underneath the dry, low permeability area. The plume is distinctly non-Gaussian with no tendency towards a more Gaussian behavior even at late times (see also chapter 9).

10.6.3 Sensitivity of Concentration Moments to Sampling Networks (Site #28)

"Dense" sampling network for all parameters (f, a, h): simulation A

In this first example, data are available at a high sampling frequency (every five nodes in each direction or $0.5\lambda_f$ in the horizontal and $1\lambda_f$ in the vertical). Both independent RFVs f and *a* are sampled at identical locations. The soil water tension h is measured at nearby locations (conditional simulation A, Table 10.1). This is the highest density measurement grid used in any of the simulations (Figure 10.5e). From a practical point of view, such a high density of observation points cannot be achieved without partially removing or destroying the

site (e.g., in the trench site experiment by Wierenga et al., 1989) But this type of conditional simulation serves as a benchmark test to illustrate by how much prediction uncertainty can be reduced in an optimally sampled field site.

As would be expected, the conditional mean concentration distribution is very similar but not identical to the actual concentration distribution (Figure 10.5e-h). The conditional solute plume shows many of the broader patterns of the actual field plume, but does not distinguish between some local random patterns. The length scale associated with the differences between the conditional plume and the actual plume is significantly larger than the scale of the sampling intervals for the f, *a*, and h data (compare actual and mean plume at, for example, t'=8). There are several reasons to explain why it is possible that the conditional simulation uncertainties go beyond the confinement of the measurement grid:

a. The available field measurements are only indirect pieces of information with respect to predicting the movement of the solute plume. Neither concentration nor velocities are measured directly to confine the predictions.

b. Even the information about the hydraulic conductivity itself is not entirely certain anywhere because head measurements are taken at different points than f and *a* measurements. A small amount of uncertainty about y remains even at the f and *a* data locations, especially in this highly heterogeneous soil (see Figure 10.3e).

c. The conditioning on the head data has been implemented only in a linear, approximate manner i.e., the conditioning algorithm does not yield a zero head variance at the head data locations (see section 10.3 and results in section 10.5).

The conditional concentration prediction from simulation A clearly shows the early diagonal displacement, the horizontal spreading along a low permeability zone in the center of the simulation domain, the breakthrough to the bottom boundary in the right half of the domain at t'=16, and the residual concentration below the low permeability zone at late time t'=31. The movement of the highest concentrations, or the plume center, is predicted very accurately.

Error in predicting lower concentrations is indicated by the slightly larger vertical and horizontal spreading of the conditional mean plume. Conditioning at this density is very useful not only for predicting the movement of the center of a contaminant plume but perhaps more importantly the general patterns of the fringes of the contamination plume (indicated by the $c/c_{max}(t') = 0.01$ contour line). The approach seems particularly useful to identify possible preferential transport paths on one hand and solute retention areas on the other hand.

To assess the difference between prediction and actual plume the absolute nodal error measure E is introduced:

$$E = \sum_{x \in \Omega} |c_f(x) - \langle c(x) \rangle^c| \qquad \textbf{(10-2)}$$

where Ω indicates the simulation domain, $\langle c(x) \rangle^c$ is the conditionally simulated mean concentration, and $c_f(x)$ is the actual field-site concentration at node location x. For the four output times t' = 4, 8, 16, and 31 in Figure 4.5e-h, the absolute nodal error in the conditional simulation is E = 5.4, 4.7, 3.9, and 2.8, respectively. This is approximately 40% less than in the unconditional simulation with E = 9.0, 8.0, 8.7, and 4.0, respectively (Figure 10.7i-m). Note, that the nodal error measure emphasizes errors in the regions of high concentrations. Errors occurring away from the center of the conditional plume are small and therefore insignificant with respect to E and cannot be reflected by such a measure. Often, however, very low concentrations are of equal concern. Then a "success" measure like E can be very misleading.

A statistically important measure of the quality of the simulated prediction is the concentration coefficient of variation CV_c where $CV_c = std_c / m_c$, the ratio of the concentration sample standard deviation over the sample mean concentration. Figure 10.8e-h depicts the dynamics of the CV_c plume for conditional simulation A. The CV_c plume depicts areas of least uncertainty (darkest colors). At the $CV_c = 2$ contour line, it is generally as wide or wider in the horizontal direction as the mean concentration plume at the 1% $c/c_{max}(t')$ contour line, but

vertically less extensive than the mean plume. This is consistent with the $0.5\lambda_f$ horizontal sampling density vs. a $1.0\lambda_f$ vertical sampling density and the general anisotropic structure of the soil. It is also consistent with the fact that the head correlation scale is larger in the horizontal direction than in the vertical direction. Conditioning reduces concentration uncertainty stronger into the horizontal distances than into the vertical distances from the measurement point. The minimum coefficient of variation in the center of the CV_c plume increases with time from 0.35 at t'=4 to 0.56 at t'=31 indicating increased uncertainty near the center of the plume. The minimum CV_c location coincides with the location of the peak mean concentration. Like in the unconditional simulations of chapter 9 (see also Figure 10.7i-m), the area of low uncertainty defined by the CV_c=2 contour increases with increasing mean plume size and time (compare Figure 10.8e-h with Figure 10.5e-h).

Numerical mass balance problems contribute approximately 0.1 to the CV_c. This value is estimated by computing the coefficient of variation of the mass balance variability between different realizations. Initially the numerical mass balance error $CV_{bal}(t) = std_{bal}(t) / mass_{tot}$ (standard deviation of the total mass balance in the domain divided by the total initial mass) is zero, then rapidly increases at early time and reaches a relatively stable plateau of 0.1. The mass balance error is inherent to the modified method of characteristics and must be attributed to the heterogeneous velocity field, for which the fourth order Runge-Kutta travel path integration is known not to be accurate (see chapter 5).

Not sampling α, dense grid

Simulation B (Figure 10.5i-m) uses the same f and h data as simulation A, but assumes that nothing is known in situ about $\log\alpha$. Only its unconditional mean and variance and the form of its pdf are given. The difference between the conditional concentration moments of simulation A and B is small, because the variance of $\log\alpha$ is not very large and the soil is

rather wet. The information about K_s and h gives reasonably accurate estimates of the unsaturated hydraulic conductivity even without measurements of α. The mean plume is slightly larger with a smaller peak concentration. At early time (t'=4), simulation B has 25% higher CV_c than simulation A, but as time proceeds, the differences in CV_c decrease (Figure 10.8i-m).

Sampling saturated hydraulic conductivity only

The uncertainty reduction relative to the unconditional MCS that is achieved from saturated hydraulic conductivity measurements alone is considerably smaller than in the previously discussed conditional simulations A and B. When sampled in a dense network (simulation C, Figure 10.6a-d), the minimum CV_c at t'=4 is 0.81, almost double as large as in simulation B, which includes the head measurements in addition to the data used in simulation C. The ratio of the minimum CV_c in simulation C over that in the unconditional simulation decreases only slightly with time. Since the variance of *a* is moderate, f data are helpful in discriminating the most probable fast flow paths from likely slow flow areas. The diagonal flow path near the source is obvious in the conditional mean prediction, and so is the low permeability area in the center of the cross-section. Clearly, the peak concentrations in C are lower than in simulations A and B due to the larger concentration variability. When f is sampled only on the sparse network (not shown) the results are almost identical to those shown in Figure 10.6e-h for conditional simulation D with f and *a* data on the sparse network. The indifference between the two simulations is again due to the moderate variability of *a*, its relatively small mean value, and the relative wetness of the soil (the unsaturated hydraulic conductivity differs little from the saturated hydraulic conductivity). Compared to the dense sampling network for f (simulation C), the conditional solute plume D is considerably more disperse, particularly at later time. The minimum CV_c=0.88 at t'=4 is a less than 10% increase

over simulation C but CV_c=1.29 at t'=16 is a 30% increase over simulation C. These values approach those for the unconditional simulation, even exceed them at t'=16. The CV_c away from the plume center, however, is always less in conditional simulation D than in the unconditional simulation.

Sampling soil water tension only

For the conditional simulation G, three hypothetical tensiometer nests are installed three meters or one correlation length apart with tensiometers placed every one meter or two correlation lengths in the vertical (sparse sampling network). The forty head measurements are used for conditioning the f and *a* input random fields. Sparse sampling network G yields the least conditioned simulation in this study. Nevertheless the tensiometer data cause a significant improvement in the mean concentration prediction compared to the unconditional mean concentration prediction (compare Figure 10.7e-h and Figure 10.7i-m). The mean plume movement indicates the initial diagonal movement, the split of the plume into two lobes and it hints at a low permeability zone in the center of the simulation domain. The peak concentrations are much closer to the actual peak concentration than in the unconditional simulation. The estimates of both the front and the tail of the plume are more realistic than in the unconditional simulation.

If the number of tensiometers is doubled in both the vertical and horizontal direction and extended over a larger cross-section (conditional simulation F, Figure 10.7a-d), the prediction of the expected concentration does not improve very much. This shows that additional measurements of the tension are not associated with an equal amount of uncertainty reduction. The minimum CV_c at t'=4 are 0.50 and 0.65, respectively, compared to 0.95 in the unconditional simulation. Similar ratios between the minimum CV_c of the different simulations are obtained at later times. The minimum CV_c in both simulations F and G are significantly

lower than in simulation C (dense f data, direct conditioning) (0.50, 0.65 vs. 0.81). In terms of uncertainty it therefore appears that soil water tension data by themselves yield a greater improvement of the prediction than saturated hydraulic conductivity data. Only at t'=31, the minimum CV_c in simulation G is higher than in simulation C, while the minimum CV_c in simulation F (dense h data, indirect conditioning) remains below that in simulation C. This is in partial contrast to the mean concentration prediction, which - particularly at t'=16 and t'=31 - seems significantly better in simulation C than in either simulation F or G. The relatively lower minimum CV_c in simulations F and G is probably caused by the smaller horizontal spreading of the mean concentration plumes and its higher peak concentration.

Also, for both the sparse and the dense sampling networks, the conditional CV_c plumes seemingly "know" more about the actual plume behavior than the respective m_c plumes, since their spatial pattern better mimic the actual plume. This latter observation is partially coincidence, partially due to the particularly strong horizontal spreading of the plume around t'=16. Horizontal velocity components have a stronger horizontal correlation than vertical velocity components. Similar observations are not made in MCSs of other field sites.

The results underline the importance of soil water tension data in the conditional simulation of transport in highly heterogeneous flow fields. They also indicate that the minimum CV_c alone can only serve as a guideline to measure reduction in prediction uncertainty.

Other sampling network combinations for f, a and h

Figure 10.6i-m shows the mean concentration results for conditional simulation E based on a sparse network of f and *a* measurements combined with a dense network of h measurements. Again, the results are almost identical to those with sparse f data alone together with a dense h measurement network (conditional simulation H, Figure 10.21a-d). The spatial

concentration distribution is significantly better predicted than in either simulation D or F alone. The mean plume is much less dispersed resulting in higher concentrations at the center of the plume. The improvement is particularly visible at t'=16, when both the actual and the mean plume exhibit the strongest horizontal spreading. The visual information is supported by the results for CV_c (Figure 10.9i-m). The minimum CV_c for simulation E at t'=4, for example, is 0.43 compared to 0.88 and 0.50 in simulations D and F, respectively. The simulation results are also better than those obtained from conditioning on a dense f sampling network (simulation C) and very similar to simulation B which utilizes dense network data for both f and h. Compared with simulation F, the additional saturated hydraulic conductivity information particularly helps to outline the extremely high and extremely low permeability areas, since the spatial variability of α is not very strong. But the comparison between simulations B and E also points to the fact that there is no gain in increasing the number of f measurements from 40 to 320, when so many head data are already available for conditioning. This is particularly important, since saturated hydraulic conductivity measurements are much more difficult to implement in situ than head measurements. The results from this simulation indicate that a combination of in situ h and f data, with more h measurements than f measurements, may be the most economical approach to design a monitoring or sampling network.

10.6.4 Comparison to a Dry, Anisotropic Field Site of Equivalent Variability in y

Field site #15 has a much smaller textural variability than field site #28: The variance of f and a are only 1 and 0.01, respectively, instead of 2.25 and 0.04 at site #28 (see chapter 8). However, the increased dryness (mean head H = -1000 cm) leads to a strong increase in the unsaturated hydraulic conductivity unconditional variance, which is 1.5 compared to an unconditional variance of 1.8 at field site #28. The head variances are also similar: Field site #15 has an unconditional head variance of 4400 cm^2 vs. 4900 cm^2 at field site 28.

Figure 10.11a-m shows the actual plume at the field site and the conditional mean concentration for the highest density and lowest density data simulations discussed above (simulations A and G). Not surprisingly the tortuosity of the spatial path taken by the plume is very similar to field site #28. The agreement between the conditional mean plumes A and G and the actual plume is comparable to the findings at field site #28. This visual impression is confirmed by the concentration coefficients of variation, which are very similar to those found in the equivalent conditional simulations of field site #28 (Note that the output times for field site 15 are slightly different: 5, 10, 20, and 40 instead of 4, 8, 16, and 31). At similar variances of the unsaturated hydraulic conductivity and soil water tension and for the same mean α and correlation structure, the effects of conditioning on a set of f, a, and h data (simulation A) or on h data alone (simulation g) are similar, regardless of the mean soil water tension and the variability of the soil saturated hydraulic conductivity.

However, conditioning on f alone (conditional simulation C) neither improves the mean concentration prediction, nor reduces the minimum CV_c as much as in the wet soil #28 when compared to the unconditional simulation (Figure 10.11n-u; Figure 10.12n-u). Relative to simulation G, the mean concentration in simulation C has a much larger longitudinal and transverse extension indicating significantly more uncertainty about the actual travel velocity and the travel path. The higher uncertainty is caused by the weak correlation between saturated and unsaturated hydraulic conductivity in dry soils, if f and a are uncorrelated. In contrast, the soil water tension data as in site #28 provide information not so much on the unsaturated hydraulic conductivity but on the gradient field and hence the approximate travel path of the plume. If data on a and f are not available or if data on only one of the two parameters is available, soil water tension data must therefore be considered an important source of information for more accurate transport predictions.

10.7 Unsaturated Hydraulic Conductivity Variance and the Effect of Conditioning Data

Increasing the unsaturated hydraulic conductivity and head variance leads to increased solute spreading and increased uncertainty in the prediction of the mean travel path of a solute plume. This theoretical result (Russo, 1993a) has been confirmed in the previous chapter. Here, a qualitative analysis is given of the effect of soil variability on the *conditional* concentration moment prediction. The concentration moments of two field sites are compared with those discussed in the previous section. All field sites have the same anisotropic correlation structure for f and a and the same mean F and A (see previous section, chapter 8). Field site #12 is a moderately heterogeneous soil with correlated f and a, an unsaturated hydraulic conductivity variance $\sigma_y^2 = 0.53$ and a head variance of 1900 cm^2 with a mean head H = -150 cm. Field site 21 is the same as field site 12, but in a very dry condition (H=-3000 cm), resulting in $\sigma_y^2 = 3.2$ and a head variance 7600 cm^2. In terms of σ_y^2, field site 12 ranks lowest and field site 21 highest among the sites tested. Note that ρ_{af}=1, which means that f data perfectly predict a at the same location.

The unconditional plume for field site #12 is much less dispersed than those at other field sites (Figure 10.13a-d). Consequently the unconditional simulation itself is a fairly good description of the actual plume (at least compared to the conditional simulation results at field site #28), although ergodicity (zero concentration variance) is not achieved even for this moderately heterogeneous soil. The most obvious difference between the unconditional mean plume and the actual plume is the rate of displacement. At t'=20, for example, the center of the actual plume has traveled significantly further than the center of the unconditional plume (compare Figure 10.13a-d to Figure 10.15a-d). The conditional simulation A (high data density, Figure 10.15e-h) captures the actual rate of displacement of the field plume as well as its particular shape. In contrast, the conditional simulation G (sparse head data only, Figure 10.15i-m) offers little improvement over the unconditional simulation. This is again reflected

in the concentration coefficient of variation (Figure 10.14a-d and Figure 10.16e-h,i-m). At t'=20, the minimum coefficient of variation in the unconditional simulation is 0.79, which decreases by less than 25% to 0.63 in conditional simulation G, but by more than 75% to 0.19 in conditional simulation A. Similar observations can be made at other output times. This is a much better improvement in conditional simulation A compared to the results for field site #28, but much less of an improvement in conditional simulation G. The difference is caused by the changing information content of the data that are used for conditioning: In the heterogeneous soil #28, the flow path of the plume is rather tortuous and hence dictated primarily by the spatial distribution of the soil water tension. In this soil (#12), flow is almost parallel, a situation which has been conceptualized in many stochastic soil flow and transport models as the "parallel column model" (c.f. Destouni, 1993). Here, the uncertainty is reduced to predicting the rate of solute displacement while the travel path is well-known. The vertical velocity is then primarily controlled by the saturated hydraulic conductivity and α. In simulation G, these values are conditioned indirectly through the h data. In simulation A both are known at a high density and combined with the lower variability of the soil result in a lower CV_c than the comparable simulation for site #28.

For the same reasons, h data are even more important in simulating site #21 than in simulating site #28. The unconditional mean concentration prediction (Figure 10.13e-h) has a very high variability (Figure 10.14e-h). Nevertheless, the characteristic features of the actual plume are well captured even by conditional simulation G (compare Figure 10.17i-m with Figure 10.17a-d): The initial diagonal displacement (t'=5), the characteristic s-shape at t'=10, and the residual concentration not far below the source. Although conditional simulation A (Figure 10.17e-h) offers considerable improvements over simulation G, the uncertainty associated with an unconditional simulation is so large that the three tensiometer nests for simulation G alone offer almost as much improvement in prediction accuracy as all the data in simulation A together. Again, the visual impression from the mean plume maps are confirmed

quantitatively by the CV_c. At t'=5, the unconditional minimum CV_c is 1.51 (Figure 10.14e), which improves by over 50% in simulation G to 0.73 (Figure 10.18i), and by almost 70% to 0.47 in conditional simulation A (Figure 10.18e). Similar results occur at t'=10. At t'=20, the minimum CV_c of the unconditional simulation reduce to 1.37, while those for the conditional simulations further increase relative to earlier time.

The two field sites #12 and #21 are particularly educational in that they illustrate how the information content of field data with respect to the conditional moments of the concentration changes with soil water content. Both sites represent the same type of soil, but under different mean soil water tension conditions. Depending on H, the same amount of on-site field data yields distinctly different improvements in the conditional plume prediction relative to an unconditional stochastic plume prediction. Conditioning on tensiometer measurements is particularly useful in soils with highly heterogeneous flow paths i.e., in soils with a high degree of textural heterogeneity, in very dry soils, or in soils with a steep average slope α of the logK(h) function. In soils with almost exclusively parallel vertical flow and therefore only mildly heterogeneous unsaturated hydraulic conductivity fields, the same tensiometer measurements have almost negligible effects. In contrast, saturated hydraulic conductivity data and data defining α are important data to reduce uncertainty in soils with more or less vertical parallel flow. But they loose their information content (measured in terms of minimum CV_c reduction relative to the unconditional minimum CV_c) in soils with very tortuous flow paths.

10.8 Anisotropy Ratio and the Effect of Conditioning Data

The isotropic soil site 3 is chosen for comparison with the conditional simulation results of the previous two sections. Relative to the horizontal correlation scale, the horizontal plume spreading is much larger in the isotropic soil than in the anisotropic soil #28, even though σ_y^2

at site 3 is only half of that at site #28 (see chapter 9). Note, that the vertical to horizontal scale ratio for all site 3 maps is 3:1 (half the aspect ratio $\lambda_{fh}/\lambda_{fz}$ of the anisotropic soils) instead of 1:1 (as in all maps of the anisotropic soil sites). Thus, the horizontal correlation scale for the site #3 maps appears as half the absolute length of the correlation scale for the maps of the anisotropic soils.

Since flow path tortuosity (Figure 10.19a-d) contributes considerably to the uncertainty in the concentration prediction, in situ head measurements significantly reduce the prediction uncertainty (compare Figures 10.13i-m, 10.14i-m to Figures 10.19i-m, 10.20i-m). The minimum CV_c reduction at t'=5 is more than 50% from 1.07 to 0.51 with simulation G, and more than 85% from 1.07 to 0.14 with simulation A. Curiously, however, in this particular case the tensiometer data increase the error in the mean concentration prediction near the source at t' > 10: In simulation G, a secondary concentration peak appears and remains immediately underneath the source. Since the CV_c in this area is very high, the anomaly is probably caused by an outlier and should be neglected.

10.9 Conditional Simulation under Parameter Uncertainty

In all of the previous simulations it is assumed that the stochastic parameters describing the first and second moment of the input parameters f and a are known with certainty. In actuality, these parameters must be derived from a sample population of field and laboratory measurements. Generally, these sample populations are very small and the estimated mean and covariance are themselves RFVs (see chapters 3 and 8) i.e., their actual value is associated with a degree of uncertainty that is best measured in terms of the theoretical sampling error. Note that sampling errors are not the same as measurement errors. The effect of measurement errors, although important, has not been considered here. Parameter uncertainty in a conditional stochastic framework has been addressed by Smith and Schwartz (1981b) who implemented a

specific type of conditional Monte Carlo analysis of saturated flow and transport to assess the additional uncertainty introduced by the sample estimation of the saturated hydraulic conductivity. Their objective was to assess the difference in the moments of the solute flux and concentration distribution introduced to the unconditional stochastic analysis by parameter uncertainty. Their approach was too CPU expensive to address the combined effect of parameter uncertainty and measurement network design. The conceptual limits imposed on their study are the same for this study. Therefore, an alternative method is implemented to understand - at least qualitatively - the effect of parameter uncertainty in the conditional framework presented here.

Unlike the method by Smith and Schwartz (1981b) it is not the objective of this exercise to define quantitatively the increase in concentration variance or the change in mean concentration due to parameter uncertainty (which is computationally not feasible for the conditional case). Instead the problem is tackled from the following point of view: How different is a MCS result, if the sample moments, which are used as input to the MCS, are "far off" the actual ensemble moments? As in Smith and Schwartz (1981b), the exercise here will be restricted to the assessment of the effect of parameter uncertainty in the mean and the variance of the input RFVs f and a and in the mean H of the soil water tension. It is still assumed that f and a are known to be Gaussian distributed, that they are independent of each other ($\rho_{af} = 0$), and that the correlation functions of f and a are known with certainty. For the purpose of this exercise, "far off" sample moments are defined by the 95% confidence interval of the sample moment distribution. For simplicity and without loss of generality, the distribution of the sample moments is assumed to also be Gaussian (instead of e.g. the t-distribution most commonly used). Then the standard deviation ε_G of the sample mean G of g (g=f,a,h) is the square root of (8-3) and the standard deviation $\varepsilon_{s,g}$ of the sample standard deviation std_g is the square root of (8-5) (chapter 8). The "far off" sample moments are the means $m_{g,95} = \mu_g \pm 2\varepsilon_G$ and the standard deviation $std_{g,95} = \sigma_g \pm 2\varepsilon_{s,g}$, where μ_g is the ensemble

mean and σ_g is the ensemble standard deviation of g. Theoretically, the sample moments are "worse" i.e., more different from the ensemble moments, in only one of twenty sampling campaigns.

Data for the conditional simulation H of soils site #28 are chosen to demonstrate the method. Conditional simulation H consists of 40 measurements of f, 40 measurements of a, and of 320 measurements of h (Table 10.1). Since the f and a measurements are taken at least one correlation length apart, one can reasonably assume independence. Using (8-3) and (8-5), ε_P = 0.24, ε_A = 0.032, $\varepsilon_{s,f}$ = 0.17, $\varepsilon_{s,a}$ = 0.022. Hence, with a 95% probability the sample mean estimates of f and a are within the intervals [-0.5, 0.5] and [-4.7, -4.5], respectively (two standard deviations about the mean). Note that the uncertainty about the mean of α is so small that it can be neglected. With the same probability, the sample standard deviations of f and a must be within the intervals [1.2, 1.8] and [0.16, 0.24], respectively. The soil water tension data exhibit a much stronger correlation and are available at a much denser grid. It is conservatively assumed that the 320 correlated head data are equivalent to only 50 independent head data. From chapter 8, the unconditional head standard deviation is known (70 cm). Then $\varepsilon_H \approx$ 10 cm.

Four Monte Carlo simulations are implemented. The first one (simulation I) is implemented with overestimated parameters for the variances of f and a (σ_f=1.8, σ_a=0.24). It also strongly overestimates the mean of a. Although A can be determined very accurately under the above assumptions, it is the most difficult one to estimate in the field, since it is generally derived from fitting theoretical equations such as Gardner's (chapter 4) to measurements of unsaturated hydraulic conductivity or the soil water retention curve. In the first simulation, mean logα is therefore set to -4.0, simulating a type of measurement error of half an order of magnitude. Thus the unsaturated hydraulic conductivity is expected to be lower than in the actual field site due to the steeper average slope of the unsaturated conductivity function. Figure 10.21e-h shows the conditional mean concentration for this case in comparison

to the simulation with the correct parameters (Figure 10.21a-d). Due to the reduced mean vertical flux (lower mean conductivity), the plume moves much slower, but along the same path as in the perfect parameter case. The higher variance in f and *a* does not contribute significantly to the spreading of the mean concentration. The higher variance in f is offset by the conditioning effect of the actual field data (which are exactly the same as in the perfect parameter case). The higher variance in *a* is still relatively low and doesn't affect the overall result significantly.

In the opposite case with underestimated variances (σ_f^2=1.2, σ_a^2=0.16) and with a very small mean logα=-5.2 (simulation J, Figure 10.21i-m), the plume moves much faster than the actual plume. The unconditional mean vertical velocity is 6.8 times faster than in the previous case I and almost twice as large as at the actual site. But the plume moves again along the same travel paths and with only a small decrease in plume spreading. Since the travel paths are essentially the same in simulations H, I, and J, the differences in plume spreading are best compared for travel times that correspond to similar travel-distances: Conditional simulation H at t'=8 against I at t'=31 (to be accurate it should be t'=28) against J at t'=4. The differences in the plume spreading caused by erroneous assumptions about the soil variability are obvious. Note that the different output times use different contouring levels.

Figure 10.22e-h shows the mean plume prediction from a simulation that again overestimates the variances of f and *a*, but has the correct A (mean of *a*) and an overestimate of F, the mean of f (conditional simulation K). Due to the conditioning, the plume moves only slightly faster than in the perfect parameter case (Figure 10.22a-d) and again with little extra spreading. Similar results are found, if the f and *a* parameters are estimated correctly, but the mean soil water tension is too wet (conditional simulation L), resulting in a higher average conductivity (Figure 10.2i-m).

These results show that conditioning not only reduces the uncertainty due to spatial heterogeneity, but also reduces the unknown errors that arise from a limited knowledge of the

overall soil properties. Conditioning data tend to neutralize the parameter estimation error. With a high amount of tension data and some conductivity data, mean and variance estimation becomes a relatively minor source of uncertainty compared to the uncertainty arising from the spatial variability of the parameters. The effect of uncertainty in the correlation function needs to be explored in a future study.

10.10 Conditional Mean Displacement Variance and Conditional Moment of Inertia

The concentration moments are a function of both space and time. The Monte Carlo analysis of concentration moments is therefore associated with large amounts of data storage and data handling. It is also cumbersome - particularly in three dimensions - to visualize the results in an efficient manner. The spatial moments of the solute plume i.e., the center of mass and the moment of inertia (chapter 9), are a much more concise measure of the concentration distribution and of the uncertainty about the plume location. They reduce the multiple plots of two- or three-dimensional concentration fields to a single-valued function of time. Dagan (1984), Rubin (1991c), and Zhang and Neuman (1994c) use the second spatial moments of the mean solute plume to illustrate the effect of conditioning in mildly heterogeneous porous media. They show that the second moment of the mean concentration plume decreases towards the size of the actual plume as the number of conditioning points increases, since the spreading of each individual plume is smaller than that of the mean plume.

In chapter 9, three measures related to the position and size of the solute plume were introduced: the mean vertical and horizontal spreading of each plume around its center, $<M_{zz}>$ and $<M_{xx}>$; the variance of the plume center displacement in the vertical and horizontal direction, $var(M_z)$ and $var(M_x)$; and the vertical and horizontal spreading of the mean concentration plume, X_{zz} and X_{xx}, which is computed as the sum of the two former measures (eqn. 9-3, see also Fisher et al., 1979). Figure 10.23 shows these moments for the actual plume

at field site #28 as a function of dimensionless time $t'=tV_z/\lambda_{fz}$ (solid curve) with those from the corresponding Monte Carlo simulations A (dense grid of f, *a*, h data; long dashed curve), H (dense grid of h data, sparse grid of f data; short dashed curve), and G (sparse grid of h data; dash-dotted curve), and for the unconditional simulation of this site (dotted curve). The dimensionless moments (indicated by an apostrophe ') are normalized by dividing the actual moments with the product of the square of the vertical correlation scale of f and the variance of f, ($\lambda_{fz}\sigma_f^2$) (see also chapter 9).

The average plume spreading $<M_{zz}>$ and $<M_{xx}>$ are determined primarily by the variability and correlation scale of the soil texture (Russo, 1993a). The moments of individual plumes may vary in many different ways, particularly since the spatial distributions of the solute plumes are generally non-Gaussian for the hypothetical field sites studied here. At site #28, the horizontal spreading of the actual plume has a small step increase at early time t' (0.5 - 1.5) which stems from the diagonal plume movement, and a very large increase after t'=8 to almost 8 times the value for the vertical spreading at t'=15 (Figure 10.23a,b) indicating the horizontal plume movement observed in the map of the actual concentration distribution (Figure 10.5a-b). The vertical spreading indicates a strong expansion-contraction cycle between t'=8 and t'=16. Since the expansion is seen for both the horizontal and the vertical moment, there is likely an accelerated diagonal movement of parts of the plume after t'=8 (no concentration data are available for the time between t'=8 and t'=16 to exactly explain the anomaly in M_{zz}). Curiously, $<M_{zz}>$ from simulation A shows exactly the opposite anomaly at the same time (Figure 10.23a): a strong contraction followed by some expansion. While the actual plume has a vertical spreading comparable to the unconditional plume, all conditional plumes significantly underpredict the vertical spreading of the solute. In contrast, the conditional data improve the prediction of horizontal spreading that occurs after t'=8 (Figure 10.23b). At earlier times, the horizontal spreading predicted is very similar for all three types of conditioning and for the unconditional simulation.

The variance var(M_z) of the vertical displacement of the plume center decreases significantly as the number of data increases (Figure 10.23c). The unconditional simulation has a very large center displacement variance, much larger than the average spreading $<M_{zz}>$ of the individual plumes. For t'<7 the horizontal center displacement variance var(M_x) also decreases (Figure 10.23d). However, due to the strong horizontal spreading of the mean plume after t'=7, the conditional horizontal plume spreading increases with the number of conditioning points, and so does var(M_x). At t'>12 var(M_x) is larger in conditional simulation A than in the unconditional simulation.

From those results it follows that the vertical spreading X_{zz} of the mean plume (Figure 10.23e), which is the sum of the average plume spreading and the plume center displacement variance, shows - for most parts - the expected decrease as the number of conditioning points increases. The decrease in X_{zz} stems mainly from the decrease in the plume center displacement variance var(M_z). But due to the difference between $<M_{zz}>$ and the actual vertical spreading of the field plume, X_{zz} becomes smaller than that of the actual plume for conditional simulation A at t'>8. For the horizontal X_{xx}, the results are ambiguous at early time (t'<8). Only at later times, X_{xx} comes closer to the actual horizontal plume spreading as the number of conditioning points increases. Due to the strong horizontal spreading of the actual plume, the horizontal spreading of the mean plume actually increases with the number of conditional data available (t'>8). Although not shown, it is found that the spatial moments obtained from the conditional mean concentration plume are in good agreement with the sum $X_{ii} = <M_{ii}> +$ var(M_i) (Figure 10.23e,f).

Overall the results indicate that the plume moments do not very accurately reflect the prediction improvement as demonstrated by the conditional concentration moments in previous sections. The discrepancy between the quality of the moment prediction and the amount of conditional data invested is caused primarily by the non-Gaussian shape of the plume. Multiple peaks, meandering, parting of the plume and many other particular features of solute plumes

in moderately to highly variable soils cannot be characterized by the spatial moments of the plume. The larger the plume deviates from the Gaussian shape the less information is contained in the first and second moment, since it becomes very sensitive to the particular distribution of the plume i.e., to higher order spatial plume moments. This explains why the increase in conditioning points does not necessarily improve the accuracy of the moment prediction.

In soils with a less variable flow field, the spatial concentration distribution is much closer to the Gaussian form, and hence the above three measures of plume spreading are increasingly helpful in describing the actual contribution of conditioning i.e., in describing the actual plume movement. This is demonstrated in the spatial analysis of the concentration distribution at site #12 (Figure 10.24), which has an only moderate variability in the unsaturated hydraulic conductivity ($\sigma_y^2 = 0.5$). But even here it is seen that at different times, the accuracy of the predictions do not necessarily reflect the degree of conditioning (e.g. the prediction of X_{xx} in Figure 10.24f at time t'=5). This is consistent with findings of Zhang and Neuman (1994c).

In soils with flow fields that are even more variable than at site #28, the value of using spatial moments of the concentration distribution to assess the plume movement via conditional simulation becomes questionable due to the highly irregular shape of the actual solute plume, as demonstrated for site #21 (Figure 10.25), where $\sigma_y^2 = 3.2$.

10.11 Conditional Local Solute Travel Time

From a regulatory point of view, the spatial distribution of solute concentration is in many cases not as much of interest as the arrival time distribution of the solute at some compliance surface. For transport through the unsaturated zone, the compliance surface is mostly the aquifer water table, since the aquifer rather than the soil itself is the resource that is protected under many environmental regulations. In this section the focus is the solute flux

breakthrough at a certain depth below surface as a function of time and location on the compliance surface. In the two-dimensional simulations the compliance surface reduces to a horizontal compliance axis (CL). The compliance axis in all simulations is located across the center of the two-dimensional, vertical simulation domain (z/λ_{fz} = 11.6). In chapter 9, two measures to characterize solute breakthrough at each horizontal location x of the CL were introduced: The time t_p of arrival of the peak solute flux and the time t_a of first exceedance of a certain compliance solute flux.

Figure 10.26 shows the peak time of solute flux at the field site and the mean and variance of the peak time obtained from the conditional and unconditional MCSs. The vertical time axis is normalized by the mean unconditional travel time $t = V_z/z$ where z is the distance from the source to the compliance surface directly underneath the source. At the field site, the main features of solute breakthrough are two areas of relatively fast breakthrough i.e., early peak solute flux time, at x≈-200 cm and at 400cm < x < 1000 cm (horizontal distances are measured with respect to the point directly under the solute source). This corresponds to the two advancing fronts of the solute plume seen in Figure 10.5 at t'=8 and t'=16. Prediction of these two distinct and quickly advancing fronts would seem critical for regulatory purposes.

None of the conditional simulation predicts an advancement of peak travel time as fast as it actually occurs at the field site. The best predictions are by conditional simulation A, which predicts peak concentrations of the two advancing fronts to occur approximately 10% later. Peak times at other locations of the compliance axis are estimated conservatively by simulation A. Conditional simulation H (dense head data, sparse f data) predicts peak arrival generally later than A and shows much less distinction for the two advancing fronts. Conditional simulation G (sparse head data) makes a better distinction between the two advancing fronts and gives a fairly accurate prediction of the location of breakthrough of these fronts, but at later time than the other two conditional simulations. The variance of the peak time increases with less conditional data due to the increase in concentration variance seen

previously. Between simulation A and the unconditional simulation, the difference in variance is approximately a factor 2 near the center of the compliance axis.

A more detailed picture of solute breakthrough is given by the arrival time t_a or first exceedance of the compliance solute flux s/s_0. In Figure 10.27 these times are mapped for various compliance solute flux levels. The lowest s/s_0 levels are first exceeded i.e., arrive first. The white area outside the plume indicates that the compliance level was never exceeded (see chapter 9). The advancement of the two split fronts of the solute plume is again seen in the map for the field site: The arrival time of all but the highest s/s_0 levels is much earlier at -200 cm < x < 0 cm and 400 cm < 600 cm than at x = 200 cm. Conditional simulation A is the only simulation that reproduces a similar split pattern. But even for this high data density, the arrival times of any particular s/s_0 level is underestimated by approximately 20%. Also, at most lower s/s_0 levels, the conditional simulation predicts an earlier breakthrough of the left front when compared to the right front, while in reality the opposite is true. The distinction between two advancing fronts is entirely lost in the other conditional simulations, which show the arrival time of any s/s_0 level to be the shortest to the left of the center of the compliance axis, and then longer the further away from the center. The unconditional simulation has the largest error in predicting the arrival time of s/s_0 levels due to the fact that the actual plume moves overall faster than the average velocity. Again the variance increases for less conditioning data.

Much of the insensitivity of the travel time moments may be due to the particular location of the compliance surface at field site #28: It coincides with the region of strong horizontal movement, which is well predicted with simulation type A, but less explicit and at slightly different locations with simulation types G and H. At field site #21, the compliance surface coincides with strong vertical solute movement on the left site of the center of the compliance line. In this case, a much higher sensitivity of the solute arrival moments e.g., the mean arrival time t_a of s/s_0 is found, although the soil flux is much more variable.

In summary, the mapping of the two time parameters to characterize the solute flux

breakthrough as a function of location on the compliance axis may not nearly be as sensitive to conditioning as the local concentration moments are. If strong horizontal flux occurs at or near the compliance surface, the results of the travel time analysis may be very vague. Ideally the compliance surface should be located such that solute flux is known to be predominantly normal to the compliance surface. Otherwise the effect of conditioning may only be weak in the arrival time of certain solute flux compliance levels or the peak concentration. While conditioning works well to predict the general spatial distribution of the concentration, this shows that it may be less effective for predicting solute flux arrival times or breakthrough curves, since the amount of data necessary to predict these accurately can under circumstances be enormous. And depending on the flux pattern across the compliance surface, the improvement in the mean time predictions due to sparse conditioning may be relatively small or very significant.

10.12 Conditional Integrated Solute Breakthrough Curves

Given that the local breakthrough curves are not necessarily sensitive to conditioning, the question arises whether the integrated solute breakthrough curve (BTC) is similarly insensitive. The solute breakthrough curve represents total mass flux across the compliance surface at any given time. The data are compiled not only at the compliance surface in the center of the domain, but also at every other quartile of the domain depth (1/4 depth or $5.4\lambda_{fz}$ travel distance, 3/4 depth or $17.8\lambda_{fz}$ travel distance, and bottom boundary or $23.8\lambda_{fz}$ travel distance). The actual breakthrough curve at field site #28 is plotted against the mean breakthrough curves of the conditional simulations A, H, G, and the breakthrough curve of the unconditional simulation (Figure 10.28a-d). The mean breakthrough curves clearly show the effect of conditioning, particularly at the two top compliance axes (Figure 10.28a,b). At those two levels, the actual plume BTC has an almost Gaussian shape, and increasing the data density

leads to less dispersed mean BTCs in the conditional simulation with the result that the peak concentration is much better predicted if more data are used for conditioning. At the 3/4 depth and the bottom of the simulation domain, the BTC of the actual plume significantly deviates from the Gaussian shape due to the very heterogeneous shape of the solute plume. The conditional breakthrough curves give results of variable accuracy, which cannot be related to the number of conditioning points (Figure 10.28c,d). This is not surprisingly similar to the insensitivity of the spatial plume moments at later time, since the temporal plume moments are related to the spatial plume moments and suffer from similar disadvantages. Note that the variance of the breakthrough curves nevertheless decrease as the number of conditioning points increases (Figure 10.28e-h). Also, as the number of conditioning points increases, the time span of high standard deviations of the BTC decreases. This indicates that the while the prediction about the average solute flux at a given time does not necessarily improve with the amount of data used for conditioning, the uncertainty about the prediction decreases almost always. Similar observations are made for field site #21 (Figure 10.30). In contrast, the effect of conditioning is very obvious in the mean BTCs for the moderately heterogeneous site #12 (Figure 10.29) as found by other researchers in the past (Smith and Schwartz, 1981b; Gutjahr et al., 1994; Zhang and Neuman, 1994c).

10.13 A Deterministic Geostatistical Inverse Approach in Comparison

It may be argued that with a reasonable amount of information - such as that in sampling scheme A - the stochastic technique is superfluous and a reasonable prediction can be made through deterministic approaches alone. This argument may be appropriate if one is interested in a prediction of solute transport without an estimation of the associated uncertainty. With deterministic modeling uncertainty cannot be quantified. If a model is only needed to give an approximate prediction of the solute plume movement, methods other than the

stochastic technique should be considered.

By generating a zero variance unconditional realization of f and *a* and by assuming that all other pertinent statistical moments are known (F, Γ, cov_f, cov_a, cov_h, $ccov_{fh}$, $ccov_{ah}$, where cov is the covariance and ccov is the cross-covariance), the conditional simulation algorithm of section 10.3 (Figure 10.1) reduces to the geostatistical inverse modeling approach described similarly for saturated groundwater flow by Neuman and Yakowitz (1979), Kitanidis and Vomvoris (1983): The measurements of f, *a*, and h are used to estimate the remaining unknown f and *a* data in the simulation grid through the linear, unbiased, cokriging estimator introduced earlier. The steady-state head solution and solute transport is then computed for the cokriged f and *a* field. The geostatistical inverse modeling technique is only one of several other indirect inverse modeling techniques (Schweppe, 1973; Neuman and Yakowitz, 1979; Carrera and Neuman, 1986; Peck et al., 1988).

The geostatistical inverse approach (cokriging) is applied to field site #28 given the same data as used for the conditional simulation A of that site. Since the measured data density is relatively exhaustive, the f and *a* parameter estimation is associated with only small errors (see section 10.5). Like any random realization of the conditional simulation A (section 10.6), the concentration distribution predicted from the geostatistical inverse model is a very good approximation of the overall plume movement (compare Figures 10.31e-h, 10.31i-m). The solute plume predicted by the inverse model is less dispersed than the conditional mean solute plume since it is not an average concentration. It is also less dispersed than the actual plume, since the underlying parameter fields for f, *a*, and h are subject to minimal perturbation given the conditional data. A less tortuous travel path and a mass balance error in the transport simulation of up to +13% lead to higher predicted peak concentrations in the inverse model than observed at the field site.

10.14 Summary and Conclusions

A number of studies presented in the literature analyze the uncertainty associated with predicting transport of solutes in heterogeneous unsaturated soils. Both analytical and numerical models have been developed to address this issue. But without exception in situ measurement data have not been incorporated in the stochastic analysis except to determine the unconditional parameters of the statistical models that describe soil heterogeneity. Neither has any study to date taken advantage of the available in situ information for soil water tension or other data indirectly related to the soil textural heterogeneity (indirect data) to reduce the prediction uncertainty associated with the unconditional stochastic approach to modeling solute transport. Most recently, Neuman and Loeven (1994) have introduced a new approach that allows one to derive the conditional moments of the soil water tension, soil water content, and soil water flux. But the approach has not yet been applied to also derive conditional concentration moments. With the conditional approach developed in this work a model is provided to compute the spatial distribution of estimation errors associated with solute transport predictions subject to in situ data measurements of either direct data (K_s and/or α) or indirect data (soil water tension) or a combination of both.

The difficulties that have prevented conditional simulation of nonlinear unsaturated flow and transport in the past are overcome by introducing an approach called conditional ASIGNing. The method is based on the ASIGNing technique (Harter and Yeh, 1993; chapter 7), which generates not only unconditional random fields of f and a, but also an approximate linearized solution h_L to accelerate the CPU-time for the finite element solution h of Richards equation. In this chapter, the ASIGNing method is combined with the geostatistical approach in general (Matheron, 1971; Journel, 1974; Delhomme, 1979) and cokriging in particular (Myers, 1982; Carr and Myers, 1985). The key to the efficiency of the new conditional simulation algorithm is the use of the first order perturbation approach described in chapters 4

and 7 to compute an unconditional head random field h_L that is approximately consistent with the unconditional random fields f and a. h_L is an intermediate result in the conditioning algorithm (Figure 10.1). The h_L field is necessary to condition the corresponding f and a realizations (eqn. 10-1) on soil water tension data and to construct a geostatistical estimate of the conditional soil water tension realization h_L^c as initial estimate to again accelerate the CPU-time for the finite element solution h^c of Richards equation. Although the linearized, first order head solution is only an approximation of h, the results indicate that its application in the conditioning process is justified since the conditional moments of f^c and a^c are also linear estimates (cokriged estimates). Like other (linear) conditional algorithms conditional ASIGNing does not lead to solutions h^c of the flow equation (given the conditional f^c and a^c) that perfectly honor the measured head data. But the conditional variance of the head at the measurement points are at the most 5%-10% of the unconditional head variance. Forcing the correct heads at the points of measurement by imposing internal boundary nodes would lead to ill-conditioned gradient and velocity fields.

In this chapter, conditional ASIGNing has successfully been applied to the Monte Carlo simulation of conditional stochastic transport in a number of hypothetical soil types with varying degrees of textural variability, anisotropy, and moisture content. Conditional moments were analyzed not only of the spatial distribution of the concentration mean and variance at time t, but also of the overall plume spreading and of the arrival time of the solute as measured by a number of different parameters such as the solute breakthrough curve at a hypothetical compliance surface. In summary of the Monte Carlo simulation (MCS) results I have the following conclusions:

From a numerical-technical point of view, conditioning even on a few indirect data is an important tool to eliminate some of the most unlikely possible plume travel dynamics in the Monte Carlo sampling procedure. Most importantly, conditioning on either direct or indirect data at the source removes the outlier problem in unconditional Monte Carlo simulations of

highly heterogeneous soils. Outliers of concentration levels occur near the source due to sometimes extremely low conductivities at or near the solute source. Outliers of permeability values far from the source are generally no problem, since the travel path of the plume avoids such stagnant areas. Conditioning on near source information greatly reduces the risk of outliers that may bias the sample statistics. In addition, less realizations are necessary per MCS to achieve the same level of sample moment accuracy due to the decrease in the ensemble variability. Conditional simulations are therefore computationally less expensive than unconditional simulations, although additional CPU time is needed for the conditioning of each realization. In this analysis, 150 conditional realizations gave very accurate sample estimates, if either h or f or both are measured in a dense grid. If only sparse sampling data are available, the number of realizations was increased to 300, the same number as in the unconditional simulations (chapter 9).

The most important difference between unsaturated and saturated conditioning is the physical nature of unsaturated hydraulic conductivity, which is not an independent property of the soil, but determined by the soil water content and soil water tension and by a number of textural properties of the soil. The unsaturated conductivity cannot be conditioned directly unless it is measured in situ. It is here assumed to be dependent on two parameters besides the soil water tension h, which are often measured at different locations. If both parameters $f=\log K_s$ and $a=\log\alpha$ of the K(h) function (4-8) are known at one location, and if the soil water tension is measured nearby ($0.25\,\lambda_f$), then the conditional variance of the unsaturated hydraulic conductivity reduces to almost negligible values. But if a is not measured, the uncertainty about K at the f measurement points may be significantly larger depending on the mean and variance of a and depending also on the mean soil water tension.

In this study it is assumed that unsaturated steady-state flow occurs under unit gradient conditions with the major anisotropy axis transverse to the mean flow direction. The steep mean gradient and the transverse anisotropy have a stabilizing effect on the flow pattern.

Hence, for anisotropic soils with moderately heterogeneous flow ($\sigma_y^2 < 1$) the assumption of one-dimensional vertical flow (parallel column model) is mostly justified. In such soils the unconditional simulation approach yields results that are a relatively good approximation of the actual plume even if the plume is from a small source (provided the source location is known). The uncertainty about the solute plume movement is reduced primarily to uncertainty about the vertical travel velocity. Since moderately variable flow is mostly restricted to wet soils, the travel velocity is strongly correlated with the saturated hydraulic conductivity. Conditioning on f will therefore reduce uncertainty more than conditioning on a or h. In moderately heterogeneous, anisotropic soils conditioning on head data alone will not significantly improve the unconditional prediction of solute transport.

In soils with strongly heterogeneous, anisotropic flow fields ($\sigma_y^2 \geq 1$) i.e., in very heterogeneous soils or in dry soils, the travel path significantly deviates from the vertical direction and is characterized by a significant amount of horizontal displacement and tortuosity. In isotropic soils, similar observations are made even for moderately heterogeneous flow fields ($\sigma_y^2 > 0.5$). Solute plumes of small initial lateral dimensions (0.3λ) are found to have multiple peaks, multiple fronts, and are generally of a very erratic shape. With the unconditional stochastic transport approach, the uncertainty about the plume movement in both the horizontal and vertical direction leads to very large mean concentration plumes (see chapter 9). While an unreasonable amount of data would have to be retrieved from the soil to accurately predict the solute movement in such highly heterogeneous soils, conditioning on either a few indirect or a few direct data will significantly improve the prediction of the mean concentration plume and reduce the prediction uncertainty as measured by the spatial distribution of concentration mean and concentration coefficient of variation.

The information content (i.e., the ability to reduce uncertainty in a conditional simulation) of f alone decreases not only with increasing heterogeneity but also as the soil dries out, particularly if the mean and variability of a is large and if a is not strongly correlated with

f. Then the information content of the head becomes important for two reasons: The spatial distribution of the head carries information about the head gradient field in the soil and therefore about the travel path of a solute plume. Secondly, soil water tension data help to better estimate the unsaturated hydraulic conductivity, which controls both travel velocity and travel path. Hence, in soils with highly variable flow fields, conditioning with head data significantly reduces transport prediction uncertainty despite the fact that the conditioning technique itself relies on a strong linearization of the physical process, which becomes less valid as the flux variability increases (Kitanidis and Vomvoris, 1983). In very heterogeneous soils it appears that soil water tension data reduce the solute movement prediction uncertainty (as measured by the minimum CV_c) more than the same amount of saturated hydraulic conductivity data. The positive effect of head conditioning in very heterogeneous porous media was also observed for saturated groundwater flow (Gutjahr et al., 1994).

This is a very encouraging result since the cost of equipment and labor associated with soil water tension data is generally lower than that associated with obtaining saturated hydraulic conductivity data. It is more likely to find in situ head data than to find in situ information about the saturated hydraulic conductivity. The simulations suggest that a combined network with a relatively high sampling/monitoring rate for soil water tension and a relatively sparse sampling/monitoring rate for saturated hydraulic conductivity leads to a significant decrease in prediction uncertainty about the concentration. From the examples in this study it appears that the combined uncertainty reduction due to a combination of h and f data is beyond the additive impact of head data by themselves and f data by themselves.

The minimum concentration coefficient of variation CV_c is used as a summary measure of the conditioning effect on uncertainty reduction. The changes in the minimum CV_c appear to be approximately consistent with the visual changes on the concentration maps. Future research must address the question of converting the large amount of information about $c(x,t)$ into other representative parameters. In this context I would also like to point out that an exact

definition and quantification of the term "uncertainty" is very difficult, an issue that should be addressed in future research.

The spatial moments of the mean concentration plume are another example of a compact measure to study the impact of conditioning on solute transport in heterogeneous porous media (Dagan, 1982, 1984; Rubin, 1991a; Zhang and Neuman, 1994c). The analysis of the spatial moments of solute plumes in moderately variable flow fields indicated that conditional data primarily reduce the uncertainty about the center of the plume. The uncertainty about the mean spreading of the solute plume is fairly small and the spatial distribution of the actual solute concentration is not much unlike a Gaussian plume. In mildly to moderately heterogeneous, anisotropic soils, conditional spatial moments of the mean solute plume and conditional mean breakthrough curves therefore accurately reflect the effect of conditioning on the solute transport prediction. In strongly heterogeneous flow fields, however, and in isotropic soils with moderate heterogeneities, the significance of the spatial moments of the conditional mean plume is strongly diminished due to the erratic (non-Gaussian) shape both of the individual solute plume realizations and of the mean solute plume. It becomes therefore difficult to quantitatively assess the effects of conditioning by analyzing the spatial solute plume moments alone.

Similarly, the effect of conditioning on the arrival time or breakthrough of a solute at a compliance surface or compliance point some distance away from the solute source is often felt much less direct than in the spatial pattern of the conditional mean concentration, if the flow patterns are strongly heterogeneous. While a significant decrease is found in the variance of these measures, the actual shape of the conditional mean breakthrough curve (locally and integrated) may or may not be similar to the actual breakthrough curve, even with a dense sampling grid for f, a, and h. If the solute flux across the compliance surface is not predominantly normal to the surface, the mean solute flux and arrival time become very sensitive to small changes in the conditional mean flow field, and the effect of conditioning

becomes ambiguous. It therefore appears that the conditional simulation of breakthrough curves in highly heterogeneous porous media must be accompanied by the concentration mean and variance maps to help explain what is seen in the breakthrough curve and to evaluate the effect of conditioning on the breakthrough. Breakthrough curves of solute transport from small sources in strongly heterogeneous soils should therefore not be expected to be very accurate, even when the amount of conditional data is large.

Besides spatial heterogeneity, the estimation of the statistical parameters f, a, and h and the associated estimation error introduces additional uncertainty into the solute transport prediction. The impact of parameter uncertainty is found to diminish with the amount of data available in situ, because of reduced sampling error and more constraints on the stochastic simulation. Parameter uncertainty about the variance of f and a is mainly responsible for increasing the overall spreading of the mean plume. In contrast, errors in the sample mean of f, a, and h result in an error about the mean flux prediction and consequently the error will be not in the travel path of the plume, but merely in the travel time. Overall, however, it appears that the uncertainty of the solute transport prediction arising from soil heterogeneity is much more significant than the uncertainty arising from parameter uncertainty.

In this study, several simplifications are made not only to be able to compare numerical with analytical solutions (see chapters 8 and 9), but also to be able to establish some fundamental relationships between monitoring/sampling network and the heterogeneity of the soil. Future work must address the effect of variable moisture content and transient flow conditions. Measurement errors, parameter estimation errors, particularly about the correlation structure, and error in assuming the wrong models describing the K(h) and h(θ) relationship further increase prediction uncertainty and should be addressed in future research. Thus, it may be expected that the effects of conditioning become smaller. The geostatistical conditional simulation model must be recognized not to be a perfect measure of uncertainty itself, because it is based on a linearization of a nonlinear physical problem (see section 10.2 and 10.3) and

on several important assumptions about the concept of spatial variability in soils (see chapter 2). A field validation of the conditional stochastic approach suggested here is therefore necessary. However, the model is based on statistical concepts, and it seems at this time impossible to implement such a field validation rigorously, because many field experiments (samples) would be needed to judge about the goodness of the stochastic model.

From a practical point of view, the results are both encouraging and disappointing. They are encouraging in that they show that with less computational effort than in the classic unconditional approach, and with data that are relatively simple to obtain in situ (soil water tension), the uncertainty about the predicted plume movement in space can be drastically reduced, particularly for applications to highly heterogeneous soils. It is encouraging also in that the conditional mean concentration predictions are pinpointing to areas where the plume displacement significantly differs from the typical downward movement. This helps to identify locations from which additional data may be taken. If the unsaturated flow field is very heterogeneous conditioning on a few indirect or direct data will greatly improve the stochastic predictions associated with unconditional simulation and with macrodispersion analysis (see chapter 9). But the results are discouraging in that the simulations have shown how difficult it is to describe the (conditionally simulated) plume movement in highly heterogeneous soils by simple measures such as the spatial moments of the mean solute plume or the minimum concentration coefficient of variation. The study has also underlined the difficulty of predicting solute breakthrough at some compliance depth even when conditioning on a high density of direct and indirect data. Further research needs to be done to address these disadvantages. It appears from the results presented in this chapter that even with an enormous amount of field sampling it will be very difficult to predict every detailed aspect of solute transport in moderately to highly heterogeneous soils, particularly the prediction of very low levels of solute concentration either in front of an advancing contamination plume or as residual.

Table 10-1

Classification of the conditional simulation types. Conditional simulations A through H are based on different sampling networks for the parameters f, a, and h. Simulations I through L are applied to field site 28 only toa assess the effect of erroneous statistical iput parameters.

conditional simulation type	sampling density f	sampling density a	sampling density h
A	dense	dense	dense
B	dense	-	dense
C	dense	-	-
D	sparse	sparse	-
E	sparse	sparse	dense
F	-	-	dense
G	-	-	sparse
H	sparse	-	dense
I (as H)	but: (σ_f^2 = 1.8, σ_α^2 = 0.24, $\langle \log\alpha \rangle$ = 4.0)		
J (as H)	but: (σ_f^2 = 1.2, σ_α^2 = 0.16, $\langle \log\alpha \rangle$ = 5.2)		
K (as H)	but: (σ_f^2 = 1.8, σ_α^2 = 0.24, F = 0.5		
L (as H)	but: (H = -140 cm)		

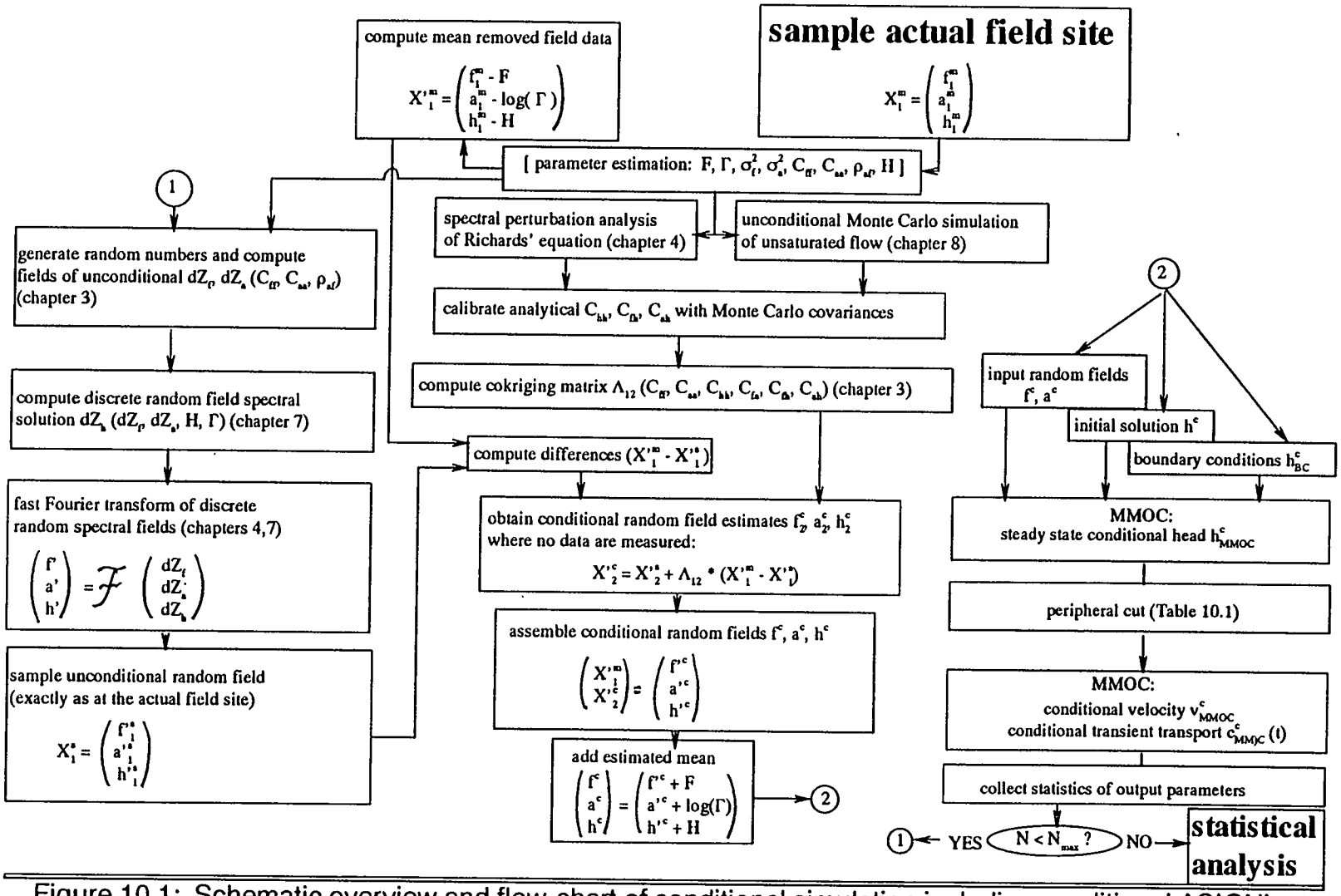

Figure 10.1: Schematic overview and flow-chart of conditional simulation including conditional ASIGNing.

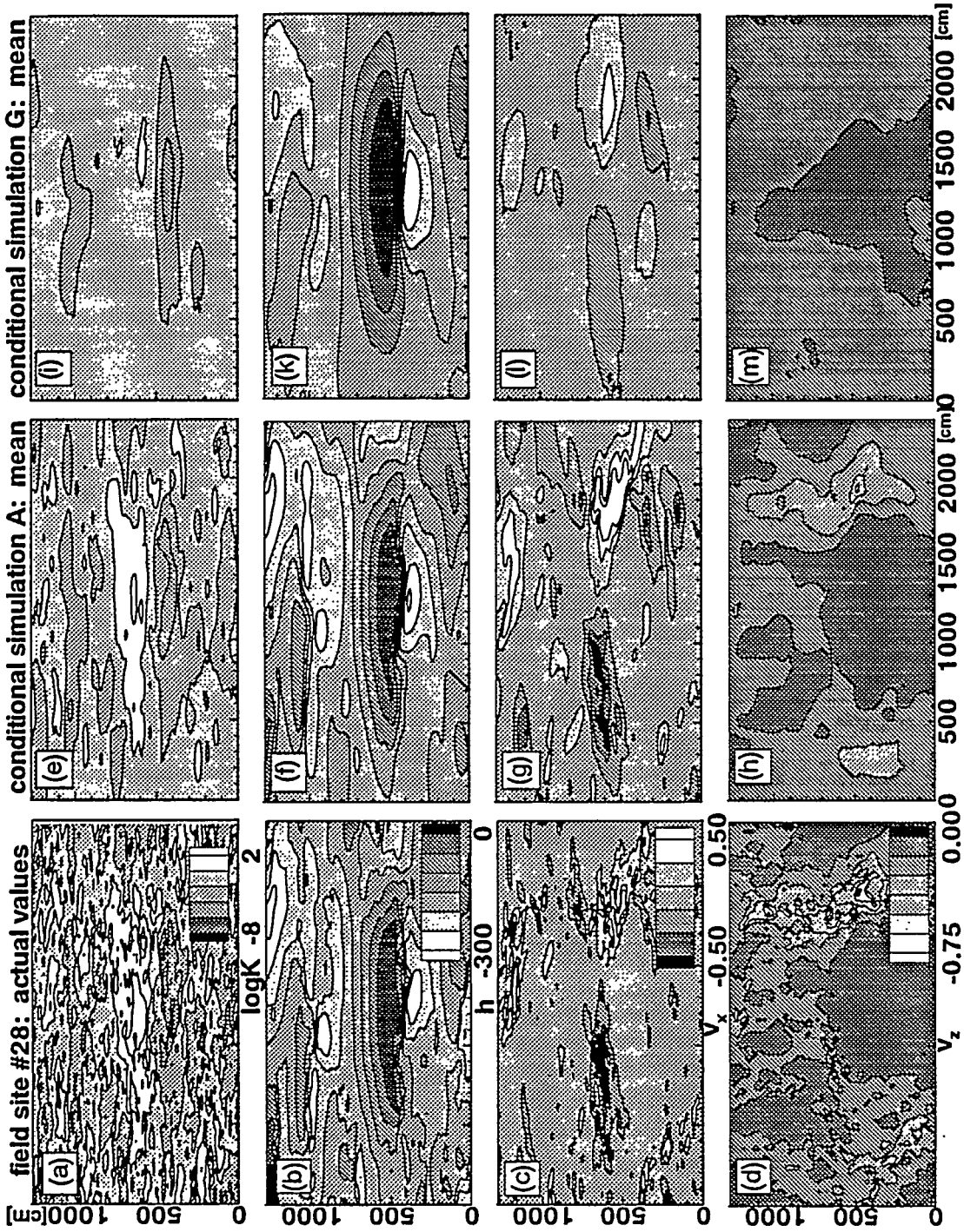

Figure 10.2: Actual field site #28 (a-d), conditional simulation A (e-h), and conditional simulation G (i-m) for the parameters logK (a,e,i), h (b,f,k), v_x (c,g,l), and v_z (d,h,m). Contour labels are idential throughout each row.

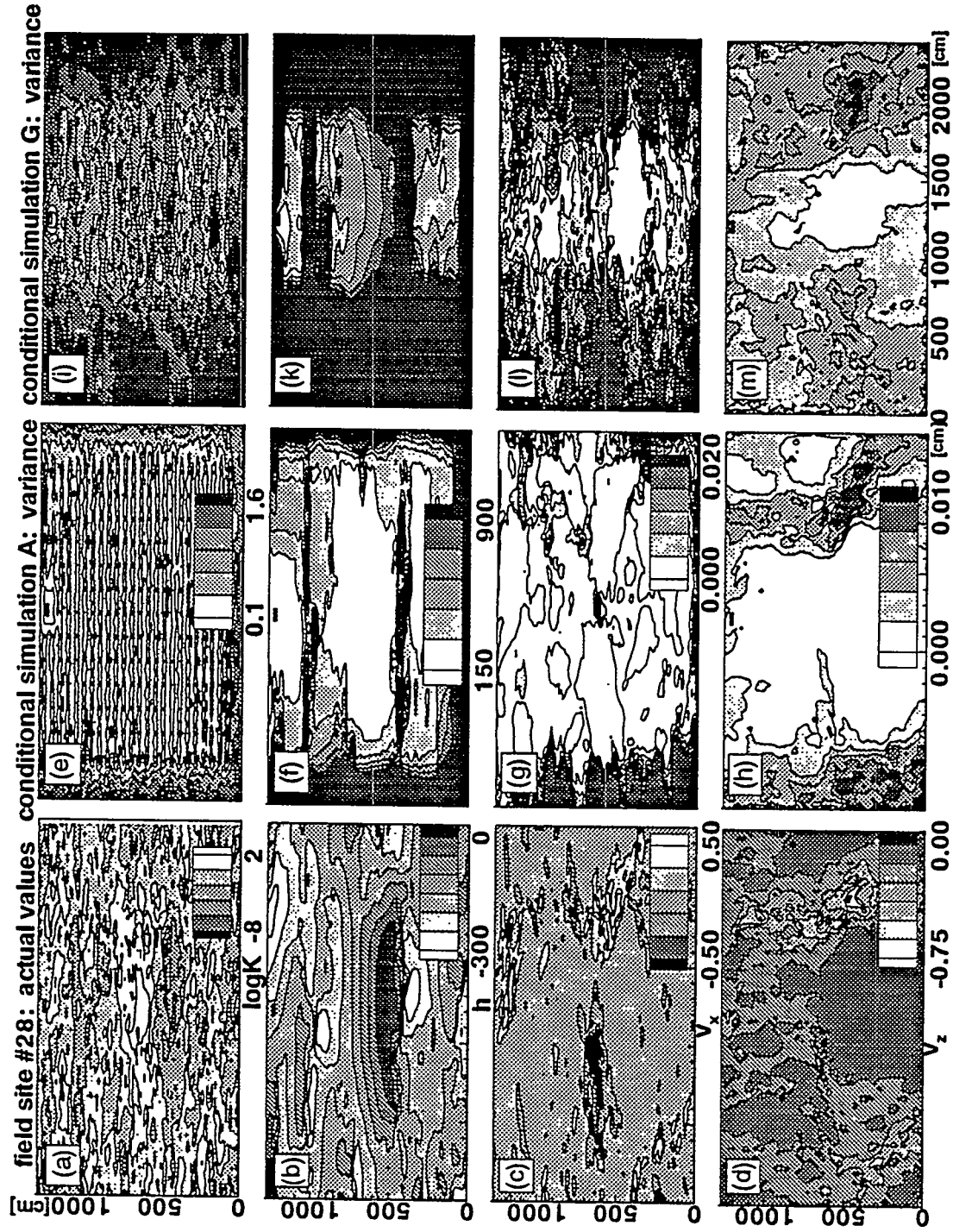

Figure 10.3: Field site #28 (left) and variances for conditional simulation A (center) and G (right).

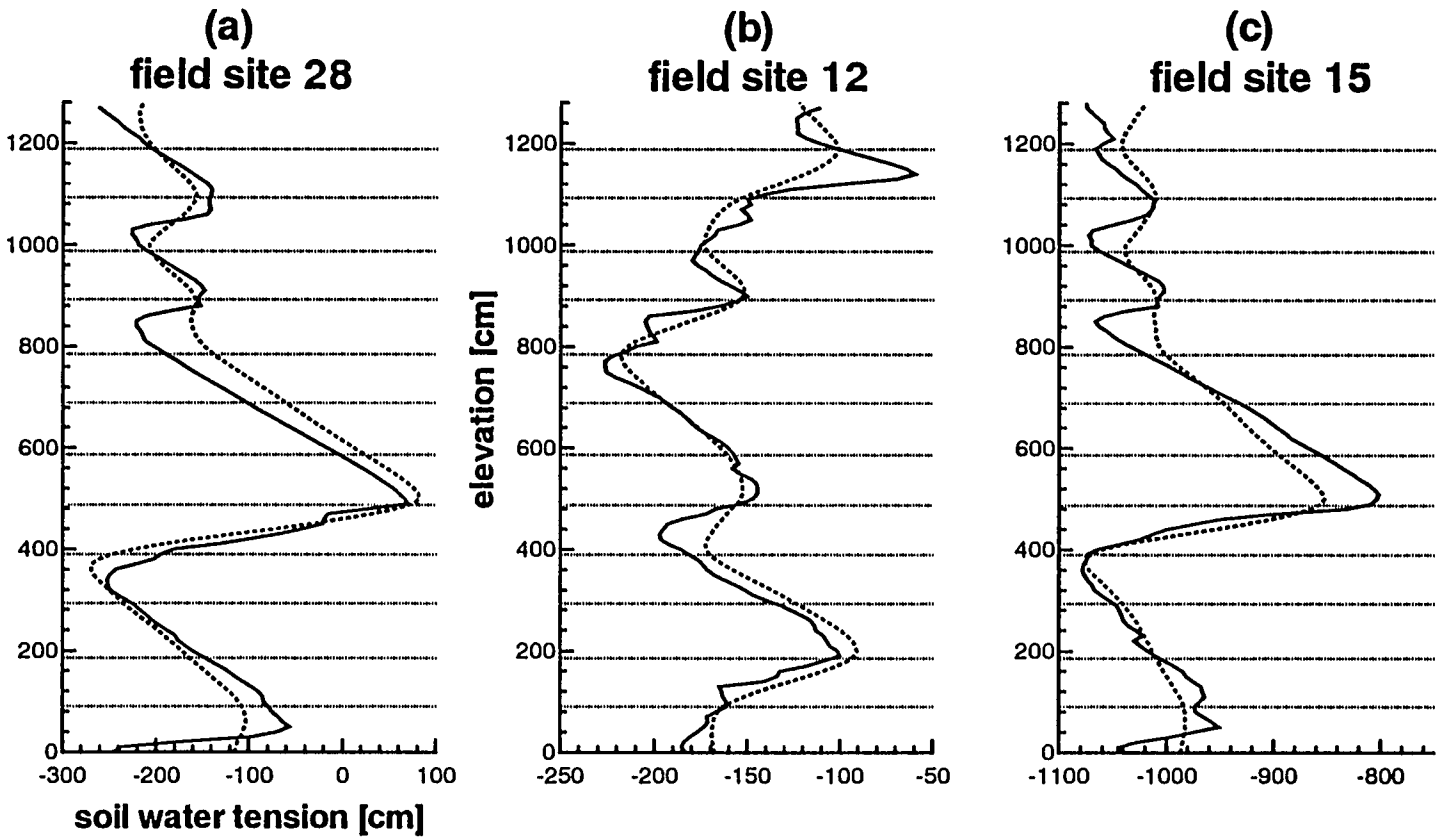

Figure 10.4: Conditional simulation type G - Conditional mean (dashed line) and actual (solid line) soil water tension along the third of three tensiometer nests for three different field sites. The vertical location of the tensiometer data are indicated by dotted lines. Field site #28 and #12 are wet soils with high and moderate variability in $\log K_s$, respectively. Field site #15 is a dry soil with similar textural variability as site #12, but a head variance comparable to site #28.

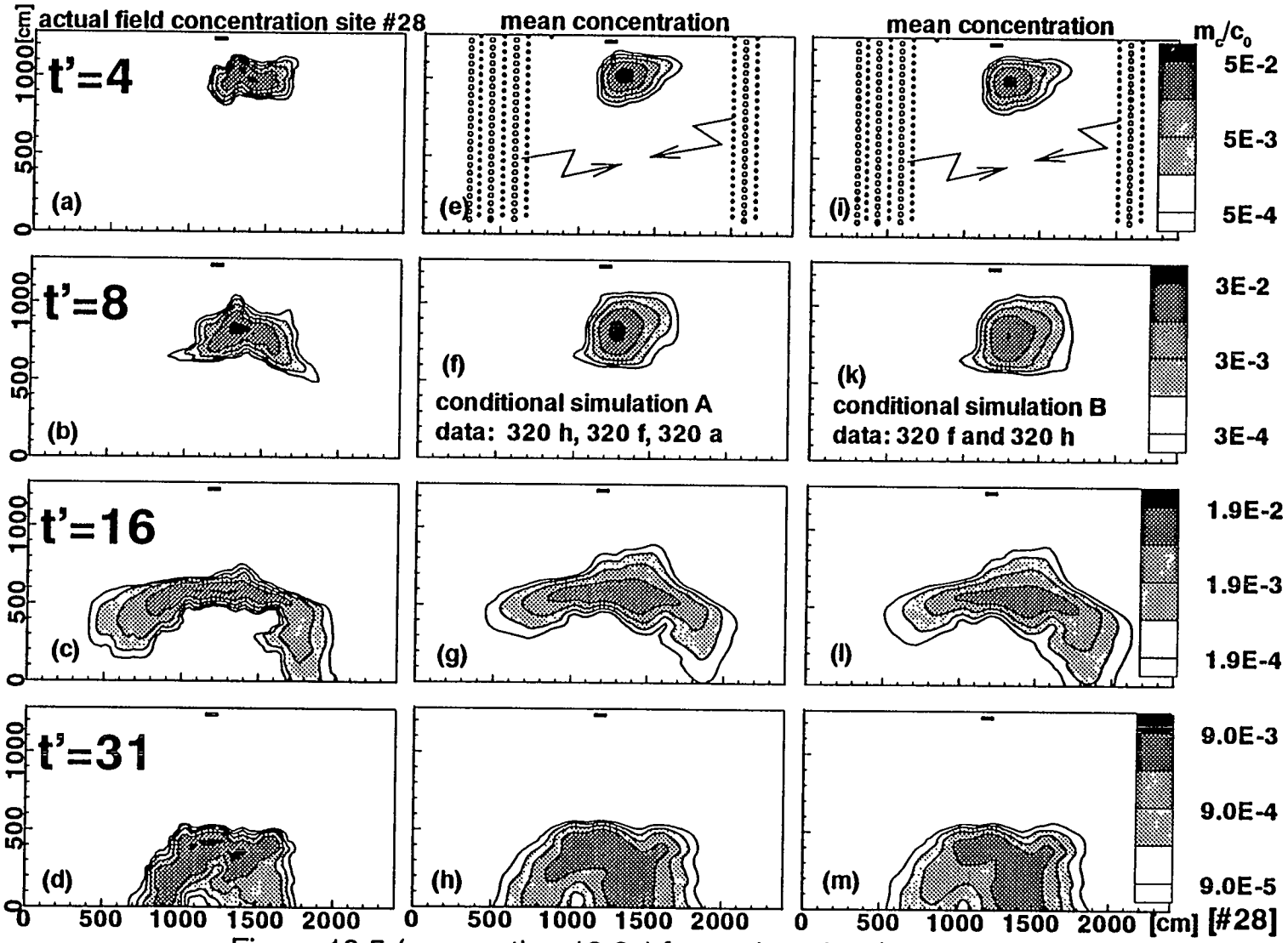

Figure 10.5 (see section 10.6.1 for explanations).

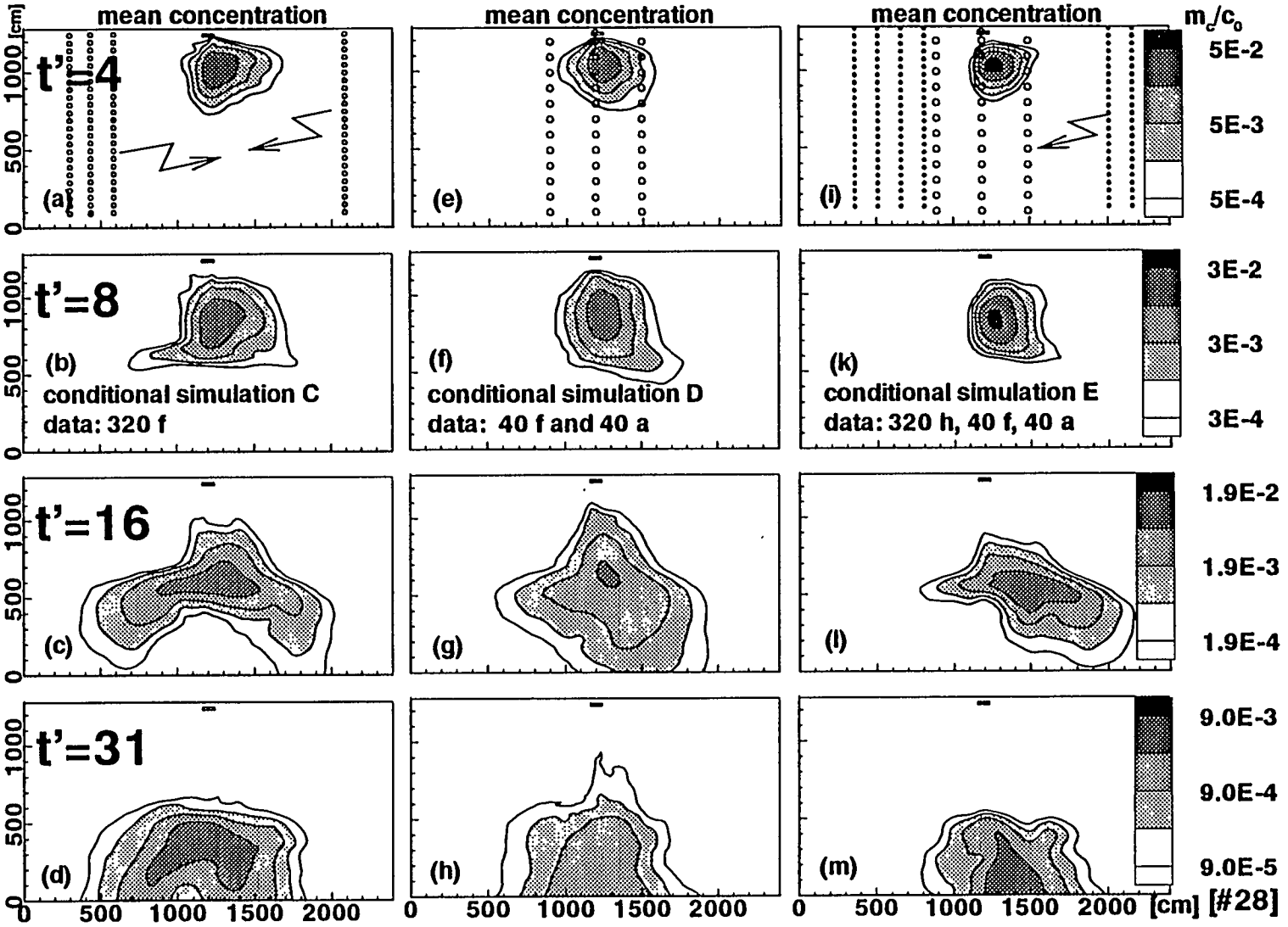

Figure 10.6 (see section 10.6.1 for explanations).

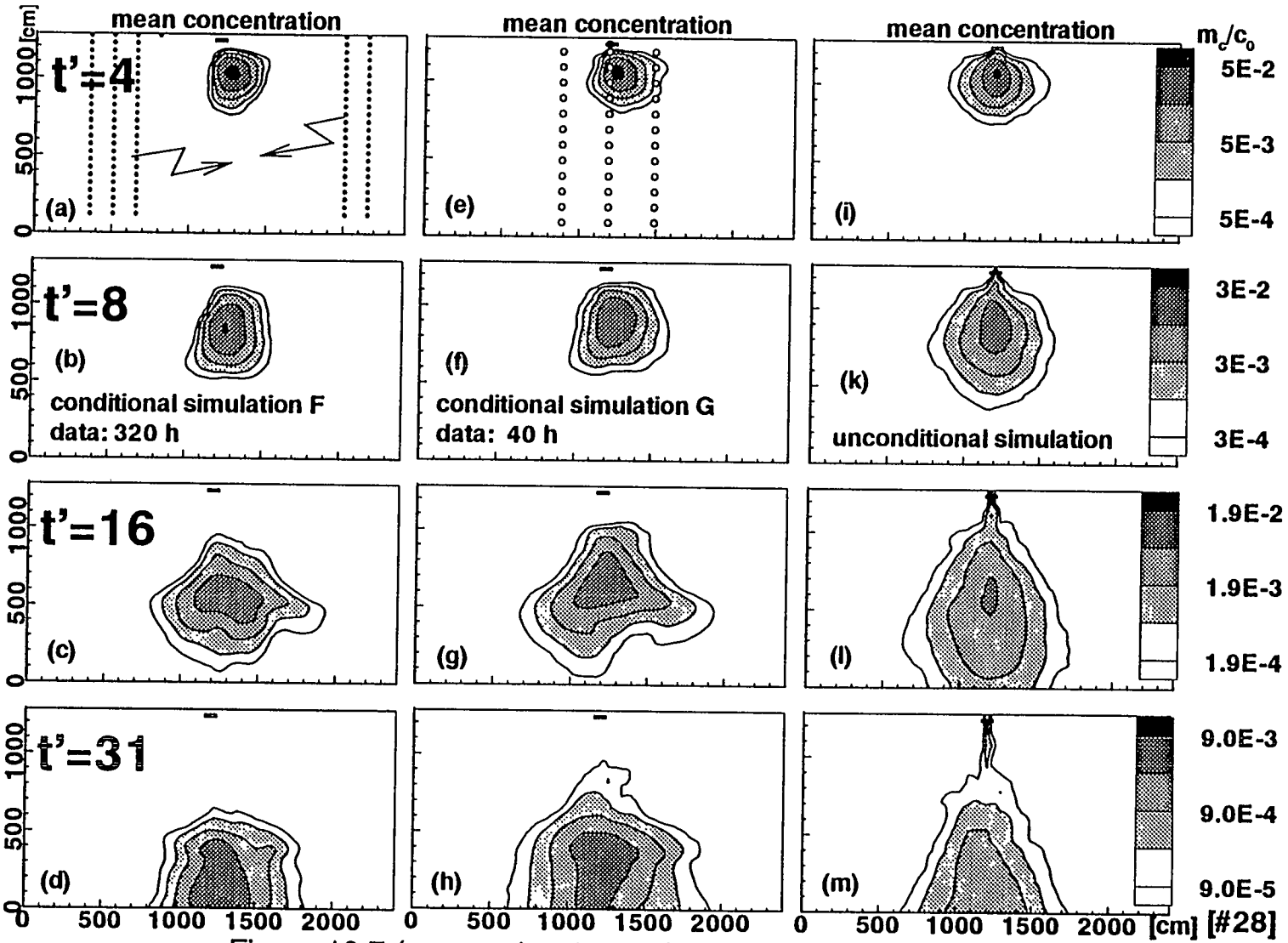

Figure 10.7 (see section 10.6.1 for explanations).

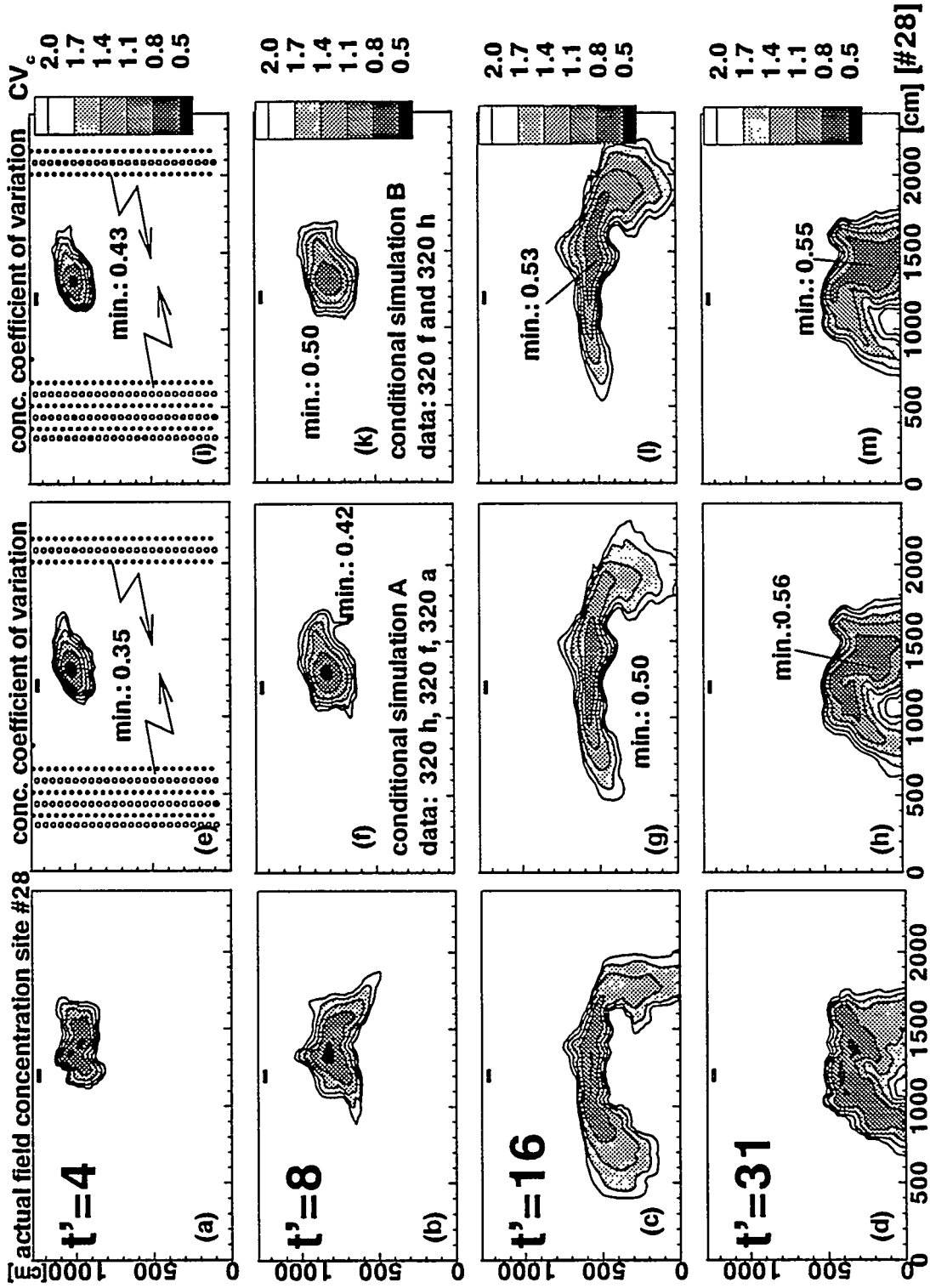

Figure 10.8 (see section 10.6.1 for explanations).

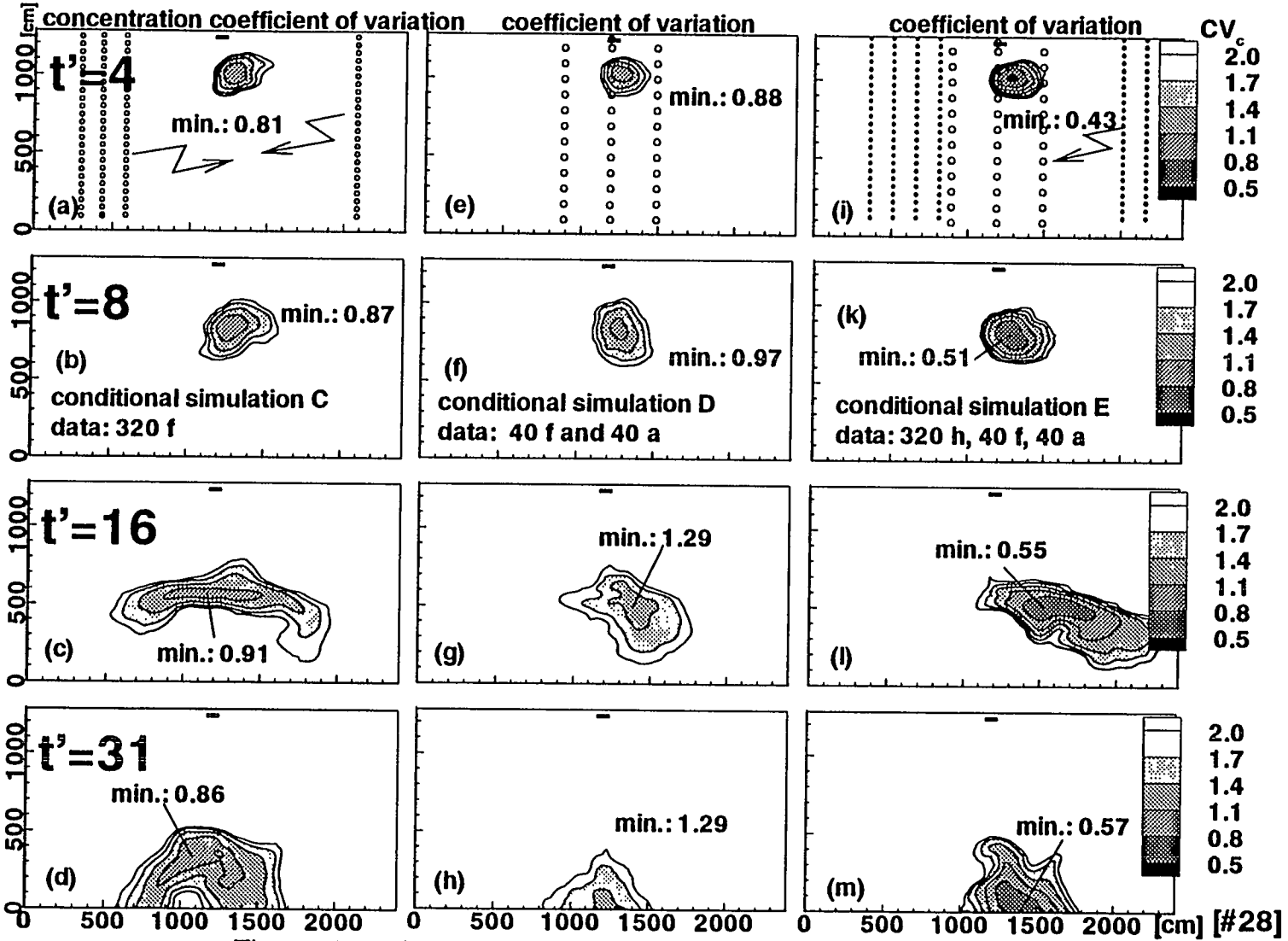

Figure 10.9 (see section 10.6.1 for explanations).

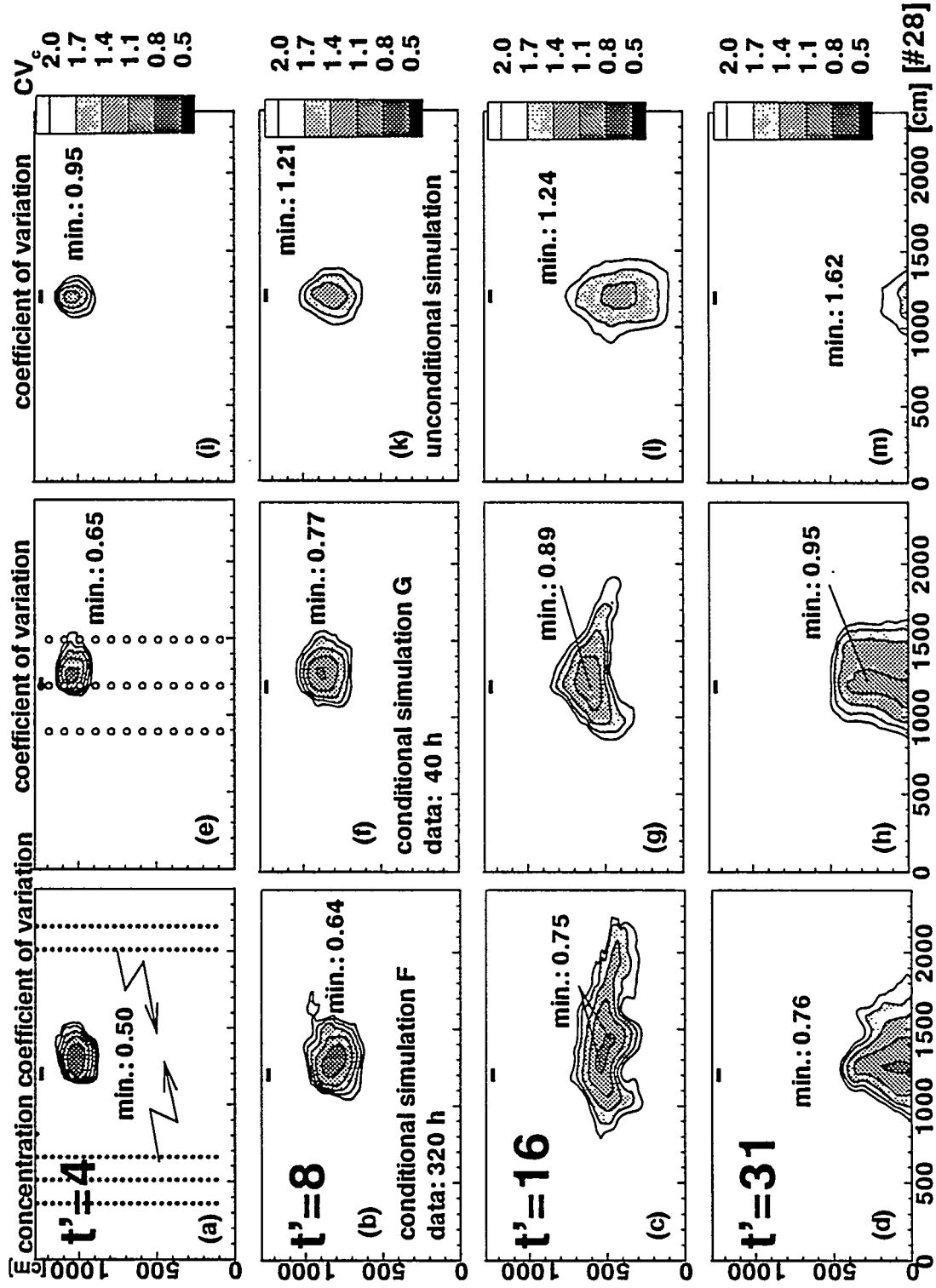

Figure 10.10 (see section 10.6.1 for explanations).

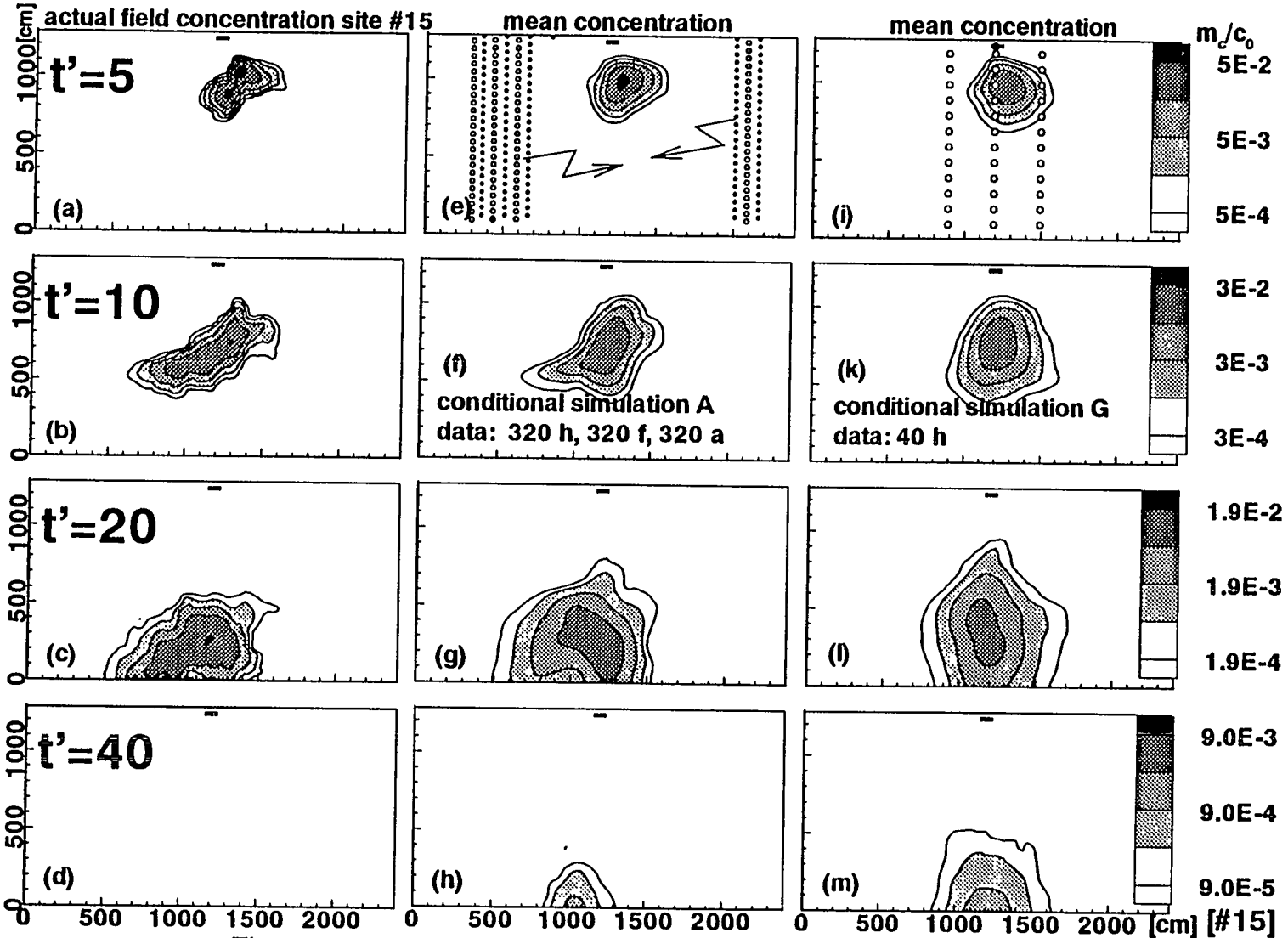

Figure 10.11 (see section 10.6.1 for explanations).

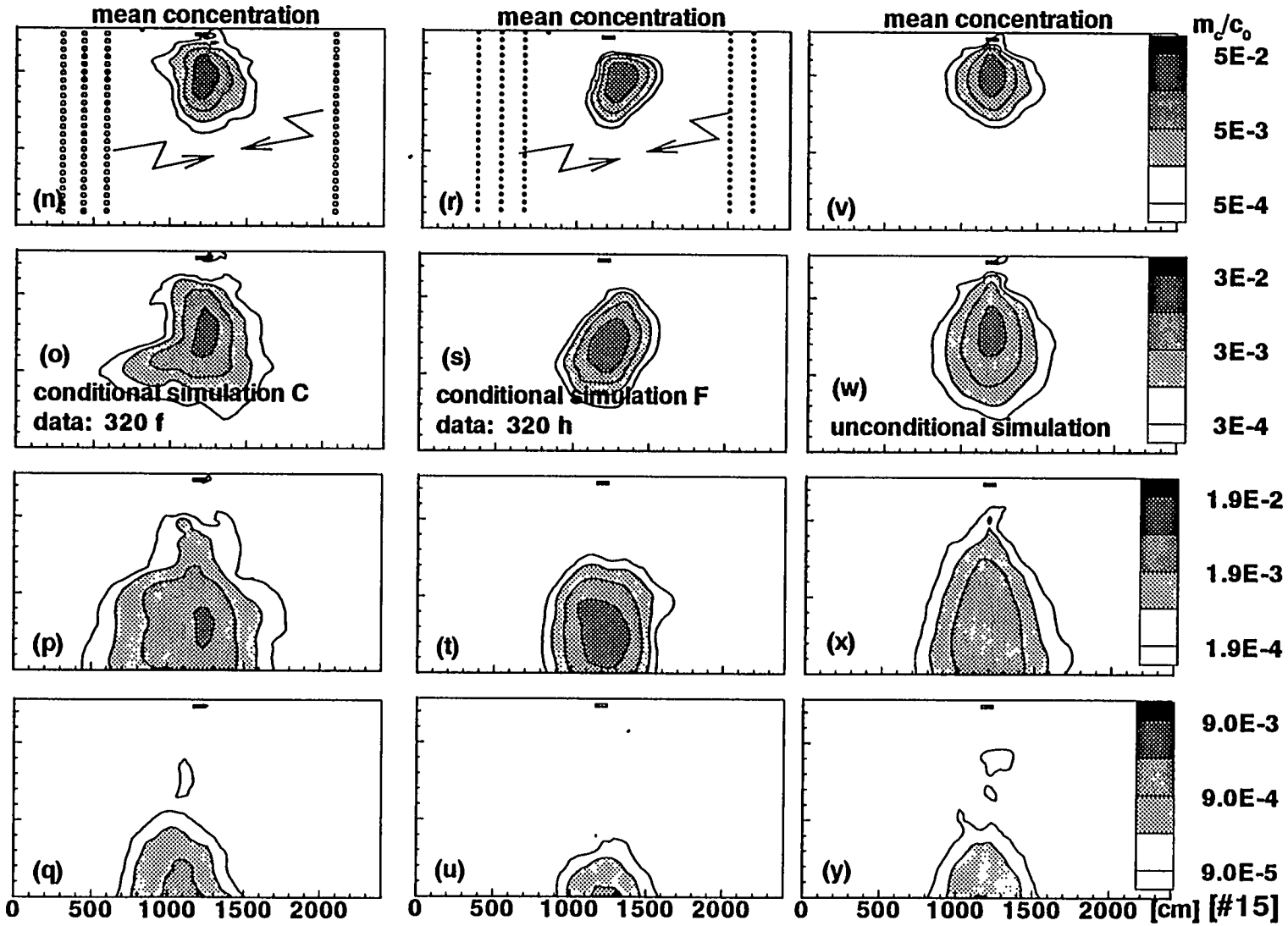

Figure 10.11 (continued, see section 10.6.1 for explanations).

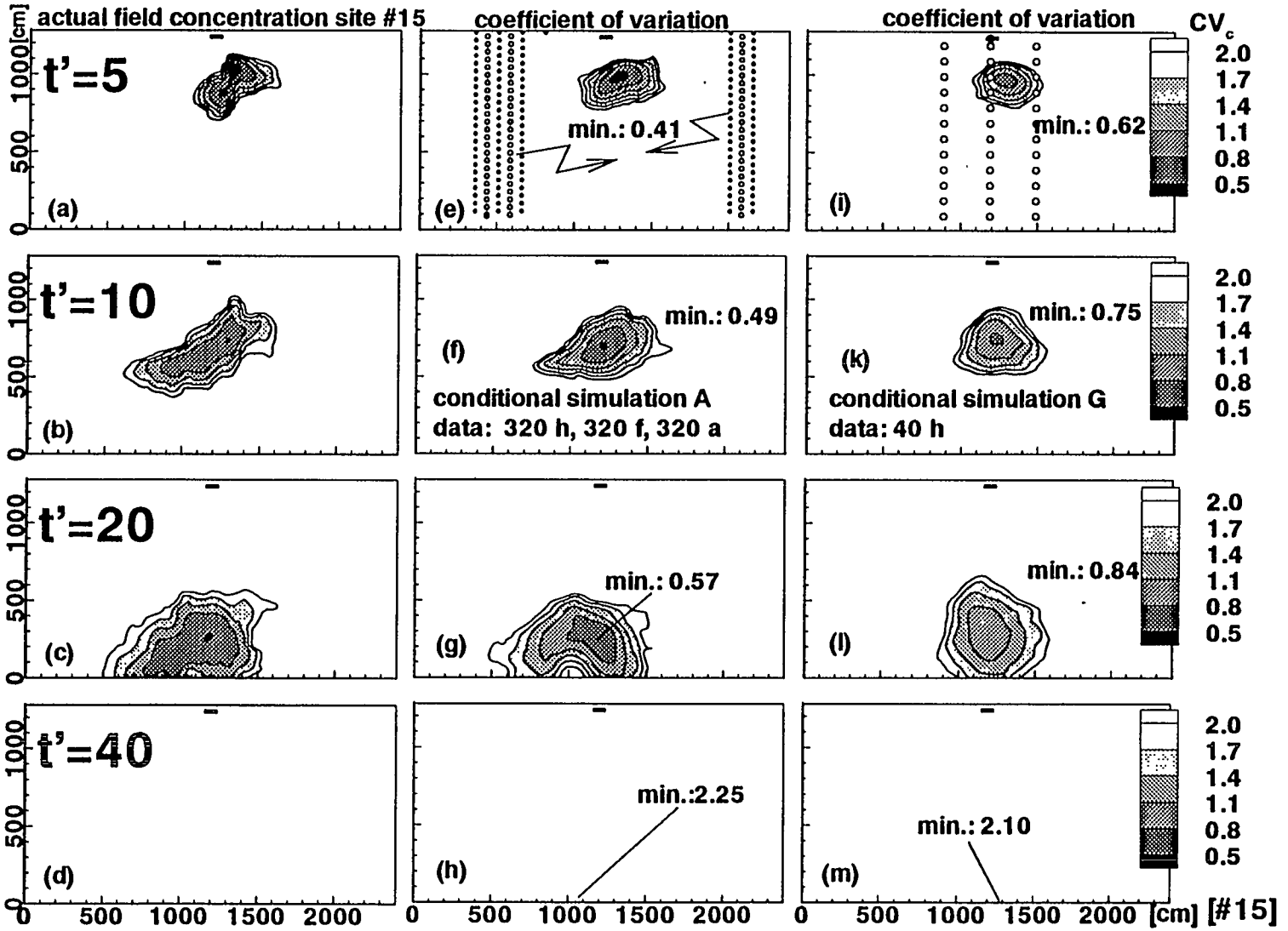

Figure 10.12 (see section 10.6.1 for explanations).

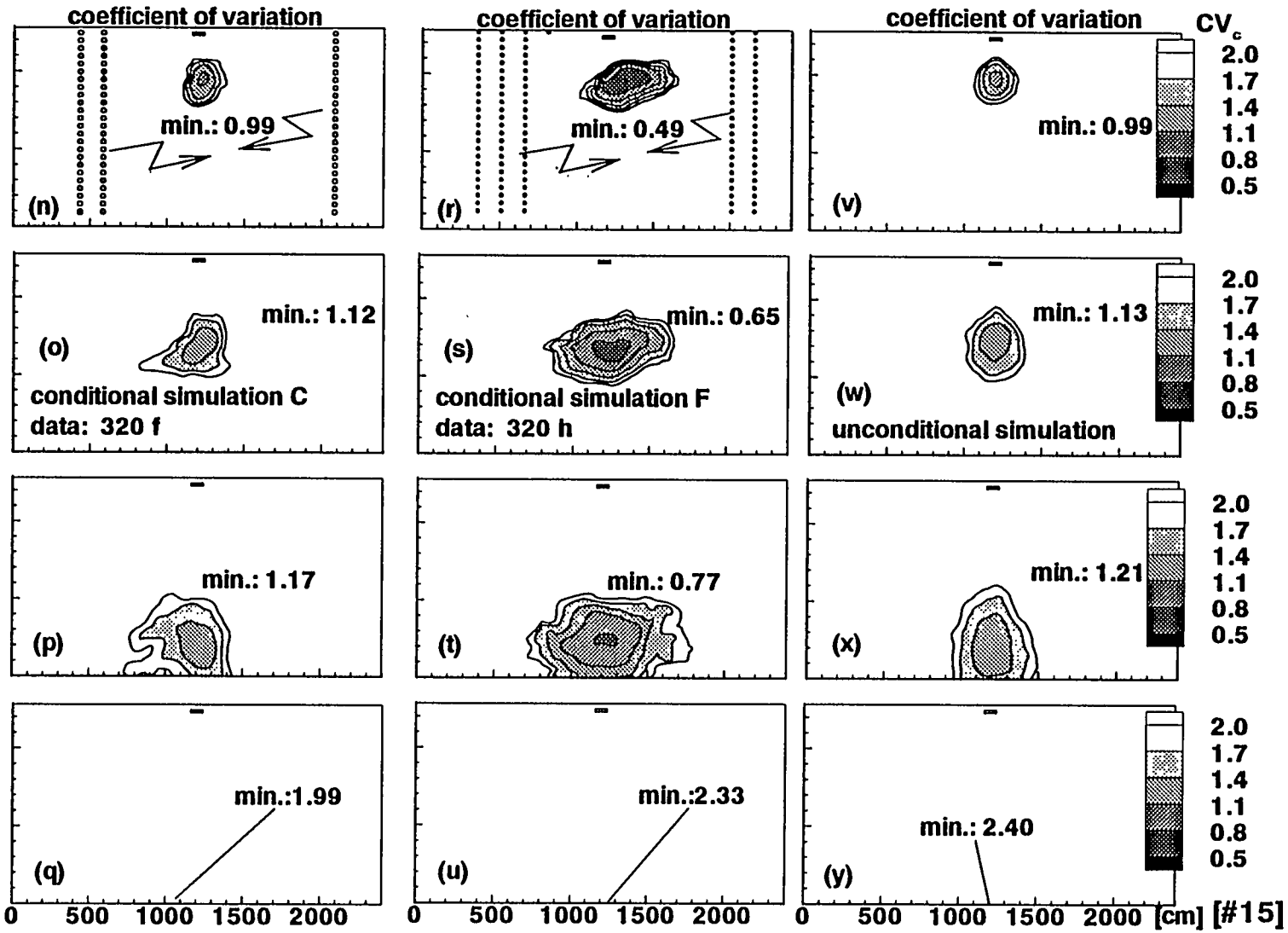

Figure 10.12 (continued, see section 10.6.1 for explanations).

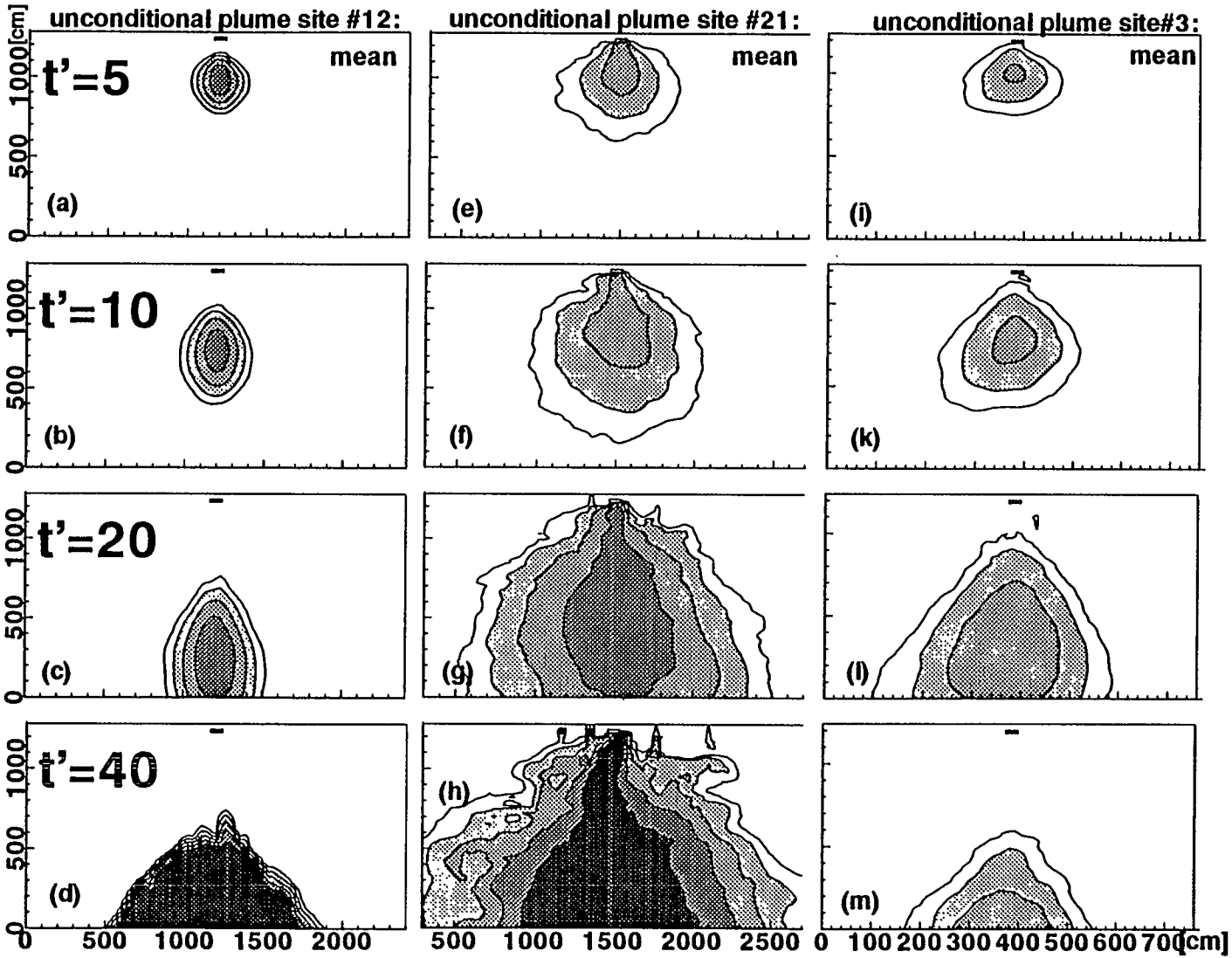

Figure 10.13 (see section 10.6.1 for explanations).

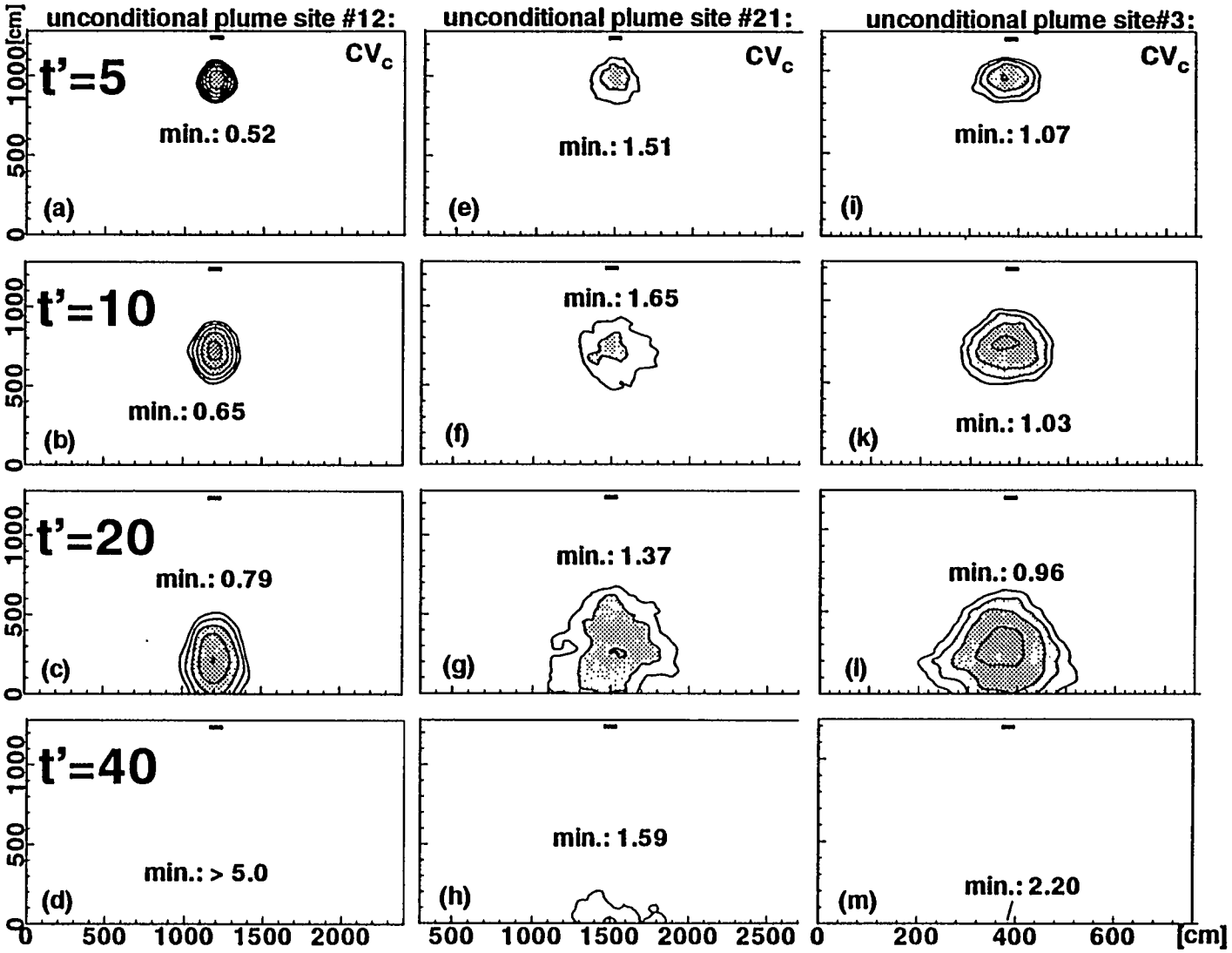

Figure 10.14 (see section 10.6.1 for explanations).

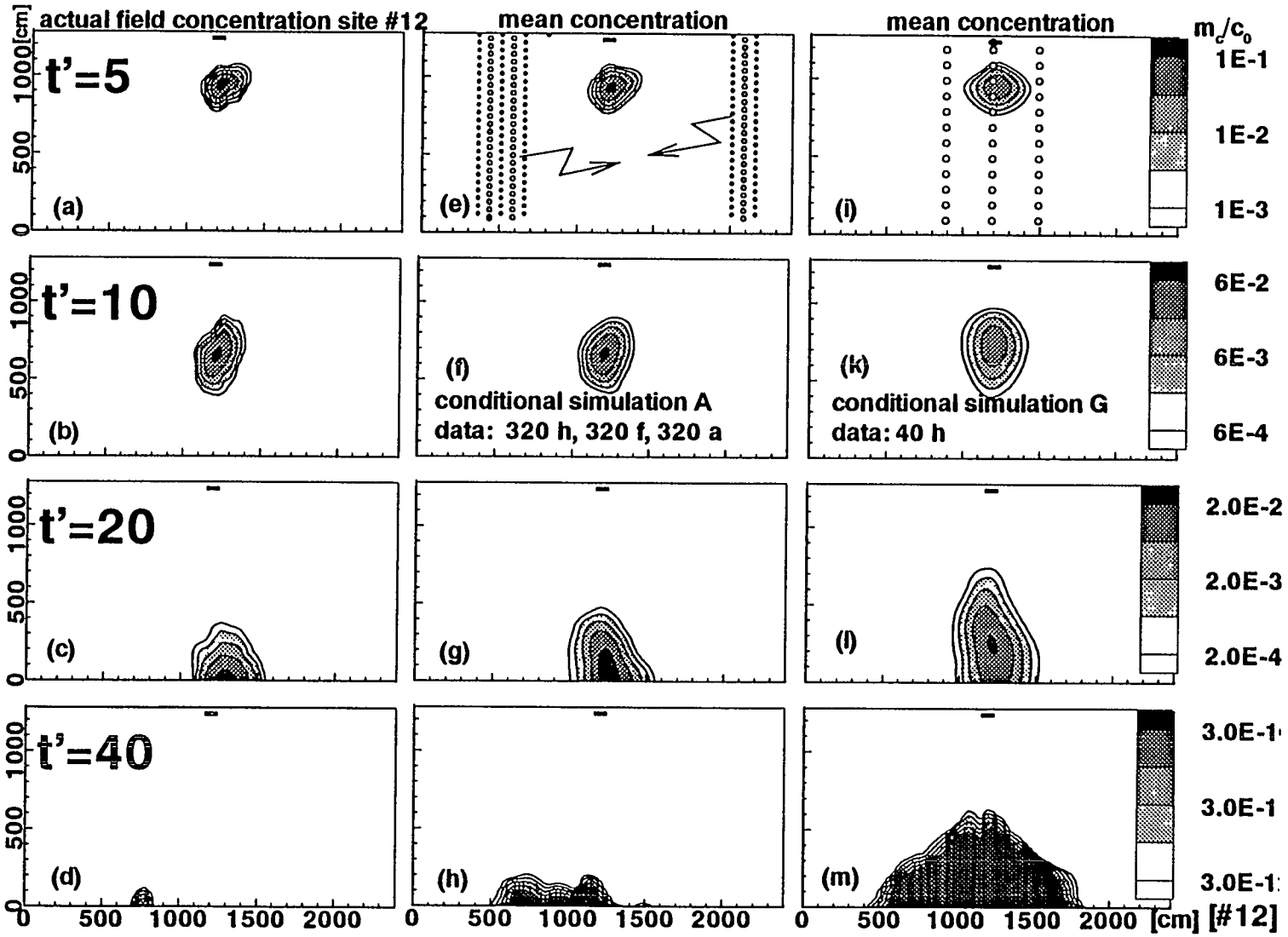

Figure 10.15 (see section 10.6.1 for explanations).

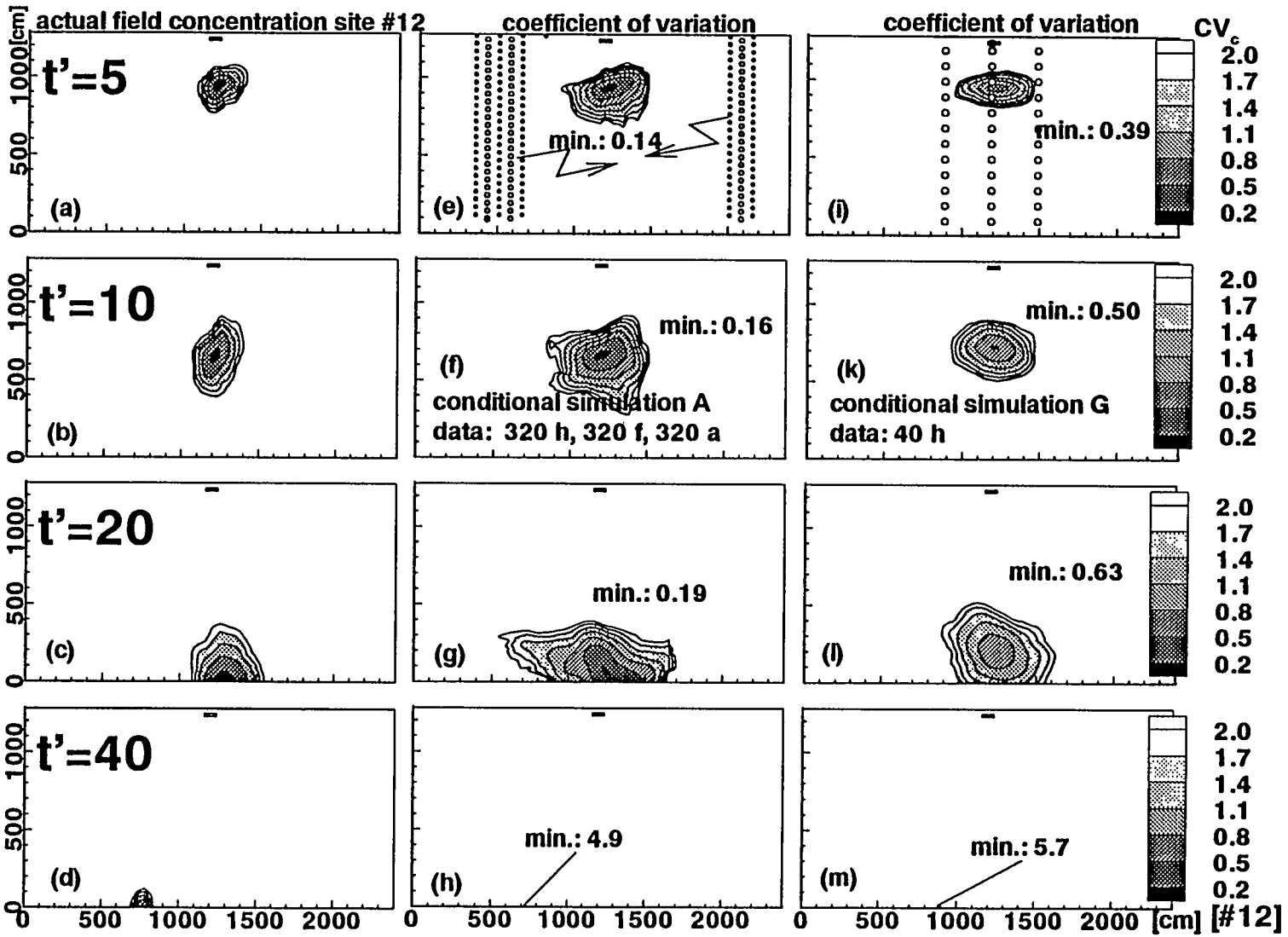

Figure 10.16 (see section 10.6.1 for explanations).

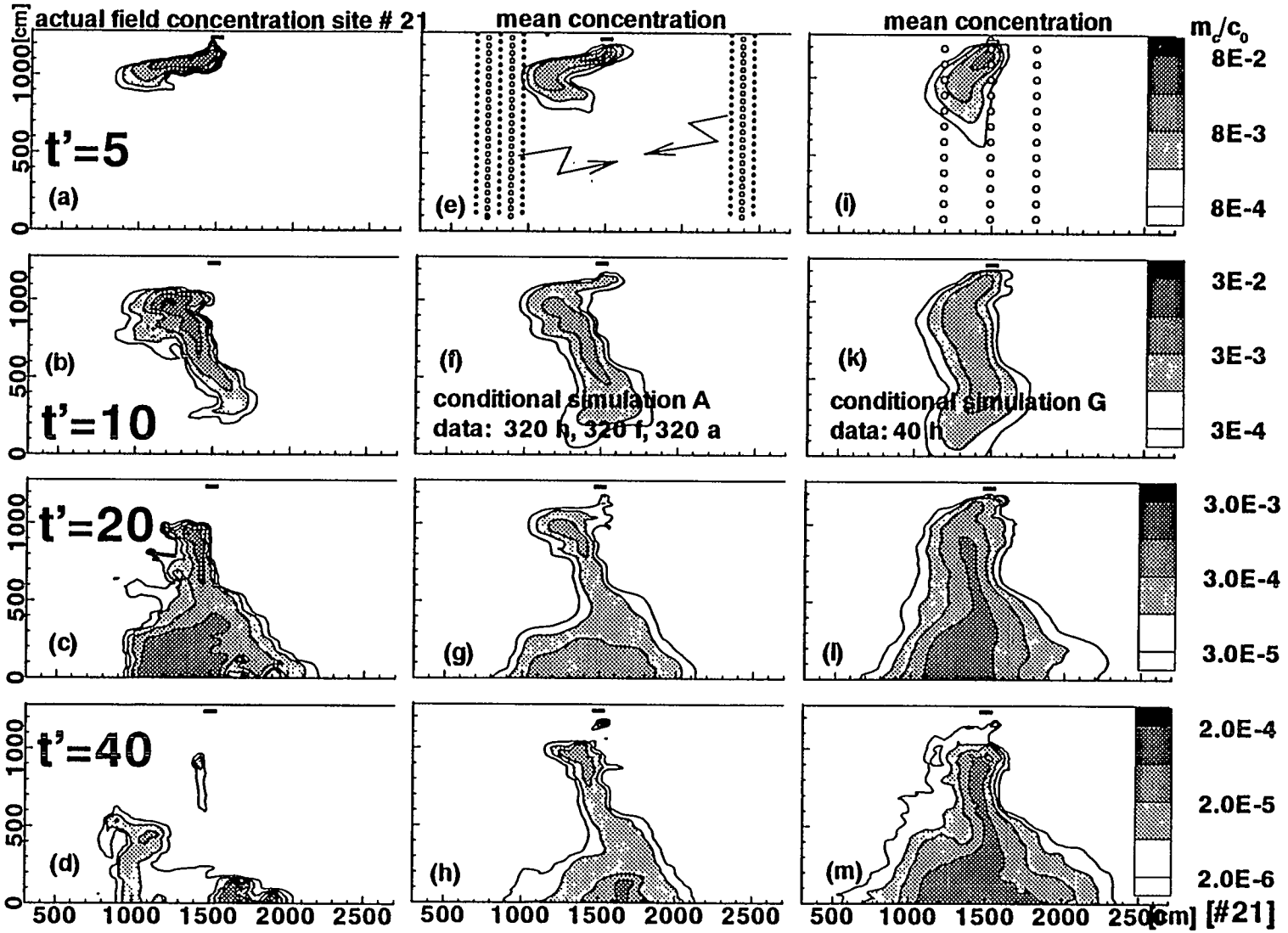

Figure 10.17 (see section 10.6.1 for explanations).

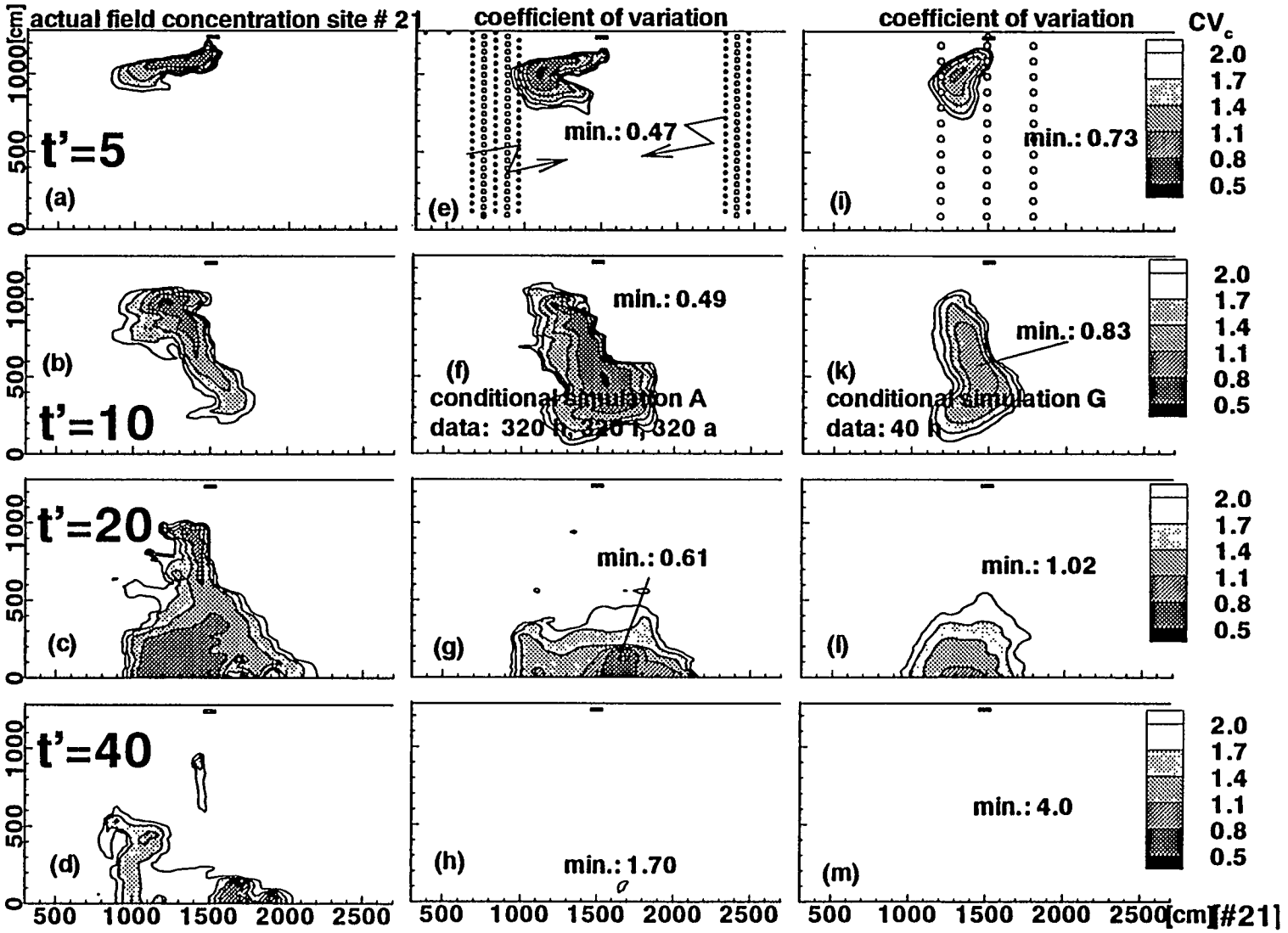

Figure 10.18 (see section 10.6.1 for explanations).

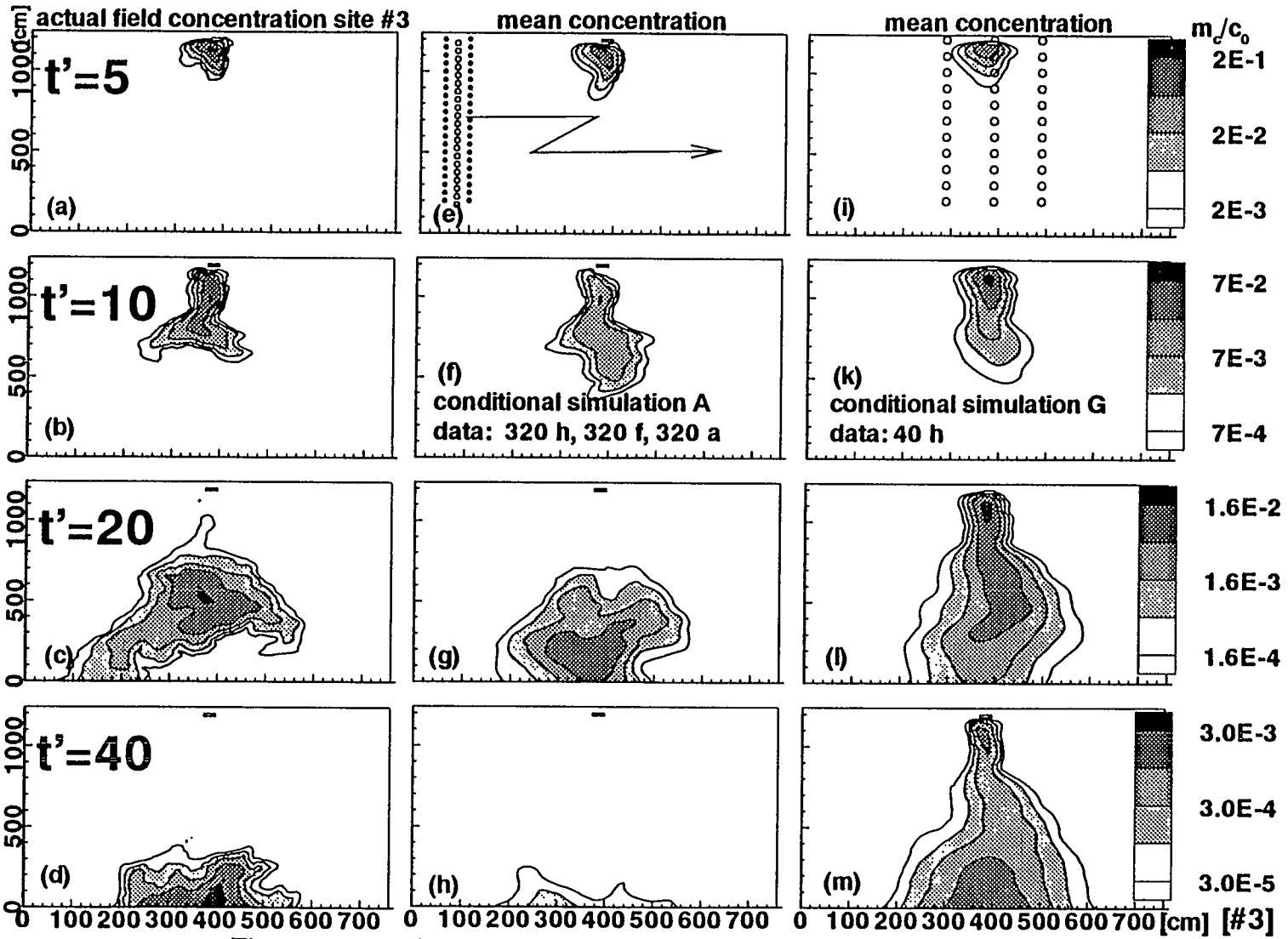

Figure 10.19 (see section 10.6.1 for explanations).

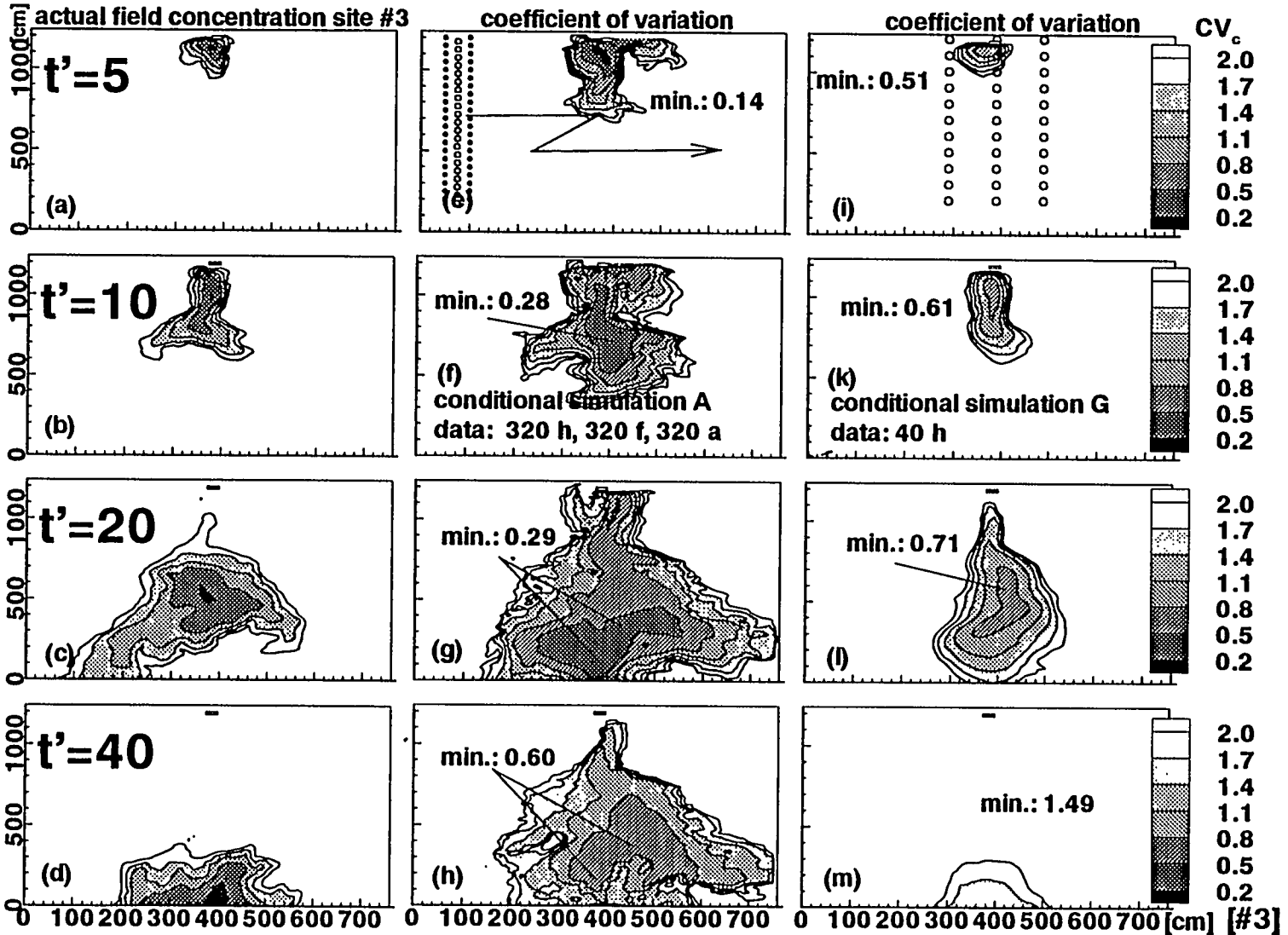

Figure 10.20 (see section 10.6.1 for explanations).

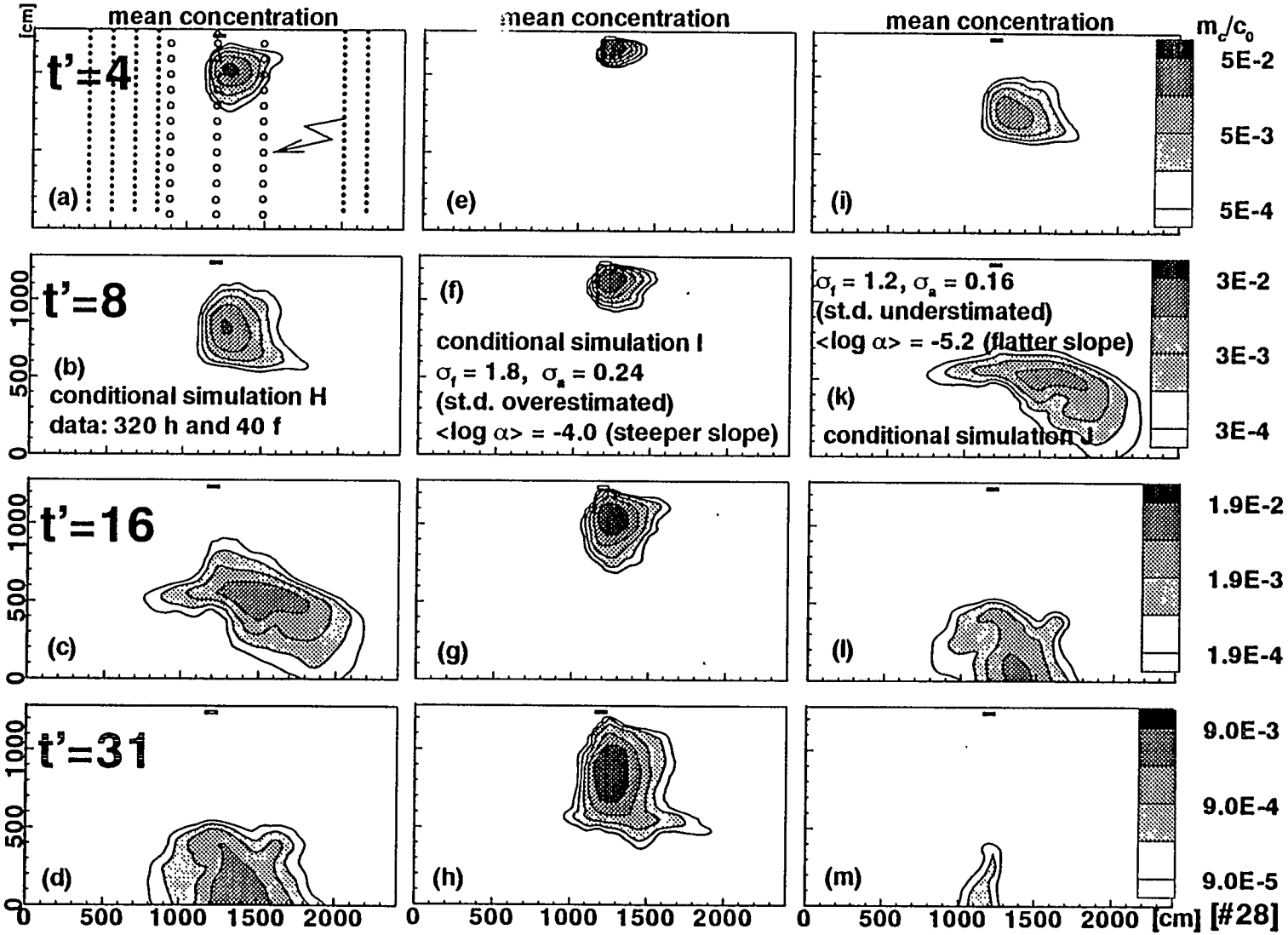

Figure 10.21 (see section 10.6.1 for explanations).

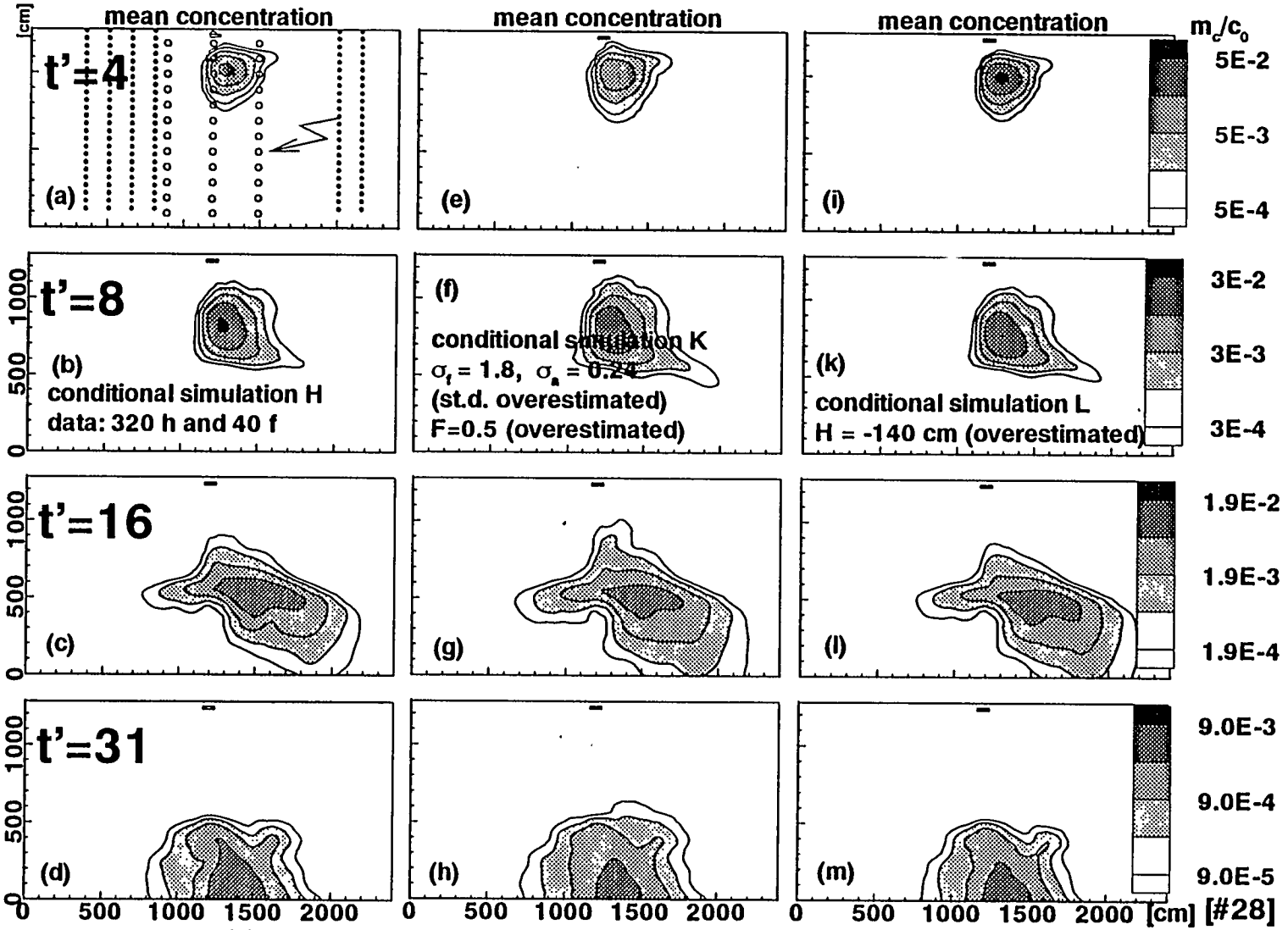

Figure 10.22 (see section 10.6.1 for explanations).

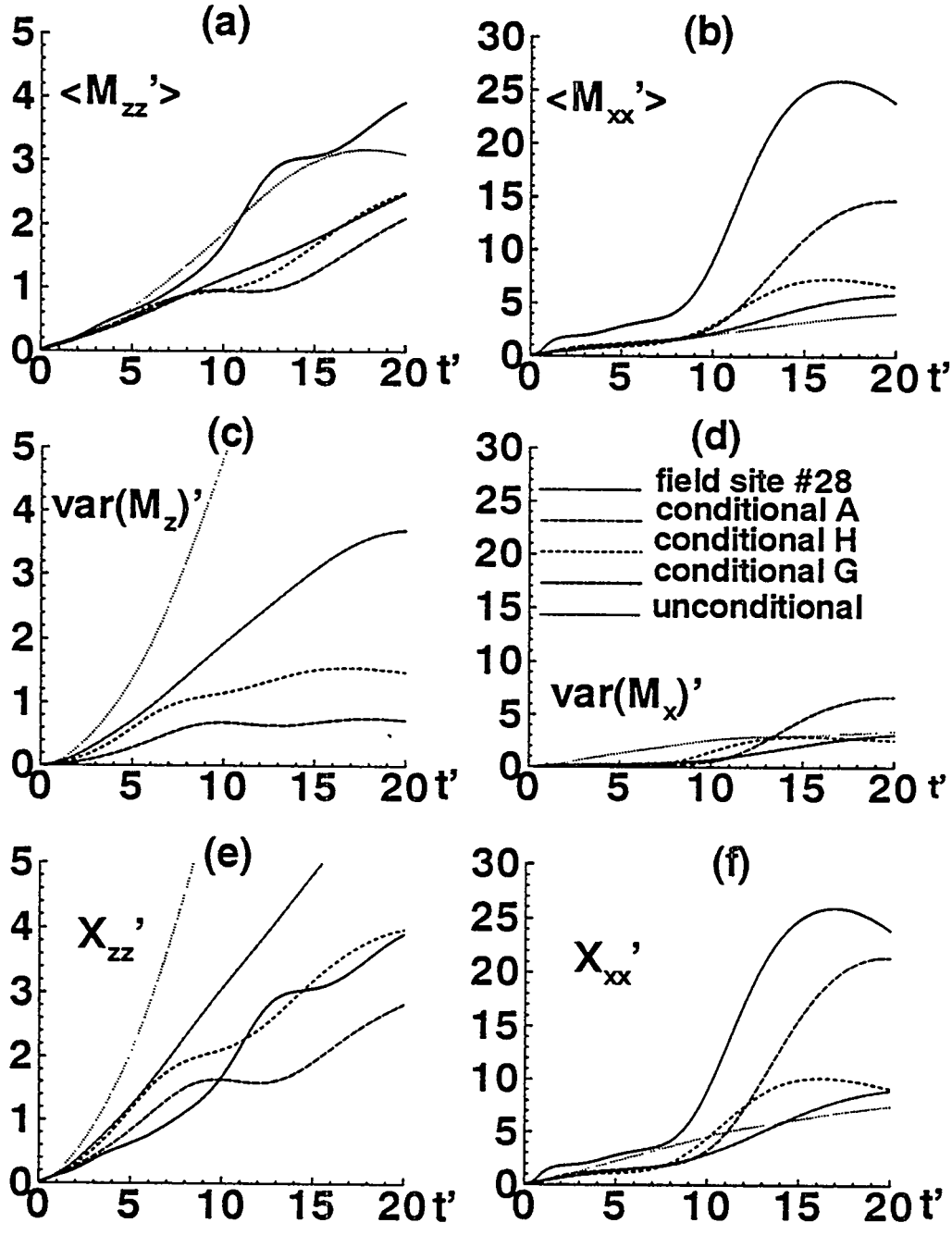

Figure 10.23: Average moment of inertia of individual plumes (a,b), variance of the plume center of mass (c,d), and moment of inertia of the mean plume (e,f) in the vertical (left column) and horizontal dimension (right column). All moments are normalized (') by ($\lambda_{fz}\,\sigma_f^2$).

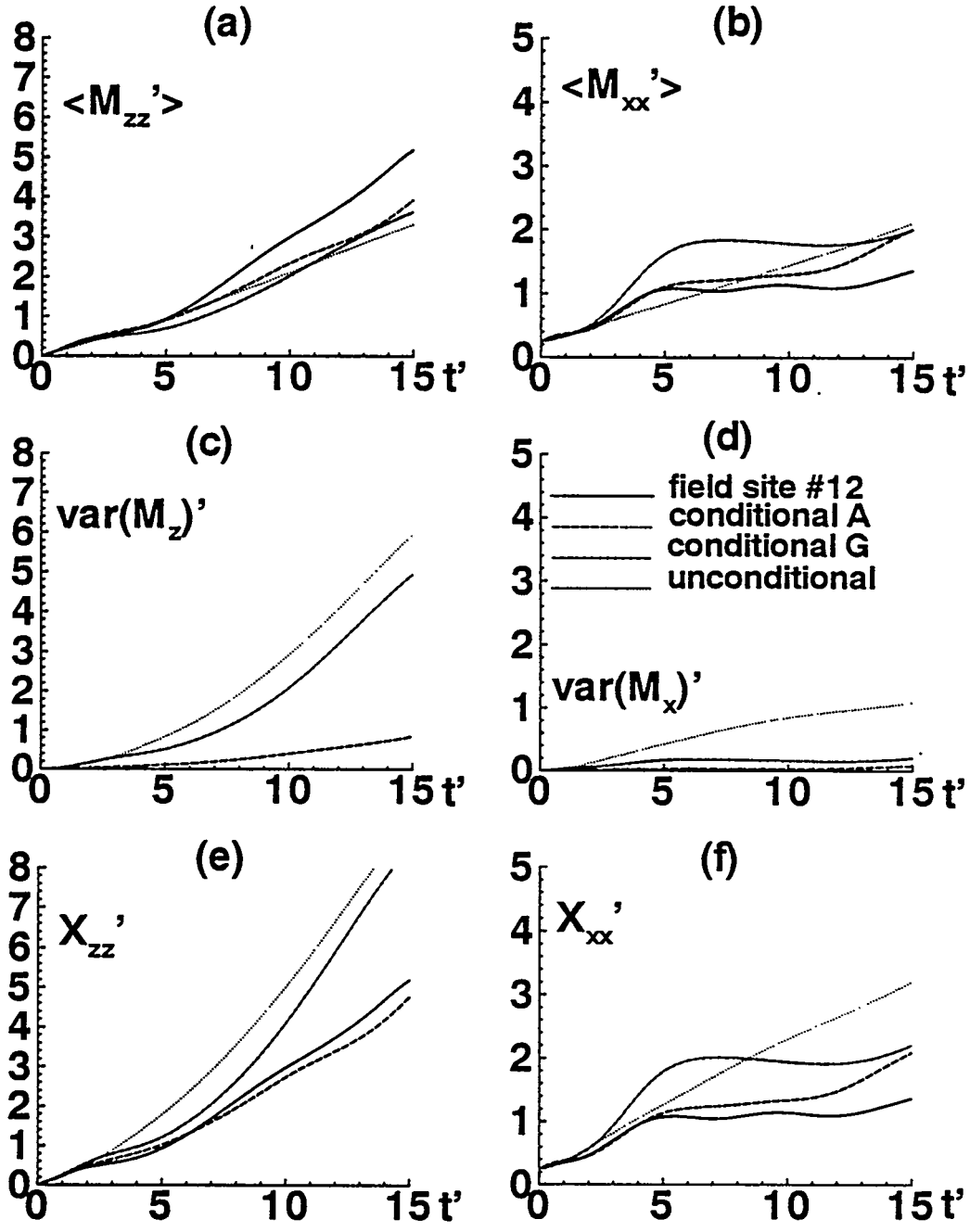

Figure 10.24: Average moment of inertia of individual plumes (a,b), variance of the plume center of mass (c,d), and moment of inertia of the mean plume (e,f) in the vertical (left column) and horizontal dimension (right column). All moments are normalized (') by ($\lambda_{fz}\,\sigma_f^2$).

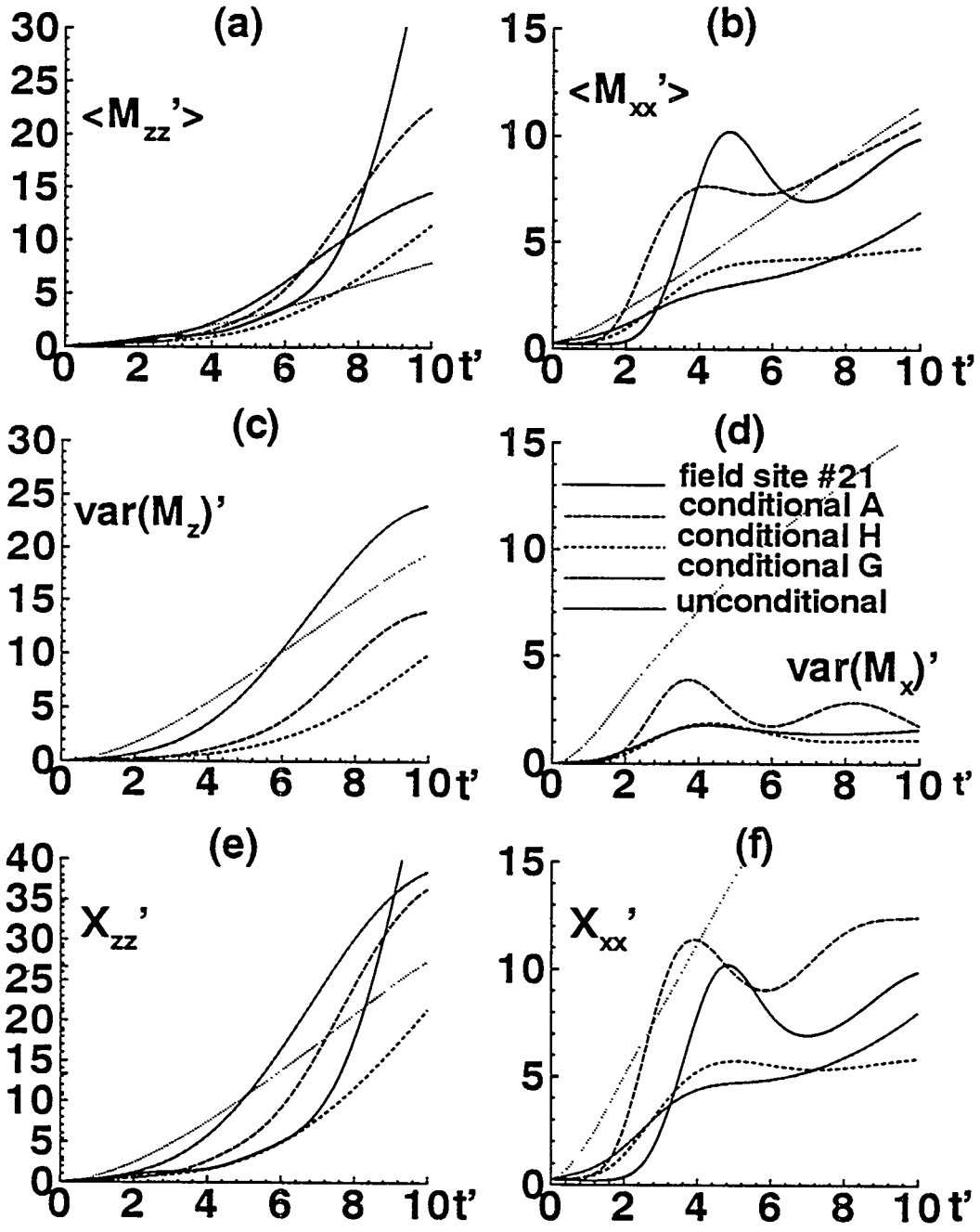

Figure 10.25: Average moment of inertia of individual plumes (a,b), variance of the plume center of mass (c,d), and moment of inertia of the mean plume (e,f) in the vertical (left column) and horizontal dimension (right column). All moments are normalized (') by ($\lambda_{fz}\ \sigma_f^2$).

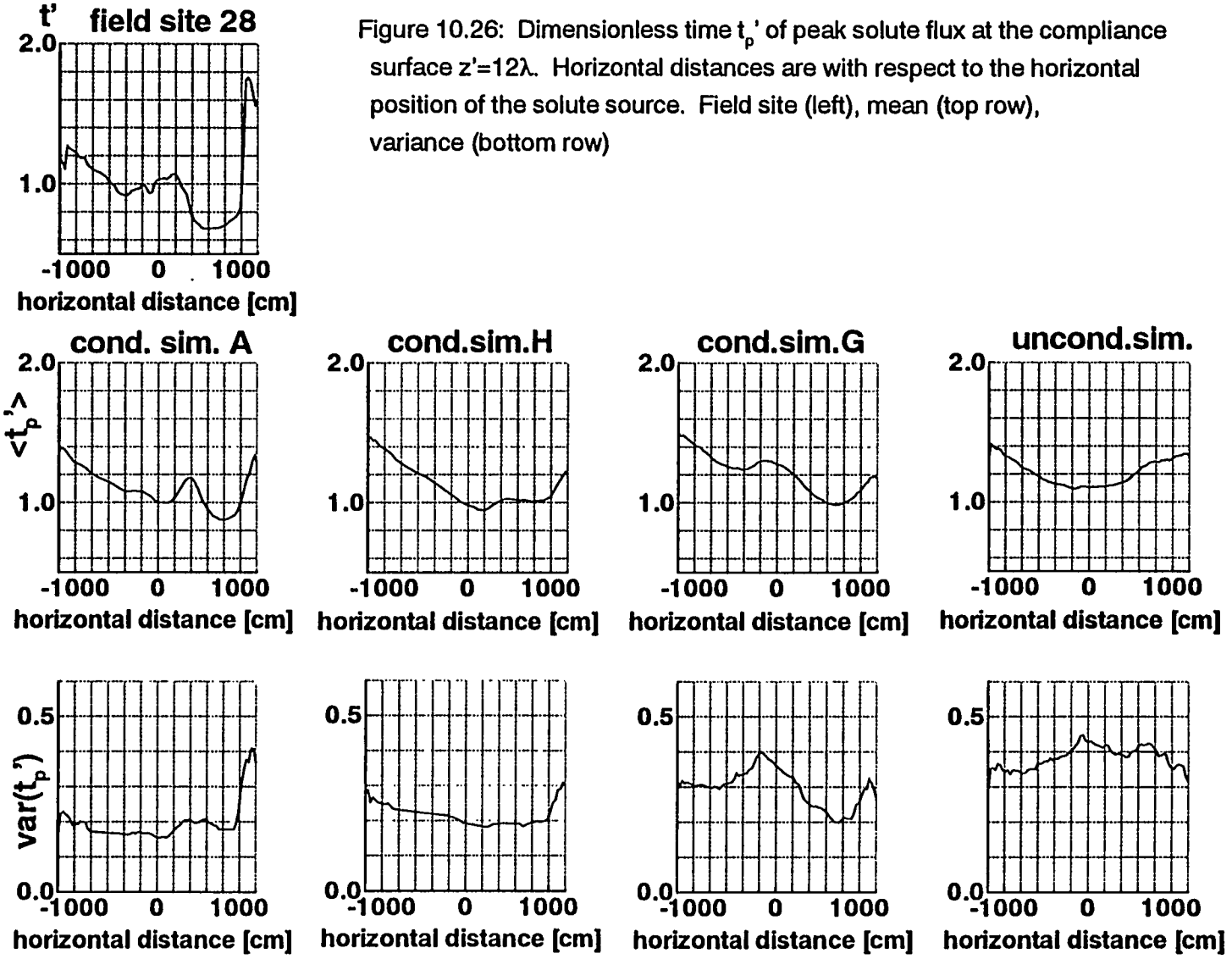

Figure 10.26: Dimensionless time t_p' of peak solute flux at the compliance surface $z'=12\lambda$. Horizontal distances are with respect to the horizontal position of the solute source. Field site (left), mean (top row), variance (bottom row)

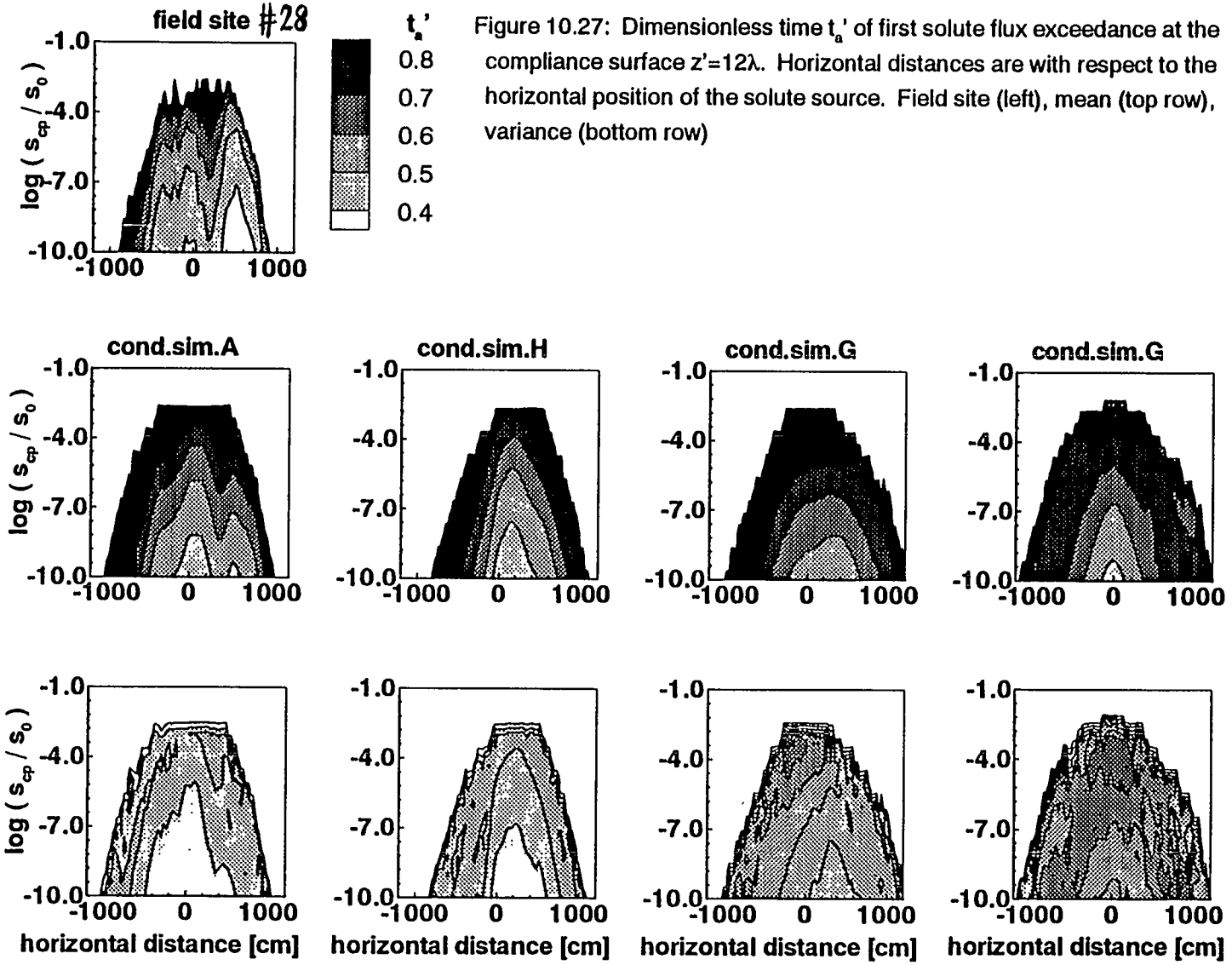

Figure 10.27: Dimensionless time t_a' of first solute flux exceedance at the compliance surface $z'=12\lambda$. Horizontal distances are with respect to the horizontal position of the solute source. Field site (left), mean (top row), variance (bottom row)

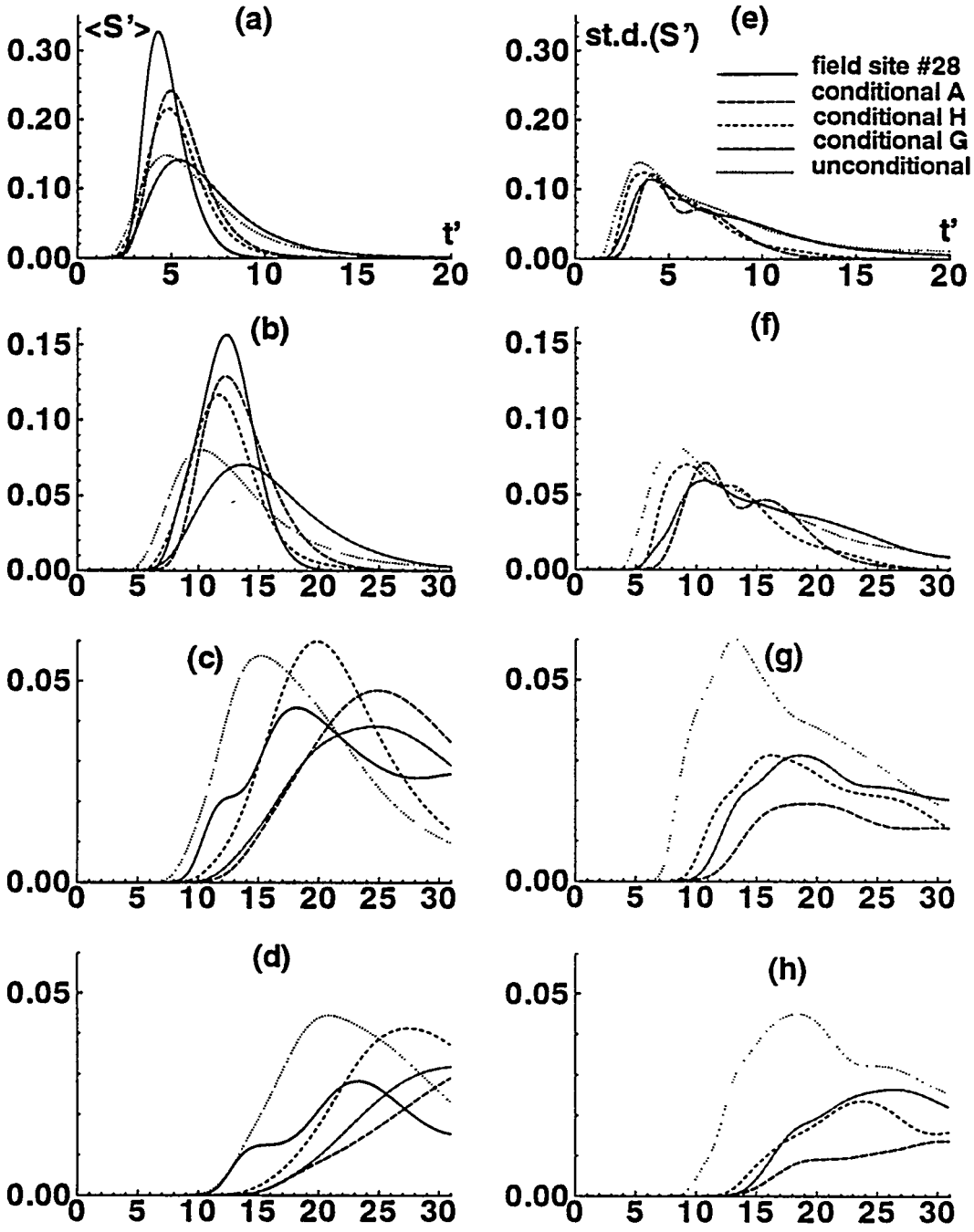

Figure 10.28: Normalized mean breakthrough curve <S'(t')>, and standard dev. of the breakthrough curve st.d.(S') at different depth: $5.4\lambda_{fz}$ (top row), $11.6\lambda_{fz}$ (second row), $17.8\lambda_{fz}$ (third row), and $23.8\lambda_{fz}$ (bottom row). The breakthrough curve for the field site is only plotted in the left column.

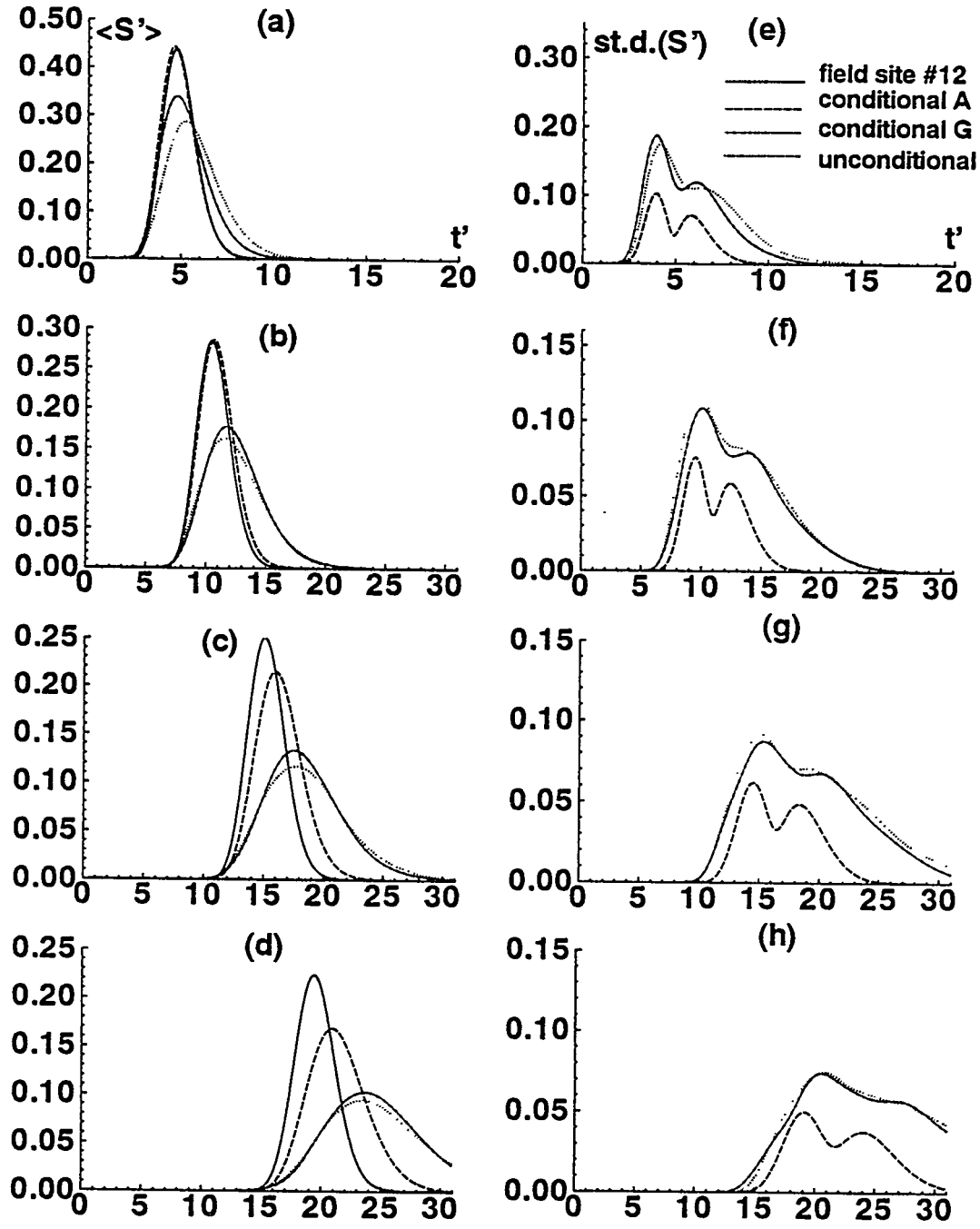

Figure 10.29: Normalized mean breakthrough curve <S'(t')>, and standard dev. of the breakthrough curve st.d.(S') at different depth: $5.4\lambda_{Iz}$ (top row), $11.6\lambda_{Iz}$ (second row), $17.8\lambda_{Iz}$ (third row), and $23.8\lambda_{Iz}$ (bottom row). The breakthrough curve for the field site is only plotted in the left column.

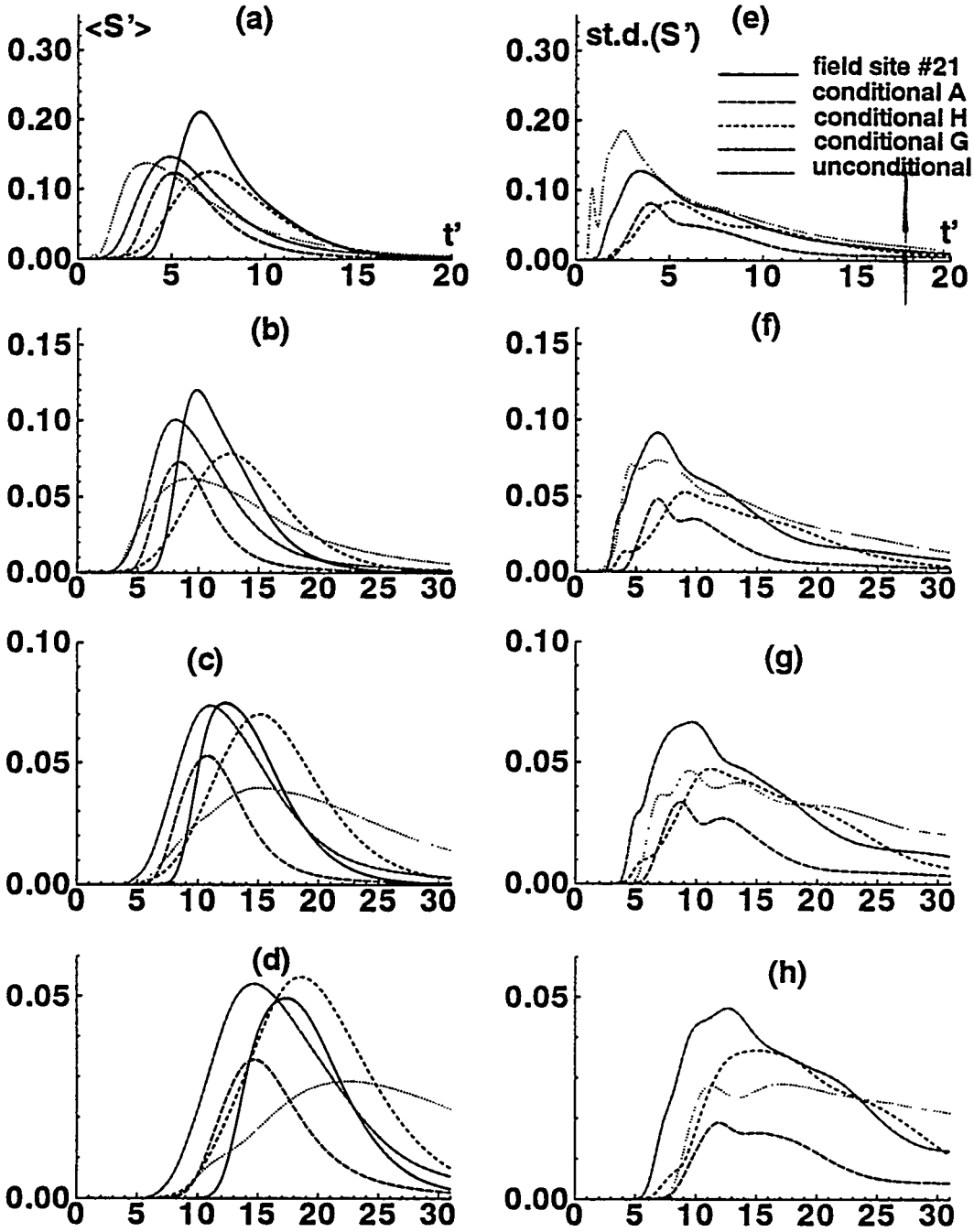

Figure 10.30: Normalized mean breakthrough curve <S'(t')>, and standard dev. of the breakthrough curve st.d.(S') at different depth: $5.4\lambda_{fz}$ (top row), $11.6\lambda_{fz}$ (second row), $17.8\lambda_{fz}$ (third row), and $23.8\lambda_{fz}$ (bottom row). The breakthrough curve for the field site is only plotted in the left column.

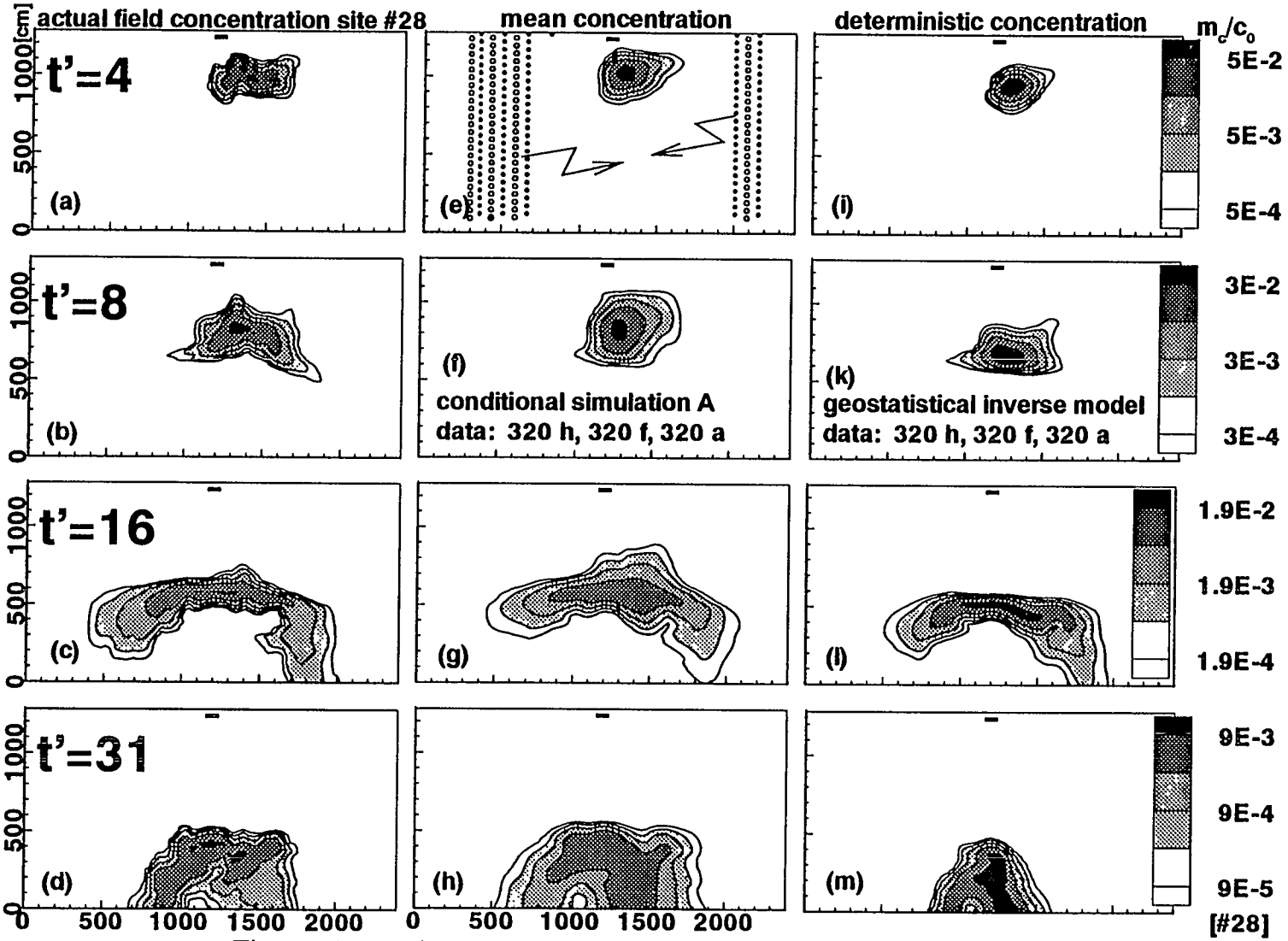

Figure 10.31 (see section 10.6.1 for explanations).

11. REFERENCES

Ababou, R., Three-dimensional flow in random porous media, Ph.D. thesis, Dep. of Civ. Eng., Mass.Inst. of Technol., Cambridge, Mass., 1988.

Ababou, R., Stochastic analysis of unsaturated flow and transport, in "Report on research activities for the quarter April 1 through June 30, 1991", Edited by Wesley C. Patrick, Center for Nuclear Waste Regulatory Analyses, San Antonio, Texas, August, 1991.

Ahuja, L.R., J.W. Naney, D.R. Nielsen, Scaling soil water properties and infiltration, *Soil Science Soc. Am. J., 48*, 970-973, 1984.

Alabert, F., The practice of fast conditional simulations through the LU decomposition of the covariance matrix, *Mathematical Geology, 19*, 369-386, 1987.

Amoozegar-Fard, A., D.R. Nielsen, A.W. Warrick, Soil solute concentration distribution for spatially varying pore water velocities and apparent diffusion coefficients, *Soil Sci. Soc. Amer. J., 46*, 3-9, 1982.

Anderson, M.P., Comment on "Universal scaling of hydraulic conductivities and dispersivities in geologic media", *Water Resour. Res., 27*, 1381-1382, 1991.

Anderson, M.P., W. W. Woessner, *Applied groundwater modeling: simulation of flow and advective transport*, Academic Press, San Diego, 1992.

Anderson, S. H., D. K. Cassel, Statistical and autoregressiv analysis of soil physical properties of Portsmouth sandy loam, *Soil Sci. Soc. of Am. J., 49*, 1096-1104, 1986.

Armstrong, M., G. Matheron, Disjunctive kriging revisited: part I, *Mathematical Geology, 18*, 711-728, 1986.

Bakr, A. A., L. W. Gelhar, A. L. Gutjahr, and J. R. McMillan, Stochastic analysis of the effect of spatial variability in subsurface flows, 1: Comparison of one- and three-dimensional flows, *Water Resour. Res., 14*, 263-271, 1978.

Bear, J., *Dynamics of fluids in porous media*, Elsevier, New York, 1972.

Bellin, A., P. Salandin, A. Rinaldo, Simulation of dispersion in heterogeneous porous formations: statistics, first-order theories, convergence of computations, *Water Resour. Res., 28*, 221-2227, 1992.

Binsariti, A. A., Statistical analysis and stochastic modeling of the Cortaro aquifer in Southern Arizona, Ph.D. disseration, Dep. of Hydrology and Water Resources, University of Arizona, Tucson, Arizona , 1980.

Bras, R. L., I. Rodríguez-Iturbe, *Random functions and hydrology*, Addison-Wesley, Reading, Massachussetts, 1985.

Bresler, E., G. Dagan, Convective and pore scale dispersive solute transport in unsaturated heterogeneous fields, *Water Resour. Res., 17*, 1683-1693, 1981.

Brigham, E. O., *The fast Fourier transform and its applications*, Englewood Cliffs, N.J., 1988.

Brooker, P.I., Two-dimensional simulation by turning bands, *Mathematical Geology, 17*, 81-90, 1985.

Burden, D.S., H.M. Selim, Correlation of spatially variable soil water retention for a subsurface soil, *Soil Science, 148*, 436-447, 1989.

Butters, G.L., W.A. Jury, Field scale transport of bromide in an unsaturated soil, 2. Dispersion modeling, *Water Resour. Res., 25*, 1583-1589, 1989.

Byers, E., D.B. Stephens, Statistical and stochastic analysis of hydraulic conductivity and particle size in a fluvial sand, *Soil Science Soc. Am. J., 47*, 1072-1080, 1983.

Cameron, D.R., Variability of soil water retention curves and predicted hydraulic conductivities on a small plot, *Soil Science, 126*, 364-371, 1978.

Carr, J.R., D.E. Myers, COSIM: A FORTRAN IV program for coconditional simulation, *Computers and Geosciences, 11*, 675-705, 1985.

Carrera, J., S.P. Neuman, Estimation of aquifer parameters under transient and steady-state conditions, 1. Maximum likelihood method incorporating prior information, *Water Resour. Res., 22*, 199-210, 1986.

Ciollaro, G., V. Comegna, Spatial variability of soil hydraulic properties of a psammetic palexeralf soil of South Italy, *Acta Horticulturae, Int. Soc. for Horticultural Science, 228*, 61-71, 1988.

Clifton, P.M., S.P. Neuman, Effects of kriging and inverse modeling on conditional simulation of the Avra Valley aquifer in southern Arizona, *Water Resour. Res., 18*, 1215-1234, 1982.

Cushey, M.A., A. Bellin, Y. Rubin, Predicting cumulative distribution functions of concentrations for non-reactive solute transport in heterogeneous porous media, *EOS, Transactions, American Geophysical Union, 74, Supplement*, p.312, October 26, 1993.

Cvetkovic, V., A.M. Shapiro, G. Dagan, A solute flux approach to transport in heterogeneous formations, 2. Uncertainty analysis, *Water Resour. Res., 28*, 1377-1388, 1992.

Dagan, G., E. Bresler, Solute dispersion in unsaturated heterogeneous soil at field scale, 1. Theory, *Soil Science Soc. Am. J., 43*, 461-467, 1979.

Dagan, G., Stochastic modeling of groundwater flow by unconditional and conditional probabilities, 1. Conditional simulation and the direct problem, *Water Resour. Res., 18*, 813-833, 1982a.

Dagan, G., Stochastic modeling of groundwater flow by unconditional and conditional probabilities, 2. The solute transport, *Water Resour. Res., 18*, 835-848, 1982b.

Dagan, G., Solute transport in heterogeneous porous formations, *J. Fluid Mechnics, 145*, 151-177, 1984.

Dagan, G., A note on higher-order corrections of the head covariances in steady aquifer flow, *Water Resour. Res., 21*, 573-578, 1985.

Dagan, G., Statistical theory of groundwater flow and transport: pore to laboratory, laboratory to formation, and formation to regional scale, *Water Resour. Res., 22*, 120S-134S, 1986.

Dagan, G., Theory of solute transport by groundwater, *Ann. Rev. Fluid Mech., 19*, 183-215, 1987.

Dagan, G., Time-dependent macrodispersion for solute transport in anisotropic heterogeneous aquifers, *Water Resour. Res., 24*, 1491-1500, 1988.

Dagan, G., Transport in heterogeneous porous formations: spatial moments, ergodicity, and effective dispersion, *Water Resour. Res., 26*, 1281-1290, 1990.

Dagan, G., V. Cvetkovic, A.M. Shapiro, A solute flux approach to transport in heterogeneous formations, 1. The general framework, *Water Resour. Res., 28*, 1369-1376, 1992.

Davis, M.W., Production of conditional simulations via the LU decomposition of the covariance matrix, *Mathematical Geology, 19*, 91-98, 1987.

Delhomme, J.P., Spatial variability and uncertainty in groundwater flow parameters: a geostatistical approach, *Water Resour. Res., 15*, 269-280, 1979.

Desbarats, A.J., Spatial averaging of hydraulic conductivity in three-dimensional heterogeneous porous media, *Math. Geol., 24*, 249-267, 1992.

Destouni, G., V. Cvetkovic, The effect of heterogeneity on large scale solute transport in the unsaturated zone, *Nordic Hydrol., 20*, 43-52, 1989.

Destouni, G., V. Cvetkovic, Field-scale mass arrival of sorptive solute into the groundwater, *Water Resour. Res., 27*, 1315-1325, 1991.

Destouni, G., Prediction uncertainty in solute flux through heterogeneous soil, *Water Resour. Res., 28*, 793-801, 1992.

Ellsworth, T.R., W.A. Jury, F.F. Ernst, P.J. Shouse, A three-dimensional field study of solute transport through unsaturated, layered porous media, 1. Methodology, mass recovery, and mean transport, *Water Resour. Res., 27*, 951-965, 1991.

Field J. A., J. C. Parker, N. C. Powell, Comparison of field- and lab-measured and predicted hydraulic properties of a soil with macropores, Soil Sci. 138, 385-396, 1984.

Fischer, H.B., E.J. List, R.C.Y. Koh, J. Imberger, N.H. Brooks, *Mixing in inland and coastal waters*, 483 pp., Academic Press, San Diego, 1979.

Fletcher, C. A. J., Computational techniques for fluid dynamics, Volume 1, Springer-Verlag, 1988.

Freeze, R.A., A stochastic-conceptual analysis of one-dimensional groundwater flow in non-uniform, homogeneous media, *Water Resour. Res., 11*, 725-741, 1975.

Gardner, W. R., Some steady state solutions of unsaturated moisture flow equations with applications to evaporation from a water table, *Soil Sci., 85*, 228-232, 1958.

Gelhar, L.W., P.Y. Ko, H.H. Kwai, J.L. Wilson, Stochastic modeling of groundwater systems, *R.M. Parsons Laboratory for Water Resources and Hydrodynamics Report 189.* Cambridge, Mass,: MIT, 1974.

Gelhar, L. W., Effects of hydraulic conductivity variations on groundwater flows, in: *Proceedings, Second International IAHR Symposium on Stochatic Hydraulics, International Association of Hydraulic Research, Lund, Sweden*, 1976.

Gelhar, L. W. and C. L. Axness, Three-dimensional stochastic analysis of macrodispersion in aquifers, *Water Resour. Res., 19*, 161-180, 1983.

Gelhar, L.W., Stochastic subsurface hydrology from theory to applications, *Water Resour. Res., 22*, 135S-145S, 1986.

Glass, R.J., T.S. Steenhuis, J.-Y. Parlange, Wetting front instability as a rapid and far-reaching hydrologic process in the vadose zone, *J. of Contam. Hydrol. 3*, 207-226, 1988.

Gomez-Hernandez, J.J., R.M. Srivastava, ISIM3D: an ANSI-C three-dimensional multiple indicator conditional simulation program, *Computers and Geosciences, 16*, 395-440, 1990.

Gomez-Hernandez, J.J., A stochastic approach to the simulation of block conductivity fields conditioned upon data measured at a smaller scale, Ph.D. dissertation, Department of Applied Earth Sciences, Standford University, 351 pp., 1991.

Graham W., D. McLaughlin, Stochastic analysis of nonstationary subsurface solute transport, 1. Unconditional moments, *Water Resour. Res., 25*, 215-232, 1989a.

Graham W., D. McLaughlin, Stochastic analysis of nonstationary subsurface solute transport, 2. Conditional moments, *Water Resour. Res., 25*, 2331-2355, 1989b.

Gray, R.M., L.D. Davisson, *Random processes: a mathematical approach for engineers*, 305pp., Prentice-Hall, Englewood-Cliffs, New Jersey, 1986.

Greminger, P.J., Y.K. Sud, D.R. Nielsen, Spatial variability of field-measured soil-water characteristics, *Soil Science Soc. Am. J., 49*, 1075-1082.

Gutjahr, A.L., L.W. Gelhar, A.A. Bakr, J.R. McMillan, Stochastic analysis of spatial variability in subsurface flows. Part II: Evaluation and application, *Water Resources Research, 14*, 953-960, 1978.

Gutjahr, A.L., Fast Fourier transforms for random field generation, *Project Report for Los Alamos Grant to New Mexico Tech, Contract number 4-R58-2690R*, Department of Mathematics, New Mexico Tech, Socorro, New Mexico, 1989.

Gutjahr, A. L., Q. Bai, S. Hatch, Conditional simulation applied to contaminant flow modeling, *Technical Completion Report*, Department of Mathematics, New Mexico Institute of Mining and Technology, Socorro, New Mexico, 1992.

Gutjahr, A.L., B. Bullard, S. Hatch, L. Hughson, Joint conditional simulations and the spectral approach for flow modeling, submitted to: *Journal of Stochastic Hydrology*, 1994.

Harter, Th., Conditional simulation: a comprehensive review of some important numerical techniques, *preliminary examination report*, personal communication, 1992.

Harter, Th., T.-C. J. Yeh, A. L. Gutjahr, Conditional simulation of unsaturated flow-fields for assessing contaminant transport in heterogeneous soils, *EOS, Transactions American Geophysical Union, Supplement*, p.127, October 27, 1992.

Harter, Th., T.-C.J. Yeh, Conditional simulation of unsaturated transport in highly heterogeneous soil profiles, *EOS, Transactions, American Geophysical Union, 74, Supplement*, p.308, October 26, 1993.

Harter, Th., T.-C.J. Yeh, An efficient method for simulating steady unsaturated flow in random porous media: using an analytical perturbation solution as initial guess to a numerical model, *Water Resour. Res., 29*, 4139-4149, 1993.

Haan, C.T., *Statistical methods in hydrology*, 378 pp., Iowa State University Press, Ames, Iowa, 1977.

Hern, C.S., S.M. Melancon, *Vadose zone modelling of organic pollutants*, Lewis Publishers, Chelsea, Michigan, 1986.

Hillel D., *Fundamentals of soil physics*, 413 pp., Academic Press, New York, 1980.

Hills, R. G., P. J. Wierenga, D. B. Hudson, M. R. Kirkland, The second Las Cruces trench experiment: Experimental results and two-dimensional flow predictions, *Water Resour. Res., 27*, 2707-2718, 1991.

Hopmans, J. W., H. Schukking, P. J. J. F. Torfs, Two-dimensional steady state unsaturated water flow in heterogeneous soils with autocorrelated soil hydraulic properties, *Water Resour. Res.*, 24, 2005-2017, 1988.

Hopmans, J. W., J. N. M. Stricker, Stochastic analysis of soil water regime in a watershed, *J. of Hydrology, 105*, 57-84, 1989.

IBM, *Engineering and scientific subroutine library, guide and reference,* IBM publication, 1993.

IMSL, *International mathematical and statistical library, edition 2.1*, Houston, Texas, IMSL Ltd., 1989.

Isaaks, E.H., R.M. Srivastava, *An introduction to applied geostatistics*, 559 pp., Oxford University Press, Oxford, 1989.

Journel, A.G., Geostatistics for conditional simulations of ore bodies, *Econ. Geol., 69*, 673-687, 1974.

Journel, A.G., Ch.J. Hujibregts, *Mining Geostatistic*, 600 pp., Academic Press, San Diego, 1978.

Journel, A.G., Non-parametric estimation of spatial distributions, *Mathematical Geology, 15*, 445-468, 1983.

Journel, A.G., *Fundamentals in geostatistics in five lessons*, Stanford Center for Reservoir Forecasting, Applied Earth Sciences Department, Stanford, California, 1988.

Journel, A.G., J.J. Gomez-Hernandez, Stochastic imaging of the Wilmington clastic sequence, *64th Annual Technical Conference and Exhibition of the Society of Petroleum Engineers*, San Antonio, Texas, October 8-11, 1989, SPE 19857, p. 591-606, 1989.

Jury, W.A., G. Sposito, R.E. White, A transfer function model of solute transport through soil, 1. Fundamental concepts, *Water Resour. Res., 22*, 243-247, 1986.

Jury, W. A., W. R. Gardner, W. H. Gardner, *Soil physics*, New York (Wiley), 1991.

Kalos, M.H., P.A. Whitlock, *Monte Carlo methods, volume 1: basics*, 186pp., John Wiley, New York, 1986.

Kim, Y.C., Advanced geostatistics for highly skewed data, Department of Mining and Geological Engineering, University of Arizona, Tucson, Arizona, 1988.

Kitanidis, P.K., E.G. Vomvoris, A geostatistical approach to the inverse problem in groundwater modeling (steady state) and one-dimensional simulations, *Water Resour. Res., 19*, 677-690, 1983.

Kitanidis, P.K., The concept of the dilution index, submitted to *Water Resour. Res.*, 1994.

Knuth, D. E., Seminumerical algorithms, 2nd ed., vol. 2 of *The Art of Computer Programming*, Reading, Mass, 1981.

Lauren, J.G., R.J. Wagenet, J. Bouma, J.H.M. Wonston, Variability of saturated hydraulic conductivity in a glossaquic hapludalf with macropores, *Soil Science, 145*, 2005-2017.

Levin, O., Stochastic analysis of flow and transport in three-dimensional heterogeneous media, preliminary draft, Ph.D. disseration, University of Arizona, 1994.

Li, S.-G., D. McLaughlin, A nonstationary spectral method for solving stochastic groundwater problems: unconditional analysis, *Water Resour. Res., 27*, 1589-1605, 1991.

Maclaren, N.M., The generation of multiple independent sequences of pseudorandom numbers, *Appl. Statist., Royal Statist. Soc., 38*, 351-359, 1992.

Mantoglou, A., J.L. Wilson, The turning bands method for simulation of random fields using line generation by a spectral method, *Water Resour. Res., 18*, 1379-1394, 1982.

Mantoglou, A., L.W. Gelhar, Stochastic modeling of large-scale transient unsaturated flow systems, *Water Resour. Res., 23*, 37-46, 1987a.

Mantoglou, A., L.W. Gelhar, Capillary tension head variance, mean soil moisture content, and effective specific soil moisture capacity of transient unsaturated flow in stratified soils, *Water Resour. Res., 23*, 47-56, 1987b.

Mantoglou, A., L.W. Gelhar, Effective hydraulic conductivities of transient unsaturated flow in stratified soils, *Water Resour. Res., 23*, 57-67, 1987c.

Mantoglou, A., Digital simulation of multivariate two- and three-dimensional stochastic processes with a spectral turning bands method, *Mathematical Geology, 19*, 129-149, 1987.

Marsily, G., *Quantitative hydrogeology, groundwater hydrology for engineers*, 440pp., Academic Press, San Diego, 1986.

Matheron, G., *The theory of regionalized variables and its applications*, 211 pp., Ecole des Mines, Fontainebleau, France, 1971.

Matheron, G., The intrinsic random functions and their applications, *Advan. Appl. Probab., 5*, 438-468, 1973.

Matheron, G., Effet proportionnel et lognormalité, *Int. Rep. N-374*, Ecole des Mines, Fontainebleau, France, 1974.

McCord, J.T., D. B. Stephens, and J. L. Wilson, Hysteresis and state-dependent anisotropy in modeling unsaturated hillslope hydrologic processes, *Water Resour. Res., 27*, 1501-1518, 1991.

Mizell, S.A., A.L. Gutjahr, L.W. Gelhar, Stochastic analysis of spatial variability in two-dimensional steady groundwater flow assuming stationary and nonstationary heads, *Water Resour. Res., 18*, 1053-1067, 1982.

Moreno, L., Y.W. Tsang, C.F. Tsang, F.V. Hale, I. Neretnieks, Flow and tracer transport in a single fracture: A stochastic model and its relation to some field observations, *Water Resour. Res., 24*, 2033-2048, 1989.

Mualem, Y., A new model for predicting the hydraulic conductivity of unsaturated porous media, *Water Resour. Res., 12*, 513-522, 1976.

Mulla, D.J., Estimating spatial patterns in water content, matric suction, and hydraulic conductivity, *Soil Science Soc. Am. J., 52*, 1547-1553, 1988.

Myers, D.E., Matrix formulation of co-kriging, *J. Math. Geology, 14*, 249-257, 1982.

NAG, *Numerical algorithms group*, Mark 14, routine G05AAF, Oxford: Numerical Algorithms Group, 1974, 1992.

Naney, J.W., R.D. Williams, L.R. Ahuja, Variability of soil water properties and crop yield in a sloped watershed, *Water Resources Bulletin, AWRA, 24*, 281-288, 1988.

Neuman, S.P., Saturated-unsaturated seepage by finite elements. *ASCE J. Hydraul. Div., 99 (HY2)*, 2233-2251, 1973.

Neuman, S.P., S. Yakowitz, A statistical approach to the inverse problem of aquifer hydrology, 1. Theory, *Water Resour. Res., 15*, 845-860, 1979.

Neuman, S.P., Adaptive Eulerian-Lagrangian finite element method for advection-dispersion, *Int. J. of Numer. Meth. Eng., 20*, 321-337, 1984.

Neuman, S.P., C.L. Winter, C.M. Newman, Stochastic theory of field-scale Fickian dispersion in anisotropic porous media, *Water Resour. Res., 23*, 453-466, 1987.

Neuman, S.P., Universal scaling of hydraulic conductivities and dispersivities in geologic media, *Water Resour. Res., 26*, 1749-1758, 1990.

Neuman, S.P., Y.-K. Zhang, A quasi-linear theory of non-Fickian and Fickian subsurface dispersion, 1. Theoretical analysis with application to isotropic media, *Water Resour. Res., 26*, 887-902, 1990.

Neuman, S.P., Reply, *Water Resour. Res., 27*, 1383-1384, 1991.

Neuman, S.P., On the relationship between information content and model structure: advective travel (time) versus dispersion, *manuscript*, FIfth NRC Workshop on Flow and Transport through Unsaturated Fractured Rocks Related to High-Level Radioactive Waste Disposal, Tucson, Arizona, January 7-10, 1991.

Neuman, S.P., Eulerian-Lagrangian theory of transport in space-time nonstationary velocity fields: exact non-local formalism by conditional moments and weak approximation, *Water Resour. Res., 29*, 633-645, 1993.

Neuman, S.P., C. Loeven, Exact conditional moment expressions for transient unsaturated flow in randomly heterogeneous soils with scalable moisture retention characteristics, in: *Numerical Methods in Water Resources, Proc. CMWR'94*, edited by A. Peters, G. Wittum, B. Herrling, and U. Meissner, Kluwer, Academic Publ., 1994.

Nielsen, D.R., J.W. Biggar, K.T. Erh, Spatial variability of field measured soi-water properties, *Hilgardia, 42*, 215-260, 1973.

Orr S., Stochastic approach to steady state flow in nonuniform geologic media, Ph.D. dissertation, Department of Hydrology and Water Resources, University of Arizona, Tucson, Arizona, 1993.

Ortega, J. M., W. C. Rheinbolt, *Iterative solution of nonlinear equations in several variables*, Academic Press, New York, 1970.

Papoulis, A., *Probability, random variables, and stochastic processes, 2nd edition*, 576 pp., McGraw-Hill, New York, 1984.

Parker, J.C., M.Th. vanGenuchten, Determining transport parameters from laboratory and field tracer experiments, *Virginia Agricultural Experiment Station, Bulletin 84-3*, 96 pp., May 1984.

Peck, A., S. Gorelick, G. de Marsily, S. Foster, V. Kovalevsky, *Consequences of spatial variability in aquifer properties and data limitations for groundwater modelling practice*, 272 pp., IAHS Publication No. 175, Washington, D.C., 1988

Polmann, D.J., D. McLaughlin, S. Luis, L.W. Gelhar, R. Ababou, Stochastic modeling of large-scale flow in heterogeneous unsaturated soils, *Water Resour. Res., 27*, 1447-1458, 1991.

Press, W.H., W.T.Vetterling, S. A. Teukolsky, B.P. Flannery, *Numerical recipes in FORTRAN, 2nd edition*, Cambridge University Press, Cambridge, 1992.

Priestley, M. B., *Spectral analysis and time series*, Academic Press, San Diego, pp. 890, 1981.

Robin, M.J.L., A.L. Gutjahr, E.A. Sudicky, J.L. Wilson, Cross-correlated random field generation with the direct Fourier transform method, *Water Resour. Res., 29*, 2385-2397, 1993.

Rubin, Y., G. Dagan, Stochastic analysis of boundaries effects on head spatial variability in heterogeneous aquifers, 1. Constant head boundary, *Water Resour. Res., 24*, 1689-1697, 1988.

Rubin, Y., G. Dagan, Stochastic analysis of boundaries effects on head spatial variability in heterogeneous aquifers, 2. Impervious boundary, *Water Resour. Res., 25*, 707-712, 1989.

Rubin, Y., Stochastic modeling of macrodispersion in heterogeneous porous media, *Water Resour. Res., 26*, 133-14, 1990.

Rubin, Y., J.J. Gomez-Hernandez, A stochastic approach to the problem of upscaling of conductivity in disordered media: theory and unconditional numerical simulations, *Water Resour. Res., 26*, 691-701, 1990.

Rubin, Y., Prediction of tracer plume migration in disordered porous media by the method of conditional probabilities, *Water Resour. Res., 27*, 1291-1308, 1991a.

Rubin, Y., Transport in heterogeneous porous media: prediction and uncertainty, *Water Resour. Res., 27*, 1723-1738, 1991b.

Rubin, Y., The spatial and temporal moments of tracer concentration in disordered porous media, *Water Resour. Res., 27*, 2845-2854, 1991c.

Rubin, Y., G. Dagan, Conditional estimation of solute travel time in heterogeneous formations: impact of transmissivity measurements, *Water Resour. Res., 28*, 1033-1040, 1992.

Russo, D., E. Bresler, Soil hydraulic properties as stochastic processes, 1. an analysis of field spatial variability, *Soil Science Soc. Am. J., 45*, 682-687, 1981.

Russo, D., A geostatistical approach to solute transport in heterogeneous fields and its applications to salinity management, *Water Resour. Res., 20*, 1260-1270, 1984.

Russo, D., Determining soil hydraulic properties by parameter estimation: On the selection of a model for the hydraulic properties, Water Resour. Res., 24, 453-459, 1988.

Russo, D., Stochastic analysis of simulated vadose zone solute transport in a vertical cross section of heterogeneous soils during nonsteady water flow, Water Resour. Res. 27, 267-284, 1991.

Russo, D., G. Dagan, On solute transport in a heterogeneous porous formation under saturated and unsaturated water flows, *Water Resour. Res., 27*, 285-292, 1991.

Russo, D. E. Bresler, U. Shani,, J. C. Parker, Analyses of infiltration events in relation to determining soil hydraulic properties by inverse problem methodology, Water Resour. Res 27, 1361-1373, 1991.

Russo, D., Stochastic modeling of macrodispersion for solute transport in a heterogeneous unsaturated porous formation, *Water Resour. Res., 29*, 383-397, 1993a.

Russo, D., Stochastic modeling of solute flux in a heterogeneous partially saturated porous formation, *Water Resour. Res., 29*, 1731-1744, 1993b.

Saddiq, M.H., P.J. Wierenga, M.H. Hendricks, M.Y. Hussain, Spatial variability of soil water tension in an irrigated soil, *Soil Science, 140*, 126-132, 1985.

Schweppe, F.C., *Uncertain dynamic systems*, 563 pp., Prentice-Hall, New Jersey, 1973.

Shinozuka, M., Monte Carlo simulation of structural dynamics, *Computers and Structures, 2*, 855-875, 1972.

Shinozuka, M., G. Deodatis, Simulation of stochastic processes by spectral representation, *Appl., Mech. Rev., 44*, 191-204, 1991.

Smettem, K.R.J., Characterization of water entry into a soil with a contrasting textural class: spatial variability of infiltration parameters and influence of macroporosity, *Soil Science, 144*, 167-174, 1987.

Smith, L., R.A. Freeze, Stochastic analysis of groundwater flow in a bounded domain, 2. Two-dimensional simulations, *Water Resour. Res., 15*, 1543-1559, 1979.

Smith, L., F.W. Schwartz, Mass transport, 1. A stochastic analysis of macrodispersion, *Water Resour. Res., 16*, 303-313, 1980.

Smith, L., F.W. Schwartz, Mass transport, 2. Analysis of uncertainty in prediction *Water Resour. Res., 17*, 351-369, 1981a.

Smith, L., F.W. Schwartz, Mass transport, 3. Role of hydraulic conductivity data in prediction, *Water Resour. Res., 17*, 351-369,1981b.

Srivastava, R. and T.-C. J. Yeh, Analytical solutions for one-dimensional, transient infiltration toward the water table in homogeneous and layered soils, *Water Resour. Res., 27*, 753-762, 1991.

Tompson, A.F.B., R. Ababou, L.W. Gelhar, Implementation of the three-dimensional turning bands random field generator, *Water Resour. Res., 25*, 227-2243, 1989.

Tompson, A.F.B., L.W. Gelhar, Numerical simulation of solute transport in three-dimensional, randomly heterogeneous porous media, *Water Resour. Res., 26*, 2541-2562, 1990.

Tripathi, V. S., G.T. Yeh, A performance comparison of scalar, vector, and concurrent vector computers including supercomputers for modeling transport of reactive contaminants in groundwater, *Water Resour. Res., 29*, 1819-1823, 1993.

Ünlü K., D.R. Nielsen, J.W. Biggar, Stochastic Analysis of Unsaturated Flow: One-dimensional Monte Carlo simulations and comparisons with spectral perturbation analysis and field observations, *Water Resour. Res. 26*, 2207-2218, 1990.

Van Genuchten, M. Th., A closed-form equation for predicting the hydraulic conductivity of unsaturated soils, *Soil Sci. Soc. Am. J., 44*, 892-898, 1980.

Vieira, S.R., D.R. Nielsen, J.W. Biggar, Spatial variability of field measured infiltration rate, *Soil Science Soc. Am. J., 45*, 1040-1048, 1981.

Wagenet, R.J., T.M. Addiscott, Estimating the varibility of unsaturated soil hydraulic conductivity using simple equations, *Soil Science Soc. Am. J., 51*,42-47, 1987.

Warrick, A.W., G.J. Mullen, D.R. Nielsen, Predictions of soil water flux based upon field-measured soil-water properties, *Soil Science Soc. Am. J., 41*, 414-419, 1977.

Warrick, A. W. and T.-C. J. Yeh, One-dimensional, steady vertical flow in a layered soil profile, *Adv. Water Resour., 13*, 207-210, 1990.

White I. and M. J. Sully, On the variability and use of the hydraulic conductivity alpha parameter in stochastic treatments of unsaturated flow, *Water Resour. Res., 28*, 209-213, 1992.

Wiener, N., Generalised harmonic analysis, *Acta Math., 55*, 117-258, 1930.

Wierenga, P. J., A. F. Toorman, D. B. Hudson, J. Vinson, M. Nash, R. G. Hills, Soil physical properties at the Las Cruces trench site, *NUREG/CR-5441*, 1989.

Wierenga, P. J., R. G. Hills, D. B. Hudson, The Las Cruces trench site: Characterization, experimental results, and one-dimensional flow, *Water Resour. Res., 27*, 2695-2706, 1991.

Yeh, T.-C. J., L. W. Gelhar, A. L. Gutjahr, Stochastic analysis of unsaturated flow in heterogeneous soils, 1: Statistically isotropic media, *Water Resour. Res., 21*, 447-456, 1985a.

Yeh, T.-C. J., L. W. Gelhar, A. L. Gutjahr, Stochastic analysis of unsaturated flow in heterogeneous soils, 2: Statistically anisotropic media with variable α, *Water Resour. Res., 21*, 457-464, 1985b.

Yeh, T.-C. J., L. W. Gelhar, P. J. Wierenga, Observations of spatial variability of soil-water pressure in a field soil, *Soil Science, 142*, 7-12, 1986.

Yeh, T.-C. J., One-dimensional steady state infiltration in heterogeneous soils, *Water Resour. Res., 25*, 2149-2158, 1989.

Yeh, T.-C. J., D.J. Harvey, Effective unsaturated hydraulic conductivity of layered sands, *Water Resour. Res., 26*, 1271-1279, 1990.

Yeh, T.-C. J., R. Srivastava, A. Guzman, Th. Harter, A numerical model for two-dimensional water flow and chemical transport, *Ground Water, 32*, 2-11, 1993.

Yeh, T.-C. J., A.L. Gutjahr, M. Jin, An iterative co-conditional simulation method for solute transport in heterogeneous aquifers, *EOS, Transactions, American Geophysical Union, 74, Supplement*, p.251, October 26, 1993.

Yevjevich, V.M., *Stochastic processes in hydrology*, Water Resources Publications, Fort Collins, Colorado, 1972.

Zhang, R., A.W. Warrick, D.E. Myers, Variance as a function of sample support size, *Mathematical Geology, 22*, 107-121, 1990 .

Zhang, D., S.P. Neuman, Eulerian-Lagrangian analysis of transport conditioned on hydraulic data: 1. Analytical-numerical approach, submitted to *Water Resour. Res.*, 1994a.

Zhang, D., S.P. Neuman, Eulerian-Lagrangian analysis of transport conditioned on hydraulic data: 2. Effects of log transmissivity and hydraulic head measurements, submitted to *Water Resour. Res.*, 1994b.

Zhang, D., S.P. Neuman, Eulerian-Lagrangian analysis of transport conditioned on hydraulic data: 3. Spatial moments, travel time distribution, mass flow rate and cumulative release across a compliance surface, submitted to *Water Resour. Res.*, 1994c.

Zhang, D., S.P. Neuman, Eulerian-Lagrangian analysis of transport conditioned on hydraulic data: 4. Uncertain initial plume state and non-Gaussian velocities, submitted to *Water Resour. Res.*, 1994d.

Zhang, D., S.P. Neuman, Information-dependent prediction of solute transport in heterogeneous geologic media, in: *Numerical Methods in Water Resources, Proc. CMWR'94*, edited by A. Peters, G. Wittum, B. Herrling, and U. Meissner, Kluwer Acad. Public., 1994e.

Zimmermann, D.A., J.L. Wilson, *TUBA: A computer code for generating two-dimensional random fields via the turning bands method, A: User Guide*, Seasoft, Albuquerque, New Mexico, 1990.